Title
Out-of-equilibrium dynamics and phases of matter in Atomic, Molecular and Optical systems

Permalink
https://escholarship.org/uc/item/1v3702xn

Author
Leal Machado, Francisco

Publication Date
2022

Out-of-equilibrium dynamics and phases of matter in Atomic, Molecular and Optical
systems

by

Francisco Leal Machado

A dissertation submitted in partial satisfaction of the

requirements for the degree of

Doctor of Philosophy

in

Physics

in the

Graduate Division

of the

University of California, Berkeley

Committee in charge:

Professor Norman Yao, Chair
Professor Joel Moore
Professor Umesh Vazirani

Spring 2022

Out-of-equilibrium dynamics and phases of matter in Atomic, Molecular and Optical
systems

Abstract

Out-of-equilibrium dynamics and phases of matter in Atomic, Molecular and Optical systems

by

Francisco Leal Machado

Doctor of Philosophy in Physics

University of California, Berkeley

Professor Norman Yao, Chair

The past few decades have witnessed an explosive development of atomic, molecular and optical (AMO) platforms. Previously restricted to a single qubit, quantum coherent manipulation is now available across large arrays of quantum particles. This unprecedented control over many-body quantum matter has enabled the direct study of isolated quantum dynamics away from equilibrium, and has opened an entirely new landscape for exploring different physical phenomena in AMO systems. In this thesis, I explore this landscape by focusing on three different classes of dynamics: many-body localization, prethermalization, and hydrodynamics. Using a combination of analytical and numerical tools, I will discuss the stability of different out-of-equilibrium phases of matter, as well as different universal dynamical phenomena. Examples include, time crystalline order in both many-body localized and periodically driven prethermal systems, prethermal phases of matter in long-range interacting systems systems, and diffusive and superdiffusive dynamics in isolated quantum systems. At the same time, I will also discuss the experimental realization of different dynamical phenomena in AMO platforms.

To my family and friends,
for joining me in this long ride

Contents

II Phases of matter in non-equilibrating systems   57

III Prethermalization and out-of-equilibrium phases of matter   97

List of Figures

List of Tables

Acknowledgments

And what a wild ride it has been. The past 6 years have been a professional and personal roller coaster, the extent of which I could have never imagined. I am still trying to fully grasp how life's twists and turns transformed scrappy 21-year-old me into the person that is now writing this dissertation. More than any other period of my life, graduate school made me realize how much we change, sometimes by our own will, sometimes by whatever life throws our way; often by a combination of two. I can't help but feel excited (and a fair amount nervous) to think what the next five, ten and twenty years will bring.

At its core, this journey has only been this rich and full (of successes, laughs and many other moments) because of the people I had the pleasure and good fortune to surround myself with. Although this is not an extensive list, I would like to take a moment to acknowledge some key figures and take a moment to thank them.

First and foremost, I would like to thank my advisor Prof. Norman Yao. Not out of need to thank my advisor first, but because very few (if any) single person has impacted my time in Berkeley as much as Norm. Thank you for constantly reminding me of the joy of exploring, the thrill of the hunt and the importance of being open to all the physics (and science) around me; you have made me a better scientist but also a more interested and engaged person with the world and with ideas. At the same time, you have been my biggest champion; whether in giving me opportunities I did not even know were possible, or placing your trust in me [and thus helping a little bit in the battle against that impostor syndrome lurking the back of one's mind]. In you, I see not only a mentor, but also a friend and a worthy Magic opponent.

Second, I would like to thank the Yao group for fostering an environment where science was fun and where the success of each individual success was the success of us all. To Bingtian Ye, thank you for being an amazing and patient collaborator, who endured my nit picky comments and sometimes ludicrous ideas. It was a pleasure to collaborate with you. To Greg Kahanamoku-Meyer, for always bringing a smile to a conversation and a cool fact about supercomputers or CS. To the theorists [Tommy Schuster, Bryce Kobrin, Kamphol (Best) Akkaravarawong, Maxwell Block, Marcus Bintz, Sabrina Chern and Helia Kamal], thank you for helping me explore my own projects as well as a vast banquet of other amazing physics. To the experimentalists [Thomas Mittiga, Prabudhya (Pra) Bhattacharyya, Yuanqi Lyu, Satcher Hsieh, Weijie Wu], thank you for embracing me and my (sometimes wild) ideas. To the (former and current) postdocs in our group [Prof. Chong Zu, Emily Davis, Jack Kemp, Prof. Shubhayu Chatterjee, Prof. Soonwon Choi, Prof. Quntao Zhuang, Prof. Snir Gazit], thank you for treating me as an colleague rather than an underling—feeling that my contributions were measured against their intrinsic worth and not their origin allowed me to be more confident and bold as a scientist and learn how to stick to my guns! And thank you Rahul Sahay for giving me the chance to mentor you. Seeing you develop as a scientist and as a person (and feeling I had at least a small part in that) has been one of my most satisfying "projects" during graduate school.

tant: Shannon Haley, Venkatesh Chandrasekar, and Vickie Ye. Thank you all for being an anchor on which I was able to build a sense of self untethered from work and its rat race.

Thank you to Pratik Rath and Nikola Maksimovic teaching me modesty and humbleness, and for humoring me while I tried (really hard) to win a full set of squash games of a weekly basis—next time, I'm sure I'll get you! To the Physcal IM soccer team (Aashrita Mangu, Nikola Maksimovic, captain Andreas Biekert, Philipp Kempski, Max Smiley, Kayla Currier, Lorenzo Vergari, Christopher Madsen, Tomohiro Soejima, and others), thank you for letting me run around for a few hours every week, but most importantly for the comradery.

Last, but definitely not least, I would like to thank my family. First and foremost for your support. Even though I "shipped" myself to another continent 9 years ago (and decided to drift even further out to California), you continue to always be there for me, being my biggest fan and my safe harbor. Life is made of sacrifices and choices that affect not only ourselves but those around us—I know that being away was not always been easy for me nor for you. Yet, you always welcome me back with open arms as if I had just been gone for a week. It's hard to express how much that is important to me.

And on that note, so long, and thanks for all the fish!

Citations to Previously Published Work

Most of the work presented in this thesis is adapted from previously published work. In order of appearance:

Chapter 7 is adapted from:
J. Randall et al. "Observation of a Many-Body-Localized Discrete Time Crystal with a Programmable Spin-Based Quantum Simulator". In: *Science* 374.6574 (2021), pp. 1474–1478. DOI: 10.1126/science.abk0603. arXiv: 2107.00736

Chapter 8 is adapted from:
Rahul Sahay et al. "Emergent Ergodicity at the Transition between Many-Body Localized Phases". In: *Physical Review Letters* 126.10 (2021), p. 100604. DOI: 10.1103/PhysRevLett.126.100604. arXiv: 2008.08585

Chapter 9 is adapted from:
Quntao Zhuang et al. "An Absolutely Stable Open Time Crystal". In: *arXiv* (2021). arXiv: 2110.00585

Chapter 10 is adapted from:
Francisco Machado et al. "Exponentially Slow Heating in Short and Long-range Interacting Floquet Systems". In: *Physical Review Research* 1.3 (2019), p. 033202. DOI: 10.1103/PhysRevResearch.1.033202. arXiv: 1708.01620

Chapter 11 is adapted from:
Dominic V. Else et al. "An Improved Lieb-Robinson Bound for Many-Body Hamiltonians with Power-Law Interactions". In: *Physical Review A* 101.2 (2020), p. 022333. DOI: 10.1103/PhysRevA.101.022333. arXiv: 1809.06369

Chapter 12 is adapted from:
Francisco Machado et al. "Long-Range Prethermal Phases of Nonequilibrium Matter". In: *Physical Review X* 10.1 (2020), p. 011043. DOI: 10.1103/PhysRevX.10.011043. arXiv: 1908.07530

Chapter 13 is adapted from:
Antonis Kyprianidis et al. "Observation of a Prethermal Discrete Time Crystal". In: *Science* 372.6547 (2021), pp. 1192–1196. DOI: 10.1126/science.abg8102. arXiv: 2102.01695

Chapter 14 is adapted from:
Bingtian Ye, Francisco Machado, and Norman Y. Yao. "Floquet Phases of Matter via Classical Prethermalization". In: *Physical Review Letters* 127.14 (2021), p. 140603. DOI:

10.1103/PhysRevLett.127.140603. arXiv: 2104.13927

Chapter 15 is adapted from:
Bingtian Ye et al. "Emergent Hydrodynamics in Non-Equilibrium Quantum Systems". In: *Physical Review Letters* 125.3 (2020), p. 030601. DOI: 10.1103/PhysRevLett.125.030601. arXiv: 1902.01859

Chapter 16 is adapted from:
C. Zu et al. "Emergent Hydrodynamics in a Strongly Interacting Dipolar Spin Ensemble". In: *Nature* 597.7874 (7874 2021), pp. 45–50. DOI: 10.1038/s41586-021-03763-1

Chapter 17 is adapted from:
Bingtian Ye et al. "Universal Kardar-Parisi-Zhang Dynamics in Integrable Quantum Systems". In: *arXiv* (2022). arXiv: 2205.02853

Chapter 18 is adapted from:
David Wei et al. "Quantum Gas Microscopy of Kardar-Parisi-Zhang Superdiffusion". In: *arXiv* (2021). arXiv: 2107.00038

Chapter 19 is adapted from:
Emily J. Davis et al. "Probing Many-Body Noise in a Strongly Interacting Two-Dimensional Dipolar Spin System". In: *arXiv* (2021). arXiv: 2103.12742

Part I

Introduction

Chapter 1

Making sense of a constantly changing complex world

Our day-to-day experience of the physical world is one of constant change and motion; different objects interact with one another, altering their positions and velocities. Although the underlying equations of motion are well-known (e.g. Newton's second law, Schrödinger equation, etc.), their solution is daunting when going beyond a small number of degrees of freedom. More fundamentally, even with such solution in hand, it remains difficult (or perhaps impossible) to obtain any meaningful insights into the phenomena of interest: going from the detailed dynamics of each individual molecule in the atmosphere to insights into the sources and effects of climate change is, by no means, a straightforward task. To this end, we need to simpler models that cut through this complexity and give us insight into the physics at hand. One particularly useful idea has been that of *universality*—different phenomena can be grouped into different universal categories whose elements have the same (qualitative) behavior [270]. Such an approach enables us to build precise mappings between disparate physical systems, and allows us to make generic statements about a class of physical systems rather than restrict the scope of an investigation to a single particular instance.

This simple idea lies behind the success in the investigation and characterization of *equilibrium* phenonema (i.e. systems that have been brought to equilibrium due to the presence of a bath). In this context, the Landau theory (and later the renormalization group theory) gives us the theoretical framework for understanding different phases of matter in terms of the symmetries of the system (with topology being appreciated more recently) [315, 271, 574, 575, 576]. For example, universality explains why all Ising ferromagnets behave alike when becoming paramagnetic; but also why they behave exactly like a coexisting liquid/gas phase—even though the two phenomena occur in different physical settings and appear, at first glance, completely unrelated.

The success of this approach in the equilibrium setting suggests a natural follow-up question: can one extend this idea to *dynamical* phenomena of systems *away from equilibrium*? Unfortunately, the complexity of out-of-equilibrium systems makes an immediate translation unclear. One fundamental hurdle is that complex many-particle systems often rapidly

approach an equilibrium state, precluding the possibility of any long-lived dynamical phe-
nomena. For example, when you slap your hand on the table, the table makes some sound
as vibrations travel through it, but the noise quickly subsides as the table returns to a
static equilibrium state, as if nothing ever happened. This highlights that many strongly
interacting many-particle systems, brought out of equilibrium, do not experience long-lived
dynamical phenomena, but rather transient responses.

This expectation is motivated by our experience when interacting with systems coupled
to the external bath that is the rest of the universe. The ability to exchange energy with
such external and uncontrollable degrees of freedom leads to the loss of information of (most)
details of the initial out-of-equilibrium state—this phenomena is known as equilibration or
thermalization. One might then posit that, in isolated systems, the deterministic, reversible
nature of the equations of motion implies that equilibration is impossible—this logic turns
out to be too simplistic and its resolution depend on the classical/quantum nature of the
underlying system—we expand on this point in Chapter 2.

While some of these concerns date back to the development of quantum mechanics [493,
559], the recent explosion in atomic, molecular and optical (AMO) platforms offers a new
experimental lens with which to study these questions, as well a new set of tools to spark
theorists' imagination. The ability to isolate a physical system from its environment, as well
as control the microscopic details of the interactions and initial state (all while maintaining
quantum coherence), has opened the doors to studying out-of-equilibrium phenomena in a
controllable and systematic way. At the same time, the complementarity of the different
platforms across this broad landscape of experiments enables one to leverage the different
characteristics of each system to probe different types of out-of-equilibrium phenomena.

The goal of this dissertation is to develop our understanding of out-of-equilibrium phe-
nomena, using atomic, molecular and optical platforms as a natural laboratory for exploring
these questions.

As alluded above, given the importance of equilibration in the possible out-of-equilibrium
phenomena, effort will be made in understanding what determines a system's ability to
equilibrate, and relate that to the possibility of interesting dynamical phenomena, such as
novel out-of-equilibrium phases of matter. To this end, this dissertation is divided into four
different parts:

- In this part, we present an overview of different concepts and ideas pertaining to the
  equilibration and dynamical behavior of isolated quantum systems, setting the stage
  for the work presented in the latter parts. In Chapter 2, we discuss how equilibration
  can occur in such systems even though the equations of motion are deterministic and
  reversible. In Chapter 3, we take an aside to introduce the physics of periodically
  driven systems, introducing the main concepts and ideas used later in this disserta-
  tion. In Chapter 4, we discuss the many-body localized phase as an example of a class
  of interacting quantum systems where equilibration is arrested and some of its more
  fundamental properties. In Chapter 5, the concept of prethermalization is presented
  as a mechanism whereby equilibration is not arrested, but delayed. Understanding

the properties of this equilibrating phenomena and the phases of matter it can support (with particular emphasis in long-range interacting systems), will be the goal of Part III. Finally, in Chapter 6, we discuss hydrodynamics, highlighting how the presence of locally conserved quantities can fundamentally alter the equilibration dynamics and induce important and non-trival dynamical phenomena that can last parametrically long.

- In Part II, we focus on the study of systems where equilibration is arrested and dynamical phenomena are allowed to persist to arbitrary late times; the long lifetime of such phenomena is thus enabled by the system's inability to "lose" its memory of its initial state. We will begin in Chapter 7, with an experimental exploration of how many-body localized systems, under the presence of a drive, can exhibit entirely novel phases of matter. To this end, we present the observation of a *many-body-localized discrete time crystal*, an intrinsically out-of-equilibrium phase of matter with no equilibrium analogue, where the system's response exhibits a robust, interaction driven sub-harmonic response that breaks the underlying discrete time translation symmetry of the equations of motion. In Chapter 8, we consider the robustness of the equilibration arresting behavior upon changes to the underlying order of the system. We find that many-body localization is destabilized as the system approaches a transition between two different phases, suggesting that any transition between two different kinds of many-body localized order occurs via a small, but important ergodic/thermalizing phase. Finally, in Chapter 9, we move beyond isolated, quantum mechanical systems and consider whether ergodicity breaking can occur in *open, classical* models. We devise a construction of continuous classical particles coupled to a bath at finite temperature that allows us to simulate the dynamics of cellular automata that are robust to the presence of (a low rate of) arbitrary errors. We numerically observe that the classical model inherits the stability of the underlying cellular automaton being simulated, enabling the realization of robust out-of-equilibrium phases of matter in classical open system. Assuming this stability is independent of the cellular automaton used, this opens the tantalizing possibility of leveraging results in theoretical computer science to realize finite temperature ordered phases of matter in one dimensional short-range driven systems, evading the expectations of Mermin-Wagner-like theorems that preclude order in one dimension [188, 476].

- In Part III, we focus our attention on periodically driven (or Floquet) prethermal behavior, where the frequency of the drive provides an *exponential* control over the heating/equilibration time of the system. In Chapter 10, we begin by considering the dynamics of isolated quantum mechanical systems, studying the properties of this exponentially long equilibration process. In particular, motivated by the a wide range of AMO platforms, we focus on the prethermal dynamics of long-range interacting system. Having understood the equilibration process, we zoom into the particular class of Flo-

quet systems whose stroboscopic dynamics approximately generates a global rotation. It was previously shown that, in short-range interacting systems [161], such a setting leads to the emergence of long-lived symmetries that can be used to stabilize out-of-equilibrium phenomena for an exponentially long time. We study the generalization of these results to long-range interacting systems, building a new set of theoretical results that shed light on the propagation of information in long-range interacting systems (Chapter 11), as well, identify the situations where prethermal phases of matter are provably stable (Chapter 12). We use these analytical insights to numerically study a new phase of matter with no static analogue, the *prethermal discrete time crystal*. These theoretical results motivate the experimental exploration of a prethermal discrete time crystal, a result which is summarized in Chapter 13. We conclude with Chapter 14 by studying the importance of quantum mechanics in the observation of prethermal phases of matter; leveraging the mapping of large-S quantum spins to classical spins, we demonstrate that prethermal phases of matter can also occur in classical systems, although no effective static dynamical description exists.

- In Part IV, we turn to systems where equilibration is neither arrested nor delayed; even such systems can exhibit interesting long-lived dynamical phenomena. The most important example of this feature is falls under the moniker of *hydrodynamics*—whenever an equilibrating system hosts locally conserved quantities (i.e. energy, charge, momentum, etc), the late-time, coarse-grained motion of such quantities follows a simple set differential equation description, even if the underlying dynamics are very complicated. In Chapters 15 and 16, we study the emergence of that description in the dynamics of isolated quantum systems. In the former, we leverage a novel tensor method to simulate the large scale dynamics of a periodically driven spin chain, observing and characterizing the late-time hydrodynamical behavior. In the latter, we observe the emergent hydrodynamics in an strongly interacting, disordered spin system. Using both nitrogen-vacancy centers and substitutional nitrogen spin defects in diamond, we prepare spatially inhomogenous spin polarization profile and observe their relaxation. We observe the characteristic signature of diffusive dynamics and, complementing our observations with a numerical treatment of the dynamics, we study how the diffusion is modified by a combination of strong disorder and long-range interactions. Having discussed the emergence of regular diffusion, we turn to consider more exotic hydrodynamical phenomena. To this end, we turn to the study of one-dimensional integrable magnets, where the presence of non-Abelian symmetries has been shown to lead to superdiffusive dynamics of the conserved spin charge [613, 333, 334, 253]. In Chapter 17, we extend previous work on characterizing the universality class of this dynamical phenomena. We observe, that the resulting spin transport falls under the Kardar-Parisi-Zhang universality class, not only for the previously studied Heisenberg model, but for all types of non-Abelian symmetric integrable spin systems. Curiously, our results extend to other contexts that had not been explored in the past: supersymmet-

ric as well as periodically driven models. In Chapter 18, we discuss the experimental observation of this phenomena in an atomic gas microscope, where spin degrees of freedom can be encoded in the hyperfine levels of atoms cooled into a Mott insulator. The ability to spatially resolve the spin state across the entire chain provides a direct observation of superdiffusive nature of transport, as well as characterize its non-linear nature, offering new insights into the observed dynamics. Finally, we conclude this part with Chapter 19, where the investigate the dynamics of noise in a strongly interacting spin system. We introduce a formalism that can be utilized to characterize ensembles of spin defects in solids, as well as elucidate the nature of the noise dynamics of the system.

Chapter 2

Equilibration in physical systems

In this chapter, we will discuss the notion of equilibration and how it can arise in isolated physical systems. We will separate this chapter into two broad sections: first, we discuss equilibrium as it arises from the statistical analysis of a physical system; second, we will consider how equilibrium can (and cannot) be reached via a system's dynamics. This will allows us to be precise about what is meant when a physical system reaches equilibrium via its own dynamics and what are the necessary and sufficient ingredients for its observation.

2.1   Equilibrium in statistical physics

A physicist's first foray into the analysis of equilibrium comes from the study of thermodynamics. There, the guiding principle is that there is a small set of macroscopic thermodynamic quantities, such as temperature, pressure and entropy, that allow us to characterize the equilibrium state of a particular system, even though it might be composed of an Avogadro's number of particles. At first glance, it is surprising that such a simple analysis can have a good qualitative and quantitative descriptive power—somehow, ignoring the details of all $\sim 10^{23}$ particles does not affect our ability to understand the physical behavior of the system.

Statistical physical provides a framework for understanding why this can be true. Namely, when dealing with a large number of particles, the precise details of each constituent become irrelevant because the quantities of interest can be understood in a *statistical sense*. For example, if one has N gas molecules confined to a room, there are configurations of these particles where there are no molecules on the, say, left side of the room. However, *assuming all configurations of the positions are equally likely*, the probability of such event to occur is exponentially small (2^{-N} to be precise), while the probability of each side having the same number of particles is $2^{-N}\binom{N}{N/2}$, a *factorially* larger probability (in the number of particles). Not only is the average case more likely, but the relative size of the fluctuations *decreases* with an increasing number of particles [Fig. 2.1]! This means that the likelihood of observing a substantial fluctuation of the number of particles becomes negligible as one considers an
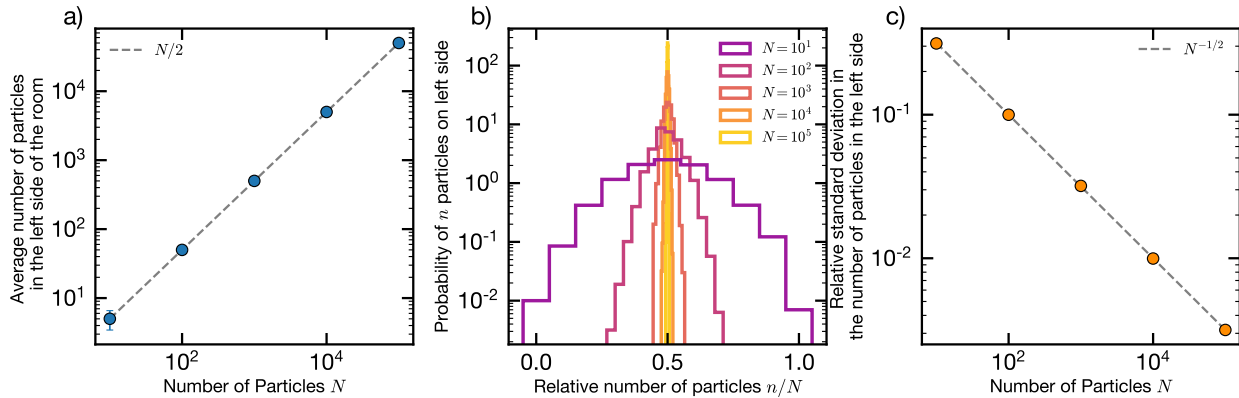
Figure 2.1: **Example of a statistical physics analysis.** Likelihood of finding n gas particles in the left half of a room *assuming all positional configurations are equally likely.* **a)** Average number of particles is exactly half the number of total particles. **b)** Crucially, the distribution of relative number of particles n/N sharpens, implying that the size of fluctuations in the relative number of particles decreases with the number of particles N. **c)** The relative standard deviation of the distribution decreases as $N^{-1/2}$, making precise the decrease in the relative fluctuation of particles.

increasing number of particles—for a large enough number of particles they do not affect any observations.

This example highlights why, in everyday life, we do not worry the air escaping to one side of the room, and displays the power of thinking of the equilibrium situation as an *ensemble* of possible configurations, which attributes to each configuration a particular probability of occurring. Physical consequences arise from the statistical properties of such an ensemble.

From this discussion, a natural question arises: what ensemble should one consider? In the next few sections, we consider a few examples that will be important for future discussions. For a more in-depth discussion see Ref. [277].

Microcanonical ensemble

Let us begin by consider an *isolated* system that cannot exchange energy or particles with the outside world—in this case, the energy E of the system remains fixed. By specifying the system's energy, we can immediately build an ensemble of configurations consistent with that value of energy E. In this case, we define the *microcanonical ensemble* as the ensemble of all microscopic configurations with energy E and all weighted equally likely to occur:

$$p(\boldsymbol{x}) = \begin{cases} 1/\Omega(E) & H(\boldsymbol{x}) = E \\ 0 & H(\boldsymbol{x}) \neq E \end{cases} \tag{2.1}$$

where $\boldsymbol{x}$ corresponds to the configuration of the system, $\Omega(E)$ is the number of configurations (or the volume of phase space) with energy E, and $H(\boldsymbol{x})$ the energy of the configuration $\boldsymbol{x}$.

While conceptually simple, from such construction one can already understand the thermodynamic properties of many physical systems (albeit with some computational effort owing to having to describe all configurations consistent with $H(\boldsymbol{x}) = E$) [277].

More fundamentally, this construction already encodes the notion temperature as a relationship between energy and entropy. To see this, consider dividing the system into subsystems A and B. Then the total number of states can be computed by the configurations on both subsystems of the system, conditional that the energies sum to E:

$$\Omega(E) = \int dE_A \Omega_A(E_A) \int dE_B \Omega_B(E_B) \delta[E - (E_A + E_B)] = \int dE_A \Omega_A(E_A) \Omega_B(E - E_A) \ .$$

Crucially, the number of states is directly related to the entropy of the system:

$$S_A(E_A) = k_b \log \Omega_A(E_A) \tag{2.2}$$

where k_b is the Boltzmann constant. Writing in terms of the entropy of each subsystem (S_A and S_B):

$$\Omega(E) = \int dE_A \exp\left\{ \frac{1}{k_b} [S_A(E_A) + S_B(E - E_A)] \right\}$$

Since the entropy is an extensive quantity (alternatively, the number of microstates grows exponentially with the number of particles), the integrand is expected to be sharply peaked—the total integration is then dominated by the contribution at this value (saddle point approximation). This can be thought similarly to the example above in Fig. 2.1, in that $S_A(E_A) + S_B(E - E_A)$ is sharply peaked for a particular value of $E_A = E_A^*$ and becomes sharper in the thermodynamic limit. The maximum of the integrand can then be obtained by maximizing the exponent, which must satisfy:

$$\frac{d}{dE_A} [S_A(E_A) + S_B(E - E_A)]|_{E_A = E_A^*} = 0$$

$$\Rightarrow \frac{dS_A(E)}{dE}\bigg|_{E=E_A^*} = \frac{dS_B(E)}{dE}\bigg|_{E=E-E_A^*} = \frac{1}{T} \ . \tag{2.3}$$

Such equality must hold regardless of the partition made. This allows us to define a quantity, which we define to be the temperature T, that must be constant across the entire system—it is then an intrinsic quantity.

Conceptually, this analysis also sheds some light into the distribution of the probabilities between different configurations. While all global microscopic configurations of fixed energy are equally likely, the number of configurations where the energy is "well-divided" (subsystem A has energy E_A^* and subsystem B has energy $E_B^* = E - E_A^*$), dominate over the extremal ones (i.e. $E_A = E$ and $E_B = 0$). At the same time, we saw how the notion of temperature—usually associated with the presence of a bath or a reservoir—emerges naturally in the context of an *isolated system*.

Canonical (Gibbs) ensemble

Having considered the case of an isolated system where energy is fixed, we now consider the conjugate setup: a system that is allowed to exchange energy with a reservoir that is kept at a fixed temperature T. In this case, we can compute the probability of a particular configuration in the system $\boldsymbol{x}_S$, by including the system and reservoir within larger, isolated system. The probability of the system having a particular configuration is then the ratio between the number of configurations of the total system (system + reservoir) that are consistent with a fixed total energy E_{tot}:

$$p(\boldsymbol{x}_S) = \frac{1}{\Omega(E_{\text{tot}})} \Omega_R[E_R = E_{\text{tot}} - H_S(\boldsymbol{x}_S)]$$
$$= \frac{1}{\Omega(E_{\text{tot}})} \exp\left\{\frac{1}{k_b} S_R[E_{\text{tot}} - H_S(\boldsymbol{x}_S)]\right\} \tag{2.4}$$

Since the system is much smaller than the reservoir, we can Taylor expand the exponent, yielding:

$$p(\boldsymbol{x}_S) \approx \frac{1}{\Omega(E_{\text{tot}})} \exp\left\{-\frac{1}{k_b} S_R[E_{\text{tot}}]\right\} \exp\left\{-\frac{H_S(\boldsymbol{x}_S)}{k_b} \left.\frac{\partial S_R(E)}{\partial E}\right|_{E=E_{\text{tot}}}\right\}$$
$$\propto \exp\left\{-\frac{H_S(\boldsymbol{x}_S)}{k_b T}\right\} \tag{2.5}$$

which recovers the well-known Boltzmann weight. Note that this setting corresponds to the more colloquial notion of equilibrium–a system that is allowed to couple to a reservoir that fixes the an overall temperature $k_b T = \beta^{-1}$. Because the system is allowed to exchange energy with the reservoir, it is allowed, in principle, to be in configurations with any energy, although higher energetic configurations are (exponentially) less likely. This was also the case when we considered the division of an isolated system into two subsystems. In this case, one subsystem serves as an effective reservoir for the other, allowing the local energy to exhibit a distribution, even though it is fixed globally.

For the remainder of this work, we shall work in units where the Boltzmann constant is unity, $k_b = 1$.

2.2 Equilibration as a dynamical process

In the previous section we focused in understanding how statistical physics leverages the use of ensembles of states/configurations to predict physical properties of a system at equilibrium. However, this approach does not tell us anything about the origin of these ensembles, nor how a physical system evolves in a way that mimics such equilibrium ensembles. Indeed, one might worry that this approach is misguided—we expect reality to be in a particular state/configuration that is constantly evolving into other configurations according to the

equations of motion. From a practical perspective, one might worry that such stark differ-ence leads to qualitative and quantitative differences between the dynamical setting and the ensemble setting. More fundamentally, one should understand why such an ensemble pic-ture provides such a powerful and effective description of the world, and why such ensemble perspective captures the properties of a strongly interacting system in constant motion. In this section we will discuss this tension and some ideas that allow us to bridge this gap, as well as some remaining open questions.

Equilibration in classical systems

We begin by considering the dynamics of an isolated classical system. In such setting, the system is characterized by a set of coordinated $\{q_i\}$ and their corresponding conjugate momenta $\{p_i\}$. Dynamics are then generated by the Hamiltonian $H(\{q_i\}, \{p_i\})$ of the system via Hamilton's equations of motion [199]:

$$\frac{dq_i}{dt} = \frac{\partial H}{\partial p_i} \quad , \quad \frac{dp_i}{dt} = -\frac{\partial H}{\partial q_i} \ . \tag{2.6}$$

Such equations induce a continuous transformation of the coordinates—this is the *trajectory*, $\{q_i(t), p_i(t)\}$, of the system in phase space.

   If we want the system to ever exhibit any equilibrating dynamics, two conditions must be immediately met: the system must be both *chaotic* and *ergodic*. Chaos is a statement of the behavior of nearby points of phase space under the system's dynamics. More precisely, a system is dubbed chaotic if nearby trajectories deviate *exponentially* in time [199]:

$$\left\| \ \boldsymbol{q}_i(t)|_{\boldsymbol{q}_i(t=0)=\boldsymbol{q}_0} - \boldsymbol{q}_i(t)|_{\boldsymbol{q}_i(t=0)=\boldsymbol{q}_0+\delta\boldsymbol{q}} \ \right\| \sim |\delta\boldsymbol{q}| e^{\lambda t} \tag{2.7}$$

where λ is the Lyaponov exponent that measures the strength of the chaotic behavior. The importance of chaos for equilibration is that it ensures that details of any initial state are quickly made inaccessible. In particular, trying to reconstruct the past configuration (a time t before) becomes exponentially difficult, because all quantities have to be measured exponentially well to ensure the backward time simulation of the dynamics is not dominated by the chaotic divergence of the trajectories. This behavior implies that the details of the initial state are "hidden" exponentially well with time.

   Ergodicity, on the other hand refers to the trajectory's ability to explore all of the phase space available to it in a random and uniform way [199]. As such, even a system starting in one particular configuration, will explore all available configurations in an random and unbiased way. Such condition is needed for equilibration to occur because it ensures that the dynamics are able to explore the totality of the phase space as time progresses.

   Note that a system can be chaotic but not ergodic if the dynamics are constrained to a particular subset of phase space, but within that subspace they still exhibit chaotic dynamics. The simplest example of this behavior occurs in the context of slightly perturbed integrable systems. The KAM theorem [301, 383, 24] states that such system should still preserve some

integrable orbits, leading to "integrable islands" in a sea of chaos—the fact that an initial state within the chaotic sea is unable to explore such islands implies that the system is not fully ergodic (see Ref. [364] for a recent example).

At the same time, a system can be ergodic but not chaotic; the simplest example oscillating with various incommensurate frequencies. The quasi-periodicity of the dynamics ensures that the system explores all of phase space available at fixed energy, but nearby trajectories will remain close owing to simple and separable nature of the dynamics.

However, these conditions are not sufficient for a single trajectory to approach an equilibrium state; fundamentally, at any one point in time, any single observable $q_i(t)$ or $p_i(t)$ is usually far away from its equilibrium value because it is dependent of the details of the dynamics. To this end, there is no way of discussing classical equilibration as occurring at *one single point of time for a single trajectory*. Understanding equilibration then requires zooming out of the details of the microscopic dynamics. This can be accomplished in different ways, some of which discussed below and summarized in Fig. 2.2.

Looking at coarse grained quantities—Although the details of each individual quantity q_i can be very different from the expected equilibration value, one can consider the properties of groups of particles (e.g. $Q_A = \sum_{i \in A} q_i$). While each quantity faces the same problems as those discussed above, the *averaging* over different quantities offers an ensemble-like approach that enables the averaged quantity to approach the equilibrium value.

Indeed, we can return to the case of N gas particles in a box to gain some intuition. Let us assume we consider a particularly troublesome state where all the particles are in the right-hand side of the box. Then all quantities, both q_i but also averaged quantities like Q_A, will not be in their equilibrium value. However, through the dynamics, the ergodic nature of the system implies that the state of the system is, statistically, given by a random configuration all possible accessible phase space. While the location of any one particle will still not have approached its equilibrium value (it is zipping along at some position), the average of an extensive number of particles will (by the same logic as in Fig. 2.1): after a while the center of mass of the gas moves to the center of the box.

The averaging over the different quantities can then be thought as building an ensemble of trajectories $\{q_i(t)\}$ and sampling from it. Assuming that the dynamics are ergodic, any initial correlations that might exist in $\{q_i(t)\}$ disappear and the averaging process mimics the behavior of an equilibrium ensemble.

Building an ensemble in time—The above prescription is useful when we are interested in the average properties of a system of interest. In this case, we can ignore the details of the microscopic degrees of freedom and focus on coarse-grained quantities, even for a single trajectory of the dynamics (this prescription is used later on to motivate a hydrodynamic description for the dynamics of conserved quantities). However, this prescription is insufficient if we are interested in the properties of one particular degree of freedom (think of a particular massive particle in a see of smaller particles).

The ergodic condition offers a possibility: since a single trajectory will explore all of the
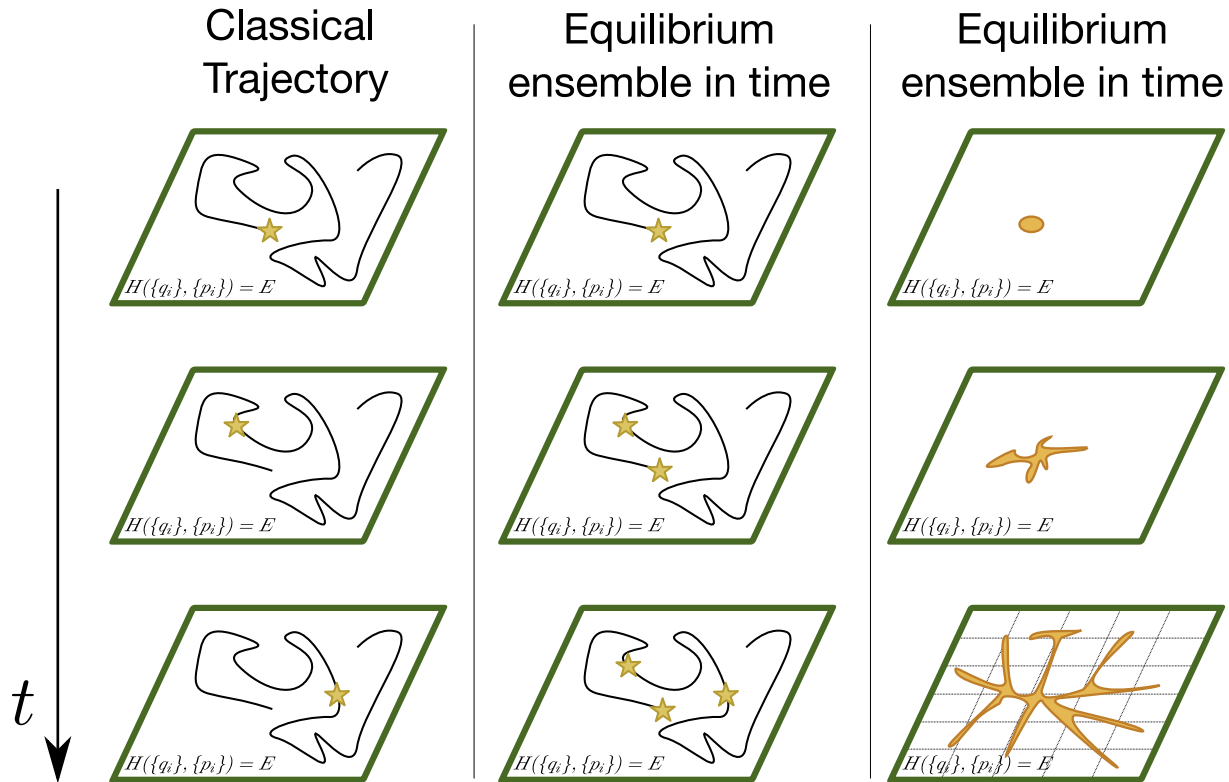
Figure 2.2: **Equilibration dynamics in classical systems.** In order to discuss equilibrium within classical systems, one must zoom out from the details of a single trajectory (left column), where the system's variables take one particular value and can appear to be far from equilibrium. One possibility is to consider the time averaged dynamics of the system, building an ensemble of configurations by sampling a single trajectory of the dynamics (middle column). Alternatively, one can consider the dynamics of a distribution of initial states (right column). Although Louiville's theorem states that the volume of phase occupied by this distribution never changes and thus the distribution can never exactly match the much more extensive equilibrium distribution, chaos and ergodicity ensures that the distribution, at late times, exhibits a fractal structure that enables it to be near all regions of the equilibrium phase despite having a very small volume. Averages over this distribution can then match averages over the equilibrium distribution.

phase accessible to it, we can build an appropriate equilibrium ensemble by sampling the trajectory at different times (middle column of Fig. 2.2). The equilibrium properties can then be obtained by computing them against such ensemble.

One limitation of this approach is that, in general, it only captures the equilibrium properties but not necessarily the approach to equilibrium. An important class of problem where this is not the case is when the system exhibits some notion of *local equilibration* before approaching the late-time equilibrium state. For example, consider the case where energy is *locally* conserved, meaning that it is a sum of local quantities. In such systems, although total energy is conserved, the energy density profile need not be. For example, the initial state might exhibit an energy density imbalance that is homogenized by the system's dynamics. Crucially, the time scale of homegenization is determined by the speed of energy diffusion in the system τ_{en}, which can be much longer than the local dynamics time scale τ_J and much shorter then the global thermalization process τ_{global}. Indeed, when $\tau_{\mathrm{global}} \gg \tau_{\mathrm{en}} \gg \tau_J$, then the local dynamics can explore the phase space associated with the local equilibrium state of the system, providing an accurate measure of the local equilibrium state, as it evolves towards the global equilibrium state.

Starting with an initial distribution in phase space—Finally, we consider what occurs when we do not consider the dynamics of a single trajectory, but rather the trajectory of an initial ensemble of trajectories. This corresponds to looking at the dynamics, not of a single point in phase space, but rather a distribution within phase space [third column Fig. 2.2].

One might worry that the resulting dynamics will exhibit the same constraints as the single trajectory case. Since we are only considering a finite region of phase space and the volume of phase space is conserved, how can the late time ensemble distribution accurately describe the equilibrium state? Once again, chaos and ergodicity provide the answer.

Since chaos imposes that nearby trajectories diverge exponentially, then any initial ensemble distribution in phase space will get highly distorted by the dynamics, with nearby points of the distribution moving apart very quickly. As such, one observes the formation of small structures that protrude out of the distribution, allowing the small volumed distribution to extend across wide regions of the total phase space. A very simple picture of this behavior is present in the case of an anharmonic oscillator, where an initially simple gaussian distribution stretches owing to the different, Fig. 2.3. Indeed, in more complex systems, the changing shape can actually exhibit a fractal like dimension, allowing a small volume of phase space to cover a much larger region [531]. At late times, even though the initial distribution has not spread homogeneously through phase space, it can occupy a portion of any finite region of phase space. In order words, if we divide phase space into cells, there is some ensemble distribution is present in most cells. As a result, the probability distribution of any quantity measured with respect to this phase space distribution mirrors the probability distribution of the full equilibrium state.
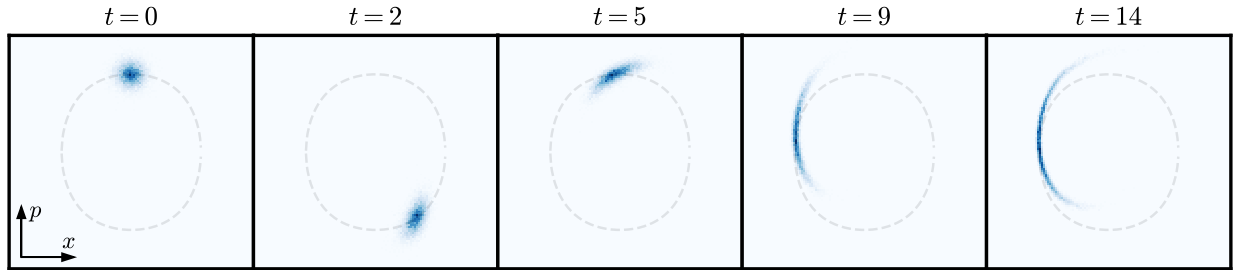
Figure 2.3: **Dynamics of a trajectory ensemble distribution in phase space.** Starting from an initial Gaussian distribution in phase space, one observes the stretching and deforming of the original round distribution owing to the system's ergodic (but not chaotic) dynamics. Chaos ensures that such a process is even more violent as nearby points in phase space must diverge exponentially fast in time. Dashed line corresponds to a cut of phase space with fixed energy.

Equilibration in quantum mechanical systems

Having discussed how equilibration can occur in classical system, we now contrast it with equilibration in an isolated quantum mechanical system. The main distinction will arise from the ability of the system to host a *superposition* of different configuration states that immediately confers "ensemble"-like structure to the calculation of local quantities—*even if the system is globally in a pure state.*

This idea is best exemplified by considering the local properties of a Bell pair state over two sites (A and B): $|\psi_B\rangle = \frac{1}{\sqrt{2}} [|\uparrow_A\uparrow_B\rangle + |\downarrow_A\downarrow_B\rangle]$. In this case, the system is in a pure state and exhibits important two-body correlations, for example:

$$\langle\psi_B|\sigma_z^A\sigma_z^B|\psi_B\rangle = 1 \ .$$

However, when looking at properties spanning only a single site (e.g. site A), all observables are zero.

$$\langle\psi_B|\sigma_x^A|\psi_B\rangle = \langle\psi_B|\sigma_y^A|\psi_B\rangle = \langle\psi_B|\sigma_z^A|\psi_B\rangle = 0 \ .$$

As a result, the subsystem A appears to be in a fully mixed state (i.e. a state where all configurations are equally likely to occur), which corresponds to an infinite temperature equilibrium state.[1] This mapping can be made precise by considering the density matrix that describes subsystem A. This can be obtained by *tracing out* its complement, which here corresponds to subsystem B:

$$\rho_A = \sum_{b\in\{|\uparrow_B\rangle,|\downarrow_B\rangle\}} \langle b|\psi_B\rangle\langle\psi_B|b\rangle = \frac{1}{2} (|\uparrow_A\rangle\langle\uparrow_A | + |\downarrow_A\rangle\langle\downarrow_A |) = \frac{\mathbb{1}_A}{2} \ . \tag{2.8}$$

---

[1]Note that although in this case we do not have a notion of Hamiltonian and energy, we can still discuss the infinite temperature state as it always refers to the fully mixed state.

Indeed, if one restricts their attention to only subsytem A, measurements of local observables cannot distinguish between $|\psi_B\rangle$ and an infinite temperature state—the subsystem appears to have approached an equilibrium state.

This discussion highlights that it is possible for a pure quantum state in an isolated quantum system to exhibit the features of an equilibrium ensemble *as long as one focuses on subsystem properties*. Note that this is impossible in the context of a single classical trajectory, because there is not "tracing out" operation capable of generating an ensemble like description of the system—any local quantity takes one particular value at some time. However, this discussion raises many important concerns:

- How generic is the feature that the system's dynamics push the system towards a state that displays the equilibration property described above?

- At the same time, dynamics will continuously lead to the evolution of the quantum state. If a subsystem approaches an equilibrium state, will it remain in the same equilibrium state or will it move between different equilibrium state or even "unequilibrate"?

- How is the equilibrium state dependent on the initial state considered? Are they special states that fail to equilibrate?

We will address these questions in the next section, introducing the eigenstate thermalization hypothesis as a theoretical framework for understanding the equilibration dynamics of isolated quantum systems.

Understanding the limitations of equilibration in generic isolated quantum systems

Let us first consider evolution of the expectation value of a generic observable for a pure state undergoing unitary dynamics, $|\psi(t)\rangle = e^{-iHt}|\psi(t=0)\rangle$:[2]

$$\langle\psi(t)|\hat{O}|\psi(t)\rangle = \sum_{a,b} c_a^* c_b \langle a|\hat{O}|b\rangle e^{-i(\epsilon_b - \epsilon_a)t} = \sum_a |c_a|^2 O_{aa} + \sum_{a\neq b} c_a^* c_b O_{ab} e^{-i(\epsilon_b - \epsilon_a)t} , \quad (2.9)$$

where $|a\rangle$ is the eigenstate of H with energy ϵ_a, c_a are the coefficients of the eigenstate decomposition, $|\psi(t=0)\rangle = \sum_a c_a |a\rangle$, and O_{ab} is a short-hand for $\langle a|\hat{O}|b\rangle$, the matrix element of the operator in the eigenstate basis.

While the above prescription is generic, we are interested in the special case where $|\psi\rangle$ is "simple". By this, we mean that it is a state that can be easily preparable and characterized— note that this notion can change as our capabilities of controlling quantum matter improve. An important class of such states are product states: states that can be written as the tensor

---

[2]In this section we focus on the case of dynamics generated by a static Hamiltonian. The presence of a conserved quantity (energy) allows us to define equilibrium states that are not necessarily trivial, i.e. the infinite temperature state.

product of its constituents. In the context of spins systems, this corresponds to preparing each individual spin in a different orientation. Since such states are rarely eigenstates of the evolution, dynamics will then lead to the rotation and decay of the polarization of the spin according to Eq. 2.9.

While Eq. 2.9 might just account for some algebraic manipulation, it provides a glimpse into why the dynamics of a local observable may decay to a constant value. While the first term of Eq. 2.9 is always time independent, the second term corresponds to the sum of many oscillating terms. Unless the energy gaps $\epsilon_b - \epsilon_b$ exhibit some structure (or some particular correlation with $c_a^* c_b$ and/or O_{ab}), we expect the different oscillating terms to cancel one another and the second sum being approximately zero (with some fluctuations). As a result, at late times we expect any observable to approach a constant value given by:

$$O_{\text{cte}} = \sum_a |c_a|^2 O_{aa}$$

A few remarks are in order. First, in order for the dynamics to lead to the equilibration of the system, the late time value of the dynamics must match the *equilibrium value*. Assuming energy is conserved, this should correspond to the expectation value of the canonical ensemble *at the same energy*:

$$O_{\text{cte}} = \sum_a |c_a|^2 O_{aa} = \frac{\text{tr}\left[\hat{O} e^{-\beta H}\right]}{\text{tr}\left[e^{-\beta H}\right]} \tag{2.10}$$

with temperature β^{-1} implicitly defined by energy conservation

$$\langle \psi(t=0)|\, H\, |\psi(t=0)\rangle = \langle \psi(t)|\, H\, |\psi(t)\rangle = \frac{\text{tr}\left[H e^{-\beta H}\right]}{\text{tr}\left[e^{-\beta H}\right]}$$

That Eq. 2.10 can be satisfied for most, if not all, initial states is quite surprising, as it appears to be highly dependent on the choice of the initial state—one might worry that one can pick states with different distribution of c_a which would reflected in different O_{cte}, but that exhibit the same value of energy and thus should approach the same equilibrium state. At present, there is not generic toolset or framework for ensuring that Eq. 2.10 can be satisfied for all simple initial states, but in Chapter 2.2 we will introduce a theoretical condition that will help us better understand when such equality is expected to occur.

Second, although we expect the oscillating terms to cancel out, they will, in general, exhibit fluctuations around the constant value. Indeed, we expect the size of these fluctuations to be directly related to the number of oscillating terms in the second sum; the larger the number of oscillating terms, the more effective the cancellation will be and the closer the value approaches a constant term. Physically, this agrees with the expectation that equilibration is more effective in larger system sizes and becomes precise in the thermodynamic limit.

Third, given a system with a *finite* number of levels/degrees of freedom, the number of gaps $\epsilon_b - \epsilon_a$ will also be finite. As a result, there is a finite number of frequencies (and

corresponding periods). As such, we expect that there is a large enough time one can wait such that all the periodic contributions "refocus" back to the original value, that is, there should exist some time such that $t(\epsilon_b - \epsilon_a) \sim k_{ab}2\pi$ for some $k_{ab} \in \mathbb{N}$ and for all a and b. Crucially, this time must be, at least, as long as the longest period (the inverse of the smallest gap). In a quantum mechanical *extensive* system, such a gap decreases exponentially with the number of particles (linearly in the size of the Hilbert space), ensuring that any revivals take at least and exponentially long-time to be observed–even in "small" systems sizes, we expect this phenomena to occur at very late times.

Fourth, the discussion above is quite heuristic because we have been implicitly assuming that there is no structure in c_a and O_{ab}. In fact, one can easily build edge cases that break the expectations delineated above—understanding these edge cases will help us sharpen the conditions and requirements for discussing equilibration in isolated systems.

Choosing the operator $\hat{O}$ carefully— In the above discussion we made no particular reference to the type of operator one should consider. In principle the only feature we seem to require is that O_{ab} does not have particular correlations with the energy gaps. However, if we choose the operator of interest to be a projection operator to a particular eigenstate subspace A (i.e. $\hat{O}_{\mathrm{proj}} = \sum_{a \in A} |a\rangle \langle a|$), then the dynamics of the operator are markedly different:

$$\langle \psi(t)| \, \hat{O}_{\mathrm{proj}} \, |\psi(t)\rangle = \sum_{a \in A} |c_a|^2 \tag{2.11}$$

In particular, the system does not exhibit any dynamics. Crucially, the value of the resulting constant is highly dependent on the details of the initial state chosen. That is, even two states that have the same energy can have wildly different values for the expectation value of the $\hat{O}_{\mathrm{proj}}$, leading to an approach to different equilibration values. Such behavior undermines our expectation of equilibration dynamics: either it signals that equilibration in intrinsically impossible, or that it highlights that under unitary dynamics not all observables approach their equilibrium value.

We take the latter perspective, and use it to sharpen our notion of equilibration. This immediately demands us to ask why we might expect some observables to equilibrate while others fail to do so. To highlight this point, we consider a somewhat convoluted but insightful example. Instead of considering a fixed observables, let us consider the expectation value of a particular time-evolved operator, $O_t = e^{-iHt}\hat{O}e^{+iHt}$. Crucially, owing to the time-evolution, the expectation value of such operator $\langle \psi(t)| \, O_t \, |\psi(t)\rangle$ will remain constant for all times–this means that the evolution of $|\psi(t)\rangle$ retains some information of the initial state. Making this example more explicit, take $|\psi(t = 0)\rangle$ to be a product state of spins up and down, and consider the corresponding O_t operators for each σ^z operator. Crucially, the expectation value of such an operator will always be in either ± 1, never equilibrating.

One gains some insight into what is occurring by analysing the structure of $\sigma^z(t)$. While in general this is very difficult, we can start by considering the short-time expansion of the

operator:

$$e^{-iHt}\sigma^z e^{iHt} = \left[\sum_{n=0}^{\infty} \frac{(-iHt)^n}{n!}\right] \sigma^z \left[\sum_{m=0}^{\infty} \frac{(+iHt)^m}{m!}\right]$$

$$= \sigma^z + (-it)[H, \sigma^z] + \frac{(-it)^2}{2}[H, [H, \sigma^z]] + \dots \quad (2.12)$$

with higher order terms (in t) inducing more nested commutators. Crucially, if the H is interacting and couples different degrees of freedom, each action of the commutator leads to a more complicated operator that acts on more degrees of freedom of the system. Using this picture, we can think that any information encoded in the initial state tends to move towards more complicated, higher-body operators, where it becomes inaccessible to usual measurement schemes. Indeed, while theoretically, such operators are valid observables one can consider, their experimental observation is very complicated if not impossible in most settings. For example, within condensed matter experiment, one is often limited to the study of one and two body correlation functions via response/scattering experiments. In the context of atomic, molecular and optical experiments, the local control over all degrees of freedom opens the doors such a measurement. However, the complexity of such a measurement increases with the size of the operator of interest, as well as the number of terms that constitute it (since they have to be measured separately). To this end, one is often interested in the dynamics of small, simple observables.

Indeed, this perspective immediately tells us that we expect equilibration not to occur for all observables, but rather almost all operators. More precisely, smaller sized operators will exhibiting faster/more complete thermalization.

So far, we have focused on understanding equilibration via the dynamics of the expectation value of observables. However, if we believe that equilibration is only sensible/meaningful to discuss in the context of few-body/simple observables, this opens a different framework for understanding/studying equilibration as a property of states. Namely, segment the system into a small subsystem A of size k and its complement B of size $N - k$. Crucially, if all the observables with support in A have approached their equilibrium values, then the state is locally indistinguishable from an equilibrium state. That is because measuring all d^{2k} operators in subsystem A allows us to uniquely describe the local density matrix of the system.

$$\forall_{\hat{O}_A} \ \langle\psi(t)| \hat{O}_A |\psi(t)\rangle = \frac{\text{tr}\left[\hat{O}_A e^{-\beta H}\right]}{\text{tr}[e^{-\beta H}]} \Rightarrow \text{tr}_B\left[|\psi(t)\rangle \langle\psi(t)|\right] = \text{tr}_B \frac{e^{-\beta H}}{\text{tr}[e^{-\beta H}]} \quad (2.13)$$

This provides an alternate description for testing the equilibration of system, allowing to cast it as a simple yes or no question that is straight-forward to compute. It also provides a direct picture of the origin of the equilibration dynamics—a subsystem A which might be initially in an out-of-equilibrium state, exchanges energy with the much larger subsystem B. Under such dynamics, in a classical system, the subsystem A will still remain in a

specific configuration. By contrast, under quantum dynamics, entanglement between the two subsystems is generated via interactions which generates non-local correlations that cannot be accessed by either of the subsystems individually. If one only has access to subsystem A, the system can appear to be in an equilibrium state, even though the full system remains in a pure state.

At the same time, this state-based view of equilibration provides some insight into the nature of the steady state behavior of thermalizing systems. For example, since the late-time steady state approaches a Gibbs/canonical ensemble, the entanglement entropy between subsystems A and B will exhibit *volume-law scaling* (i.e. the entanglement entropy scales with the number of degrees of freedom within the system). We will return to this prediction when discussing the eigenstate thermalization hypothesis in Chapter 2.2.

Let us conclude by introducing yet another perspective into the thermalizing dynamics. A different viewpoint for why not all operators can equilibrate has to do with the reversibility of unitary dynamics. Indeed, since we can always perform the backward time-evolution, any information initially encoded in the system will remain present for all times. Alternatively, one can always reconstruct that the underlying state is a pure state rather than equilibrium mixed state (at worst, one can perform the full tomography of the state, build the corresponding density matrix $\rho = |\psi(t)\rangle \langle \psi(t)|$ and confirm that $\rho^2 = \rho$). However, such information is encoded in highly non-local correlations in the state, rather than in the properties of few-body observables, making it inaccessible to observation. This perspective also highlights why there can be many different pure states that appear to approach the same equilibrium state: as long as any initial information is "hidden" within large, multi-body operators, it is irrelevant which precise operator it is as they are all inaccessible. The role of the dynamics can be understood as moving information from simple to complex operators and then move it between different complex operators. Indeed, just from combinatorics analysis we expect this to be a generic feature: there are $\sim N^k$ k-local operators, but a total of d^{2N} possible operators (where d is the local Hilbert space dimension), if the dynamics move maps operators to other operators randomly, it is more likely that an operator becomes more complex rather than less complex. This perspective in terms of the complexity of the operators has arisen recently within the context of building notions of complexity of quantum dynamics [426], but also in the study of out-of-ordered time correlators as probes of quantum chaos and equilibration, with intriguing connections to the black hole and high-energy physics (see Ref. [525] for a recent perspective).

Choosing the Hamiltonian H carefully— Critical to the equilibration dynamics are the properties of the generator of the dynamics itself.[3] Indeed, we expect some dynamics to *not exhibit* any form of equilibration. The simplest example is that of a combination of

---

[3]In this discussion, we assume that dynamics are generated by a static Hamiltonian, but the features introduced here are also more general.

different simple Harmonic oscillators:

$$H_{HO} = \sum_\lambda \hbar\omega a_\lambda^\dagger a_\lambda \ ,$$

where ω_λ is the frequency of the λ oscillator and $a_\lambda^\dagger(a_\lambda)$ is the corresponding bosonic creation/annihilation operator. In such a system, each oscillator will evolve separately with a frequency ω_λ. As a result, whenever a system is prepared in an out-of-equilibrium state, all observables exhibit persistent oscillations with frequencies ω_λ, precluding equilibration.

One can also think of the lack of equilibration as a consequence of the presence of simple conservation laws: the number of excitations in each oscillator $\hat{n}_\lambda = a_\lambda^\dagger a_\lambda$ remains a constant of motion. As a result, one can label all eigenstates of the system via the number of excitations in each harmonic oscillator.

This is different from a generic equilibrating system where conserved quantities also arise in the form of the overlap with the eigenvalues, but the associated observables O_{proj} are incredibly complex and non-local.

Another example that will be instructive is that of free-fermions (in one dimension for simplicity):

$$H_{\mathrm{ff}} = -t\sum_j c_j^\dagger c_{j+1} + h.c. + \Delta \sum_j c_j^\dagger c_{j+1}^\dagger + h.c. \tag{2.14}$$

where t describes the hopping strength and Δ is a pairing energy that creates or destroys pairs of fermions. The presence of a hopping term, means that a fermion initially placed in site n, will hope between different sites, and delocalize. However, it turns out that, much like H_{HO}, H_{ff} hosts a series of conserved quantities in the form of fermionic Bogoliubov modes, obtained by considering the system in momentum space and mixing between $c_k^\dagger$ and c_{-k}.[4] Crucially, the presence of such modes implies that the occupation of each of these extensive number of modes will never change. Moreover, the dynamics of the system can always be written in terms of the propagation of such modes through the lattice. In this context, all details of the initial state are encoded in the occupation of such modes which are accessible—the system will not approach an equilibrium state—even if, in this case, the most transparent description of subspaces is not necessarily in real space, but rather momentum space.

Indeed, the examples above can be cast in terms of a broader class of non-equilibrating systems—integrable systems. Integrable systems correspond to models where there exist quasi-local conserved quantities that can be used to enumerate the eigenstates and understand the dynamics. The important feature of these systems is that the conserved quantities can interact with one another but the dynamics does not lead to their creation or annihilation.

Owing to the complexity of underlying conserved quantities, the physics of integrable systems is best understood in terms of the properties of scattering of excitations, motivated

---

[4]For details see Ref. [295].
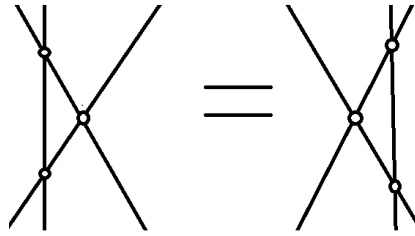
Figure 2.4: **Schematic of the Yang-Baxter equation.** Different orderings of two-body scattering processes are equivalent [12]. This is necessary condition for the Bethe ansatz approach of describing any higher-body scattering process as a combination of two-body processes.

by the Beth Ansatz and encoded in the Yang-Baxter equation, here represented visually in Fig. 2.4—we do not cover these topics in full in this dissertation, but rather point the interested reader to Refs. [40, 143, 327] and references therein. For the purposes of this work, a simple physical intuition suffices: The Bethe ansatz can be thought of as a statement that all scattering processes are reducible to a series of two-body scattering processes—the Yang-Baxter equation serves as a consistency condition: it does not matter how a three body scattering process is divided into different two-body scatterings because the result is the same. Crucially, in one dimensional systems, conservation of energy and momentum ensures that a two-body scattering process can only exchange the momenta of the particles and induce a phase factor. As a result, soliton-like modes (that can be, but are not necessarily, simple one body fermion/bosonic modes) do not decay owing to interactions with other solitonic modes—at most they can pick up a phase value from such collisions that either speeds them up or slows them down. The simplest visualization of this behavior is that of classical rods in one dimension, Fig. 2.5. When such rods interact, they exchange energy and momentum: however if instead of tracking each rod individually, we track the rod moving with some particular velocity, then each collision leads to a quick jump of its position (either forwards or backwards). As a result, much like the excitations number in H_{HO} or the Bogoliubov modes in H_{ff}, such systems exhibit a large set of (quasi)-local conserved quantities that can be used to identify and label the state of the system. However, since such particles are not independent—they acquire phase shifts as they scatter from one another—this means that their dynamics can be much more intricate. Understanding what the late-time dynamics of such systems and, in particular, how ensembles of such particles exhibit an equilibration process, has received a large amount of attention recently owing to the insights gained from Generalized Hydrodynamics [148], and the ability to study the transport dynamics theorerically [253] and numerically [333, 593].

The simplest example of one such interacting integrable model that displays complex
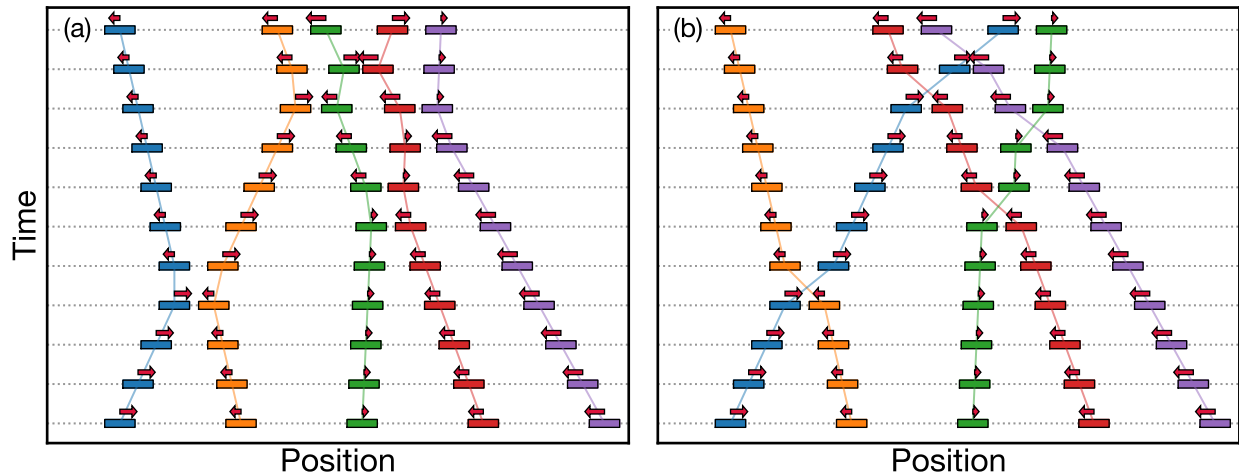
Figure 2.5:   **Dynamics in classical interacting integrable system of interacting hard rods. (a)** Upon a collision, the different rods (different colors) exchange their velocity. As a result their motion appears very complicated because it depends acutely on the details of the positions of the other rods. **(b)** If instead we identify each rod by its velocity, we see that each collision does not alter the direction of motion, it simply leads to a jump of the size of the rods. In the corresponding quantum dynamics, this process can be thought of as an additional phase shift imparted by the scattering process.

conserved quantities is the one dimensional spin-1/2 XXZ model:

$$H_{XXZ} = J \sum_i S_j^x S_{j+1}^x + S_j^y S_{j+1}^y + \Delta S_j^z S_{j+1}^z \ ,$$

where S_j^α are α spin operators on site j and Δ the anisotropy. In Chapters 17 and 18 we will return to the study of this model (and others), focusing on the details of the spin transport.

Note that the examples above are often considered fine-tuned examples, in that the presence of additional interacting terms breaks integrability and leads to the decay of any conserved quantities. Over the past two decades, a different class of models has been investigated whereby the presence of strong disorder (or energy mismatch in the case of quasi-periodic systems), leads to the localization of excitations and the breakdown of equilibration. Known as Many-body Localization, this phenomena provides a different mechanism for halting equilibration. In Chapter 4, we will discuss the physics of such phenomena in preparation for the work presented in Chapters 7 and 8.

Choosing the initial state carefully— We now turn to discussing how the choice of a specific initial state can put into question the generality of equilibration to initial states. This is made clearest when considering the initial state to be an eigenstate (i.e. the λ eigenstate)

of the system:

$$c_a = \begin{cases} 1 & a = \lambda \\ 0 & \text{otherwise} \end{cases} \tag{2.15}$$

In this case, the dynamics are trivial—the eigenstate remains unchanged (up to a phase) by the time evolution and thus the expectation value remains constant: $\langle \psi(t)| \hat{O} |\psi(t)\rangle = O_{\lambda\lambda}$. While very specific, this choice of initial state corresponds to the choice of microcanonical ensemble in the context of a quantum system (assuming no degeneracies). However, applying Eq. 2.10 to each individual eigenstate places strong constraints on the matrix elements of local operators: for each eigenstate the matrix element must match its value in the corresponding equilibrium state. This simple observation underlies the eigenstate thermalization hypothesis, introduced and discussed more in-depth below in Chapter 2.2. The previous discussions will help us better understand under what conditions we expect such hypothesis to hold and help us build intuition into its consequences.

Let us highlight that there are contexts where equilibration can exhibit important initial state dependence. The most famous example is that of many-body scars [46, 502]. In systems exhibiting such scars, there is a small subset of eigenstates that are (approximately) equally spaced in energy and display a small amount of entanglement. As a result, there are simple product state states that have most of their overlap with these states, leading to local observables exhibiting a long-lived oscillating behavior that highlights the breakdown from a simple equilibrating picture. Crucially, under the preparation of slightly different product states, equilibration is fast and not oscilations are present. For more details, see Ref. [502] and references therein.

Eigenstate Thermalization Hypothesis

Having discussed some of the expectations of thermalization in the dynamics of isolated quantum system, we now present a analytical conjecture that provides a framework for bringing all these aspects together: the Eigenstate Thermalization Hypothesis (ETH) [139, 517].

Statement of the Eigenstate Thermalization Hypothesis— The Eigenstate Thermalization Hypothesis corresponds to an ansatz for the matrix elements of local operators O in the basis of the system's eigenstates ($H |n\rangle = E_n |n\rangle$). It reads:

$$O_{nm} = \langle n| \hat{O} |m\rangle = O(E)\delta_{nm} + e^{-S(E)/2} f(E, \omega) R_{nm} \tag{2.16}$$

where $E = (E_n + E_m)/2$ is the average energy between the levels and $\omega = E_m - E_n$ its difference. $O(E)$ is a smooth function that relates the energy of the spectrum with the corresponding equilibrium value $O(E) = \text{tr}[\hat{O}e^{-\beta H}]/Z$ with $E = \text{tr}[He^{-\beta H}]/Z$, $S(E)$ is a measure of the entropy of the system at energy E (proportional the logarithm of the density of states), $f(E, \omega)$ is a smooth function (odd in ω) and R_{nm} are Gaussian random values with unit variance [140, 388].

Such form for the matrix elements immediately provides a mechanism for understanding why equilibration is so generic. If one considers the behavior of eigenstates, Eq. 2.16 describes that they are already expected to be at equilibrium since any local observable, measured with respect to any eigenstate returns the equilibrium value at the same energy density.

More broadly, it also explains why generic initial states will also approach the correct equilibrium value. From Eq. 2.11, the late-time behavior of a local observable is given an average of the eigenstates expectation value, weighted by $|c_a|^2$, the weight of a particular eigenstate in the $|\psi\rangle$ eigenvalue decomposition. However, for most preparable states, the distribution of the eigenvalue weights $|c_a|^2$ follow a sharp distribution around the energy of the state $|\psi\rangle$.[5] By the equivalence of different ensembles, this averaging reproduces the equilibrium value and thus the system at late times approaches the correct equilibrium state.

Curiously, Eq. 2.16 also provides an insight into the entanglement behavior of eigenstates. If all local operators follow Eq. 2.16, then the local density matrix associated with any eigenstate will be indistinguishable from the equilibrium density matrix. The entanglement entropy between two regions of the system will then be given by the entropy of the equilibrium state of the smaller region, which scales with the size of the region—this is known as the *volume-law* scaling of entanglement. This immediately highlights how eigenstates of thermalizing systems and fundamentally very complicated, non-seperable states. This makes their global description very complicated; however, if one is only interested in their local properties, the fact that they simply reproduce the equilibrium expectation suggests that there are effective descriptions of such that can capture local properties efficiently. In Chapter 15, we take this philosophy into heart to study the dynamics of thermalizing systems in one dimension using matrix product methods.

Let us note that the validity of ETH across the entire spectrum of the system is known as *strong ETH*. By contrast, there are systems where ETH holds for most, but not all eigenstates in the system—this is known as *weak ETH*. The most famous example of such behavior are, the aforementioned, many-body scarred systems; the presence of an extensive number of low-entanglement eigenstates equidistantly placed in the spectrum leads to long-lived persistence of oscillations when the system is prepared in an appropriate initial simple product state.

Effect of conserved quantities in equilibration

Throughout this chapter, we have focused on the equilibration dynamics of systems where energy is conserved. The exchange of energy between different parts of the system, subject to its overall conservation is what entered into the derivation of the Gibbs ensemble form earlier in the chapter. Indeed, the presence of additional conservation laws lead to a modification of the equilibrium ensemble by adding the appropriate thermodynamic conjugate variable (e.g.

---

[5]The preparation of more complex distributions of $|c_a|^2$ (for example a bimodal distribution) is expected to be very difficult, because it requires preparing the coherent superpositions of states that have very different local properties—this is akin to the preparation of cat states. Although such states may fail to equilibrate, their preparation and importance in experiments is unclear except in fine tuned examples (as the previously discussed many-body scarred systems).

for particle number there is the chemical potential). In integrable systems, there is one such parameter for each of the extensive number of the conserved quantities; the study of such ensembles has lead to recent advances in transport in integrable systems using Generalized Hydrodynamics.

On the opposite limit, we can consider what occurs when the system does not exhibit any conservation law, not even energy. In this case there is no constrains in the dynamics of the system and we expect the system to explore the *full* Hilbert space. In this case the only possible equilibrium state is that which weighs all configurations equation, the infinite temperature mixed state. In this case, Eq. 2.16 loses its dependence on the energy E, and all eigenstates are expect to have zero expectation for all local observables (with small fluctuations). We expand on this point in Chapter 3.

Chapter 3

Periodically driven (Floquet) systems

In the previously chapters we have mainly discussed the physics of static systems (i.e. where the Hamiltonian is constant in time). In this chapter, we instead focus on periodically driven systems, where the equations of motion (or the Hamiltonian) are periodic in time. Our goal is to introduce some fundamental concepts and notation, as well as discuss some aspects of their equilibration dynamics.

3.1   Main ideas and definitions

Our starting point will be a time-periodic Hamiltonian $H(t+T) = H(t)$, characterized by its period T, or equivalently, its frequency $\omega = \frac{2\pi}{T}$. Such a system is often termed a *periodically driven system* (because the periodic change of the equations of motion can be thought of a driving field acting on the system), or a *Floquet system* (in honor of Gaston Floquet for hist study of differential equations with periodically changing coefficients). Note that, in the quantum setting, the resulting dynamics remain unitary, and thus, the system remains isolated from the outside world in that it cannot build entanglement with external degrees of freedom, even though there is no notion of energy that remains conserved.[1]

Given this context, an important first question is to consider the settings whether such framework can accurately capture the dynamics of any physical system of interest. Indeed, it is usually emphasized that the laws that govern the universe are constant in time (at least in the timescales we probe them) and, thus, we expect a system's equations of motion to be constant in time. This suggests that the variation of the equations of motions arises from an external modulation of the system, and thus requires the action of an external agent (usually a hard-working experimentalist).

As a result, we should consider systems that are periodically modulated according to some protocol. One might then worry about the details of such modulation. In particular,

---

[1]Remember that energy is the conserved quantity associated with the continuous time translation symmetry (via Noether's theorem). The breaking of this symmetry by the time varying equations of motion means that energy is no longer well-defined.

any physical change to a system of interest arises from an interaction to the outside world, giving the chance of the system of interest to couple with the external world and generate entanglement. In general, this is exactly what one expects. However, the most remarkable feat of modern atomic, molecular and optical setups is the ability to prepare and isolate quantum systems, while retaining the ability to control them without generating spurious entanglement with the outside world. The most important tool in this endeavor is the invention of the laser, which prepares light in a highly coherent state. Crucially, coherent states of light interact with system in a very "classical" way in that entanglement is not formed between the system and the photonic degrees of freedom and the system can be manipulated in a unitary fashion.[2] This is in contrast to both incoherent light (where the lack of a definite phase brings the system to a mixed state owing to our ignorance of the phase information), as well as single photon interactions (where the presence of only a few photonic excitations means that the details of the entanglement is crucial to the dynamics). Indeed, the ability to manipulate a quantum system without affecting the purity of the state is why atomic, molecular and optical systems have emerged as the leading platforms for quantum information processing and the study of out-of-equilibrium dynamics in driven quantum systems.

Having motivated the form of $H(t) = H(t+T)$ as a physically realizable and meaningful system to consider, we now turn to the study of its properties. Many of the properties of interest of a Floquet system are encoded in the *Floquet unitary*, the unitary that describes the time evolution of a system after one period of the drive:

$$U_F = \mathcal{T} \exp\left[-i \int_0^T dt\ H(t)\right] . \tag{3.1}$$

where $\mathcal{T}$ refers to the time ordered product of the exponential expansion. This object allows us to study system at *stroboscopic* times $t = nT$. To access the dynamics between the periods of the system, i.e. at $t = nt+\tau$, one can complement the evolution with an additional unitary that captures the evolution within a period:

$$U(nT + \tau) = U(\tau)U_F^n \text{ where } \quad U(\tau) = \mathcal{T} \exp\left[-i \int_0^\tau dt\ H(t)\right] \tag{3.2}$$

thus constructing the time evolution operator for all times.

Because we are focused on the universal dynamical properties of the system, we will ignore the details of the behavior between periods and focus on the stroboscopic evolution $(t = nT)$.

---

[2]The intuitive argument for this fact is that atom-photon interactions usually take the form $\propto a^\dagger \sigma^- + a\sigma^+$, where $a^\dagger(\sigma^+)$ is the creation operator of a photon(atom) excitation and $a(\sigma^-)$ its hermitian conjugate. The crucial property of the coherent state of light is that it is an eigenstate of a and an approximate eigenstate of $a^\dagger$. The error in the latter condition decays with the expectation number of photons in the laser light $N_{\rm ph}$ as $1/\sqrt{N_{\rm ph}}$. Shining a green laser ($\lambda = 512$ nm) with power of 1 mW laser for 10 ns yields $\sim 10^7$ photons, making this error negligible and thus the light degrees of freedom are unchanged.

The properties of U_F can analyzed by looking at its eigenvectors $|\phi_j\rangle$ and corresponding eigenvalues λ_j. Because U_F is unitary, the eigenvalues must have unit norm, and thus can be written in terms of phases $\lambda_j = e^{-i\epsilon_j}$. ϵ_j are often referred to as *quasi-energies* in analogy to quasi-momentum in crystalline systems and their relationship to free-space momentum upon the breaking of continuous translation symmetry to a discrete translation symmetry (exactly what is done in the Floquet systems when a drive is introduced).

An important conceptual quantity directly obtainable from U_F is the *Floquet Hamiltonian* H_F defined as:

$$U_F = e^{-iTH_F} \quad \Rightarrow \quad TH_F = -i\log U_F \ = \sum_j \epsilon_j |\phi_j\rangle \langle\phi_j| \tag{3.3}$$

One should immediately note that the Floquet Hamiltonian is not uniquely defined owing to the 2π arbitrariness in the quasi-energy ($\epsilon_j \to 2\pi + \epsilon_j$ does not modify U_F but it modifies H_F). At the same time, the logarithm is often computationally and analytically difficult to study, motivating the introduction of the Floquet Magnus expansion as a formal series expansion for the Floquet Hamiltonian [54]:

$$TH_F = \int_0^T dt\ H(t) + \frac{1}{2i}\int_0^T dt_1\ \int_0^{t_1} dt_2 [H(t_1), H(t_2)]+ \tag{3.4}$$

$$-\frac{1}{6}\int_0^T dt_1 \int_0^{t_1} dt_2 \int_0^{t_2} dt_3 \left\{ [H(t_1), [H(t_2), H(t_3)]] + [H(t_3), [H(t_2), H(t_1)]] \right\} + \dots$$

One can think of such a series as a perturbative expansion in $T\|H\|$ (where $\|H\|$ captures a suitable norm of the Hamiltonian), and thus better behaved in the short period or high frequency limit. Nevertheless, even for arbitrary small T, the Magnus expansion is (generally) not convergent, owing to the growing number of terms arising from the nested commutators that overwhelm the exponential decaying expansion coefficient $[T\|H\|]^n$.

While the radius of convergence of the series is difficult to analyze formally, one can understand the breakdown of this series in terms of the equilibration dynamics of periodically driven systems.

3.2   The Floquet Hamiltonian and its effects on equilibration dynamics

One of the main expectations we have developed in Chapter 2 is that the equilibrium state a system approaches is only constrained/determined by the conserved quantities of the system. When the dynamics are generated by a static Hamiltonian, energy is necessarily conserved since the Hamiltonian commutes with the time evolution operator, and thus the equilibrium system is characterized by an appropriate temperature. Similar thermodynamic quantities arise whenever the system exhibits other conserved quantities (e.g. chemical potential for conserved number of particles). However, because energy is no longer conserved in driven

systems, a generic driven system exhibits no local conservation laws, implying that there is only one meaningful equilibrium state to consider—the fully mixed infinite temperature state. Physically, this corresponds to the drive imparting "energy" to the system (measured with respect to any local observable) until the system is unable to absorb more energy; at this point, the system is at infinite temperature.

This expectation provides a physical intuition for the breakdown of the Magnus expansion in generic driven system: if the Magnus expansion converged, one could define a (quasi-)local Hamiltonian that is preserved under the dynamics and thus the system would equilibrate with respect to the energy measured according to such H_F. Indeed, the Magnus expansion converges in systems where equilibration is not expected such as integrable systems.

Nevertheless, even though the Magnus expansion does not necessarily converge, it still provides a useful analytical tool and can provide important insights into the physics of a dynamical system, as discussed in Chapter 5.

3.3 Periodic driving as a tool

The ability to periodically modulate the equations of motion of a system has also emerged as an important tool for the controlled manipulation of physical systems. This approach has seen a particularly important renaissance owing to the need to control and isolate quantum systems. Indeed, techniques first developed within the context of magnetic resonance spectroscopy, such as dynamical decoupling pulse sequences, have been now applied to other atomic, molecular and optical systems to suppress unwanted interactions, both within a system's own degrees of freedom, as well as with an external environment [509, 213, 566, 460, 350, 461, 554, 548, 608, 98]. At the same time, periodic driving has become a staple as a tool for engineering the types and strength of interactions in both condensed matter and atomic physics settings. This has enables the realization of topological insulators from nominally trivial band structures [255, 331, 562, 264, 530], as well as the generation of new types of many-body interactions in atomic systems [259, 190, 198, 13, 120, 331].

Chapter 4

Many-body localization

As discussed in the previous chapter, ETH provides a framework for understanding the equilibration dynamics of an isolating quantum system undergoing Hamiltonian dynamics. Its breakdown offers the possibility to observe non-trivial late-time behavior that differs from the equilibrium behavior, and thus the tantalizing possibility for observing long-lived dynamical phenomena.

In this chapter we introduce Many-Body Localization as a generic class of systems that do not satisfy ETH. We will start by motivating its existence as a perturbation of the Anderson localization phenomenon in non-interacting particle systems. This will lead us to build an effective model in terms of *emergent* quasi-local conserved quantities that will help to describe the most important properties of this phenomena. We will then describe how such phenomena can be used as a jumping board to a different kind of order and phase transitions that are not present in equilibrium systems coupled to a bath at some temperature T. Finally, we will discuss the stability of this phenomena.

4.1 Anderson localization and the ℓ-bit model for MBL

We begin by considering the problem of fermions hopping in a disordered system [20] (here implemented by a random onsite energy ϵ_j), Fig. 4.1:

$$H_{\text{Anderson}} = \sum_j \epsilon_j c_j^\dagger c_j - t \sum_{\langle n,m \rangle} c_n^\dagger c_m + h.c. \tag{4.1}$$

where $c_j^\dagger$ are the creation operators for a fermion on site j, and t is hopping amplitude that permits the fermions to occupy more than one site in the chain. Owing to the single particle nature of this model, it can be easily numerically solved by writing the single particle transition matrix and diagonalizing it, [in Fig. 4.1(b), we consider the one dimensional case]. Remarkably, in low dimension ($d \leq 2$), *any amount of disorder* leads to the observation of
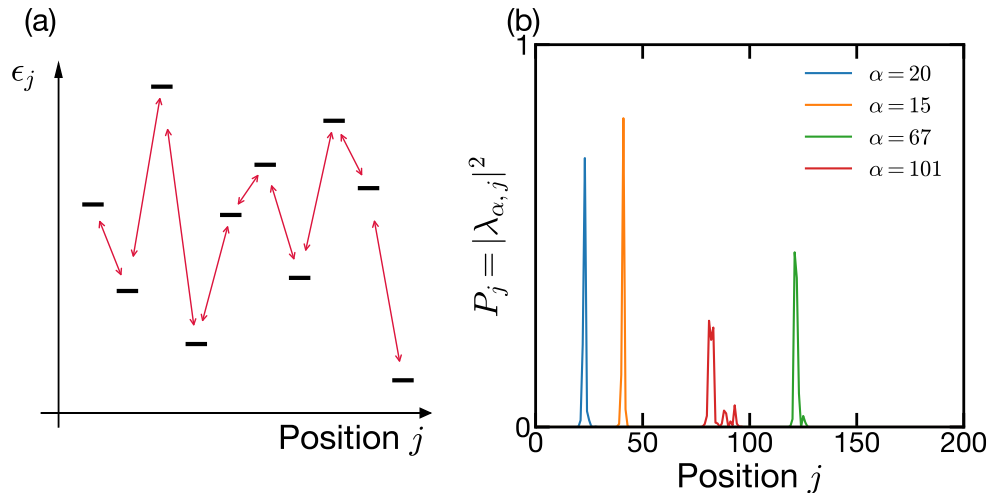
Figure 4.1: **Schematic of Anderson localization.** **(a)** Prototypical model exhibiting Anderson localization: fermions hopping with constant strength in a random landscape of local energies ϵ_j. **(b)** Upon solving for the eigenstates of the systems $\phi_\alpha^\dagger = \sum_j \lambda_{\alpha,j} c_j^\dagger$, we observe localization as evinced by the support of the eigenmodes being exponentially localized around a central site (which depends on the eigenmode considered).

localization of the different single-particle modes around a particular site of the chain (for $d = 3$, the disorder strength has to be above a particular critical value, for more details see Ref. [10]).

There are two different intuitions for understanding the presence of this localized behavior. On the one hand, thinking in terms of the wave nature of the particle, each energy mismatch leads to a wave-like scattering process. Assuming that there is no correlation in the disorder, these scattering processes cancel one another and prevent a particle, initially at some location, to delocalize through the entire system. Indeed, this intuition explains the observation of Anderson-like localization in wave phenomena as well [498]. On the other hand, we can obtain the phenomenology of disorder by considering the effect of hopping as a perturbation on top of a large disorder potential. Under only the energy potential, fermions are exactly localized, with hopping perturbatively allowing the fermion to move to a nearest neighbor site. However, such process will be very off-resonant, leading to a hybridization of the orbitals on the order t/W where W is a measure of the average energy difference between different sites. Delocalization to further away sites then comes at the cost of considering higher order perturbative processes. When disorder is large, all these perturbative processes will be off resonant, so the mixing between site j and site $j+r$ is expected to decay as $\sim (t/W)^r$, leading to exponentially localization around the initial site.

Let us emphasize an aside. Note that for the above argument to hold, we did not place strict requirements on the type of disorder. Intuitively, it is not the disorder itself that

induces the localization, but rather sites of the chain being off-resonant. Curiously this can be accomplished by considering *quasi-periodic* potentials: $\epsilon_j = V \cos(\omega j + \alpha)$ with $\omega/2\pi$ being a irrational number. In such systems, the strength of the energy potential cannot be arbitrarily small and V must be larger than a critical to observe localization [26].

So far we have focused on the single-particle case, precluding the discussion of this phenomena as a proper, robust phase of matter with interactions. To this end, it is important to understand the stability of the localized behavior to the presence of interactions such as:

$$V_{\text{int}} = \sum_{\alpha,\beta,\gamma,\delta} V_{\alpha\beta\gamma\delta} c_\alpha^\dagger c_\beta^\dagger c_\gamma c_\delta \tag{4.2}$$

Crucially, the presence of interactions offers additional channels through which the perturbation theory can "find" resonant conditions and delocalize the eigenstates. Understanding the importance of interactions/finite density of particles was a concern brought up immediately in Anderson's original work [20], but whose progress required almost 40 years. A series of works [18, 205, 37] tackled this question by trying to understand the low temperature properties of disordered electronic systems. Starting from a localized single-particle systems, these works studied the effect of interactions, showing that localization would persist at low energy densities. The localized nature of the electronic modes translated into an absence of any conductivity in the system, leading to a finite temperature *metal to insulating transition.*

Let us remark, that in the context of this transition, energy and temperature are often used interchangeably, meaning that temperature should be thought of as setting the energy scale below which localization remains robust. We emphasize this point to clarify that we are considering the transport in an *isolated* system and, thus, there is no bath with which the system can exchange energy. Indeed, the presence of a bath fundamentally alters the transport behavior since energy exchange with the bath enables any off-resonant condition to be overcome. As a result, one observes thermally activated hopping between different localized modes which induces a finite conductivity, this constitutes the central idea behind Mott's theory of variable range hopping [385].

On the heels of these works, it was numerically found that such localization behavior can occur for the *entire spectrum* in systems with a local, bounded Hilbert space (e.g. spin systems) [406], marking the presence of an infinite-temperature transition between localized and delocalized systems. Later on, a breakthrough result in mathematical physics proved the existence of the many-body localized phase in a one dimensional interacting spin system [254]. This result brought a analytical, non-perturbative positive result to the literature of many-body localization, boolstering people's understanding of this phenomenon even further.[1] These results opened the doors to the numerical study of the many body localization phase and brought a series of works that helped us hone the consequences and limits of this phase. In this present work, we will not present a comprehensive review of the literature (we point the interested reader to the reviews in Refs. [395, 6]), but rather focus on the salient features and consequences.

---

[1]We make the small caveat that this proof requires a physically motivated assumption on the limited attraction between different energy levels.

A particularly helpful framework for understanding the many-body localized phase is that of ℓ-bits, a description of the emergence quasi-local conserved quantities. Once again, these are best understood starting from the Anderson localization problem; by diagonalizing the hopping matrix, one is able to easily obtain the fermion modes corresponding to the localized modes (as illustrated in Fig. 4.1): $\phi_\alpha^\dagger = \sum_j \lambda_{\alpha,j} c_j^\dagger$. These operator allow us to build the conserved quantities of the system as the occupations of each such localized mode: $\hat{n}_\alpha = \phi_\alpha^\dagger \phi_\alpha$, where $[H_{\text{Anderson}}, \hat{n}_\alpha] = 0$ and $[\hat{n}_\alpha, \hat{n}_\beta] = 0$ for all α and β. In a similar fashion we hope to build operators, the ℓ-bits, that generalize this idea to the interacting case. The major hurdle in this construction is that the presence of interactions immediately dictates that the structure of the conserved charges will be much more complex; because of interactions, $\hat{\phi}_\alpha$ must be replaced by a new operator that is not only a superposition of single fermion creation operators, but includes terms that create and destroy many fermion modes.

Nevertheless, we expect the quantities to obey certain generic conditions for them to represent localized modes. Most importantly, they should remain (quasi)-local in space, meaning that most of their support is centered around a particular position. As a result, terms of the ℓ-bit with large support and/or far away from the localization center are expected to decay exponentially with distance.

In the language of a spin model, where the non-interacting localized modes corresponds to σ_j^z (e.g. owing to a large onsite random field), the form of the ℓ-bits is expected to be [503]:

$$\tau_\alpha^z = Z\sigma_j^z + \sum_{n=0}^{\infty} V^{(n)} O^{(n)} \tag{4.3}$$

where Z is an $\mathcal{O}(1)$ coefficient and $O^{(n)}$ is an normalized operator ($\text{tr}(O^\dagger O)/\mathcal{D} = 1$, where $\mathcal{D}$ is the Hilbert space dimension) with non-trivial support a distance n sites away. Crucially, the coefficient of these terms decays exponentially, $V^{(n)} \sim e^{-n/\xi}$ where ξ corresponds to the localization length, highlighting the locality of the mode. Note that, in analogy to the relationship between σ^z and $\sigma^{x,y}$, we can define $\tau^{x,y}$ with which we can build creation and annihilation operators, $\tau^{+,-}$.

Crucially the ℓ-bits must commute with one another and with the Hamiltonian, $[\tau_\alpha^z, \tau_\beta^z] = [\tau_\alpha^z, H] = 0$. This allows us to write the most general form of the Hamiltonian as:

$$H_{\ell-\text{bit}} = \sum_j h_j \tau_j^z + \sum_{j,k} J_{jk} \tau_j^z \tau_k^z + \sum_{j,k,l} J_{jkl} \tau_j^z \tau_k^z \tau_l^z + \ldots \tag{4.4}$$

It is important to emphasize an addition condition on the interaction terms. Owing to the short-range nature of the interactions, as well as the localized nature of the ℓ-bits, we expect the interaction strength to preserve a similar notion of locality. As a result, the interaction terms should decay exponentially in the distance between the ℓ-bits, signifying that the local integrals of motion interact locally as well[2].

---

[2]We note that in principle the lengthscale associated with the decay of interactions need not be the same as the lengthscale of the ℓ-bit. Understanding all the lengthscales associated with the many-body localized phase, as well as their distributions, remains an open question.

One key property of the ℓ-bits τ_i^z is that their dynamics are markedly distinct from their conjugate $\tau_i^{x,y}$ operators. Indeed, since τ_i^z are conserved quantities of the dynamics, they remain unchanged under the dynamics:

$$\tau_i^z(t) = e^{iH_{\ell-\mathrm{bit}}t}\tau_i^z e^{-iH_{\ell-\mathrm{bit}}t} = \tau_i^z$$

On the other hand, the conjugate quantities can have much more complex dynamics owing to the interactions between the τ_i^z operators:

$$\frac{d}{dt}\tau_i^x = i[H_{\ell-\mathrm{bit}}, \tau_i^x] = -\sum_j h_j\tau_j^y + \sum_{j,k} J_{jk}(\tau_j^y\tau_k^z + \tau_j^z\tau_k^y) + \sum_{j,k,l} J_{jkl}(\tau_j^y\tau_k^z\tau_l^z + \tau_j^z\tau_k^y\tau_l^z + \tau_j^z\tau_k^z\tau_l^y) + \dots$$

Dynamics of the $\tau^{x,y}$ operators transforms the operator into higher-body, more complex operators, leading to a decay of any initial non-zero expectation value. This highlights that although the MBL phase is able to encode classical information in τ_i^z (any initial value of $\langle\tau^z\rangle$ is preserved throughout the dynamics), any coherence (encoded in the $\tau^{x,y}$ operators) *is not protected*. As a result, although it features non-thermalizing behavior, MBL cannot be straightforwardly used as a quantum memory.

Armed with the ℓ-bit picture of the many-body localized phase, we now turn to exploring some of its consequences and features.

4.2 MBL in periodically driven systems

So far we have focused on the MBL phase in static systems. However, the robustness of MBL is not limited to this setting and it carries over also when considering periodically driven systems [439, 440]. In these systems, the breakdown of equilibration leads to an even starker effect, since eigenstates that previously could not have any structure (owing to ETH), can now exhibit emergent locally conserved quantities and thus approach very non-trivial late-time steady states very different from the infinite temperature, fully mixed equilibrium state. Crucially, such behavior occurs in the context of system that is intrinsically pushed out-of-equilibrium by the constant action of the drive. In such settings one can even observe entirely new phases of matter that have no static analogue, as discussed below in Section 4.6.

4.3 Breakdown of ETH

In the previous section, we already alluded to MBL's non-equilibrating behavior in the context of the τ_i^z operators. We can extend this analysis to generic local operators $\hat{O}$ by considering their decomposition in terms of the $\tau_i^{x,y,z}$ operators and their products:

$$\hat{O} = \underbrace{\sum_j Z_j\tau_i^z + \sum_{j,k} Z_{jk}\tau_j^z\tau_k^z + \dots}_{\text{Conserved under dynamics}} + \underbrace{\sum_{\substack{\alpha\in\{x,y\}\\j}} \lambda_j^\alpha\tau_i^\alpha + \sum_{\substack{\alpha_j\in\{x,y\}\\\alpha_k\in\{x,y,z\}\\j,k}} V_{jk}^{\alpha_j\alpha_k}\tau_j^{\alpha_j}\tau_k^{\alpha_k} + \dots}_{\text{Decoheres owing to the dynamics}} \quad (4.5)$$

From the discussion above, any overlap with $\tau_i^{x,y}$ decays to zero as the operator evolves to larger operator size. However, any overlap with the ℓ-bits or their products, leads to a finite, constant value. Crucially the choice of this value is highly dependent on the initial state considered and *uncorrelated* to the energy density of the initial state; that is, picking different states of similar energy density can lead to wildly different late time values of the operator $\hat{O}$, signaling the breakdown of thermalization.

This discussion allows us to directly consider the behavior of eigenstates and thus make a direct connection between MBL and ETH. Indeed, owing to the existence of an extensive number of conserved, local and commuting operators, the eigenstates of the system can be labeled by the expectation value (± 1) for each of the ℓ-bits. Crucially, owing to the randomness in the interactions of $H_{\ell\text{-bit}}$, eigenstates of nearby energy have very different expectation values for different τ_i^z. Since these are (quasi)-local operators, they represent a breakdown of ETH, as the expectation of local operators is not a smooth function of the energy of the system.

4.4 Level statistics

A consequence of the breakdown of ETH is that any one particular eigenstate yields very little information about other nearby eigenstates. In order words, consecutive eigenstates in the spectrum will, locally, be very distinct. This has important consequences into the statistical properties of the spectrum of a many-body localized system. The study of the spectral properties of MBL has enabled a direct connection between the physics of (non-)thermalizing systems and random matrix theory. This connection provides the first step towards building a theory for the classification of infinite temperature quantum systems, by relating different dynamical systems as arising from distinct ensembles of random matrices.

To study the spectral properties of a particular system, we will consider the statistical properties of the level spacing between adjacent eigenvalues. Consider a matrix M with eigenvalues ϵ_n that are ordered by value [for the purposes of this discussion we take ϵ_n to be real—in physical systems this corresponds to a (quasi-)energy so this does not limit the scope of our discussion]. Let us also define the level spacing $\delta_n = \epsilon_{n+1} - \epsilon_n$. Armed with this quantity, we define the $\langle r \rangle$-ratio as a measure of the relationship between nearby gaps:

$$\langle r \rangle = \sum_{n=1}^{\mathcal{D}-2} \frac{\min(\delta_{n+1}, \delta_n)}{\max(\delta_{n+1}, \delta_n)} \tag{4.6}$$

We can define a similar quantity without the maximization/minimization step: $\tilde{r}_n = \delta_{n+1}/\delta_n$.

Fundamentally, the $\langle r \rangle$-ratio captures a the degree of "knowledge" between the near eigenstates. This is most easily seen by thinking of small perturbations to the system. Starting from a particular matrix M with eigenvalues ϵ_n and eigenvectors $|\phi_n\rangle$, let us consider the effect of a small perturbation $\epsilon\Lambda$, where Λ is a normalized operator and ϵ captures the smallness of the perturbation. Under perturbation theory, the shift in the energy levels is
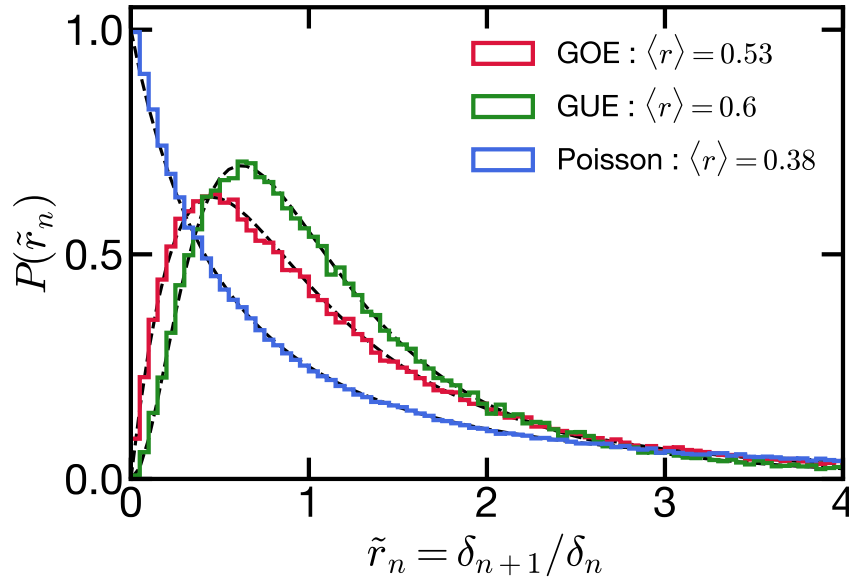
Figure 4.2: **Level spacing statistics for different random ensembles.** Distribution of the level spacing statistics $\tilde{r}$ for different random ensembles: GOE, GUE and Poisson [358]. If the ensemble has no additional structure, levels repel one another and $P(\tilde{r}) \to 0$ as $\tilde{r} \to 0$. By contrast, in the Poisson ensemble, the levels are independent of one another and thus the level spacing (and $\tilde{r}$) exhibit Poisson statistics which are maximal for $\tilde{r} = 0$. Dashed lines corresponds to analytical predictions for the different ensembles [25, 91].

given by:

$$\epsilon_n \to \epsilon_n + \epsilon \langle \phi_n | \Lambda | \phi_n \rangle + \epsilon^2 \left[-\frac{|\langle \phi_n | \Lambda | \phi_{n+1} \rangle|^2}{\delta_n} + \frac{|\langle \phi_n | \Lambda | \phi_{n-1} \rangle|^2}{\delta_{n-1}} \right] \tag{4.7}$$

As a result, the gaps modify to:

$$\delta_n \to \delta_n + \epsilon \left[\langle \phi_{n+1} | \Lambda | \phi_{n+1} \rangle - \langle \phi_n | \Lambda | \phi_n \rangle \right] + \tag{4.8}$$
$$+ \epsilon^2 \left[\frac{2|\langle \phi_n | \Lambda | \phi_{n+1} \rangle|^2}{\delta_n} - \frac{|\langle \phi_n | \Lambda | \phi_{n-1} \rangle|^2}{\delta_{n-1}} - \frac{|\langle \phi_{n+1} | \Lambda | \phi_{n+2} \rangle|^2}{\delta_{n+1}} \right]$$

Crucially, this simple calculation implies that, as long as $\langle \phi_n | \Lambda | \phi_{n+1} \rangle \neq 0$, the level spacing cannot go to zero ($\delta_n \not\to 0$) since the mixing between the two levels leads to the repulsion of their energies. This is the expected behavior in equilibrating systems respecting ETH, which predicts small (but finite) off-diagonal matrix elements for local operators, Eq. 2.16. By contrast, if the system has more structure, like conserved quantities, whether the matrix elements of Λ are non-zero depends on the relation of Λ to that structure. For example, if nearby states have different values of some conserved quantity, then Λ must,

at least, have some charge creating/destroying terms. Indeed, the same intuition explains what occurs in the many-body localized phase; the presence of an extensive number of ℓ-bits ensures that nearby eigenstates differ by a large number of ℓ-bit values, and thus Λ has to be a product of a large number of ℓ-bit creation/annihilation operators for $\langle\phi_n|\Lambda|\phi_{n+1}\rangle$ to be non-zero. The fact that nearby states can have such different properties (and thus do not "know" of each other), is what leads to qualitatively different properties for the level spacing statistics.

As a result, in an MBL system there is no level repulsion and the gaps will follow a Poisson-like distribution for their gaps. By contrast, in ETH respecting systems, level repulsion ensure that the level spacing is never "too small" and the level spacing is unlikely to be zero. In Fig. 4.2, we demonstrate this feature by considering the spectral statistics (probability distribution of $\tilde{r}$ and the value of $\langle r \rangle$) for different matrices:

- GOE (Gaussian Orthogonal ensemble) corresponds to random orthogonal matrices with real Gaussian entries.

- GUE (Gaussian Unitary ensemble) corresponds to random Hermitian matrices with complex Gaussian entries.

- Poisson refers to a system of 10 non-interacting particles each with a Gaussian, random energy.

We end this discussion by connecting the discussion about spectral statistics and the physics of MBL and non-equilibrating systems. Although we have discussed these spectral properties in terms of the physics of MBL, the same logic carries over to other integrable systems, where the eigenstates can be labelled by the content of quasi-particles. This similarity is why MBL is discussed as an example of emergent integrability (owing to strong disorder) [6]. At the same time, the $\langle r \rangle$-ratio provides of the most strightforward diagnostic for theoretically/numerically studying the equilibration properties of a quantum system, as it provides an immediate measure across the entire spectrum of the emergence of conserved quantities. Indeed, early works studying MBL leveraged spectral properties to identify the onset of MBL [406, 418].

4.5   Area law entanglement

The properties of the spectrum of the system is not the only defining feature of the excited states in the MBL phase, they also exhibit *area-law* entanglement, in contrast to the expectations from ETH (further highlighting its breakdown).

The argument for this behavior goes as follows [503]. Consider an system and divide it into regions A and B. The Hamiltonian of the system can be written as $H = H_A + H_B + H_{AB}$, where H_j is the Hamiltonian for region j and H_{AB} is the coupling between the two regions. We can understand the eigenstates of the full system H, by first considering the eigenstates of each individual region, H_A and H_B and then including the effect of the perturbations.

Since the whole system is in an MBL phase, each region of the system will also be in an MBL phase, and thus there are quasi-local conserved ℓ-bits which allow us to label the eigenstates on each side. We now consider what occurs when H_{AB} is included back into the system. Deep in each of the regions of the system, the ℓ-bits are not affected by H_{AB} since they are exponentially well localized and thus remain unchanged. The only modes that are allowed to change and hybridize are those a distance ξ from the boundary of the two regions (these are the ℓ-bits that have overlap with H_{AB}). As such the entanglement of each eigenstate is bounded by the number of ℓ-bits that hybridize across the boundary, which grows with the size of the boundary between the two regions rather than the size of the regions (as happened in the thermal case).

The fact that the eigenstate of an MBL system are area-law entangled suggests that, unless there is some topological restriction, they can be preparable from a product state via the application of a low-depth quantum circuit. This provides additional intuition for MBL as corresponding the stability of Anderson localization to interactions: the single-particle conserved quantities can then be rotated to their many-body versions by such a, not too complex, unitary.

4.6 Eigenstate Order

The existence of a low-depth, quasi-local unitary that transforms product states into the localized many-body eigenstates has important consequences to the type of phenomenology we expect in such systems. For example, it means that any (even deep in the spectrum) MBL eigenstate is the ground state of a different quasi-local Hamiltonian.

To see this, consider the following construction. Imagine you want the Hamiltonian where the eigenstate $|n\rangle$ is the ground state and we know that there is quasi-local unitary U that transforms product states into the many-body eigenstates. We can then obtain the product state $|\text{prod}_n\rangle$ that generates $|n\rangle$ by acting $|n\rangle$ with U^{-1}:

$$|\text{prod}_n\rangle = U^{-1} |n\rangle \tag{4.9}$$

Since $|\text{prod}_n\rangle$ is a product state, it is easy to build a Hamiltonian where $|\text{prod}_n\rangle$ is the ground state using local fields, let this Hamiltonian be H_{prod_n}. We can go back to the eigenbasis by rotating H_{prod_n} with U:

$$H_n = U H_{\text{prod}_n} U^{-1} \tag{4.10}$$

Since U is a low-depth unitary, the resulting Hamiltonian will be composed of terms that are (quasi-)local and $|n\rangle$ is the corresponding ground state since the unitary rotation does not change the spectrum of the system.

The equivalence between MBL excited states and the ground states of gapped quasi-local Hamiltonians has important consequences. On the one hand, it provides a different perspective for the origin of the area-law scaling of entnaglement. Indeed, ground states of gapped systems exhibit area-law scaling of entanglement entropy [157], a fact which underpins many

of the numerical approaches towards solving the ground state of strongly interacting quantum systems, and provides theoretical insight into the exponential decay of correlations (formalized for one dimensional systems in Ref. [227]).

On the other hand, it offers the tantalizing opportunity of observing quantum order across the entire spectrum. The lack of an ordered phase for high-temperatures or low dimensions is a consequence of thermodynamic considerations. However, the breakdown of equilibration in MBL systems means that such considerations do not apply and order can survive. The survival of order in high energy eigenstates can also be understood in the terms of the construction above: even high energy eigenstates correspond to the ground of a particular local Hamiltonian and thus can host order [39, 249].

Indeed, upon this realization different proposals emerged for models exhibiting different types of order ranging from topological order to $\mathbb{Z}_2$ symmetry breaking [89, 296, 429]. The stability of the MBL phase in periodic systems also enabled the proposal of intrinsically out-of-equilibrium phases of matter, most notably the discrete time crystal (DTC) [160, 290, 590]. The DTC phase arises when a periodically driven system, exhibiting discrete time translation symmetry of period T, exhibits a robust sub-harmonic response with period NT—the response breaks the underlying discrete symmetry of the dynamics. The observation of this phase in an ensemble of highly controllable nuclear spins in diamond will be the topic of Chapter 7.

The presence of different orders within the MBL phase highlights that MBL is a broader mechanism which can be combined with other notions of order to stabilize a new set of phases of matter. Understanding the transition between different MBL phases of matter is the topic of Chapter 8.

4.7 Stability of MBL

Up until now, we have not discussed the transition between the MBL and the ergodic/thermalizing phase, nor have we delved into the conditions on which MBL is stable, focusing on the phenomenology of this phase of matter. However, the conditions under which the MBL phase is stable remain an important open problem with recent renewed interest. We take this opportunity to briefly overview the main ideas following this discussion.

The main impediment towards the existence of a stable MBL phase is the existence of a external bath with which the system can interact. As already alluded to in Chapter 4.1, when a localized system is connected to a bath, energy exchange with the bath is able to overcome any off-resonant condition between the modes inducing transport [385].[3] This results in the breakdown of localization and restores ergodicity. To this end, one of the requirements towards the thermodynamic stability of MBL is that a quantum system remains isolated from its environment.

---

[3]Although some recent proposal argue that a weak coupling to a non-thermal bath can help observe some features of the MBL phase and its transition [322].

This stringent requirement explains why only recently the MBL phase has been explored both analytically and experimentally. The advent of highly coherent quantum simulation platforms enable the direct study of such dynamics in a variety of physical settings [492, 97, 510, 467].

Having discussed the importance of a lack of bath to the stability of MBL, we now discuss the converse point, i.e. the positive evidence for the existence of such a phase. Since the proof that localization is perturbatively robust to interactions [205, 37], there has been an explosion of work exploring the MBL phase and its consequences. The resulting literature is thus vast (and we do not attempt to present a comprehensive review), but evidence can be broadly divided into three different categories:

- Numerical and experimental studies of finite sized systems—One of the most used technique in the theoretical study of the MBL phase is exact diagonalization numerics. Starting from a particular set of interactions, one can extract the entire spectrum and study the properties of the eigenstates of the systems (such as the entanglement entropy, and the $\langle r \rangle$-ratio), enabling the observation of the transition between ergodic and MBL regime. Unfortunately, owing to the exponentially growth of the Hilbert space of the system, such numerics are often limited to small size $\lesssim 16$ spins. Owing to the prohibitive cost of considering larger systems, alternative approaches have been considered to study the breakdown of equilibration. Examples include the analysis of subsets of spectrum [340], the direct study of the equilibrium dynamics [131], and the study of the susceptibility of the eigenstates to perturbations [386]. We also emphasize that the probing the equilibration dynamics is an approach that has been taken in experimental works, where the direct probe of the spectral properties is difficult but the dynamics of large system sizes are amenable [492, 97, 510, 467]. We note that, because no experimental platform is fully decoupled from the outside would, one is always limited to the observation of localized behavior until the decoherence time of experiment. Below we discuss how the timescale at which equilibration occurs may be exponentially large in the system size limiting one's ability to make progress via the direct study of the equilibration dynamics of chosen observables.

- Renormalization group for excited state / thermalization properties—The previous numerical approaches have the advantage that they are exact (or at least the error can be controlled). However, this comes at the cost of being limited to small system sizes or finite times. To this end, there has been an effort in building renormalization group techniques (akin to those employed in the study of equilibrium phases of matter), to better understand the MBL phase and its transition. Indeed, such approaches have been developed to study the properties of excited states in localized systems [429], as well as build procedures for studying the MBL-to-ergodic transition [603, 204, 381]. Although such methods provide insights into the nature of the transition, they implicit assume that the MBL phase is stable in the limit of infinite disorder, studying in a self-consistent manner the resulting phase transition, and properties of the localized phase.

- A mathematical proof by Imbrie—Perhaps the most solid evidence of the stability of the MBL phase lies in the work by Imbrie [254], where the stability of the MBL phase was proven for a class of disordered one dimensional systems under a simple assumption that limits the attraction between energy levels. By constructing a quasi-local unitary that diagonalizes the system, one is able to prove different properties of the eigenstates of the MBL phase such as their closeness to eigenstate of the corresponding non-interacting model, the exponential decay of connected correlations, and the ability to label the eigenstate in terms of ℓ-bits (termed metaspins).

At the time, the one dimensional constraint in the proof in Ref. [254] was seen as a technical issue arising from the difficulty of the diagonalization in higher dimension. However, a few years later, a non-perturbative argument was put forward for the *instability* of the MBL phase in dimensions greater than one [130]—this came to be known as the avalanche instability.

At its core the avalanche instability arises from an attempt to understand the presence of small thermal regions within a larger MBL system and how that can destabilize localization. The broad argument goes as follows: Consider a large D-dimensional system where MBL is obtained via some form of disorder. Owing to the randomness in the couplings, there is a small, but finite probability of a region of size N to have low disorder; if this is the case, that portion of the system will be unable to localize and instead its degrees of freedom will be delocalize across that region—we call this a thermal bubble. We then want to understand the effect of this thermal bubble to nearby ℓ-bits. Are they able to remain localized or will they hybridize with the thermal bath and "grow" the thermal bubble?

To this end, consider segmenting the system into two initially non-interacting regions, a thermal region, where the system is delocalized and ergodic, and a region where the system is in the MBL phase with ℓ-bits of localization length ξ. We now turn on the interactions between the two regions. Owing to the localized nature of the ℓ-bits, the interaction with the thermal bath decays exponentially with the distance from the thermal bubble $J_r = e^{-r/\xi}$.

Owing to interactions, nearby ℓ-bits might hybridize with this thermal bubble. Such hybridization is efficient whenever the interaction strength is larger than the energy difference between the levels. To understand the scaling of the interaction strength, we need to be mindful of properties of the thermal bubble and the localized modes. From the former, ETH (Eq. 2.16) informs us that the matrix element decays with the square root of the density of states, $e^{-S(E)/2} \sim \sqrt{\frac{1}{\rho}} \sim \sqrt{\frac{1}{2^N}}$. From the latter, the localization of the ℓ-bits tells us that the interaction strength must decay exponentially with distance of the ℓ-bit to the thermal bubble $J_r \sim e^{-r/\xi}$ where r is the distance in lattice lengths. At the same time, the level spacing is given by the many-body level spacing in the thermal bubble, $\Lambda \sim 2^{-N}$; Since the system is in the ergodic regime, all eigenstates (at similar energy density) have the same properties and thus can hybridize the system equally well. For the hybridization not to occur, we must have:

$$\frac{J}{\Lambda} = C\frac{e^{-r/\xi}2^{-N/2}}{2^{-N}} < 1 \Rightarrow Ce^{-r/\xi}2^{N/2} < 1 \tag{4.11}$$

where C includes overall constant factors we have ignored throughout the exposition above.

In general, we are unable to analyze the hybridization of a single ℓ-bit, since it depends on the details of the particular realization (as measured by C). However, we can consider whether, having hybridized spins at distance j, the system be more or less likely to hybridize the next set of ℓ-bits. In D dimensions, there are $c_D r^{D-1}$ ℓ-bits a distance j from the thermal bubble. If all these ℓ-bits are absorbed $N \to N + c_D r^{D-1}$, while the distance only increase by one. Then we have that:

$$\frac{J_{j+1}/\Lambda_{j+1}}{J_j/\Lambda_j} = \frac{e^{-(r+1)/\xi} 2^{(N+c_D r^{D-1})/2}}{e^{-r/\xi} 2^{N/2}} = \frac{2^{c_D r^{D-1}/2}}{e^{1/\xi}} \tag{4.12}$$

From this expression, one immediately expects localization to *not* be stable in $D > 1$. In this setting, as the system absorbs a layer of ℓ-bits around the thermal bubble, the decrease in the many-body level spacing decays much faster than the interaction. As a result, for large enough bubbles (and thus r), the thermal bubble will start absorbing nearby ℓ-bits which makes the absorption condition for the next set of ℓ-bits easier, initiating a runaway process—this is why this is called an avalanche instability.

The only option for the hybridization process to stop occurs in $D = 1$. For this process to stop, we then require:

$$\frac{\sqrt{2}}{e^{1/\xi}} \leq 1 \Rightarrow \xi \leq \frac{2}{\log 2} \tag{4.13}$$

This implies that, even in one dimension, the localization length of the ℓ-bits cannot be too large, otherwise the presence of thermal bubbles in the system are able to proliferate and destroy all localized modes.

This argument provides a potent perspective on why thermalization is so hard to overcome; even small thermal systems can lead to the late-time delocalization of a large region of the system. At the same time, it brought to the forefront how *non-perturbative* effects can destabilize the MBL phase at long-times. Indeed, since the couplings considered in the argument above are on the order of the *many-body* level spacing, the resulting time scales for this hybridization process grow *exponentially* with the system size, ensuring that their observation, for reasonably sized systems stands outside the reach of experimental efforts and theoretical approaches that study the MBL via direct dynamical probes.

Nevertheless, this work has sparked a renewed interest in better understanding and characterizing the MBL-to-ergodic transition. Since then, different probes and analysis have been put forward with disagreement emerging on their interpretation as well as their significance to determining the stability of the MBL phase [522, 1, 500, 382, 501].

More broadly, this tension highlights the need of new ideas and techniques for analyzing the breakdown of ergodicity and ETH in ways that are not limited to small system sizes or finite times.

Chapter 5

Prethermalization

As discussed in Chapter 2, we expect generic interacting systems to approach the late time equilibrium state characterized by the conserved quantities of the system (e.g. energy, particle number, etc.). However, our discussion did not address the *timescale* at which such approach occurs. When this time scale is long, the approach to the late-time equilibrium state can exhibit complex and interesting thermalization dynamics. A particularly amenable setting for this behavior is strongly disordered systems, where equilibration is expected to take a very long time as the system needs to "explore" microscopically distinct configurations with similar energy (understanding this complex equilibration process is one of the motivations behind the analysis of glassy systems).

A different setting occurs when the system exhibits very distinct energy scales and one can divide the system into "fast" and "slow" degrees of motion. In such systems, the equilibration towards the equilibrium state occurs in a two-step process (Fig. 5.1): within a time scale τ_{pre}, the fast modes approach an equilibrium state, ρ_{pre}, with respect to almost static configuration of the slow modes; at a much later time τ^*, the slow modes have had time to equilibrate, bringing the whole system to the true equilibrium state, ρ_{eq}.

As a result of this separation of time scales, between τ_{pre} and τ^*, the system is in an equilibrium-like intermediate state with respect to an effective, prethermal Hamiltonian H_{pre}. Because the system arrives at a thermal state, before approaching its true final equilibrium state—this phenomena is known as *prethermalization* with the intermediate time being termed the prethermal regime.

This idea, formalized recently in the context of nuclei collisions [45], underpins the Born-Oppenheimer approximation for molecular dynamics (for understanding the dynamics of electrons in molecules, one can assume the nuclear positions are fixed owing to the large difference in masses between the particles) [60].

In this chapter, we briefly introduce the main ideas and concepts behind prethermalization leaving a more detailed and extensive analysis for Part III.
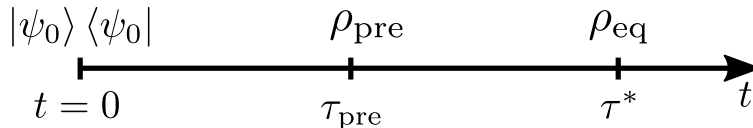
Figure 5.1:   **Schematic of prethermalization dynamics.** A particular initial state evolves towards an equilibrium state ρ_{pre} that is different from the late-time equilibrium state ρ_{eq}, which is only reached at a much later time τ^*. The duration of the prethermal regime (corresponding to the time between τ_{pre} and τ^*) as well as the nature of the prethermal state ρ_{pre} is deeply connected to the mechanism that suppresses the equilibration process.

In static systems

Let us consider first consider the very broad setting of a time independent Hamiltonian:

$$H = H_0 + gV \tag{5.1}$$

where H_0 is a "reference" Hamiltonian and V is a small perturbation, whose strength is controlled by the unitless parameter g. We will assume that g is small throughout this discussion. Following the discussion above, we expect that the equilibration of the system will exhibit first an equilibration to H_0, followed by an equilibration to the entire Hamiltonian H. However, owing to the small difference between H and H_0, one might worry that the resulting equilibrium states exhibit an equally small difference. This need not be the case. For example, if the dynamics generated by H_0 are constrained by a conservation law, the resulting prethermal equilibrium is dictated by the initial value of those conserved quantities; if V does not respect the same symmetries, the system is later allowed to equilibrate across a much larger region of the Hilbert space and, thus, the final equilibrium state can be quite distinct, even if the Hamiltonians' difference is small. This perspective has motivated the study of dynamics in systems of the form of Eq. 5.1 in different settings where H_0 is non-interacting, integrable, or hosted symmetries [300, 400, 348].

Crucially, in all these settings, the timescale of the approach to the late-time equilibrium system decays polynomially with the perturbation strength, as g^{-2}. This motivates the picture that the late time equilibration is driven by Fermi's golden rule-like processes that weakly mix previously disjoint portions of the Hilbert space.

Another important class of static prethermal models occur when the dynamics are dominated by a term with an equidistant spectrum [5]. More precisely, let us consider a Hamiltonian of the form:

$$H = \lambda \hat{N} + H_0 \tag{5.2}$$

where $\hat{N}$ is an operator with integer spectrum, λ controls the energy scale, and H_0 is a generic interacting term. We are interested in the limit where λ is much larger than the local energy scale J_{local} of the interacting Hamiltonian H_0. However, this condition does imply that the spectrum separated into different "bands" for different eigenstates of $\hat{N}$. Crucially, in the

thermodynamics the *many-body* bandwidth of H_0 scales with the system size and, thus, will always be larger than any particular λ.

In this regime, Eq. 5.2 exhibits remarkable equilibration properties. Most notably, even though $\hat{N}$ is not a conserved quantity of the system, its decay to its equilibrium value takes an exponentially long time in λ, signaling that $\tau^* \sim e^{\lambda/J_{\text{local}}}$. This exponentially large prethermal regime is a consequence of the large energy mismatch between λ and J_{local}. Although H_0 does not conserve $\hat{N}$, changing the expectation value of $\hat{N}$ by one unit corresponds to an energy shift of λ, which must be compensated by H_0 to ensure that energy is conserved. However, since the $J_{\text{local}} \ll \omega$ such compensation would require a $n \sim \lambda/J_{\text{local}}$ number of local rearrangements, a process which is exponentially suppressed in n—requiring an exponentially long time for $\hat{N}$ to reach its equilibrium value.

This offers a different setting where the physics of prethermalization can have a much more striking effect on the equilibration dynamics of static systems. At the same time, this framing also makes a connection between the physics of prethermalization and strong zero modes [165, 426, 282].

In driven (Floquet) system

In driven systems, the presence of a drive induces a naturally tunable energy scale with respect to study the system. In such systems, the breaking of continuous time translation symmetry means that energy is no longer a conserved quantity and (in the absence of additional conservation laws), the late time equilibrium corresponds to the fully mixed, infinite temperature state. The source of this late time equilibrium state is easy to intuit: the driving can continuously impart energy into the system's degrees of freedom, heating the system without bound.

This immediately offers a mechanism for understanding how prethermalization can arise in driven sytems. If the heating rate of the system is very small, the time independent interactions between the system's degrees of freedom can equilibrate, before the system is able to heat up. This can be accomplished into two ways, either reducing the strength of the driving field, or increasing the frequency of the drive. The former exhibits a phenomenology that is similar to the static case, whereby the heating rate is polynomially controlled by the strength of the coupling—in the small coupling limit, we can think of heating as occurring via a Fermi's golden rule process and thus scale quadratically with the strength of the driving field. The latter exhibits a much more intriguing effect that we now discuss.

In the limit of infinite frequency, the drive affects the system so fast, that the system's degrees do not have time to respond to the changing equations of motion and absorb energy from the drive. Effectively, the system experiences a modified static like system. Note that even in this case, the drive can have a stark effect by changing the stability of the system. The Kapitza's pendulum is the most striking example of this phenomena—by vertically shaking the pivot point of pendulum very quickly, it modifies the potential landscape of the pendulum and the upside down configuration becomes a stable equilibrium point [275].

As one considers large, but finite, frequency, the system is now capable of absorbing energy from the drive, albeit very slowly. Remarkably, the rate of energy absorption/the heating rate, $\frac{1}{\tau^*}$, decays *exponentially* with increasing frequency ω. Fundamentally this arises from a energy mismatch condition between the drive frequency and the local interaction energy scale of the system J_{local}: When $\omega \gg J_{\text{local}}$, absorbing on quanta of energy $\hbar\omega$ from the drive requires many local rearrangements of the system. Crucially, this is an off-resonant process and thus exponentially suppressed with the number of such rearrangements $n \sim \omega/J_{\text{local}}$ leading to an exponential suppression in frequency. Alternatively we can think that the heating time scale grows exponentially in the frequency of the drive, $\tau^* \sim e^{\omega/J_{\text{local}}}$. This offers exquisite control over the equilibration behavior of the system using an easily accessible experimentally parameter.

Here we note that the phenomenology is very similar to that discussed above for the static system with an integer spectrum. This connection can be made even more precisely by extending the system with an additional, fictional dimension that counts the number of energy quanta absorbed from the drive [103]. The system exhibits an integer spectrum with regards to the position along this fictitious direction, and the exponentially small heating rate can be then understood as a statement that the system requires an exponentially long time to equilibrate along this direction.

Having discussed how long the prethermal regime will last, we now turn to briefly discussing the nature of the prethermal Hamiltonian H_{pre}. The Magnus expansion analysis of discussed in Chapter 3 provides a useful framework for understanding the form of this Hamiltonian. Crucially, to zero-th order in ω^{-1}, the prethermal Hamiltonian is given by the time-averaged Hamiltonian throughout the period of the evolution. On top of this, higher order corrections arise from the non-commuting nature of the evolution at different points in time.

Although this expansion fails to converge (owing to the thermalizing nature of the dynamics), its truncation to finite order remains useful [312]. In this context, the terms of the Magnus expansion decay exponentially up until order $n^* \sim \omega/J_{\text{local}}$, beyond which their magnitude grows leading to the divergence of the formal series. By truncating the Magnus expansion, one obtains an approximation to the full Floquet unitary, generated by an effective or prethermal Hamiltonian H_{eff}. Crucially, it can be proven that H_{eff} remain exponentially well conserved under the dynamics, defining the energy with respect to which one can measure the heating rate. Moreover, this Hamiltonian does not only correspond to the meaningful conserved energy, but it also is the approximate generator of the dynamics, a much stringent condition! Chapters 10, 11 and 12 will discuss this point at length, relating its validity to the locality of the interactions of the underlying system, and the presence of prethermal phases of matter.

Chapter 6

Hydrodynamics as a dynamical approach to equilibrium

Up until now, we have focused on the physics of non-equilibrating systems as originating interesting behavior that persists for long times. However, normal equilibrating systems can also exhibit interesting and varied phenomena. In this context, although at late-times, the system approaches an equilibrium state which can no longer exhibit interesting dynamics, the *approach* to that equilibrium state can exhibit distinct phenomena and behaviors.

The most familiar of such phenomena is that of hydrodynamics. In this chapter we introduce some of the main elements of hydrodynamics in the hopes of better contextualizing the work in Chapters 15, 16, 17 and 18.

6.1 Hydrodynamics as an effective dynamical description of changing local equilibriums

Perhaps the most straightforward picture for understanding hydrodynamics is in terms of an effective theory that describes how local equilibrium changes. To this end, we should think of dividing a system size of size L, into many different cells of size ξ_{cell}, each of which is in (local) equilibrium and thus determined by the locally conserved quantities of the system [e.g. energy density $\epsilon(\boldsymbol{x})$, particle density, magnetization density, etc.], Fig. 6.1. Implicitly, this construction needs to assume a particular hierarchy of lengthscales in the problem:

$$L \gg \xi_{\text{cell}} \gg \xi_{\text{micro}} \tag{6.1}$$

where ξ_{micro} refers to the lengthscale associated with the microscopic details of the system (e.g. interparticle spacing, lattice constant, etc.).

The dynamics of conserved quantities of the system, and thus the changing local equilibrium, is mediated through exchange of that conserved quantity between nearby cells. Crucially, such exchange depends only on the equilibrium description of the different cells
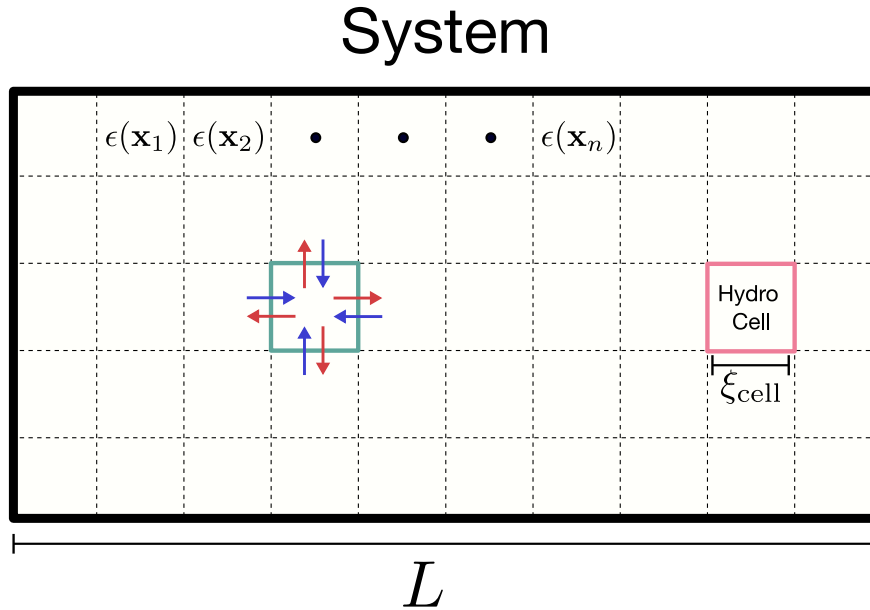
System

Figure 6.1: **Framework for an hydrodynamic description.** A system of size L is divided into a large number of hydrodynamic cells of size ξ_{cell}, which are in a local equilibrium state described by the conserved quantities, e.g. energy density $\epsilon(\boldsymbol{x})$. The dynamics of such a system are mediated by the exchange of the conserved quantity out to (red arrows) or from (blue arrows) nearby cells.

and thus, one expects to write an effective description of the dynamics solely in terms of conserved quantity. For example, if there is a single conserved quantity ϵ that depends on the position of the cell n, we have:

$$\partial_t \epsilon(\boldsymbol{x}_n) = f_{\text{hydro}}[\{\epsilon(\boldsymbol{x}_m)\}] \tag{6.2}$$

Note that, already at this level, we have already performed an immense simplification of the problem. Each cell, being in local equilibrium, should be constituted of a macroscopic number of particles. However, we are assuming that describing it in terms only on one number $\epsilon(\boldsymbol{x}_n)$ is sufficient to capture the physics of the changing landscape of local equilibrium.

For such a prediction to be valid, we expect the equilibrium states of nearby cells to be very close to one another (if this is not the case, the choice of cell boundaries will be crucial to describe the system well). As such, we expect that the discrete set of values $\epsilon(\boldsymbol{x}_m)$, can be replaced by a continuous and smooth function $\epsilon(\boldsymbol{x})$ which will provide the basis for our hydrodynamical description.

Finally, since we expect interactions to be local, the hydrodynamical equation of motion f_{hydro} can be well approximated in terms of a derivative expansion of around the point of interest. Owing to the complicated nature of the underlying interactions, deriving the
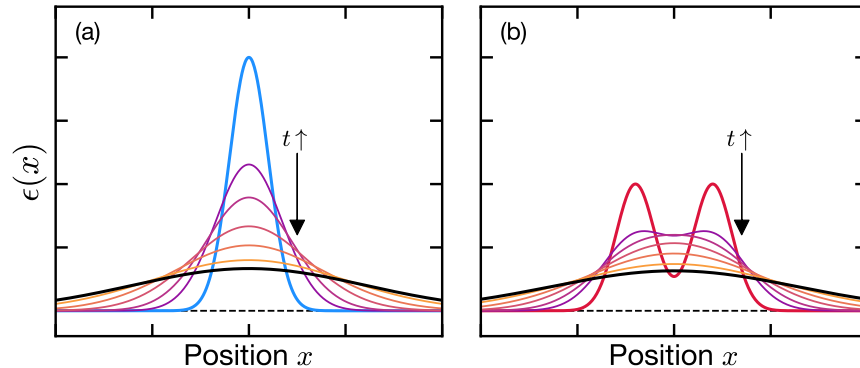
Figure 6.2: **Diffusion dynamics for different initial configurations.** Dynamics under Eq. 6.4 for two distinct initial conditions [blue curve in (a) and red curve in (b)]. Despite looking very different, the late time behavior (black curve) looks identical, highlighting the contractive nature of the dynamics.

exact form is often intractable, and one must appeal to symmetry arguments to understand which terms are allowed or not. The associated expansion coefficients (known as transport coefficients) can then be extracted by comparing the hydrodynamical description to the observed dynamics.

For the case of the dynamics of a single conserved quantity in a translationally and rotationally invariant system the hydrodynamic description should take the form of:

$$\partial_t \epsilon = D\nabla^2 \epsilon + C_1 (\nabla^2)^2 \epsilon + C_2 (\nabla \epsilon)^2 + C_3 \epsilon \nabla^2 \epsilon + \dots \tag{6.3}$$

where we suppressed the argument for notational simplicity. Keeping the lowest order terms (which are the relevant terms to the late time dynamics close to global equilibrium), in both ϵ and derivative, yields the diffusion/heat equation.

$$\partial_t \epsilon = D\nabla^2 \epsilon \tag{6.4}$$

A few remarks are in order.

Irreversibility—A common feature of a hydrodynamical description is the emergence of irreversible dynamics. For example, in Eq. 6.4, all initial states [with finite total energy $E = \int d\boldsymbol{r} \epsilon(\boldsymbol{r})$] eventually approach the same late-time state of equilibrium at $\epsilon(\boldsymbol{x}) \to 0$, Fig. 6.2. This is a signature of contractive dynamics.

That different initial states approach the same late-time dynamics offers the tantalizing possibility of categorizing seemingly different hydrodynamic descriptions by this *universal* late-time behavior. Under this program, there exists a function $f(\zeta)$ which captures the late time behavior of the system upon a *time rescaling* of the conserved quantity and the
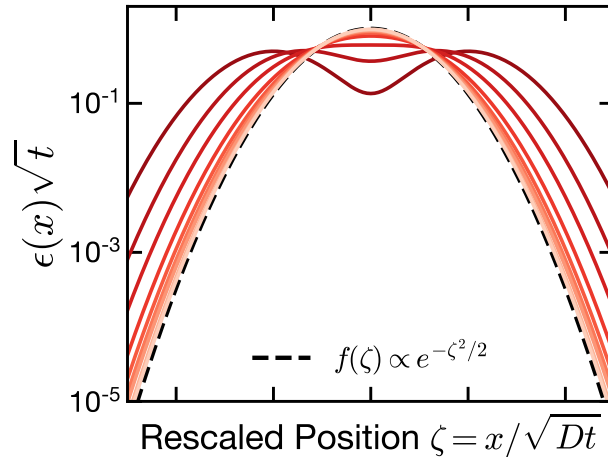
Figure 6.3: **Rescaled dynamics of diffusion converges to a universal distribution.**
Rescaled dynamics of the bimodal initial configuration considered in Fig. 6.2(b). Lighter
colors represent later times. As the dynamics progress, the rescaled dynamics of the system
approach a unique scaling function $f(\zeta)$ [dashed black line], which characterizes the universal
properties of the hydrodynamical description in Eq. 6.4.

distance, Fig. 6.3. In the case of diffusion, the exponent associated with this rescaling
can be understood in terms of the linear growth of the mean-squared displacement in a
random walk: $\langle x^2 \rangle = 2dDt$, where d is the dimensionality of the system and D the diffusion
coefficient [Eq. 6.4]. This implicitly tells us that the lengthscale of the distribution grows
with the square-root of time and thus the proper rescaled quantity is $\zeta = x/\sqrt{Dt}$. The
associated exponent $z = 2$ is known as the dynamical exponent of the system as it relates
changes in time and space $x^z \sim t$. In parallel, the conserved quantity has spread over a
volume of size x^d, and thus its density decays as $t^{-d/z}$ where d is the dimensionality of the
system. Indeed, we see that for the bimodal initial distribution considered in Fig. 6.2, the
late time rescaled distribution converges to a Gaussian function $f(\zeta) \propto e^{-\zeta^2/2}$.

Currents of conserved quantities—In our motivation for a hydrodynamical descrip-
tion, we focused only on the building an effective description of the local equilibration dy-
namics in terms of the conserved quantities in the system. However, the derivative expansion
provides little intuition to the nature of the different terms. A more physically motivated
analysis considers the evolution of the conserved quantity in the cell in terms of *currents* $\boldsymbol{j}$
of said quantity across the cell's boundaries. Crucially, if the quantity is conserved, the rate
of change of a conserved quantity in a particular cell must be compensated by the current

of that conserved across the cell's boundaries. More formally we expect:

$$\partial_t \int_{\text{cell}} d\boldsymbol{x} \ \epsilon(\boldsymbol{x}) = - \int_{\partial\text{cell}} d\boldsymbol{S} \ \boldsymbol{j}_\epsilon(\boldsymbol{x}) \cdot \hat{n} = - \int_{\text{cell}} d\boldsymbol{x} \ \nabla \cdot \boldsymbol{j}_\epsilon(\boldsymbol{x})$$

$$\Rightarrow \int_{\text{cell}} d\boldsymbol{x} \ (\partial_t\epsilon(\boldsymbol{x}) + \nabla \cdot \boldsymbol{j}_\epsilon(\boldsymbol{x})) = 0 \tag{6.5}$$

Since such relation should not depends on the particular choice of cell boundaries chosen, the integrand should equal zero everywhere, leading to a continuity condition:

$$\partial_t\epsilon(\boldsymbol{x}) + \nabla \cdot \boldsymbol{j}_\epsilon(\boldsymbol{x}) = 0 \tag{6.6}$$

Interpreting $\boldsymbol{j}_\epsilon$ as a current, provides a simple picture for what occurs in diffusion. In this case:

$$\boldsymbol{j}_\epsilon(\boldsymbol{x}) = -D\nabla\epsilon(\boldsymbol{x}) \tag{6.7}$$

meaning that the current counteracts the gradient of the energy density. The current then attempts to move the conserved quantity from regions of large quantity to regions of lower quantity—exactly our expectation for what the equilibration process should do.

One physical picture for understanding the tendency of the current to homogenize the conserved quantity, is to think of ϵ as a density of particles. Zooming into the dynamics between two particular hydrodynamic cells (A and B), the number of particles moving from cell A to cell B is proportional to the density of particles in cell A. If both cells A and B have the same density, each cell loses and gains the same number of particles and ϵ is unchanged. However, if cell A has a higher density of particles, then it will lose more particles than it gains from B, leading to an overall homogenization between the two.

The picture of current is also valuable in the case where the currents themselves are conserved quantities. For example, in the case of a dissipationless fluid, both mass and momentum are conserved, however, the transport of mass is proportional to the momentum of the particles, intrinsically coupling the hydrodynamical descriptions. In this work we will not focus on this case; however, this notion is important in the case of hydrodynamics in integrable models where there is an extensive number of conserved quantities and thus a hierarchy of currents.

Effect of long-range interactions—In the previous discussion, we implicitly assumed a notion of locality to ensure that the derivative expansion of f_{hydro} was sensible. However, there are systems where transport can occur with non-local interactions that couple spatially distinct regions of the system. A particularly important example is that of dipolar interacting spin systems, whose long-range decay $\sim 1/r^3$ enables the transport of spin across long-distances. Whether such interactions modify the universality class of the resulting hydrodynamics depends on both the dimensionality and the power-law decay of the transport. When the power-law decay is fast (the exponent is much larger than the dimensionality of the system), the long-range interactions result in a higher modification of Eq. 6.4 not

fundamentally modifying the universality class. As the power-law exponent decreases and the transport becomes more non-local, such correction become more meaningful, until they dominate over the simple diffusive behavior. In this case, the universality class of the dynamics changes and the system enters the Lévy flight regime, which signals the breakdown of the applicability of the Central limit theorem [329].

We return to this point in Chapter 16 and an additional analysis of the conditions where such change happens can be found in Appendix C.2.

The many kinds of hydrodynamics

So far, we have focused on diffusion as a form of hydrodynamics and how long-range interactions can modify the universality class making the system exhibit Lévy flight behavior. However, this simple examples of linear hydrodynamics are not the only possibilities and indeed, and the entire landscape of hydrodynamical model is much more vast.

The most simple example of a different class is that of ballistic transport in systems with stable quasi-particles. Such phenomena is usually characteristic of integrable systems, where the conserved quantities corresponds to propagating modes that can carry some conserved charge.

Another important universality class is the Kardar-Parisi-Zhang (KPZ) universality class. First studied in the context of surface growth, the interplay between randomness, smoothing and non-linearity induces an entirely distinct behavior of the fluctuations and two-point correlation functions [278]. Since then, the KPZ class has been observed in myriad phenomena, from the propagation of fire fronts to traffic models [453, 220, 106]. More recently, a striking connection has been made between the KPZ class and the infinite temperature spin transport of integrable quantum (and classical) magnets. We will discuss this connection in detail in Chapters 17 and 18.

By contrast, the presence of more additional constraints in the dynamics can make the transport of conserved quantities more difficulty leading to sub-diffusive behavior $z > 2$ [176]. More broadly, there are also constructions that generate leverage non-linear fluctuating hydrodynamics to build different universality classes for different ratios of consecutive elements of the Fibonnacci sequence [441].

6.2 Emergence of hydrodynamics in isolated quantum systems

In Chapter 2.2, we discussed how the equilibration of local observables can be understood in terms of a dynamical transformation of the initially simple observable into a much more complex, inaccessible object. While such picture holds in general, if the dynamics respect the conservation of some quantity, this picture is greatly modified and we expect a hydrodynamic description to emerge. To see how such a prescription can emerge, let us consider a spin-1/2 system where the total spin polarization $(\hat{S}_{\text{tot}}^z = \sum_i \sigma_i^z)$ is conserved, and for specificity, let

us consider the dynamics of an infinite temperature state perturbed such that the spin in site r_0 is fully polarized. The corresponding density matrix is straightforwardly written as:[1]

$$\rho_{\text{init}} \propto \mathbb{1} + \sigma_{r_0}^z$$

The dynamics of this state provides is then generated by $U(t) = e^{-iHt}$:

$$\rho(t) = U(t)\rho_{\text{init}}U^\dagger(t) = \mathbb{1} + \sum_i \lambda_i \sigma_i^z + \lambda_{\text{rest}}\delta\rho(t) \tag{6.8}$$

where $\delta\rho(t)$ corresponds to the more complex terms generated by the dynamics, normalized such that $\text{tr}[(\delta\rho)^2] = 0$. The conservation of S_{tot}^z, immediately imposes constrains on the values of λ_i:

$$\text{tr}\left[S_{\text{tot}}^z \rho(t)\right] = \text{tr}\left[S_{\text{tot}}^z \rho_{\text{init}}\right] \Leftrightarrow \sum_i \lambda_i \text{tr}\left[\sigma_i^z \sigma_i^z\right] = \text{tr}\left[\sigma_{r_0}^z \sigma_{r_0}^z\right]$$

$$\sum_i \lambda_i = 1 \tag{6.9}$$

As a result, even under equilibrating dynamics, small, local observables maintain a significant weight—the conservation law ensures that the dynamics cannot hide the information about the conserved quantity into more complex and inaccessible higher-body operators.

Indeed, the conservation of the purity of the state $\text{tr}[\rho^2(t)] = \text{tr}[\rho_{\text{init}}^2]$, gives rise to an addition relationship that allows us to further comprehend the effect of the conservation law:

$$\text{tr}[\rho^2(t)] = \lambda_{\text{rest}}^2 + \sum_i \lambda_i^2 = 1 \tag{6.10}$$

As a result, λ_{rest} is maximized when λ_i are minimized which occurs when $\lambda_i = 1/L$ and thus:

$$\lambda_{\text{simple}} = \sum_i \lambda_i^2 = \sum_i \frac{1}{L^2} = L^{-1} \quad \Rightarrow \quad \lambda_{\text{rest}} = \sqrt{1 - L^{-1}}$$

Even though the Hilbert space grows exponentially with system size L, the state maintains a polynomially large overlap with simple local observables. This characterizes the late-time equilibrium state whereby an initially localized charge is spread out homogeneously throughout the entire system.

The form of Eq. 6.8 also provides a direct glimpse into why we might expect the emergence of a hydrodynamical description. Without additional constraints, we expect that $\delta\rho$ will be a complicated operator that will drive the system to local equilibration. As a result, after some early time behavior where λ_{rest} is small and the dynamics of few body operators

---

[1]Throughout this section we ignore the normalization by the Hilbert space size $\mathcal{D}$ to simplify notation, assuming it is included within the definition of the different operators to ensure such that $\text{tr}[P_i P_j] = \delta_{ij}$ where P_i describes a Pauli string.

dominate, we expect that locally the system has approached a local equilibrium state solely characterized by local value of the spin polarization. This follows the same idea for building the hydrodynamic description illustrated in Fig. 6.1, but rather than equilibrium arising from the ignorance of the details of the hydrodynamical cell, in this case, it arises from the entanglement generated between different cells and prevents properties of the system from being locally accessible. Under such assumption, one can hope to build an effective dynamical model for the dynamics of the locally conserved quantities λ_i, by first coarse-graining and then building the appropriate derivative expansion theory, like in Eqs. 6.2 and 6.3.

In essence the ability of a quantum system to hide information offers a mechanism for ensuring local equilibration occurs quickly and effectively, without the need of additional averaging or the presence of a bath.

Coarse-grained procedure is not precise—In the previous discussion, we perform and coarse-graining prescription by separating the operator evolution into its few-body local terms, and a large many-body non-local term. The former terms are the quantity one can measure and keep track, while the latter cannot be accessed (except via an exponentially costly tomography of the system).

In reality, it remains unclear how to perform such a separation and whether there is natural lengthscale on which to perform this operation. Fundamentally, the dynamics of k-local operators is related to the dynamics of $k+j$ local operators [with $j \in \{-(b-1), \ldots, (b-1)\}$ and b the size of the operators/unitary that generates the dynamics], via the observables equations of motion [i.e. $\partial_t \hat{O}(t) = i[H, \hat{O}(t)]$ and $\hat{O}(t+1) = U^\dagger \hat{O} U$].

Understanding how this hierarchy of operators interacts with one another and how to account for the "back-flow" from the large complex operators to the simple observables remains an important open question [426, 456, 556].

Let us note here, that the availability of highly isolated and coherent quantum platforms provides the perfect platform for exploring this question and better understand the equilibration process and the emergence hydrodynamics in quantum mechanical systems. Indeed, in Chapter 16, we discuss some work attempting to bridge this gap within strongly interacting spin ensembles, and in Chapter 18, we investigate the hydrodynamics associated with the spin dynamics of a Mott insulator in an optical lattice.

Emergent irreversibility—We finish this chapter by reemphasizing the fundamental tension in the study of equilibration and hydrodynamics in isolated quantum systems: although the underlying dynamics are deterministic and reversible, the system displays behavior which seem entirely irreversible. While the discussion above provides broad brush strokes towards an understanding of equilibration and hydrodynamics, there is still no unifying principle or theoretical tools for to predict which portions of the Hilbert space are crucial towards accurately capturing dynamical phenomena. Indeed, while the details of complex many-body operators do not appear to affect the dynamics, efforts in translating this seemingly simplicity into numerical and analytical tools to accurately compute transport coefficients remains an important open problem. We discuss some of our work in this

direction in Chapter 15.

Part II

Phases of matter in non-equilibrating systems

Chapter 7

Experimental observation of a Many-Body Localized Discrete Time Crystal (MBL DTC)

As alluded in Part I, one of the most exciting possibilities offered by non-thermalizing systems is their ability to serve as a platform for observing novel, entirely out-of-equilibrium phases of matter. Perhaps the simplest and most striking example of such a phase is the *time crystal* [572, 504, 565]—a phase of matter where the system spontaneously breaks the underlying time translation symmetry of the system. Such symmetry breaking behavior is evinced in the observation of robust, persistent oscillations with a period that does not match the system's period. In the case of a static, time-independent system, any form of oscillation suffices since it immediately breaks the underlying *continuous* time translation symmetry into a *discrete* time translation symmetry (much like a solid breaks the continuous spatial translation symmetry of interactions). In the case of a periodically driven system, the oscillation's period of the dynamics becomes a multiple of drive's period and the system exhibits a sub-harmonic response—this is known as *discrete time crystal* (DTC) owing to the breaking of a *discrete* time translation symmetry.

Understanding the requirements for such a phase, and the contexts under which it can emerge has motivated a flurry of theoretical and experimental work over the past decade [565, 287, 164, 201, 589, 285, 601, 313, 100, 405, 468, 419, 511, 27, 182]. One of the most fruitful settings for the study of this phase has been in periodically driven, isolated quantum systems [160, 290, 590, 287, 164], which enables the DTC to evade the constraints affecting the existence of time crystalline order in static systems [565]. One key requirement for the thermodynamic stability of the DTC order is that equilibration must be fully arrested, rather than exponentially delayed [161, 345, 430, 313, 589]. At present, the only known mechanism for such ergodicity breaking is the many-body localized phase [Chapter 4]. In this context, DTC order is not restricted to a subset of the eigenstates, but rather occurs throughout the full Floquet eigenspectrum; as a result, time-crystalline dynamics occurs for generic initial states [160, 290, 6, 287, 163, 119, 590]. The experimental demonstration of such robust DTC

order has remained an outstanding challenge [287, 256].

In this chapter, we present the observation of the hallmark signatures of the many-body-localized DTC phase in a periodically driven isolated quantum system. We develop a quantum simulator based on individually controllable and detectable ^{13}C nuclear spins in diamond, which can be used to realize a range of many-body Hamiltonians with tunable parameters and dimensionalities. We implement a Floquet sequence in a one-dimensional (1D) chain of $L = 9$ spins, and observe the characteristic period doubling associated with the discrete time crystal. By combining the ability to prepare arbitrary initial states with site-resolved measurements, we observe the DTC response for a variety of initial states up to $N = 800$ Floquet cycles. This robustness for generic initial states provides a key signature to distinguish the many-body-localized DTC phase from prethermal responses, which only show a long-lived response for particular states [161, 345, 313, 256].

7.1 Experimental setup and protocol

Our experiments are performed on a system of ^{13}C nuclear spins in diamond close to a nitrogen-vacancy (NV) center at 4 K [Fig. 7.1(A)]. The nuclear spins are well-isolated qubits with coherence times up to tens of seconds [63]. They are coupled via dipole-dipole interactions and are accessed through the optically addressable NV electronic spin [63, 9]. With the electronic spin in the $m_s = -1$ state, the electron-nuclear hyperfine interaction induces a frequency shift h_j for each nuclear spin, which — combined with an applied magnetic field B_z in the $\hat{z}$-direction — reduces the dipolar interactions to Ising form. We additionally apply a radio-frequency (rf) driving field to implement nuclear-spin rotations. The nuclear-spin Hamiltonian is then given by $H = H_{\text{int}} + H_{\text{rf}}$, where H_{int} and H_{rf} describe the interaction and rf driving terms respectively:

$$
\begin{aligned}
H_{\text{int}} &= \sum_j (B_z + h_j)\sigma_j^z + \sum_{j<k} J_{jk}\sigma_j^z\sigma_k^z \\
H_{\text{rf}} &= \sum_j \Omega(t)\sigma_j^x.
\end{aligned}
\tag{7.1}
$$

Here, σ_j^β $(\beta = x, y, z)$ are the Pauli matrices for spin j, $B = \gamma_c B_z/2$ is the magnetic field splitting, γ_c is the ^{13}C gyromagnetic ratio, J_{jk} is the Ising component of the dipole-dipole interaction between spins j and k, $\Omega(t)$ is the applied time-dependent rf field and we set $\hbar = 1$. The system has previously been characterized in detail [9]; for 27 ^{13}C spins the hyperfine shifts h_j, the spatial coordinates, and the 351 interaction terms J_{jk} are known.

To investigate the DTC phase, we apply a Floquet unitary consisting of free evolution $U_{\text{int}}(\tau) = \exp(-iH_{\text{int}}\tau)$, interleaved with global spin rotations $U_x(\theta) = \exp\left(-i\theta \sum_j^L \sigma_j^x/2\right)$. To realize the global rotations, we develop multi-frequency rf pulses that simultaneously rotate a chosen subset of spins (H_{rf} in Eq. 7.1). We symmetrize the Floquet unitary such that $U_F = U_{\text{int}}(\tau) \cdot U_x(\theta) \cdot U_{\text{int}}(\tau)$, and apply N cycles of this basic sequence [Fig. 7.1(B)].
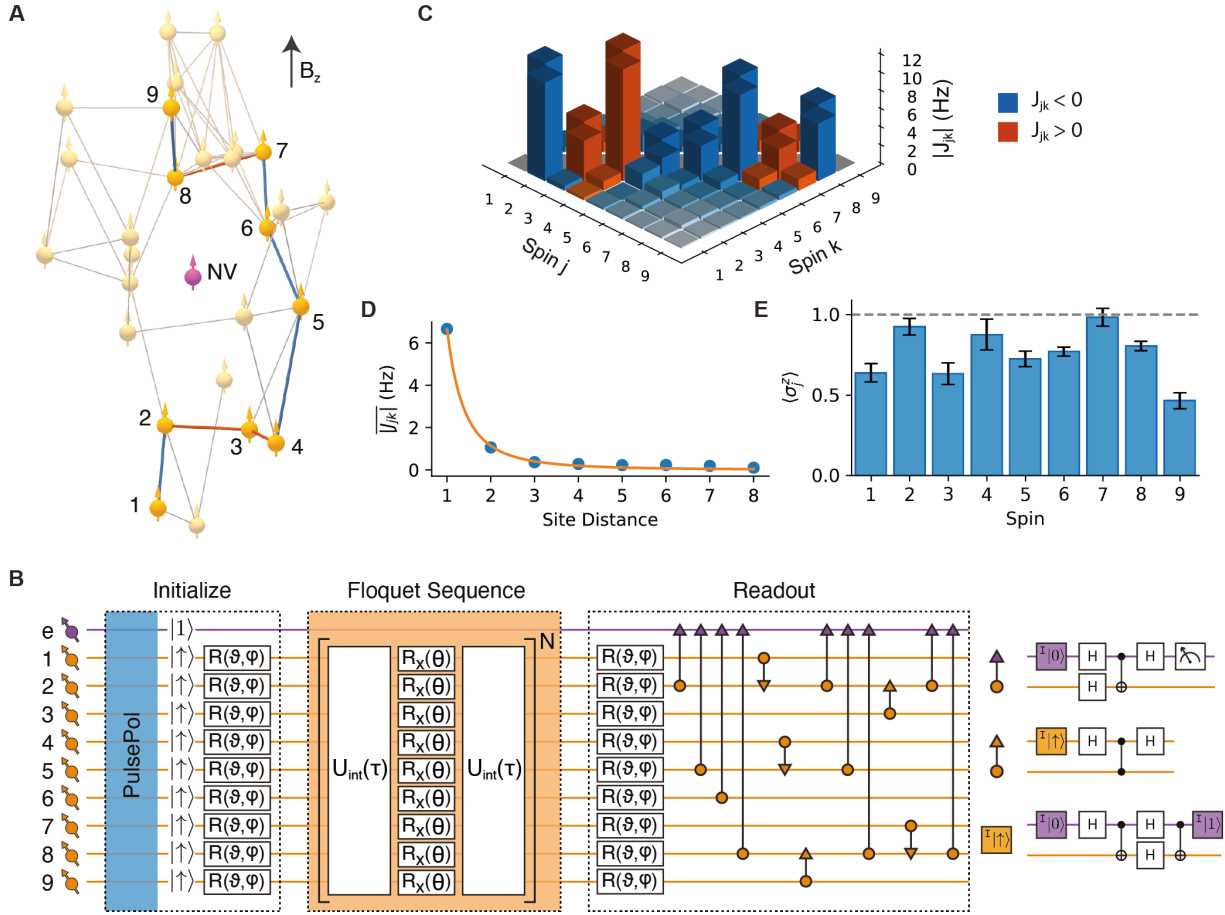
Figure 7.1:   **Programmable spin-based quantum simulator.** (**A**) We program an effective 1D chain of 9 spins in an interacting cluster of 27 ^{13}C nuclear spins (orange) close to a single NV center. Connections indicate nuclear-nuclear couplings $|J_{jk}| > 1.5$ Hz, and blue (red) lines represent negative (positive) nearest-neighbor couplings within the chain [9]. Magnetic field: $B_z \sim 403$ G. (**B**) Experimental sequence: The spins are initialized by applying the PulsePol sequence [496], followed by rotations of the form $R(\vartheta, \varphi) = \exp\left[-i\frac{\vartheta}{2}(\sin(\varphi)\sigma^x + \cos(\varphi)\sigma^y)\right]$. After evolution under N cycles of the Floquet unitary $U_F = U_{\text{int}}(\tau) \cdot U_x(\theta) \cdot U_{\text{int}}(\tau)$, the spins are sequentially read out through the NV electronic spin using electron-nuclear and nuclear-nuclear two-qubit gates. Colored boxes with 'I' denote re-initialization into the given state. (**C**) Coupling matrix for the 9-spin chain. (**D**) Average coupling magnitude as a function of site distance across the chain. Orange line: least-squares fit to a power-law function $J_0/|j - k|^\alpha$, giving $J_0 = 6.7(1)$ Hz and $\alpha = 2.5(1)$, confirming that the chain maps to an effective 1D system. (**E**) Measured expectation values $\langle \sigma_j^z \rangle$ after initializing the state $|\uparrow\uparrow\uparrow\uparrow\uparrow\uparrow\uparrow\uparrow\uparrow\rangle$. The data is corrected for measurement errors.
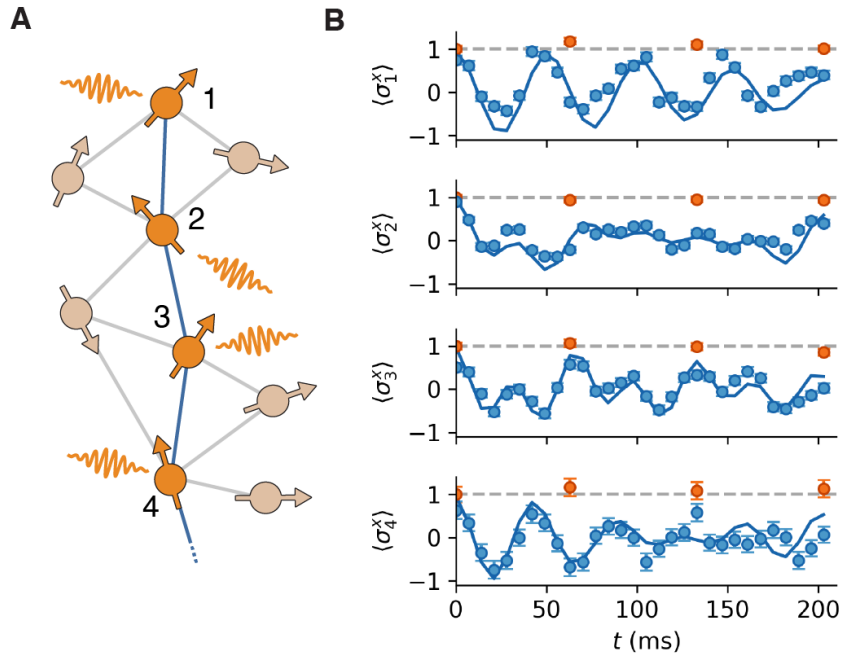
Figure 7.2: **Isolating spin chains.** (**A**) We test the programming of interacting spin
chains for the first 4 spins of the 9-spin chain [Figs. 7.1(A,C,D)]. For $\theta \sim \pi$, the Floquet
sequence $[U_F]^N$ decouples the spin chain from its environment, but preserves the internal
interactions. (**B**) Measured expectation values $\langle \sigma_j^x \rangle$ after initializing the state $|{+}{+}{+}{+}\rangle$ and
applying $[U_F]^N$ with $\theta = \pi$. Here $t = 2\tau N$ is varied by fixing $\tau = 3.5\,\mathrm{ms}$ and varying N. The
blue (orange) points show the evolution with (without) spin-spin interactions. Blue lines:
numerical simulations of only the 4-spin system. Measurements in this figure and hereafter
are corrected for state preparation and measurement errors.

For $\theta \sim \pi$, this decouples the targeted spins from their environment, while preserving the
internal interactions.

To stabilize MBL, the Floquet sequence $[U_F]^N$ should satisfy two requirements. First,
the system should be low-dimensional and short-range interacting [591, 78, 256, 130][1]. This
requirement is not naturally met in a coupled 3D spin system [Fig. 7.1(A)]. To resolve
this, we program an effective 1D spin chain using a subset of 9 spins [Figs. 7.1(A,C,D)],
sufficiently large to exhibit the hallmark exponential divergence of the MBL DTC lifetime
[160]. Second, since the periodic rotations approximately cancel the on-site disorder terms
h_j, the system must exhibit Ising-even disorder to stabilize MBL in the Floquet setting [590,
287, 256]. This is naturally realized in our system since the Ising couplings, J_{jk}, inherit

---

[1]We note that avalanche instabilities might destabilize MBL in power-law interacting systems, although
such effects are outside of current experimental and numerical capabilities [130].

the positional disorder of the nuclear spins. The disorder in the magnitude of the nearest-neighbor couplings is distributed over a range $W \sim 10$ Hz. The ratio of disorder to average nearest-neighbor coupling is therefore $W/J_0 \sim 1.5$, comparable with previous theoretical studies of DTC order in MBL systems [160, 256, 287].

To reveal the signature spatiotemporal order of the DTC phase, one must prepare a variety of initial states and perform site-resolved measurements [160, 256]. We use a combination of new and existing methods to realize the required initialization, single-spin control, and individual single-shot measurement for all spins in the chain [Fig. 7.1(B)].

First, we initialize the spins through a recently introduced dynamical-nuclear-polarization sequence called PulsePol [496]. This sequence polarizes nuclear spins in the vicinity of the NV center and prepares the 1D chain in the state $|\uparrow\uparrow\uparrow\uparrow\uparrow\uparrow\uparrow\uparrow\uparrow\rangle$. Subsequently, each spin can be independently rotated to an arbitrary state by selective rf pulses.

Second, after Floquet evolution, we read out the spins by sequentially mapping their $\langle \sigma_j^z \rangle$ expectation values to the NV electronic spin, and measuring the electronic-spin state via resonant optical excitation [63]. Spins j=2,5,6,8 can be directly accessed using previously developed electron-nuclear two-qubit gates [63]. To access the other spins (j=1,3,4,7,9), which couple weakly to the NV, we develop a protocol based on nuclear-nuclear two-qubit gates through spin-echo double resonance. We use these gates to map the spin states to other, directly accessible spins in the chain. Figure 7.1(E) shows the measured $\langle \sigma_j^z \rangle$ expectation values after preparing the state $|\uparrow\uparrow\uparrow\uparrow\uparrow\uparrow\uparrow\uparrow\uparrow\rangle$.

We verify that we can isolate the dynamics of a subset of spins by studying the first 4 spins of the 9-spin chain [Fig. 7.2(A)]. We prepare the superposition state $|{+}{+}{+}{+}\rangle$, where $|+\rangle = (|\uparrow\rangle + |\downarrow\rangle)/\sqrt{2}$, and apply $[U_F]^N$ with $\theta = \pi$. We first verify that the state is preserved when each spin is individually decoupled to remove interactions [Fig. 7.2(B)]. In contrast, with internal interactions, the four spins entangle and undergo complex dynamics. The measured evolution matches a numerical simulation containing only the 4 spins, indicating that the system is strongly interacting and protected from external decoherence.

7.2   Observation of an MBL DTC

With this capability confirmed, we turn to the 9-spin chain and the DTC phase. The expectation for the DTC phase is a long-lived period-doubled response that is stabilized against perturbations of U_F through many-body interactions. To illustrate this, we set $\theta = 0.95\pi$, a perturbation from the ideal value of $\theta_{\text{ideal}} = \pi$, and tune the system through the DTC phase transition by changing τ, which effectively sets the interaction strength [Figs. 7.3(A-C)].

We first investigate the state $|\uparrow\uparrow\uparrow\uparrow\uparrow\uparrow\uparrow\uparrow\uparrow\rangle$ and consider the averaged two-point correlation function $\overline{\chi} = \frac{1}{L}\sum_{j=1}^{L}\langle \sigma_j^z(N)\rangle \mathrm{sgn}[\langle \sigma_j^z(0)\rangle]$, where $\langle \sigma_j^z(N)\rangle$ is the expectation value at Floquet cycle N for spin j. Without interactions, the deliberate under-rotations ($\theta < \pi$), in combination with naturally present noise in the applied control fields, lead to a rapid decay [Figs. 7.3(B,C)]. By introducing moderate interactions ($\tau = 1.55$ ms), the system is on the
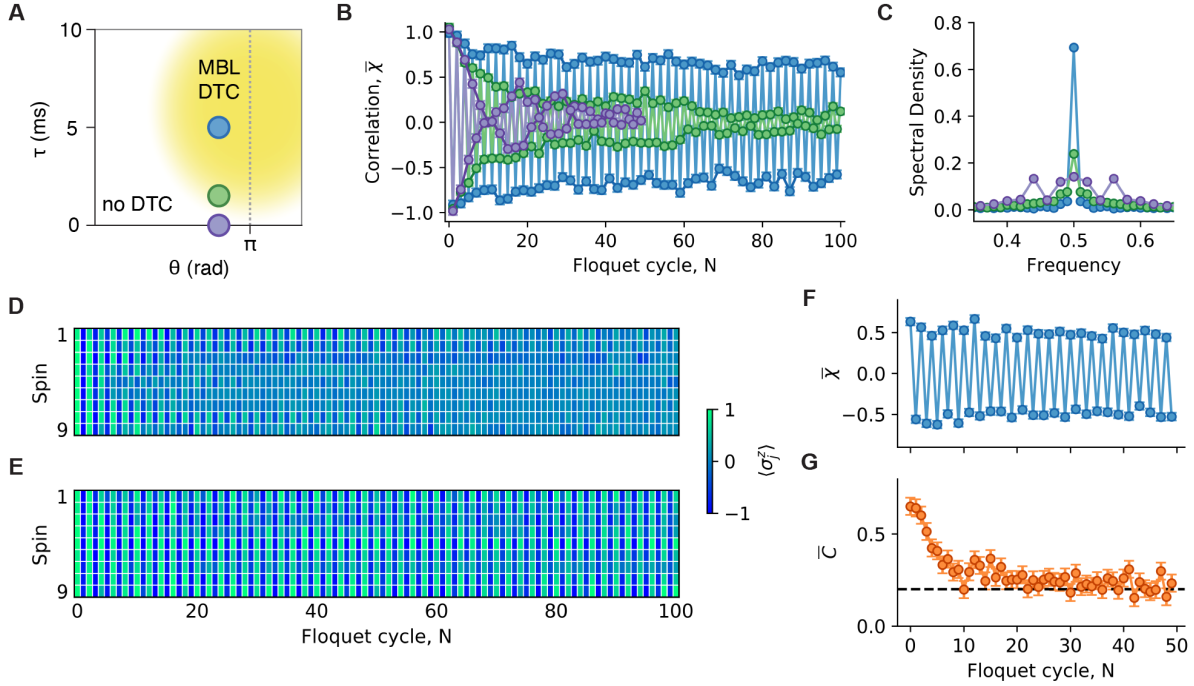
Figure 7.3: **Discrete time crystal in the 9-spin chain.** (**A**) Sketch of the phase diagram
as a function of τ and θ when applying the Floquet sequence $[U_F]^N$ [Fig. 7.1(B)] [287]. The
yellow region indicates the many-body-localized DTC phase. The colored points mark three
combinations of $\{\theta,\tau\}$ that illustrate the DTC phase transition. (**B**) Averaged two-point
correlation $\overline{\chi}$ as a function of the number of Floquet cycles N, for $\theta = 0.95\pi$ and initial
state $|\uparrow\uparrow\uparrow\uparrow\uparrow\uparrow\uparrow\uparrow\uparrow\rangle$. Without interactions (purple), $\overline{\chi}$ decays quickly. With small interactions
($\tau = 1.55$ ms, green), the system is on the edge of the transition to the DTC phase. With
strong interactions ($\tau = 5$ ms, blue), the subharmonic response is stable and persists over all
100 Floquet cycles. (**C**) The corresponding Fourier transforms show a sharp peak at $f = 0.5$
emerging as the system enters the DTC phase. (**D** and **E**) Individual spin expectation
values $\langle\sigma_j^z\rangle$ for interaction times $\tau = 1.55$ ms (D) and $\tau = 5$ ms (E). (**F** and **G**) Averaged
two-point correlation $\overline{\chi}$ (F) and coherence $\overline{C}$ (G) after preparing the superposition state
$[\cos(\pi/8)\,|\uparrow\rangle + \sin(\pi/8)\,|\downarrow\rangle]^{\otimes 9}$ and applying $[U_F]^N$ with $\tau = 5$ ms. The subharmonic response
in $\overline{\chi}$ is preserved, while $\overline{C}$ quickly decays due to interaction-induced local dephasing. The
dashed line in (G) indicates a reference value for $\overline{C}$ measured after preparing the state $|\uparrow\rangle^{\otimes 9}$.

edge of the phase transition, and the interactions begin to stabilize the subharmonic response
[Figs. 7.3(B,C,D)]. Finally, for strong interactions ($\tau = 5$ ms), the subharmonic response
is stabilized despite the perturbations of θ [Figs. 7.3(B,C,E)]. The individual spin measure-
ments confirm that the spins are synchronized and the signature long-lived spatiotemporal
response is observed [Fig. 7.3(E)].

To rule out trivial non-interacting explanations, we prepare the superposition state
$[\cos(\pi/8)\left|\uparrow\right\rangle + \sin(\pi/8)\left|\downarrow\right\rangle]^{\otimes 9}$ and perform full single-qubit tomography for each spin for
different values of N [160]. The two-point correlation $\overline{\chi}$, shows a persistent subharmonic
response similar to the initial state $\left|\uparrow\uparrow\uparrow\uparrow\uparrow\uparrow\uparrow\uparrow\uparrow\right\rangle$ [Fig. 7.3(F)]. In contrast, the coherence
$\overline{C} = \frac{1}{L}\sum_{j=1}^{L}\sqrt{\langle\sigma_j^x\rangle^2 + \langle\sigma_j^y\rangle^2}$ shows a quick decay on a timescale of approximately 10 Flo-
quet cycles, indicating rapid local dephasing due to internal many-body interactions that
generate entanglement across the system [Fig. 7.3(G)].

While the results shown in Fig. 7.3 are consistent with a DTC, these measurements alone
do not distinguish the many-body-localized DTC phase from prethermal responses [287, 256,
313]. In particular, the hallmark of the MBL DTC phase is robust time crystalline order for
generic initial states. Conversely, prethermal responses only exhibit long-lived oscillations
for a particular range of initial states [161, 313, 256].

We study a range of generic initial states of the form $\bigotimes_j^L\left|m_j\right\rangle$, $m_j \in \{\uparrow,\downarrow\}$, including
the Néel state $\left|\uparrow\downarrow\uparrow\downarrow\uparrow\downarrow\uparrow\downarrow\uparrow\right\rangle$ [Fig. 7.4(A)] and 9 additional random states [Figs. 7.4(B,C)].
To illustrate that a variety of states are considered, we evaluate their energy density $\mathcal{E} = \langle H_{\mathrm{eff}}\rangle/J_0 L$, where J_0 is the average nearest-neighbor coupling strength [Fig. 7.1(D)] and H_{eff}
is the leading order term in the Floquet-Magnus expansion of U_F. The selected initial states
extend across the energy spectrum [Fig. 7.4(D)].

The response up to $N = 800$ shows a stable period-doubled signal for all states, consistent
with a DTC stabilized by MBL [Figs. 7.4(A,B)]. The 1/e decay value averaged over the states
is $N_{1/e} = 463(36)$ Floquet cycles — corresponding to a time of ~ 4.6 s [Fig. 7.4(B)], and little
initial state dependence is observed [Fig. 7.4(C)]. In contrast, numerical calculations for a 9-
spin chain with the same average couplings, but without disorder (and thus no MBL phase),
show a strongly state-dependent response. Some initial states show a rapid decay, falling to
1/e within ~ 30 Floquet cycles, and crossing through $\overline{\chi} = 0$ within 300 cycles, showing that
such a prethermal response would be well distinguished within the experimental lifetime.

While the DTC phase in an ideal system is predicted to persist to arbitrary times, any
experimental implementation inevitably decays due to finite-size effects or environmental de-
coherence. Numerical calculations for the spin chain without decoherence yield a long-lived
response (up to $\sim 10^6$ Floquet cycles), showing that the finite size of the chain does not limit
the observed DTC lifetime. A characterization of the decoherence ($T_2 > 4800(900)$ periods)
and relaxation (T_1, none observed) times for the spins shows that these are negligible over
the timescale of the experiments. Therefore, the observed decay likely originates from resid-
ual interactions with the spin environment due to imperfect decoupling under the Floquet
sequence with $\theta \neq 0$. Such decoherence might be mitigated in the future with improved
decoupling sequences.
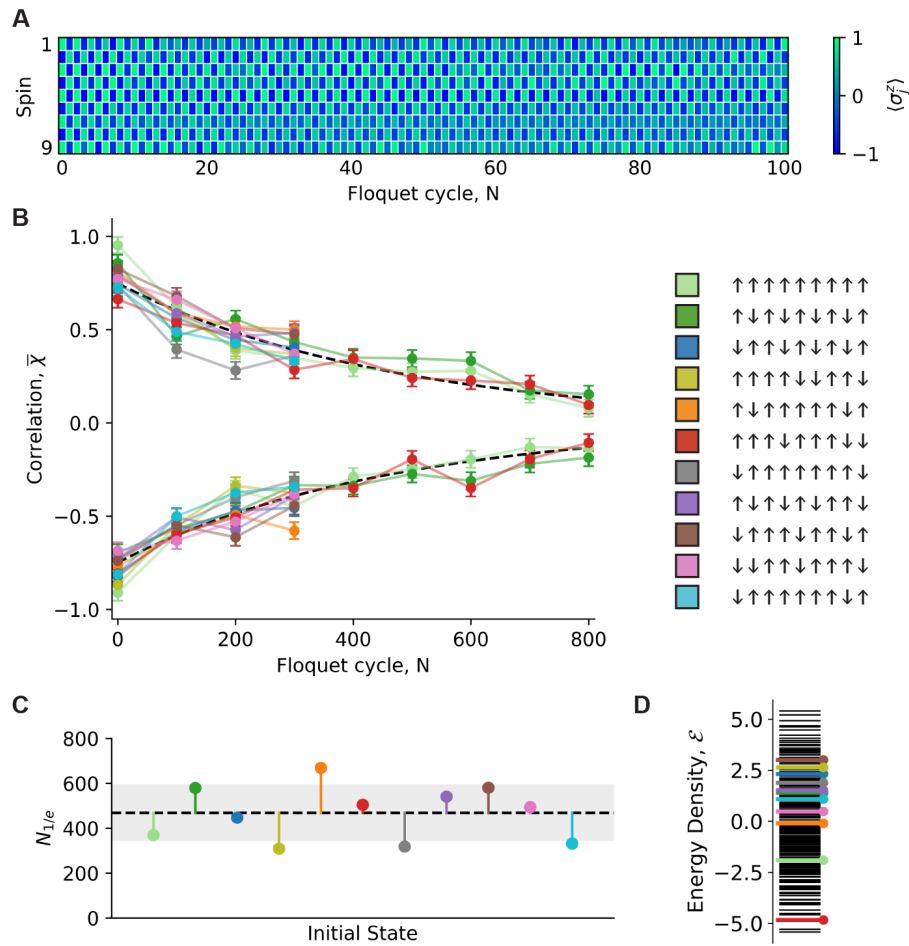
Figure 7.4: **Observation of the DTC response for generic initial states.** (**A**) Individual spin expectation values $\langle \sigma_j^z \rangle$ as a function of N after initializing the spins in the Néel state $|\uparrow\downarrow\uparrow\downarrow\uparrow\downarrow\uparrow\downarrow\uparrow\rangle$ and applying $[U_F]^N$ for $\theta = 0.95\pi$ and $\tau = 5\,\text{ms}$. (**B**) Average correlation for even (upper curve) and odd (lower curve) N for 9 randomly chosen initial states, plus the polarized state and the Néel state (indicated in the legend) with $\theta = 0.95\pi$ and $\tau = 5\,\text{ms}$. Each data point is the average over even/odd integers in the range N to $N + 10$. Three of the states are measured up to $N = 800$, the others to $N = 300$. The dashed black line is a fit of $|\overline{\chi}|$, averaged over all states using a phenomenological function $f(N) = Ae^{-N/N_{1/e}}$, giving $A = 0.75(2)$ and $N_{1/e} = 463(36)$. (**C**) $N_{1/e}$ for each initial state, extracted from a fit to $f(N)$ for the data in (B). The gray shaded region indicates the measurement uncertainty ($\pm 2\sigma$ around the mean) obtained through a Monte Carlo sampling of the fitting procedure. (**D**) Calculated energy density $\mathcal{E}$ (with respect to H_{eff}) for all possible states of the form $\bigotimes_j^L |m_j\rangle$, $m_j \in \{\uparrow, \downarrow\}$ (black lines). Colored lines: states indicated in the legend shown in (B).

7.3 Conclusion

We have present an observation of the hallmark signatures of the many-body-localized DTC phase, complementing subsequent work on a superconducting qubit platform [363]. Compared with previous experiments, the observed time crystalline response is stable for generic initial states, demonstrating robust DTC order across the many-body spectrum. This result highlights the how many-body interactions and disorder culminate in the ergodicity breaking behavior necessary for stabilizing the MBL-DTC phase. This offers a first step towards the realization and understanding of out-of-equilibrium phases of matter in isolated quantum systems. The developed methods also provide new opportunities to investigate other Floquet phases of matter, including topologically protected phases [287], and time-crystalline order in a variety of settings complementary to MBL, such as open systems where the interplay between dissipation and interactions leads to distinct DTC phenomena [201, 589, 321].

From a broader perspective, this work introduces a quantum simulator based on individually controllable solid-state spins that is naturally suited to studying many-body dynamics, adding to the growing toolbox of atomic, molecular and optical platforms for the study of quantum dynamics and computing. By connecting different subsets of spins, larger one-dimensional chains and two- and three-dimensional systems can be realized [548, 98]. The combination of complete programmability through universal individual control, excellent coherence, and site-selective measurement enables the realization of a wide variety of many-body Hamiltonians. Future scalability beyond tens of spins might be achieved by exploiting spins external to the diamond [80, 337], by linking multiple electronic-spin defects through dipolar coupling [144], by photonic remote entanglement [438], or by combinations of these methods.

Chapter 8

Emergent ergodic region between MBL phases

So far in this dissertation, we have focused on the existence and properties of non-thermalizing phases of matter, with a special emphasis on the MBL phase, the only (currently known) robust non-ergodic phase [139, 517, 82, 158]. In this class of systems, the non-thermalizing nature of the dynamics places important constraints on the properties of its eigenstates, such as the area-law scaling of their entanglement entropy and their description as the ground state of quasi-local Hamiltonians [503, 39]. More striking (as experimentally explored in Chapter 7), such systems can also exhibit order that is not limited to its ground or low temperature states, but rather that extends throughout the full spectrum [249, 39, 423, 89, 296, 429]. From a practical perspective, this offers the prospect of preparing and observing the consequences of ordered phases (even topological order) in atomic, molecular and optical platforms, where the lack of a bath makes the preparation of low temperature states difficult [30, 588, 590, 160, 444].

More fundamentally, the presence of order throughout the entire eigenspectrum—dubbed *eigenstate order*—offers an entirely new landscape of ordered phases that is not captured by any previous theoretical framework of phases of matter and their transitions. A particularly intriguing open question is the nature of the phase transition between different types of MBL eigenstate order. Crucially, understanding such transition requires navigating a delicate balance between the properties of localization and phase transitions. On the one hand, the stability of MBL is contingent upon the existence of an extensive number of quasi-*local* conserved quantities ("ℓ-bits") [503, 248, 130]. On the other hand, a well-known property of second-order phase transitions is that correlation length *diverges* as one approaches the transition [477]. Understanding this tension remains an outstanding challenge: while certain studies suggest the presence of a direct transition between distinct MBL phases [296, 429, 552, 184, 551, 590], others have found signatures of delocalization at the transition [290, 88, 561].

In this chapter, we conjecture that any transition between distinct MBL phases is invariably forbidden and that an intervening ergodic phase always emerges [Fig. 8.1(a)]. This
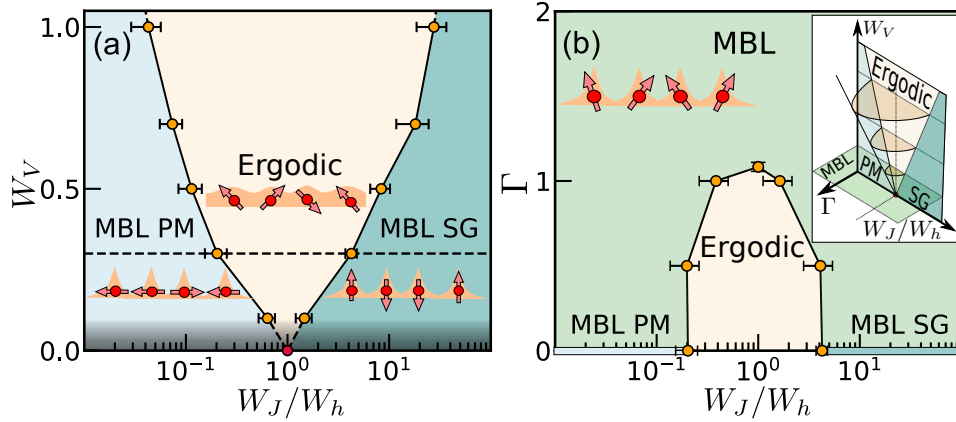
Figure 8.1: **Phase diagram for $\mathbb{Z}_2$ symmetric, disordered, interacting model. (a)** Phase diagram of the symmetry breaking model, Eq. 8.1, as a function of W_J/W_h and interaction strength W_V. For all numerically accessible W_V (outside the shaded region), we observe a finite width ergodic region between the two different MBL phases (PM and SG). At $W_V = 0$, the system is non-interacting and exhibits a critical point at $W_J/W_h = 1$ (red point). **(b)** Phase diagram as a function of a symmetry breaking field Γ and W_J/W_h for $W_V = 0.3$. With increasing Γ, the size of the ergodic region decreases until the system remain localized for all W_J/W_h. (inset) Schematic of the full phase diagram as a function of W_J/W_h, W_V and Γ.

conjecture is motivated by an extensive numerical study of three classes of MBL transitions: (i) a symmetry-breaking transition, (ii) a symmetry-protected topological (SPT) transition, and (iii) a discrete time crystalline transition (in a Floquet system). By systematically constructing the various phase diagrams, we show that an intervening ergodic region emerges for all numerically-accessible interaction strengths. Moreover, we demonstrate that this emergent ergodicity is intimately tied to the presence of a phase transition; a *disorder-less*, symmetry-breaking field suppresses the intervening ergodic phase. In addition to numerics, we analyze two instabilities which could induce thermalization near the putative transition: (i) the proliferation of two-body resonances [37, 18, 396] and (ii) the run-away of avalanches [130, 114]. We find that the latter is marginal. Finally, we propose and analyze an experimental platform capable of directly exploring the emergence of ergodicity at the transition between MBL phases. Our proposal is motivated by recent advances in Rydberg-dressed, neutral-atom quantum simulators [35, 97, 598, 46, 105, 135, 573, 346]; we demonstrate that the phase diagram depicted in Fig. 8.1 can be directly probed via quench dynamics of local observables within experimental decoherence time-scales.
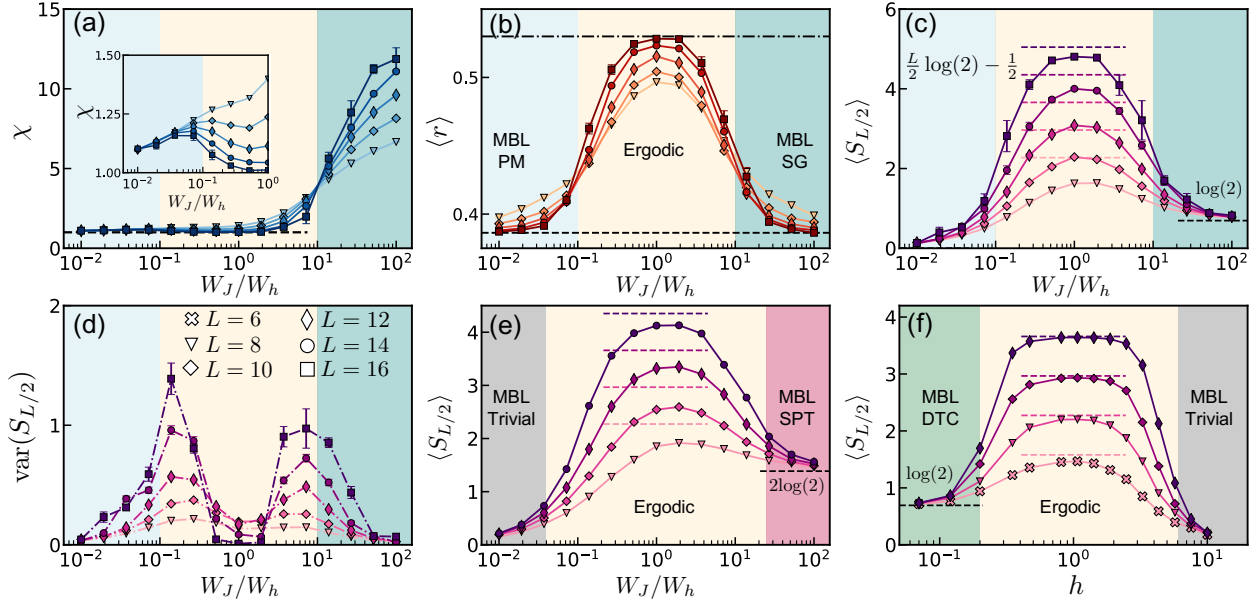
Figure 8.2: **Evidence for intermediate ergodic phase between any two MBL phases.**
(a-d) Characterization of the symmetry breaking model, Eq. 8.1, for $W_V = 0.7$. **(a)** For $W_J/W_h \gtrsim 10$, χ increases with system size evincing the SG nature of the phase. In the PM phase, χ approaches a finite constant, albeit exhibiting two distinct behaviors (inset). **(b)** $\langle r \rangle$-ratio as a function of W_J/W_h reveals an intervening ergodic phase surrounded by two localized phases. The dash-dotted [dashed] line corresponds to the GOE [Poisson] expectation. **(c)** The half-chain entanglement entropy $S_{L/2}$ increases with system size for intermediate W_J/W_h, in agreement with the expected thermal volume-law. In the two localized phases, $S_{L/2}$ saturates to different values, highlighting the distinct nature of the underlying eigenstate order. **(d)** The variance of $S_{L/2}$ exhibits two distinct peaks in agreement with the presence of two distinct transitions. **(e)[(f)]** $S_{L/2}$ for the SPT [DTC] model of Eq. 8.2 [Eq. 8.3] also demonstrates the presence of an intervening ergodic phase. Each data point corresponds to averaging over at least 10^3 disorder realizations.

8.1 Symmetry-breaking MBL order

Let us begin by considering the paradigmatic example of a disordered one dimensional spin chain, which hosts two distinct MBL phases:

$$H = \sum_i J_i \sigma_i^z \sigma_{i+1}^z + \sum_i h_i \sigma_i^x + \sum_i V_i (\sigma_i^x \sigma_{i+1}^x + \sigma_i^z \sigma_{i+2}^z), \qquad (8.1)$$

where $\vec{\sigma}$ are Pauli operators and all coupling strengths are disordered, with $J_i \in [-W_J, W_J]$, $h_i \in [-W_h, W_h]$, and $V_i \in [-W_V, W_V]$.[1] We choose to work with the normalization $\sqrt{W_J W_h} = 1$ and perform extensive exact diagonalization studies up to system size $L = 16$. In the absence of V_i, the system reduces to the non-interacting, Anderson localized limit and for sufficiently strong disorder (in J_i and h_i), this localization persists in the presence of interactions.

The Hamiltonian (Eq. 8.1) exhibits a $\mathbb{Z}_2$ symmetry corresponding to a global spin-flip, $G = \prod_i \sigma_i^x$. In the many-body localized regime, two distinct forms of eigenstate order emerge with respect to the breaking of this symmetry. For $W_h \gg W_J, W_V$, the transverse field dominates and the system is in the MBL paramagnetic (PM) phase. The conserved ℓ-bits simply correspond to dressed versions of the physical σ_i^x operators. For $W_J \gg W_h, W_V$, the Ising interaction dominates and the eigenstates correspond to "cat states" of spin configurations in the $\hat{z}$ direction. Physical states break the associated $\mathbb{Z}_2$ symmetry, the ℓ-bits are dressed versions of $\sigma_i^z \sigma_{i+1}^z$, and the system is in the so-called MBL spin-glass (SG) phase [249, 296].

These two types of eigenstate order can be distinguished via the Edwards-Anderson order parameter which probes the presence of long-range Ising correlations in eigenstates $|n\rangle$, $\chi = \langle\langle L^{-1} \sum_{i,j} \langle n| \sigma_i^z \sigma_j^z |n\rangle^2 \rangle\rangle$, where $\langle\langle \cdots \rangle\rangle$ denotes averaging over disorder realizations [296, 551]. In the SG phase, this order parameter scales extensively with system size, $\chi \propto L$, while in the PM phase, it approaches a constant $\mathcal{O}(1)$ value. Fixing $W_V = 0.7$, χ exhibits a clear transition from PM to SG as one tunes the ratio of W_J/W_h [Fig. 8.2(a)]. The finite-size flow of χ is consistent with the presence of a *single* critical point at $W_J = 3.2, W_h = 0.32$ ($W_J/W_h \approx 10$).

However, thermalization diagnostics tell a different story. In particular, we compute the $\langle r \rangle$-ratio, a measure of the rigidity of the many-body spectrum:

$$\langle r \rangle = \langle\langle \min\{\delta_n, \delta_{n+1}\}/\max\{\delta_n, \delta_{n+1}\} \rangle\rangle,$$

where $\delta_n = E_{n+1} - E_n$, E_n is the nth eigenenergy and averaging is also done across the entire many-body spectrum [406, 418]. In the MBL phase, energy levels exhibit Poisson statistics with $\langle r \rangle \approx 0.39$, while in the ergodic phase, level repulsion leads to the GOE expectation $\langle r \rangle \approx 0.53$ [6, 395, 517]. Unlike χ, which exhibits a single transition, the $\langle r \rangle$-ratio exhibits two distinct critical points, each characterized by its own finite-size flow [Fig. 8.2(b)]. This demarcates three distinct phases: two many-body localized phases (for $W_J/W_h \lesssim 0.1$ and

---

[1] We remark that up to edge effects, the model is dual under the Kramers-Wannier map ensuring that any direct transition between the MBL SG and MBL PM phases must occur at $W_J/W_h = 1$.

$W_J/W_h \gtrsim 10$) separated by an intervening ergodic phase. Interestingly, the location of the ergodic-MBL transition at $W_J/W_h \approx 10$ matches the location of the spin-glass transition observed via χ. The fact that an additional ergodic-MBL transition is observed in the $\langle r \rangle$-ratio, but not in χ, suggests that the PM regime has slightly more structure.

In order to further probe this structure, we turn to the half-chain entanglement entropy, $S_{L/2} = -\text{Tr}[\rho_s \log(\rho_s)]$, where $\rho_s = \text{Tr}_{i \le L/2}[|n\rangle \langle n|]$ [296, 6, 6, 340, 503, 338, 508, 289, 150, 15, 532]. The behavior of $S_{L/2}$, illustrated in Fig. 8.2(c), allows us to clearly distinguish three phases: the MBL paramagnet, the ergodic paramagnet, and the MBL spin-glass. For $W_J/W_h \ll 0.1$, the eigenstates are close to product states and the entanglement entropy $S_{L/2}$ is independent of L, consistent with a localized paramagnet. Near $W_J/W_h \approx 1$, $S_{L/2}$ increases with system size, approaching $(L \log 2 - 1)/2$, consistent with an ergodic paramagnet [416]. Finally, for $W_J/W_h \gg 10$, the half-chain entanglement again becomes independent of L and, for very large W_J/W_h, approaches $\log 2$, consistent with the cat-state-nature of eigenstates in the MBL SG phase.

A few remarks are in order. First, the variance of $S_{L/2}$ across the ensemble of disorder realizations provides a complementary diagnostic to confirm the presence of two distinct ergodic-MBL transitions [Fig. 8.2(d)] [296, 340, 338, 508, 290, 289, 150, 15, 532]. Indeed, one observes two well-separated peaks in $\text{var}(S_{L/2})$, whose locations are consistent with the transitions found in the $\langle r \rangle$-ratio. Second, although χ only scales with system size in the SG phase, one expects its behavior to be qualitatively different in the MBL versus ergodic paramagnet. In particular, in the MBL paramagnet, the ℓ-bits have a small overlap with $\sigma_i^z \sigma_j^z$ and one expects $\chi > 1$; meanwhile, in the ergodic paramagnet, for a state chosen at the center of the many-body spectrum, one expects that $\chi \to 1$ rapidly with increasing system size (owing to the eigenstate thermalization hypothesis) [517, 139, 463, 518]. This is indeed borne out by the numerics, as shown in the inset of Fig. 8.2(a).

Diagnostics in hand, we now construct the full phase diagram as a function of W_V and W_J/W_h [Fig. 8.1(a)]. Even for the smallest interaction strengths accessible $W_V \sim 0.07$ (i.e. where the minimum interaction coupling remains larger than the mean level spacing) one observes a finite width region where the $\langle r \rangle$-ratio increases with system size [420, 6, 421, 89, 225].

Effect of symmetry breaking field

To verify that the presence of a phase transition is indeed responsible for the intervening ergodic region, one can explicitly break the $\mathbb{Z}_2$ symmetry in Eq. 8.1. We do so by adding a *disorder-less*, on-site longitudinal field, $\Gamma \sum_i \sigma_i^z$. Despite the fact that the field is uniform, it causes the $\langle r \rangle$-ratio to systematically decrease [Figs. 8.3(a,b)], and for a sufficiently large symmetry breaking field, all finite-size flow tends toward localization. This allows us to construct the phase diagram in the presence of finite Γ, as depicted in Fig. 8.1(b).
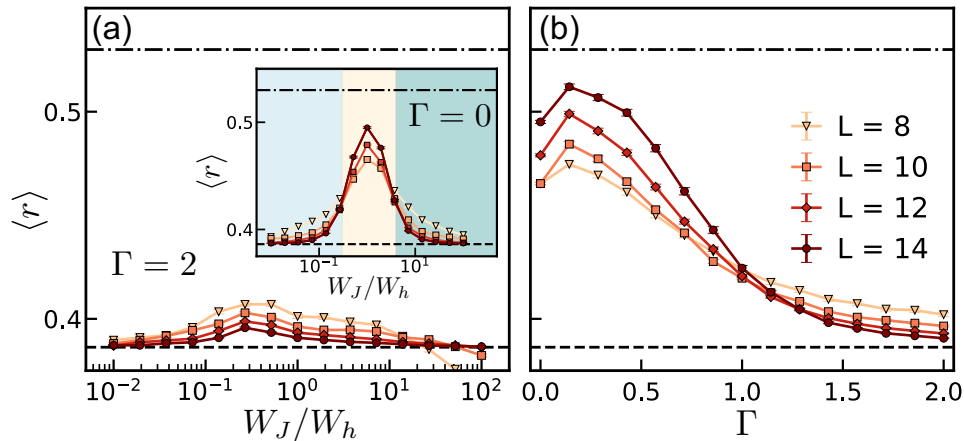
Figure 8.3: **Presence of a symmetry breaking field increases robustness of MBL phase.** **(a)** $\langle r \rangle$-ratio as a function of W_J/W_h at $W_V = 0.3$ in the presence of an explicit symmetry breaking field $\Gamma = 2$. The dash-dotted [dashed] line corresponds to the GOE [Poisson] expectation. Unlike the symmetry respecting case ($\Gamma = 0$, inset), the system remains localized for all values of W_J/W_h. **(b)** Within the ergodic region (here with $W_J/W_h = 1$), an increasing symmetry-breaking field drives the system towards localization. Each data point corresponds to averaging over at least 3×10^2 disorder realizations.

8.2 Other types of MBL order

To understand the generality of an emergent ergodic region between many-body localized phases, we now consider two additional types of MBL transitions: a symmetry-protected topological (SPT) transition and a discrete time-crystalline (DTC) transition. The Hamiltonian of the SPT model is given by:[2]

$$H_{\mathrm{SPT}} = \sum_i J_i \sigma_{i-1}^z \sigma_i^x \sigma_{i+1}^z + \sum_i h_i \sigma_i^x$$
$$+ \sum_i V_i (\sigma_i^x \sigma_{i+1}^x + \sigma_{i-1}^z \sigma_i^y \sigma_{i+1}^y \sigma_{i+2}^z) \ , \tag{8.2}$$

with $J_i \in [-W_J, W_J]$, $h_i \in [-W_h, W_h]$, and $V_i \in [-W_V, W_V]$. H_{SPT} exhibits a $\mathbb{Z}_2 \times \mathbb{Z}_2$ symmetry, which gives rise to an MBL SPT (Haldane) phase for $W_J \gg W_h, W_V$ and a topologically-trivial MBL phase for $W_J \ll W_h, W_V$ [29, 89, 30]. For the DTC model, we consider the Floquet unitary evolution $U_F = \mathcal{T} \exp\left(-i \int_0^T dt \ H_F(t)\right)$ generated by the stro-

---

[2]We chose the form of our interaction such that, in the thermodynamic limit, the MBL SPT and MBL PM are dual to one another under the duality transformation $\sigma_i^z \to \sigma_i^z \sigma_{i+1}^x$ and $\sigma_i^x \to \sigma_{i-1}^x \sigma_i^x \sigma_{i+1}^z$.

boscopic Hamiltonian:

$$H_F(t) = \begin{cases} \sum_i J_i \sigma_i^z \sigma_{i+1}^z + h_i \sigma_i^x + V_i \sigma_i^z & t \in [0, T/2] \\ -\frac{\pi}{T} \sum_i \sigma_i^x & t \in [T/2, T) \end{cases} \tag{8.3}$$

where $J_i \in [0.5, 1.5]$, $T = 2$, $h_i \in [0, h]$ and $V_i \in [0, 2V]$. When $h \ll 1$, the Floquet system spontaneously breaks time-translation symmetry and is in the so-called DTC phase, while for $h \gg 1$, the system is in a Floquet paramagnetic phase [160, 590, 290, 439, 602, 3]. We analyze each of these models using the four diagnostics previously described: (i) the order parameter, (ii) the $\langle r \rangle$-ratio, (iii) the half-chain entanglement, and (iv) the variance, $\text{var}(S_{L/2})$. We observe the same qualitative behavior for both transitions across all diagnostics: An intervening ergodic phase emerges which terminates at the non-interacting critical point. This is illustrated in Figs. 8.2(e,f) using $S_{L/2}$ for both the SPT model (for an eigenstate of H_{SPT} at zero energy density) and the DTC model (for an eigenstate of U_F at π quasi-energy). We have also analyzed the finite-size effects arising from small couplings, which we believe underlie previous numerical observations of apparent direct transitions [590, 184, 551, 552].

8.3 Experimental realization

Motivated by recent advances in the characterization and control of Rydberg states, we propose an experimental protocol to directly explore the emergence of ergodicity between MBL phases. Our protocol is most naturally implemented in one dimensional chains of either alkali or alkaline-earth atoms [35, 97, 598, 46, 105, 135, 573, 346]. To be specific, we consider ^{87}Rb with an effective spin-1/2 encoded in hyperfine states: $|\downarrow\rangle = |F = 1, m_F = -1\rangle$ and $|\uparrow\rangle = |F = 2, m_F = -2\rangle$. Recent experiments have demonstrated the ability to generate strong interactions via either Rydberg-dressing in an optical lattice (where atoms are typically spaced by ~ 0.5 μm) or via Rydberg-blockade in a tweezer array (where atoms are typically spaced by ~ 3 μm) [35, 97, 598, 46, 105, 135, 573, 346]. Focusing on the optical lattice setup, dressing enables the generation of tunable, long-range soft-core Ising interactions, $H_{ZZ} = \sum_{i,j} J_{ij} \sigma_i^z \sigma_j^z$, with a spatial profile that interpolates between a constant at short distances (determined by the blockade radius) and a $1/r^6$ van der Waals tail.

A particularly simple implementation of a PM-SG Hamiltonian (closely related to Eq. 8.1) is to alternate time evolution under H_{ZZ} and $H_X = \sum_i h_i \sigma_i^x$, with the latter being implemented via a two-photon Raman transition [Fig. 8.4(a)]. In the high frequency limit, the dynamics are governed by an effective Hamiltonian:

$$H_{\text{eff}} = \frac{\tau_1}{\tau_1 + \tau_2} \sum_i h_i \sigma_i^x + \frac{\tau_2}{\tau_1 + \tau_2} \sum_{ij} J_{ij} \sigma_i^z \sigma_j^z \; , \tag{8.4}$$

where H_X is applied for time τ_1, H_{ZZ} is applied for time τ_2, and the Floquet frequency $\omega = 2\pi/(\tau_1 + \tau_2) \gg h_i, J_{ij}$. This latter inequality ensures that both Floquet heating and higher-order corrections to H_{eff} can be safely neglected on experimentally relevant time-scales
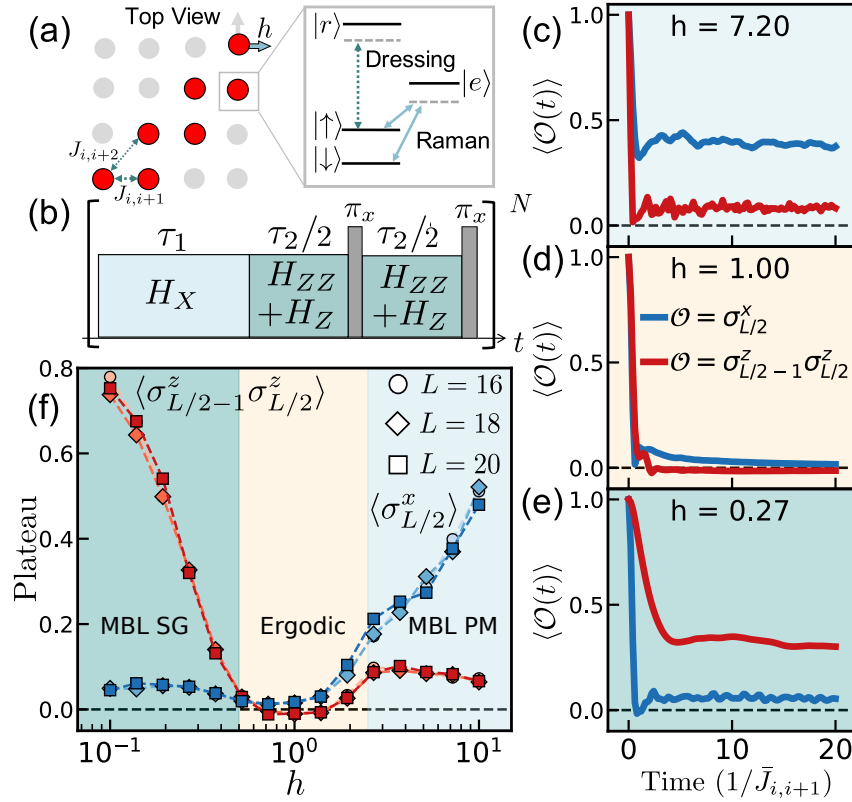
Figure 8.4: **Experimental proposal for observing intervening ergodic phase. (a)** Schematic of the proposed experimental protocol. Within an optical lattice, neutral atoms are prepared along two adjacent diagonals (i.e. with a gas microscope), defining a zig-zag spin chain configuration. Dressing with a Rydberg state $|r\rangle$ leads to H_{ZZ} with an additional onsite field $H_Z \propto \sum_i \sigma_i^z$, while a two-photon Raman transition mediated by an excited state $|e\rangle$ leads to H_X. **(b)** By combining rapid spin echo pulses with Floquet evolution under H_X and $H_{ZZ} + H_Z$, one can engineer H_{eff} (Eq. 8.4). **(c-e)** Dynamics of $\sigma_{L/2}^x$ (blue) and $\sigma_{L/2-1}^z\sigma_{L/2}^z$ (red) under H_{eff} starting with initial states $|\psi_x\rangle$ and $|\psi_{zz}\rangle$, respectively. Different panels correspond to representative behaviors for the three distinct phases (tuned via h). **(f)** The height of the late-time plateau distinguishes between the three phases. Each data point corresponds to averaging over at least 10^2 disorder realizations.

[4, 344]. Note that unlike the DTC model (Eq. 8.3), here Floquet engineering is being used to emulate a static MBL PM-SG Hamiltonian [444, 98].

Although our prior analysis has focused on eigenstate properties, we will now demonstrate, that the phase diagram can also be characterized via the dynamics of local observables. To investigate this behavior, we use Krylov subspace methods [361, 233, 232, 33] to numerically simulate the dynamics of H_{eff} with $\tau_1 = \tau_2 = 1$, $J_{i,i+1} \in [-1, -3]$, $J_{i,i+2} = 0.6J_{i,i+1}$

and $h_i \in [h, 3h]$. We note that the ratio of the nearest- to next-nearest-neighbor coupling strength is chosen based upon the experimentally measured Rydberg-dressing-interaction profile and a 1D zig-zag chain geometry [Fig. 8.4(a)] [598, 210].[3]

For system sizes up to $L = 20$, we compute the dynamics of initial states $|\psi_x\rangle$ and $|\psi_{zz}\rangle$;[4] both states are easily preparable in experiment, close to zero energy density, and chosen such that $\langle\psi_x|\sigma^x_{L/2}|\psi_x\rangle = 1$ and $\langle\psi_{zz}|\sigma^z_{L/2-1}\sigma^z_{L/2}|\psi_{zz}\rangle = 1$. Starting with $|\psi_x\rangle$ as our initial state and large h, we observe that $\langle\sigma^x_{L/2}(t)\rangle$ plateaus to a finite value at late-times, indicating the system is in the MBL PM phase [Fig. 8.4(c)]. Analogously, for $|\psi_{zz}\rangle$ and small h, we observe that $\langle\sigma^z_{L/2-1}(t)\sigma^z_{L/2}(t)\rangle$ plateaus to a finite value at late-times, indicating the system is in the MBL SG phase [Fig. 8.4(e)]. For $h \sim 1$, *both* observables decay to zero, indicating the system is the ergodic phase [Fig. 8.4(d)]. The plateau value of the two observables as a function of h clearly identifies the intervening ergodic region [Fig. 8.4(f)].

To ensure that one can observe the intervening ergodic phase within experimental coherence times, we now estimate the time-scales necessary to carry out our protocol. Previous experiments using Rydberg dressing have demonstrated coherence times $T_2 \sim 1$ ms, with nearest neighbor couplings $J_{i,i+1} \sim (2\pi) \times 13$ kHz and a microwave-induced π-pulse duration ~ 25 μs [598]. Taken together, this leads to an estimate of ~ 55 μs for the Floquet period [Fig. 8.4(b)]. Crucially, within T_2 (i.e. ~ 20 Floquet cycles), all observables approach their late-time plateaus.

8.4 Analytic discussion

We now turn to discussing previous analytical results and how they may shed light on the origins of the intervening ergodic phase. For more details see Appendix A. In the absence of interactions, the Hamiltonian transitions we consider all fall into infinite-randomness universality classes characterized by both a divergent single-particle density of states (DOS, $D(\varepsilon) \sim |\varepsilon \log^3 \varepsilon|^{-1}$ near zero single-particle energy ε) and single-particle orbitals with diverging mean and typical localization lengths ($\xi_{\text{mean}} \sim |\log^2 \varepsilon|$ and $\xi_{\text{typ}} \sim |\log \varepsilon|$ respectively) [170, 179, 34, 355, 404, 311]. These divergences suggest that two-body resonances might directly destabilize MBL upon the introduction of interactions; however, a simple counting of resonances in typical blocks does not produce such an instability: In a block of length l, there are $lN(\varepsilon)$ "active" single particle orbitals with $\xi_{\text{typ}}(\varepsilon) \geq l$, where $N(\varepsilon) = \int^\varepsilon d\varepsilon' \, D(\varepsilon')$ is the integrated DOS [396, 591]. These orbitals overlap in real space and are thus susceptible to participating in perturbative two-body resonances. A perturbative instability of the localized state arises if lN diverges as $\varepsilon \to 0$; even for arbitrarily small interactions, a large network of resonant pairs can be found at low enough energy. Using the DOS and local-

---

[3]An analogous behavior can be found in a linear geometry where the ration between nearest and next-nearest neighbor interactions is $J_{i,i+2} = 0.2J_{i,i+1}$.

[4]$|\psi_x\rangle$ is polarized along $+\hat{y}$ except at sites $L/2, L/2+1$ where it is polarized in the $+\hat{x}$ and $-\hat{x}$ direction respectively. Analogously $|\psi_{zz}\rangle$ is polarized along $+\hat{y}$ except at sites $L/2 - 1$ through $L/2 + 2$ where the spins are polarized in the $\hat{z}$ direction with the pattern $\uparrow\uparrow\downarrow\downarrow$.

ization lengths of the infinite-randomness transition, we find $lN \sim 1/|\log \varepsilon|$ which vanishes slowly as $\varepsilon \to 0$.

Alternatively, one might consider the susceptibility to 'avalanches' due to rare thermal bubbles induced by the interactions [339, 533, 130]. For a system with a distribution of localization lengths, it has recently been shown that the *average* localization length controls this instability [114]: for $\overline{\xi} > 2/\log 2$, thermal bubbles avalanche. However, this is within a model where the orbitals have a single localization center. Near the infinite-randomness transition, the orbitals have two centers whose separation is controlled by ξ_{mean} but whose overlap onto a putative thermal bubble is controlled by ξ_{typ}. Thus, while $\overline{\xi_{\mathrm{mean}}}$ diverges logarithmically, the more appropriate $\overline{\xi_{\mathrm{typ}}}$ remains finite and this criterion does not produce an absolute instability.

Finally, let us note that the direct numerical observation of avalanche instabilities remains extremely challenging [130, 443]; the presence of a robust intervening ergodic region in our study suggests that an alternate mechanism might be at the heart of our observations.

8.5 Conclusion

Our work provides a systematic study of the nature of the transition between different MBL phases, finding evidence that no direct MBL-to-MBL phase transition occurs. Instead, the system's ability to overcome thermalization is challenged near phase transitions, owing to the increase in the system's correlation length which induces new resonance processes that are leveraged to restore the ergodicity of the system. Curiously, owing to the system size limitations of our study, we expect the observed behavior to not be related to the avalanche instability [130]. This offers the tantalizing possibility, that there are other, more dominant, mechanisms that drive the system towards ergodicity—at least near phase transitions.

Chapter 9

An absolutely stable open time crystal

One of the main focuses of this dissertation is understanding how novel out-of-equilibrium phenomena emerge; in particular, when are novel out-of-equilibrium phases of matter stable and what are their properties. An important setting for such phenomena is that of interacting periodically-driven (Floquet) systems [445, 290, 160, 590, 601, 100, 163], where the time-dependent nature of the equations of motion implies that any steady state will exhibit interesting non-equilibrium-like dynamics (unless the system approaches the trivial infinite temperature state).

Thus far, the study of such out-of-equilibrium phenomena has been largely focused on two scenarios: First, within the context of quantum "many-body-localized" (MBL) Floquet phases [296, 395, 439, 290, 160, 590, 6]. The ergodicity-breaking nature of MBL prevents the periodic drive from heating the system to infinite temperature, and thus the system does not need to be coupled to a dissipative bath to dissipate energy. As a result, although the dynamics are driven, they remain purely unitary [70, 3, 568]. An immediate consequence, as discussed in Chapter 4, is that the eigenstates of the Floquet evolution have area-law entanglement, which allows their mapping to the dynamics and properties to those of quantum ground states, where order and phases of matter can be more easily understood [249, 89, 30, 444]. Second, there are "prethermal" Floquet phases which heat only exponentially slowly due to a mismatch between the driving frequency and the natural frequencies of the un-driven system [4, 161, 600, 379, 344, 345, 313, 592, 435, 163]. During the exponentially long time-scale before heating, these systems can exhibit behavior which is analogous to order in finite temperature equilibrium phases [161, 345, 592, 435]. However, prethermal Floquet phases are not, in a strict sense, true thermodynamic phases of matter, because they are distinguished from disordered behavior via crossovers, rather than sharp transitions [163], despite exhibiting the phenomenology of finite temperature equilibrium phases for an exponentially long window in time. In Part III, we return to the discussion of prethermal phases of matter.

The most paradigmatic example of a Floquet phase of matter is the so-called discrete time crystal (DTC)—starting from a generic initial state, at long times the DTC relaxes into a steady state with a temporal periodicity which is a multiple of the drive's [290, 160, 590] (see
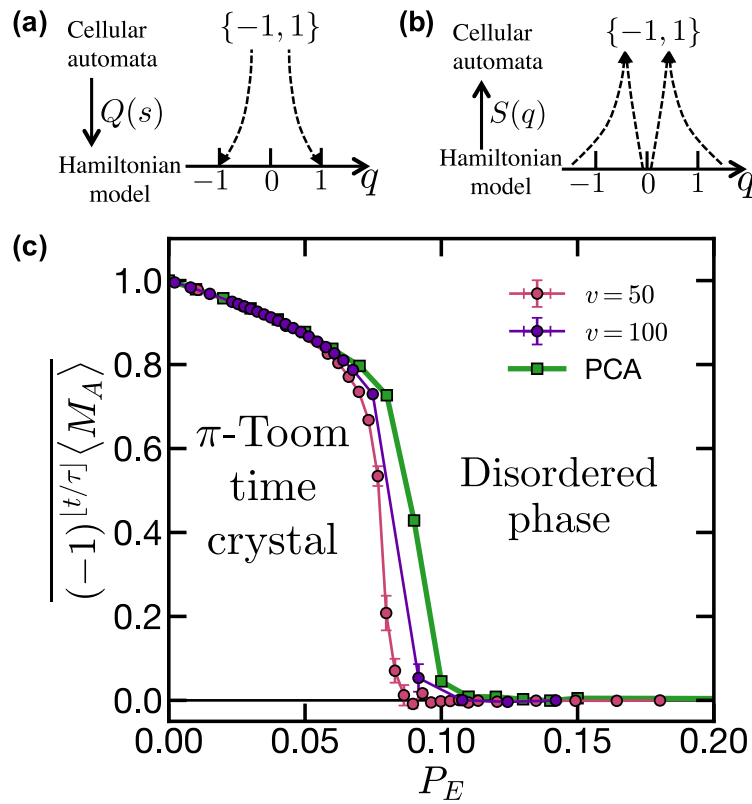
Figure 9.1: **Discrete time crystalline order in a driven, dissipative classical system.** **(a,b)** Schematic of the translation between the discrete state space of a cellular automata and the continuous state space of a Hamiltonian model. **(c)** Time crystalline order parameter (e.g. stroboscopic magnetization) as a function of the error probability. The phase transition from a discrete time crystal to the disordered phase is shown for both a Floquet Langevin simulation of the π-Toom model with pinning potential $v = 50, 100$, as well as for a direct implementation of the probabilistic cellular automata (PCA).

Chapter 7 for a discussion of its experimental observation). This behavior is stable to small perturbations of the dynamics that respect the underlying time-translation symmetry of the drive, and thus, is "rigid" in the same way that equilibrium phases of matter are. We note that, somewhat similar behavior has been studied within the context of non-linear dynamics and falls under the name of "subharmonic entrainment" or "asymptotic periodicity" [317, 336, 195, 427]; for a discussion of how this earlier work differs from results in the quantum many-body regime, we refer the reader to [589, 163, 287].

It is natural to then ask if "true", thermodynamically stable time crystals exist beyond MBL. Without MBL to prevent heating, stabilizing time crystalline order presumably require coupling to a dissipative bath [320, 609, 405, 284, 499, 321, 57, 285]. Combining periodic driving and a dissipative bath introduces the full complexity of non-equilibrium dynamics [320, 543, 335, 69, 112, 193, 192, 321, 141, 284, 285, 526].

Thinking microscopically, classical driven dissipative systems are described by Hamiltonian dynamics coupled to a finite-temperature Langevin bath, or in the quantum case, periodically driven Lindbladian evolution. A key feature of both these contexts is that, if the bath is dissipative, at finite temperature it is also accompanied by noise due to the fluctuation-dissipation theorem. At zero temperature, where there is damping but no noise, many-body time crystals can occur rather trivially by analogy to the "period doubling" behavior of coupled iterated logistic maps [273, 276, 77, 272, 274]. In this chapter we will then focus on the following key question: *Can true time crystals exist in a periodically driven system of locally interacting particles coupled to an equilibrium bath at finite temperature?*

We argue in the affirmative: finite-temperature time crystals [572, 504], with an *infinite* auto-correlation time, can exist even in translation-invariant arrays of classical, non-linear, locally interacting oscillators. To do so, we leverage non-trivial results in the field of probabilistic cellular automata (PCA) [580]. A PCA is a deterministic cellular automata (CA) perturbed by stochastic errors, mimicking the effect of finite temperature, making it a simplified model of finite-temperature non-equilibrium dynamics. Using results of Gács (1D) [188, 207] and Toom (2D) [537, 43, 347], we show that that local PCAs can exhibit time crystalline behavior stable to arbitrary small perturbations. Unlike MBL or prethermal time crystals, such time crystalline order is "absolutely stable", in the sense that it remains robust *even* in the presence of perturbations that break the discrete time-translation symmetry of the periodic drive.

However, one may wonder whether these PCA results can be applied to the physical setting of interest — classical Langevin dynamics—which is constrained, for example, by the symplectic structure of Hamiltonian's dynamics and the fluctuation-dissipation theorem. To this end, we show how classical Langevin dynamics can be used to "simulate" PCA dynamics, and further provide numerical evidence that the errors due to Langevin noise are of a type covered by Gács' and Toom's mathematical results. Applying this to a 2D array of locally interacting mechanical oscillators, Langevin simulations reveal a finite-temperature phase transition between a discrete time crystal and a disordered phase, Fig. 9.1.

Our work demonstrates that discrete time crystals can exist in driven classical systems coupled to a bath, even when the periodic drive is imperfect. In contrast to previous mecha-

nisms for realizing DTC order, including many-body localization and prethermalization, the perturbations can even systematically violate the time-translation symmetry of the drive, making such behavior "absolutely stable" in the strongest possible sense.

9.1 Time crystals in a PCA: the π-Toom and π-Gács models

We begin by reviewing the definition of a PCA, and explain how the results of Gács and Toom imply the existence of time crystals in this setting [537, 188, 207, 209]. Much like a CA, the state of a PCA is given by a particular configuration $\{\eta(x)\}$, where $x \in \Lambda$ labels sites in a regular lattice Λ and each $\eta(x)$ corresponds to the state of that sites and takes values in a set $\mathcal{S} = \{1, 2, \cdots, d\}$. In a CA, the dynamics are governed by a deterministic, local transition rule [546, 401],

$$\{\eta(\boldsymbol{x}, t+1)\} = \mathcal{T}[\{\eta(\boldsymbol{x}, t)\}] \tag{9.1}$$

[Fig. 9.2(a)]. In a PCA, the dynamics are generalized to be a Markov process described by the transition matrix $M_{\eta \to \eta'}$, which characterizes the *probability* to evolve from configuration η to η' [536, 124, 189]. M should be also be local in the sense that the update distribution of a local state depends only on the state of sites on some finite range "neighborhood" $\mathcal{N}$.

A particularly natural class of PCAs arise by starting with a deterministic CA and perturbing it with an "error rate" ϵ. More concretely, at each step, the system follow the rule $\mathcal{T}$ (as in Eq. 9.1), and then, with a probability bounded by ϵ, some error can occur that changes the system to a different state. One can think of the resulting Markov process as a perturbation to the deterministic one, $M = \mathcal{T} + \epsilon \Delta M$, where ΔM determines the precise error distribution. The mathematical results we will describe can also account for even more general (non-Markovian) error models, as we will describe shortly [188, 187].

A time crystal be easily realized in a deterministic CA with $\mathcal{S} = \{-1, 1\}$: for example, the rule $1 \leftrightarrow -1$. In fact, since CA are capable of universal classical computation, they can realize any dynamical phenomena which can be programmed on a computer [104]. Whether a PCA can realize a stable time crystal is significantly more subtle. The long-time dynamics of a PCA are described by the stationary probability distributions $\mathcal{P}[\eta]$ of M, (i.e. $M\mathcal{P}[\eta] = \mathcal{P}[\eta]$). We say M exhibits an n-fold subharmonic response if there are $n > 1$ distinct distributions, $\mathcal{P}_i[\eta]$, such that $M\mathcal{P}_i[\eta] = \mathcal{P}_{i+1}[\eta]$, with $\mathcal{P}_n = \mathcal{P}_0$. This simply formalizes the notion of long-time oscillations: at long times a generic initial state will relax into to a non-uniform convex combination $\sum_i p_i \mathcal{P}_i$ which is stationary under M^n, but not M. Such behavior has also been referred to as asymptotic periodicity [317]. In this context, a time crystal is defined to be a local PCA with a *stable* n-fold subharmonic response: for sufficiently small but arbitrary local perturbations ΔM, $M + \Delta M$ should retain its n-fold subharmonic response. This motivates the following sharp question: Do PCA time crystals exist [44]?

To see why the this question is subtle, one can consider what happens when CA rule $1 \leftrightarrow -1$ is perturbed by random errors at rate ϵ. Over a timescale $\sim 1/\epsilon$, each spin will

forget its initial state and relax to the maximally mixed distribution. As a result, one has to leverage interactions to induce stability. Indeed, systems that are characterized by long-range interactions can stabilize DTC behavior [349, 433]. However, even with local interactions, Bennett et al. [44] argued that PCAs could give rise to stable subharmonic responses—a result we exploit in recent work [193]. A particularly simple candidate for a PCA with time translation symmetry breaking is a Majority-vote rule followed by a cyclic permutation [193]. However, as pointed out by Bennett et al. [44], this rule is not a stable time crystal for any period $k > 2$.

Ergodicity breaking in a PCA

One prerequisite for a time crystal is ergodicity breaking. A PCA is "ergodic" if it has a unique stationary distribution, so that at long times the state is independent of the initial spin configuration. A time crystal necessarily breaks ergodicity because M^n has n stationary distributions, so the system remembers which of the n states in the orbit it is in.

Ergodicity-breaking PCAs were first proved to exist in 2D by Toom [536, 537], and much later in 1D by Gács [188]. Since stable ergodicity breaking is impossible in a zero dimensional model with a finite state space [431, 185], the results of Toom and Gács necessarily require interactions and dimension $D \geq 1$ (where the thermodynamic limit is well defined). We discuss Toom's model first because of its simplicity. The Toom model is a 2D CA with a binary state space, $\mathcal{S} = \{-1, 1\}$, and a "majority vote" transition rule in the Northern-Eastern-Center (NEC) neighborhood $\mathcal{N} = \{(1, 0), (0, 1), (0, 0)\}$ (the $(\Delta x_i, \Delta y_i) \in \mathcal{N}$ denote the relative locations of the cells in the neighborhood). Namely, the new state of cell $\boldsymbol{x}$ is determined by the majority value of the three NEC neighbors, $\boldsymbol{x} + \mathcal{N}$. Crucially, in this model, it was proven that there are two "phases" (i.e. stationary distributions), corresponding to states "all $+1$" and "all -1", which are stable against arbitrary stochastic perturbations below a critical error rate ϵ. The origin of this stability can be intuitively understood: without any errors, the NEC majority vote eliminates any finite island of errors in a short time; as long as the error rate ϵ is small enough, the system can eliminate an island before another equally large island appears [43, 347, 187].

We emphasize that the coexistence of two stable phases in the Toom model is of a much *stronger* nature than the coexistence of equilibrium phases (i.e. all up and all down) in, for example, the 2D Ising model; this is because the coexistence in the Toom model is stable even if the errors are *biased*. For example, while the deterministic Toom CA happens to have a transition rule with an Ising symmetry, one can perturb using two different error rates, $\epsilon_1 < \epsilon_{-1}$, for states to flip to ± 1, respectively. Despite this bias, at long times, two separate stationary distributions $\mathcal{P}_+, \mathcal{P}_-$ persist. This is in contrast to equilibrium systems (i.e. the 2D Ising model), where coexistence is always fine-tuned, either via a symmetry, or by tuning to the boundary of a first order phase transition.

Armed with Toom's result, a simple modification we call the "π-Toom" model turns his construction into a time crystal: instead of an NEC majority vote, we take as our rule the NEC anti-majority vote. Or equivalently, we consider the model in which we interleave a
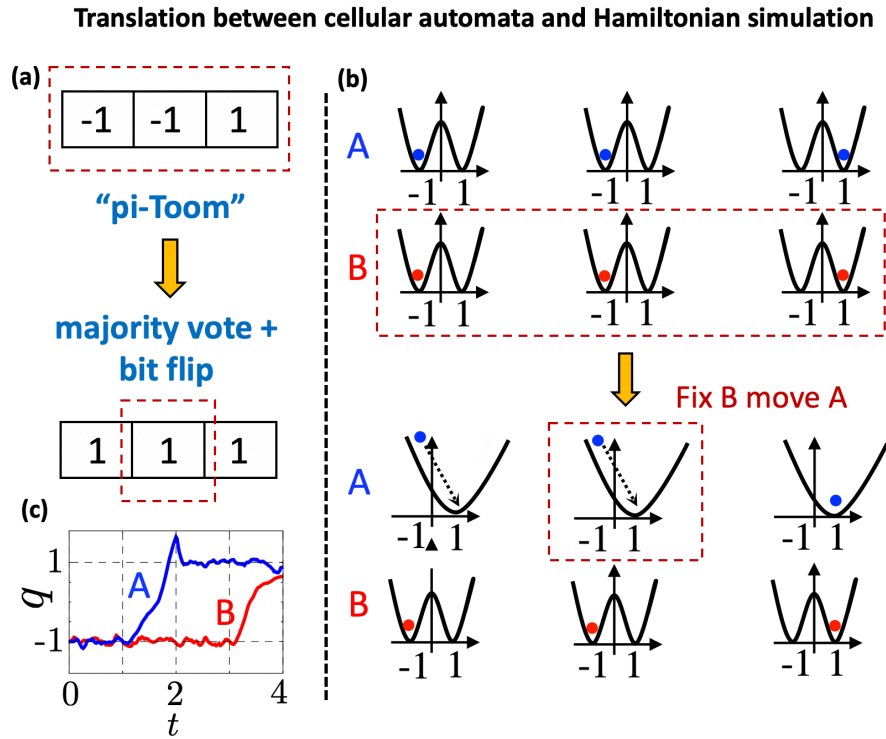
Figure 9.2: **Mapping between cellular automata and continuous Hamiltonian dynamics.** **(a)** Shows a single step of a one dimensional version of the "π-Toom" rule, which consists of a majority vote and a bit flip. **(b)** In the Hamiltonian setting, we consider two sets of oscillators, A (blue) and B (red). The corresponding Hamiltonian simulation proceeds in two steps. First, there is a "relaxation" step followed by local interactions which implement the "anti-majority vote". In this second step, the B oscillators are fixed, while the state of the A oscillators is updated. **(c)** Trajectory $q_{A/B}(t)$ during an error correction step of the Toom model for a 32×32 lattice with $v = 50$ and $T = 2$. The vertical dashed lines divide time into four steps as described in the text; an error of the form $q \sim -1$ gets corrected to be $q \sim 1$.

spin flip, $1 \leftrightarrow -1$, between each Toom step. Because Toom has proved that his construction can successfully "error-correct" against minority islands, one can immediately conclude the π-Toom model is a period-doubled time crystal below a critical error rate ϵ, even if the noise breaks the Ising symmetry. Above this error rate, there is a transition into a disordered phase, analogous to the ergodicity-breaking phase transition of the Toom model. We will numerically confirm this transition exists in the π-Toom model in Section 9.3. We note that the potential for the Toom rule to stabilize periodic behavior in PCAs was pointed out well before the recent interest in time crystals [44, 195].

Time crystalline order in a 1D PCA

As with conventional phases of matter, the possibility of a stable, discrete time crystal depends on the spatial dimension. Thus, it is natural and interesting to ask if a PCA time crystal can also exist in one dimension ($D = 1$). Note that in the quantum case, while the 1D MBL discrete time crystal is well established [290, 160, 590, 457, 363], the stability of MBL in 2D, and hence the existence of a 2D MBL DTC phase, remains controversial [130, 114].

Unfortunately, Toom's route to stability cannot be generalized to 1D. Since each island of errors is only separated by two domain walls in one dimension, locally one cannot efficiently tell which side corresponds to the error and which side to the correct region. This intuition is not specific to the Toom model, and in fact for many decades it was conjectured that all 1D, finite-range and finite-state PCAs were generically ergodic, i.e. the so-called "positive-rates conjecture" [207].

Surprisingly, in 1998, this longstanding conjecture was proven incorrect by Gács [188]. Gács constructed a 1D translation invariant PCA, with nearest neighbor interactions, with the following remarkable property: on a chain of length L, the dynamics exhibit 2^L stable stationary measures (intuitively, one can think of these as fixed points) in the limit $L \to \infty$; said another way, Gács' PCA can "remember" one bit per unit length! Each cell/site of the PCA has a large state space, likely somewhere between 2^{24} and 2^{400} [207, 188]. Roughly speaking, each cell contains one bit that it is trying to remember, and the remaining 399 bits (taking e.g. the 2^{400} state space) are involved in a highly collective error correction protocol. As in the Toom model, the stochastic errors can be biased so long as they remain below some finite threshold, above which a dynamical phase transition will restore ergodicity.

Even more remarkably, not only is the Gács model an error-corrected memory, it can execute Turing-complete operations on the protected state space. In other words, his construction demonstrates that a *stochastic* 1D PCA can be used to simulate a deterministic CA, and hence error-corrected classical computing is possible in 1D. This immediately implies the existence of the "π-Gács time crystal:" In particular, one can simply use the Gács construction to emulate a CA with the rule: $1 \leftrightarrow -1$. His mathematical results then imply that this is an absolutely stable discrete time crystal, with infinitely long-lived temporal order as $L \to \infty$.
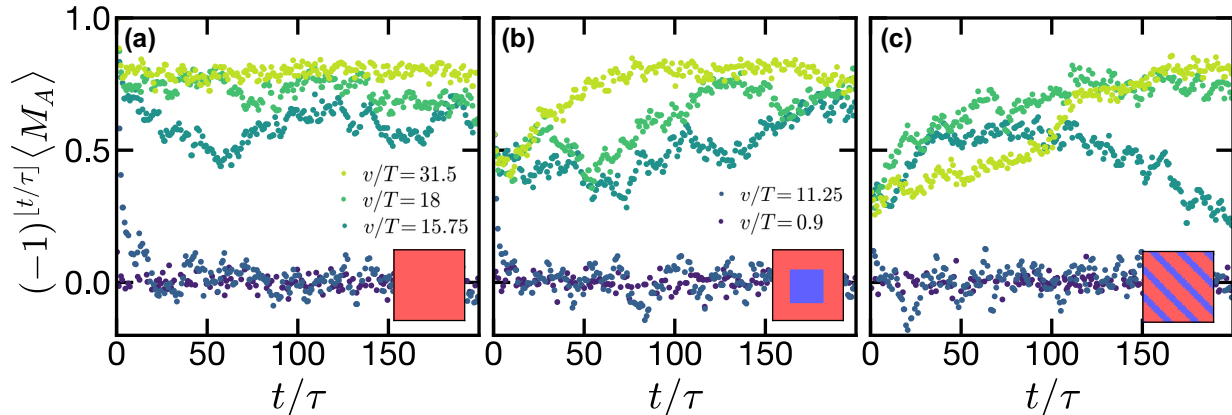
Figure 9.3: **Stability of discrete time crystalline behavior to different initial states.** Floquet Langevin simulation of the π-Toom model for a two dimensional lattice of size $32{\times}32$, with $v = 50$. For each panel, the inset depicts the initial configuration (for both A and B oscillators), where red indicates $q = +1$ and blue indicates $q = -1$. **(a)** For a uniform initial state, at low temperatures, the time crystalline order parameter remains finite at late times. At high temperatures, the time crystal quickly melts into a disordered phase. **(b)** For an initial state with a central island of errors (i.e. oscillators in $q = -1$), at low temperatures, the Floquet Langevin dynamics "error correct" and the time crystalline order grows toward a plateau at late times. At high temperatures, the time crystal again melts into a disordered phase. **(c)** For an initial state with stripes of errors, one sees the same qualitative behavior as in panel (b). As expected, near the transition (data set with $v/T = 15.75$), it becomes difficult to tell whether the time crystalline order will eventually decay or plateau to a finite value.

Gács' result (and Toom's) is mathematically rigorous, and as such, there are assumptions about the error model, which we outline here [537, 188, 187]. Since the PCA is viewed as a perturbation to a CA rule $\mathcal{T}$, given a particular spatio-temporal history $\eta(\boldsymbol{x}, t)$, we say an "error" E_u occurred at space-time point u if it didn't follow the update rule $\mathcal{T}$; instead, the state of u is chosen according to some noise distribution. $E_{u_1} \wedge E_{u_2}$ then denotes the situation where errors have occurred at both u_1 and u_2. Gács only requires that the probability that errors (of any type) occurring at k space-time points $\{u_\ell\}$ satisfy the bound $P_{\wedge_{\ell=1}^k E_{u_\ell}} \leq \epsilon^k$ for some constant ϵ [188]. The Gács model is non-ergodic below a finite critical ϵ, *irrespective* of the further details of $P_{\wedge_\ell^k E_{u_\ell}}$. Thus, Gács' error model is extremely general — it does not even require that the errors come from a Markov process.

To understand why most physical systems would naturally satisfy this bound, one can expand Gács' error condition using the chain rule for conditional probabilities, $P_{X \wedge Y} =$

$P_{X|Y}P_Y$, which yields

$$P_{\wedge_{\ell=1}^k E_{u_\ell}} = \prod_{\ell=1}^k P_{E_\ell|E_{\ell-1}\cdots E_1} \leq \epsilon^k. \tag{9.2}$$

Thus, a sufficient condition is simply to require that each $P_{E_\ell|E_{\ell-1}\cdots E_1} \leq \epsilon$; if we choose ℓ to be ordered in time, this will be satisfied if the probability for an error to occur at ℓ, conditioned on all of the past errors, is below some constant ϵ. This will *always* be the case for a Markov model of the form, $M = \mathcal{T} + \epsilon\Delta M$, for arbitrary (local) entries $|\Delta M_{\eta\to\eta'}| < 1$. Thus, the "stability to errors" of the Gács model can be understood, more generally, as the stability to local perturbations.

9.2 Translating a PCA into Floquet-Langevin Dynamics

Our goal in this section is to bridge the gap between the preceding results from theoretical computer science and systems more familiar to many-body physics. Specifically, we aim to map the π-Toom and π-Gács models to a classical Floquet Hamiltonian coupled to a Langevin bath which instantaneously satisfies detailed balance. A well-known mapping from D-dimensional CA to $D+1$-dimensional *equilibrium* models was studied in the 1980s [43, 166, 145]; however, these mappings introduce an extra spatial dimension corresponding to the history of the CA. Thus, time-translation breaking in the original CA does not actually give rise to time crystalline order in the resulting Hamiltonian.

So here we take a different approach. We should say at the outset that there is nothing particularly special about our strategy, and other proposals may work equally well. In fact the problem can be understood as a constrained instance of the well-studied "embedding problem:" we aim to realize a discrete-time Markov process (the PCA) via the stroboscopic dynamics of a continuous time Monte Carlo chain (CTMC) satisfying local detailed balance (LDB) [449, 323, 581].

The dynamics we consider take the general Langevin form,

$$\dot{q}_i = \partial_{p_i}H(\{p,q\};t)$$
$$\dot{p}_i = -\partial_{q_i}H(\{p,q\};t) + R_i(t) - \gamma p_i$$
$$\langle R_i(t)R_j(t')\rangle_{\text{noise}} = 2\gamma T\delta_{ij}\delta(t-t'), \tag{9.3}$$

where (q_i, p_i) are the conjugate variables of a mechanical oscillator at site i. As depicted in Fig. 9.1(a,b), roughly speaking we will encode the discrete state of the CA, η_i, as the integer part of the position, $\eta_i = \lfloor q_i \rfloor$. The Hamiltonian will take the familiar form $H(t) = \sum_i \frac{p_i^2}{2m} + U(\{q\}, t)$, with $U(t)$ engineered so that one Floquet cycle, $H(t+\tau) = H(t)$, will enact one cycle of the CA update $\mathcal{T}$. In order to satisfy the fluctuation-dissipation theorem at each instant in time, $R_i(t)$ is a stochastic force whose variance is proportional to the

friction coefficient γ and the temperature T. This stochastic force will sometimes lead to "errors" in the Hamiltonian simulation of the CA, making it effectively a PCA.

Let us begin by defining the precise mapping between the state s of a single site in the CA and the phase space (q, p) of a single oscillator. Each sites takes on values within the discrete state space $\mathcal{S}$, while the oscillators take on continuous values, $q \in \mathbb{R}$. To map from the CA to the oscillator $(Q : \mathcal{S} \to \mathbb{R})$, we use $Q(s) = s$ [Fig. 9.1(a)]. To map from the oscillator to the CA $(S : \mathbb{R} \to \mathcal{S})$, we use the following prescription: given a position q, the corresponding state $S(q) = s$ is given by the closest $Q(s)$ such that $S(q) = \arg\min_s |Q(s) - q|$ [Fig. 9.1(b)]. We note that the oscillator-to-CA mapping is many-to-one; indeed, it is completely independent of the momentum p.

When building Hamiltonian dynamics that simulate the CA, we encounter a challenge. Unlike the discrete time evolution of the CA, where the update of the global state is immediate, in a continuous-time Hamiltonian system, one needs a way to "store" the previous global state throughout the update cycle. This is essential in order to give the dynamics enough time to identify what the new state of the system should be. To solve this issue, we promote each CA cell at position $\boldsymbol{x}$ to *two* oscillators (A and B) with coordinates $(q_{\boldsymbol{x}}^A, p_{\boldsymbol{x}}^A)$, and $(q_{\boldsymbol{x}}^B, p_{\boldsymbol{x}}^B)$. At each step, we will view one set of oscillators (say A) as the "memory", while the other set (B) will undergo evolution to the new state $B = \mathcal{T}(A)$, driven by $U(t)$. We then exchange the role of A and B and repeat. In a sense, our protocol condenses the extra history dimension of the equilibrium construction [43, 166, 145] to a constant overhead in the state-space size. Interestingly, it was recently shown that such ancillary "hidden" degrees of freedom are necessary in any CTMC realization of a sufficiently non-trivial discrete-time Markov chain, including the "bit-flip" process (e.g. a time crystal) [581].

Within this protocol, one Floquet cycle ($A \to B \to A$) can actually execute *two* CA steps. However, when considering discrete time crystals, where we want the Floquet period to enact a single CA step, one can always make one of the steps equivalent to either the "do-nothing" ($\mathcal{I}$) or Toom CAs. This would result in an interleaving of the form: $(\mathcal{I}\mathcal{T})(\mathcal{I}\mathcal{T})\cdots$.

Building the Floquet dynamics

We now turn to building the Floquet dynamics, which simulates the transition rules of the cellular automata. We begin with the oscillators at site $\boldsymbol{x}$ in the state $(q_{\boldsymbol{x}}^{A/B}, p_{\boldsymbol{x}}^{A/B}) = \left(Q(\eta(\boldsymbol{x}, t)), 0\right)$. From there, the dynamics evolve via a 4-step process.

Step 1: Relaxation. The goal of the first step is to leverage dissipation in order to reduce fluctuations in the system. In particular, we envision turning on a one-body potential, $V_{\mathrm{pin}}(q)$, which has a local minimum at $Q(s)$ for all $s \in \mathcal{S}$. At sufficiently low temperatures, the dissipative dynamics [Eq. 9.3] will relax the oscillator's positions, $q_{\boldsymbol{x}}$, toward valid values of $Q(s)$ with low momenta (with fluctuations of order the equipartition scale $\sim k_B T$). The

precise form of V_{pin} is not important; however, for concreteness we will utilize

$$V_{\text{pin}}(q) = v_{\text{pin}} \prod_{s \in \mathcal{S}} (Q(s) - q)^2 \tag{9.4}$$

where the overall magnitude of the pinning potential is set by v_{pin}.

Step 2: Fix A, move B. As illustrated in Fig. 9.2, the second step of the Floquet dynamics implements the cellular automata transition $B = \mathcal{T}(A)$. We will keep q^A fixed using the pinning potential, V_{pin}. For the B oscillators, however, we turn off V_{pin}, and turn on an interaction V_I between q^A and q^B. This interaction is engineered such that each $q_{\boldsymbol{x}}^B$ sees only a single potential minimum corresponding to the desired CA update rule; in general, this will depend on the state of the A oscillators in the associated neighborhood, $\{q_{\boldsymbol{x}+\mathcal{N}}^A\}$.

Defining the location of this minimum to be $\widetilde{\mathcal{T}}(\{q_{\boldsymbol{x}+\mathcal{N}}^A\})$, we can then specify an interaction of the form:

$$V_I(\{q_{\boldsymbol{x}+\mathcal{N}}^A\}, q_{\boldsymbol{x}}^B) = \frac{v_I}{2} \left(\widetilde{\mathcal{T}}(\{q_{\boldsymbol{x}+\mathcal{N}}^A\}) - q_{\boldsymbol{x}}^B \right)^2, \tag{9.5}$$

where the interaction strength is characterized by v_I. This is a highly non-linear but local interaction between each $q_{\boldsymbol{x}}^B$ and a finite set of A oscillators, $\{q_{\boldsymbol{x}+\mathcal{N}}^A\}$, within the neighborhood, $\mathcal{N}$. In particular, as shown in Fig. 9.2(b), for the example of $\widetilde{\mathcal{T}}$ being an "anti-majority vote", the interaction would correspond to an $|\mathcal{N}| + 1$ body coupling.[1]

Step 3: Relaxation. In the third step, we turn off the interaction, V_I, while ramping up the pinning potential, V_{pin}. As in the first step, dissipation relaxes and pins the positions of the oscillators.

Step 4: Fix B move A. In the final step, we implement "$A = \mathcal{T}(B)$" by repeating step two with the role of A and B reversed.

After these four steps, our Floquet dynamics have implemented two steps of the cellular automata update rule, $\mathcal{T}$. This block naturally forms a single period of the Floquet drive, which can then be repeated. As aforementioned, one can also replace the transition $\mathcal{T}$ in step two with the "do-nothing" CA rule if one wants to implement only a single CA update, $\mathcal{T}$, per Floquet cycle.

We now have all of the ingredients to explicitly define our Langevin dynamics, governed by:

$$H(t) = \sum_{\boldsymbol{x}} \frac{p_{\boldsymbol{x}}^{A2}}{2m} + \frac{p_{\boldsymbol{x}}^{B2}}{2m} + U\left(t, \{q_{\boldsymbol{x}}^A, q_{\boldsymbol{x}}^B\}\right), \tag{9.6}$$

---

[1]Naively, one could set $\tilde{\mathcal{T}}(\{q_{\boldsymbol{x}+\mathcal{N}}^A\}) = Q\Big(\mathcal{T}\big(S(q_{\boldsymbol{x}+\mathcal{N}}^A)\big)\Big)$. However, the discontinuities in $S(q)$, and hence V_I, lead to isolated points with infinite force, which makes any analysis or numerical simulation significantly more troublesome. To remedy this, we smooth the interaction using an interpolation.

where the potential $U(t, \{q_{\boldsymbol{x}}^A, q_{\boldsymbol{x}}^B\})$ has a Floquet period of $\tau = 4$:

$$U\left(t, \{q_k^A, q_k^B\}\right) = \begin{cases} \sum_{\boldsymbol{x}} V_{\mathrm{pin}}(q_{\boldsymbol{x}}^A) + V_{\mathrm{pin}}(q_{\boldsymbol{x}}^B) & \text{if} \quad \mathrm{mod}\left(\lfloor t \rfloor, 4\right) = 0, 2; \\ \sum_{\boldsymbol{x}} V_{\mathrm{pin}}(q_{\boldsymbol{x}}^A) + V_I\left(q_{\boldsymbol{x}+\mathcal{N}}^A, q_{\boldsymbol{x}}^B\right) & \text{if} \quad \mathrm{mod}\left(\lfloor t \rfloor, 4\right) = 1; \\ \sum_{\boldsymbol{x}} V_I\left(q_{\boldsymbol{x}+\mathcal{N}}^B, q_{\boldsymbol{x}}^A\right) + V_{\mathrm{pin}}(q_{\boldsymbol{x}}^B) & \text{if} \quad \mathrm{mod}\left(\lfloor t \rfloor, 4\right) = 3. \end{cases} \quad (9.7)$$

Without loss of generality, we set the mass, $m = 1/2$, in the remaining discussions.

9.3 Discrete Time Crystal in the π-Toom model

Within the PCA setting, the π-Toom model (an anti-majority vote in the NEC neighborhood) is a discrete time crystal, and in the preceding section, we have described a procedure for "simulating" this model using continuous-time Floquet-Langevin dynamics. At zero temperature, $T = 0$, where the dynamics are damped and deterministic, our protocol will faithfully simulate the π-Toom model, as long as the friction coefficient is chosen "correctly" relative to v_I, v_{pin} and the Floquet period. More precisely, one should choose γ to ensure that the oscillators' relaxation occurs on a time-scale that is short relative to the Floquet period.

The possible flaw at finite temperature is that the errors due to Langevin noise (e.g. thermally activated escape out of the pinning potentials) may not satisfy the requirements of the Gács and Toom error models. Even though Langevin noise is Markovian, the effective error model for our simulated PCA dynamics is not because the oscillator-to-CA mapping is many-to-one and thus, the system possesses extra memory that can induce correlations between the errors. The worry is that there may then be "avalanches" of errors; for example, if an oscillator makes an error during one step, it *could* be more likely for it to make another error in a subsequent step. Such correlations are harmless so long as they satisfy the bound in Eq. 9.2.

We will return to a detailed analysis of error correlations in Sec. 9.4, but let us begin by numerically exploring time crystalline order in a Floquet-Langevin simulation of the π-Toom model.

Consider a binary CA on a two dimensional square lattice, with state-space $\mathcal{S} = \{-1, 1\}$, and a CA-to-oscillator mapping, $Q(s) = s$, as previously discussed. We take the pinning potential to be: $V_{\mathrm{pin}}(q) = v_{\mathrm{pin}}(q-1)^2(q+1)^2 + Fq$, where $F = 10^{-4}$ breaks the accidental Ising symmetry of the π-Toom model. Parameterizing the magnitude of the interaction strength and the pinning potential as $v_{\mathrm{pin}} = 4v_I = v$, we numerically solve the Floquet-Langevin dynamics Eq. 9.3 via a first-order Euler-stepper. The noise term, $R_i(t)$, is implemented via random momentum kicks with variance $2\eta T dt$, where dt is chosen to ensure that the relative momentum change within each step is small. Finally, γ is chosen such that the dynamics are tuned to critical damping relative to both V_{pin} and V_I.

In order to ensure that a single Floquet period implements only one π-Toom update, we utilize the following interleaving strategy: in step two, we choose $\widetilde{\mathcal{T}}$ to be the Toom update rule, while in step four, we choose $\widetilde{\mathcal{T}}$ to be the π-Toom update rule. We probe the resulting
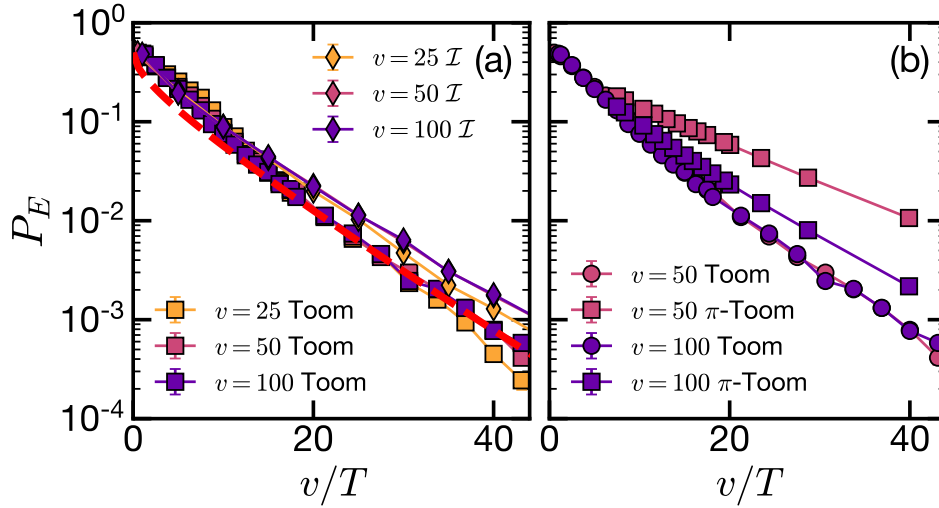
Figure 9.4: **Scaling of error with the rescaled height of the barrier.** Error probability P_E versus the ratio of the pinning potential to the temperature, v/T, in simulations of (**a**) the do-nothing ($\mathcal{I}$) and Toom CAs. The dashed-red line indicates the equilibrium estimate of Eq. 9.8. (**b**) The π-Toom CA. While P_E apparently depends on the simulated CA, as v increases the π-Toom error rate converges toward the Toom error rate. In all cases, we find an exponential decay in the error rate as a function of v/T. Data are obtained from a 32×32 system by averaging over 25 Floquet cycles after an initial evolution of 200 Floquet cycles.

dynamics by measuring the average "magnetization", $\langle M_A | M_A \rangle \equiv \frac{1}{N} \sum_k \text{sign}(q_k^A)$, where N is the system size. Time crystalline order corresponds to stable period-doubling of the magnetization and manifests as a late-time plateau in the order parameter: $(-1)^{\lfloor t/\tau \rfloor} \langle M_A | M_A \rangle$.

To investigate the emergence of DTC order, we compute the Floquet-Langevin dynamics starting from three distinct initial states: (i) a uniform input state with all oscillators in $q = +1$ [Fig. 9.3(a)], (ii) a state which contains an island of $q = -1$ oscillators in the center [Fig. 9.3(b)], and (iii) a state which consists of diagonal stripes of $q = -1$ oscillators [Fig. 9.3(c)].[2] In the language of the π-Toom PCA, for each of these initial states, one can think of the oscillators with $q = -1$ as "errors", which will either be "corrected" by our Floquet Langevin dynamics (for sufficiently low bath temperatures) or not.

For the uniform initial state [Fig. 9.3(a)], the DTC order parameter, $(-1)^{\lfloor t/\tau \rfloor} \langle M_A | M_A \rangle$, begins at unity for all temperatures. At high temperatures, the order parameter quickly decays to zero, indicating that the Floquet Langevin dynamics drive the system toward the disordered phase. On the other hand, for sufficiently low temperatures, the time crystalline

---

[2]Note that for perfect stripes, even the deterministic Toom model cannot not correct it. However, there are a measure zero set of such fine-tuned initial conditions.
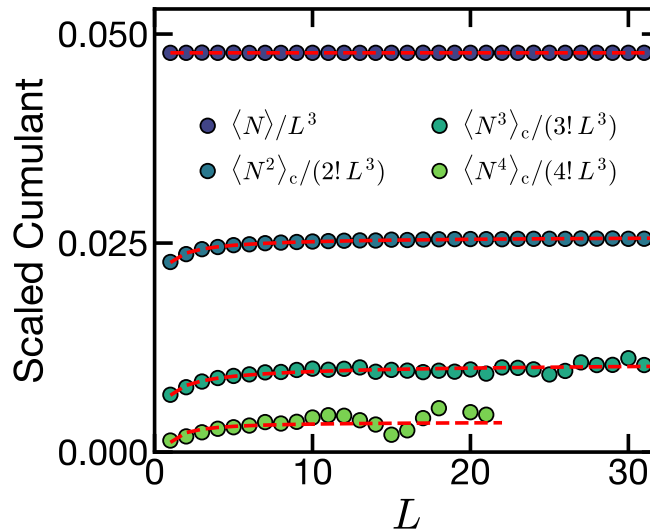
Figure 9.5:   **Analysis of error correlations via calculation of cumulants of the error distribution.** Cumulants, $\langle N_V^n \rangle_c$, of the error distribution from a Floquet Langevin simulation of the π-Toom model for $L \times L \times L$ space-time volumes. The dashed curves are fits to $\langle N_V^n \rangle_c / L^3 = c_n - b_n L^{-\eta_n}$. We find $\eta > 0$ (Table 9.1), indicating convergence to a finite c_n. Each data point was estimated from the statistics of 3000 independent Langevin trajectories ($T = 5.17, v = 100$), with 1000 $L \times L \times L$ blocks sampled from each trajectory.

order evolves toward a finite plateau value at late-times, indicative of a DTC. In Fig. 9.3(b), we show the analogous dynamics starting from an initial state with a central island of errors. For low temperatures, the Floquet Langevin dynamics correct these errors and the DTC order parameter grows, with the system approaching a time crystalline state. Again, above a critical temperature, time crystalline order "melts" and the stroboscopic magnetization decays to zero. Finally, Fig. 9.3(c) depicts the dynamics starting from a striped error configuration; the qualitative features are identical to Fig. 9.3(b), although the competition between the DTC phase and the disordered phase is more apparent at intermediate temperatures.

In order to characterize the phase transition between the time crystal and the disordered phase as a function of temperature, we compute the late time Floquet Langevin dynamics up to time-scale, $t \sim 10^4$, starting from a uniform initial state. We define the plateau value of the DTC order parameter as the late-time average of the stroboscopic magnetization, $\overline{(-1)^{\lfloor t/\tau \rfloor} \langle M_A | M_A \rangle}$; in particular, we average $(-1)^{\lfloor t/\tau \rfloor} \langle M_A | M_A \rangle$ starting at $t = 3000$ for ~ 500 Floquet cycles and ~ 50 noise realizations.

One can immediately observe the DTC phase transition by plotting the time crystalline order parameter, $\overline{(-1)^{\lfloor t/\tau \rfloor} \langle M_A | M_A \rangle}$, versus T. However, in order to compare our Floquet

n	c_n	b_n	η_n
1	0.048	0	—
2	0.052	0.007	0.60
3	0.067	0.026	0.46
4	0.088	0.060	0.90

Table 9.1: Fitting parameters for the dashed curves in Fig. 9.5.

Langevin simulation with a direct implementation of the π-Toom PCA, we first translate the temperature, T, to an effective error rate P_E (per space-time cell). To do so, for each temperature, we examine the ensemble of all simulated Langevin trajectories and count the number of errors under the continuous to discrete mapping S; this allows us to empirically determine the error rate, $P_E(T)$. As shown in Fig. 9.1(c), the time crystalline order parameter exhibits a sharp phase transition as a function of P_E.

Although there is clearly a phase transition, the question remains: How accurate is the Floquet-Langevin simulation of the π-Toom model? To answer this question, we directly implement the π-Toom PCA, assuming an error rate P_E (associated with the transition for each space-time point) with no correlations in space or time. As depicted in Fig. 9.1(c), the functional form and location of the DTC phase transition are in excellent agreement between our Floquet Langevin simulation and the π-Toom PCA (with improving agreement for larger pinning potential v). However, some discrepancy can be seen near the transition, where there is a residual dependence on the pinning potential even as $P_E(T)$ is held fixed. As we will see, this discrepancy arises because the Floquet-Langevin errors are spatio-temporally *correlated*. In order to claim that Toom and Gács' rigorous PCA results apply to our Floquet Langevin simulation in the thermodynamic limit, a more careful analysis of these error correlations is needed—a task to which we now turn.

9.4 The nature of errors in Floquet-Langevin dynamics

Due to the presence of a finite temperature bath, the Floquet-Langevin simulation of the π-Toom model is intrinsically noisy. Large thermal fluctuations can lead to an "error" in the subsequent state $\tilde{\eta}(\boldsymbol{x}, t)$ relative to the noiseless transition $\mathcal{T}\big(\tilde{\eta}(\boldsymbol{x} + \mathcal{N}, t-1)\big)$. Fortunately, our overall goal is to simulate the noisy PCA version of the π-Toom model. However, even then, the distribution of errors arising from the Floquet-Langevin dynamics need not (a priori) be consistent with the error model considered in the context of e.g. Gács' and Toom's mathematical results on stability. To this end, we now characterize the nature of errors in our Floquet-Langevin simulation.

Our goal is to obtain numerical evidence that: (1) the errors arising from the Floquet-

Langevin dynamics satisfy the condition in Eq. 9.2 for some constant $\epsilon(T)$ and (2) the error bound $\epsilon(T)$ can be made arbitrarily small as $T \to 0$, to ensure the error threshold for Toom or Gács' results can be obtained.

To begin, we first examine the temperature dependence of the error *rate* per space-time cell $P_E = \langle E_x \rangle$, where $E_x \in \{0, 1\}$ is the indicator function for an error at x, and show that $P_E(T)$ decays exponentially as $T \to 0$. Note that due to the spatio-temporal correlation of errors, the error rate is not the same as the error bound, $P_E \neq \epsilon$, but P_E will nevertheless play an important roll in the analysis. In Fig. 9.4(a), we show the empirically measured error rate $P_E(T)$ as a function of v/T for two simulated PCAs which are usually static: the "do-nothing" CA $\mathcal{I}$ and the Toom CA. We find P_E decays exponentially in v/T, suggesting that the errors arise from activated tunneling over the V_{pin}, V_I barriers. For the parameters studied here, we expect the dominant error source arises from the transition between the "Fix A (B) move B (A)" step and the relaxation step enforced by V_I. To predict the rate of such errors, suppose that the interaction potential is driving an oscillator to the state $q = -1$, so that $V_I(q) = \frac{v_I}{2}(q+1)^2$. When the dynamics switch to the pinning potential $V_{\text{pin}}(q)$, an error will occur if the oscillator has a position $q \in [0, \infty)$. Assuming the system reaches local equilibrium with respect to V_I, the probability of this error can be estimated from the Boltzmann distribution as:

$$P_E\left(\frac{v_I}{T}\right) \equiv \frac{\int_0^\infty e^{-V_I(q)/T}}{\int_{-\infty}^\infty e^{-V_I(q)/T}} = \frac{1}{2}\text{Erfc}\left(\sqrt{\frac{v_I}{2T}}\right), \qquad (9.8)$$

which asymptotically gives exponential decay $P_E \sim e^{-v_I/2T}$. In Fig. 9.4(a), we show that this prediction (dashed red line) gives good agreement with the observed decay.

In Fig. 9.4(b), we examine $P_E(T)$ for the $\pi-$Toom CA, which involves considerable motion during each cycle. For small v_I, the $\pi-$Toom CA error rate is higher than the Toom CA, suggesting that non-equilibrium effects beyond the estimate of Eq. 9.8 are important. As v increases, the π-Toom error rate approaches that of the static CA. Regardless, in all cases we find that decreasing the temperature leads to an exponential decay in P_E, implying that for strong potentials and low temperatures, arbitrarily small P_E can be obtained.

We now turn to the crucial issue of spatio-temporal correlations. Consider an arbitrary space-time volume V containing $|V|$ points. Letting $P(N_V)$ denotes the probability that N_V errors occur in the volume V, we aim to provide empirical evidence that there is a constant ϵ such that $P(N_V = |V|) \leq \epsilon^{|V|}$ for all V. However, measuring $P(N_V = |V|)$ directly is difficult because for large $|V|$ such "large deviations" [138, 550, 242, 538] are too rare to collect statistics. To make progress, we will instead relate $P(N_V = |V|)$ to the connected n-point functions of the errors, which are feasible to estimate for low enough n. Roughly speaking, if the connected n-point functions decay fast enough, the desired bound will be satisfied.

To do so, we consider the scaled cumulant generating function (SCGF) $\lambda_V(k)$ defined by $\langle e^{kN_V} \rangle = e^{|V|\lambda_V(k)}$. The SCGF upper bounds $P(N_V = |V|) \leq e^{-|V|(k-\lambda_V(k))}$ for any choice of
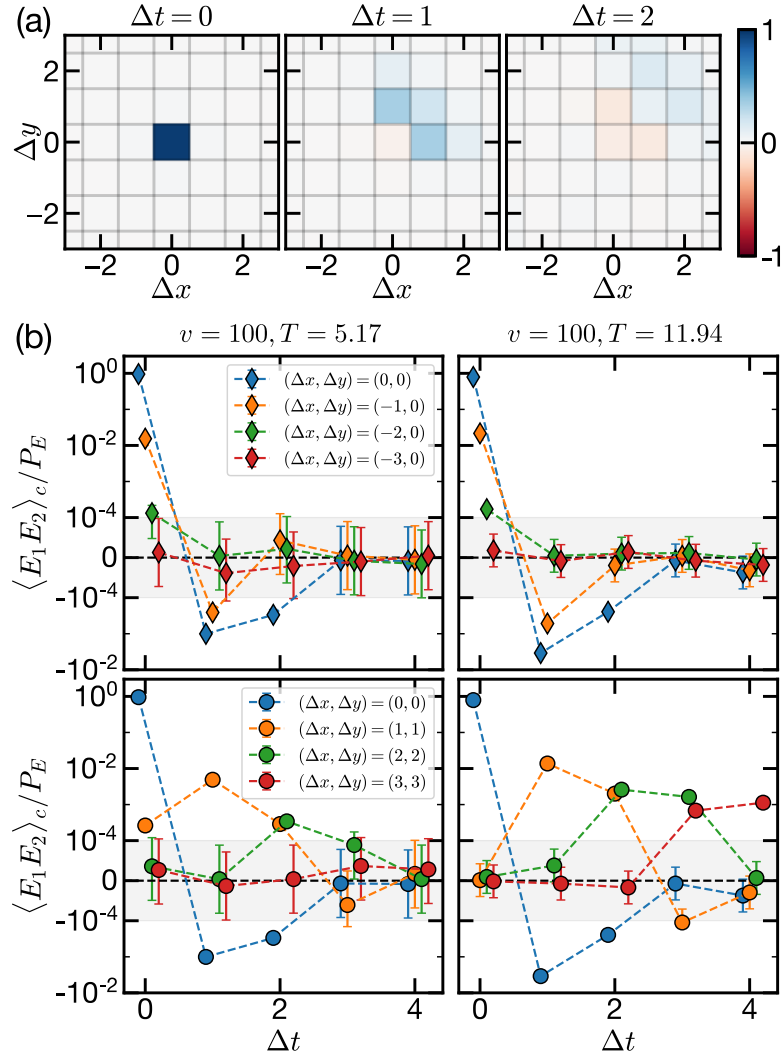
Figure 9.6: **Connected two-point correlations of the error distribution. (a)** Error correlation in real space for $v = 100$ and $T = 5.17$. The connected correlation, $\langle E_1 E_2 \rangle_c / P_E$, for different time separations Δt is shown as a function of the spatial separations. The color map range is rescaled by 1.0, 0.025, 0.004 for the left, middle and right panels respectively. **(b)** Connected correlations between errors for different types of space separations (top and bottom) and different temperatures (left and right).

$k \geq 0$. The error bound can then be defined by a min-max principle

$$\log \frac{1}{\epsilon} = \min_V \max_{k \geq 0} (k - \lambda_V(k)). \tag{9.9}$$

The Taylor series of the SCGF gives the n-th cumulants of N_V, $\lambda_V(k) = |V|^{-1} \sum_{n=1}^{\infty} \langle N_V^n \rangle_c \frac{k^n}{n!}$. The cumulants are in turn related to the connected correlations, e.g., $\langle N_V^2 \rangle_c = \sum_{x,y \in V} \langle E_x E_y \rangle_c$. If the correlations decay, we expect the cumulants to scale as $\langle N_V^n \rangle_c = |V| c_n(V)$, where $c_n(V)$ depends on the geometry of V but does not grow with $|V|$ (in particular, $c_1(V) = P_E$). Let us suppose that their growth is upper bounded by a constant $c_n \equiv \max_V c_n(V)$. Furthermore, suppose that the resulting c_n grow slower than $n!$, so that we obtain a bound $\lambda_V(k) \leq \lambda(k) \equiv \sum_{n=1}^{\infty} c_n \frac{k^n}{n!}$ for all $k \geq 0$. It would then follow that $\log(1/\epsilon) = \max_{k \geq 0}(k - \lambda(k))$. Since $\lambda(0) = 0$ and $\lambda'(k) = P_E < 1$, the maximal value is positive and finite, ensuring Eq. 9.2 is satisfied for some $\epsilon < 1$.

Our goal, then, is to provide empirical evidence that $\langle N_V^n \rangle_c$ does not grow faster than $|V|$ or $n!$. Rather than enumerating over all V, we restrict our attention to space-time boxes of dimension $|V| = L \times L \times L$ (note that such compact volumes are the most likely to show violations, as they contain the most correlations). In Fig. 9.5, we show the estimated cumulants of our Floquet Langevin simulation of the π-Toom model for $L = 2 - 32$. They converge to a finite c_n with a power law correction in $1/L$. While it is difficult to estimate the cumulants beyond $n > 3$, from the available data the $n!$ bound on c_n is safely satisfied.

It is interesting to note that the errors are power-law correlated and non-Gaussian. In Fig. 9.6, we present data on the two-point correlations $\langle E_{\Delta t, \Delta x, \Delta y} E_{0,0,0} \rangle_c$ of the π-Toom simulation. We see that an initial error causes an increased likelihood for errors at nearby space-time points, with correlations which propagate outward in a anisotropic manner consistent with Toom's NEC-rule. While it is again difficult to obtain estimates for large spatio-temporal separations, fitting the three available points to a line, the decay is consistent with a power-law, in agreement with the power-law convergence of the cumulants $\langle N^n \rangle_c$.

Finally, we turn to whether the error bound $\epsilon(T) \to 0$ as $T \to 0$. One sufficient condition is the existence of a T-independent, continuous, and strictly increasing function $\Lambda(k)$ such that $\lambda(k) \leq P_E(T)\Lambda(k)$ for all $k, T \geq 0$, with $\Lambda(0) = 0$. To see why, note the min-max principle gives

$$\log \frac{1}{\epsilon(T)} \geq \max_{k \geq 0} \left(t - P_E(T)\Lambda(k) \right). \tag{9.10}$$

Since Λ is invertible on $\mathbb{R}^+$, we may define $k_*(P_E) = \Lambda^{-1}(1/P_E)$. Eq. 9.10 then provides the bound $\log(1/\epsilon(T)) \geq k_*(P_E(T)) - 1$. Finally, note $\lim_{P_E \to 0} k_*(P_E) = \infty$, because the inverse of a strictly increasing function is itself strictly increasing. Thus, the existence of such a $\Lambda(k)$, combined with our earlier evidence that $\lim_{T \to 0} P_E(T) = 0$, would imply $\lim_{T \to 0} \epsilon(T) = 0$.

To verify the existence of such a $\Lambda(k)$, it would be sufficient to show that the scaled cumulants are bounded as $c_n(T) \leq P_E(T)C_n$, with C_n growing slower than $n!$, so that $\Lambda(k)$ has an infinite radius of convergence (Poisson statistics corresponds to $C_n = 1$, $\Lambda(k) =$

e^k). However, due to the small statistics, numerically estimating c_n at low temperatures is extremely demanding. A preliminary comparison of $T = 5.17, 11.94$ finds $c_2(T)/P_E(T) = 1.24$ at $T = 11.94$, while $c_2(T)/P_E(T) = 1.08$ at $T = 5.17$, consistent with an approach to $C_2 \sim 1$, but a comprehensive investigation remains a work in progress.

In summary, despite errors which are power-law correlated and non-Gaussian, we find compelling evidence that Langevin-Floquet dynamics can simulate a PCA with an error bound $\epsilon(T)$ that satisfies Eq. 9.2, so that Toom and Gács' results may be applied to this setting. Of course we cannot rule out that for some anomalously large volume $|V|$, cumulant order n, or inverse temperature $1/T$, the observed behavior will change course and violate the bound—a caveat common to any numerical finite-scaling approach. Obtaining a rigorous proof of this bound thus remains an interesting future direction.

9.5 Discussion and outlook

There is a long history of understanding computation as a fundamentally physical process, and the subsequent constraints which arise from thermodynamics: "Computers may be thought of as engines for transforming free energy into waste heat and mathematical work" [316, 42, 581]. In this point of view, a time crystal can be understood as a physical realization of the second-simplest possible computer program: a global NOT-gate. By demanding that the program execute perfectly despite faulty (noisy) gates, and when restricting to physical implementations that rely only on local interactions, the execution of such a program can be understood as a non-equilibrium "phase of matter," and the error threshold as a non-equilibrium phase transition into a time crystalline phase.

It is interesting to speculate about extensions of this approach to the quantum setting, where a discrete-time Markov process is promoted to a quantum channel, and the Langevin bath to a Lindbladian. On the one hand, any classical Markov process, such as the Toom or Gács PCA, can be realized as a quantum channel which dephases and acts diagonally on populations. When assessing stability in the quantum setting, however, it remains to be shown that the ergodicity breaking is robust to imperfect dephasing. On the other hand, error-corrected quantum computing can be realized as a purely local autonomous process in the thermodynamic limit [224, 122] and by analogy to the discussion above, one may realize a time crystal by running the program "NOT" on an error-corrected quantum computer. In this sense, the existence of time crystals in open systems is an elementary application of deeper results regarding the physical possibility of error-correction in autonomous, locally interacting systems.

More broadly, our work highlights how the interplay between driving and dissipation can lead to entirely new phenomena, most notably by allowing a system to overcome Mermin-Wagner type constraints on the existence of order [476]. At present, there are no frameworks for understanding the defining features of the Gács and Toom models that enable them to "tame" the effect of noise in the bath. Building such framework will be a necessary step

for the categorization of all non-ergodic behavior and subsequently all out-of-equilibrium phenomena in classical and quantum systems.

Part III

Prethermalization and out-of-equilibrium phases of matter

Chapter 10

Exponentially Slow Heating in Short and Long-range Interacting Floquet Systems

One feature we emphasized in Chapter 3 is that the dynamics of a periodically driven quantum system is fundamentally distinct from its static counterpart. The presence of a driving field breaks the normal *continuous* time translation symmetry into a *discrete* one, and, as a result, energy is no longer a conserved quantity. Crucially, this modifies not only the equilibration dynamics, but also the late-time equilibrium state.

When a generic many-body interaction system is periodically driven, it typically absorbs energy from the driving field and heats up to an infinite temperature state [451, 450, 118, 319, 119, 70, 439, 72, 568, 339]. However, when the driving frequency is high, the Floquet system can only absorb energy from the drive by creating multiple local excitations—an inefficient process that results in an extremely long thermalization time [4, 380, 312, 5, 161, 5, 237]. While the system does *eventually* thermalize, during this intermediate time interval, it settles into a "prethermal" state [45, 373, 208, 351, 168] that exhibits the hallmarks of thermal *equilibrium*, albeit at a lower entropy than the true infinite temperature thermal state. In this chapter, we characterize and elucidate the mechanism of Floquet thermalization with an emphasis on the high-frequency regime.

Using massively parallel Krylov subspace methods, we explore the late time dynamics of periodically-driven spin chains with both short and long-ranged interactions. In both cases, seminal recent results [380, 312, 5, 161, 5] have proven that the thermalization time, τ^*, increases at least exponentially with the frequency of the drive.[1] We provide the first concrete demonstration of this. To this end, our results are consistent with those of [71], which also observed slow heating; but additionally, by directly observing the *exponential scaling* of the thermalization time, we can extract the effective energy scale controlling the Floquet heating rate. This is enabled by going to sufficiently large system sizes such that

---

[1]An exponentially long heating time scale with logarithmic corrections was proven in [5, 161, 5].
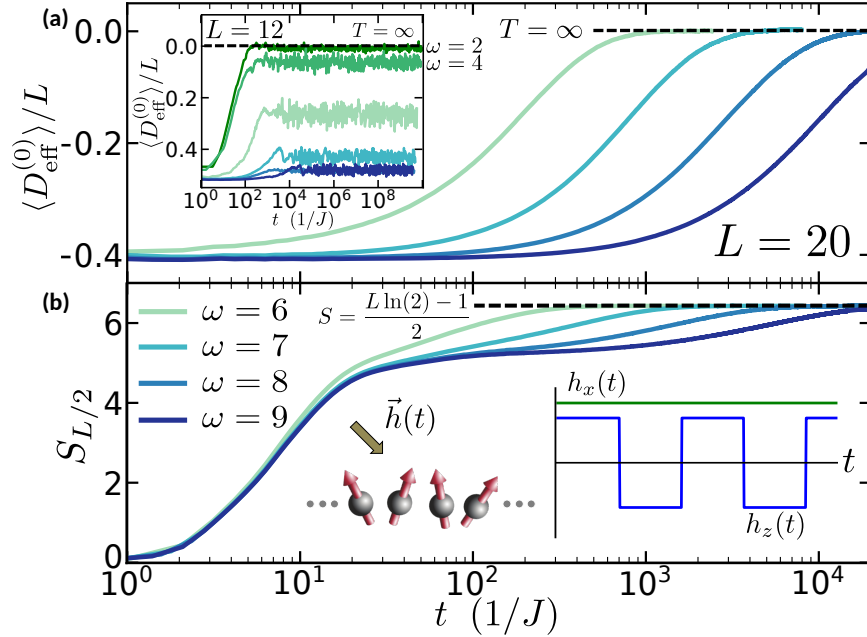
Figure 10.1: **Exponentially slow Floquet thermalization dynamics.** Floquet thermalization dynamics of a long-range interacting spin model with $L = 20$ using the parameters $\{J, J_x, h_x, h_y, h_z, \alpha\} = \{1, 0.19, 0.21, 0.17, 0.13, 1.25\}$. **(a)** As the driving frequency is increased, one observes an *exponential enhancement* in the time scale at which the system approaches infinite-temperature as diagnosed by the energy density, $\langle D_{\text{eff}}^{(0)}\rangle/L \to 0$. (inset) For smaller system sizes, full thermalization to infinite temperature is never observed even at late times. **(b)** The same exponentially slow thermalization is seen in the time scale where the half-chain entanglement entropy reaches its infinite temperature value, $\frac{L}{2}\log(2) - 0.5$ [416]. (inset) Each spin is periodically driven by a time-dependent magnetic field which exhibits a square pulse shape.

there is a clear separation of scales between the local bandwidth, the driving frequency and the global many-body bandwidth;[2] indeed, for small system sizes, moderate driving frequencies are already above the many-body bandwidth, and the system is trivially blocked from heating up to infinite temperature, Fig. 10.1(a) inset.

Moreover, we demonstrate that, at high frequency, the half-chain entanglement entropy, $S_{L/2}(t)$, quickly reaches a plateau value consistent with a prethermal state before saturating to its infinite-temperature value at exponentially-late times [380, 312, 5, 161, 5]. On this prethermal plateau, there is an emergent time-independent Hamiltonian, D_{eff}, that is conserved and generates the time evolution of the system at stroboscopic times $t = mT$ (where T is the period of the drive). For short-range interactions, these observations are in direct

---

[2]While the global bandwidth is infinite in the thermodynamic limit, it is finite for a finite system size.
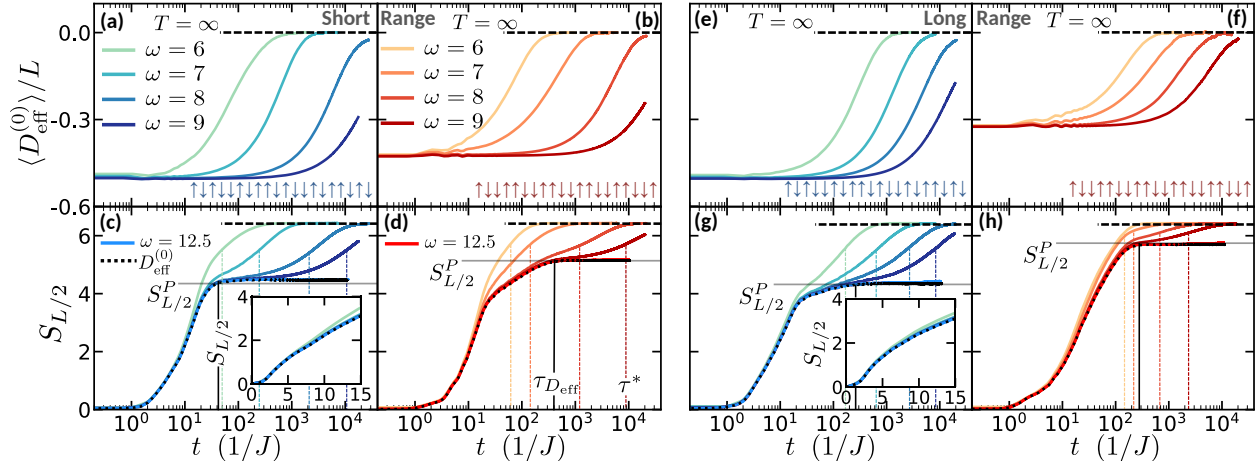
Figure 10.2: **Generality of slow Floquet thermalization.**   Floquet evolution of
both short and long-range interacting systems with $L = 20$ using the parameters
$\{J, J_x, h_x, h_y, h_z, \alpha\} = \{1, 0.19, 0.21, 0.17, 0.13, 1.25\}$. **(a,b)** [**(e,f)**] Energy density as a func-
tion of time for short-range [long-range] interactions, as measured with respect to the prether-
mal Hamiltonian $D_{\text{eff}}^{(0)}$ for a low temperature (a[e]) and a high temperature (b[f]) initial state.
As one increases the frequency of the periodic drive, one observes an exponential increase
in the thermalization time (to infinite temperature). **(c,d)** [**(g,h)**] The half-chain entan-
glement entropy $S_{L/2}$ as a function of time for short-range [long-range] interactions. Two
distinct timescales emerge: $\tau_{D_{\text{eff}}}$ and τ^*. τ^* corresponds to the thermalization time and is
estimated via the colored, dashed vertical lines. $\tau_{D_{\text{eff}}}$ corresponds to the time-scale where
the system reaches the prethermal Gibbs state (with entropy $S_{L/2}^P$) of the effective Hamilto-
nian D_{eff}, and is indicated via a solid, black vertical line.At higher frequency, $\omega = 12.5$, the
system's entanglement entropy dynamics faithfully captures the prethermal plateau owing
to its long thermalization time scale (not accessible within the time scale of the numerics)
and the dynamics follows that from of the evolution under the infinite frequency prether-
mal Hamiltonian $D_{\text{eff}}^{(0)}$ (dotted black line). (inset, c[g]) Early time evolution of $S_{L/2}$ for the
short-range [long-range] model.

agreement with recent rigorous proofs [380, 312, 5, 161, 5].

Intriguingly, for long-range interacting systems (with power-law $1 < \alpha < 2$), we *also* observe the emergence of a time-independent D_{eff} that generates the dynamics of the system until exponentially late times. This result *extends* beyond previous analytical bounds, where the lack of a Lieb-Robinson bound with a polynomial light-cone for long-ranged systems $d < \alpha < 2d$ (where d is the spatial dimension) precluded the study of this regime [542]. Our observations, thus, suggest that the Lieb-Robinson bound might be too strict of a condition to understand the equilibration dynamics of generic systems from generic states, and different bounds (such as those encoded in the Frobenius norm [539]) may provide important new insights into the prethermalization/equilibration dynamics of long-range interacting systems. Our results are also of particular relevance to experiments in isolated quantum optical systems of atoms, ions and molecules, where strong interactions often take the form of long-range Coulomb, dipolar, or van der Waals couplings [586, 598, 152, 490].

10.1 Model and probes

We analyze one-dimensional spin chains whose Floquet evolution is governed by a Hamiltonian with power-law interactions:

$$H_\ell(t) = J \sum_{i<j} \frac{\sigma_i^z \sigma_j^z}{|i-j|^\alpha} + \vec{h}(t) \cdot \left[\sum_i \vec{\sigma}_i \right] + J_x \sum_{\langle i,j \rangle} \sigma_i^x \sigma_j^x \qquad (10.1)$$

where $\vec{h}(t) = \vec{h}(t+T)$ and $\vec{h}(t) = h_x \hat{x} + (h_y \hat{y} + h_z \hat{z})[1 - 2\theta(t - T/2)]$ for $t \in [0, T)$ [Fig. 10.1(b) inset] induces a "bang-bang" protocol as considered in previous studies on quantum thermalization [119, 439, 440], σ_i^γ are Pauli operators and $\omega = 2\pi/T$ is the driving frequency [380, 312, 5, 161, 5]. We also consider a short-range interacting model, $H_s(t)$, realized by truncating the Ising interaction in $H_\ell(t)$ to nearest and next-nearest neighbor. Throughout this work we consider the parameters $\{J, J_x, h_x, h_y, h_z, \alpha\} = \{1, 0.19, 0.21, 0.17, 0.13, 1.25\}$. The inclusion of non-zero J_x and h_x ensures the static part of the Hamiltonian is not trivially diagonal in the σ_i^z basis, controlling the time scale $\tau_{D_{\text{eff}}}$ of the approach to the prethermal plateau, as well as the local energy scale. We emphasize that our results are neither sensitive to the particular choice of parameters nor to the details of our driving protocol, nature of the couplings and symmetries of the Hamiltonian and the same phenomenology occurs with different choices of parameters and long-range interactions.

To characterize the Floquet thermalization dynamics, we begin with two diagnostics (Fig. 10.1). First, we use the increase of the energy averaged over a period of the drive: $D_{\text{eff}}^{(0)} \equiv \frac{1}{T} \int_0^T dt \, H_\ell(t) = J \sum_{i<j} \frac{\sigma_z^i \sigma_z^j}{|i-j|^\alpha} + h_x \sum_i \sigma_x + J_x \sum_{\langle i,j \rangle} \sigma_x^i \sigma_x^j;$[3] we note that $D_{\text{eff}}^{(0)}$ is actually the first term in an expansion for the prethermal Hamiltonian, $D_{\text{eff}} = D_{\text{eff}}^{(0)} + D_{\text{eff}}^{(1)}/\omega + D_{\text{eff}}^{(2)}/\omega^2 + \cdots,$

---

[3]In the short-range case, $D_{\text{eff}}^{(0)}$ only contains the nearest and next nearest neighbor Ising terms.

which contains a large but finite number of terms [380, 312, 5, 161, 5]. To set notation, let us also define $\mathcal{D}_{\text{eff}}^n$ as the truncation of D_{eff} to n-th order in $1/\omega$. As a second diagnostic, we investigate the growth of the half-chain entanglement entropy as a function of time: $S_{L/2} \equiv \text{Tr}(-\rho_{L/2} \ln \rho_{L/2})$ where $\rho_{L/2} \equiv \text{Tr}_{1 \leq i \leq L/2}(|\psi(t)\rangle\langle\psi(t)|)$.

10.2 Exponentially slow thermalization

We directly compute the Floquet evolution of up to $L = 26$ spins using massively parallel Krylov subspace techniques [33, 233, 232]. We consider initial product states with spins polarized along $\hat{z}$ and control the energy density of the initial state by varying the number of equally-spaced domain walls that are present. We begin with the short-range model, $H_s(t)$ and compute the time evolution of $\langle D_{\text{eff}}^{(0)}(t) \rangle / L$ for $L = 20$ spins at a variety of driving frequencies (significantly larger than the local energy scales of the Hamiltonian but smaller than the global many-body bandwidth). Unlike the small size ($L = 12$) exact diagonalization results, Fig. 10.1(a) inset, one observes a clear approach to infinite temperature ($\langle D_{\text{eff}}^{(0)} \rangle / L \rightarrow 0$) at late times for a wide range of frequencies, Fig. 10.2(a), allowing us to study the effect of frequency in the infinite temperature thermalization. Later in this work, we further verify that indeed $L = 20$ captures both the large system size thermalization dynamics (Fig. 10.5) and long-range nature of the interactions (Fig. 10.6). We define the thermalization time τ_{En}^* as the time at which the energy density is halfway from its initial value to its infinite temperature value, $\langle D_{\text{eff}}^{(0)}(\tau_{En}^*) \rangle = 0.5 \langle D_{\text{eff}}^{(0)}(t = 0) \rangle$. For both low, Fig. 10.2(a), and high temperature, Fig. 10.2(b), initial states, one observes an exponential enhancement of τ_{En}^* as a function of increasing driving frequency.

To further probe the exponentially slow heating of the system, we investigate the growth of the half-chain entanglement entropy as a function of time. We expect the evolution of $S_{L/2}(t)$ to be characterized by three distinct regimes: an initial growth period beginning from $S_{L/2}(0) = 0$; an intermediate plateau where the entropy reaches its prethermal value, $S_{L/2}^P$; and a final plateau once the system has fully thermalized to infinite temperature, $S_{L/2}^{T=\infty} = (L \ln(2) - 1)/2$ [416]. This is indeed born out by the numerics, Fig. 10.2(c,d). The time scale $\tau_{S_{L/2}}^*$ at which the entropy is halfway from its prethermal plateau value to its infinite temperature value gives us an alternate estimation of the thermalization time τ^*, $S_{L/2}(\tau_{S_{L/2}}^*) = S_{L/2}^P + \frac{1}{2}[S_{L/2}^{T=\infty} - S_{L/2}^P]$, and has the virtue of not relying upon the choice of operator (such as $\mathcal{D}_{\text{eff}}^n$) used to probe the state of the system. For both low, Fig. 10.2(c), and high, Fig. 10.2(d), temperature initial states, one observes an exponentially-long heating time scale consistent with that extracted from $\langle D_{\text{eff}}^{(0)} \rangle / L$. To this end, Fig. 10.3(a) shows just how well $\tau_{S_{L/2}}^*$ fits an exponential dependence for a variety of different initial states. Let us emphasize that, as the system leaves the prethermal plateau and heats toward its final infinite temperature state, the entanglement entropy closely follows the expected thermal value, suggesting that the system evolves between different global thermal states with respect to the prethermal Hamiltonian D_{eff}.
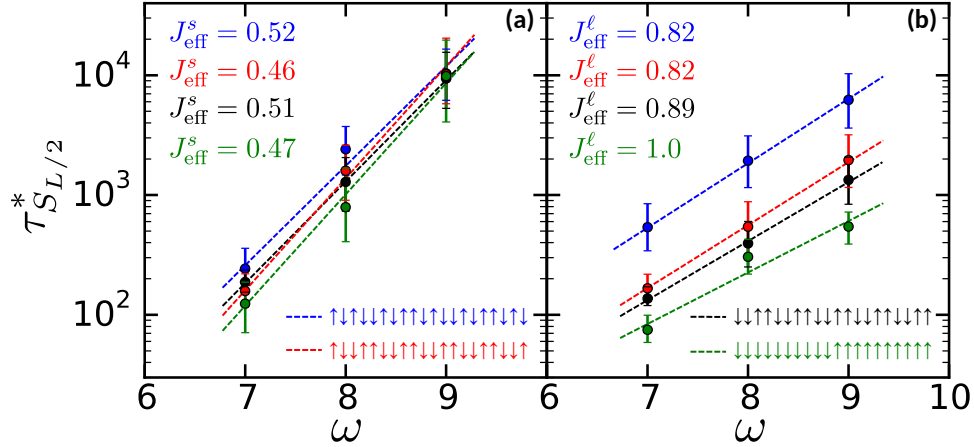
Figure 10.3: **Exponential dependence of the heating time on the drive's frequency.**
The thermalization time $\tau^*_{S_{L/2}}$, as extracted from $S_{L/2}$, as a function of driving frequency for
both (a) short and (b) long-range interactions. The slope provides a direct estimate of J_{eff},
the energy scale controlling the slow thermalization dynamics. The extracted J_{eff} is largely
independent of initial state (different colors) and is consistent with its interpretation as an
effective local energy scale of the system. Initial states near the edge of the spectrum exhibit
slightly larger $\tau^*_{S_{L/2}}$, which can be qualitatively attributed to a reduction of the density of
states at these energies.

There is a second time scale in the problem; namely, the time, $\tau_{D_{\text{eff}}}$, at which the en-
tanglement entropy reaches its prethermal plateau value, $S^P_{L/2}$, as depicted in Fig. 10.2(c,d).
This is the time at which the system *globally* establishes the prethermal equilibrium-like
Gibbs state of D_{eff} and is expected to be greater than the *local* thermalization time of D_{eff}
by a factor of order $\sim L$. The value of the plateau entropy, $S^P_{L/2}$, depends on the inverse
temperature of the prethermal ensemble, β_{eff}, which in turn can be directly estimated using
energy density, ϵ, of the initial state: $\epsilon L = \langle D_{\text{eff}}(t=0)\rangle \approx \text{Tr}\left[D_{\text{eff}}\ e^{-\beta_{\text{eff}} D_{\text{eff}}}\right]/\text{Tr}[e^{-\beta_{\text{eff}} D_{\text{eff}}}]$.

To quantitatively verify this relationship, we perform imaginary time evolution of random
initial states (infinite temperature-like states) in order to estimate the entanglement entropy
of the thermal state. In the case of short-range interactions, this approach predicts $S^P_{L/2} = $
4.34 and $S^P_{L/2} = 5.13$ for low and high temperature initial states, respectively, both in
excellent agreement with the numerically observed plateau, Fig. 10.2(c,d).

We now turn to the long-range interacting model, $H_\ell(t)$, with power-law $\alpha = 1.25$, where
we again compute $\langle D^{(0)}_{\text{eff}}(t)\rangle/L$ and $S_{L/2}(t)$. As aforementioned, recent results have proven
exponentially slow heating in Floquet systems with power-law interactions [380, 312]. The
intuition is that the system still requires many rearrangements, each with a few-body (albeit
long-ranged) interaction [380, 312], in order to absorb energy ω from the drive. Indeed,
for both low, Fig. 10.2(e,g), and high, Fig. 10.2(f,h), temperature initial states, we observe

exponentially slow heating times as a function of frequency, analogous to the short-range
case.

A few remarks are in order. First, the approach of the entanglement entropy to its
prethermal plateau can exhibit a "shoulder" with slow growth, which only flattens into a
true plateau for larger frequencies. This phenomena can occur for both short-range and long-
range interactions, Fig. 10.2(d,g). Much like the short-range case, for long-range interactions
the prethermal plateau is in excellent agreement with the value computed via imaginary
time evolution, $S_{L/2}^{P} = 4.31$ and $S_{L/2}^{P} = 5.74$ for low and high temperature initial states
respectively. Second, while both the short and long-range systems exhibit exponentially
slow thermalization, there is a clear quantitative difference between the heating rates in the
two cases.

We directly extract the energy scale controlling the exponentially slow heating (i.e. the
effective local bandwidth), by fitting $\tau_{S_{L/2}}^{*}$ to $\tau_{S_{L/2}}^{*} \sim e^{\omega/J_{\text{eff}}}$, as depicted in Fig. 10.3. Moti-
vated by the results in Fig. 10.2, we do not consider the $\omega = 6$ data, as they do not exhibit
an approach to the prethermal plateau for any initial state. In the case of short-range inter-
actions, both low and high temperature initial states give $J_{\text{eff}}^{s} \approx 0.5 \pm 0.1$. For the long-range
interacting model, one finds a larger value $J_{\text{eff}}^{\ell} \approx 0.9 \pm 0.1$. Intriguingly, these heating rates
yield a ratio, $J_{\text{eff}}^{\ell}/J_{\text{eff}}^{s} \approx 1.8 \pm 0.2$, which is consistent with the ratio of the average strength
of the Ising interactions emanating from each site, $\left[\sum |i - j|^{-1.25}\right]/\left[1 + 2^{-1.25}\right] \approx 1.6$. We
note that the prefactor of the exponential in τ^{*} is larger for initial states near the edges of
the spectrum, which could arise from the smaller density of states there.

10.3   Long-range prethermal effective Hamiltonian

We now demonstrate that the time-independent prethermal Hamiltonian D_{eff} is indeed the
generator of Floquet dynamics at stroboscopic times up to τ^{*}. Here, we focus on the more
surprising long-range case. Unlike the question of slow heating, a proof of the existence of
a time-independent D_{eff} that approximately generates the dynamics of local observables in
the prethermal regime may need to employ Lieb-Robinson bounds, which cannot exhibit a
power-law cone $d < \alpha < 2d$ [230, 231, 159, 200, 181, 354, 163, 542]. As aforementioned, we
not only observe the same exponentially-slow approach to the maximum entropy (consistent
with $\langle D_{\text{eff}}^{(0)}(t)\rangle/L$), but also the presence of a prethermal plateau (for both low and high
temperature initial states), indicative of the existence of D_{eff} even for long-range interact-
ing systems, Fig. 10.2(g,h)! Such result is not expected to hold generically in the $d < \alpha$
regime, where super-extensivity of the energy and loss of locality leads to a breakdown of
the analytical understanding of prethermalization—a single local rearrangement is capable
of absorbing an arbitrarily large amount of energy.

Further evidence for the existence of a time-independent D_{eff} comes from comparing the
system's evolution under the full Floquet unitary, $U_{f} \equiv \mathcal{T} \, e^{-i \int_{0}^{T} H_{l}(t)dt}$, to evolutions under
truncations of the Magnus expansion: $D_{\text{eff}} = D_{\text{eff}}^{(0)} + D_{\text{eff}}^{(1)}/\omega + D_{\text{eff}}^{(2)}/\omega^{2} + \cdots$ at leading order
$(\mathcal{D}_{\text{eff}}^{0})$, at second order $(\mathcal{D}_{\text{eff}}^{2})$, and at fourth order $(\mathcal{D}_{\text{eff}}^{4})$.
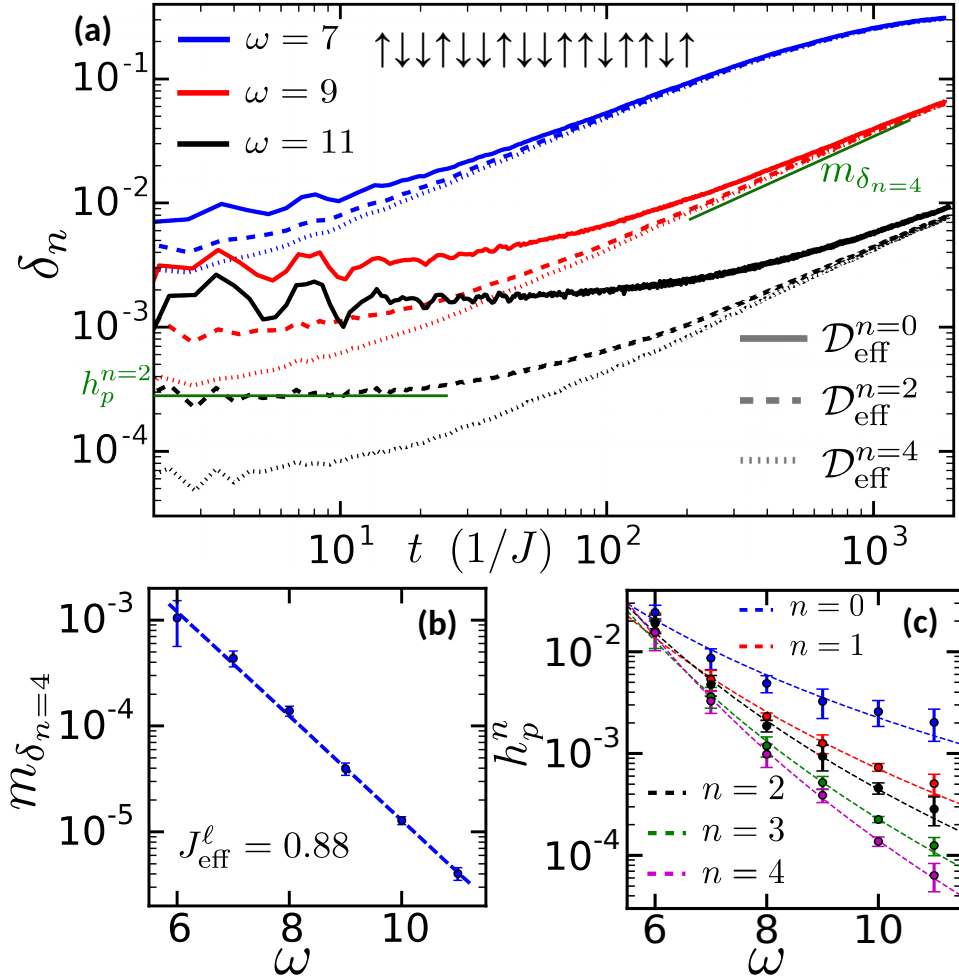
Figure 10.4: **Effective Hamiltonian governing Floquet dynamics.** (a) The difference,
δ_n, of the expectation value of $\mathcal{O} = D_{\text{eff}}^{(0)}/L$ as a function of time, for a chain of length $L = 16$,
with different frequencies (colors) and different Magnus truncation orders (line style) using
the parameters $\{J, J_x, h_x, h_y, h_z, \alpha\} = \{1, 0.19, 0.21, 0.17, 0.13, 1.25\}$. Two distinct regimes
are observed: an initial plateau at short times and a linear increase at late times. (b)
Extracted slope of the late time linear regime of δ_n as a function of frequency. This provides
an independent estimate for J_{eff}^{ℓ} which is in excellent agreement with that calculated from
$\tau_{S_{L/2}}^{*}$. (c) Plateau height $h_{pl}^{(n)}$ for different Magnus truncation orders, n, as a function of
frequency. The results are consistent with an n-dependent power-law.

In Fig. 10.4(a), we plot the difference $\delta_n = |\langle \mathcal{O} \rangle_{U_f} - \langle \mathcal{O} \rangle_{\mathcal{D}_{\text{eff}}^n}|$, as a function of time for different frequencies and different Magnus truncation orders n, with operator $\mathcal{O} = D_{\text{eff}}^{(0)}/L$ (different local operators exhibit analogous results but this one has the cleanest numerics). Here, $\langle \mathcal{O} \rangle_H$ is the expectation value of $\mathcal{O}$ evolved under H; thus, $\delta_n(t)$ captures the time-dependent difference in the expectation value of $\mathcal{O}$ evolved under the full Floquet unitary versus under different approximations to D_{eff}. Inspection reveals two essential features: a short time plateau whose value depends on both n and ω,[4] followed by linear growth at late times that seems to converge for the different truncation orders. To understand these features, we note that there are two contributions to $\delta_n(t)$.

First, even at short times, one expects a finite discrepancy to arise simply from the fact that the nth order Magnus approximation $\mathcal{D}_{\text{eff}}^n$ still differs from D_{eff} (e.g. by terms such as $D_{\text{eff}}^{(n+1)}/\omega^{n+1} + D_{\text{eff}}^{(n+2)}/\omega^{n+2} + \cdots$). As a result, by either increasing n or ω, the effect of higher-order terms in the expansion is decreased, and so is the height of the early time difference plateau. Indeed, measuring the plateau height h_p as a function of frequency, we find that it is consistent with $h_p \sim \omega^{-\gamma(n)}$, where γ is an n-dependent power-law [Fig. 10.4(c)].

Second, since D_{eff} approximates the full Floquet evolution only up to a time scale $\tau^* \sim e^{\omega/J_{\text{eff}}}$, one expects the exponentially slow accumulation of errors, $\delta \sim t e^{-\omega/J_{\text{eff}}}$. Indeed, this linear growth of $\delta_n(t)$ is observed, Fig. 10.4(a), enabling an independent extraction of J_{eff}. In particular, by plotting the slope of the late time growth of $\delta_n(t)$ as a function of the frequency, Fig. 10.4(b), one obtains $J_{\text{eff}}^\ell \approx 0.88 \pm 0.05$ consistent with that calculated via the entanglement entropy in Fig. 3.

10.4 Discussion of numerical methods

Throughout our discussions, we have emphasized the importance of considering sufficiently large systems sizes to ensure that the thermalization behavior we observe is generic and indicative of the thermodynamic limit. Here, we expand upon this point and present additional results carefully quantifying finite-size effects in our numerics. At the same time, we detail the methodology used to extract the various thermalization time scales and their associated uncertainties.

To this end, we consider the impact of system size on the thermalization dynamics of an initial product state (Fig. 10.5). Focusing on energy density $\langle D_{\text{eff}}^{(0)}(t) \rangle/L$ and entanglement entropy $S_{L/2}(t)$, we observe significant finite size effects for $L < 18$; even at moderate driving

---

[4]The nature of the short time dynamics is dependent on both the operator considered and the truncation order of D_{eff}. That there is a plateau at short times arises from the close relationship between $D_{\text{eff}}^{(0)}$ and $\mathcal{D}_{\text{eff}}^n$. As the systems thermalizes with respect to $\mathcal{D}_{\text{eff}}^n$, the expectation value of $D_{\text{eff}}^{(0)}$ will not change significantly as it approaches its thermal average $\langle D_{\text{eff}}^{(0)} \rangle_{\mathcal{D}_{\text{eff}}^n} = \text{Tr}(D_{\text{eff}}^{(0)} e^{-\beta_{\text{eff}}^n \mathcal{D}_{\text{eff}}^n})/Z$. The value of the plateau then corresponds to the difference in the thermal value of $D_{\text{eff}}^{(0)}$ calculated with respect to $\mathcal{D}_{\text{eff}}^n$ and the full D_{eff}. By varying n, one changes both the Hamiltonian to which the system thermalizes as well as the effective temperature of the prethermal regime β_{eff}^n, leading to a non-trivial dependence of the plateau value with both n and ω (but expected to monotonically decrease as either increases).

$$\langle D_{\text{eff}}^{(0)}(t)\rangle \;/\; \langle D_{\text{eff}}^{(0)}(t=0)\rangle \qquad\qquad \delta S_{L/2}(t) \;/\; S_{L/2}^{T=\infty}$$
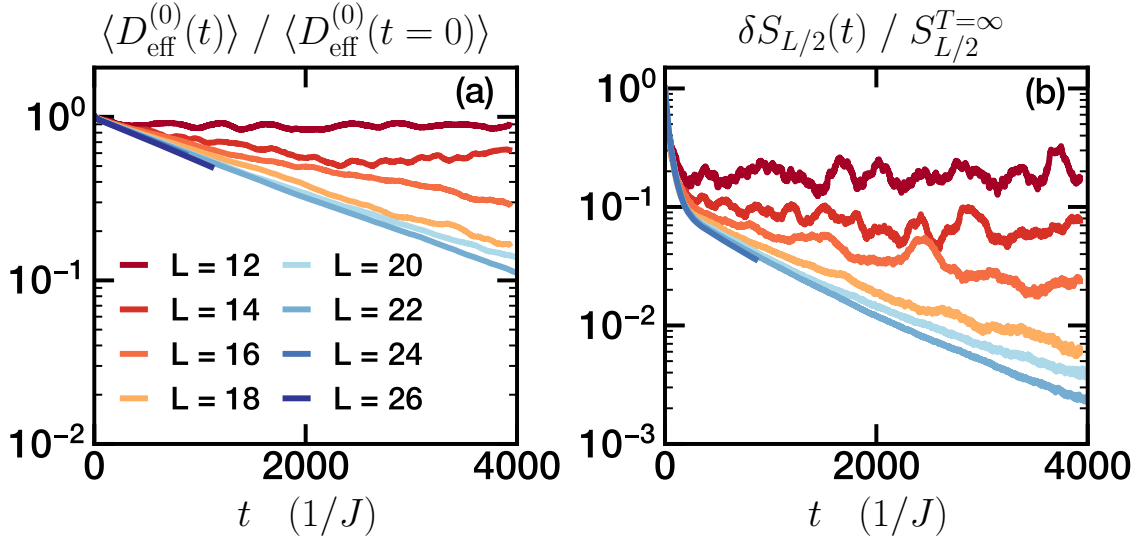
Figure 10.5: **Finite system size effects on thermalization dynamics.**   (a)[(b)] Finite system size effect on the thermalization dynamics of energy $D_{\text{eff}}^{(0)}/L$ [entanglement entropy $\delta S_{L/2}(t) = S_{L/2}(t) - S_{L/2}^{T=\infty}$] using parameters $\{J, J_x, h_x, h_y, h_z, \alpha, \omega\} = \{1.0, 0.19, 0.21, 0.17, 0.13, 1.25, 8\}$ and a Néel-like initial state with a domain wall every two spins. After the system has approached the prethermal state ($t > \tau_{D_{\text{eff}}} \sim 300$), the dynamics for different system sizes $L \gtrsim 18$ converge to a simple exponential decay—the associated decay rate captures the thermalization time scale of the system.

frequencies the system fails to exhibit a simple universal approach to infinite temperature and the late time dynamics is characterized by the presence of fluctuations and a plateau. As one considers larger systems sizes, $L \gtrsim 18$, such features are greatly reduced and the dynamics converge; indeed, both quantities approach their infinite temperature value as a simple exponential. The characterization of the dynamics via a single thermalization time scale demonstrates that our results capture the underlying heating dynamics due to the drive and are not limited by the finite system size.

Having established that the system size considered in our analysis does not affect the observed thermalization dynamics, we now demonstrate it is also large enough to capture the long-range nature of the interactions, Eq. 10.1. Unlike the short-range case, long-range interactions can induce a finite temperature ordered phase in one dimensional systems which leads to distinct late time thermalization dynamics. In Fig. 10.6, we probe this distinction by studying the magnetization dynamics, $M(t) = L^{-1}\sum_i \langle \sigma_i^z(t)\rangle$, under the static Hamiltonian $D_{\text{eff}}^{(0)}$, where, for power-law $\alpha < 2$, a ferromagnetic phase exists near the edge of the spectrum [153]. Indeed, when considering $\alpha = 1.13$, $M(t)$ remains non-zero at late times—consistent with an approach toward a spontaneously symmetry broken equilibrium state with non-zero
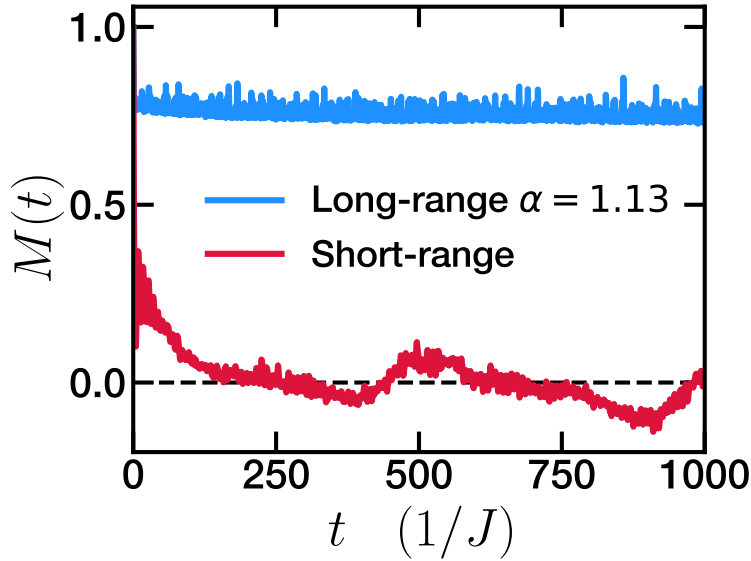
Figure 10.6: **Prethermalization to symmetry-broken state.** Dynamics of the average magnetization $M(t)$ using the parameters $\{J, J_x, h_x, h_y, h_z\} = \{1, 0.75, 0.21, 0.17, 0.13\}$ and the same initial product state (near the edge of the spectrum), for different range of interactions: (blue) long-range with power-law $\alpha = 1.13$, and (red) short-range with nearest and next nearest neighbor interactions $\{J_{NN}, J_{NNN}\} = \{1.0, 2^{-1.13}\}$. When considering the evolution under the long-range static $D_{\text{eff}}^{(0)}$, $M(t)$ remains non-zero at late times—this is consistent with the equilibration of the system toward ferromagnetic state. In contrast, when considering the short-range $D_{\text{eff}}^{(0)}$, we observe that $M(t)$ quickly decays to zero as no ferromagnetic equilibrium state exists.

net magnetization. In stark contrast, when considering the short-range case, $M(t)$ quickly decays to zero—consistent with the lack of an ordered phase. Such difference demonstrates that the dynamics are sensitive to the long-range nature of the interactions at the system size considered.

Finally, we detail our methodology for measuring the different quantities extracted from our numerics:

- Heating time scale τ^* — for both energy density and entanglement entropy we measure the heating time scale τ^* (τ_{En}^* and $\tau_{S_{L/2}}^*$ respectively) as the time at which the quantity is midway between its prethermal and final infinite temperature value. To estimate the uncertainty, we also measure the times τ_{min}^* and τ_{max}^* at which each quantity is 35% and 65% between its prethermal and infinite temperature value, respectively; the uncertainty is taken as the larger of the two deviations, $|\tau^* - \tau_{min}^*|$ and $|\tau^* - \tau_{max}^*|$.

- Late time error slope m_{δ_n} — we divide the late time linear regime into six equally sized

sub regions, and within each region we perform a linear fit to δ_n to extract a slope. The final value m_{δ_n} is given by the average of the six extracted slopes with an uncertainty given by twice the standard deviation.

- Initial error plateau $h_p^n - h_p^n$ is given by the average deviation δ_n within the time window between $2J^{-1}$ and $5J^{-1}$, while the uncertainty is twice the standard deviation.

10.5 Conclusion

Despite their ubiquity, periodically-driven Floquet systems have generally not shown distinct phases of matter. This is largely due to their tendency to heat up to infinite temperature, except in certain exceptional cases, such as free fermion systems (e.g. topological insulators [255, 331, 562, 264, 530]), and strongly-disordered one-dimensional systems in the many-body localized phase [37, 205, 249, 30, 89, 395]. In the high-frequency limit, however, we have shown that there is an exponentially-long time interval during which a system may, as it would in true thermal equilibrium, realize phases of matter and phase transitions between them, including certain phases that do not exist in undriven systems [161, 602, 100].

In the next few chapters, we focus on this question by studying prethermal phases in *long-range* interacting systems. Owing to the importance of the Lieb-Robinson bound for building an analytical understanding of the prethermal dynamics, we devote Chapter 11 to improving Lieb-Robinson bound for multi-body long-range interacting systems [163]. These results will become crucial when, in Chapter 12, we prove the existence and stability of prethermal phases of matter in long-range interacting systems. We complement this analysis with a numerical investigation of a prethermal phase. We conclude our analysis of quantum prethermalization in Chapter 13 by discussing the experimental observation of a prethermal phase of matter—the prethermal discrete time crystal [345]. Finally, in Chapter 14, we take a step back and consider the broader question of Floquet prethermal dynamics in *classical* systems, and demonstrate that, although there is no effective, static description for the stroboscopic dynamics, prethermal phases of matter are still well defined and stable—using large scale numerics, we study their properties [592].

Chapter 11

Lieb-Robinson bounds for long-range interacting quantum systems

The speed of light sets an upper bound on the speed at which information can spread; a fundamental fact that is encoded in the structure of the relativistic quantum field theories that describe the universe. When considering non-relativistic discrete systems, however, there is no notion of "speed of light" and thus information can, in principle, move arbitrarily fast. The *Lieb-Robinson bound* [330, 390, 230, 65, 392, 389, 391] is a formal statement that establishes the existence of a analogous "light-cone" for the spread of quantum information, recovering the notion of locality in non-relativistic quantum systems. Such constraints on the spread of information, in addition to being physically important in their own right, have also been used as ingredients in the rigorous mathematical proof of key results about discrete quantum systems [228, 390, 229, 230, 412, 392, 65, 227, 66, 64, 28, 365, 5], including the exponential decay of correlations in the ground states of gapped Hamiltonians [390, 230] and the stability of topological order [65, 66, 64, 365].

More recently, numerical and analytical works have investigated the existence of analogous Lieb-Robinson bounds in discrete spin systems where interactions *do not* have a finite range, but rather fall off as a power of the spin separation [230, 231, 159, 462, 181, 486, 519, 354, 86, 324, 87, 342]. Such long-range interactions arise in a wide variety of experimental platforms, ranging from solid-state spin defects [474, 281, 595] to quantum optical systems of trapped ions [55], polar molecules [384], and Rydberg atoms [479]. While the majority of previous studies have focused on few-body physics, recent advances have enabled a number of these platforms to begin probing the many-body dynamics and information propagation of strongly interacting, long-range systems [586, 462, 598].

Motivated by the development of these physical platforms, in this work, we improve Lieb-Robinson bounds for generic power-law interactions. Specifically, let us consider a system of spins on a set of sites Λ governed by a Hamiltonian H, which can be written as a sum $H = \sum_Z H_Z$ of terms acting on subsets of sites $Z \subseteq \Lambda$ in d-dimensional space. Moreover, we assume (among other conditions described in Section 11.1) that there exists a constant

Reference	Multi-body Hamiltonians	Asymptotic Spatial Decay	LC1	LC2
Ref. [181]	✗	$r^{-(\alpha+d)}$	$\alpha > d$	$\alpha > d$
Ref. [354]	✓	$r^{-(\alpha-d)/(\eta+1)}$	$\alpha > d$	$\alpha > 2d$
Our work	✓	$r^{-\alpha}$	$\alpha > d$	$\alpha > d$

Table 11.1: **Summary of power-law Lieb-Robinson bounds for $\alpha > d$.** Note that the LC1 and LC2 columns describe the power-law regime where these light-cones exist and are power-law.

J such that

$$\sup_{z \in \Lambda} \sum_{Z \ni z : \text{diam}(Z) \geq R} ||H_Z|| \; \leq \; \frac{J}{R^\alpha}, \tag{11.1}$$

where $\text{diam}(Z)$ is the greatest distance between any two points in Z. A familiar example [601, 100] is the long-range Ising interaction,

$$H = H_{\text{short-range}} + \widetilde{J} \sum_{i \neq j} \frac{1}{|\mathbf{r}_i - \mathbf{r}_j|^{d+\alpha}} \sigma_i^z \sigma_j^z. \tag{11.2}$$

Note that in this chapter we are following the convention of Ref. [354] in the definition of the power-law, α. This differs from the definition of "α" previous chapters and in Ref. [181], which would be equal to $\alpha + d$ in this convention.

An early result on Lieb-Robinson bounds in power-law interacting systems was proved in Ref. [230], which demonstrated the existence of a light-cone whose size grows exponentially in time for any $\alpha > 0$. More recently, this result was improved in Refs. [181] and [354], where it was shown that a *power-law* light-cone emerges for $\alpha > d$, where d is the spatial dimension.

However, each of these results has certain limitations (Table 11.1). On the one hand, Ref. [181] assumes a two-body Hamiltonian, where each term acts on at most two spins. This assumption limits the usage of this result in analyzing multi-body effective Hamiltonians of broad interest in condensed matter physics. Such Hamiltonians can arise in a number of different contexts: for example, ring-exchange interactions may be important in solid ³He [534] and are known to stabilize certain topological phases [369, 422]; multi-body Hamiltonians arise in explicit constructions of various results in mathematical physics [229, 66, 64, 5]; and higher-body interactions naturally emerge in the effective description of periodically-driven two-body Hamiltonians [70, 5].

On the other hand, while Ref. [354] overcomes this two-body assumption, it proves a significantly weaker result regarding the power-law decay of information outside the light-

cone (Table 11.1).[1] In particular, for $\alpha \gtrsim d$, the bounds of Ref. [354] ensure only a relatively slow decay outside the light-cone; which can limit its applicability to some important results, e.g. bounding the difference in operators time evolved under slightly different Hamiltonians.

In this chapter, we prove a Lieb-Robinson bound that addresses both of the above concerns. We demonstrate that for multi-body interactions with $\alpha > d$, the spatial decay of a time evolved operator, outside the light-cone, scales arbitrarily closely to $\sim 1/r^\alpha$ (Table 11.1). While this bound is not as strong as the $\sim 1/r^{\alpha+d}$ decay obtained in Ref. [181], our combination of an improved scaling (over Ref. [354]) and applicability to arbitrary multi-body Hamiltonians, enables the usage of this Lieb-Robinson bound to prove new results in mathematical physics [345].

An important comment is in order. Unlike either short-range or exponentially decaying interactions, power-law interactions are characterized by Lieb-Robinson bounds with power-law tails which lack a natural notion of a length scale. This implies that one must be particularly careful when defining an associated light-cone for such long-range interacting systems. One possible definition of a light-cone (used in Refs. [181, 354]) is the following: at late times, the propagation of a local operator to any one point outside the light-cone is small. From here on, we will refer to this as light-cone 1 (LC1). For short-range interacting systems, LC1 is the only length-scale associated with time evolution. For power-law interacting systems, one can already get a sense of the insufficiency of LC1 by noting the following: despite the differences between the asymptotic spatial decays obtained in Refs. [181], [354] and this work (Table 11.1), they all yield the same LC1 (Table 11.2).

To this end, we introduce a second light-cone, LC2, which properly captures these differences. In particular, LC2 ensures that at late times, the evolution of a local operator is not affected by changes to the Hamiltonian outside of LC2. For short-range interacting systems, LC1 and LC2 coincide, but for long-range interacting systems, they can be quite different. More specifically, Ref. [181] exhibits a finite, power-law LC2 for $\alpha > d$, while Ref. [354] only has a finite LC2 for $\alpha > 2d$, despite both having the same power-law LC1. Intuitively, the lack of an LC2 for $\alpha > d$ in Ref. [354] stems from the aforementioned slow asymptotic spatial decay of quantum information. This highlights the importance of our improved decay; it enables us to prove our second main result, which is the existence of a power-law LC2 for $\alpha > d$ for arbitrary multi-body Hamiltonians (Table 11.1).[2]

This chapter is divided into two main sections. In Section 11.1, we present an improved Lieb-Robinson bound for multi-body long-range interacting systems. We introduce the necessary notation and assumptions used in its derivation. After stating the final bound, we present its detailed proof. In Section 11.2, we introduce the definition of a new light cone (LC2), discussing its differences from the light-cone usually considered in the literature (LC1), as well as its physical motivation and how it relates to previous work. We conclude with a brief summary and discussion in Section 11.3.

---

[1]The $\sim 1/r^{(\alpha-d)/(\eta+1)}$ decay can be improved arbitrarily close to $\sim 1/r^{\alpha-d}$ at the cost of widening the light-cone.

[2]We note that this extension comes at the expense of a worse LC2 exponent compared to Ref. [181] (Table 11.2)

11.1 Improved Lieb-Robinson bound

Assumptions and notation

Our notation will be similar to that of Ref. [354]. We consider a set of sites Λ with a metric
$d(x,y)$ for $x, y \in \Lambda$, and a Hamiltonian H written as a sum of terms $H = \sum_Z H_Z$, where
H_Z is supported on the set $Z \subseteq \Lambda$. We extend the notation of the metric to sets, denoting
$d(X, Y)$ as the minimum distance between any two elements of the sets $X, Y \subseteq \Lambda$, as well
as between sets and sites, denoting $d(X, y) = d(X, \{y\})$. We define a function $f(R)$ that
captures the power-law decay of interactions:

$$f(R) := \sup_{z \in \Lambda} \sum_{Z \ni z : \mathrm{diam}(Z) \geq R} \|H_Z\| \, , \tag{11.3}$$

where

$$\mathrm{diam}(Z) = \sup_{x,y \in Z} d(x, y) \, , \tag{11.4}$$

and we assume there are constants J and $\alpha > d$ (the dimensionality of the system) such
that $f(R) \leq J R^{-\alpha}$. We also require that the sum of the operator norms of all of the terms
involving any site be finite:

$$\mathcal{C}_0 := \sup_{x \in \Lambda} \sum_{y \in \Lambda} \sum_{Z \ni x, y} \|H_Z\| < \infty \, . \tag{11.5}$$

Finally, we assume certain conditions on the set of sites Λ and its metric. Specifically,
we assume that Λ can be embedded in Euclidean space $\mathbb{R}^d$, so that for each $z \in \Lambda$ there is a
corresponding $\mathbf{r}_z \in \mathbb{R}^d$, such that $d(x, y) = |\mathbf{r}_x - \mathbf{r}_y|$. Moreover, we assume there is a smallest
separation a such that $d(x, y) \geq a$ for any $x, y \in \Lambda$ unless $x = y$. We choose to work in units
such that $a = 1$. Despite an emphasis on this class of physically motivated sets of sites and
metrics, the strategy and arguments developed in this work should extend to more general
Λ and $d(x, y)$, as in Ref. [354]

Let us also define $\tau_t^H(O)$ as the operator O time-evolved according to the Heisenberg
representation

$$\tau_t^H(O) = e^{itH} \, O \, e^{-itH}. \tag{11.6}$$

Throughout this chapter we will use "C" to refer to any constants that depends only on
σ (the parameter introduced in the statement of the theorem) and Λ. It will not necessarily
be the same constant each time it appears.

Statement of main result

Theorem 1. *Given the assumptions stated above, let observables A and B be supported on
sets X and Y respectively. Then for any $(d + 1)/(\alpha + 1) < \sigma < 1$:*

$$\|[\tau_t^H(A), B]\| \leq \|A\| \|B\| \left\{ 2|X| e^{vt - r^{1-\sigma}} + C_1 \frac{\mathfrak{G}(vt)}{r^{\sigma\alpha}} \right\}, \tag{11.7}$$

where $r = d(X,Y)$ and $v = C_2 \max(J, \mathcal{C}_0)$. Moreover, there exists a constant C_3 such that:

$$\mathfrak{G}(\tau) \leq C_3(\tau + \tau^{1+d/(1-\sigma)})|X|^{n^*+2}, \tag{11.8}$$

where

$$n^* = \left\lceil \frac{\sigma d}{\sigma \alpha - d} \right\rceil \tag{11.9}$$

Here, all C_i are constants only dependent on σ and Λ.

By choosing σ arbitrarily close to 1 we obtain a decay of the Lieb-Robinson bound that approaches $\sim r^{-\alpha}$ for large r.

Proof

Iteration Procedure

The main challenge in understanding the spread of a local operator in long-range interacting systems is being able to differentiate the contribution from strong "short" range terms and the weak "long" range terms in a problem with no natural length scale. As a result, there is no single separation between "short" and "long" range terms of the Hamiltonian that yields a strict bound. To this end, we develop a construction that iteratively introduces a new short scale [181, 354], enabling us to better account for the spatial decay of interactions in the Hamiltonian and obtain an improved Lieb-Robinson bound.

As a starting point, we consider a truncated version of our long-range Hamiltionian with a cutoff R, $H^{\leq R}$:

$$H^{\leq R} = \sum_{Z:\mathrm{diam}(Z)\leq R} H_Z \ . \tag{11.10}$$

At the end of our construction we can make $R \to \infty$, recovering the full Hamiltonian. Because $H^{\leq R}$ has finite range R, a Lieb-Robinson bound for short-ranged Hamiltonians can be applied. However, this is clearly not the optimal bound, as it assumes all interactions of range up to R are equally strong, ignoring their decay with range. Nevertheless, this provides the starting point for our iterative process.

An outline of this procedure is as follows. At each iteration step, the Hamiltonian $H^{\leq R}$ is split into a short and a long-range piece using a new cutoff R':

$$H^{\leq R} = H^{\leq R'} + H^{R';R} \tag{11.11}$$

$$\text{where} \quad H^{R';R} = \sum_{Z:R'<\mathrm{diam}(Z)\leq R} H_Z \ . \tag{11.12}$$

Then, following the strategy of Refs. [181] and [354], the time-evolution of an operator A is separated into a contribution from the short-range part $H^{\leq R'}$ and the long-range part $H^{R';R}$.

The role of these two terms can be intuited by considering the long-range part as a weak perturbation on top of the short-range part: under evolution via $H^{\leq R'}$ alone, the operator spreads with a linear light-cone as per short-range Lieb-Robinson bounds, Fig. 11.1(a); the weak $H^{R';R}$ part then leads to a faster spreading by directly connecting this growing operator with the outside of its light-cone, Fig. 11.1(b).

This picture is made precise in Lemma 3.1 in Ref. [354], where the total spread of the operator is bounded as a contribution from the short-range part $H^{\leq R'}$, as well as an *additional* contribution due to the long-range part $H^{R';R}$:

$$\|[\tau_t^{H^{\leq R}}(A), B]\| \leq \|[\tau_t^{H^{\leq R'}}(A), B]\|+$$
$$+ 2\|B\| \int_0^t \|[\tau_{t-s}^{H^{\leq R'}}(A), H^{R';R}]\| \ ds \tag{11.13}$$

This procedure enables us to better distinguish the contribution of the strong short-range terms and the weak long-range terms of the evolution, improving upon the initial naive bound. Once this iteration step is concluded and an improvement is obtained, one can perform the procedure again further reducing the contribution from the long-range piece of Eq. 11.13 and improving the spatial decay of the Lieb-Robinson bound. We note this iterative process recovers the argument of Ref. [354] after one iteration; by iterating multiple times we can improve on their results. We make this iterative construction more precise with the following Lemma:

Lemma 1. *Fix a set $X \subseteq \Lambda$ and a time t. Suppose that we have a function $\lambda^{(R)}(r)$ such that for all $0 \leq s \leq t$, $Y \subseteq \Lambda$ and observables A and B supported on sets X and Y respectively, the bound*

$$\|[\tau_s^{H^{\leq R}}(A), B]\| \leq \lambda^{(R)}(d(X,Y))\|A\|\|B\| \tag{11.14}$$

is satisfied. We assume that $\lambda^{(R)}(r)$ is monotonically increasing in R and decreasing in r. Then, for any $R' > 0$, Eq. 11.14 is also satisfied with λ replaced by $\widetilde{\lambda}$, defined according to

$$\widetilde{\lambda}^{(R)}(r) = \lambda^{(R')}(r) + C\Theta(R - R')\,|X|\,t\,f(R')\,\mathcal{I}[\lambda^{(R')}], \tag{11.15}$$

where $f(R)$ is given in Eq. (11.3); C is a constant independent of $R, R', |X|$ and t; $\Theta(x)$ is the Heaviside theta function and:

$$\mathcal{I}[\lambda] = \lambda(0) + \int_{1/2}^{\infty} \rho^{d-1}\lambda(\rho) \ d\rho. \tag{11.16}$$

Proof. For $R' \geq R$, the result follows directly from the monotonicity with respect to R. On

the other hand, for $R' < R$ we have, from Eq. 11.13:

$$\|[\tau_t^{H^{\leq R}}(A), B]\| \leq \|[\tau_t^{H^{\leq R'}}(A), B]\| + 2\|B\| \int_0^t ds \; \|[\tau_{t-s}^{H^{\leq R'}}(A), H^{R';R}]\|$$

$$\leq \|[\tau_t^{H^{\leq R'}}(A), B]\| + 2\|B\| \int_0^t ds \sum_{Z:R'<\text{diam}(Z)\leq R} \|[\tau_s^{H^{\leq R'}}(A), H_Z]\|$$

$$\leq \lambda^{(R')}(d(X,Y))\|A\|\|B\| + 2t\|B\| \sum_{Z:R'<\text{diam}(Z)\leq R} \lambda^{(R')}(d(X,Z))\|H_Z\|\|A\|$$

$$\leq \lambda^{(R')}(d(X,Y))\|A\|\|B\| + 2t\|A\|\|B\| \sum_{z\in\Lambda} \sum_{Z\ni z:R'<\text{diam}(Z)\leq R} \lambda^{(R')}(d(X,z))\|H_Z\|$$

$$\leq \lambda^{(R')}(d(X,Y))\|A\|\|B\| + 2t\|A\|\|B\|f(R') \sum_{z\in\Lambda} \lambda^{(R')}(d(X,z))$$

$$\leq \lambda^{(R')}(d(X,Y))\|A\|\|B\| + 2\|A\|\|B\|tf(R')|X| \sup_{x\in X} \sum_{z\in\Lambda} \lambda^{(R')}(d(x,z))$$

$$\leq \lambda^{(R')}(d(X,Y))\|A\|\|B\| + 2\|A\|\|B\|tf(R')|X|\mathcal{I}[\lambda^{(R')}] \; . \tag{11.17}$$

In going from the second to the third inequality, it is helpful to recall that $\lambda^{(R')}(d(X,Y))$ is independent of s (but dependent on t). In going from the fourth to the fifth inequality, we used:

$$\sum_{z\in\Lambda} \sum_{Z\ni z,R'<\text{diam}(Z)<R} \lambda^{(R')}(d(X,z))\|H_Z\| \tag{11.18}$$

$$= \sum_{z\in\Lambda} \lambda^{(R')}(d(X,z)) \sum_{Z\ni z,R'<\text{diam}(Z)<R} \|H_Z\| \tag{11.19}$$

$$\leq f(R') \sum_{z\in\Lambda} \lambda^{(R')}(d(X,z)). \tag{11.20}$$

To obtain the final result, we have replaced the sum by an integral in the last inequality of Eq. (11.17).

Finally, let us emphasize that the simplest bound for $\lambda^{(R')}(d(X,Y))$ corresponds to the short-range Lieb-Robinson bound where the interactions have at most range R', and, thus, can always be used as the first term of Eq. 11.13. $\qquad\square$

We now iteratively apply Lemma 1. Eq. 11.15 says that a Lieb-Robinson bound $\lambda^{(R)}$ for an interaction with maximum range R can be rewritten as the sum of two contributions: a Lieb-Robinson bound $\lambda^{(R')}$ for an interaction of maximum range R', which can be interpreted as the "short-range part of the evolution"; and an additional contribution due to "long-range hops", which have range between R' and R and maximum strength $f(R')$. However, these "long-range hops" need not originate in the support of the original A itself but, rather, in the support of the time-evolved A under the short-range part of the interaction. This additional effect, depicted in Fig. 11.1, is captured by the $\mathcal{I}[\lambda^{(R')}]$ term.

At each iteration we replace the short-range contribution by the short-range Lieb-Robinson bound. We make use of the bound proven in Theorem A.1 of Ref. [354] which state that, for observables A and B supported on sets X and Y, respectively:

$$\|[\tau_t^{H^{\leq R'}}(A), B]\| \leq 2|X| \exp[vt - d(X,Y)/R']\|A\|\|B\| . \tag{11.21}$$

Finally, we are free to choose R' in Eq. 11.15. In particular, we choose it to be a function of r; specifically, at the n-th iteration we take $R' = r^{\sigma_n}$, with $d/\alpha < \sigma_n < 1$. The resulting bound no longer depends on any cut-off R' and when used again in Eq. 11.15, leads to a faster decaying $\mathcal{I}[\lambda]$ and an improved bound.

Therefore, at the n-th iteration we obtain the bound:

$$\|[\tau_s^{H^{\leq R}}(A), B]\| \leq \lambda_n^{(R)}(d(X,Y))\|A\|\|B\|, \tag{11.22}$$

where the iteration equation is:

$$\lambda_n^{(R)}(r) = \Delta_r \left(2|X| \exp\left[vt - r^{1-\sigma_n}\right] + C\Theta(R - r^{\sigma_n})|X|t\, f(r^{\sigma_n})\mathcal{I}[\lambda_{n-1}^{(r^{\sigma_n})}] \right) , \tag{11.23}$$

where

$$\Delta_r(u) = \begin{cases} 2 & r < 1 \text{ or } u > 2 \\ u & \text{otherwise} \end{cases} \tag{11.24}$$

This choice of Δ_r ensures that we always use the trivial bound on the commutator when $r = 0$ or when it is the most stringent bound. Now, it only remains to carry out the iteration.

Analyzing the iteration

To begin the iterative process we can invoke the generic Lieb-Robinson bound for finite-range Hamiltonians, as described in Eq. 11.21. Taking into account the trivial case,

$$\|[\tau_t^{H^{\leq R}}(A), B]\| \leq 2\|A\|\|B\|, \tag{11.25}$$

we begin the iteration with the initial bound:

$$\lambda_0^{(R)}(r) = \Delta_r(2|X|e^{vt-r/R}). \tag{11.26}$$

We then find:

$$\mathcal{I}[\lambda_0^{(R')}] \leq C|X|\left[1 + (vtR')^d\right] \tag{11.27}$$

Taking Eq. 11.23 and setting $R' = r^{\sigma_1}$, we have:

$$\lambda_1^{(R)}(r) \leq \Delta_r\left[2|X|e^{vt-r^{1-\sigma_1}} + C\Theta(R - r^{\sigma_1})\,|X|^2 Jtr^{-\sigma_1\alpha}[1 + r^{\sigma_1 d}(vt)^d]\right] \tag{11.28}$$
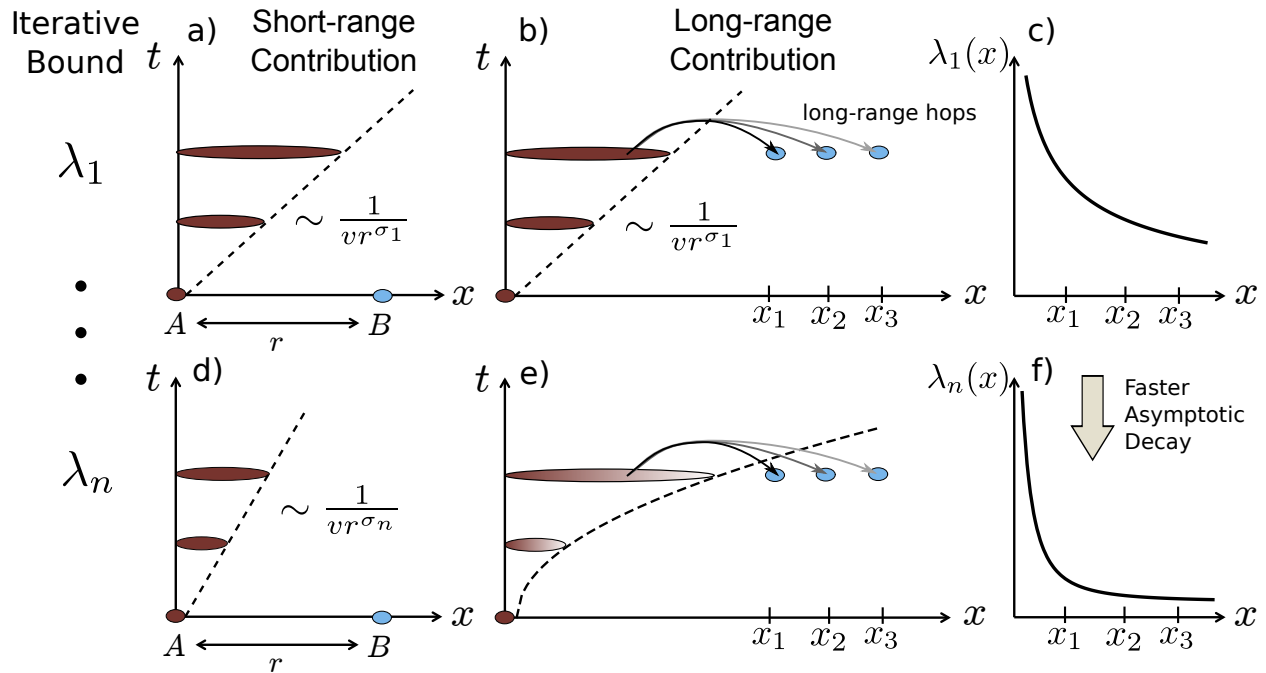
Figure 11.1: **Schematic of the iteration step in proof.** The Lieb-Robinson bound captures the spread of quantum information during evolution by bounding the commutator of a time evolved local operator A with another operator B a distance r away. The spread the operator A can be apportioned into the spread due to interactions of range shorter than R' (left column) and long-range hops due to interactions of range larger than R' (center column). The long-range hops connect the short-range time evolved operator A with strength at most $f(R')$ but they can originate from any location that A has spread to, so the total contribution of these long-range hops is weighted by the integral $\mathcal{I}[\lambda]$ (see Lemma 1). At the first iterative step, which yields λ_1, the short-range interactions can always be characterized by an exponentially decaying bound with a sharp light-cone with slope $(vR')^{-1}$, Eq. 11.21. This corresponds exactly to the short-range contribution to λ_1, **(a)**. The long-range contribution arises from the long-range hops that connect the inside of the light-cone to the support of B, **(b)**. By choosing the cut-off R' as a function of the operator distance, $R' = r^{\sigma_1}$, the resulting bound becomes the sum of exponential and power-law decaying terms, Eq. 11.28, the latter of which dominate the long distance decay of the bound, **(c)**. This choice of R' leads to the light-cone slope of $(vr^{\sigma_1})^{-1}$ of panel **(a)**. At the n-th iteration step, which yields λ_n, we choose a new cut-off $\tilde{R}'$. As before, we obtain a short-range contribution that yields a linear light-cone with slope $(v\tilde{R}')^{-1}$, **(d)**. More importantly, the long-range hops will now be weighted by the power-law decay of the previous bound λ_{n-1}, illustrated by the dark shading in **(e)**. It is the combination of these two power-law decays that enables our iterative procedure to improve the asymptotic decay of the bound λ_n after specifying the cut-off as $\tilde{R}' = r^{\sigma_n}$ **(f)**. This choice of $\tilde{R}'$ leads to the light-cone slope of $(vr^{\sigma_n})^{-1}$ of panel **(d)**.

which recovers the results in Ref. [354] with an appropriate choice of σ_1. From this point,
we proceed by induction. Indeed, suppose at the n-th iteration we have:

$$\lambda_n^{(R)}(r) \leq \Delta_r\left(2|X|e^{vt - r^{1-\sigma_n}} + C\Theta(R - r^{\sigma_n})\sum_{i=1}^{2}\mathfrak{F}_i^{(n)}(vt)\,r^{\mu_i^{(n)}}\right). \tag{11.29}$$

Note that, according to Eq. 11.28, this is satisfied for $n = 1$ if we take

$$\mu_1^{(1)} = \sigma_1(-\alpha + d) \tag{11.30}$$

$$\mu_2^{(1)} = -\sigma_1\alpha \tag{11.31}$$

$$\mathfrak{F}_1^{(1)}(\tau) = C\tau^{d+1}|X|^2 \tag{11.32}$$

$$\mathfrak{F}_2^{(1)}(\tau) = C\tau|X|^2 \tag{11.33}$$

(Here we used the fact that $J/v \leq C$ given the definitions of these quantities.) Then, so long
as $\mu_1^{(n)} + d > 0$ and $\mu_2^{(n)} + d < 0$ we have:

$$\mathcal{I}[\lambda_n^{(R')}] \leq C\left[|X|(1 + (vt)^{d/(1-\sigma_n)}) + \mathfrak{F}_2^{(n)}(vt)\,(vt)^{(d+\mu_2^{(n)})/(1-\sigma_n)} + \mathfrak{F}_1^{(n)}(vt)\,(R')^{(\mu_1^{(n)}+d)/\sigma_n}\right] \tag{11.34}$$

and therefore, using Eq. 11.23 and setting $R' = r^{\sigma_{n+1}}$:

$$\lambda_{n+1}^{(R)}(r) \leq \Delta_r\Bigg(2|X|e^{vt-r^{1-\sigma_{n+1}}} + C\Theta(R - r^{\sigma_{n+1}})|X|Jtr^{-\sigma_{n+1}\left(\alpha - \frac{\mu_1^{(n)}+d}{\sigma_n}\right)}\mathfrak{F}_1^{(n)}(vt) +$$

$$+ C\Theta(R - r^{\sigma_{n+1}})|X|Jtr^{-\sigma_{n+1}\alpha}\left\{|X|(1 + (vt)^{d/(1-\sigma_n)}) + \mathfrak{F}_2^{(n)}(vt)\,(vt)^{(d+\mu_2^{(n)})/(1-\sigma_n)}\right\}\Bigg). \tag{11.35}$$

By choosing $\sigma_{n+1} \leq \sigma_n$ we ensure that the spatial decay of the exponential term does not
increase in performing the iterative procedure.

So at the next iteration we have

$$\mu_1^{(n+1)} = \sigma_{n+1}\left(-\alpha + (\mu_1^{(n)} + d)/\sigma_n\right) \tag{11.36}$$

$$\mu_2^{(n+1)} = -\sigma_{n+1}\alpha \tag{11.37}$$

$$\mathfrak{F}_1^{(n+1)}(\tau) = C\tau|X|\,\mathfrak{F}_1^{(n)}(\tau) \tag{11.38}$$

$$\mathfrak{F}_2^{(n+1)}(\tau) = C\tau|X|\left\{|X|[1 + \tau^{d/(1-\sigma_n)}] + \mathfrak{F}_2^{(n)}(\tau)\,\tau^{(d+\mu_2^{(n)})/(1-\sigma_n)}\right\} \tag{11.39}$$

Iteratively applying Eq. 11.36 to the initial condition of Eq. 11.30 yields:

$$\mu_1^{(n)} = \left(1 + \frac{1}{\sigma_1} + \frac{1}{\sigma_2} + \dots\frac{1}{\sigma_{n-1}}\right)\sigma_n d - n\sigma_n\alpha. \tag{11.40}$$

At each iteration, $\mu_1^{(n)}$ is made smaller (i.e. more negative) at the cost of increasing the leading power of τ in $\mathfrak{F}_1^{(n)}(\tau)$, so long as $\mu_1^{(n)} > -d$. By choosing appropriate σ_j, we eventually reach an iteration step $n = n^*$ such that $\mu_1^{(n^*)} + d < 0$ and Eq. 11.34 no longer holds [and neither will the iteration equations Eqs. (11.36) - (11.39)]. For $n > n^*$, $\mathcal{I}[\lambda_n^{R'}]$ becomes independent of R':

$$\mathcal{I}[\lambda_{n \geq n^*}^{R'}] \leq C\left[|X|(1 + (vt)^{d/(1-\sigma_n)}) + \mathfrak{F}_1^{(n)}(vt)\ (vt)^{(d+\mu_1^{(n)})/(1-\sigma_n)} + \mathfrak{F}_2^{(n)}(vt)\ (vt)^{(d+\mu_2^{(n)})/(1-\sigma_n)}\right] \tag{11.41}$$

which leads to new iterative steps where the spatial decay of both polynomial terms is the same:

$$\mu_1^{(n+1)} = \mu_2^{(n+1)} = -\sigma_{n+1}\alpha \tag{11.42}$$

$$\mathfrak{F}_1^{(n+1)}(\tau) = \tau^{1+(d+\mu_1^{(n)})/(1-\sigma_n)}|X|\ \mathfrak{F}_1^{(n)}(\tau) \tag{11.43}$$

$$\mathfrak{F}_2^{(n+1)}(\tau) = \tau|X|\left\{|X|[1 + \tau^{d/(1-\sigma_n)}] + \mathfrak{F}_2^{(n)}(\tau)\tau^{(d+\mu_2^{(n)})/(1-\sigma_n)}\right\} . \tag{11.44}$$

At this point in the iterative procedure, further iterations do not improve on the power-law decay of the Lieb-Robinson bound since they are set by $-\sigma_n\alpha$.

With regards to the time dependence of the bound, at each iteration step n, one can choose $\sigma_n > (1 - \sigma_{n-1} + d)/\alpha$, reducing the time dependence of $\mathfrak{F}_i^{(n)}(vt)$ in Eqs. (11.39), (11.43) and (11.44). For such choices of σ_n and enough iterations steps, the leading temporal dependence arises from the $\tau^{1+d/(1-\sigma_n)}$ term introduced each iteration step in Eq. 11.44. As a result, there is some iteration number $m > n^*$ above which the most meaningful terms of the bound do not change. At this point, the bound $\lambda_m^{(R)}(r)$ is given by:

$$\lambda_m^{(R)} \leq \Delta_r\left(2|X|e^{vt-r^{1-\sigma_m}} + C\Theta(R - r^{\sigma_m})r^{-\sigma_m\alpha}\left\{|X|^2(vt)^{1+d/(1-\sigma_m)} + \ldots\right\}\right), \tag{11.45}$$

where $\ldots$ are terms with lower power in vt, but higher power in $|X|$.

We can make the previous considerations more concrete by analyzing the case where σ_j are all made equal, $\sigma_j = \sigma > (d + 1)/(\alpha + 1)$. This inequality ensures the reduction of the time dependence of $\mathfrak{F}_i^{(n)}(vt)$.

For this choice of $\{\sigma_j\}$, Eq. 11.40 simplifies to:

$$\mu_1^{(n)} = (n - 1 + \sigma)d - n\sigma\alpha \tag{11.46}$$

further leading to $n^* = \lceil \sigma d/(\sigma\alpha - d) \rceil$.

For $n > n^*$, the time dependence is encoded in:

$$\mathfrak{F}_1^{(n)}(\tau) \sim \tau^{1+d/(1-\sigma)}\left[\tau^{[1+d-\sigma(1+\alpha)]/[1-\sigma]}\right]^{n-1} + \ldots \tag{11.47}$$

$$\mathfrak{F}_2^{(n)}(\tau) \sim \tau^{1+d/(1-\sigma)} + \ldots \tag{11.48}$$

where ... correspond to lower power of τ. Then, $\mathfrak{F}_2(\tau)$ becomes the dominant term immediately for iteration step $n^* + 1$ as the term $[\ \cdot \ ]^{n-1}$ reduces the leading term of $\mathfrak{F}_1^{(n)}(\tau)$ to be smaller than $\mathfrak{F}_2^{(n)}(\tau)$. Because different terms have different dependences on $|X|$, to ensure all constants are independent of $|X|$, we include the largest power of $|X|$ emerging from our construction in front of the time dependence. Finally, taking $R \to \infty$ yields the final result as expressed in Theorem 1.

11.2 Power-law light-cones

In short-range interacting systems, the length scale associated with the exponential decay of the Lieb-Robinson bound, Eq. 11.21, provides a natural definition for a light-cone. In contrast, Lieb-Robinson bounds in long-range interacting systems are characterized by power-law decays that lack a natural length scale.[3] As a result, the precise notion of a light-cone will depend on which properties we wish to capture.

One way to define a light-cone is in terms of the "spread of information": that is, suppose we consider the time evolution of two states $|\psi\rangle$ and $O|\psi\rangle$, where O is a local operator that perturbs the initial state. The light-cone is the region of radius $R_{\mathrm{LC1}}(t)$ around the support of O, outside which, both time-evolved states yield nearly identical local observables. It is a direct measure of the spread of the influence of the perturbation O across the system as a function of time t. We refer to this light-cone as LC1.

A different way to define a light-cone is in terms of the region of the system that can affect the evolution of local observables appreciably. More specifically, consider the time evolution of an operator O under two different Hamiltonians, H and $H + \Delta H$. Intuitively, if ΔH only acts very far away from O, it will not have a significant impact on the evolution of O at short times. One can make this intuition precise and guarantee that the evolution of O does not change appreciably, until time t, if ΔH only acts a distance $R_{\mathrm{LC2}}(t)$ away from O. $R_{\mathrm{LC2}}(t)$ then characterizes the "zone of influence" of the evolution of operator O. We refer to this light-cone as LC2. Strictly speaking, LC2 is not a light-cone. However, this "zone of influence" is intimately connected with a *modified* notion of the past light-cone. Our usual understanding of such a past light-cone consists of all events (points in space-time) where acting with a *local operator* can influence the current event. The modified past light-cone that is naturally associated with LC2 corresponds to all events where a change in the *Hamiltonian* can influence the current event. In long-range systems, these two light-cones need not be equal, as even a local change to the Hamiltonian can affect the system non-locally.

In general, in power-law interacting systems, LC2 will be greater than LC1. Intuitively, as the operator O expands outwards, the number of terms of ΔH it can interact with increases dramatically. As a result, it is not only necessary that the operator is mostly localized to a

---

[3]Such power-law decays are present in current Lieb-Robinson bounds for long-range interacting systems, both in Refs [230, 181, 354] and this work.

Reference	LC1 ($d < \alpha$)	LC2 ($d < \alpha \leq 2d$)	LC2 ($2d < \alpha < \alpha_M$)	LC2 ($\alpha_M \leq \alpha$)
Ref. [181]	$\beta_{\text{FF}}^{\text{LC1}} = \dfrac{\alpha+1}{\alpha-d}$	$\beta_{\text{FF}}^{\text{LC2}} = \dfrac{\alpha+d}{\alpha}\dfrac{\alpha+1}{\alpha-d} + \dfrac{1}{\alpha}$	$\beta_{\text{FF}}^{\text{LC2}} = \dfrac{\alpha+d}{\alpha}\dfrac{\alpha+1}{\alpha-d} + \dfrac{1}{\alpha}$	$\beta_{\text{FF}}^{\text{LC2}} = \dfrac{\alpha+d}{\alpha}\dfrac{\alpha+1}{\alpha-d} + \dfrac{1}{\alpha}$
Ref. [354]	$\beta_{\text{M}}^{\text{LC1}} = \dfrac{\alpha+1}{\alpha-d}$	✗	$\beta_{\text{M}}^{\text{LC2}} = \dfrac{\alpha+2}{\alpha-2d}$	$\beta_{\text{M}}^{\text{LC2}} = \dfrac{\alpha+2}{\alpha-2d}$
Present Work	$\beta^{\text{LC1}} = \dfrac{\alpha+1}{\alpha-d}$	$\beta_{\text{FF}}^{\text{LC2}} < \beta^{\text{LC2}} = \tilde\beta$	$\beta_{\text{FF}}^{\text{LC2}} < \beta^{\text{LC2}} = \tilde\beta < \beta_{\text{M}}^{\text{LC2}}$	$\beta^{\text{LC2}} = \dfrac{\alpha+2}{\alpha-2d}$

Table 11.2: **Summary of the power-law light-cone exponents of LC1 and LC2 for both previous literature and our work.** We use the subscript FF and M to refer to the light-cone exponents from the bounds of Refs. [181] and [354] respectively. Here $\tilde\beta = \frac{2}{(\alpha-d)^2} \times \left[\alpha - d + \alpha d(1 + \sqrt{1+2/d-2/\alpha}) \right]$ and $\alpha_M = \frac{3d}{2}\left[1 + \sqrt{1+\frac{8}{9d}}\right]$.

particular region, but also that the spatial profile of the operator spread decays fast enough to counteract the increasing number of terms that can modify its dynamics.

We now make these definitions more precise. In order to simplify the notation in this section, we write the Lieb-Robinson bound between two operators A and B, such that $d(A, B) = r$, and with at least one of $|A|$ or $|B|$ bounded by a constant C, as:

$$\frac{\|[\tau_t^H(A), B]\|}{\|A\|\|B\|} \leq \mathcal{C}(r, t), \tag{11.49}$$

This allows us to formally define LC1 as the light-cone used in previous literature:

Definition 1. *Let **light-cone 1 (LC1)** be defined as a relation $r = f(t)$ such that:*

$$\lim_{t \to \infty} \mathcal{C}(f(t), t) = 0. \tag{11.50}$$

The meaning of LC1 is that the propagation of an operator outside the light-cone is small and gets smaller as $t \to \infty$.[4] Because we are interested in the asymptotic behavior, we focus on power-law light-cones, $f(t) = t^\gamma$, which characterize the Lieb-Robinson bounds considered here. The smallest light-cone is characterized by the exponent β^{LC1}, the infimum of the γ which satisfy Eq. 11.50.

In contrast we wish to define LC2 as the region outside which changing the Hamiltonian of the system has no significant impact in the evolution of the operator. To obtain a precise condition for LC2, we consider how changing the Hamiltonian H to $H + \Delta H$ impacts the evolution of an operator. More specifically, we consider modifying the Hamiltonian only a distance r_{min} away from the operator of interest O. The difference in the time evolved operators is bounded by:

$$\|e^{iHt}Oe^{-iHt} - e^{i(H+\Delta H)t}Oe^{-i(H+\Delta H)t}\| \leq C\Delta J\|O\|t \int_{r_{min}}^{\infty} dr \; r^{d-1}\mathcal{C}(r, t) \tag{11.51}$$

where ΔJ quantifies the local norm of ΔH.

LC2 is then given by the relationship between r_{min} and t that ensures that operator difference, bound in Eq. 11.51, remains small and goes to zero in the long time limit. This immediately motivates the definition of LC2 as follows:

Definition 2. *Let **light-cone 2 (LC2)** be defined as a relation $r = f(t)$ such that:*

$$\lim_{t \to \infty} \; t \int_{f(t)}^{\infty} dr \; r^{d-1}\mathcal{C}(r, t) = 0, \tag{11.52}$$

where d is the dimensionality of the system.

---

[4]Let us note that this has been measured in different forms in different results. More specifically, Ref. [181] requires the probe operator B to be localized at one site, measuring the spread of the operator A to any *one site*, while in Ref. [354] the probe operator need not be local. Our bound follows this second convention, more common in previous literature.

Again, we will focus on polynomial light-cones, $f(t) = t^\gamma$ and define β^{LC2} as the infimum of the γ which satisfy Eq. 11.52.

In short-ranged interacting systems, where $\mathcal{C}(r,t) \propto e^{vt-r/R}$, the exponential suppression of $\mathcal{C}(r,t)$ at large r is insensitive to the extra volume term in the definition of LC2, Eq. 11.52, leading to the same linear light-cone for both LC1 and LC2. This result is an immediate consequence of the natural length scale in $\mathcal{C}(r,t)$.

However, in long-range interacting systems, $\mathcal{C}(r,t)$ has a power-law decay in space which *is* sensitive to the extra volume term in LC2. For example, for Eq. 11.52 to converge and ensure a power-law LC2, the Lieb-Robinson bound must decay *faster* than r^{-d}; for LC1 there is no such requirement. As a result, for slowly-decaying Lieb-Robinson bounds one may have a power-law LC1 but no LC2, i.e. there is no power-law $f(t)$ that satisfies Eq. 11.52. This is the case for the bound in Matsuta et al. [354], where LC2 does not exist for $d < \alpha < 2d$, yet LC1 matches that of Foss-Feig et al. [181]. LC2 is able to capture the difference between these two results.

By comparison, our result supports both an LC1 and LC2 for $\alpha > d$, extending the existence of an LC2 in long-range multi-body Hamiltonians to $d < \alpha < 2d$. In this regime both our Lieb-Robinson bound and that of Ref. [181] lead to a finite LC2, albeit our bound exhibits a larger light-cone exponent. Much like the difference in decay profile, this might be inherent to our treatment of the more general case of arbitrary multi-body interactions.

In Table 11.2 and Fig. 11.2, we compare the different light-cone exponents obtained from both our work and previous literature for different values of α. In Fig. 11.2, we plot the exponent of LC2 of the different works as a function of α for dimension $d = 1$.

11.3 Discussion

In this chapter, we have proven an improved Lieb-Robinson bound for generic multi-body long-range interactions, characterized by a faster asymptotic spatial decay. The importance of this improvement is captured by the notion of LC2, a definition of light-cone that provides a stricter definition of locality for the growth of operators, in particular, that their evolution is not affected by the outside region for large t. Our work extends the existence of an LC2 light-cone for generic multi-body interacting systems for $d < \alpha < 2d$.

This improvement has important implications for understanding prethermalization and Floquet phases of matter in periodically-driven systems. In such systems (especially in the high frequency regime), one can capture the evolution under a time-dependent Hamiltonian $H(t)$ using a time-independent approximation. Even when the original $H(t)$ has strictly two-body terms, the time-independent approximation will naturally exhibit multi-body terms. The results which establish the accuracy and limitations of such approximations require Lieb-Robinson bounds for multi-body power-law interactions with a rapid decay outside the light-cone [345]. We discuss this construction and its consequences in Chapter 12.

Finally, let us note that during the preparation of this work, we became aware of a new Lieb-Robinson bound [540] that improves upon Ref. [181]. The bound in Ref. [540]
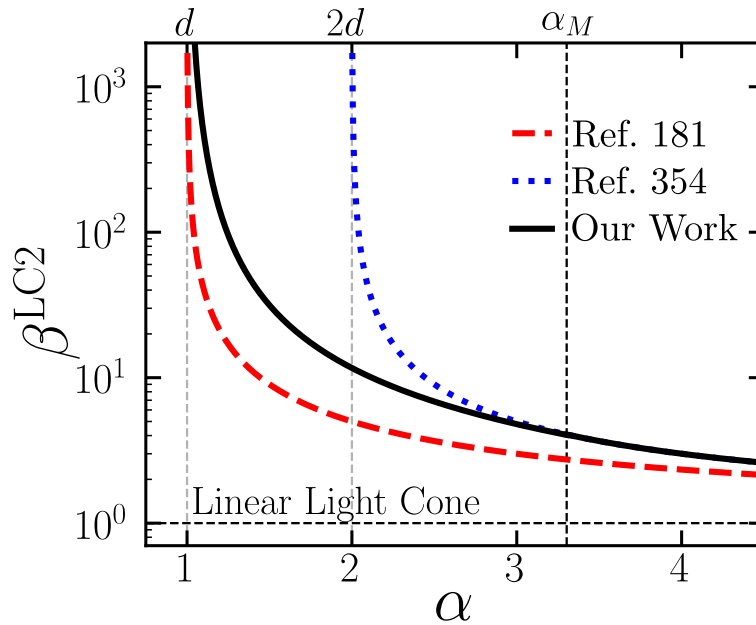
Figure 11.2: **Power-law light-cones for long-range interacting systems.** Power-law
LC2 exponent for the present work and Refs. [181] and [354] for $d = 1$ as a function of
α. While Ref. [354] has a finite power-law LC2 for $\alpha > 2d$, Ref. [181] and our work have a
power-law LC2 for all $\alpha > d$. For $\alpha < \alpha_M$ our work leads to a better LC2 than Ref. [354],
while matching it for $\alpha \geq \alpha_M$. The horizontal dashed line corresponds to a linear light-cone.

has an LC1 exponent of $\alpha/(\alpha - d)$ under similar assumptions as Ref. [181], namely, two-
body interactions. However, their result (phrased in terms of commutators) does not yield
a finite LC2 for $d < \alpha < 2d$. Nevertheless, the structure of their arguments is intriguing
and understanding how to generalize their results to multi-body interactions is a promising
direction for future study.

Chapter 12

Prethermal phases of matter in long-range interacting systems

As we have been exploring in this dissertation, periodically driven (Floquet) systems offer a distinctly different setting for exploring new physical phenomena. One particularly interesting possibility is that of entirely new phases of matter that have no equilibrium analogue; this is enabled by both a novel dynamical structure, as well as a novel underlying symmetry (the driving field breaks the continuous time translation symmetry into a discrete symmetry). Unfortunately, studying and observing such novel phases has been notoriously challenging [374, 164, 223]. One major hurdle is that the framework of statistical mechanics, normally used to characterize phases of matter, is largely restricted to the exploration of systems at or near *equilibrium*. Floquet systems do not fit this category. Rather, they can continuously absorb energy from the driving field, ultimately approaching an infinite-temperature thermal state at late times [451, 450, 118, 319, 119, 70, 439, 72, 58, 568, 339, 215, 609]. As a result, at late times, a many-body Floquet systems is expected to behave trivially from the perspective of phases of matter. However, recent work have called this assumption into question.

For example, the presence of strong disorder in one dimension can arrest thermalization by inducing a many-body localized (MBL) phase [396, 6]. When an MBL phase occurs in a Floquet system [118, 439, 440, 3] it can prevent energy absorption from the drive and lead to novel, intrinsically out-of-equilibrium phases of matter [290, 558, 557, 555, 162, 445, 160, 590]. However, the dual constraints of strong disorder and low dimensionality significantly limit the scope of both the experiments and models that one can consider, naturally raising the question: can interesting Floquet phase structure survive in periodically driven systems *without* disorder?

An affirmative answer has emerged [161] in the context of Floquet prethermalization [4, 312, 380, 5, 2, 237]. For sufficiently large driving frequencies, a many-body Floquet system can enter a so-called "prethermal regime", where its dynamics are well captured by an *effective* static Hamiltonian. This static Hamiltonian description necessitates the existence of a conserved energy, which prevents the driven system from heating to an infinite

(c) Range of interactions	Short-range	Long-range $\alpha > 2d$	Long-range $\alpha > d$
Exponentially long thermalization	Refs. [5, 312, 380]		
Local observables captured by D^*	Refs. [5, 312, 380]	Ref. [312]	Limited by Lieb-Robinson bounds
Local observables captured by D^* with emergent symmetry	Ref. [161]	This work	Limited by Lieb-Robinson bounds
Prethermal phases of matter	Ref. [161]	This work	This work*
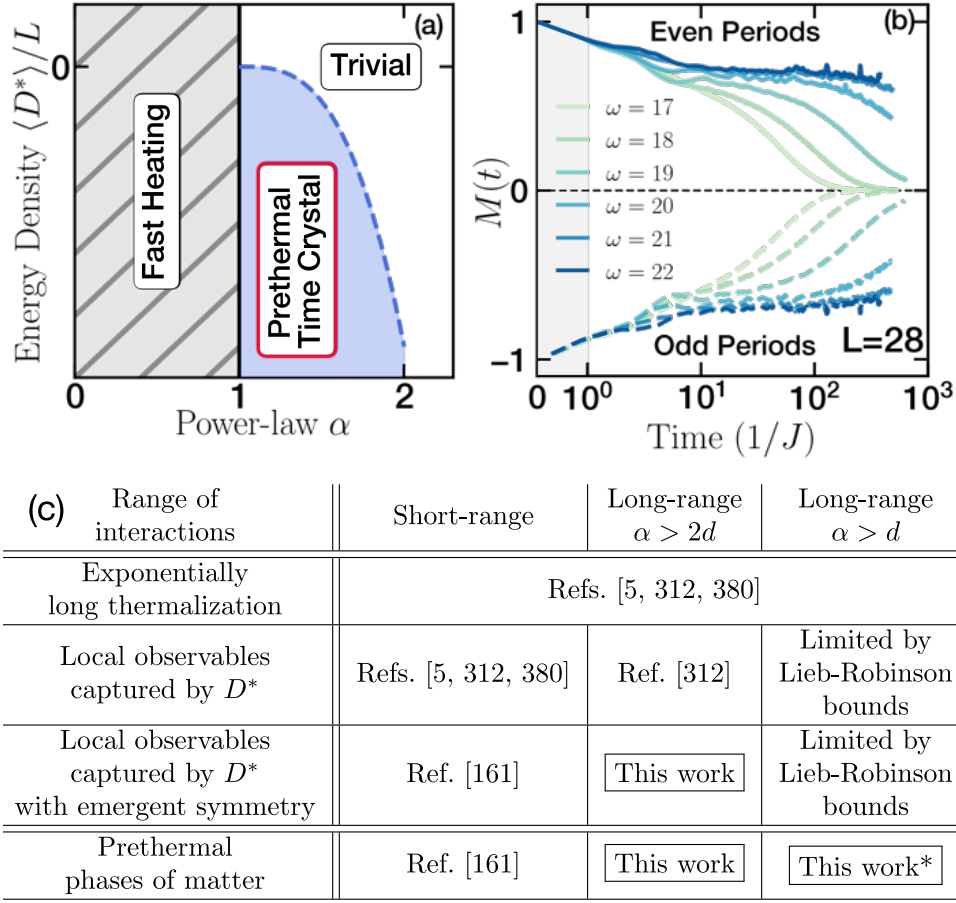
Figure 12.1: **Prethermalization in long-range interacting systems.**   (a) Schematic
phase diagram for a one-dimensional prethermal discrete time crystal (PDTC) as a function
of interaction power-law and energy density. The 1D PDTC can only exist for long-range
interactions (i.e., $J_{ij} \propto |i - j|^{-\alpha}$) with power-law $1 < \alpha < 2$ and an energy density that
lies in the symmetry broken phase of the prethermal Hamiltonian D^*.   (b) PDTC Floquet
dynamics depicting the magnetization $M(t)$ for a system size $L = 28$. The robust period
doubling behavior, which survives for *exponentially* long times in the frequency of the drive
ω, signals prethermal time crystalline order.   (c) Table summarizing our analytical results.
The star (*) indicates that for this case, prethermal phases exist provided that we assume
that local observables to relax to the Gibbs state of D^*, which we expect since this is the
state that maximizes the entropy subject to the constraint of conservation of energy.

temperature state. Crucially, the *lifetime* of this prethermal regime has been proven to be *exponentially* long in the frequency of the drive, providing a parametrically robust mechanism to delay the onset of Floquet heating.

Although such results further cement the power of periodic driving as a technique for Hamiltonian engineering [269, 359, 408, 325], we hasten to emphasize that these results *are necessary but not sufficient* for proving the existence of intrinsically non-equilibrium, prethermal Floquet phases of matter. Let us unpack this last statement. Our focus in this chapter is on phases of matter that *cannot* exist in equilibrium. This means that the Floquet nature of the system is not simply being used as an engineering tool to stitch two disparate Hamiltonians together, but rather, as a *prerequisite ingredient* for the existence of a phase with no direct analog in thermal equilibrium. This latter point is most easily summarized as follows: the phase must, at its core, be protected by the discrete time translation symmetry of the drive [162, 445, 161].

Thus, in order to prove the existence of prethermal Floquet phases, one must first demonstrate that the prethermal regime can actually preserve the symmetry structure of the driven system. With this in mind, it has precisely demonstrated the existence of *emergent symmetries* during the prethermal window [161]. The existence of these symmetries can be viewed as a direct manifestation of the discrete time-translation symmetry of the drive. This theoretical framework provides the perfect landscape for realizing prethermal non-equilibrium phases of matter, including prethermal versions of discrete time crystals [290, 160], Floquet symmetry protected topological phases [162, 558, 445, 444], and possibly many others [535, 437, 495, 399]. However, this framework leaves open one fundamental challenge, in that it cannot be applied to long-range interacting systems.

More specifically, one cannot ensure that the resulting effective prethermal Hamiltonian possesses any meaningful sense of locality. Without this notion of locality, the evolution of local operators may not be well-approximated by the prethermal Hamiltonian. As a result, the usual assumption that the system will evolve to the prethermal Gibbs state and exhibit the phase structure of local and power-law interacting Hamiltonians may not hold. The overarching goal of our work is to tackle this concern, *proving* the existence of prethermal Floquet phases in many-body systems that exhibit long-range, power-law interactions (i.e. Coulomb, dipolar, van der Waals, etc) [55, 318, 308, 135, 384].

This goal is motivated from two complementary fronts. On the experimental front, many of the platforms most naturally suited for implementing Floquet dynamics exhibit long-range interactions, including dipolar spins in the solid-state, trapped ions, ultracold polar molecules, and Rydberg atom arrays [601, 586, 46, 384, 100, 468]. Understanding the prethermal properties of this broad class of systems could unlock a myriad of new experimental techniques for Floquet quantum simulation. On the theoretical front, even in equilibrium, it is well known that long-range interactions can lead to symmetry-breaking in qualitatively different regimes than that allowed by short-range interactions. This suggests the possibility of finding prethermal Floquet phases that can *only* be realized in long-range interacting systems.

Our main results are three fold. First, we prove the existence of prethermal Floquet

phases of matter (Fig. 12.1) in long-range interacting systems, so long as the interactions decay as a power-law with exponent $\alpha > d$, where d is the dimension of the system. Second, we predict the existence of a novel, disorder-free, prethermal discrete time crystal (PDTC) in one dimension. This phase is strictly forbidden in any of the three contexts that we discussed earlier: equilibrium, Floquet MBL, and *short-range* interacting prethermal Floquet. Indeed, the 1D PDTC can only be realized in a *long-range* interacting, prethermal Floquet system! Finally, leveraging large-scale Krylov subspace methods, we perform extensive numerics characterizing the emergence of a 1D PDTC in a long-range interacting spin chain. In this context, we highlight one of the key (experimentally observable) differences between the prethermal time crystal and the MBL time crystal, namely, the presence of a phase transition as a function of energy density of the initial state (Fig. 12.1 and Table 12.1).

This chapter is organized as follows. In Sec. 12.1, we lay the framework for understanding Floquet prethermalization both with and without an emergent symmetry (although only the former admits non-equilibrium phases of matter). Moreover, we review and contextualize a number of prior results with a particular emphasis on their implications for understanding the dynamics within the prethermal regime. This allows us to formalize the two essential properties for proving the existence of long-range interacting, prethermal phases. Building upon these discussions, in Sec. 12.2, we begin by introducing new machinery to carefully keep track of the spatial structure of the long-range interactions. Leveraging these new tools, we ultimately prove three theorems, which in combination, demonstrate the existence of long-lived, non-equilibrium prethermal phases of matter in long-range interacting systems with power-laws $\alpha > d$. Within this context, we also introduce a novel phase of matter: the 1D prethermal discrete time crystal. In Sec. 12.3, we perform an exhaustive numerical investigation of a one dimensional Floquet spin chain and demonstrate that it exhibits a PDTC phase, only when the system harbors sufficiently long-range interactions. Using a combination of Krylov subspace methods and quantum Monte Carlo calculations, we identify one of the unique signatures of a PDTC (as compared to an MBL discrete time crystal), namely, that it displays a phase transition as a function of the energy density of the initial state. Finally, we provide a short summary of some of the implications and interpretations in Sec. 12.4.

12.1 Prethermalization

In an interacting, many-body quantum system, one generally expects dynamics to push the local state of the system toward equilibrium via a process known as thermalization [139, 517, 463].[1] However, in certain cases, the time scale, τ^*, at which thermalization occurs can be significantly larger than the timescale associated with the intrinsic local interactions of the Hamiltonian, $1/J_{\text{local}}$.[2] In such cases, before full thermalization actually occurs (i.e. for

---

[1]Counter-examples of this broad phenomenology are integrable models or those displaying a many-body localized phase.

[2]Throughout this work we work in natural units $\hbar = 1$ and thus frequency carries units of energy.

times $t < \tau^*$), the system can first approach a *different* equilibrium state determined by an effective Hamiltonian—this process is called *prethermalization*; the time interval associated with it is known as the *prethermal regime*, while the effective Hamiltonian is referred to as the *prethermal Hamiltonian.*

Systems exhibiting prethermalization generally have two distinct energy scales. In static systems, this typically requires the underlying Hamiltonian to exhibit two very different couplings which lead to both "fast" and "slow" degrees of freedom. Prethermalization can then be understood as the equilibration of the "fast" degrees of freedom with respect to a slowly varying background arising from the dynamics of the "slow" degrees of freedom. In this case, τ^* is expected to depend *algebraically* on the ratio of the energy scales.[3]

Exponentially long Floquet heating time

Unlike static systems, Floquet systems always exhibit two distinct energy scales: the local energy scale, J_{local}, and the frequency of the drive, ω. To this end, a Floquet system can almost naturally be expected to exhibit a long-lived intermediate prethermal regime when these two energy scales are sufficiently different; our focus is of course, on the case in which $\omega \gg J_{\text{local}}$. In that case (typically referred to as Floquet prethermalization), τ^* scales *exponentially* with the ratio of these two energy scales, ω/J_{local}, rather than algebraically [4, 312, 380, 5, 2].

The physical intuition for this exponential scaling is simple. Given a local energy scale J_{local}, the many-body system requires ω/J_{local} rearrangements in order to absorb a single quantum of energy from the drive. When interactions are local, the system cannot efficiently make a large number of correlated local rearrangements. Thus, the associated rate of energy absorption (i.e. Floquet heating) is exponentially small in ω/J_{local}, leading to a heating time scale, $\tau^* \sim e^{\omega/J_{\text{local}}}$. This physical picture also helps to explain why long-range interacting Floquet systems with power-laws $\alpha < d$ cannot exhibit a prethermal regime. In such systems, the energy scale associated with a single local rearrangement diverges as a function of the system size (i.e. the system exhibits a super-extensive many-body spectrum), implying that a single rearrangement can, in principle, absorb an energy quantum from the drive regardless of the magnitude of the driving frequency.

Approximation of local Floquet dynamics

While we have focused above on the existence of an exponentially long Floquet prethermal regime, as we alluded to earlier (while emphasizing the importance of locality), this is not the only constraint that one needs to worry about. Rather, just as important is whether one can prove that there actually exists a local prethermal Hamiltonian, D^*, that approximately generates the dynamics of the Floquet system during the prethermal regime. A bit more

---

[3]In special cases, however, it can depend exponentially on the ratio of the energy scales. An example occurs in models with near integer spectrum [5, 161, 283, 165, 425]

precisely— to approximate the unitary time evolution operator, U_f, that generates the *exact* Floquet dynamics during a single driving period T, should be approximated by

$$U_f \approx U_f^{\text{app}} = e^{-iD^*T} \ . \tag{12.1}$$

And, more importantly, one hopes that this approximation correctly captures the dynamics of local observables until the Floquet heating time scale. A priori, this need not be the case and, in fact, the exact Floquet dynamics might not have any effective Hamiltonian description.

Indeed, the difference between proving the existence of a conserved energy (i.e. measured with respect to the prethermal Hamiltonian) versus proving that the prethermal Hamiltonian correctly generates the local dynamics is stark. For example, although the Floquet heating time, τ^*, has been proven to be exponentially long in generic systems with extensive energy scales (including long-range interacting systems [312, 380, 5, 2, 161] and even classical systems [379]), proving that the associated prethermal Hamiltonian describes the dynamics of local observables has only been achieved for a significantly smaller class of systems [312, 5, 161].[4] In fact, in certain systems it has been shown that the prethermal Hamiltonian *does not* generate the actual Floquet dynamics [379].

Generalizing to the case of an emergent symmetry

Up to now, we have focused on how an effective *static* description of the Floquet system (governed by the prethermal effective Hamiltonian) can emerge during the prethermal regime, both in the context of a conserved energy as well as in the context of generating local dynamics. While powerful in and of itself, this description limits Floquet systems to mimicry of equilibrium-like physics within the prethermal regime. This is because, at the moment, our effective static description has forgotten about the structure of the original time periodic drive. Luckily, this need not be the case!

Before formalizing this last statement, let us illustrate it with a simple example. Consider an $S = 1/2$ spin undergoing a $\pi/2$ rotation every period T. In the absence of any perturbing field, the spin will return to its original orientation every four periods. Crucially, it turns out that even in the presence of small interactions (with respect to the driving frequency $\sim \omega = 2\pi/T$), this picture remains true for an extremely long time scale. One can gain some intuition for this by noting that all of the interactions which fail to commute with the $\pi/2$-rotation get "echoed out" (i.e. they average to zero in the toggling frame that rotates by $\pi/2$ each Floquet period), which means that at leading order in the inverse frequency,

---

[4]Previous proofs that the dynamics of local observables are correctly captured by the prethermal Hamiltonian (within the prethermal regime) can be divided into two categories: those applicable in prethermal regimes with no emergent symmetry, and those applicable in prethermal regimes with an emergent symmetry. In the former, proofs exist for short [312, 5, 161] and long-range interacting systems with power-law $\alpha > 2d$ [312]. In the latter, proofs only exist for short-range interacting systems [161]. Our work considers the latter category, extending current results to long-range interacting systems with power-law $\alpha > 2d$.

they do not contribute to the dynamics. We emphasize, however, that the general results we eventually consider will hold not just at leading order, but also at higher orders.

Armed with this simple example, let us now formalize how extra symmetry-structure can emerge in the prethermal regime of Floquet systems. In particular, if U_f contains a large rotation, X, that returns to itself after N periods, $X^N = \mathbb{1}$ (in our example with the $\pi/2$-rotation, $N = 4$) and *generic* interactions (whose strength is much smaller than the driving frequency), then U_f can be *exponentially well* approximated by a much simpler evolution [161]:

$$U_f \approx U_f^{\text{app}} = \mathcal{U} \widetilde{U}_f^{\text{app}} \mathcal{U}^\dagger,$$
$$\widetilde{U}_f^{\text{app}} = X e^{-iTD^*} \quad \text{with} \quad [D^*, X] = 0, \tag{12.2}$$

where D^* is the effective prethermal Hamiltonian that commutes with the rotation X, and $\mathcal{U}$ is a time-independent unitary change of frame, which is close to the identity. Note that we will often choose to work directly in the rotated frame given by $\mathcal{U}$, so that the evolution is (approximately) given by $\widetilde{U}_f^{\text{app}}$ rather than U_f^{app}.

The above discussion encodes a few important consequences. First, since D^* commutes with X, it remains an *exactly* conserved quantity under this approximate evolution. Taking into account the exponentially small error terms (which track the differences between this approximate evolution and the exact Floquet evolution) leads to D^* being exponentially well conserved. Second, while X was not a symmetry of the original evolution, it has become a $\mathbb{Z}_N$ symmetry of the approximate time evolution, $\widetilde{U}_f^{\text{app}}$; this emergent symmetry is protected by the underlying discrete time translation symmetry of the Floquet evolution operator. As we discuss later, one can leverage this emergent symmetry to realize novel Floquet phases within the prethermal regime, including phases like the time crystal, which break the discrete time translation symmetry of the underlying drive. Third, let us emphasize that the presence of X within $\widetilde{U}_f^{\text{app}}$ ensures that for every period, the system undergoes a non-trivial rotation that remains finite even in the high-frequency limit, $\omega \to \infty$; this corresponds to the remnant "Floquet structure" that remains within the prethermal regime. However, when one considers the evolution every N periods, one finds that the dynamics are simply generated by the static prethermal Hamiltonian D^*:

$$(\widetilde{U}_f^{\text{app}})^N = e^{-iNTD^*} . \tag{12.3}$$

Finally, we emphasize that the emergent $\mathbb{Z}_N$ symmetry is relevant only within the prethermal regime, where the total energy is also exponentially well conserved.

Prethermal emergent symmetry as a framework for non-equilibrium phases of matter

In this section, we further elucidate the role of the emergent symmetry and how it provides a natural framework for realizing non-equilibrium phases of matter. Since the time evolution

every N periods is captured by the prethermal Hamiltonian D^* (Eq. 12.3), there exists a time scale, τ_{pre}, after which the system has "prethermalized" into a Gibbs state of D^* and thus, is locally described by $\rho \propto e^{-\beta D^*}$, with a temperature β^{-1} determined by the system's initial energy density.

Let us now examine the evolution of this equilibrium state under a single period of $\widetilde{U}_f^{\text{app}}$. In general, ρ will evolve trivially because the equilibrium state respects the emergent symmetry X:

$$\rho \; \to \; Xe^{-iD^*T}\rho e^{iD^*T}X^\dagger = X\rho X^\dagger = \rho \;. \tag{12.4}$$

However, if D^* exhibits a spontaneously symmetry broken (SSB) phase with respect to X, ρ can instead approach the equilibrium state within a particular symmetry-breaking sector; let us refer to such a spontaneously symmetry broken state as ρ_{SSB}. In this case, although ρ_{SSB} evolves trivially under D^*, the action of X is to rotate ρ_{SSB} into a distinct symmetry-breaking sector, ρ'_{SSB}:

$$Xe^{-iD^*T}\rho_{\text{SSB}}e^{iD^*T}X^\dagger = X\rho_{\text{SSB}}X^\dagger = \rho'_{\text{SSB}} \neq \rho_{\text{SSB}} \;. \tag{12.5}$$

During each period, the state rotates between the different symmetry-breaking sectors, only coming back to its original sector after N periods ($X^N = \mathbb{1}$). The sub-harmonic nature of this behavior becomes transparent by measuring the order parameter, which is a local observable whose expectation value is different in each of the symmetry sectors.

In the language of time crystals, the fact that the underlying Floquet evolution has a period of T, while observables exhibit an enlarged periodicity NT, precisely corresponds to the discrete breaking of time translation symmetry [290, 160, 590, 555, 601, 161]. For the remainder of this section, we continue to use the example of time crystalline order to highlight some of the unique features of prethermal non-equilibrium phases (Table 12.1).

First, in order to meaningfully label the prethermal time crystal as a phase of matter, one needs to show that it remains stable under small perturbations. This is guaranteed so long as the discrete time translation symmetry of the drive is not broken; in particular, this symmetry protects the emergent $\mathbb{Z}_N$ symmetry, and we know that a phase that spontaneously breaks a $\mathbb{Z}_N$ symmetry should be stable with respect to perturbations that do not explicitly break the symmetry.

Second, because our construction requires the system to prethermalize to an SSB state of D^*, the observation of a prethermal time crystal depends on the choice of initial state (Table 12.1). In particular, the initial energy density must correspond to a temperature below the critical temperature of the SSB phase transition. We emphasize that, because the underlying transition of D^* is *sharp* in the thermodynamic limit, there is an equally *sharp* transition between the prethermal time crystal and the trivial prethermal regime as a function of energy density (as long as $\tau^* \gg \tau_{\text{pre}}$).[5]

---

[5]As long as τ_{pre} diverges at most algebraically near the transition, we are guaranteed (owing to the exponential scaling of τ^*) that the transition will be exponentially sharp in the frequency of the drive.

Third, as the system begins absorbing energy from the drive at τ^*, the temperature of the system will eventually cross the critical temperature of the SSB transition, leading to the loss of time crystalline order—the prethermal time crystal phase will always have a finite (but large) lifetime. To this end, depending on the energy density of the initial state, the lifetime of the time crystalline behavior can exhibit two distinct behaviors. If the energy density is below the critical SSB temperature, the system prethermalizes to the SSB phase and the time scale τ_{TC} at which the time crystalline order parameter decays is similar to the heating time scale: $\tau_{TC} \sim \tau^* \sim e^{\omega/J_{\text{local}}}$. If, on the other hand, the energy density is above the critical SSB temperature, the system will simply prethermalize to the symmetry preserving (trivial) phase and any transient time crystalline order can only occur before prethermalization, $\tau_{\text{TC}} \lesssim \tau_{\text{pre}} \sim \mathcal{O}(J_{\text{local}}^{-1})$.

Differences between the many-body localized and prethermal discrete time crystal

We end this section by juxtaposing the above discussions about the prethermal discrete time crystal with its many-body localized counterpart. Our focus is on highlighting the key differences between the two phases, as summarized in Table 12.1. These differences can be divided into two categories: 1) the stability of the time crystal and 2) the restrictions on systems that can host a time crystal. Concerning the former, in contrast to the exponentially long lifetime of the PDTC, the ergodicity-breaking properties of Floquet many-body localization enable the MBL time crystal to persist to infinite times. Moreover, while the stability of the MBL time crystal can be independent of the initial state, the PDTC can only occur for a finite range of initial energy densities.

Let us now turn to the restrictions on systems that can realize an MBL versus a prethermal time crystal. In the MBL case, such systems are required to have strong disorder[6] and are unstable to the presence of an external bath [394], long-range interactions [591, 130], and higher dimensions [130]. By contrast, the prethermal time crystal suffers from none of these restrictions and requires only two ingredients: a Floquet frequency that is larger than the local bandwidth and the existence of a static Hamiltonian D^* with a spontaneously symmetry broken phase. Crucially, in one dimension, this latter ingredient *requires* us to consider long-range interacting systems with power-law $1 < \alpha < 2$ [153]; for such power-laws, it is known that even a 1D system can exhibit finite temperature SSB phase, skirting the conventional Landau-Peierls argument that discrete symmetry breaking is forbidden for short-range interacting systems in 1D.

Prethermalization in long-range interacting systems

Before proving the existence of long-range interacting, prethermal phases of matter, we briefly contextualize a number of prior results with a particular emphasis on their implications for understanding the dynamics within the prethermal regime.

---

[6]Or a disorder-like potential such as a quasi-periodic potential.

	MBL TC	Prethermal TC
Lifetime	$\tau \to \infty$	$\tau \sim e^{\omega/J_{\text{local}}}$
Initial State	Any	Below T_c
Requires Disorder	Yes	No
Interaction Range	Short-range*	Long-range $1 < \alpha \le 2$

Table 12.1: **Differences between MBL and prethermal discrete time crystalline order in one dimensional systems.** The star (*) next to short-range indicates that the range of the interaction must only be sufficiently short so that MBL is preserved.

In particular, we now formalize the two different properties (for which we previously gave intuition) that U_f^{app} should satisfy in order to be of the broadest interest and most useful. We simplify the following discussion by focusing on the case without an emergent symmetry, Eq. 12.1, but our analysis carries over to the case with an emergent symmetry [Eq. 12.2] by rotating into the frame $\mathcal{U}$: $U_f \to \widetilde{U}_f = \mathcal{U} U_f \mathcal{U}^\dagger$ and $U_f^{\text{app}} \to \widetilde{U}_f^{\text{app}}$.

(a) **Exponentially long heating time**—For U_f^{app} to be a good approximation to U_f, a naive first requirement is that the difference between the two unitaries be small. This can be encoded in a bound of the form:

$$\|U_f - U_f^{\text{app}}\| \le \mathcal{O}(\Lambda e^{-\omega/J_{\text{local}}}) \,, \tag{12.6}$$

where Λ is the volume of the system. Such a result would ensure that the error associated with the approximation in Eq. 12.1 is exponentially small in the frequency of the drive.

However, owing to its volume dependence, this bound, at first, suggests that U_f^{app} is not meaningful in the thermodynamic limit, $\Lambda \to \infty$. In particular, if one simply computes the overlap between wavefunctions evolved under the approximated and the true evolution, it would go to zero:

$$\lim_{\Lambda \to \infty} \langle \psi | U_f^\dagger U_f^{\text{app}} | \psi \rangle = 0 \,. \tag{12.7}$$

But, of course, one is typically not interested in capturing the dynamics of the *full quantum wave-function* (which cannot be measured), but rather in the dynamics of *local observables*. Unfortunately, by itself, Eq. 12.6 is insufficient to analyze the error in the evolution of generic local observables.

Nevertheless, it can still be used to prove important results on the dynamics of *extensive quasi-conserved quantities*. Of particular interest is the dynamics of the energy density,

D^*/Λ. Since it remains constant under U_f^{app}, bounding the error growth of this observable provides an immediate upper bound on the heating rate under the true evolution!

To this end, by combining knowledge of the structure of the approximate unitary [Eq. 12.1] with the error in the unitaries [Eq. 12.6], one can immediately conclude that D^*/Λ remains exponentially well conserved under the evolution:

$$\frac{1}{\Lambda}\left|\langle U_f^{-m} D^* U_f^m\rangle - \langle D^*\rangle\right| = \mathcal{O}(mTe^{-\omega/J_{\mathrm{local}}}) \ . \tag{12.8}$$

As promised, this formalizes the statement that the energy of the system is conserved up to an exponentially long time-scale τ^* and thus, that the infinite temperature state cannot be reached before τ^*. Note that for other extensive quantities conserved by D^*, similar bounds can also be derived.

(b) **Approximation of local dynamics**—At this point, we have not yet formalized the statement that U_f^{app} is the correct "effective" generator of the true Floquet dynamics, only that the energy density remains conserved.[7] By filling in this gap, we would be able to rigorously connect the prethermal regime with the equilibrium properties of D^*. This can be achieved by bounding the error in the dynamics of a generic local observable O as:

$$\|U_f^{-m} O U_f^m - (U_f^{\mathrm{app}})^{-m} O (U_f^{\mathrm{app}})^m\| \leq \mathcal{O}(\ (mT)^\delta e^{-\omega/J_{\mathrm{local}}}\ ) \ , \tag{12.9}$$

for some finite δ. Crucially, this result is *independent* of the volume of the system, meaning that it remains applicable even in the thermodynamic limit. This formalizes the intuition that, even if the global wave-function is not perfectly captured by U_f^{app} [Eq. 12.7], the local properties remain correct. Supplementing this result with an understanding of the equilibrium properties of D^* as well as the structure of the unitary evolution (i.e. the emergent symmetry) will ultimately enable us to prove the existence of long-range, prethermal phases of matter.

Having formalized these two properties, we are now in a position to contextualize prior results on prethermalization in long-range interacting systems, *without* an emergent symmetry. In the case of an exponentially long thermalization time [property (a) above], the approximate unitary U_f^{app} has been proven to satisfy Eq. 12.8 for power-laws $\alpha > d$ [312, 380]. For approximating local dynamics [property (b) above], the approximate unitary U_f^{app}, has been proven to satisfy Eq. 12.9 for power-laws $\alpha > 2d$ [312, 380]. The discrepancy between these two regimes arises from the fact that Lieb-Robinson bounds with power-law light-cones have been proven only for $\alpha > 2d$ [181, 354, 540, 163]. When attempting to extrapolate to the case with an *emergent symmetry* in the prethermal regime, the above prior techniques do not appear readily generalizable [312, 380].

---

[7]This is a crucial point when attempting to describe phases of matter within the prethermal regime, because without it, one cannot precisely determine the equilibrium properties of the system during prethermalization.

Indeed, even for *short-range interactions* [161], generalizing to the case of an *emergent symmetry* requires the use of an alternate construction [5]. Curiously, although not explicitly discussed, many of the arguments found in this construction [5], generalize directly to the long-ranged case with little modification. In particular, the construction depends on the *number of lattices sites* each interaction term couples, which remains small even for long-range interactions (e.g. the long-range Ising interaction found in trapped ion experiments only couples pairs of sites [601]). As a result, one can directly use this construction for any power-law $\alpha > d$, to create the approximate Floquet unitary U_f^{app}, and to prove that it satisfies property (a), i.e. that it exhibits an exponentially long thermalization time scale. Extending to the case of an emergent symmetry then naturally follows by using the arguments found in Ref. [161].

Key challenge

Unfortunately, since the construction found in Ref. [5] retains no spatial information about D^*, one is unable to prove that U_f^{app} satisfies property (b), i.e. that the dynamics of local observables are accurately captured.

Crucially, the lack of spatial information about D^* prevents the application of Lieb-Robinson bounds, implying that any bound on the error of local observables diverges with the system size. To better understand the essential role of the Lieb-Robinson bounds, let us recall that the Floquet unitary is given by the *exact* expression [5]:

$$U_f = \mathcal{T} \ e^{-i \int_0^T dt \ D^* + V^*(t)} \ , \tag{12.10}$$

where $\mathcal{T}$ denotes time ordering and $V^*(t)$ is a time-dependent interaction such that the sum of terms acting on any one site is exponentially small in frequency. One then builds the approximate unitary evolution, U_f^{app}, by disregarding the role of the exponentially small $V^*(t)$.

To understand how much error is accrued in this approximation, it is crucial to understand how a local operator O "spreads" under the evolution generated by D^*. The bigger the volume of O, the larger the number of terms in $V^*(t)$ it can overlap with and whose contribution we are missing when we disregard the role of $V^*(t)$. As such, the rate of error growth is simply bounded by the sum of the local terms of $V^*(t)$ within the support $\Lambda_{O(t)}$ of the operator $O(t)$, while the total error $\delta O(t)$ is the integral: $\delta O(t) \sim e^{-\omega/J_{\mathrm{local}}} \int_0^t dt' \ \Lambda_{O(t')}$.

The role of the interaction range is now apparent. If the original Floquet evolution is *short-range*, both the resulting D^* and $V^*(t)$ are also short-range and the evolution exhibits a finite Lieb-Robinson velocity v_{LR}. The volume of the operator $O(t)$ is then bounded by $\propto (v_{\mathrm{LR}} t)^d$, and the error $\delta O(t) \sim t^{d+1} e^{-\omega/J_{\mathrm{local}}}$ remains small for an exponentially long time in the frequency.

In contrast, when the original Floquet evolution is *long-range*, the volume of the operator O can grow much faster than $\mathcal{O}(t^d)$. For example, for interactions decaying with power-laws $\alpha \leq 2d$, only an exponential light cone has been proven, $\Lambda_{O(t)} \sim e^{d\eta t}$ [230]. In this case, the

error $\delta O \sim e^{-\omega/J_{\text{local}}+d\eta t}$ remains small for only a short time *proportional* to the frequency of the drive. For $\alpha > 2d$, a power-law light cone has been proven [181, 354, 540, 163], suggesting that if D^* can be shown to exhibit an $\alpha > 2d$ spatial decay, one can immediately apply current Lieb-Robinson bounds. Of course, we hasten to remind the reader that in order to apply these long-range Lieb-Robinson bounds, one must first extend prior results (in the context of an emergent symmetry [5, 161]) to determine the spatial decay of D^* which, *a priori*, may be quite different from the decay of $H(t)$.

Prethermal phases in finite size systems

Up until to now, our discussion has focused on the thermodynamic limit, where Lieb-Robinson bounds are required to prove that local dynamics are captured by U_f^{app}. However, in finite system sizes, Eq. 12.6 can actually be enough to guarantee that the prethermal Hamiltonian properly captures the dynamics. In particular, by setting the frequency of the drive large enough, i.e., $\omega \gg \log \Lambda$, the approximate Floquet unitary is close to the full unitary evolution and the global wavefunction of the system is well approximated, *regardless of the locality of the interactions*. In this case, *any* observable (local or not) is well captured by the prethermal Hamiltonian until a time scale $\tau_O \sim \Lambda^{-1}e^{\omega/J_{\text{local}}}$ (which remains smaller than the thermalization time scale τ^* by a factor of Λ). Nevertheless, as long as τ_{pre} is smaller than τ_O, the system is guaranteed to approach the Gibbs state of D^* and this intermediate window ($\tau_{\text{pre}} < t < \tau_O$) can host prethermal phases of matter.

Summary of key analytical results

Our main analytical results are twofold. First, we present a new construction for D^* that explicitly retains information about the spatial locality of the interactions. Our construction naturally addresses the case where D^* hosts an emergent $\mathbb{Z}_N$ symmetry, extending prior results [161] to the case of long-range interactions. Second, using this novel construction, we are able to apply appropriate long-range Lieb-Robinson bounds to ensure that the prethermal Hamiltonian captures the local dynamics within the prethermal regime [property (b)] and thus, to prove the existence of long-range prethermal phases of matter.

For $\alpha > 2d$, the existence of power-law-light-cone Lieb-Robinson bounds allows us to prove that the local dynamics are accurately captured by U_f^{app} up to the Floquet heating time scale, $\tau^* \sim e^{\omega/J_{\text{local}}}$ [third row of table in Fig. 12.1]. This ensures that within the prethermal regime, the system will approach the equilibrium state of the prethermal Hamiltonian D^*; combined with the existence of an emergent symmetry (protected by the time translation symmetry of the drive), this proves the existence of *prethermal phases of matter* [fourth row of table in Fig. 12.1(c)].

For $d < \alpha < 2d$, we are not be able to directly invoke such power-law-light-cone Lieb-Robinson bounds. In this case, the equilibration dynamics within the prethermal regime are less clear. Nevertheless, one expects that the approximate conservation of energy density means that local observables still relax to the Gibbs state of D^*, since this is the state

that maximizes the entropy subject to the constraint of conservation of energy. Under this assumption, we show that the robustness of prethermal phases of matter extends to power-laws $d < \alpha < 2d$ as well [fourth row of table in Fig. 12.1(c), where the star indicates this additional assumption]. Moreover, in *finite-size* systems, one can prove rigorous statements without making this assumption, as discussed in the previous section.

In summary, our work demonstrates that prethermal phases of matter exist for all extensive power-law interacting systems ($\alpha > d$).

12.2 Rigorous statement and proof of prethermalization in long-range systems

In this section, we describe our novel analytic construction, which extends prior results on prethermal phases [5, 161] to the long-range interacting case. At its heart, this construction *exactly* transforms the initial time-dependent Hamiltonian into a new Hamiltonian composed of a static term D^* (with an emergent $\mathbb{Z}_N$ symmetry) in addition to small error terms. Crucially, this transformation captures two complementary properties: First, it ensures that the error terms are exponentially small in the frequency of the drive. Second, it guarantees that D^* and the small error terms inherit the same locality properties as the original Hamiltonian; if the original Hamiltonian is long-ranged, the transformed Hamiltonian will also be long-ranged.

As discussed in Sec. 12.1, the first property allows us to prove an exponentially long thermalization time scale, in agreement with previous bounds [312, 380, 5, 161]. Meanwhile, the second property enables us to prove a much stronger statement, namely that local observables remain well approximated by the long-range prethermal Hamiltonian throughout the prethermal regime (for power-laws $\alpha > 2d$)—a statement which has not been addressed in any prior literature for long-range interacting, prethermal systems with an emergent symmetry.

To guide the reader through this rather technical section, we present a short road map below. We begin by providing a careful treatment of previous results on prethermalization. This introduces the necessary context to discuss the novel ideas required for our construction. Next, we will precisely state the key result of our construction in the form of Theorem 2. Finally, we discuss three immediate consequences of our construction: (1) that local observables are well captured by the approximate Floquet unitary for $\alpha > 2d$ (Theorem 3), (2) how prethermal phases of matter arise even for $\alpha > d$ (Theorem 4), and (3) how our ideas can be directly generalizable to static systems with a near integer spectrum.

Previous results

Analyzing the Magnus expansion

In Refs. [312, 380], the main theoretical tool used to analyze the prethermal regime is the formal Magnus expansion of the single period time evolution operator U_f. This procedure defines the Floquet Hamiltonian H_F as a formal series expansion in the period of the drive T:

$$U_f \equiv e^{iH_F T} \quad \text{where} \quad H_F = \sum_{m=0}^{\infty} T^m K_m \ , \tag{12.11}$$

with K_m being operators and m the order of the Magnus expansion. Although such a series will, in general, not converge (otherwise there is a quasi local Hamiltonian H_F which is conserved under the dynamics of the system), understanding its truncation remains very useful.

First, by truncating the Floquet Hamiltonian at the correct order $n_0 = \mathcal{O}(\omega)$, $H_F^{(n_0)} = \sum_{m=0}^{n_0} T^m K_m$, one obtains an *exponentially* good approximation to the full unitary evolution, $U_f \approx e^{-iTH_F^{(n_0)}}$. This implies that, over a single period of the evolution, the energy density $\langle H_F^{(n_0)} \rangle / \Lambda$ remains exponentially well conserved in the frequency of the drive; this corresponds to property (a) of Sec. 12.1. Because this analysis relies only on the few-bodyness of the interaction and the existence of a finite local energy scale, it holds for both short- and long-range interacting systems with $\alpha > d$.

Second, for power-laws $\alpha > 2d$, one can use Lieb-Robinson bounds with power-law light cones [181, 354, 540, 163] to prove that $H_F^{(n_0)}$ is also the approximate generator of the dynamics of local observables for exponentially long times; this corresponds to property (b) of Sec. 12.1. Combining these two conclusions, one proves the existence of a long-lived prethermal regime whose dynamics are well captured by the prethermal Hamiltonian for short and long-range interacting systems with power-law $\alpha > 2d$ [first and second rows of the table in Fig. 12.1(c)]. Again, we emphasize that this construction does not prove the existence of an emergent symmetry in the prethermal regime; to obtain this result requires (to the best of our knowledge) a different approach.

Rotating into an appropriate frame

To this end, a different approach [5] was pursued which enabled the proof of an emergent symmetry in the prethermal regime [161]. The main idea is to find a sequence of frame rotations where each rotation reduces the magnitude of the driven part of the evolution. Stopping the iteration at the correct step minimizes the driven component and proves the existence of a long-lived prethermal regime.

In more detail, one begins by separating the Hamiltonian $H(t) = H_0(t)$ into two components: a static D_0 and a driven $V_0(t)$ term. Performing a rotation into a new frame, one obtains a new Hamiltonian $H_1(t)$ that *exactly* describes the evolution, but where the norm of the driven term $V_1(t)$ is reduced (while the static component D_1 is slightly modified); repeat-

ing such a process for n steps reduces the magnitude of the drive $V_n(t)$ exponentially in n. However, much like the Magnus expansion result, this process cannot continue indefinitely or the system would be described by a static local Hamiltonian and thus fail to thermalize to the infinite temperature state. The optimal iteration step is given by $n^* \sim \mathcal{O}(\omega/\ln^3 \omega)$, leading to the final Hamiltonian $H_{n^*}(t)$:

$$H_{n^*}(t) = D_{n^*} + V_{n^*}(t) \quad \text{where} \quad \|V_{n^*}(t)\| \leq \|V_0\|(2/3)^{n^*} .$$

Since the local terms of the driven part $V_{n^*}(t)$ are exponentially small, the full evolution is approximately generated by the static component, $U_f \approx e^{-iD_{n^*}T}$. Analogous to the Magnus expansion approach, one can prove that D_{n^*}/Λ remains exponentially well conserved under a single period:

$$\frac{1}{\Lambda}\|U_f^{-1}D_{n^*}U_f - D_{n^*}\| \leq CT\left(\frac{2}{3}\right)^{n^*} , \tag{12.12}$$

for some volume and frequency independent constant C; the thermalization time scale is then exponentially long in the frequency of the drive.

Using this approach, one can also prove that the prethermal Hamiltonian can approximate the dynamics of local operators *provided that the original evolution is governed by a Hamiltonian with short-range interactions*. The source of this additional restriction is that, unlike the Magnus expansion approach, this construction cannot keep track of the range of interactions due to the way it accounts for the size of the Hamiltonian terms. More specifically, the proof ensures that any one operator does not grow to act on too many sites, without bounding the distance between the sites it acts on. In short-range interacting systems, this distinction is unimportant because the two measures of size are proportional; it is then guaranteed that D_{n^*} remains short-ranged and that the appropriate Lieb-Robinson bounds can be used to show it approximately generates the dynamics of local operators. However, this distinction becomes crucial in long-range interacting systems where these two measures can be very distinct leading to the breakdown of the proof.

Generalizing to a prethermal emergent symmetry

Understanding the limitations of this construction [5] is crucial because it provides the only path (to our knowledge) to prove the emergence of symmetries in the prethermal regime [161]. The main insight for this generalization is that the previous construction can be slightly modified to preserve the structure of the original Floquet unitary. Consider a Floquet unitary of the form:

$$U_f = \mathcal{T}e^{-i\int_0^T dt[H_0(t)+V(t)]} = X \; \mathcal{T}e^{-i\int_0^T dt[D_0+E_0+V_0(t)]} , \tag{12.13}$$

$$\text{where} \quad \mathcal{T}e^{-i\int_0^T dt \; H_0(t)} = X , \; X^N = \mathbb{1} \tag{12.14}$$

where E_0 corresponds to the static terms of the evolution that *do not* commute with the symmetry X. In this case, E_0 and $V_0(t)$ are both the error terms we wish to minimize (in this

language, the original construction corresponds to the specific case when $N = 1$, $X = \mathbb{1}$, and $E_0 = 0$ [5]). To adapt their construction, one first rotates the system such that E_0 becomes time periodic, while keeping D_0 unchanged; the system is now fully characterized by D_0 and a new drive $V_0'(t)$. One can now directly employ the previous construction to reduce the magnitude of the newly defined driven part [161]. The resulting new Hamiltonian contains terms E_1 and $V_1(t)$ whose magnitude is reduced and a static D_1 whose magnitude slightly increases. Applying this procedure n^* times reduces the size of E_{n^*} and $V_{n^*}(t)$ optimally, such that the unitary evolution is well approximated by the action of X and an evolution under the final static term $D_{n^*} = D^*$ [Eq. 12.2]. Let us emphasize that this picture is exact in a slightly rotated frame $\mathcal{U} \approx \mathbb{1} + \mathcal{O}(\omega^{-1})$ arising from the small rotation necessary to transform each E_n into a driven term.

Because this analysis follows the results of Ref. [5], the results have the same scope with regards to the range of the interactions. In particular, the heating rate of the system is exponentially slow in frequency for both short and long-range interactions with power-law $\alpha > d$; however, local observables are only provably well captured by the prethermal Hamiltonian in short-range interacting systems. Proving this result in full generality is the goal of the next few sections and will open up an entirely new landscape for investigating non-equilibrium phases of matter and their quantum simulation in long-range interacting quantum optical platforms.

Main ideas of proof for long-range generalization

In this section, we outline the novel ideas required to extend prior results [5, 161] to long-range interacting systems; our main result is summarized in Theorems 2 and 3. The detailed proofs can be found in Appendix B.

The main hurdle in generalizing the previous results to long-range interacting systems is to understand how the spatial structure of the interactions changes as one performs the necessary frame rotations.

We highlight, with a simplified example illustrated in Fig. 12.2, the importance of the range of interactions to the spread of operators. Although this example uses time evolution, the intuition carries over to the case of a frame rotation generated by some short- or long-range operator. Consider an operator $O = \sigma_i^x$ and a short-range interacting Hamiltonian $H^{\mathrm{sr}} = \sum_j \sigma_j^z \sigma_{j+1}^z$. At early times, the spread of the operator is given by

$$
\begin{aligned}
O \;\rightarrow\; e^{itH^{\mathrm{sr}}} O e^{-itH^{\mathrm{sr}}} &= O + it[H^{\mathrm{sr}}, O] + \mathcal{O}(t^2) \\
&= \sigma_i^x - 2t\sigma_i^y \left(\sigma_{i+1}^z + \sigma_{i-1}^z\right) + \mathcal{O}(t^2) \;.
\end{aligned}
\tag{12.15}
$$

Crucially, the growth of the operator can happen only where it fails to commute with the Hamiltonian. Because the Hamiltonian is short-ranged, the range (spatial extent R) of the time-evolved operator is proportional to the size of the support of the operator (number of sites k it acts non-trivially on). This distinction may not seem meaningful for short-range interacting systems, but in long-range systems it becomes crucial. For example, if we

consider long-range interactions such as

$$H^{\mathrm{lr}} = \sum_{i \neq j} \frac{\sigma_i^z \sigma_j^z}{|i-j|^\alpha},$$

(12.16)

then the spread of the operator is given instead by

$$O \rightarrow e^{itH^{\mathrm{lr}}} O e^{-itH^{\mathrm{lr}}} = O + it[H^{\mathrm{lr}}, O] + \mathcal{O}(t^2)$$

$$= \sigma_i^x - 2t\sigma_i^y \sum_{j \neq i} \frac{\sigma_j^z}{|i-j|^\alpha} + \mathcal{O}(t^2) .$$

(12.17)

In this case, the time-evolved operator immediately becomes a sum of terms that connect
two very distant points. While each term is two-bodied—i.e. the size of the support remains
small with $k = 2$—it can connect two points that are arbitrarily far away—i.e. the range R
is arbitrarily large.

We now connect this intuition to a careful analysis of the prethermal Hamiltonian. Start-
ing from two-body interactions [such as Eq. 12.16], the usual construction performs a rotation
(informed by the driven part of the Hamiltonian) that generates a new Hamiltonian with
higher-body and further extended terms [5, 161]. To properly characterize the resulting final
prethermal Hamiltonian, it is crucial to account for both the support size k and the spatial
extent R of the terms, as these two properties play different roles in our result.

In particular, we need to ensure that terms that have either a large support size or a
large range have a small magnitude. More precisely, if their magnitude decays exponentially
with support size k, one can prove that there is a prethermal Hamiltonian exhibiting an
exponentially long heating time scale. If their magnitude *also* decays with R with sufficiently
large power-law, one can employ the necessary Lieb-Robinson bounds to prove that the
prethermal Hamiltonian is the approximate generator of the dynamics. In our work, we
prove that this condition holds even when there is an emergent symmetry.

This latter point has eluded previous results [5, 161] because their construction was
unable to keep track of the spatial structure of interactions; in particular, a distinction is
not made between an operator that acts on many sites (large k) and a few-body interaction
that acts on sites far apart (large R).

To overcome this issue, our strategy is to imbue the construction with extra structure
that enables us to keep track of the range and the size of the operator separately. To this
end, we introduce the definition of an *R-ranged set* and use it to build *R-ranged operators*.
By representing the Hamiltonian in terms of R-ranged operators, we will ultimately be able
to keep track of both the range R as well as the size k of the rotated Hamiltonian throughout
the construction.

Let us begin by defining an R-ranged set. Schematically, an R-ranged set is a union of
"clusters," each separated by distance at most R. As a result, any two of its sites are con-
nected via a sequence of "jumps" of size at most R through the set, as shown in Fig. 12.2(c).
Formalizing this picture, we define an *R-ranged set* as a set Z_R of sites of our system, such
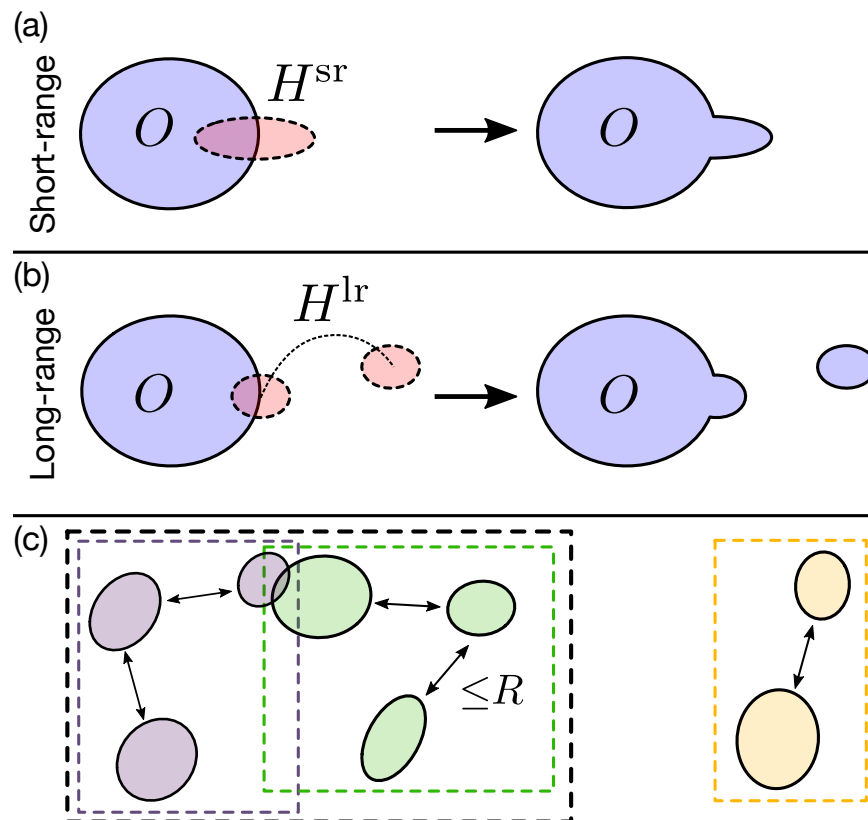
Figure 12.2: **Schematic of operator expansion under dynamics.** **(a)** [**(b)**] Illustration
of operator spread via the action of a short- [long]-range Hamiltonian, Eqs. 12.15 [12.17].
In the short-range case (a), the operator remains close to its original location. For the
operator to spread to a far away location, it requires many actions of H^{sr} which leads to
a correspondingly large increase in its support; the range and support are closely related
notions of size. In the long-range case (b), this need not be the case. The operator can very
quickly spread across the system without a significant increase to its support; the range and
the support of the operator capture very different notions of size. **(c)** An R-ranged set is
a set where any two elements can be connected via a sequence of "jumps" (within the set)
of size no greater than R. We illustrate this concept with the gray, green and orange sets,
each representing a different R-ranged set. Crucially, this definition is closed: when two
R-ranged sets have a non-empty intersection, their union is also an R-ranged set (e.g. the
gray and green sets). If they do not intersect, the union of two R-ranged sets need not form
an R-ranged set (e.g. the green and orange sets).

that for $x, x' \in Z_R$, there exists a sequence of elements $(x_1, \ldots, x_n)$ with $x_i \in Z_R$ such that
$x_1 = x$, $x_n = x'$ and $\mathrm{dist}(x_i, x_{i+1}) \leq R$.

At first sight, this definition appears more involved than simply characterizing a set
based on its diameter (i.e. largest distance between two of its elements). This is on purpose.
Indeed, our definition of an R-ranged set has the following crucial property: if two R-ranged
sets have a non-trivial intersection, then their union is itself an R-ranged set. The same is
not true for two sets with diameter at most R.

To see the importance of this property, let us first define an R-*ranged operator* as an
operator whose (non-trivial) support is an R-ranged set. The previous property of R-ranged
sets immediately manifests in the following: if one takes two R-ranged operators A_{R_1}, B_{R_2},
then $e^{A_{R_1}} B_{R_2} e^{-A_{R_1}}$ will be a $\max(R_1, R_2)$-ranged operator. If we consider an operator written
as a sum of R-ranged terms, then we can easily keep track of the range of each term as we
perform a frame rotation (here, corresponding to $e^{A_{R_1}}$). When applied to the construction
of the prethermal Hamiltonian, we can easily keep track of the R-rangeness of each term of
the original Hamiltonian throughout the different rotations.

The idea now is that we will consider potentials made up of a *hierarchy* of different-
ranged interactions, decaying in an appropriate way with range. Specifically, we introduce a
parameter $\sigma > 0$ (the value of which we will choose later), and define a sequences of ranges
$R_l = e^{\sigma l}$. Then we will define a *range-indexed potential* to be a formal sum:

$$\Phi = \sum_{l=0}^{\infty} \sum_{Z \in \mathcal{Z}_{R_l}} \Phi_{Z,l} \, , \tag{12.18}$$

where $\Phi_{Z,l}$ is supported on the R_l-ranged set Z. Here we have introduced $\mathcal{Z}_{R_l}$, the collection
of all possible R_l-ranged sets.

Now we introduce a norm whose finiteness ensures our desired condition, namely, that
the strength of the interactions decays exponentially in the size of their support k and as a
power-law in the range R. Specifically, we define a norm that depends on two parameters
$\kappa, \gamma > 0$ according to

$$\|\Phi\|_{\kappa,\gamma} = \sup_{x \in \Lambda} \sum_{l=0}^{\infty} R_l^{\gamma} \sum_{Z \in \mathcal{Z}_{R_l}, x \in Z} e^{\kappa|Z|} \|\Phi_{Z,l}\| \, , \tag{12.19}$$

where γ characterizes the power-law of the long-range decay. This is a generalization of the
norm used in Refs. [5, 161],

$$\|\Phi\|_{\kappa} = \sup_{x \in \Lambda} \sum_{Z \ni x} e^{\kappa|Z|} \|\Phi_Z\| \tag{12.20}$$

which did not keep track of the decay with range.

As an example, we note that for a two-body long-ranged Hamiltonian such as Eq. 12.16,
our new norm Eq. 12.19 is finite in the thermodynamic limit provided that $\gamma < \alpha - d$. To

see this, note that we can set

$$\Phi_{Z,l} = \begin{cases} \frac{1}{r^\alpha}\sigma_i^z\sigma_j^z & Z = \{i,j\}, r = \text{dist}(i,j), l = l(r) \\ 0 & \text{otherwise} \end{cases}, \tag{12.21}$$

where $l(r)$ is the smallest l such that $R_l \geq r$. Then we have that

$$\|\Phi\|_{\kappa,\gamma} = e^{2\kappa} \sum_{l=0}^{\infty} R_l^\gamma \sum_{i,j:R_{l-1}<\text{dist}(i,j)\leq R_l} \frac{1}{\text{dist}(i,j)^\alpha} \tag{12.22}$$

On a d-dimensional lattice, we have

$$\sum_{i,j:r<\text{dist}(i,j)\leq r'} \frac{1}{\text{dist}(i,j)^\alpha} \leq \frac{C}{r^{\alpha-d}} \tag{12.23}$$

for some constant C, and hence we find

$$\|\Phi\|_{\kappa,\gamma} \leq Ce^{2\kappa}\left(R_0^\gamma + \sum_{l=1}^{\infty} \frac{R_l^\gamma}{R_{l-1}^{\alpha-d}}\right) \tag{12.24}$$

$$= Ce^{2\kappa}\left(1 + \frac{e^{\sigma(\alpha-d)}}{1 - e^{\sigma(\gamma-\alpha+d)}}\right) < \infty, \tag{12.25}$$

provided that $\gamma < \alpha - d$.

However, we emphasize that our results also hold for Hamiltonians that are not just two-body! The only condition is that they decay fast enough with distance such that the norm in Eq. 12.19 is finite.

Statement of the prethermalization theorem for long-range interacting systems

We have now set up all of the requisite tools. Our key contribution is developing the techniques required to analyze the range of the Hamiltonians produced by the aforementioned iterative construction, which leads to the following two main results (for details, see the appendices).

First, we show that, by revisiting systems with *short-range* interactions, we can obtain stronger bounds by simply replacing the particular sequence of numbers "κ_n" chosen in Ref. [5] with a more optimized version. Second, by leveraging the properties of R-ranged operators and our particular choice of the sequence R_l, we encode the information of the two-parameter norm Eq. 12.19, which captures the long-range nature of the interactions, back into the original one parameter norm Eq. 12.20. This enables us to make use of the *exact* same analysis as in the short-range case, while keeping track of the long-range nature of the interactions via this encoding. Our final result is:

Theorem 2. *Suppose we have a time-periodic Hamiltonian $H(t+T) = H(t)$ which induces
a Floquet evolution over a period T:*

$$U_f = \mathcal{T} \exp\left[-i \int_0^T dt\ H(t)\right] \tag{12.26}$$

$$= X\ \mathcal{T} \exp\left[-i \int_0^T dt\ (D + E + V(t))\right] \tag{12.27}$$

such that D and E are time-independent and

$$X^N = \mathbb{1} , \tag{12.28}$$

$$[D, X] = 0 . \tag{12.29}$$

Fix some $\kappa_0, \gamma > 0$, and define

$$\lambda = T \max\{\|D\|_{\kappa_0,\gamma}, \|E\|_{\kappa_0,\gamma}, \|V\|_{\kappa_0,\gamma}\}, \tag{12.30}$$

*Now fix any $0 < \mathfrak{C} < 1$. Then there exist constants $C_1, \ldots, C_5 > 0$, depending only on $\mathfrak{C}$ and
κ_0, with the following properties.*
*If $\lambda \leq C_1$ (the high-frequency regime), then there is a unitary transformation $\mathcal{U}$ which
transforms the evolution to:*

$$\mathcal{U}^\dagger U_f \mathcal{U} = X\ \mathcal{T} \exp\left[-i \int_0^T dt\ (D^* + E^* + V^*(t))\right] \tag{12.31}$$

where:

$$\|D - D^*\|_{\kappa_*,\gamma_*} T \leq C_3 \lambda^2, \tag{12.32}$$

$$\|V^*\|_{\kappa_*,\gamma_*} T \leq C_2 \lambda^2 \left(\frac{1}{2}\right)^{n_*}, \tag{12.33}$$

$$\|E^*\|_{\kappa_*,\gamma_*} T \leq C_2 \lambda^2 \left(\frac{1}{2}\right)^{n_*}, \tag{12.34}$$

and

$$\kappa_* = \mathfrak{C}\kappa_0, \quad \gamma_* = \mathfrak{C}\gamma, \quad n_* = \left\lfloor \frac{C_4}{\lambda} \right\rfloor. \tag{12.35}$$

Moreover, $\mathcal{U}$ is locality-preserving and close to the identity in the following precise sense:

$$\|\mathcal{U}\Phi\mathcal{U}^\dagger - \Phi\|_{\kappa_*,\gamma_*} \leq C_5 \lambda \|\Phi\|_{\kappa_0,\gamma}. \tag{12.36}$$

for any range-indexed potential Φ.

We emphasize that, because $\lambda = \mathcal{O}(\omega^{-1})$, we have that $n_* = \mathcal{O}(\omega)$; Eqs. 12.33 and 12.34
then reflect the exponential suppression (in frequency) of the "error terms" $V^*(t)$ and E^*.

Consequences of Theorem 2

Approximate form of the Floquet unitary

The end goal of Theorem 2 is to prove that the discussion in Sec. 12.1 for realizing prethermal phases of matter (e.g. the prethermal time crystal) carries over to systems with power-law decaying interactions.

To this end, we build the approximate Floquet unitary evolution, $U_f \approx \mathcal{U} X e^{-iD^*T} \mathcal{U}^\dagger :=$ U_f^{app}, by discarding the exponentially small [in $\lambda^{-1} = \mathcal{O}(\omega)$] error terms in Eq. 12.31 [E^* and $V^*(t)$]. As emphasized in Sec. 12.1, it is important to consider in what sense $U_f \approx U_f^{\mathrm{app}}$ is a good approximation. In particular, we can consider the difference between the two unitaries

$$\|U_f^{\mathrm{app}} - U_f\| \le \Lambda T \|V^* + E^*\|_{\kappa_*,\gamma_*} = \mathcal{O}(\Lambda 2^{-n_*}) \ . \tag{12.37}$$

It then follows that property (a) from Sec. 12.1 is satisfied: the energy density $\langle D^* \rangle / \Lambda$ remains approximately conserved until the heating time $\tau^* \sim 2^{n_*}$. At this point, this just recovers an already obtainable result (even for long-range interactions) directly from the arguments of Ref. [161], albeit with an improved bound on the heating time since n_* now lacks any logarithmic corrections in λ.

Crucially, however, our choice of norm *also* guarantees that the interactions in D^* [as well as E^* and $V^*(t)$] remain power-law decaying in space. This allows us to consider how well U_f^{app} approximates the dynamics of local observables [property (b) in Sec. 12.1] which requires the use of Lieb-Robinson bounds.

Approximation of local observables

As previously discussed in Sec. 12.1, proving that local dynamics are well captured by the prethermal Hamiltonian requires the existence of Lieb-Robinson bounds with power-law light-cones. However, such bounds, in turn, require the prethermal Hamiltonian to exhibit the correct locality properties; its terms must decay, at most, as a power-law of their range.

In our construction, this is guaranteed by the finiteness of our two-parameter norm [captured in Eqs. 12.32-12.34], where the power-law decay of each term is characterized by the parameter γ_*. Crucially, Theorem 2 guarantees that γ_* can be chosen arbitrarily close to the parameter γ that characterizes the power-law decay of the original Hamiltonian of the system. This ensures that the prethermal Hamiltonian exhibits the same locality properties as the original Hamiltonian. Let us emphasize, however, that in the case where the original Hamiltonian contains two-body interactions, γ does *not* correspond to the exponent α that appears directly in the magnitude of each individual term (as in Eq. 12.16); rather, as we found in Eq. 12.25, γ must be smaller than $\alpha - d$.

This language also enables us to immediately use Lieb-Robinson bounds available in the existing literature for multi-body long-range interacting Hamiltonians, and that we discussed in the previous chapter [163]. In particular, any long-range interacting Hamiltonian H with bounded norm $\|H\|_{\kappa,\gamma}$ and $\gamma > d$ satisfies the assumptions of Ref. [163], and therefore obeys

a power-law-light-cone Lieb-Robinson bound. We emphasize the requirement of a Lieb-Robinson bound for interactions with *arbitrary* k-bodyness since our construction does not guarantee that the k-bodyness of the original Hamiltonian is preserved by the prethermal Hamiltonian.

Combining our knowledge of the locality of the prethermal Hamiltonian with the necessary Lieb-Robinson bounds we prove the second main result of our work: all local observables are accurately captured by the approximate unitary U_f^{app} throughout the entire prethermal regime. This statement is formalized into the following theorem:

Theorem 3. *Approximation of local observables* *Consider the scenario described in Theorem 2. Define $\widetilde{U}_f = \mathcal{U}^\dagger U_f \mathcal{U}$, where $\mathcal{U}$ is the rotation constructed in Theorem 2, and define the corresponding approximate unitary $\widetilde{U}_f^{app} = Xe^{-iD^*T}$ by discarding the E^* and V^* terms in Eq. 12.31. Suppose that $\gamma_* > d$, where d is the spatial dimension. Then for any η satisfying $\frac{d+1}{\gamma_*+1} < \eta < 1$, and for any local observable O supported on a set Y, we have*

$$\|(\widetilde{U}_f^{\mathrm{app}})^{-m}O(\widetilde{U}_f^{\mathrm{app}})^m - \widetilde{U}_f^{-m}O\widetilde{U}_f^m\| \leq \mathcal{C}\|O\|m\lambda 2^{-n_*}\left(1 + \tau^{1+d/(1-\eta)}\right), \qquad (12.38)$$

where $\tau = (C_6\lambda)m$, where C_6 is a constant that depends only on κ_* and γ_*, and $\mathcal{C}$ is a constant that depends only on the geometry of the system (but not its volume), the spatial dimension d, the size of the set Y, and on η.

Before concluding this section, we hasten to emphasize that if novel multi-body Lieb-Robinson bounds can be extended to power-laws $\gamma > 0$, the construction presented in this work will immediately carry over. Such improvements would be in agreement with previous numerical and experimental results [462, 87, 344, 342], as well as a recent proof for the particular case of two-body long-range interacting systems in one dimension [93].

Prethermal phases for power-laws $d < \alpha < 2d$

Unfortunately, we cannot prove a result as strong as Theorem 3 for $0 < \gamma_* < d$ (corresponding to initial two-body Hamiltonians with $d < \alpha < 2d$). Nevertheless, we can at least show that the dynamics of local observables are well-approximated by $\widetilde{U}_f^{\mathrm{app}}$ at short times.

Theorem 4. *Approximation of local observables (for short times)*. *Consider the scenario described in Theorem 2. Define $\widetilde{U}_f = \mathcal{U}^\dagger U_f \mathcal{U}$, where $\mathcal{U}$ is the rotation constructed in Theorem 2, and define the corresponding approximate unitary $\widetilde{U}_f^{app} = Xe^{-iD^*T}$ by discarding the E^* and V^* terms in Eq. 12.31. Then for any local observable O supported on a set S, we have, for any positive integer m satisfying $m\lambda \leq C_7$,*

$$\|(\widetilde{U}_f^{\mathrm{app}})^{-m}O(\widetilde{U}_f^{\mathrm{app}})^m - \widetilde{U}_f^{-m}O\widetilde{U}_f^m\| \leq C_8\mathcal{C}'\|O\|\lambda^2 2^{-n_*}mT \qquad (12.39)$$

where C_7 is a constant that depends only on κ_*, and C_8 is a constant that depends only on κ_* and the size of the set S.

The assumptions of Theorem 4 differ from Theorem 3 in that Theorem 4 does not require $\gamma_* > d$, but has an upper bound on the number of periods, m, which can be considered. For small enough λ (that is, high enough frequency), $m_{\max} = \lfloor C_7/\lambda \rfloor > 1$, so one can at least accurately describe the dynamics of local observables during a *single* driving period.

The consequence of this result is as follows. Suppose that at some time $t = nT$, the local observables are approximately described by the Gibbs ensemble of D^*, or some spontaneous symmetry broken sector thereof, which we call ρ. As mentioned in Sec. 12.1, we reemphasize that is a somewhat nontrivial assumption in the absence of a proof that the approximate unitary accurately describes the dynamics of local observables during the whole approach to thermal equilibrium; however, it follows if we assume that the system maximizes its entropy subject to the constraint of conserving energy density (which remains true for exponentially long times). Then, after one more driving period, the local state is approximately described by the rotated Gibbs ensemble $\widetilde{U}_f^{\mathrm{app}} \rho (\widetilde{U}_f^{\mathrm{app}})^\dagger = X\rho X^\dagger$ (using the fact that $[\rho, D^*] = 0$). This is all we need to repeat the arguments of Sec. 12.1 about non-equilibrium prethermal phases of matter.

Extension to static systems

The long thermalization time scale of driven systems can also be generalized to static systems whose dynamics are dominated by an operator P with integer spectrum [5, 161]:

$$H = uP + D + V \ , \tag{12.40}$$

where $[D, P] = 0$, while $[V, P] \neq 0$ and u is the largest energy scale. In this setup, there is a change of frame where P becomes quasi-conversed. To intuitively understand how this conservation emerges, it is simplest to consider a infinitesimal evolution under $\Delta t = \delta t/u$:

$$U = e^{i\delta t(P + (D+V)/u)} \approx e^{-i\delta t P} e^{-i\delta t(D+V)/u} = X e^{-i\delta t(D+V)/u} \tag{12.41}$$

where the integer spectrum of P ensures that $X = e^{-i\delta t P}$ with $N = 1/\delta t$. However, we can make δt to be as small as possible, increasing the size of the emergent symmetry. In the $\delta t \to 0$ limit, where Eq. 12.41 becomes exact, $N \to \infty$ and we can think of the emergent symmetry as a continuous $U(1)$ symmetry, generated by the "number" operator P. Analogously to the driven case, a time-independent change of frame $\mathcal{U}$ ensures that this emergent symmetry is approximately conserved until an exponentially long time in $1/u$. This was proven in Ref. [5], closely following their techniques for driven systems. In a similar fashion, our construction immediately adapts to the proof of the long-lived prethermal regime in static systems, allowing its extension to long-range interactions. As an application, we note that the existence of a prethermal continuous time crystal in an undriven system [161] can now be generalized to systems with long-range interactions.

12.3 Long-range prethermal discrete time crystal in one dimension

We now turn to the example of a non-equilibrium prethermal phase, where long-range interactions are essential to its stability—the disorder free one dimensional prethermal discrete time crystal. In particular, we study a one dimensional periodically driven spin-1/2 chain with long-range interactions decaying with a power-law $d < \alpha < 2d$. Using massively parallel matrix-free Krylov methods [233, 232, 33], we compute the late time Floquet dynamics for system sizes up to $L = 28$. This enables us to highlight many of the features of prethermal phases discussed in Sec. 12.1. First, by directly comparing short- and long-range interactions, we evince the crucial role of power-law interactions for stabilizing a 1D PDTC (Fig. 12.3). Second, by varying the energy density of the initial state, we access the aforementioned transition between the PDTC and the trivial phase (Fig. 12.4). These two phases can be easily distinguished by the different scaling behavior of the time crystal's lifetime τ_{TC}: in the PDTC phase it follows the heating time scale $\tau_{\mathrm{TC}} \sim \tau^* \sim e^{\omega/J_{\mathrm{local}}}$, while in the trivial phase it is bounded by the prethermalization time scale, $\tau_{\mathrm{TC}} \lesssim \tau_{\mathrm{pre}} \sim \mathcal{O}(1/J_{\mathrm{local}})$. We corroborate that our observed finite-size crossover matches the location of the phase transition independently computed via quantum Monte Carlo calculation of the corresponding equilibrium finite-temperature phase transition. These results provide insight into the experimental signatures of the PDTC, as well as direct measures of the relevant energy and time scales.

Model and Probes

To generate Floquet dynamics that host a PDTC, the evolution must satisfy two properties: first, it must lead to a prethermal Hamiltonian D^* with a robust emergent $\mathbb{Z}_N$ symmetry, and second, D^* must exhibit a spontaneous symmetry breaking phase. We engineer a drive, motivated by current generation trapped ion experiments, that exhibits both.

To ensure that the emergent symmetry exists in the prethermal regime, we design a Floquet evolution that matches the form of Eq. 12.27 in Theorem 2. In particular, we consider time evolution under the stroboscopic application of two different Hamiltonians, H [see Eq. 12.44 below] and H_x, for times T and T_x, respectively. By choosing $H_x = \Omega_x \sum_i \sigma_i^x$, with $T_x \Omega_x = \pi/2$ and σ_i^ν the Pauli operator acting on site i, the second part of the evolution flips all spins around the $\hat{x}$ direction (in the language of NMR, this part of the evolution corresponds to a global π-pulse):

$$\exp\left[-iT_x H_x\right] = \prod_j i\sigma_j^x = X \quad , \quad X^2 = \mathbb{1} \ . \tag{12.42}$$

The resulting Floquet evolution then reads:

$$U_f = Xe^{-iTH} \ , \tag{12.43}$$
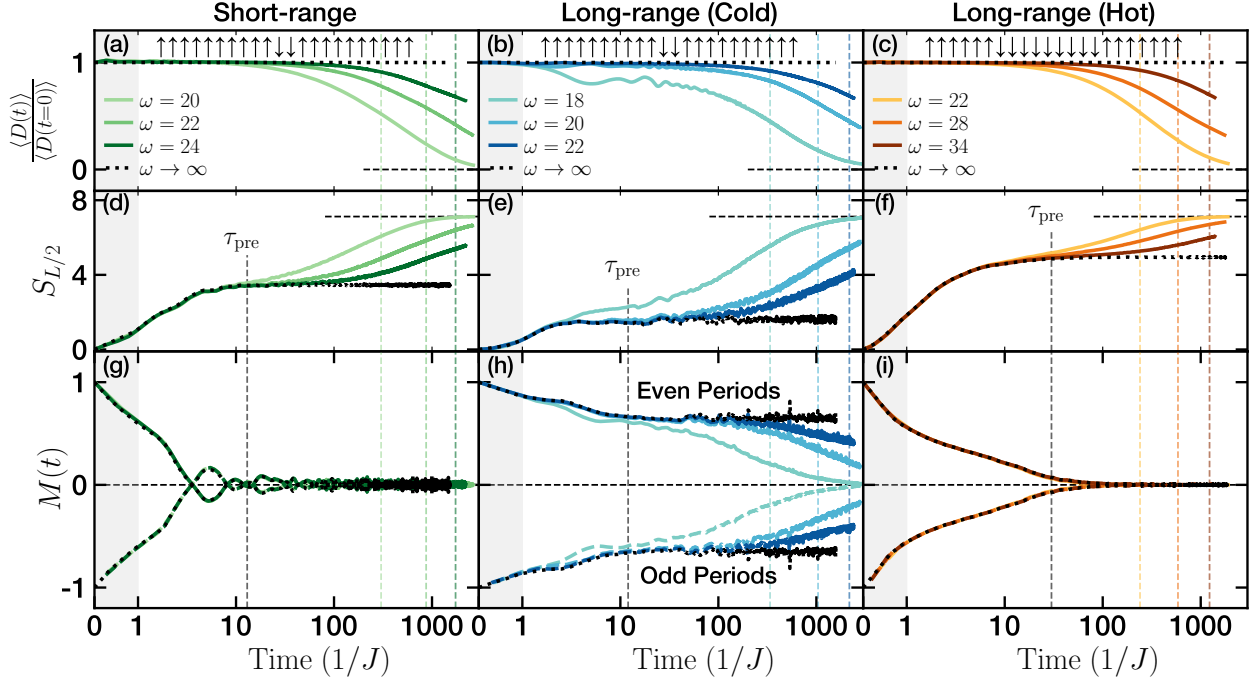
Figure 12.3: **Main ingredients for observing a prethermal discrete time crystal.**
Evolution of an L=22 spin chain under the short-range model (left column) and the long-
range model. For the latter, we consider a "cold" initial state near the top of the spectrum of
D^* (center column) and another "hot" state near the center of the spectrum (right column).
(a-c) Evolution of the energy density $\langle D \rangle / L$. Regardless of the model or initial state, the
heating time scale τ^* (which measures the approach to infinite temperature) scales *exponen-
tially* in the frequency of the drive.   **(d-f)** Evolution of the entanglement entropy $S_{L/2}$.
At intermediate times and large frequencies we observe a plateau corresponding to the en-
tanglement entropy of the prethermal state, as independently corroborated by the evolution
under the $\omega \to \infty$ limit of our Floquet evolution (captured on even periods by the evolution
under D). Analogous to the energy density, at late times $(t > \tau^*)$, the entanglement entropy
approaches its infinite temperature value of $(L \log(2) - 1)/2$ [416].   **(g-i)** Evolution of $M(t)$
for even (full line) and odd periods (dashed line). In both the short-range model (g) and the
"hot" long-range initial state (i), any period doubling behavior of the magnetization quickly
decays as the system approaches (independently of frequency) the prethermal state at τ_{pre}.
By contrast, in the "cold" long-range initial state (h), the magnetization exhibits a robust
period doubling behavior for as long as the energy density remains conserved; the decay of
both quantities occurs at $\tau^* = \mathcal{O}(e^{\omega/J_{\text{local}}})$ and the prethermal time crystal is robust. This
distinction is even clearer when considering the $\omega \to \infty$ limit of our Floquet evolution, where
the magnetization shows no signs of decay.

matching Theorem 2, with $N = 2$ and drive frequency $\omega = 2\pi/T$.[8] We emphasize that $[X, H] \neq 0$; X is *not* a symmetry of the evolution.

Next, to ensure that the associated prethermal Hamiltonian D^* exhibits a spontaneous symmetry breaking phase with respect to X, it must include long-range interactions with a power-law $d < \alpha < 2d$. However, D^* results from the construction in Theorem 2 and thus corresponds to a complicated, frequency-dependent object. Fortunately, as part of Theorem 2 we saw that D^* remains close (at high frequencies) to D, the original static symmetry respecting component of H, as defined by Eq. 12.27. Since H is time independent [Eq. 12.44], D has a very simple form: it precisely contains the terms of H that are even under X. Thus, by including a long-range Ising interaction (which commutes with X) directly in H, one can guarantee that both D and D^* exhibit a finite-temperature paramagnetic to ferromagnetic symmetry breaking phase transition [153].

Combining the long-range Ising interaction with additional generic terms (that integrability is broken) leads to the following long-range Hamiltonian H:

$$H = J \sum_{i<j}^{L-1} \frac{\sigma_i^z \sigma_j^z}{|i-j|^\alpha} + \vec{h} \cdot \sum_{i=0}^{L-1} \vec{\sigma}_i + J_x \sum_{i=0}^{L-2} \sigma_i^x \sigma_{i+1}^x \ . \tag{12.44}$$

When we compare to the "short-range version" of this Floquet evolution, we will simply truncate the Ising interaction in H to nearest and next-nearest neighbor; we denote this corresponding short-range Hamiltonian as H_s.

For the remainder of this work we consider units where $J = 1$ and use the parameters $d < \alpha = 1.13 < 2d$ and $\{J_x, h_x, h_y, h_z\} = \{0.75, 0.21, 0.17, 0.13\}$ in a spin chain of size L with periodic boundary conditions;[9] we have verified that the observed phenomena are not sensitive to this particular choice of parameters. We note that, due to our choice of an anti-ferromagnetic coupling $J > 0$, the ferromagnetic phase occurs at the *top of the spectrum* of D^*.

Finally, let us emphasize the role of the field term $h_x \sigma_i^x$ and nearest neighbor interactions $J_x \sigma_i^x \sigma_{i+1}^x$ to the thermalization properties of D^*. While favoring the disordered phase, they also ensure that, to zeroth order in ω^{-1}, D^* is not trivially diagonal and that, at large frequencies, the dynamics under D^* are generic and thermalizing; as a result, both J_x and h_x control the time scale at which the system approaches the prethermal state, τ_{pre}.

Having described our model, we now introduce the diagnostics used to characterize its Floquet evolution. First, we consider the energy density of the system. Naively, one wishes to compute the energy density with respect to the full prethermal Hamiltonian D^*; however, its numerical construction and evaluation is very costly. Therefore, we will instead measure the energy density with respect to D, which remains close to D^* at high frequencies. Second,

---

[8]Although the period of the evolution is given by $T_{\text{tot}} = T + T_x$, the evolution of the system does not depend on our choice of T_x. We then choose the limit of $T_x \to 0$ (the global π-pulse is infinitely fast) where $T_{\text{tot}} \to T$ and the drive-frequency becomes $\omega = 2\pi/T$.

[9]We slightly modify the long-range profile of the interaction to match the system's periodicity by replacing $|i-j|^{-\alpha}$ with $[(L/\pi) \sin |i-j| \pi/L]^{-\alpha}$.

we consider the half-chain entanglement entropy, $S_{L/2} = -\text{Tr}\left[\rho_{L/2}\log\rho_{L/2}\right]$ where $\rho_{L/2} = \text{Tr}_{1<i\leq L/2}|\psi\rangle\langle\psi|$, as a probe of the prethermalization and thermalization dynamics of the system.

To probe time crystalline behavior we wish to consider an observable that can exhibit a subharmonic response to our driving protocol. From our discussion in Sec. 12.1, a suitable probe should be related to the order parameter of the paramagnetic to ferromagnetic transition in our model's prethermal Hamiltonian; for example, $\langle\sigma_i^z(t)\rangle$ for some site i. However, to reduce fluctuations owing to the small support of $\langle\sigma_i^z(t)\rangle$, we find it convenient to average over the different sites of the system; let us then define

$$M(t) = \frac{1}{L}\sum_{i=0}^{L-1}\langle\sigma_i^z(0)\rangle\langle\sigma_i^z(t)\rangle \; . \tag{12.45}$$

It might have seemed more natural to consider instead the average magnetization $\overline{\sigma^z}(t) = L^{-1}\sum_{i=0}^{L-1}\langle\sigma_i^z(t)\rangle$, but $M(t)$, which corresponds to a two-time correlation function, provides a clearer window into the early time decay of the period doubling behavior. Since we consider initial product states of σ^z, $M(t=0)$ is guaranteed to be 1, its maximal value. After the system prethermalizes to D^* (for $t > \tau_{\text{pre}}$), $M(t)$ approaches a plateau whose sign will change every other period in the PDTC phase. Crucially, at this point and for translationally invariant systems (like our model), $M(t)$ becomes proportional to the average magnetization $\overline{\sigma^z}(t)$ which itself matches σ_i^z (for any i). As a result, $M(t)$ is equally sensitive to the late time decay of the time crystalline behavior (provided that the initial magnetization is nonzero).

While $M(t)$ is nonzero in the PDTC phase, it can also remains nonzero in the absence of a PDTC, e.g. in the ferromagnetic phase of a static Hamiltonian. The true order parameter for the PDTC phase must then measure the *subharmonic (i.e., period doubling) response* of $M(t)$. To this end, we introduce the PDTC order parameter:

$$\Delta M(t) = |M(t+T) - M(t)| \; . \tag{12.46}$$

In the PDTC phase, $M(t)$ will remain finite and sign changing every period and thus $\Delta M(t)$ will be nonzero. By contrast, in the symmetry-unbroken phase, all observables [including $M(t)$] quickly become T periodic and $\Delta M(t)$ approaches zero.

Exponentially long-lived PDTC

Before addressing the long-range PDTC, we begin by exploring the Floquet evolution of its short-range counterpart, H_s, where previous results have proven the existence of an exponentially long-lived prethermal regime [312, 380, 5, 2, 161]. As shown in Fig. 12.3(a), this is indeed borne out by the numerics: the energy density remains approximately constant until a late time $\tau_{D^*}^*$ when $\langle D\rangle/L$ approaches its infinite temperature value of zero. By increasing the frequency of the drive, one observes an exponential increase in $\tau_{D^*}^*$, in agreement with analytic expectations [312, 380, 5, 2, 161] and previous numerical studies [344]. These

observations are mirrored in the evolution of the entanglement entropy $S_{L/2}$ [Fig. 12.3(d)].
There, the approach to the infinite temperature value, $S_{L/2}^{T=\infty} = [L\log(2) - 1]/2$ [416], occurs
at $\tau_{S_{L/2}}^*$, which is also exponentially controlled by the frequency of the drive. The agreement
between $\tau_{D^*}^*$ and $\tau_{S_{L/2}}^*$ corroborates the existence of a single thermalization time scale τ^*
that controls the approach to the infinite temperature state. For the remainder of this work
we quantify τ^* using $\tau_{S_{L/2}}^*$.

Furthermore, $S_{L/2}$ also informs us about the equilibration with respect to the prethermal
Hamiltonian D^*; as the system evolves and approaches the prethermal state, the entangle-
ment entropy approaches a plateau that remains constant until the drive begins heating the
system at τ^*. The time scale when $S_{L/2}$ approaches this plateau value is frequency inde-
pendent. In fact, the system's prethermalization is well captured by the $\omega \to \infty$ Floquet
evolution [black dotted line in Fig. 12.3(d)]. In this limit, we have $U_f \to Xe^{-iDT}$; thus,
$U_f^2 = e^{-2iDT}$, so the evolution for even periods is *exactly* generated by the static Hamilto-
nian D; for odd periods the wave-function must be rotated by X (which does not affect $S_{L/2}$
or $\langle D\rangle/L$). This agreement with the $\omega \to \infty$ limit highlights that the dynamics within the
prethermal regime are indeed well approximated by the prethermal Hamiltonian $D^* \approx D$.

Finally, we turn to $M(t)$, our diagnostic for time crystalline order. From the discussion in
Sec. 12.1, the lack of a spontaneous symmetry breaking phase in short-range interacting one-
dimensional systems is expected to preclude the existence of the PDTC phase. In particular,
any transient period doubling behavior should quickly decay as the system approaches the
prethermal state at τ_{pre}. This is precisely what is observed in the dynamics of $M(t)$, as shown
in Fig. 12.3(g); while at very early times, even and odd periods exhibit almost opposite $M(t)$,
by the time-scale τ_{pre}, $M(t)$ has decayed to zero and the system no longer exhibits any time
crystalline behavior. Thus, the transient signatures of a time crystal "melt" as the system
equilibrates to the prethermal Hamiltonian D^*, clearly demonstrating the system's lack of a
true PDTC phase.

We now contrast this behavior to the long-range case using the same initial state, as
evinced in Figs. 12.3(b), 12.3(e) and 12.3(h). With respect to the thermalization dynamics—
captured by $\langle D\rangle/L$ and $S_{L/2}$ as shown in Figs. 12.3(b) and 12.3(e), respectively—the short-
range and long-range models exhibit qualitative agreement; an increase in the frequency of
the drive leads to an exponential increase in the thermalization time scale τ^*. We note,
however, an important quantitative difference. In particular, the value of J_{local} extracted
from the scaling $\tau^* \sim e^{\omega/J_{\text{local}}}$ is larger in the long-range system. This increase is due to the
greater number of interaction terms in the Hamiltonian and is in agreement with previous
numerical results [344]. In addition, τ_{pre} remains frequency independent and the prethermal
dynamics are in excellent agreement with the $\omega \to \infty$ time evolution [Fig. 12.3(e)].

The difference between the short and long-range interacting systems becomes apparent
when considering the PDTC order. In particular, in the long-range model, the subharmonic
response of $M(t)$ survives well beyond τ_{pre} and lasts until the heating time scale τ^*. This
behavior is robust. By increasing the frequency of the drive, the lifetime of the time crystal
increases, mirroring the exponential growth of the thermalization time scale; the decay of

time crystalline behavior is no longer determined by dynamics within the prethermal window,
but rather by heating toward infinite temperature.

Role of the initial state

Another distinct feature of the PDTC is its sensitivity to the energy density of the initial
state. Unlike the MBL time crystal [290, 557, 160, 590, 555, 602], which can exhibit period
doubling for all physically meaningful initial states, the stability of the prethermal time
crystal relies on the prethermal state's approach to the symmetry broken phase of D^*. As
a result, its stability is intimately related to the phase diagram of D^*. Because $\langle D^* \rangle / L$
remains approximately conserved until τ^*, the energy density of the initial state is equal
to the energy density of the prethermal state. With this in mind, one can then translate
the initial energy density into the temperature β^{-1} of the prethermal state via the relation
$\langle D^*(t=0)\rangle = \text{Tr}\left[D^* e^{-\beta D^*}\right]/\text{Tr}\left[e^{-\beta D^*}\right]$. By choosing initial states with different energy
densities, one can effectively vary the temperature of the prethermal state across the phase
transition; the resulting $M(t)$ dynamics display qualitatively distinct behaviors.

This difference is manifest when we compare the dynamics of a "cold" state [near the
top of the many-body spectrum,[10] Figs. 12.3(b), 12.3(e) and 12.3(h)], with the dynamics
of a "hot" state [near the center of the many-body spectrum), Figs. 12.3(c), 12.3(f) and
12.3(i)]. Despite exhibiting the same thermalization behavior to infinite temperature, the
period doubling behavior of the "hot" state decays significantly faster; indeed, the decay of
$M(t)$ [and thus $\Delta M(t)$] is frequency independent and occurs as the system approaches the
prethermal state at $t \lesssim \tau_{\text{pre}}$, well before the heating time scale τ^*. This behavior is directly
analogous to that of the short-range model.

To directly connect the stability of the prethermal time crystal to the equilibrium phase
diagram of D^*, we study the decay time scale τ_{TC} of the PDTC order parameter $\Delta M(t)$
across the spectrum of D^* (Fig. 12.4).

Crucially, τ_{TC} exhibits important differences between the short- and long-range cases
[Figs. 12.4(a) and 12.4(b), respectively]. In the short-range case, the frequency of the drive
has no discernible effect on the lifetime of $\Delta M(t)$ (except for the highest energy state, which
we discuss below).

In the long-range case, the behavior is significantly richer and modifying the driving
frequency has a different effect depending on the energy density [Fig. 12.4(b)]. The most
distinct behaviors occur deep in the paramagnetic phase (near the center of the spectrum)
and deep in the ferromagnetic phase (near the top of the spectrum). In the former, we observe
the same frequency independent behavior of τ_{TC} that characterized the short-range model—
the decay time-scale of $\Delta M(t)$ is simply determined by the prethermalization dynamics. In
the latter, the behavior is dramatically distinct: τ_{TC} increases exponentially with the drive
frequency, following the thermalization time scale τ^*; in fact, the two time scales approach

---

[10]Owing to our choice of antiferromagnetic coupling, the ferromagnetic phase exists at the top of the
spectrum.
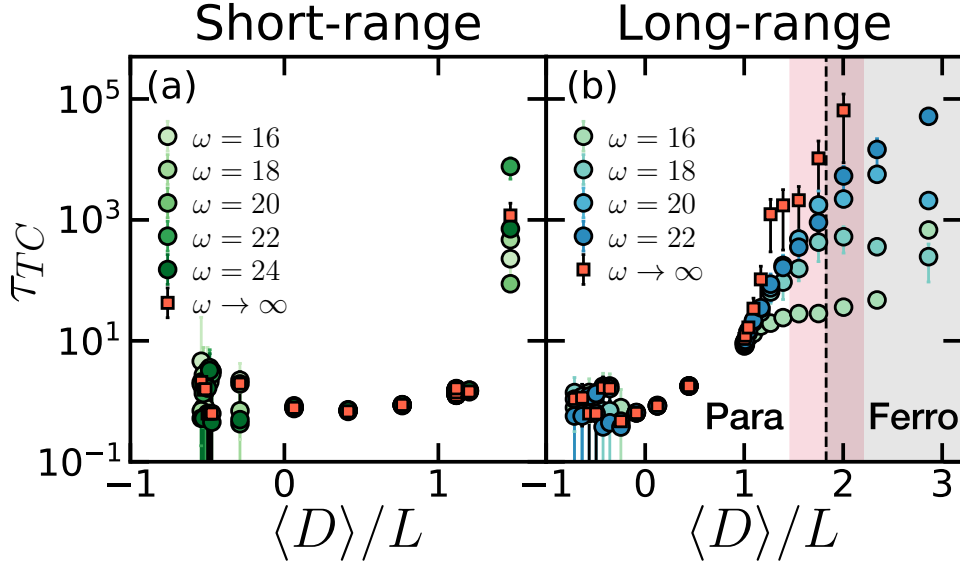
Figure 12.4: **Equilibration dynamics across transition to a prethermal discrete time crytal.** **(a[b])** Decay time scale of the time crystalline order parameter τ_{TC} as a function of the energy density of the initial state for the short[long]-range model. In the short-range model (a), τ_{TC} is fast, independent of frequency, and in agreement with the decay time scale of the magnetization $M(t)$ if the system were evolved according to D alone (red squares). In the long-range model (b), an analogous behavior occurs near the center of the spectrum. However, as one moves to higher energies across the para- to ferromagnetic phase transition (red shaded region), τ_{TC} becomes exponentially dependent on the frequency of the drive and τ_{TC} approaches τ^*. In this regime, τ_{TC} is set by the exponentially slow heating rather than the prethermal dynamics for all frequencies—the prethermal time crystal is stable.

one another with increasing frequency—this is the key signature of the PDTC phase, namely that the decay of the time crystalline order is limited only by the late time Floquet heating dynamics.

Having understood the behavior deep within each phase, we now turn to the transition between the two. At first glance, it appears that the onset of the exponential frequency scaling (and thus the transition to the PDTC phase) occurs at a lower energy density than what is expected from the phase diagram of D^* [dark shaded region of Fig. 12.4(b)]. This phase boundary is based on an independent quantum Monte Carlo calculation for the transition in D. As we explore below, this apparent inconsistency instead corresponds to a small finite frequency effect arising from the slow thermalization dynamics of D^* near the phase transition, as schematically depicted in Fig. 12.5.

As a system approaches a phase transition, critical slowing down causes its thermalization
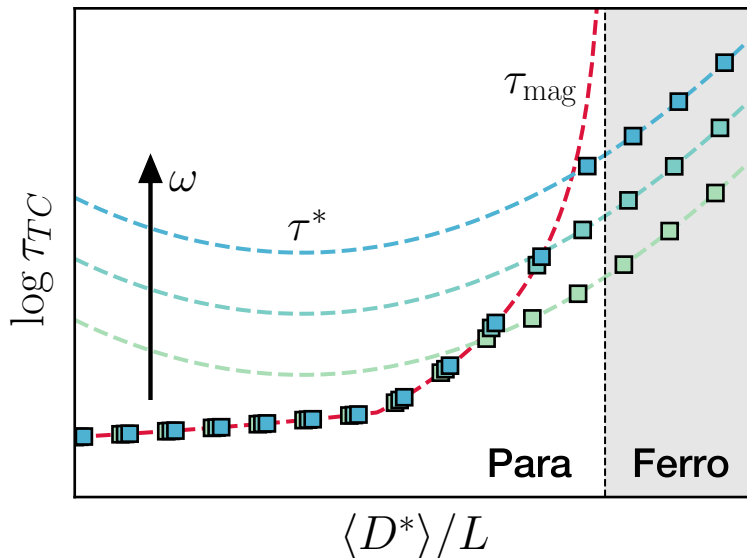
Figure 12.5: **Critical slowing down near the transition to the PDTC phase.** There
are two competing time scales: the heating time τ^*, and the magnetization decay time τ_{mag}
of the prethermal Hamiltonian D^* [captured by the red squares in Fig. 12.4(a,b)]. As the
system approaches the phase transition into the ferromagnetic phase (shaded region) from
the paramagnetic side, τ_{mag} diverges (red dashed line). The relaxation time τ_{TC} is given by
the *smaller* of these two time-scales. In (most of) the paramagnetic phase, τ_{mag} is smaller
and approximately frequency independent; while in the ferromagnetic phase, τ^* is smaller;
τ_{TC} shares its strong frequency dependence.

time scale to diverge. As a result, even in the paramagnetic phase, the decay of $\Delta M(t)$ can
occur at very late times; we refer to this decay time scale as τ_{mag}. In the paramagnetic phase
τ_{mag} is finite, while in the ferromagnetic phase, it is infinite.

At low frequencies, if the system is near the phase transition on the paramagnetic side,
τ_{mag} can be finite but much larger than τ^*. The decay of $\Delta M(t)$ is set by heating rather
than the prethermal dynamics of D^* *even though the system is in the trivial phase.* The
situation is resolved upon increasing the frequency of the drive, at which point τ^* and τ_{TC}
will both increase exponentially until they reach the magnetization decay time τ_{mag}; then, τ_{TC}
again becomes bounded by τ_{mag}, losing its frequency dependence, while τ^* keeps increasing
exponentially with frequency. Thus, at large enough frequencies, it is always the case that,
in the paramagnetic phase, the decay of $\Delta M(t)$ arises from the dynamics of D^*.

This behavior is evinced in Fig. 12.4(b) in two distinct ways. First, by directly simulating
the decay of $\Delta M(t)$ in the $\omega \to \infty$ limit (where heating cannot occur), we observe a signifi-
cant increase of the decay time near the transition. In particular, in the paramagnetic phase,
we observe a decay time scale which diverges around the transition at $\langle D \rangle / L \approx 2.0$—this

is direct evidence for the presence of slow prethermalization dynamics near the transition. Second, near the transition to the ferromagnetic phase, the disagreement between τ_{mag} (as measured by the decay of the magnetization in the $\omega \to \infty$ evolution) and τ_{TC} occurs deeper in the trivial phase smaller frequencies.

Interestingly, the above discussion also explains the long thermalization time found in the edgemost state of the short-range model, Fig. 12.4(a). In this case, the initial state is close to the zero temperature ferromagnetically ordered state, leading to a finite, but very large prethermalization time scale. This very long prethermal equilibration time might also underlie the recent observations of long lived period-doubling behavior in the prethermal regime of short-range interacting systems [600, 596, 372], where no finite-temperature phase transition or stable PDTC should occur.

12.4 Conclusion

Using a combination of analytical and numerical results, we demonstrate the existence of prethermal non-equilibrium phases of matter in long-range interacting systems with power-laws $\alpha > d$. This prethermal approach contrasts with recent MBL-based studies of Floquet phases, since it does not require disorder, nor is it limited by the dimensionality of the system. We emphasize the generality of our analytic construction, whose limitations arise only from the lack of an appropriate Lieb-Robinson bound for $d < \alpha < 2d$. However, even in this regime, on quite general grounds, we expect the system to approach the Gibbs state with respect to the prethermal Hamiltonian and, thus, for prethermal phases of matter to be well defined. Finally, we predict the existence of a novel, disorder-free, prethermal discrete time crystal in one dimension. This phase is strictly forbidden in equilibrium, Floquet MBL, and *short-range* interacting prethermal Floquet systems.

Our work provides a rigorous analysis of the stability of prethermal phases in long-range interacting quantum systems, opening the doors to the exploration of a variety of intrinsically out-of-equilibrium phases of matter. One such exploration, the first characterization of a prethermal discrete time crystal, is discussed in the next chapter [313].

For completion, we note a related complementary work, studying the locality and heating in periodically driven, power-law interacting systems [541].

Chapter 13

Observation of a Prethermal Discrete Time Crystal (PDTC)

A common theme in this dissertation is how the discrete time translation of a periodically driven (Floquet) system can be utilized to protect novel phases [408, 445, 399, 160, 590, 100, 601, 468, 511, 201, 589]. In the past chapter, we discussed how this symmetry the discrete time translation symmetry protects an emergent symmetry in the effective Hamiltonian describing the stroboscopic dynamics of a long-range interacting system. In combination with the exponentially large prethermal time window where this effective Hamiltonian remains (almost) conserved [312, 5], one obtain a framework for stabilizing intrinsically, out-of-equilibrium prethermal phases of matter [161, 345]. One example of such a phase is the prethermal discrete time crystal (PDTC), where the many-body system spontaneously breaks the discrete time translation symmetry of the drive and develops a robust sub-harmonic response.

The disorder-free PDTC exhibits a number of key differences compared to its MBL counterpart (Chapter 7), despite the similarity of their sub-harmonic response [163, 287]. When stabilized by MBL, time-crystalline order is independent of the initial state and persists to arbitrarily late times, but is believed to only occur in low dimensions with sufficiently short-range interactions [591, 130]. By contrast, the PDTC lifetime is limited by the heating timescale, τ^*, and depends on the energy density of the initial state; this energy density determines the prethermal state to which the system equilibrates for times $t > \tau_{\mathrm{pre}}$, the prethermal timescale. Crucially, if the prethermal state spontaneously breaks the emergent symmetry of H_{eff}, the many-body system also exhibits robust time-crystalline order, corresponding to an oscillation between the different symmetry sectors [161, 345]. On the other hand, if the prethermal state is symmetry-unbroken, the system will be in a trivial Floquet phase, with any signatures of time-crystalline order decaying by τ_{pre}. The requirement of a symmetry-broken phase further distinguishes the PDTC and its MBL counterpart, and highlights the PDTC's stability in higher dimensions. Indeed, in one dimension, Landau-Peierls arguments rule out the existence of a PDTC with short-range interactions [315], and long-range interactions are necessary to stabilize a prethermal time crystal [345].
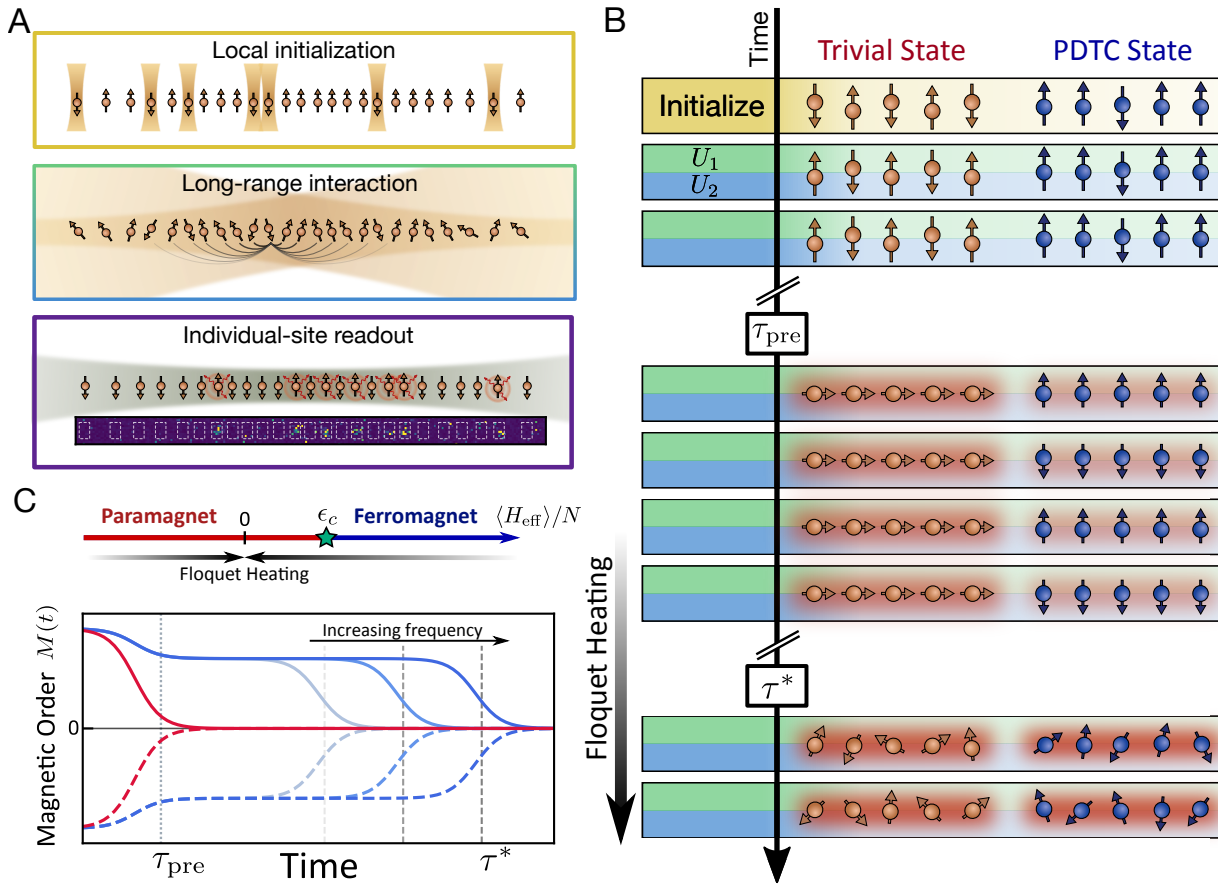
Figure 13.1: **Experimental setup and protocol. (A)** Schematic of the 25-ion chain [377].
Single-site addressing (top), global Raman beams (middle), and state-dependent fluorescence
(bottom) enable the preparation, evolution, and detection of the quantum dynamics. **(B)**
For intermediate times ($\tau_{\rm pre} < t < \tau^*$), the system approaches an equilibrium state of the
prethermal Hamiltonian $H_{\rm eff}$. In the trivial Floquet phase, the magnetization after $\tau_{\rm pre}$ decays
to zero. In the PDTC phase, the magnetization changes sign every period leading to a robust
sub-harmonic response. At times $t \gg \tau^*$, Floquet heating brings the many-body system to
a featureless infinite temperature ensemble. **(C)** Top: Phase diagram of $H_{\rm eff}$. Owing to the
anti-ferromagnetic nature of the Ising interactions $J_{ij} > 0$, the ferromagnetic phase occurs at
the top of the many-body spectrum. Bottom: Schematic of the stroboscopic magnetization
dynamics in the trivial [red] and PDTC [blue] phase (full/dashed curves represent even/odd
driving periods). When the energy density of the initial state is above the critical value $\epsilon_{\rm c}$,
the system is in the PDTC phase and its lifetime follows the frequency-dependent heating
time τ^*.

We exploit the controlled long-range spin-spin interactions of an ion trap quantum simulator to observe signatures of a one-dimensional prethermal discrete time crystal. Our main results are three fold. First, we prepare a variety of locally inhomogeneous initial states via individual addressing of ions within the one-dimensional chain [Fig. 13.1(A)]. By characterizing the quench dynamics starting from these states, we directly observe the approach to the prethermal state, enabling the experimental extraction of the prethermal equilibration time, τ_{pre}. Second, we measure the time dynamics of the energy density as a function of the driving frequency. By preparing states near both the bottom and the top of the spectrum [Fig. 13.1(B)], we observe either the gain or loss of energy as the system heats to infinite temperature (corresponding to zero energy density). Importantly, we find that the heating timescale, τ^*, increases with the driving frequency (Fig. 13.2). Finally, to probe the nature of prethermal time-crystalline order, we study the Floquet dynamics of different initial states that equilibrate to either a symmetry-broken or a symmetry-unbroken ensemble. The former exhibits robust period-doubling behavior up until the frequency-controlled heating timescale, τ^* [Fig. 13.3(B)]. In comparison, for the latter, all signatures of period doubling disappear by the frequency-independent timescale τ_{pre} [Fig. 13.3(A)]. By investigating the lifetime of the time-crystalline order as a function of the energy density of the initial state, we identify the phase boundary for the PDTC.

13.1 Experimental platform and protocol

Our system consists of a one-dimensional chain of 25 $^{171}\mathrm{Yb}^+$ ions. Each ion encodes an effective spin-1/2 degree of freedom in its hyperfine levels $|F = 0, m_F = 0\rangle$ and $|F = 1, m_F = 0\rangle$ [Fig. 13.1(A)]. Long-range Ising interactions are generated via a pair of Raman laser beams [376]. Arbitrary effective magnetic fields can be applied either locally or globally and single-site readout can be performed simultaneously across the full chain [377], enabling the direct measurement of the Floquet dynamics of both the magnetization and the energy density.

The Floquet drive alternates between two types of Hamiltonian dynamics [Fig. 13.1(B)]: (i) a global π-pulse around the $\hat{y}$ axis and (ii) evolution for time T under a disorder-free, long-range, mixed-field Ising model. This is described by the two evolution operators,

$$
\begin{aligned}
U_1 &= \exp\left[-i\frac{\pi}{2}\sum_i^N \sigma_i^y\right] \\
U_2 &= \exp\left[-iT\left(\sum_{i<j}^N J_{ij}\sigma_i^x\sigma_j^x + B_y\sum_{i=1}^N \sigma_i^y + B_z\sum_{i=1}^N \sigma_i^z\right)\right],
\end{aligned}
\tag{13.1}
$$

where σ_i^v is the v-th component of the spin-1/2 Pauli operator for the i-th ion, and we adopt the convention $\hbar = 1$. Here, $J_{ij} > 0$ is the long-range coupling with average nearest-neighbor interaction strength $J_0 = (2\pi) \times 0.33$ kHz, while $B_y = (2\pi) \times 0.5$ kHz and $B_z = (2\pi) \times 0.2$ kHz are global effective magnetic fields. The Floquet unitary $U_F = U_2 U_1$ implements the dynamics over a period of the drive and has frequency $\omega = 2\pi/T$.

Within the prethermal window in time $\tau_{\text{pre}} < t < \tau^*$, the stroboscopic dynamics of the system (every other period) are well-approximated by an effective prethermal Hamiltonian, which to lowest order in $1/\omega$ is given by [345]:

$$H_{\text{eff}} = \sum_{i<j}^{N} J_{ij}\sigma_i^x \sigma_j^x + B_y \sum_{i=1}^{N} \sigma_i^y. \tag{13.2}$$

A crucial feature of H_{eff} is that long-range Ising interactions stabilize a ferromagnetic phase along the $\hat{x}$ axis. However, owing to the anti-ferromangetic nature of the interactions ($J_{ij} > 0$), this phase does not occur at low energy density close to the bottom of the spectrum, but rather at high energy density near the top of the spectrum [Fig. 13.1(C)].

13.2   Prethermalization dynamics

We begin by characterizing the dynamics of the system as it approaches the prethermal state of H_{eff}. In particular, we prepare an initial state with all spins pointing along $\hat{x}$ (in an eigenstate of σ^x), except for two central spins, which are prepared along $\hat{z}$ [Fig. 13.2(D)]. Quench dynamics from this initial state show that the magnetization of the two central spins exhibits two-step dynamics. The $\hat{x}$-magnetization $\langle\sigma_i^x\rangle$, starting at zero, first equilibrates to the value of the neighboring spins, before decaying back to zero at late times. The convergence of the initially inhomogeneous $\hat{x}$-magnetization to a uniform finite value demonstrates that the system first reaches an intermediate-time equilibrium (i.e. prethermal) state before ultimately heating to infinite temperature. We find that this prethermal timescale is approximately given by $J_0\tau_{\text{pre}} \approx 3$.

In addition to τ_{pre}, the prethermal regime is also characterized by the timescale associated with the frequency-dependent Floquet heating, τ^*. To experimentally investigate τ^*, we measure the dynamics of the prethermal energy density, $\langle H_{\text{eff}}\rangle/(NJ_0)$, for two different initial states on opposite ends of the many-body spectrum of H_{eff}: a low-energy Néel state [Fig. 13.2(A)] and a high-energy polarized state [Fig. 13.2(B)]. In both cases, we observe the expected trend: increasing the driving frequency suppresses the heating rate [Fig. 13.2(C)]. However, the finite decoherence time of the system (induced by external noise sources) sets an upper bound on the maximum heating time scale; as a result, at large drive frequency, τ^* cannot grow exponentially with increasing drive frequency, but rather approaches a plateau value. Crucially, even in the presence of this decoherence dynamics, the separation between τ^* and τ_{pre} enables experimental access to the prethermal regime.

13.3   Observing and characterizing the PDTC phase

The demonstration of the frequency dependence of τ^* (Fig. 13.2) directly translates into our ability to control the lifetime of the prethermal time crystal. As aforementioned, the key ingredient underlying time-crystalline order is the presence of an emergent symmetry,
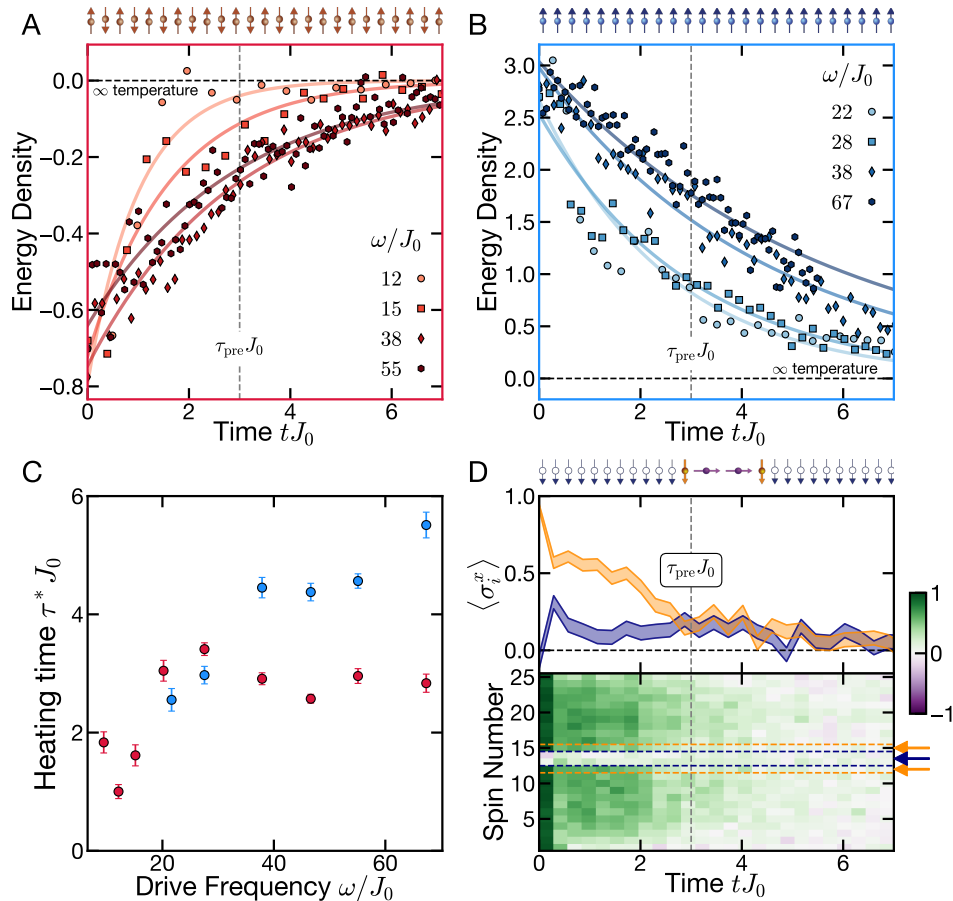
Figure 13.2:   **Characterizing the prethermal regime. (A, B)** The dynamics of the
energy density for a low-energy Néel state (left) and a high-energy polarized state (right)
highlights the frequency dependence of the heating rate. Statistical error bars are of similar
size as the point markers. **(C)** Heating time τ^* for the Néel (red) and polarized (blue) states,
extracted via an exponential fit ($\sim e^{-t/\tau^*}$) to the energy density dynamics [solid curves in (A)
and (B)]. The presence of external noise leads to a saturation of τ^* at high frequencies. Error
bars for the heating time correspond to fit errors. **(D)** Characterization of the prethermal
equilibration time, τ_{pre}, via the local $\hat{x}$-magnetization dynamics for even Floquet periods.
Top: The middle two spins (purple), initially prepared along the $\hat{z}$ axis, rapidly align with
their neighbors (orange) at time $\tau_{\mathrm{pre}}J_0 \approx 3$, signaling local equilibration to the prethermal
state. The shaded bands represent the standard error of the mean. Bottom: $\hat{x}$-magnetization
dynamics across the entire ion chain.

G, in H_{eff}, which is not a microscopic symmetry present in the Hamiltonian (Eq. 13.1), but rather, a direct consequence of the periodic driving protocol [161, 345]. In our experiment, this symmetry corresponds to a global spin flip, $G \approx U_1 \propto \prod_{i=1}^{N} \sigma_i^y$; indeed G is not a symmetry of the original evolution (Eq. 13.1) but it is present in H_{eff} (Eq. 13.2). When such emergent symmetry is present, the exact Floquet dynamics are approximately generated by evolving under H_{eff} for time T, followed by the action of G. This latter part suggests that the time-crystalline order is naturally captured by the system's magnetization dynamics; the action of G changes the sign of the order parameter $\langle \sigma_i^x \rangle$ every period. As a result, there are two possibilities for the prethermal dynamics, depending on the system's energy density [Fig. 13.1(B)]. If the prethermal state corresponds to the symmetry-respecting paramagnet, the magnetization is zero and remains unchanged across a period. Conversely, if the prethermal state corresponds to the symmetry-breaking ferromagnet, the magnetization is nonzero and alternates every period. The resulting $2T$-periodic, sub-harmonic dynamics is the hallmark of a time crystal.

We investigate these two regimes by measuring the auto-correlation of the magnetization:

$$M(t) = \frac{1}{N} \sum_{i=1}^{N} \langle \sigma_i^x(t) \rangle \langle \sigma_i^x(0) \rangle. \tag{13.3}$$

Starting with a low-energy-density Néel state [Fig. 13.3(A)], we observe that $M(t)$ quickly decays to zero at τ_{pre}, in agreement with the expectation that the system equilibrates to the symmetry-unbroken, paramagnetic phase. This behavior is frequency-independent, in direct contrast to the Floquet dynamics of the energy density [Fig. 13.2(A)]. This contrast highlights an essential point: although τ^* can be extended by increasing the driving frequency, no order survives beyond τ_{pre} when the system is in the trivial Floquet phase.

The Floquet dynamics starting from the polarized state are markedly distinct [Fig. 13.3(B)]. First, $M(t)$ exhibits period doubling, with $M > 0$ for even periods and $M < 0$ for odd periods. Second, the decay of this period-doubling behavior is directly controlled by the frequency of the drive. Third, the lifetime of the time-crystalline order mirrors the dynamics of the energy density shown in Fig. 13.2(B), demonstrating that Floquet heating ultimately melts the PDTC at late times.

By considering two additional initial states, we explore the stability of the PDTC phase as a function of energy density. Fig. 13.3(C) depicts both the heating time as well as the lifetime of the time-crystalline order. Near the bottom of the spectrum, where no symmetry-breaking phase exists, the decay of the magnetization is frequency-independent and significantly faster than the heating timescale. By contrast, near the top of the spectrum, where a symmetry-breaking ferromagnetic phase exists, the two timescales are consistent with one another and thus Floquet heating limits the PDTC lifetime. Our results are consistent with a phase boundary occurring at energy density $\langle H_{\text{eff}} \rangle / (N J_0) \approx 2$, in agreement with independent numerical calculations via quantum Monte Carlo.

In this chapter, we have described the experimental observation of robust prethermal time-crystalline behavior that persists beyond any early-time transient dynamics. Our re-
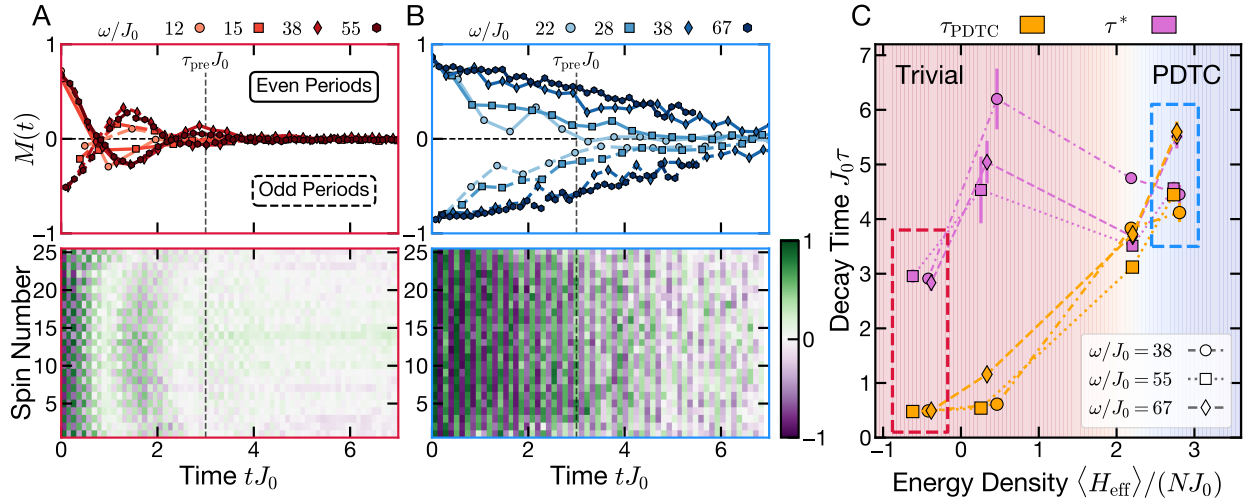
Figure 13.3: **Characterizing the PDTC phase. (A, B)** Upper plots: Magnetization dynamics, $M(t)$, for the Néel state (left) and the polarized state (right). For the Néel state, $M(t)$ quickly decays to zero at time τ_{pre} (dashed vertical line), independent of the drive frequency. For the polarized state, the sub-harmonic response ($2T$-periodicity) persists well-beyond τ_{pre} and its lifetime is extended upon increasing the drive frequency. The lifetime of the prethermal time-crystalline order τ_{PDTC} is obtained by fitting the magnetization dynamics to an exponential decay. Statistical error bars are of similar size as the point markers. Lower plots: $\hat{x}$-magnetization dynamics across the entire ion chain at $\omega/J_0 = 38$. **(C)** Heating (τ^*) and magnetization decay (τ_{PDTC}) times for four different initial states at varying energy densities. At low energy densities, τ_{PDTC} (orange) are significantly shorter than τ^* (magenta) and independent of frequency, highlighting the trivial Floquet phase. At high energies, τ_{PDTC} is similar to τ^*, highlighting the long-lived, frequency-controlled nature of the PDTC behavior. The location of the observed crossover in energy density is in agreement with an independent quantum Monte Carlo calculation (red and blue shaded regions). Error bars for the decay time correspond to fit errors, while error bars for the energy density correspond to statistical errors.

sults highlight the potential of periodic driving, in general, and prethermalization, in particular, as a framework for realizing and studying out-of-equilibrium phenomena. Even in the presence of noise, we find that the prethermal dynamics remain stable, suggesting that an external bath at sufficiently low temperature can stabilize the prethermal dynamics for infinitely long times [161]. This stands in contrast to localization-based approaches for stabilizing Floquet phases, in which the presence of an external bath tends to destabilize the dynamics. Our work points to a number of future directions: (i) exploring generalizations of Floquet prethermalization to a quasi-periodic drive [163], (ii) stabilizing Floquet topological phases [444, 165], and (iii) leveraging non-equilibrium many-body dynamics for enhanced metrology [99].

Chapter 14

Floquet phases of matter via classical prethermalization

Up until now, we have been considering the dynamics and phases of matter of *quantum* many-body Floquet systems [255, 331, 264, 160, 290, 590, 445, 444]. Owing to the lack of a locally conserved energy density, the stability of such phenomena is instrinsically connected to the ability to arrest thermalization and prevent the system from approaching a featureless, infinite temperature state [451, 450, 319, 70, 119]. One strategy discussed in Part II, was to leverage strong disorder to induce many-body localization (MBL) which enables the system to remain in a non-equilibrium steady state until arbitrarily late times [319, 119, 439, 6]. Since localization relies upon the discreteness of energy levels, this specific approach is intrinsically quantum mechanical. Given these constraints, one should naturally ask: To what extent do Floquet non-equilibrium phases require either quantum mechanics or disorder [320, 609, 265, 14, 589, 436, 321, 433, 434]?

One possible solution is the strategy explored in detail this part of the dissertation: Floquet prethermalization in disorder-free systems [45, 4, 344, 237, 312, 380, 5, 5, 593, 455, 379, 244, 238, 313]. When the driving frequency, ω, is larger than the system's local energy scale, J_{local}, Floquet heating is suppressed until exponentially late times, $\tau_{\text{heat}} \sim e^{\omega/J_{\text{local}}}$. In particular, directly absorbing energy from the drive is highly off-resonant, and heating only occurs via higher order processes that involve multiple, correlated local rearrangements. Crucially, this simple physical intuition holds for both quantum and classical systems.

However, in the quantum setting, Floquet prethermalization has an important additional feature: There exists an effective Hamiltonian that accurately captures the dynamics of the system until τ_{heat}. Whenever the periodic drive induces an emergent symmetry in this effective Hamiltonian, novel non-equilibrium prethermal phases of matter, such as discrete time crystals or Floquet symmetry-protected topological phases, can emerge [255, 331, 264, 160, 290, 590, 444, 161, 345, 313, 445, 162, 558, 470, 471, 475, 408]. Whether analogous phases are also possible in classical many-body systems is significantly more subtle; in particular, although classical prethermalization features slow Floquet heating, there is no effective Hamiltonian that accurately captures the prethermal dynamics [379].
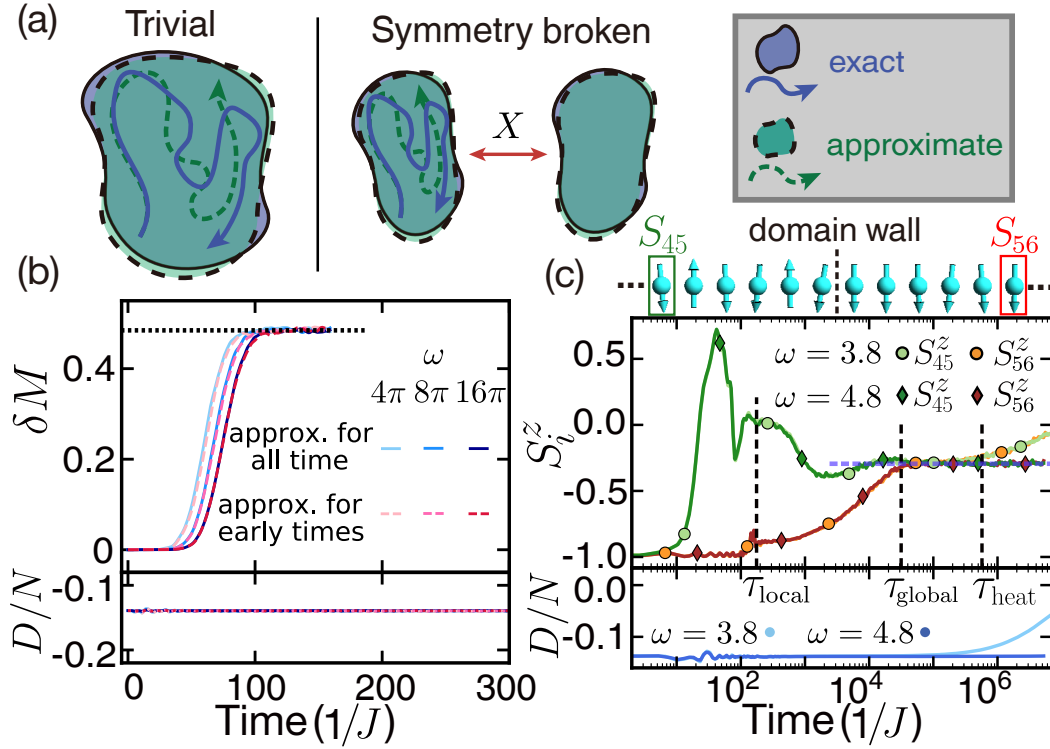
Figure 14.1: **Prethermal dynamics in a classical system.** **(a)** Schematic depicting
trajectories in a classical phase space. The exact Floquet trajectory (blue) diverges from
the approximate trajectory under the effective Hamiltonian (green). However, the exact
evolution of a *finite region* in phase space is well-captured by the effective Hamiltonian. **(b)**
The dynamics of the magnetization difference, $\delta M(t)$, and the energy density, D/N, for a
single initial state with $N = 10^4$. Solid lines depict approximate evolution under D for all
times. Dashed lines indicate approximate evolution under D for short times ($t \leq 1/J$), fol-
lowed by exact Floquet evolution. Agreement between solid and dashed curves highlights the
role of classical chaos in the growth of errors. While errors in local observables [i.e. $\delta M(t)$]
accumulate rapidly, the energy density remains conserved throughout the dynamics. **(c)**
The prethermal dynamics of an ensemble of initial states quickly converges with increasing
frequency. Before Floquet heating brings the system to infinite temperature, the magnetiza-
tion approaches the value associated with the corresponding prethermal ensemble of D (blue
dashed line, computed via Monte Carlo).

In this chapter, we show that the lack of an effective Hamiltonian does not preclude the existence of novel, non-equilibrium phases in classical Floquet systems; we highlight this by explicitly constructing a classical prethermal discrete time crystal (CPDTC). Our main results are three fold. First, we demonstrate that the inability of an effective Hamiltonian to generate the Floquet dynamics is a direct consequence of classical chaos—small errors at early times lead to exponentially diverging single trajectories. This connection to chaos suggests that one should forgo the focus on individual trajectories and rather ask whether there is an effective Hamiltonian that captures the prethermal dynamics of an *ensemble* of trajectories (Fig. 14.1). We show that this is indeed the case. Second, we prove that, much like the quantum case, the effective Hamiltonian can host an emergent symmetry which is protected by the discrete time translation symmetry of the periodic drive. Finally, we propose, analyze and numerically simulate a variety of different classical prethermal time crystals in one and two dimensions.

14.1 Theoretical Framework

Consider a classical Floquet Hamiltonian, $H_F(t) = H_F(t + T)$, with period $T = 2\pi/\omega$. For $\omega \gg J_{\text{local}}$, one can construct a perturbative expansion of the Floquet dynamics in powers of J_{local}/ω.[1] In general, this Floquet-Magnus expansion diverges, reflecting the many-body system's late-time approach to infinite temperature (via energy absorption from the drive). However, when truncated at an appropriate order, $n^* \sim \omega/J_{\text{local}}$, the expansion defines a static Hamiltonian, D, which remains quasi-conserved for exponentially long times (under the full Floquet dynamics) [4, 237, 379]:

$$\frac{1}{N}|D(t = mT) - D(t = 0)| < \mathcal{O}(mJ_{\text{local}}e^{-\omega/J_{\text{local}}}), \tag{14.1}$$

where N is the system size and $m \in \mathbb{N}$ is the number of Floquet cycles. To this end, Eq. 14.1 precisely formalizes the existence of an intermediate, prethermal regime. In particular, for times $t < \tau_{\text{heat}} \sim \mathcal{O}(e^{\omega/J_{\text{local}}})$, the energy density of the system (measured with respect to D), remains approximately constant.

Nevertheless, the question remains: Is D also the effective prethermal Hamiltonian, which generates the dynamics before τ_{heat}? In the quantum setting, the answer is yes [380, 5, 345].[2] However, in classical systems, D is only proven to faithfully reproduce the Floquet evolution

---

[1]More precisely, we note that the classical Floquet dynamics are generated by the superoperator $L(t)[\cdot] = \{\cdot, H_F(t)\}$. The time evolution operator over a single period is then given by $U_F = \mathcal{T}e^{\int_0^T L(t)dt} \equiv e^{L_F T}$, where L_F is a time-independent superoperator. The static Hamiltonian, $\mathcal{H}_F$, corresponding to L_F, is then given by $L_F = \{\cdot, \mathcal{H}_F\}$. The Floquet-Magnus expansion constructs $\mathcal{H}_F$ order-by-order in $\frac{J_{\text{local}}}{\omega}$, i.e. $\mathcal{H}_F = \sum_{n=0}^{\infty} \left(\frac{J_{\text{local}}}{\omega}\right)^n D^{(n)}$, where $D^{(n)}$ is the nth order term of the expansion. Note that the effective static Hamiltonian, D, is then defined as $D = \sum_{n=0}^{n^*} \left(\frac{J_{\text{local}}}{\omega}\right)^n D^{(n)}$

[2]Assuming that the system is extensive and power-law light-cones exist as defined via Lieb-Robinson bounds as discussed in Chapter 12.

over a *single* driving period [379]:

$$|O(T) - O'(T)| \leq \mathcal{O}(e^{-\omega/J_{local}}). \tag{14.2}$$

Here, O is a generic local observable and $O(T)$ represents its evolution under the full Floquet
Hamiltonian [i.e. $H_F(t)$], while $O'(T)$ represents its evolution under D. Note that hereon
out, observables with a prime, will always correspond to evolution under D.

Naively, one might expect the single period errors in Eq. 14.2 to accumulate additively
as one evolves to later times. However, this does not account for compounding effects, where
early-time errors propagate through the many-body system and induce additional deviations.
In the quantum case, the existence of Lieb-Robinson bounds constrains the propagation of
errors and enables one to prove that deviations grow algebraically in the number of Floquet
cycles: $|O(mT) - O'(mT)| \leq \mathcal{O}(m^p e^{-\omega/J_{\text{local}}})$; this immediately indicates that D is indeed the
effective prethermal Hamiltonian [312, 380, 5, 5, 345]. In contrast, classical systems exhibit
no such bounds—chaos causes the exponential divergence of nearby trajectories, suggesting
that errors can in principle accumulate exponentially quickly.

To sharpen this intuition, we numerically explore the Floquet dynamics of a generic
classical spin model:[3]

$$H_F(t) = \begin{cases} \sum_{i,j} J_z^{i,j} S_i^z S_j^z + \sum_i h_z S_i^z & 0 \leq t < \frac{T}{3} \\ \sum_i h_y S_i^y & \frac{T}{3} \leq t < \frac{2T}{3} \\ \sum_{i,j} J_x^{i,j} S_i^x S_j^x + \sum_i h_x S_i^x & \frac{2T}{3} \leq t < T \end{cases} \tag{14.3}$$

where $\vec{S}_i$ is a three-dimensional unit vector. Spin dynamics are generated by Hamilton's equa-
tions of motion $\dot{S}_i^\mu = \{S_i^\mu, H(t)\}$, using the Poisson bracket relation $\{S_i^\mu, S_j^\nu\} = \delta_{ij}\epsilon^{\mu\nu\rho}S_i^\rho$.
The classical dynamics of an observable O, are then given by $O(t) = \mathcal{T}e^{\int_0^t L(t')\ dt'}[O]$, where
the superoperator $L[\cdot]$ is defined by $L[\cdot] = \{\cdot, H_F\}$.[4] At lowest order in the Floquet-Magnus
expansion, the static Hamiltonian is given by:

$$D = \frac{1}{3}\left(\sum_{i,j} J_z^{i,j} S_i^z S_j^z + J_x^{i,j} S_i^x S_j^x + \vec{h} \cdot \vec{S}_i\right) + \mathcal{O}\left(\frac{1}{\omega}\right). \tag{14.4}$$

To investigate the accumulation of errors, we compare the dynamics of local observables
evolving under $H_F(t)$ and D in a one dimensional spin chain ($N = 10^4$) with nearest neighbor

---

[3]Throughout this work, we utilize the following generic set of parameters $\{J_z, J_x, h_x, h_y, h_z\} = \{-1.0, 0.79, 0.17, 0.23, 0.13\}$.

[4]We note that the multiplication of the superoperators (functions of observables) should be understood
as function composition. In particular, $(L_1 \circ L_2)[\cdot] = L_1[L_2[\cdot]]$. The nth power of L is then defined inductively
by $L^n = L \circ L^{n-1}$. Therefore, evolving under the Floquet Hamiltonian for m periods, an observable becomes
$O(mT) = \left(\mathcal{T}e^{\int_0^T L(t)dt}\right)^m [O]$. In a similar fashion, let us define X^{-1} as the inverse of the map X.

interactions.[5] Deviations from the exact Floquet dynamics are measured by computing the magnetization difference between the two trajectories: $\delta M(t) = 1 - \frac{1}{N} \sum_i \vec{S}_i(t) \cdot \vec{S}'_i(t)$. As depicted in Fig. 14.1(b) [top panel], $\delta M(t)$ quickly increases to a plateau value consistent with the spins in the two trajectories being completely uncorrelated; thus, D cannot be thought of as the effective prethermal Hamiltonian for $H_F(t)$. By contrast, the energy density remains conserved throughout the time evolution [bottom panel, Fig. 14.1(b)], demonstrating slow Floquet heating.

In order to pinpoint the role of chaos in the dynamics of $\delta M(t)$, we consider a slightly modified trajectory; in particular, starting with the same initial state, we first evolve under D for a few Floquet cycles and then under $H_F(t)$ for all subsequent times. Comparing to the exact Floquet dynamics (i.e. evolution under $H_F(t)$ for all times), this protocol only differs at very early times. Indeed, beyond an initial, exponentially-small difference in the trajectories [arising from Eq. 14.2], any additional deviation solely arises from the chaotic compounding of errors. As depicted in Fig. 14.1(b) [dashed curves], the magnetization difference between the modified trajectory and that of the exact Floquet dynamics, tracks $\delta M(t)$ for all times. Crucially, this agreement demonstrates that chaos dominates the growth of $\delta M(t)$ and prevents D from being the effective prethermal Hamiltonian.

14.2 Prethermal dynamics of ensembles of trajectories

While the evolution of a single trajectory cannot be captured by an effective Hamiltonian, we conjecture that D captures the dynamics of *ensembles* of trajectories [Fig. 14.1(a)]; by considering an initial state composed of a region of phase space (as opposed to a single point), the details of individual chaotic trajectories become "averaged out". This conjecture is made up of two separate components: (i) during the prethermal plateau, the system approaches the canonical ensemble of D (in the sense described in Chapter 2), and (ii) D accurately captures the dynamics of observables as the system evolves from local to global equilibrium. This last component highlights the two stage approach to the prethermal canonical ensemble. First, observables on nearby sites approach the same value and the system *locally* equilibrates (this occurs at time τ_{local}). Afterwards, the system becomes globally homogeneous as it approaches global equilibrium at time τ_{global}.

To investigate these components, we implement the following numerical experiment: Starting from an $N = 100$ spin chain, we construct an ensemble of initial states with a domain wall in the energy density at the center of the chain and study the Floquet dy-

---

[5]In general, the chaotic nature of D means that numerically integrating the equations of motion to later times requires exponentially better precision, making the numerical treatment very difficult. By contrast, each term of $H_F(t)$ corresponds to a precession of the spins along one of three axis, which can be straightforwardly analytically calculated without resorting to numerical integration methods.

namics of the local magnetization S_i^z and energy density D/N [Fig. 14.1(c)].[6] The presence
of a domain wall in the energy density enables us to distinguish between local and global
equilibration.

Focusing on the late time regime (but before Floquet heating), we find that the magnetization on opposite sides of the domain wall approaches the *same prethermal plateau*
[Fig. 14.1(c)]; this precisely corresponds to the global equilibration of our spin chain. Crucially, the value of this plateau *quantitatively* agrees with the mean magnetization of the
corresponding canonical ensemble of D calculated at the same energy density via Monte
Carlo [Fig. 14.1(c)]. Notably, we find agreement not only with the average value, but also
with the entire distribution, thus verifying the first component of the conjecture.

To investigate the second component, we time evolve the same ensemble of initial states
for different frequencies of the drive.[7] So long as $\tau_{\text{heat}} \gg \tau_{\text{global}}$, we find that the dynamics
of local observables rapidly converge as a function of increasing frequency [Fig. 14.1(c)].
Since the $\omega \to \infty$ limit of $H_F(t)$ precisely corresponds to Trotterized evolution under D, the
convergence observed in Fig. 14.1(c) indicates that D is indeed the prethermal Hamiltonian
for trajectory ensembles. This is in stark contrast to the dynamics of a *single* trajectory,
where local observables fail to converge with increasing frequency.

Interestingly, however, even for a single trajectory, the Floquet dynamics of either *spatially* or *temporally* averaged quantities are well captured by D. The intuition is simple:
by averaging over different times or different spatial regions, a single trajectory effectively
samples over an ensemble of different configurations [Fig. 14.1(a)]. This insight yields a particularly useful consequence, namely, that the dynamics of a *single trajectory* already encode
the prethermal properties of the many-body system.

14.3 Prethermal dynamics with symmetry breaking

Throughout our previous discussions, energy conservation is the only constraint that restricts
the many-body dynamics within phase space. However, symmetry-breaking can lead to
additional constraints; for example, if D exhibits a discrete symmetry and this symmetry
is broken at low energy densities, then phase space is naturally split into multiple disjoint
regions corresponding to different values of the order parameter. As a result, the many-body
dynamics under D are restricted to one such region.

---

[6]We initialize each spin along either $+\hat{z}$ or $-\hat{z}$ direction. By tuning the number of domain walls, we can
control the local energy density of the system. While the spins on the right half of the chain are initialized in
a completely ferromagnetic state, the spins on the left half repeat the following pattern: $\downarrow\uparrow\downarrow$. Therefore, the
energy density across the chain exhibits a domain wall at the center of the chain. To bring out the ensemble
effect, we add small random noise to the azimuthal angle and perform an average of the subsequent dynamics
over these slightly different initial states.

[7]The local equilibration time τ_{local} corresponds to the time when nearby spins approach the same value.
To identify τ_{local}, we measure the time when S_{43}^z and S_{45}^z, initially pointing in opposite directions, exhibit
the same magnetization.
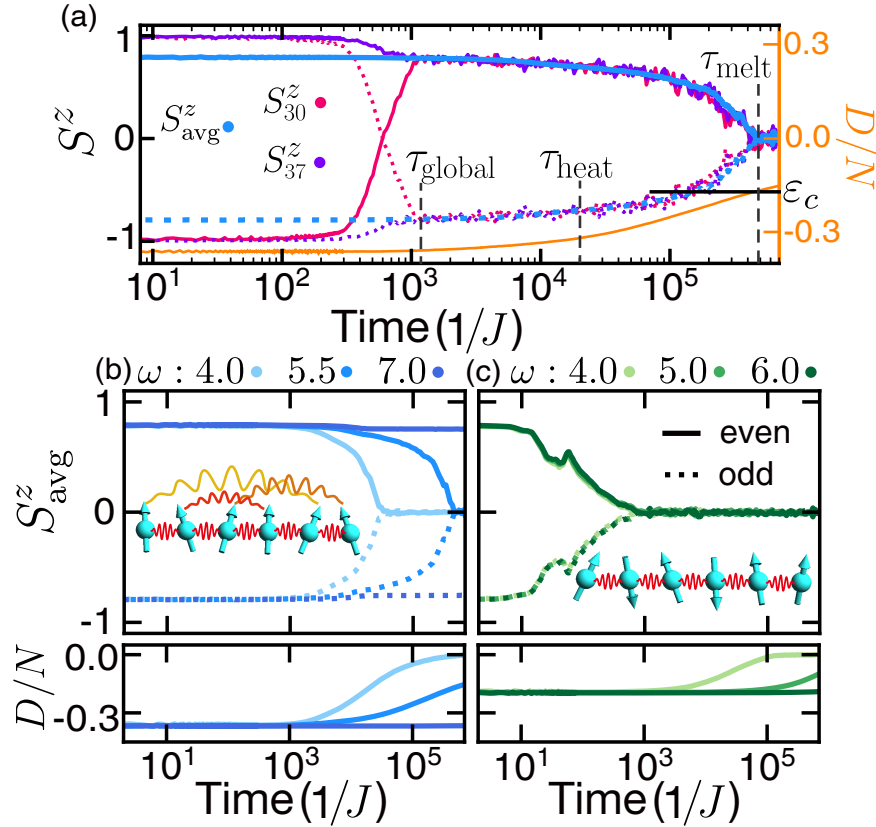
Figure 14.2: **Prethermal discrete time crystalline behavior in a classical spin
system. (a)** Dynamics of a classical prethermal time crystal in a one-dimensional long-range
interacting spin chain. At τ_{global}, different sites exhibit the same magnetization, indicating
equilibration. For an exponentially long intermediate time window, $\tau_{\text{global}} < t < \tau_{\text{melt}}$, the
system oscillates between positive and negative magnetization values for even (solid line)
and odd periods (dotted line). This subharmonic response remains stable until the energy
density crosses ε_c and the CPDTC melts. **(b,c)** Prethermal dynamics of the spin chain for
different frequencies ω with either long-range [b] or short-range [c] interactions. For long-
range interactions, the lifetime of the CPDTC is exponentially enhanced by increasing the
frequency of the drive. For short-range interactions, transient period doubling decays at
a frequency independent timescale, which is significantly shorter than the Floquet heating
time (bottom panel).

Floquet evolution complicates this story. In particular, one might worry that the micro-motion of the Floquet dynamics could move the system between different symmetry-broken regions of phase space. If this were the case, prethermal symmetry-breaking phases would not be stable. Fortunately, the ability of D to approximate the dynamics over a single period (i.e. Eq. 14.2), is sufficient to constrain the Floquet evolution to a specific symmetry-broken region.

To see this, consider, for example, a system where D exhibits a discrete $\mathbb{Z}_2$ symmetry and hosts a ferromagnetic phase whose order parameter is given by the average magnetization. When the energy density is below the critical value, the magnetization of the system can either be S_{avg}^z or $-S_{avg}^z$. Given energy conservation, under a single period of evolution, the magnetization must remain the same or change sign. However, Eq. 14.2 guarantees that the time evolved magnetization density can change, at most, by an exponentially small value in frequency. This ensures that for sufficiently large driving frequencies, the magnetization cannot change sign (i.e. move to the other symmetry-broken region) and the prethermal ferromagnet remains stable.

Crucially, symmetries of D can have two different origins: they can be directly inherited from $H_F(t)$, or they can emerge as a consequence of the time translation symmetry of the drive [161, 345]. In the latter case, this can give rise to intrinsically non-equilibrium phases of matter. To date, the study of such non-equilibrium prethermal phases has been restricted to quantum systems [325, 372, 325, 115, 475, 472, 223, 430, 313], where one can explicitly prove their stability [161, 345]. Here, we generalize and extend this analysis to classical many-body spin systems, by taking the large-S limit of the quantum dynamics [379].

Consider a Floquet Hamiltonian which is the sum of two terms, $H_F(t) = H_X(t) + H_0(t)$. During a single driving period, $H_X(t)$ generates a global rotation $X[\cdot] = \mathcal{T}e^{\int_0^T \{\cdot, H_X(t)\}dt}$, such that the system returns to itself after M periods (i.e. $X^M[\cdot] = \mathbb{I}[\cdot]$, where $\mathbb{I}$ is the identity map). $H_0(t)$ captures the remaining interactions in the system. For sufficiently large frequencies, the single period dynamics (in a slightly rotated frame) are accurately captured by $X \circ e^{T\{\cdot, D\}}$, where D is obtained via a Magnus expansion in the toggling frame; this expansion guarantees that the dynamics generated by D commute with X and thus, X generates a discrete $\mathbb{Z}_M$ symmetry of the effective Hamiltonian [161, 345]. Indeed, at lowest order, D is simply given by the time-independent terms of $H_0(t)$ that are invariant under the global rotation.

The resulting prethermal Floquet dynamics are most transparent when analyzed at stroboscopic times $t = mT$ in the toggling frame of the X rotations, wherein an observable O becomes $\widetilde{O}(mT) = X^{-m}[O(mT)]$. In this context, the dynamics of $\widetilde{O}$ are simply generated by D, i.e. $\widetilde{O}(mT) = e^{mT\{\cdot, D\}}[\widetilde{O}(t = 0)]$. Thus, if the emergent $\mathbb{Z}_M$ symmetry of D becomes spontaneously broken, the system will equilibrate to a thermal ensemble of D with a non-zero order parameter.

In the lab frame, the dynamics of O are richer: The global rotation changes the order parameter every period, only returning to its original value after M periods. As a result, the system exhibits a sub-harmonic response at frequencies $1/(MT)$ [161, 345]. This is precisely
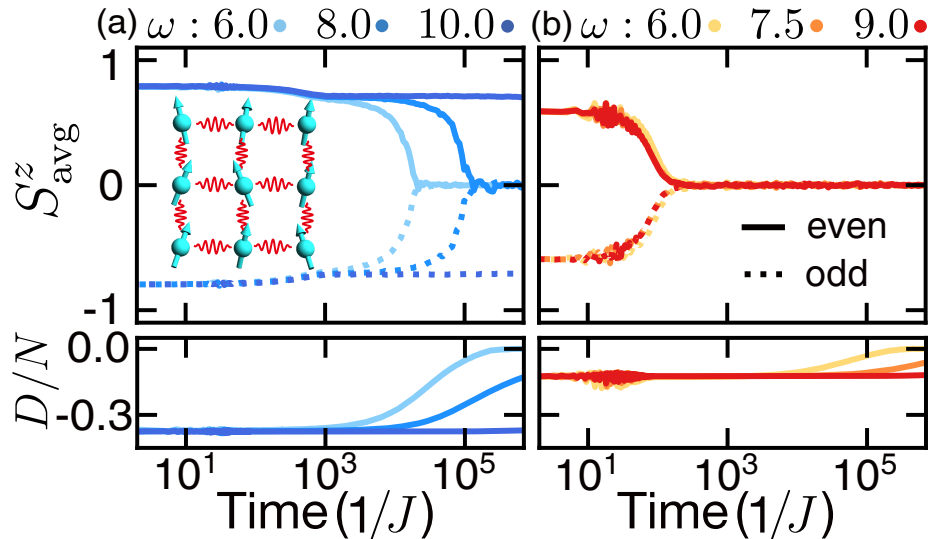
Figure 14.3: **Initial state dependence on the stability of the CPDTC.** Prethermal dynamics of a nearest-neighbor interacting classical spin model on the square lattice. **(a)** For a low-energy-density initial state, the system exhibits robust period doubling until exponentially late times. **(b)** For a high-energy-density initial state, the magnetization decays to zero rapidly, well before the Floquet heating time. This highlights the presence of a critical energy density and the importance of symmetry-breaking for the existence of a CPDTC.

the definition of a classical prethermal discrete time crystal.

14.4 Building a Classical Prethermal Discrete Time Crystal (CPDTC)

Let us now turn to a numerical investigation of the classical prethermal discrete time crystal. Consider the Floquet Hamiltonian in Eq. 14.3 with an additional global π rotation around the $\hat{x}$-axis at the end of each driving period.[8] At leading order, X corresponds to the global π rotation, while D is given by the time averaged terms of $H_F(t)$ that remain invariant under X (i.e. Eq. 14.4 with $h_y = h_z = 0$). To this end, we will utilize the energy density, D/N,

---

[8]The π rotation can be generated by a magnetic field along the $\hat{x}$ direction for time τ_π with strength $\pi/2\tau_\pi$. Since the dynamics are independent of τ_π chosen, we consider it to be an instantaneous rotation, $\tau_\pi \to 0$.

In order to better highlight the role of D throughout the prethermal regime, we consider instead a symmetrized version of $H_F(t)$ such that its first-order contribution in inverse frequency is zero and thus the dynamics are better captured by the zero-th order terms. We note that this does not change the results qualitatively.

and the average magnetization, S_{ave}^z, to diagnose the prethermal dynamics and the CPDTC
phase.

Let us begin by considering a one-dimensional system with long-range interactions $J_z^{i,j} = J_z|i-j|^{-\alpha}$; when $\alpha \leq 2$, D exhibits ferromagnetic order below a critical temperature (or, equivalently, a critical energy density ε_c which can be determined via Monte Carlo calculations) [153].[9] Taking $\alpha = 1.8$ and $N = 320$, we compute the Floquet dynamics starting from an ensemble with energy below ε_c [Fig. 14.2(a)].[10] After the initial equilibration to the prethermal state ($t \gtrsim \tau_{\text{global}}$), the magnetization becomes homogeneous across the entire chain, signaling equilibration with respect to D.[11] Crucially, as depicted in Fig. 14.2(a), throughout this prethermal regime, the magnetization exhibits robust period doubling, taking on positive values at even periods and negative values at odd periods. This behavior remains stable until the CPDTC eventually "melts" at an exponentially late time τ_{melt} when the energy density crosses the critical value ε_c of the ferromagnetic transition of D [Fig. 14.2(a)].

Three remarks are in order. First, because τ_{heat} is significantly longer than the interaction timescale, the system evolves between different thermal states of D as it absorbs energy from the drive. Second, the lifetime of the CPDTC is controlled by the Floquet heating rate and thus the frequency of the drive. Indeed, by increasing ω, the lifetime of the CPDTC is exponentially enhanced, while the global equilibration time remains constant [Fig. 14.2(b)]. Third, we emphasize that the observed CPDTC is fundamentally distinct from period-doubling bifurcations in classical dynamical maps (e.g. the logistic map) or the subharmonic response of a parametrically-driven non-linear oscillator [52, 413, 520, 273, 276, 77, 173, 458, 459, 41, 356, 303, 409, 24, 383, 301, 615, 589]. In particular, it occurs in an *isolated many-body classical system with conservative dynamics.*

Let us conclude by highlighting the central role of spontaneous symmetry breaking in observing the CPDTC. We do so by controlling the range of interactions, the dimensionality, and the energy density of the initial ensemble. To start, we consider the short-ranged version (i.e. nearest neighbor interactions) of the 1D classical spin chain discussed above. Without long-range interactions, ferromagnetic order is unstable at any finite temperature [315], and this immediately precludes the existence of a CPDTC. This is indeed borne out by the numerics [Fig. 14.2(c)]: We observe a fast, frequency-independent decay of the magnetization to its infinite-temperature value.

While nearest-neighbor interactions cannot stabilize ferromagnetism in 1D, they do so in higher dimension. To this end, we explore the same Floquet model on a two dimensional square lattice. For sufficiently low energy densities, the system equilibrates to a CPDTC

---

[9]By performing extensive Monte Carlo simulations, we obtain the critical energy density $\epsilon_c \approx -0.53$ for the transition.

[10]To prepare the initial state ensemble, we first start with the fully polarized system, flip every tenth spin, and then add a small amount of noise to the azimuthal angle. The energy density of the resulting ensemble is $\varepsilon = -1.10$

[11]We note that the fluctuations of S_i^z are local thermal fluctuations, and they decrease as we average over more realizations.

phase [Fig. 14.3(a)], while above the critical temperature, the system equilibrates to a trivial phase [Fig. 14.3(b)]. We hasten to emphasize that our framework is not restricted to the period-doubled ($M = 2$) CPDTC and it immediately ports over to more general notions of time crystalline order, including both higher-order ($M > 2$) and *fractional* CPDTCs (see supplemental material for additional numerics) [433].

Our work opens the door to a number of intriguing directions. First, it would be interesting to explore the generalization of classical prethermal time crystals to quasi-periodic driving [163]. Second, although we have presented extensive numerical and analytic evidence for the presence of an effective Hamiltonian (for trajectory ensembles), sharpening our analysis into a proof would provide additional insights in the nature of many-body classical Floquet systems.

14.5   Outlook

More broadly, our work complements the work introduced in Chapter 9, with the goal of understanding the limitations and constraints for preparing out-of-equilibrium phenomena in dynamical systems. Crucially, a recurring feature we observe is that, as along as one is able to arrest thermalization, out-of-equilibrium phases of matter can stabilized. Nevertheless, as we explored in Chapter 2, the equilibration dynamics in classical or quantum mechanical systems can be very distinct owing to the lack (or presence) of entanglement across different parts of the system. Understanding these distinctions at a more fundamental level, and how they affect the equilibration behavior and out-of-equilibrium phases of matter remain two important open questions.

Let us end this chapter by highlighting a complementary work, published at the same time, that explored prethermal phases of matter in classical spin systems [435].

Part IV

Universal equilibrating behavior

Chapter 15

Emergent hydrodynamics in non-equilibrium quantum systems

Despite the expectation, supported by centuries of evidence, that generic interacting systems exhibit a late-time hydrodynamical description, capturing both the microscopic details of short-time thermalization as well as the cross-over to late-time hydrodynamics remains an important open challenge. It is particularly difficult in strongly interacting quantum systems, owing to the complexity of the exponentially large Hilbert space [446, 560, 11, 611, 338, 286, 341, 481, 56]. Indeed no general framework exists for answering even the simplest possible question: How does one compute the classical diffusion coefficient from a quantum many-body Hamiltonian?

A setting where it is particularly difficult to tackle this question is in periodically driven (Floquet) systems, where equilibration to the featureless infinite temperature state is determined by both interactions between the different degrees of freedom, as well as energy absorption from the driving field [451, 450, 319, 119, 70, 344]. Indeed, understanding the interplay between Floquet heating, emergent hydrodynamics and microscopic thermalization represents a crucial step toward the characterization and control of non-equilibrium many-body systems [4, 380, 5, 312, 5, 161, 70, 568]. Given the complexity of this very general problem, it is useful to first consider a simpler starting point; for example, in the limit of a high-frequency Floquet drive, energy absorption is set by an extremely slow heating rate. Thus, one anticipates a relatively long timescale where the system's stroboscopic dynamics can be captured by an effective static *prethermal Hamiltonian*. This expectation immediately allow us to focus on one particular question: How do the late-time dynamics of driven quantum systems account for both the prethermal Hamiltonian's hydrodynamics and the energy absorption associated with Floquet heating?

Until now, such questions have remained largely unexplored owing to the lack of both theoretical techniques and numerical methods. However, a number of recently proposed numerical methods [571, 326, 583, 582, 597] promise to bridge this gap and directly connect microscopic models to emergent macroscopic hydrodynamics. Here, we will consider one such method — density matrix truncation (DMT) [571] — which modifies time-evolving block
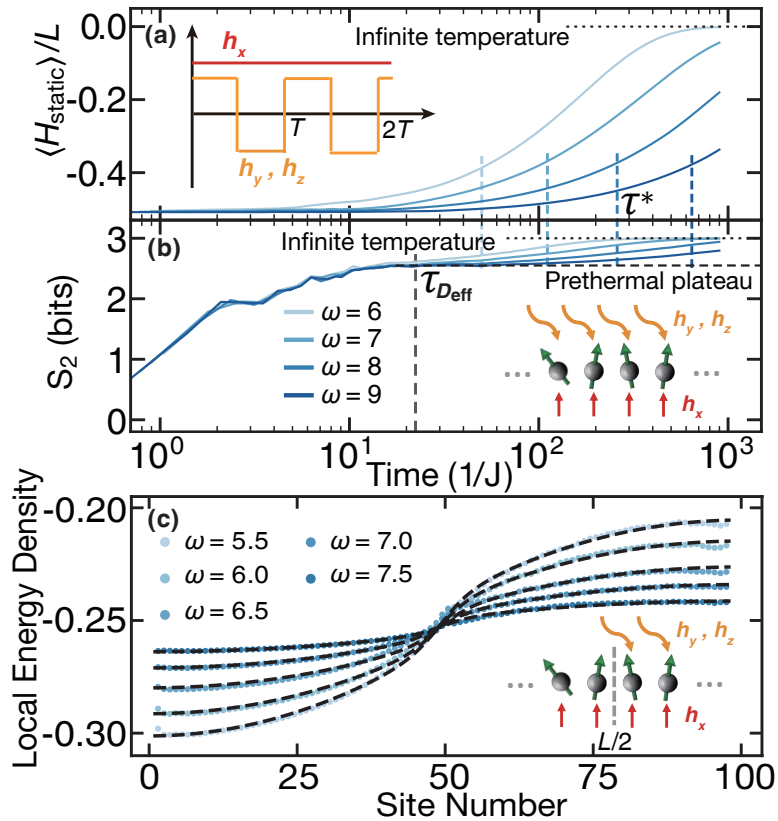
Figure 15.1: **Floquet thermalization of an** $L = 100$ **spin chain.** (a) Average energy
density measured with respect to $H_{\text{static}} \approx D_{\text{eff}}$ under a global drive. The heating timescale
τ^* is extracted from the energy's exponential approach to its infinite-temperature value and
depends exponentially on the driving frequency [for explicit scaling, see Fig. 15.4(a).] (b)
The second Rényi entropy of the leftmost three sites. The dashed lines are computed using
the prethermal Gibbs ensemble. (c) Spatial profiles of energy density under a half-system
drive with $\langle H_{\text{static}} \rangle / L = -0.25$. Insets: the drive's time dependence (a) and schematics of
the global drive (b) and the half-system drive (c).

decimation (TEBD) by representing states as matrix product density operators (MPDOs) and prioritizing short-range (over long-range) correlations.

Working with a generic, one-dimensional spin model, we use DMT to investigate a broad range of non-equilibrium phenomena ranging from Floquet heating to emergent hydrodynamics. Our main results are three fold. First, we find that DMT accurately captures two essential pieces of Floquet physics: prethermalization and heating to infinite temperature [Fig. 15.1]. Crucially, the truncation step intrinsic to DMT enables us to efficiently explore the *late-time* dynamics of large-scale quantum systems (up to $L = 100$), at the cost of imperfectly simulating the system's *early-time* dynamics. This trade-off hinges on DMT's efficient representation of local thermal states, making it a natural tool for studying emergent hydrodynamics. Our latter two results illustrate this in two distinct contexts: 1) directly measuring the energy diffusion coefficient for a static Hamiltonian, and 2) demonstrating the interplay between Floquet heating and diffusion in an inhomogeneously driven spin chain. We hasten to emphasize that such calculations are fundamentally impossible for either exact diagonalization based methods (owing to the size of the Hilbert space) or conventional TEBD methods (owing to the large amount of entanglement at late times).

15.1 Model and phenomenology

We study the dynamics of a one-dimensional spin-1/2 chain whose evolution is governed by a time periodic Hamiltonian $H(t) = H_{\text{static}} + H_{\text{drive}}(t)$, where

$$H_{\text{static}} = \sum_{i=1}^{L-1} [J\sigma_i^z \sigma_{i+1}^z + J_x \sigma_i^x \sigma_{i+1}^x] + h_x \sum_{i=1}^{L} \sigma_i^x , \qquad (15.1)$$

with σ_i^α being the Pauli operators acting on site i.[1] The drive, $H_{\text{drive}}(t) = H_{\text{drive}}(t + T)$, exhibits a period $T = 2\pi/\omega$ and corresponds to an oscillating field in the $\hat{y}$ and $\hat{z}$ directions:

$$H_{\text{drive}}(t) = \sum_{i=1}^{L} v_i(t) \, (h_y \sigma_i^y + h_z \sigma_i^z) . \qquad (15.2)$$

In this work we will consider two different driving protocols [Fig. 15.1 insets] a **global drive**, with all spins driven [$v_i(t) = \text{sgn} \cos(\omega t)$], and a **half-system drive**, with only the right half driven [$v_{i \leq L/2}(t) = 0$ and $v_{i > L/2}(t) = \text{sgn} \cos(\omega t)$]. Throughout the letter, we work in the high-frequency regime with $\omega \geq 5J$, and choose the parameters to be $\{J, J_x, h_x, h_y, h_z\} = \{1, 0.75, 0.21, 0.17, 0.13\}$. We expect our choice of the model and parameters to be generic as we observe the same phenomenology upon varying both the parameters and types of interactions in the Hamiltonian.

---

[1]While the bond terms can be mapped to a free-fermion integrable model, the additional field term breaks this integrability.
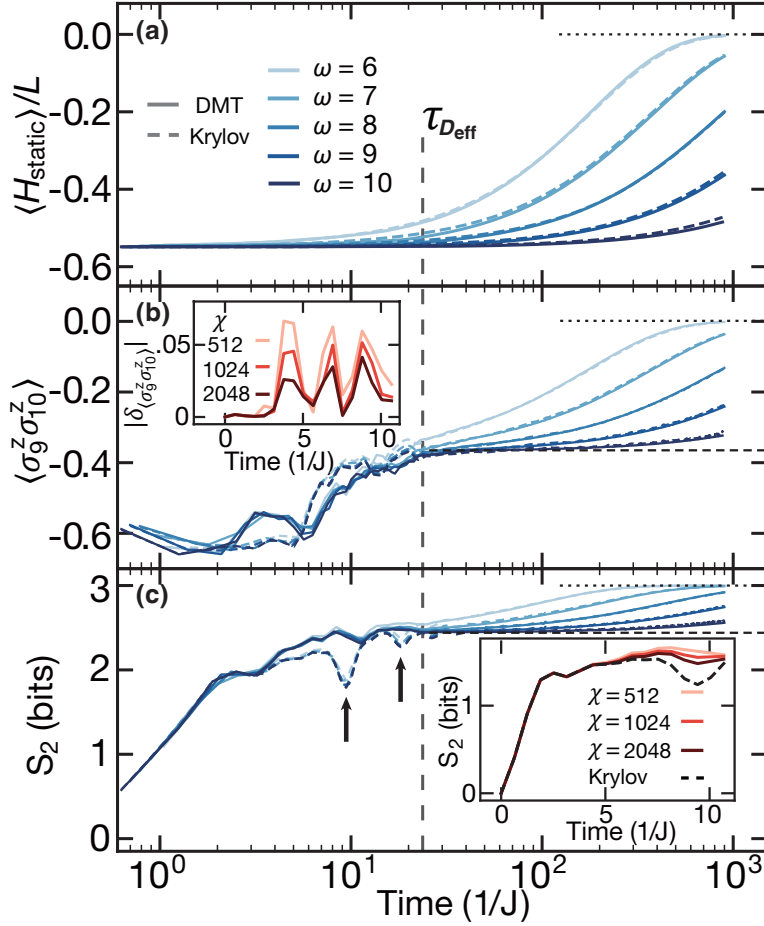
Figure 15.2: **Benchmark of dynamics computed via the density matrix truncation algorithm.** Comparison between DMT and Krylov of the time evolution of an $L = 20$ spin chain under a global drive (at fixed bond dimension $\chi = 64$). **(a)** Average energy density $\langle H_{\text{static}} \rangle / L$. **(b)** A typical local observable $\sigma_9^z \sigma_{10}^z$. **(c)** The second Rényi entropy S_2 of the leftmost three sites. The arrows mark resonance-like dips, which DMT fails to capture. The dashed lines are computed using the prethermal Gibbs ensemble. Insets (early-time behavior at frequency $\omega = 10$): (b) errors in the local observable $\delta_{\langle \sigma_9^z \sigma_{10}^z \rangle} = \langle \sigma_9^z \sigma_{10}^z \rangle_{\text{DMT}} - \langle \sigma_9^z \sigma_{10}^z \rangle_{\text{Kry}}$, (c) slow convergence of S_2 dynamics to the Krylov value highlighting that this dip is related to the coherent propagation of information through the entire system.

The quenched dynamics of a high-frequency driven system is characterized by two timescales. The heating timescale, τ^* [Fig. 15.1(a)], determines the rate of energy absorption from the drive and is proven to be at least exponential in the frequency of the drive, $\tau^* \geq \mathcal{O}(e^{\omega/J_{\text{local}}})$, where J_{local} is a local energy scale [4, 380, 312, 5, 5, 161] [see Part III]. Up until τ^*, the stroboscopic dynamics of the system is well described by the *static* prethermal Hamiltonian $D_{\text{eff}} = H_{\text{static}} + \mathcal{O}(\omega^{-1})$, which can be obtained by truncating the Floquet-Magnus expansion of the evolution operator [312, 5, 5]. The prethermalization timescale, $\tau_{D_{\text{eff}}}$ [Fig. 15.1(a,b)], determines the time at which the system approaches an equilibrium state with respect to D_{eff}. When $\tau_{D_{\text{eff}}} \ll \tau^*$, the system exhibits a well defined, long-lived prethermal regime.

In Figs. 15.1(a,b), we illustrate these two timescales by computing the dynamics of an $L = 100$ Floquet spin chain using DMT.[2] The average energy density $\langle H_{\text{static}}(t) \rangle / L$ exhibits the expected phenomenology [Fig. 15.1(a)]: it remains constant (up to ω^{-1} corrections) until τ^*, after which it begins to approach its infinite temperature value $\langle H_{\text{static}} \rangle_{T=\infty} = 0$.

To probe the prethermalization timescale $\tau_{D_{\text{eff}}}$, a different diagnostic is needed. In particular, we compute the second Rényi entropy, $S_2 = -\log_2 \text{tr}[\rho_s^2]$, where ρ_s is the reduced density matrix of the three leftmost spins. While the system begins in a product state with $S_2 = 0$, its entropy quickly approaches a *prethermal plateau*, consistent with the Gibbs state of D_{eff} at a temperature that matches the initial energy density [Fig. 15.1(b)]. The timescale at which this occurs corresponds to $\tau_{D_{\text{eff}}}$ and, indeed, we observe $\tau_{D_{\text{eff}}} \sim 1/J_{\text{local}}$ independent of the driving frequency ω. Similar to the energy density, at late times $t > \tau^*$, S_2 begins to approach its infinite temperature value, $S_2^{T=\infty} = 3$ bits.

15.2 Benchmarking the density matrix truncation method

To confirm the reliability of DMT in the simulation of Floquet dynamics, we compare it with Krylov subspace methods [233, 232, 33].[3] This analysis not only gauges the applicability of DMT, but also leads to insights into the nature of the Floquet heating process.

Time evolution with DMT proceeds via two repeating steps: a TEBD-like approximation of the time evolution unitary and a truncation of the MPDO. In the TEBD-like step, we Trotter decompose the time evolution operator into a series of local gates which we then apply to the MPDO [571]. Because each local gate application increases the bond dimension of the corresponding tensors, we must truncate them back to a fixed maximum bond dimension, which we call χ. During this truncation step, a conventional TEBD method will discard the terms which contribute the least to the entanglement [491, 411]. As a result, this truncation

---

[2] In our calculations, we consider a generic initial state, typically taken to be a Néel state with a domain wall every four spins. We have checked that our observations are independent of initial state. Based on previous studies we expect this choice of initial state to be generic and to capture the main features of Floquet heating [344].

[3] Krylov methods compute the time evolution of the state by first constructing an appropriate subspace and then using it to build a suitable rational approximation to the exponential action of the Hamiltonian.
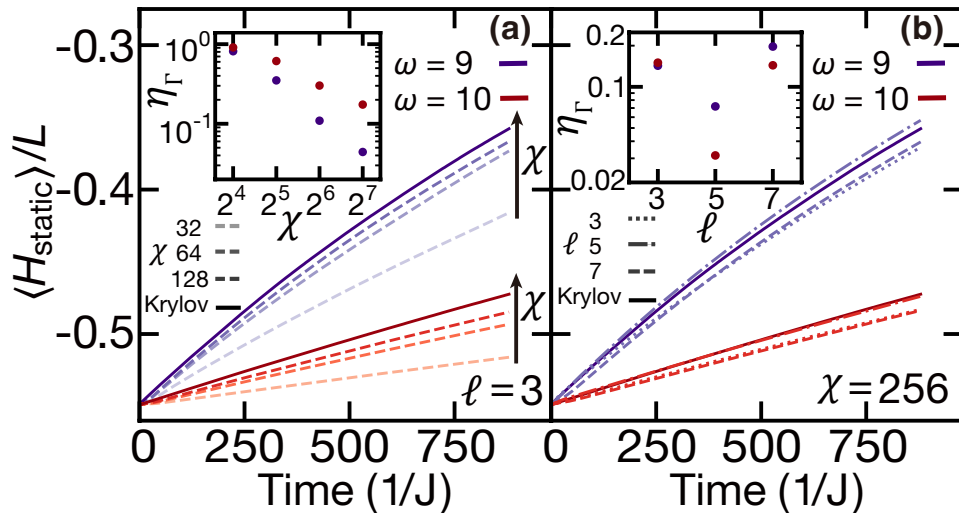
Figure 15.3: **Convergence of thermalization dynamics.** Energy density at (a) bond
dimension $\chi = 32, 64, 128$ and (b) the preservation diameter $\ell = 3, 5, 7$. Insets: relative
error in the heating rate $\eta_\Gamma = |\Gamma_{\text{DMT}} - \Gamma_{\text{Krylov}}|/\Gamma_{\text{Krylov}}$, where $\Gamma = 1/\tau_E^*$ is defined by
$\frac{d}{dt}\langle H_{\text{static}}\rangle = -\Gamma\langle H_{\text{static}}\rangle$.

is agnostic to the locality of the discarded correlations. By contrast, in DMT we explicitly
prioritize the preservation of short-range correlations [571]. To this end, DMT separates χ
into two contributions: $\chi = \chi^{\text{preserve}} + \chi^{\text{extra}}$. $\chi^{\text{preserve}} = 2^\ell$ is used to store the information of
all observables on ℓ contiguous sites around the truncated tensor—we call ℓ the *preservation
diameter*.[4] χ^{extra} is then used to preserve the remaining correlations with largest magnitude.
Crucially, the preservation of short-range correlations allows DMT to conserve (up to Trotter
errors) the instantaneous energy density and its current [571]. To be more specific, in Floquet
systems, DMT conserves $H(t)$ at each instant, but it *does not* explicitly conserve D_{eff}.

We utilize three diagnostics to compare the time evolution between DMT and Krylov:
the average energy density [Fig. 15.2(a)], local two-point correlation functions [Fig. 15.2(b)],
and the second Rényi entropy [Fig. 15.2(c)].

At early times ($t < \tau_{D_{\text{eff}}}$), one observes substantial disagreements between DMT and
Krylov [Fig. 15.2(b,c)]. This is to be expected. Indeed, the accurate description of early-
time thermalization dynamics depends sensitively on the details of long-range correlations
which DMT does not capture. An exception to this is the energy density, whose changes
are expected to be exponentially small in frequency [4, 380, 312, 5]. This is indeed born out
by the numerics where one finds that $\langle H_{\text{static}}\rangle/L$ remains quasi-conserved and in excellent
agreement with Krylov [Fig. 15.2(a)].

---

[4]Although truncation does not directly affect ℓ-sized operators, their dynamics is affected by the trun-
cation of larger sized operators via the evolution of the system.

One might naively expect the early-time disagreements to lead to equally large intermediate-time ($\tau_{D_{\text{eff}}} < t < \tau^*$) deviations. This is not what we observe. Indeed, all *three* diagnostics show excellent agreement between DMT and Krylov [Fig. 15.2]. This arises from a confluence of two factors. First, as aforementioned, DMT accurately captures the system's energy density, which in turn, *fully* determines the prethermal Gibbs state; second, DMT can efficiently represent such a Gibbs state. Thus, although DMT fails to capture the *approach* to the prethermal Gibbs state, it nevertheless reaches the same equilibrium state at $t \sim \tau_{D_{\text{eff}}}$. Afterwards (for $t > \tau_{D_{\text{eff}}}$), the system is simply evolving between different Gibbs states of D_{eff}, wherein one expects agreement between DMT and Krylov even at relatively low bond dimension [Fig. 15.2].

Small disagreements between DMT and Krylov, however, re-emerge at very late times ($t > \tau^*$) and large frequencies, reflecting the physical nature of Floquet heating [Fig. 15.2(a)]. In particular, as the frequency increases, absorbing an energy quantum from the drive requires the correlated rearrangement of a greater number of spins [4, 380, 5]. However, these longer-ranged correlations are *not* strictly preserved by DMT, leading to an artificial (truncation-induced) suppression of heating at large frequencies [Fig. 15.3].

This raises the question: How does the accuracy of DMT converge with both bond dimension and preservation diameter? As expected, increasing χ at fixed ℓ improves the accuracy of DMT since the amount of information preserved during each truncation step is greater, Fig. 15.3(a). Curiously, tuning ℓ at fixed χ can *also* affect the accuracy, despite not changing the amount of information preserved, Fig. 15.3(b). This suggests the tantalizing possibility that one can achieve high accuracy at relatively low bond dimension by carefully choosing the operators which are preserved.

15.3 Floquet heating dynamics

As a first demonstration of DMT's potential for extracting quantitative information about the Floquet dynamics, we directly measure the heating rate. We find that both $\langle H_{\text{static}} \rangle / L$ and S_2 exhibit an exponential approach toward their infinite-temperature values: $|\langle H_{\text{static}} \rangle / L| \propto e^{-t/\tau_E^*}$ and $(S_2^{T=\infty} - S_2) \propto e^{-2t/\tau_S^*}$. To this end, we extract τ_E^* and τ_S^* as independent measures of the Floquet heating timescale. Crucially, they agree with one another across all system sizes studied ($L = 20$–100), as shown in Fig. 15.4(a). Varying the frequency of the drive further allows us to extract the effective local energy scale which controls the heating dynamics: $J_{\text{local}}^E = 1.21 \pm 0.04$ and $J_{\text{local}}^S = 1.16 \pm 0.04$. This is consistent with the microscopic onsite energy scale, $\|H_{\text{static}}\|/L \simeq 1.26$.[5]

---

[5]We define the microscopic onsite energy scale as the norm of the local Hamiltonian on each bond $\|J\sigma_i^z\sigma_{i+1}^z + J_x\sigma_i^x\sigma_{i+1}^x + h_x(\sigma_i^x + \sigma_{i+1}^x)/2\|$; this differs by a (subextensive) boundary term from $\|H_{\text{static}}\|/L$.

15.4 Observing emergent hydrodynamics

Having established that DMT accurately captures the late-time thermalization of Floquet systems, we now apply it to the study of a much broader question: the emergent hydrodynamics of large (undriven) quantum spin chains ($L = 100$). In particular, our main goal here is to measure the diffusion coefficient as a function of temperature.

Our setup is the following. On top of an initial thermal state with respect to H_{static}, we add a small spatial inhomogeneity in the energy density (taken to be a Fourier mode). As the system evolves under H_{static}, one finds that the amplitude of this spatial variation decays exponentially, with a rate that scales as q^2, where q is the wave-vector of the Fourier mode. This quadratic scaling is characteristic of diffusion and confirms the emergence of hydrodynamics from our microscopic quantum Hamiltonian. By further varying the temperature of the initial Gibbs ensemble, one can also study the diffusion coefficient, $D(\epsilon)$, as a function of the energy density ϵ [Fig. 15.4(b)].[6]

We emphasize that such a numerical observation of emergent hydrodynamics is well beyond the reach of conventional numerics and fundamentally leverages DMT's ability to prepare and evolve highly-entangled states near thermal equilibrium. Moreover, we note that our procedure can also be applied to the study of *integrable* systems, where different types of anomalous transport can occur [333, 75, 202, 85, 48, 370, 197]. We highlight this by computing spin transport in the XXZ model and observing ballistic, super-diffusive and diffusive exponents as a function of the Ising anisotropy. We return to the detailed analysis of this behavior in Chapters 17 and 18.

15.5 Interplay between driving and hydrodynamics

Taking things one step further, we now combine the two previous settings and explore a situation where the interplay between Floquet heating and diffusive transport is crucial for understanding the system's thermalization dynamics. In particular, let us consider the time evolution of a spin chain where *only the right half* of the system is periodically driven [inset, Fig. 15.1(c)]. At time $t = 0$, the system is initialized in a Néel state with a domain wall every four spins.

After an initial period of local equilibration, the combination of inhomogenous driving and interactions leads to three distinct features in the dynamics of the local energy density, as illustrated in Fig. 15.4(c). First, the local energy density on the right half of the spin chain is larger, reflecting the location where driving, and thus Floquet heating, is occurring. Second, the energy density across the entire chain gradually increases in time as energy from the right half is transported toward the left half. Third, as the system approaches its

---

[6]In this setup, we also confirmed that DMT gives dynamics consistent with Krylov at small system sizes ($L = 20$). Moreover, our method, near infinite temperature ($\epsilon = 0$), matches independent calculations of the diffusion [425].
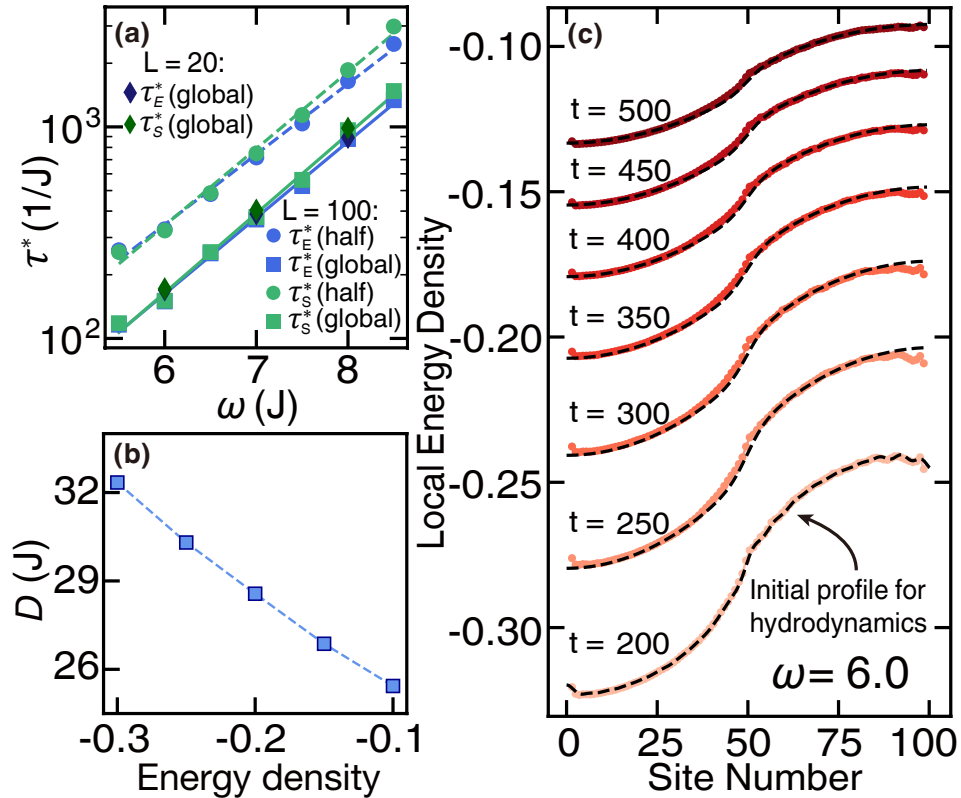
Figure 15.4: **Hydrodynamics in a large scale isolated quantum system.** **(a)** Heating timescale, τ^*, extracted in energy density (E) and subsystem entropy (S_2) for $L = 20, 100$. In agreement with theoretical prediction, τ^* depends exponentially on ω. For both driving protocols, we extract the same local energy scale $J^E_{local} \approx 1.21$. However, the half-system drive exhibits a heating timescale twice as large as the global drive. **(b)** Energy dependence of the diffusion coefficient in the undriven spin chain. **(c)** Dynamics of the energy density with half-system drive. Solid curves are computed using DMT. Dashed black curves are computed using a hydrodynamical equation, Eq. 15.3, where one feeds in the DMT-calculated energy-density profile at time $t = 200$. Subsequent time evolution under the differential equation quantitatively reproduces the exact results from DMT.

infinite temperature state, the overall energy-density inhomogeneity between the left and right halves of the system is reduced.

Leveraging our previous characterizations of both heating and transport, we combine them into such a single hydrodynamical description. The only missing element is a small correction to the transport due to the inhomogeneity of the drive, whose strength we characterize by a small, frequency dependent parameter η.

We now ask the following question: Can all three of these behaviors be *quantitatively* captured using a simple hydrodynamical equation? If so, one might naturally posit the following modified diffusion equation:

$$\partial_t \epsilon(x,t) = D(\epsilon)\partial_x^2\Big([1 + \eta g(x)]\epsilon(x,t)\Big) - g(x)\frac{\epsilon(x,t)}{\tau_E^*}. \tag{15.3}$$

Here, $g(x)$ is a step-like spatial profile which accounts for the fact that only half the spin chain is being driven.[7] The term proportional to η corresponds to the aforementioned correction to the transport owing to the inhomogeneity of the drive, while the final term in the equation captures the Floquet heating. Note that for the heating rate and the diffusion coefficient, we utilize the previously (and independently) determined values $1/\tau_E^*$ and $D(\epsilon)$, respectively [Fig. 15.4(a,b)].

In order to test our hydrodynamical description, we feed in the energy density profile computed using DMT (at time $t = 200$) into Eq. 15.3 and check whether the differential equation can quantitatively reproduce the remaining time dynamics [Fig. 15.4(c)]. Our only fitting parameter is η, and we take it to be constant across the entire evolution. We find that $\eta \ll 1$ and decreases as frequency increases, consistent with our expectation that for larger driving frequencies, D_{eff} is more homogenous across the chain. Remarkably, we observe excellent agreement for the remaining time evolution across all frequencies tested [Fig. 15.1(c) and 15.4(c)]! To this end, our results confirm that only a few coarse-grained observables are relevant to the late-time evolution of an interacting quantum system, even under a periodic drive.

15.6   Conclusion

Our work sheds light into the equilibration dynamics of isolated quantum systems. By leveraging a numerical ansatz that can only guarantee the preservation of few-body, local quantum correlations, our analysis supports the picture, introduced in Chapter 6, that the details of the complex, non-local, many-body correlations are unimportant for the emergence of the late-time hydrodynamics. Nevertheless, many questions remain open. One particularly important direction is understanding the relevant degrees of freedom / correlations when trying to capture the late-time hydrodynamical dynamics. One could then leverage those

---

[7]To be specific, $g(x) = \frac{1}{2} + \frac{1}{2}\tanh[(x - L/2)/\xi]$ with $\xi = 5$. We note that our results are not sensitive to the particular choice of $g(x)$, as long as it resembles a smoothed out step function.

insights to build generic, yet efficient numerical methods for the characterization of the quantum transport.

At the same time, our work opens two important directions of inquiry. On the one hand, our method is especially tuned to the study of one dimensional systems owing to the underlying tensor network formalism used. Are there generalizations of DMT to higher dimensional quantum systems? In particular, can one leverage recent advances in new higher dimensional tensor networks (such as Ref. [597]) to study the equilibration dynamics of higher dimensional quantum systems? On the other hand, in this work we have focused on the simplest form of hydrodynamics: simple Gaussian diffusion. What other hydrodynamical phenomena can occur in one dimensional isolated quantum systems? Indeed, the techniques and methodologies presented here can be leveraged to categorize the entire landscape of hydrodynamical phenomena. We make progress along this direction in Chapter 17, where we consider the infinite-temperature spin transport in integrable quantum magnets with complex symmetries.

Chapter 16

Emergent hydrodynamics in a strongly interacting dipolar spin ensemble

Despite recent development in numerical tools for the study of quantum dynamics (some of which were discussed in Chapter 15), many of these approaches require a set of assumptions and simplifications that, while physically motivated, are often uncontrolled [571, 426, 593, 456, 556]. Such methods are providing some of the first quantitative connections between microscopic quantum models and late-time classical hydrodynamical behavior, but we are still lacking the theoretically toolset to understand exactly how and when a late-time hydrodynamical behavior emerges. Indeed, proving that a classical hydrodynamical description captures the late-time dyanamics of isolated quantum systems (and what are the necessary requirements) has remained an enduringly hard question [22, 85, 48, 76, 582, 288, 593, 126, 47].

Addressing this question has motivated seminal advances in different context. On the theoretical front, precise analytic insights have been obtained in the context of integrable systems using generalized hydrodynamics and non-integrable systems using perturbative approaches [328, 126, 47, 398, 378, 288, 183]. On the experimental front, tremendous progress in time-resolved measurement techniques has enabled the direct observation of emergent classical diffusion in several classes of quantum systems [512, 375, 488, 604, 417, 62, 154].

There are, however, a wide variety of classical dynamical "universality classes" other than diffusion: aside from the simple case of free (ballistic) behavior, two well-known classes are Kardar-Parisi-Zhang dynamics and Sinai diffusion [278, 611, 202, 507]. Here, we report time-resolved experiments on a closed quantum system, which exhibits an unconventional approach to late-time diffusion characterized by a long-lived, non-Gaussian polarization profile.

Our experimental platform consists of two strongly-interacting species of electronic spins in diamond: substitutional nitrogen defects (P1 centers) and nitrogen-vacancy (NV) color centers [142, 217]. By controlling the relative density of these two species, we demonstrate

the ability to prepare inhomogeneous spatial profiles of a conserved spin density, as well as to locally probe the resulting nanoscale spin dynamics [Fig. 16.1]. These dynamics can be tuned via three independent controls: 1) the initial spin polarization, 2) the average spacing between spins, and 3) the magnitude of the on-site random fields.

Exploring this phase space leads us to an understanding of how the details of the microscopic spin Hamiltonian modify conventional diffusion. By tracking the local autocorrelation function of the spin polarization, $S_p(t)$, we observe the emergence of a long-time, diffusive power-law, $S_p(t) \sim t^{-3/2}$, for over an order of magnitude in time [Fig. 16.1(b)]. However, the details of this autocorrelation function over a broad range of timescales indicate that, following local initialization, the spin polarization distribution remains non-Gaussian throughout the timescales accessible in the experiment; this originates from the presence of strong disorder in our system, which leads to a *distribution* of local diffusion coefficients and a Yukawa-like spin polarization profile [Fig. 16.1(d)].

16.1   Hybrid spin platform

We choose to work with samples containing a P1 density ~ 100 ppm and an NV density ~ 0.5 ppm, leading to a geometry where each spin-1 NV center is surrounded by a strongly-interacting ensemble of spin-1/2 P1 centers [Fig. 16.1(a)]. In this geometry, the NV center naturally plays the role of both a polarization source and a local probe for nearby P1 centers. These roles rely upon two ingredients. First, the NV center can be optically initialized (to $|m_s^{\mathrm{NV}} = 0\rangle$) and read out using green laser illumination, which does not affect the P1 center. Second, the NV and P1 centers can coherently exchange spin polarization when brought into resonance via an external magnetic field [Fig. 16.2(a)] [217]; this polarization exchange is driven by the $\Delta m_s = \pm 2$ components of the magnetic dipole-dipole interaction:

$$H_{\mathrm{NV\text{-}P1}} = -\sum_i \frac{J_0}{r_{\mathrm{NV},i}^3} \left(A_i \left[S^+ P_i^+ + S^- P_i^- \right] + B_i S^z P_i^z \right), \tag{16.1}$$

where $J_0 = (2\pi) \times 52$ MHz $\cdot$ nm^3 characterizes the strength of the dipolar interaction, $r_{\mathrm{NV},i}$ is the distance between the NV center and the ith P1 center, A_i and B_i capture the angular dependence of the dipolar interaction, while $S^\pm$ and $P^\pm$ are raising and lowering operators for the NV and P1, respectively. We note that $H_{\mathrm{NV\text{-}P1}}$ corresponds to the energy-conserving terms of the dipolar interaction, upon restricting our attention to the NV spin subspace $\{|0\rangle, |-1\rangle\}$ [Fig. 16.2(a)].

In addition, the P1 centers also exhibit dipolar interactions among themselves driven by the $\Delta m_s = 0$ component:

$$H_{\mathrm{P1\text{-}P1}} = -\sum_{i<j} \frac{J_0}{r_{i,j}^3} \left(\tilde{A}_{i,j} \left[P_i^+ P_j^- + P_i^- P_j^+ \right] + \tilde{B}_{i,j} P_i^z P_j^z \right) \tag{16.2}$$

where $\tilde{A}_{i,j}$, $\tilde{B}_{i,j}$ are the analogous angular coefficients.
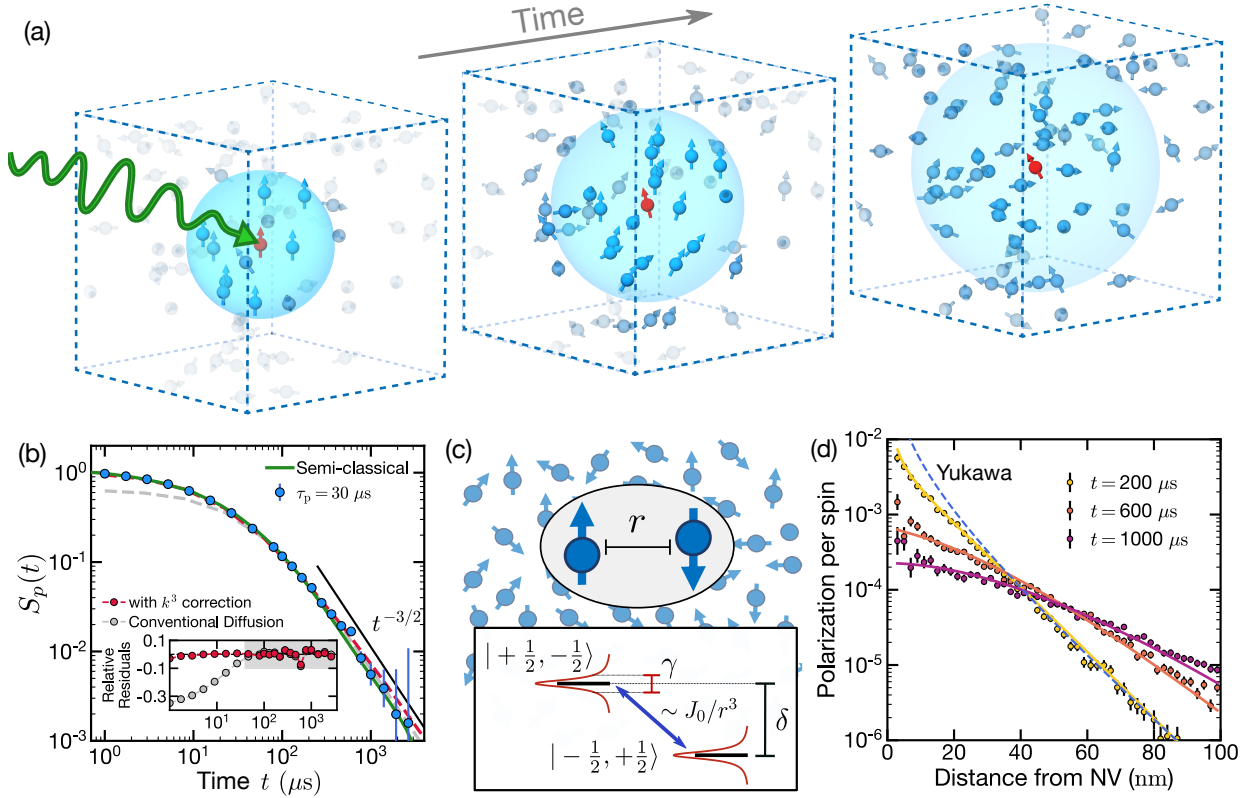
Figure 16.1: **Nanoscale spin diffusion in a long-range interacting quantum system.**
(a) Schematic depicting the emergence of hydrodynamics in a strongly interacting dipolar
spin ensemble. Through optical pumping (green arrow), the NV center (red) serves as a
polarization source for nearby P1 centers (blue), resulting in the preparation of a local,
inhomogenous spin-polarization profile. Dynamics then lead to the spreading of this profile
as a function of time. **(b)** Dynamics of the survival probability $S_p(t)$ of the $\nu = 1/3$ P1
subgroup in sample S2 at $T = 25$ K following a polarization period of $\tau_p = 30$ μs. After
an initial transient, $S_p(t)$ approaches a robust power-law decay $\sim t^{-3/2}$, indicating diffusion.
The late-time dynamics are accurately described by the diffusion equation (gray dashed
line). (inset) Relative residuals when fitting with (red) or without (grey) an additional long-
range correction $C_{lr}k^3$. In the hydrodynamical regime (grey shaded region) both models
capture the data. **(c)** Illustration of our semi-classical description for the spin-polarization
dynamics. Each pair of spins exchanges polarization via the dipolar interaction. The presence
of other nearby P1 spins leads to an energy mismatch δ and a homogeneous broadening
γ; these parameters are independently measured. **(d)** Initializing with unit polarization,
a robust non-Gaussian polarization profile emerges from the semi-classical model for all
experimentally accessible timescales. The crossover from a Yukawa to Gaussian polarization
profile is accurately captured by including the disorder-induced dynamical modification,
$C_{dyn}k^2\partial_t P_k$, in the diffusion equation with $C_{dyn} = 204 \pm 45$ nm^3.
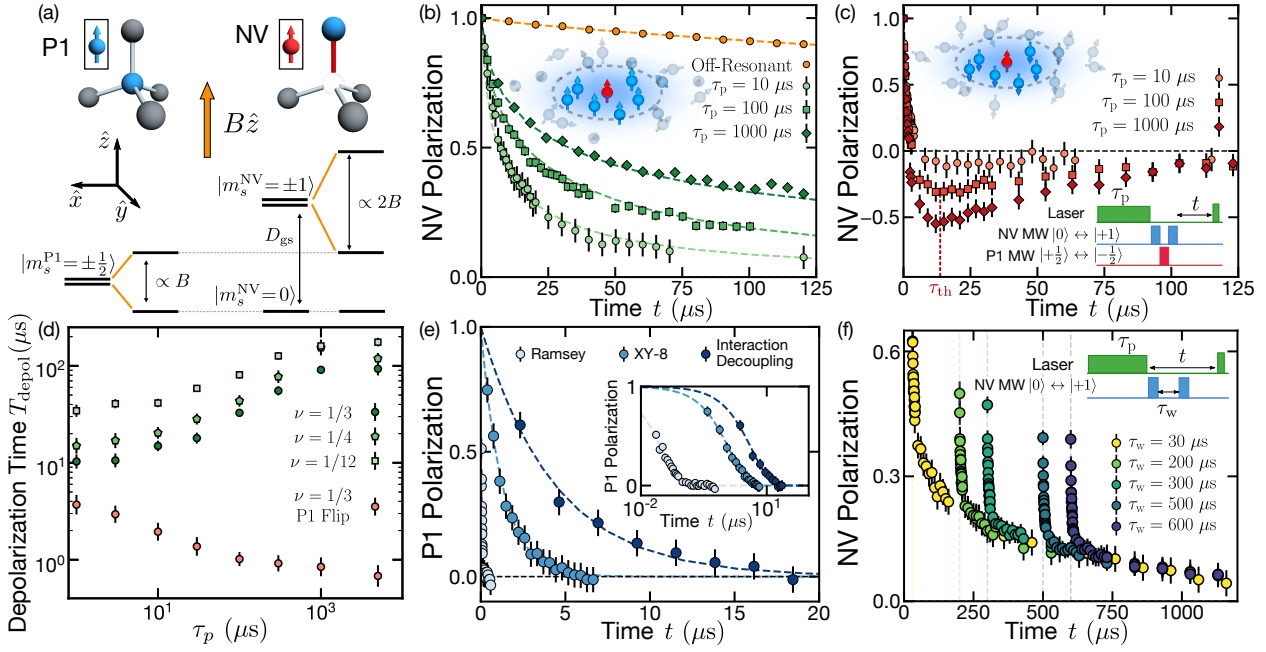
Figure 16.2: **Probing local spin-polarization dynamics using the NV center. (a)**
In the absence of a magnetic field, the P1's spin-1/2 sub-levels are degenerate, while the
NV's spin-1 sub-levels exhibit a zero field splitting, $D_{gs} = (2\pi) \times 2.87$ GHz. By applying
an external magnetic field, the P1 and NV center can be brought into resonance. **(b)**
When the NV and P1 are off-resonant (orange), $B = 360$ G, the NV exhibits a stretched
exponential decay $\sim e^{-(t/T_1^{NV})^{0.8}}$ (dashed line) with $T_1^{NV} = 2.3 \pm 0.1$ ms, consistent with spin-
phonon relaxation. When the NV is resonant with the $\nu = 1/3$ subgroup of P1s (green),
$B = 511$ G, depolarization occurs significantly more rapidly and is strongly dependent upon
the polarization time τ_p; a longer τ_p leads to a larger local polarization of P1 centers (inset)
and a correspondingly longer NV relaxation time. Dashed green lines correspond to the NV
dynamics as captured by our semi-classical model. **(c)** NV depolarization dynamics with
an anti-polarized $\nu = 1/3$ P1 ensemble (top inset). Depolarization occurs in two distinct
steps: an initial decay, $t \lesssim \tau_{th} \sim 12$ μs, corresponding to local equilibration with the P1
ensemble, followed by late-time diffusion. (bottom inset) Pulse sequence describing the
preparation of the anti-polarized P1 ensemble. **(d)** Depolarization time T_{depol} (extracted as
the $1/e$ decay time of the initial polarization) as a function of τ_p for different effective P1
densities ν. The anti-polarized case for $\nu = 1/3$ is denoted as P1 Flip [panel (c)]. As τ_p
approaches P1's $T_1 \sim 1$ ms, T_{depol} saturates. **(e)** P1 spin coherence time, T_2, for different
dynamical decoupling sequences, Ramsey $[0.032 \pm 0.005$ μs], XY-8 $[1.27 \pm 0.02$ μs] and an
interaction decoupling sequence $[4.4 \pm 0.1$ μs using DROID [608, 98]]; coherence times are
extracted from single exponential fits (dashed blue lines). (inset) Data plotted in semi-log.
(f) Depolarization dynamics for $\tau_p = 1000$ μs with variable NV-shelving time, τ_w (inset).
The τ_w-independent collapse of the late-time data confirms the NV's role as a local probe
of the P1's polarization dynamics. All data are taken using sample S1 at room temperature
$T \sim 300$ K.
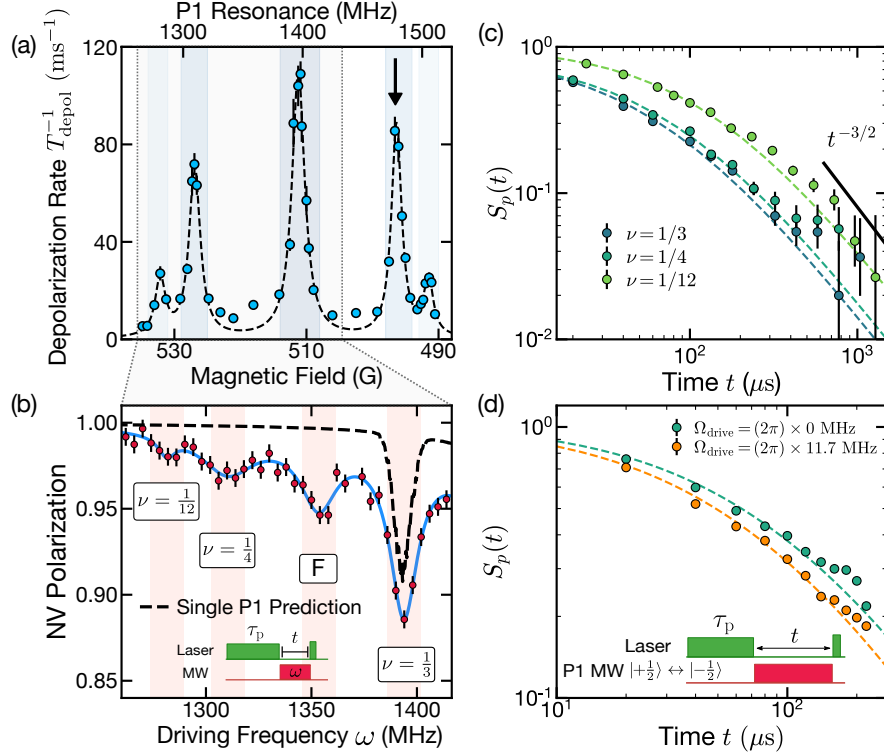
Figure 16.3:   **Controlling emergent hydrodynamics by engineering the microscopic
Hamiltonian. (a)** Depolarization rate, T_{depol}^{-1}, of the NV center as a function of magnetic field
after $\tau_{\text{p}} = 1$ μs. The NV exhibits five distinct resonances corresponding to five different subgroups
of P1s with density ratios $\nu \in \{\frac{1}{12}, \frac{1}{4}, \frac{1}{3}, \frac{1}{4}, \frac{1}{12}\}$. For panels (b,d) below, we fix the magnetic field
strength, $B = 496.5$ G, wherein the NV is resonant with a $\nu = 1/4$ P1 subgroup (indicated by
the arrow); the top axis shows the frequency of the P1 subgroups at this field strength. **(b)**
Fixing a polarization time, $\tau_{\text{p}} = 300$ μs, and an interaction time $t = 3$ μs (inset), we probe the
polarization transfer between the NV and the resonant $\nu = \frac{1}{4}$ P1 subgroup. By driving the *other*
P1 subgroups, one can effectively reduce the magnitude of the on-site disorder by "echoing" out a
portion of the Ising piece of the dipolar interactions. Sweeping the microwave driving frequency,
ω, we observe an enhanced NV decay when it is resonant with the $\nu = \frac{1}{12}, \frac{1}{4}, \frac{1}{3}$ subgroups as well
as an additional "forbidden" transition, F. By comparing against numerical simulations for a
single P1 spin (dashed black line), we conclude that—aside from the $\nu = \frac{1}{3}$ resonance where an
additional hyperfine depolarization channel plays a crucial role—echoing out disorder enhances the
coherent many-body interactions and leads to faster dynamics. **(c)** Dynamics of $S_p(t)$ for different
effective P1 densities with $\tau_{\text{p}} = 100$ μs; control over the P1 density is achieved by tuning the
external magnetic field to bring the NV into resonance with the $\nu = \frac{1}{3}, \frac{1}{4}$ and $\frac{1}{12}$ P1 subgroups.
A smaller P1 density leads to correspondingly slower spin diffusion [Table 16.1]. **(d)** Dynamics
of $S_p(t)$ for different on-site disorder strengths with $\tau_{\text{p}} = 300$ μs. Under continuous microwave
driving [$\Omega_{\text{drive}} = (2\pi) \times 11.7$ MHz] of the *other* $\nu = \frac{1}{4}$ P1 subgroup (inset), the effective disorder is
suppressed and spin diffusion is enhanced [Table 16.1]. Dashed lines in (c) and (d) correspond to
$S_p(t)$ obtained via Eq. 16.3. All experimental data are taken using sample S1 at room temperature
$T \sim 300$ K.

When the NV and P1 are off-resonant, we observe an NV depolarization timescale, $T_{\text{depol}} = 2.3 \pm 0.1$ ms, consistent with room-temperature, spin-phonon relaxation [Fig. 16.2(b)] [142]. By applying a magnetic field, $B = 511$ G, along the NV axis, the NV's $|0\rangle \leftrightarrow |-1\rangle$ transition becomes resonant with the P1's $\left|-\frac{1}{2}\right\rangle \leftrightarrow \left|+\frac{1}{2}\right\rangle$ transition [Fig. 16.2(a)], and we find that T_{depol} decreases by over two orders of magnitude to 8.9 ± 0.6 μs [Fig. 16.2(b)] [217]. We emphasize that the reduced T_{depol} should not be thought of as extrinsic decoherence, but rather as a consequence of coherent NV-P1 interactions [Fig. 16.2(e)].

16.2   Local spin polarization

By continuously repolarizing the NV center via green laser excitation, one can use $H_{\text{NV-P1}}$ to transfer spin polarization to nearby P1 centers; this polarization is further spread-out among the P1s by $H_{\text{P1-P1}}$. The duration of the laser excitation, τ_{p}, then controls the amplitude, shape and width of the local spin polarization. A longer τ_{p} leads to a larger local P1 polarization, which acts as a "frozen core" around the NV center [inset, Fig. 16.2(b)], suppressing dipolar spin exchange from $H_{\text{NV-P1}}$ [292]. This suppression suggests that T_{depol}, measured *after* P1 polarization, should be significantly enhanced. This is indeed borne out by the data. As shown in Fig. 16.2(b,d), T_{depol} is extended by an order of magnitude as a function of increasing τ_{p}. The increase saturates as τ_{p} approaches the spin-phonon relaxation time and the polarization process reaches a steady state [Fig. 16.2(d)] [527].

16.3   Probing nanoscale spin dynamics

To study the long-time dynamics associated with the dipolar-induced spreading of our initial polarization profiles, it is essential to distinguish between early-time local equilibration and late-time emergent dynamics. To this end, we introduce an experimental technique which allows us to explicitly observe local thermalization. In particular, after polarizing for τ_{p}, we utilize a microwave π-pulse to shelve the NV population from $|0\rangle$ into the highly off-resonant $|+1\rangle$ state [bottom inset, Fig. 16.2(c)]. Next, we perform a global microwave π-pulse on the $\left|-\frac{1}{2}\right\rangle \leftrightarrow \left|+\frac{1}{2}\right\rangle$ P1-transition, flipping the ensemble's spin polarization. Finally, we unshelve the NV population, effectively preparing an initial condition where the NV is antipolarized relative to the P1 ensemble [top inset, Fig. 16.2(c)].

The dynamics starting from this antipolarized configuration are markedly distinct. First, the NV polarization quickly changes sign and reaches a negative value, indicating local thermalization with the oppositely oriented P1 ensemble. Second, the larger the antipolarization (controlled by τ_{p}), the faster the NV initially decays [Fig. 16.2(c,d)]. Crucially, this allows us to extract a characteristic timescale for local thermalization, $\tau_{\text{th}} \sim 12$ μs.

Returning to the polarized case, we can now leverage the shelving technique to experimentally isolate the emergent late-time dynamics. In particular, we polarize for time τ_{p}, shelve the NV and then wait for a variable time τ_{w} to allow the P1 polarization to spread. Upon un-

shelving the NV, we observe a two-step relaxation process, as depicted in Fig. 16.2(f). After
an initial step of rapid local equilibration, the late-time dynamics exhibit a τ_{w}-independent
collapse. Crucially, this demonstrates that for $t > \tau_{\mathrm{th}}$, the NV polarization functions as a
local probe of the amplitude of the P1 polarization profile, $P(t, \boldsymbol{r})$; alternatively, one can
also think of the NV's polarization as an autocorrelation function that captures the survival
probability of the P1's polarization dynamics [247].

16.4 Observation of emergent diffusion

At late times, the conservation of total polarization and the dynamical exponent $z = 2$ deter-
mine the characteristic behavior of the survival probability in d dimensions, $S_p(t) \sim t^{-d/2}$;
the simplest hydrodynamic model capturing this corresponds to Gaussian diffusion:

$$\partial_t P(t, \boldsymbol{r}) = D\nabla^2 P(t, \boldsymbol{r}) - \frac{P(t, \boldsymbol{r})}{T_1} + Q(t, \boldsymbol{r}), \tag{16.3}$$

where D is the diffusion coefficient. The latter two terms in Eq. 16.3 are motivated by our
experiment: $Q(t, \boldsymbol{r})$ is a source term that characterizes the P1 polarization process, while
T_1 is an extrinsic relaxation time, after which the experimental signal becomes suppressed.
In order to maximize the experimental window for observing emergent hydrodynamics, we
work at low temperatures $T = 25$ K, where the NV's T_1^{NV} time extends by an order of mag-
nitude, and the P1's T_1 time extends by a factor of three [260]. The source $Q(t, \boldsymbol{r})$ contains
contributions from each of the randomly distributed NVs, whose finite density produces an
overall uniform background polarization that decays exponentially in time. Isolating the
nanoscale polarization dynamics from this background, we observe a robust power-law de-
cay of the survival probability, $S_p(t) \sim t^{-3/2}$, for over a decade in time, demonstrating the
emergence of spin diffusion [Fig. 16.1(b)] [247]. Extracting the corresponding diffusion coeffi-
cient from $S_p(t) = P_{\mathrm{total}}/(4\pi Dt)^{3/2}$ requires one additional piece of information, namely, the
total amount of spin polarization, P_{total}, transferred to the P1 ensemble. Fortunately, this is
naturally determined by combining the height of the measured polarization background with
the density of NVs, which we independently calibrate using a spin-locking experiment. This
enables us to experimentally extract the spin-diffusion coefficient: $D = 0.35 \pm 0.05$ nm^2/μs
[Table 16.1].

16.5 An unconventional approach to diffusion

While the hydrodynamic model in Eq. 16.3 captures the correct dynamical exponent, it
assumes that the dynamics follow Gaussian diffusion at all times. However, disorder in-
duces important modifications to this picture and leads to a novel dynamical correction. In
particular, around each P1 center there is a distinct local environment, arising from both
positional disorder and the presence of on-site random fields (generated by other paramag-
netic spin defects). This leads to a spatially-varying local diffusion coefficient. As an initial

polarization profile spreads, its dynamics naturally average over an increasing number of local P1 environments. This generates a *dynamical* modification to the diffusion equation, whose leading contribution is $C_{\text{dyn}}k^2\partial_t$ (for a derivation of this term see Appendix C.1):

$$\partial_t P_{\boldsymbol{k}}(t) = -\left[Dk^2 + C_{\text{dyn}}k^2\partial_t + \cdots\right] P_{\boldsymbol{k}}(t), \tag{16.4}$$

where $P_{\boldsymbol{k}}(t)$ is the Fourier component of the polarization with wavevector $\boldsymbol{k}$. This term induces two striking modifications to the diffusive dynamics. First, the early time polarization profile follows a Yukawa-like form $\sim \frac{1}{r}e^{-r/\ell}$, and only crosses over to a Gaussian at late times. Second, the relationship between the height of the polarization profile $S_p(t)$, and its width $\sim \sqrt{Dt}$, is fundamentally altered; as a result, in order to faithfully extract D from $S_p(t)$, one must account for the non-Gaussianity of the polarization profile.

   To connect our nanoscale spin dynamics to these disorder-induced hydrodynamical features, we utilize a semi-classical description of the polarization evolution based upon Fermi's golden rule [Fig. 16.1(c)]—we present the derivation of this description in Appendix D. Accounting for both positional disorder and on-site random fields, numerical simulations of the polarization dynamics exhibit excellent agreement with the experimentally measured $S_p(t)$ for over three decades in time [Fig. 16.1(b)]. Our semi-classical model also provides direct access to the spatial polarization profile, which remains robustly non-Gaussian throughout the timescale of the experiment, indicative of unconventional diffusion. Remarkably, the polarization profile precisely exhibits the predicted Yukawa to Gaussian crossover [Fig. 16.1(d)] and enables us to extract the coefficient of the dynamical modification [Eq. 16.4] as $C_{\text{dyn}} = 204 \pm 45$ nm^2. A few remarks are in order. First, this coefficient defines a physical length scale, $\ell = \sqrt{C_{\text{dyn}}} = 14.3 \pm 1.6$ nm, which sets the decay of the Yukawa form $\sim \frac{1}{r}e^{-r/\ell}$ of the polarization profile. More intuitively, ℓ can be thought of as the length-scale over which the disorder-induced variations of the local P1 environments start to become averaged out. Thus, only when the polarization expands to a characteristic size much larger than ℓ, will the dynamics approach Gaussian diffusion.

   Second, as evinced in Fig. 16.1(d), for a wide range of intermediate timescales, the polarization profile is well-described by a simple exponential, which modifies the relationship between the survival probability and the diffusion coefficient. This modification can be computed analytically and takes the form of a geometric factor $g = 2\pi^{1/3}$, wherein $D \to gD$ (Table 16.1). Crucially, the mean square displacement of the polarization profile, $\langle r^2 \rangle(t) = 6D_{\langle r^2 \rangle}t$, provides an independent measure of the diffusion coefficient [514, 156]. As highlighted in Table 16.1, only by accounting for the disorder-induced geometric factor do we observe agreement between the diffusion coefficient extracted from $S_p(t)$ and $\langle r^2 \rangle(t)$; this agreement directly demonstrates the non-Gaussian nature of the observed dynamics.

16.6   Microscopic control of emergent spin diffusion

We now demonstrate the ability to directly translate changes in the underlying microscopic Hamiltonian to changes in the emergent macroscopic behavior. In order to engineer the

Hamiltonian, we exploit the hyperfine structure of the P1 defect, enabling control over the effective density and the on-site random field disorder. In particular, sweeping the strength of the external magnetic field from 490 G to 540 G reveals five spectroscopically distinct subgroups of the P1 ensemble [142, 217], each containing a different fraction of the total P1 spins, with density ratios $\nu = \{\frac{1}{12}, \frac{1}{4}, \frac{1}{3}, \frac{1}{4}, \frac{1}{12}\}$ [Fig. 16.3(a)]. Thus, tuning the external magnetic field provides discrete control over the average spacing between resonant P1 spins. As shown in Fig. 16.3(c), the survival probability for both the $\nu = 1/4$ and $\nu = 1/12$ P1 subgroups exhibits significantly slower spin diffusion than the $\nu = 1/3$ subgroup. This is consistent with the presence of weaker interactions arising from the larger spin spacing, and leads to smaller values for the measured diffusion coefficient (Table 16.1).

Finally, one can also experimentally control the strength of the on-site random field disorder via continuous driving. Since these fields are dominated by the Ising portion of the interactions between the various P1 subgroups, rapid microwave driving of a single subgroup causes its contributions to the disorder to become averaged out [Fig. 16.3(b)]. Indeed, by bringing the NV into resonance with one of the $\nu = 1/4$ subgroups [black arrow, Fig. 16.3(a)], while driving the other $\nu = 1/4$ subgroup, we observe faster spin diffusion, consistent with a reduction in disorder [Fig. 16.3(d) and Table 16.1].

16.7   Outlook

Looking forward, the work presented in this chapter opens the door to a number of intriguing future directions. First, the presence of long-range, power-law interactions can lead to different dynamical universality classes [329]—for a detailed calculation of the long-range corrections to diffusion see Appendix C.2. Within our semi-classical model, the polarization dynamics are governed by an effective $\sim 1/r^6$ power-law. Interestingly, much like disorder, this particular power-law also leads to an unconventional approach to diffusion, albeit governed by a distinct non-analytic correction $\sim C_{\mathrm{lr}} k^3$; our data [inset, Fig. 16.1(b)] do not exhibit clear signatures of this power-law correction and we leave its exploration to future work. Second, the ability to experimentally isolate local equilibration dynamics naturally points to the study of many-body localization and Floquet thermalization [6, 379]. In long-range interacting systems, the precise criteria for delocalization remain unknown [591, 397], while in Floquet systems, the late-time dynamics involve a complex interplay between heating and hydrodynamic behaviour [593, 430]. Finally, the presence of a Yukawa-like polarization profile in our system is reminiscent of an open question in the biochemical sciences, namely, what is the underlying mechanism behind the wide-spread emergence of Fickian yet non-Gaussian diffusion in complex fluids [92, 521, 293, 102, 442, 36]; in such systems, it is notoriously difficult to change the microscopic equations of motion, suggesting the possibility for our platform to be utilized as a controllable "simulator" of soft, heterogeneous materials. A direct route for exploring this question is to leverage sub-diffraction imaging techniques or magnetic field gradients in order to measure correlation functions between spatially separated NVs [464, 23].

Within the context of equilibration dynamics, our study highlights how large scale, controllable and isolated quantum platforms can serve to explore and uncover novel equilibrating phenomena. Although we focused only on the dynamics of magnetization (a single body operator), capturing and characterizing the dynamics of more complex observables will be crucial to inspire new theoretical insights into the emergence of hydrodynamics. However, engineering large scale isolated quantum systems with a large level of microscopic control is an outstandingly difficult problem; indeed, overcoming this challenge lies at the heart of the development of general, fault-toletant quantum computers. As those technologies mature, and novel quantum simulation platforms mature (with different forms of interactions, geometries and capabilities), we hope that more experimental studies allow us to uncover different forms of hydrodynamical behavior (we discuss some work in this direction in Chapter 18).

Effective density	$\nu = 1/3$		$\nu = 1/4$		$\nu = 1/12$
					S1
Sample	S1	S2	S1 $\Omega_{\text{drive}} = 0$ MHz	S1 $\Omega_{\text{drive}} = 11.7$ MHz	S1
D [nm$^2/\mu$s]	0.28 ± 0.06	0.35 ± 0.05	0.25 ± 0.06	0.33 ± 0.09	0.11 ± 0.03
gD [nm$^2/\mu$s]	0.82 ± 0.17	1.03 ± 0.13	0.74 ± 0.18	0.95 ± 0.26	0.33 ± 0.08
$D_{\langle r^2 \rangle}$ [nm$^2/\mu$s]	0.98 ± 0.03	1.09 ± 0.02	0.66 ± 0.04	0.95 ± 0.02	0.21 ± 0.03

Table 16.1:   **Spin diffusion coefficients** across all samples, temperatures, P1 densities and disorder strengths. Accounting for the appropriate non-Gaussian geometric factor, $g = 2\pi^{1/3}$, yields agreement between the diffusion coefficient extracted from the survival probability and that extracted from the growth of $\langle r^2 \rangle$ (computed via our semi-classical model). Samples S1 and S2 both contain a P1 density of ~ 110 ppm, while their NV densities are ~ 0.7 ppm and ~ 0.3 ppm, respectively. Measurements on S1 are performed at room temperature, while measurements on S2 are taken at $T = 25$ K. For sample S1, we also consider two additional tuning parameters: (i) different effective P1 densities, $\nu \in \{\frac{1}{3}, \frac{1}{4}, \frac{1}{12}\}$, tuned via the hyperfine structure [Fig. 16.3(c)], and (ii) different disorder strengths, W, tuned via continuous microwave driving [Fig. 16.3(d)]. The reported uncertainties include propagated uncertainties from other experimentally extracted parameters (e.g. T_1 and ρ_{NV}). Despite overlapping error bars, a detailed analysis confirms that the driven diffusion coefficient is statistically larger than the undriven case [616]. Error bars represent 1 s.d. accounting statistical uncertainties.

Chapter 17

Universal Kardar-Parisi-Zhang (KPZ) dynamics in integrable quantum systems

In the previous chapters, we have focused on the emergence of diffusion-like hydrodynamics in the late-time dynamics of quantum systems. This focus is not without merit—diffusion is the prototypical example of a broader dynamical universality class that characterizes most linear stochastic processes and can be viewed as a physical manifestation of the central limit theorem. Despite its broad applicability, it is important to note that it corresponds to one example of a broader landscape of dynamical universality classes.

An example of a different dynamical universality class is the one associated with the Kardar-Parisi-Zhang (KPZ) equation [278]—termed the *KPZ universality class*. First proposed in the context of surface growth, the KPZ equation and its universality class has become central to our understanding of many interacting stochastic processes [219, 108, 107], ranging from directed polymers and traffic models to kinetic roughening [31, 81, 146, 19, 441, 109, 353, 111, 219, 132, 110, 516, 393].

Understanding the dynamical universality class of a particular phenomena then becomes an important question that allows one to build a deeper understanding by making precise comparisons and connections between disparate physical settings [515, 51, 584, 387, 167, 85, 616]. At its core, different universality classes are distinguishable by both the value of the scaling exponents and the form of the scaling functions that characterize correlations in the system. This is perhaps most familiar in the context of Brownian motion, where the diffusive late-time behavior follows a Gaussian scaling function; the width of the corresponding distribution grows as $\sim t^{1/z}$, where $z = 2$ is the dynamical scaling exponent. By contrast, the scaling functions for the KPZ universality class are significantly more complex and their exact functional form represents a relatively recent mathematical achievement [49, 447, 214, 19, 484, 109]. The associated dynamical scaling exponent is neither diffusive nor ballistic ($z = 1$), but rather superdiffusive with $z = 3/2$.

Typically, KPZ behavior is expected in non-linear, out-of-equilibrium *classical* systems
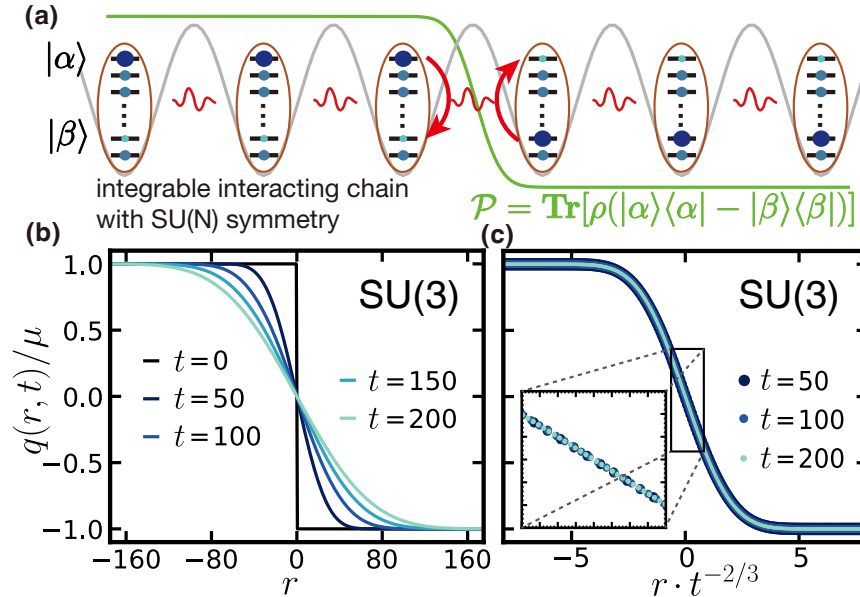
Figure 17.1: **Spin transport in an SU(3) symmetric integrable spin system. (a)**
Schematic depicting a one dimensional chain of alkaline-earth atoms (each with N-levels)
trapped in an optical lattice and interacting via nearest-neighbor super-exchange. The equi-
libration of an initial domain-wall-like imbalance encodes the underlying KPZ dynamics. **(b)**
Domain-wall dynamics as a function of time for an SU(3)-symmetric, integrable spin chain.
(c) The polarization profiles at different times collapse upon rescaling with $t^{-1/z}$. The dy-
namical exponent, $z = 3/2$, indicates superdiffusion and is consistent with KPZ transport.

subject to external noise; in this context, its observation is extremely robust and does not
require any fine-tuning or the presence of a particular symmetry [211]. To this end, the
numerical and experimental observation of KPZ universality in a one-dimensional *quantum*
spin-chain (i.e. the spin-1/2 Heisenberg model), fine-tuned for *both* integrability and SU(2)
symmetry, has attracted widespread attention [333, 252, 202, 334, 473, 253, 567, 487]. Inter-
estingly, this observation is at odds with conventional expectations for spin chain transport,
which predict diffusion [261, 7, 50, 53]. This naturally motivates the following question:
Is the Heisenberg chain an isolated exception, or the first example of a broader group of
quantum models in the KPZ universality class?

Seminal recent work has made elegant progress on this question by proving that *all*
integrable spin chains with a non-Abelian symmetry exhibit superdiffusive transport with
$z = 3/2$ [Fig. 17.1] [253]. However, a single scaling exponent does not uniquely specify the
universality class and no analysis has been able to determine the nature of the corresponding
scaling functions.

In this chapter, we present an extensive numerical investigation that supports the fol-

lowing stronger conjecture — the dynamics of all integrable spin chains with a non-Abelian symmetry belong to the KPZ universality class. Leveraging a novel tensor-network-based technique dubbed density matrix truncation (DMT) [571, 593], we demonstrate that the spin dynamics of such models are precisely *captured by the KPZ scaling function* [Fig. 17.3]. Intriguingly, our numerical observations suggest that the conjecture holds not only for static systems, but also for periodically driven (Floquet) systems [549, 334], as well as supersymmetric models.

By applying perturbations to break either the non-Abelian symmetry or the integrability, we characterize the approach to superdiffusive transport from regimes where there is analytical control on the dynamics. We reproduce these analytical results with unprecedented accuracy, both verifying and benchmarking our numerics, as well as providing independent evidence for the purported microscopic mechanism underlying superdiffusion [202, 125]. Finally, we propose an experimental implementation — based upon alkaline-earth atoms in optical lattices — capable of investigating KPZ transport in a variety of $SU(N)$-symmetric, integrable models.

In this work, we study the universality classes describing the infinite-temperature dynamics for a variety of one-dimensional quantum spin-chains. We will focus on the dynamics of a locally conserved charge $\hat{Q} = \sum_r \hat{q}_r$, typically spin. If the system is characterized by a dynamical universality class, at late times the correlation function must collapse under an appropriate rescaling of space and time:

$$\langle \hat{q}_r(t)\hat{q}_0(0)\rangle_{T=\infty} \propto t^{-1/z} f\left(\frac{r}{t^{1/z}}\right). \tag{17.1}$$

This collapse defines the dynamical scaling exponent z and the scaling function $f(\xi)$, which together determine the universality class.

17.1 Probing transport dynamics

Let us begin by exploring the dynamical exponent. While z can in principle be extracted from the behavior of $\langle \hat{q}_r(t)\hat{q}_0(0)\rangle_{T=\infty}$, a simpler and more robust numerical setup is to consider the dynamics of a domain wall. More specifically, we perturb an infinite-temperature density matrix with a weak domain-wall-like imbalance in the charge density [Fig. 17.1(a)]:

$$\rho(t=0) \propto (\mathbb{1} + \mu\hat{q})^{\otimes L/2} \otimes (\mathbb{1} - \mu\hat{q})^{\otimes L/2}, \tag{17.2}$$

where μ determines the strength of the perturbation and L is the length of the chain.

As the system equilibrates, charge crosses the domain wall—the precise details of how this occurs reveals properties of the dynamical universality class [Fig. 17.1(b)]. In particular, we focus on the spatial profile of the charge density $q(r,t) = \langle \hat{q}_r(t)\rangle$ (hereafter, denoted as polarization), as a function of time t and displacement r from the domain wall. A natural measure of transport is the total polarization transferred across the domain-wall, $\mathcal{P}(t) = \sum_{r=1}^{L/2} (\mu - q(r,t))$, which provides a robust way to determine z: $\mathcal{P}(t) \propto t^{1/z}$.

To implement the domain-wall dynamics, we represent ρ using a matrix product density operator and compute its evolution via DMT [571, 593]. The truncation procedure in DMT is specifically designed to preserve local operators, such as the energy density, polarization, and their currents; this choice makes DMT particularly amenable for probing the universality class of many-body transport dynamics.

Although we will explore a wide variety of integrable models [Fig. 17.3], let us begin by focusing our discussions on the SU(3)-symmetric, spin-1 chain [545, 314, 524]:

$$H_{\mathrm{SU}(3)} = \sum_i \vec{S}_i \cdot \vec{S}_{i+1} + (\vec{S}_i \cdot \vec{S}_{i+1})^2, \tag{17.3}$$

where $\vec{S}_i$ is the vector of spin-1 operators acting on site i. Figure 17.1(b) depicts the melting of the domain wall as a function of time, starting from the initial state, $\rho(t = 0)$ with $\hat{q} = \hat{S}^z$ [Eq. 17.2]. The corresponding polarization transfer, $\mathcal{P}(t)$, exhibits a power-law $\sim t^{2/3}$ [blue line, Fig. 17.2(b)], consistent with the expected $z = 3/2$ exponent [151]. This exponent can be independently confirmed via a scaling collapse of the polarization profile [Fig. 17.1(c)].

In order to tune the system away from superdiffusion, one can perturb the spin-chain by either breaking the symmetry of the initial state or the symmetry of the Hamiltonian. To study the former, we initialize the system in $\rho(t = 0)$ and add a uniform magnetization, δ (along the $\hat{z}$-axis) on each site. The polarization transfer exhibits markedly distinct dynamics with a ballistic exponent, $z = 1$ [orange line, Fig. 17.2(b)]. Analytically, for weak magnetizations, the velocity of this ballistic transport is expected to scale linearly with δ; this is indeed borne out by the data [Fig. 17.2(c)] [202, 129]. For the spin-1/2 Heisenberg model, an even stronger statement can be made—the velocity extracted from DMT quantitatively agrees with analytic calculations [via generalized hydrodynamics (GHD)] even in the non-linear regime [inset, Fig. 17.2(c)] [202, 125].

Next, we break the SU(3) symmetry of $H_{\mathrm{SU}(3)}$ down to U(1) by considering the so-called Izergin-Korepin family of integrable spin-1 models [257, 553, 222, 258]. We parametrize the symmetry-breaking strength by Δ, such that when $\Delta = 0$, we recover $H_{\mathrm{SU}(3)}$. For finite values of Δ, we observe diffusive transport with the polarization transfer scaling as $\mathcal{P}(t) \sim t^{1/2}$ [purple line, Fig. 17.2(b)]. In addition, the extracted diffusion coefficient, D, diverges as $\Delta \to 0$, consistent with the approach to superdiffusion [Fig. 17.2(d)]. The analogous numerical experiment in the Heisenberg model (where Δ controls the XXZ anisotropy) again quantitatively agrees with analytic calculations [202].

A few remarks are in order. First, the agreement between DMT numerics and GHD analytics (which have different underlying assumptions) serves a dual benchmarking role; in particular, it highlights DMT's ability to faithfully characterize late-time transport dynamics and GHD's ability to quantitatively compute transport coefficients in integrable models [279, 125]. Second, in addition to breaking the non-Abelian symmetry of the Hamiltonian, one can also probe the effect of integrability breaking. To this end, we perturb $H_{\mathrm{SU}(3)}$ using SU(3)-symmetry-respecting, but *integrability-breaking* next-nearest-neighbor interactions. As expected for generic non-integrable models, $\mathcal{P}(t) \sim t^{1/2}$, consistent with diffusive transport [green line, Fig. 17.2(b)] [515, 147, 183].
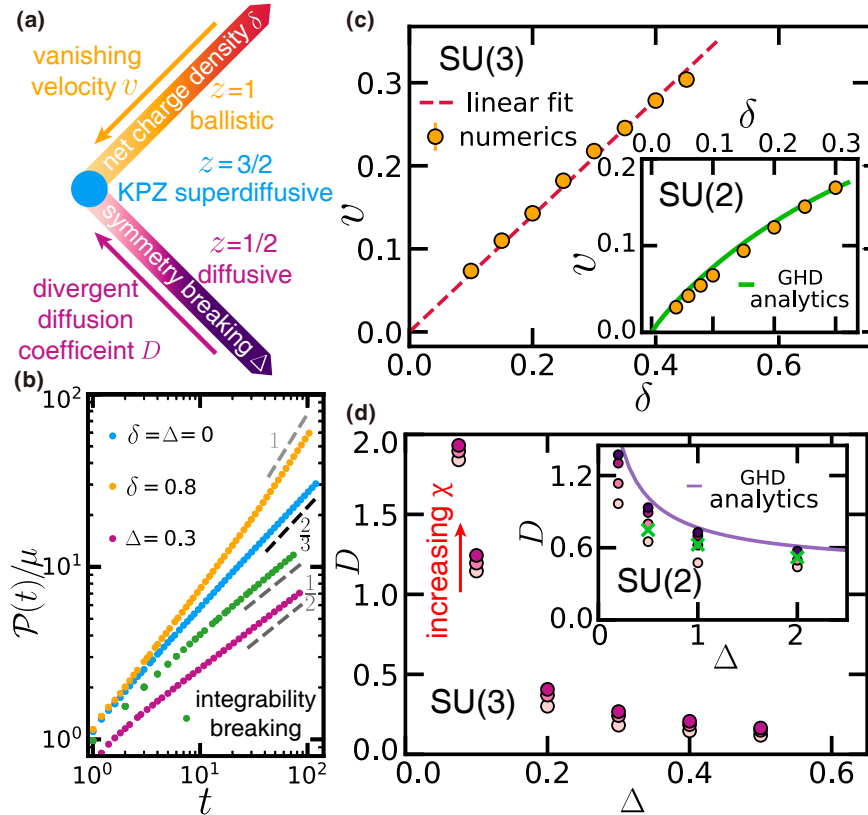
Figure 17.2: **Characterization of transport nearby superdiffusive point. (a)** Conjectured landscape of KPZ transport in integrable, non-Abelian-symmetric models (blue dot). The non-Abelian symmetry can be broken in two distinct ways, either by adding a finite charge density to the initial state (orange line) or by perturbing the underlying Hamiltonian (purple line). **(b)** The total polarization transferred across the domain wall, $\mathcal{P}(t)$, directly determines the dynamical exponent. For the integrable SU(3) model, $z = 3/2$; when either the integrability or the symmetry is broken in the Hamiltonian, $z = 2$; when the initial state has non-zero charge density, $z = 1$. The curve for the integrability breaking case (green) is shifted down for clarity. **(c)** Polarization transport velocity v as a function of charge density δ for both the SU(3) model and the SU(2) model (inset). **(d)** The diffusion coefficient, D, diverges as the integrable model approaches the SU(3) and SU(2) (inset) symmetric points. The DMT bond dimension, χ, is chosen to be $\{64, 128, 256\}$ and $\{64, 128, 256, 512\}$ for the SU(3) and SU(2) cases, respectively. Green crosses in the inset mark previous numerical results obtained from tDMRG simulations with bond dimension $\chi \sim 2000$ [279].
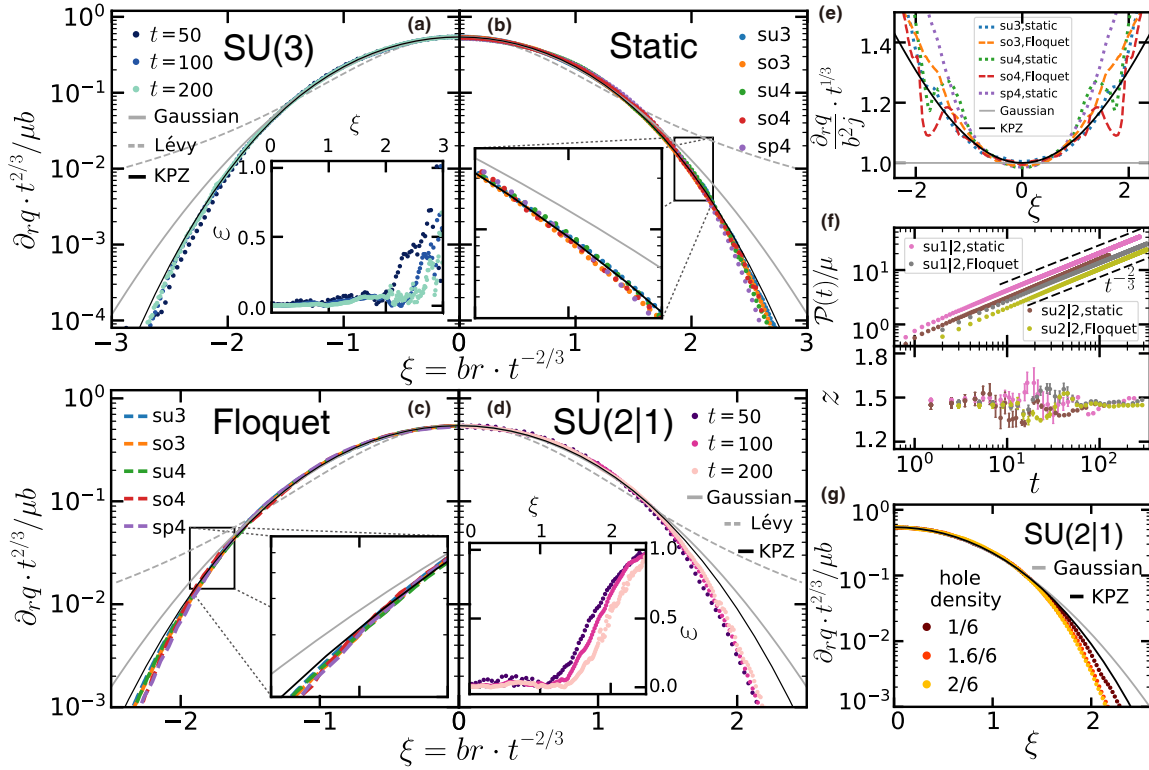
Figure 17.3: **KPZ dynamics in non-Abelian symmetric integrable spin models (and beyond). (a-d)** The KPZ scaling function emerges from a wide variety of integrable dynamics: static, non-Abelian-symmetric models, their Floquet counterparts, and supersymmetric models. **(a)[(d)]** At late times, the rescaled polarization profiles of the SU(3)[SU(2|1)] model differ from both the Gaussian and Lévy-flight expectations, but exhibit excellent agreement with the KPZ scaling function. Insets: relative difference with respect to the KPZ scaling function. We note that the agreement extends to longer length-scales as time is increased. **(b)[(c)]** Late-time, rescaled polarization profiles of static [Floquet] integrable models with different non-Abelian symmetries. For all symmetries explored, the dynamics exhibit excellent agreement with the KPZ scaling function. Insets: zoom-in of the polarization profiles. **(e)** For all models considered, the ratio between the polarization gradient and the current is inhomogeneous, in stark contrast with the expectation for any linear transport equation. The observed curvature is instead in agreement with KPZ transport. **(f)** In integrable supersymmetric models, the total charge transferred across the domain wall (upper panel) and the extracted dynamical exponent z (lower panel) are consistent with superdiffusion. **(g)** Polarization gradients in an integrable SU(2|1) model with varying hole density. At the same evolution time, systems with a smaller hole density are closer to the KPZ expectation.

17.2   Probing KPZ dynamics

While our numerical observation of a $z = 3/2$ exponent in $H_{\mathrm{SU(3)}}$ clearly establishes the presence of superdiffusion, it does not determine the system's dynamical universality class. Indeed, such an exponent can also arise in long-range interacting systems exhibiting Lévy flights, as well as rescaled diffusion [333, 334, 473, 329, 506].

To this end, we now investigate the universal scaling function. In particular, using our domain-wall dynamics, we can compute the charge correlation function from the spatial gradient of the polarization profile [334]:

$$\langle \hat{q}_r(t)\hat{q}_0(0)\rangle_{T=\infty} = \lim_{\mu \to 0} \frac{\partial_r q(r,t)}{2\mu} = \frac{b}{t^{2/3}} f\left(\frac{br}{t^{2/3}}\right), \qquad (17.4)$$

where b is a system-dependent parameter.[1]

As depicted in Figure 17.3(a), $\partial_r q(r,t)$ indeed collapses under the rescaling, $f(\xi = brt^{-2/3})$. For Lévy flights, one expects power-law tails (gray dashed line), which are manifestly inconsistent with the data. However, the difference between rescaled diffusion and KPZ is more subtle: for the former, $f(\xi)$ is Gaussian, while for KPZ, $f(\xi)$ exhibits faster decaying tails $\sim \exp\left(-0.295|\xi|^3\right)$ [447, 484, 214]. The data quantitatively agree with the KPZ prediction: The longer the evolution time, the closer $\partial_r q(r,t)$ is to the KPZ scaling function [highlighted by the relative error, Fig. 17.3(a) inset]. This agreement allows us to directly extract $b = 0.460 \pm 0.001$, which reflects the ratio between the diffusive smoothing, and the non-linear growth and noise in the KPZ equation. We emphasize that these observations apply to *any* conserved charges generated by the non-Abelian symmetry.

A complementary way to distinguish between rescaled diffusion and KPZ dynamics is to study the ratio between the spin current, $j(r,t) = -\int_{-\infty}^{r} \partial_t q(r',t)dr'$, and the polarization gradient. In rescaled diffusion, Fick's law ensures that the two are proportional, $j(r,t) \propto t^{1/3}\partial_r q(r,t)$, while the non-linearity of KPZ transport leads to the breakdown of this proportionality [447, 334]. Crucially, as illustrated in Fig. 17.3(e), we find that the ratio is not constant (as would be predicted for rescaled diffusion) and rather, is in good agreement with the KPZ prediction.

17.3   Universality of KPZ dynamics

We now turn our attention to the conjecture that KPZ dynamics emerge in several broad classes of integrable models. We will focus on three distinct settings: (i) static models with generic non-Abelian symmetries, (ii) periodically-driven (Floquet) models with non-Abelian symmetries, and (iii) supersymmetric models. In these latter two classes, even for the dynamical exponent, there are no generic results, although some particular instances are known to exhibit superdiffusion [252, 334, 151].

---

[1]We use ∂_r as a short-hand for discrete difference in the our system: $\partial_r q(r,t) = \langle \hat{q}_{r+1}(t)\rangle - \langle \hat{q}_r(t)\rangle$.

The construction of static, non-Abelian, integrable spin chains has a rich history, with different prescriptions for each of the four classes of simple Lie groups: $SU(N)$, $SO(2N)$, $SO(2N + 1)$ and $SP(2N)$ [302, 280, 253, 310]. We construct nearest-neighbor models with the following four representative symmetries, $SU(4)$, $SO(3)$, $SO(4)$ and $SP(4)$. Following our previous strategy for $H_{SU(3)}$, we analyze the transport dynamics of conserved charges for each of these models. In all cases, we observe excellent agreement with the KPZ universality class [Fig. 17.3(b,e)].

Extending this exploration to periodically driven systems requires systematically building the corresponding Floquet integrable models. Somewhat astonishingly, one can straightforwardly build such models from their static counterparts [549, 332]. The Hamiltonian is divided into terms acting on even and odd bonds (denoted as H_{even} and H_{odd}, respectively), which are then alternatingly applied, leading to a Floquet unitary: $U = e^{-iH_{odd}T/2}e^{-iH_{even}T/2}$. Using this procedure, we can extend our static analysis to the Floquet regime for all of the previous non-Abelian models [Fig. 17.3(c,e)]. Our conclusions are identical. The resulting transport falls within the KPZ universality class even though energy is no longer conserved.

Finally, let us consider integrable models where the non-Abelian symmetry is replaced with supersymmetry. Such models have been conjectured to exhibit superdiffusion, but observing this, either numerically or analytically, remains an open challenge [252, 253]. Here, we focus on a pair of spinful fermionic lattice models: the t-J model (with $t = 2J$), and the Essler-Korepin-Schoutens (EKS) model [483, 169]. These exhibit the two simplest supersymmetries, $SU(1|2)$ and $SU(2|2)$, respectively.

The defining feature of models with supersymmetry is that their conserved charges fall into two types: bosonic and fermionic, although only the bosonic charge can in principle exhibit superdiffusion [252]. For the t-J model, each lattice site can be occupied by either a spin-up fermion, a spin-down fermion, or a hole. The conserved bosonic charges are given by the total number of holes, and the total spin. Holes live in the Abelian $U(1)$ sector and thus lack particle-hole symmetry leading to a finite Drude weight and ballistic transport [252]. Therefore, we study the spin polarization, given by the difference between the number of spin-up and spin-down particles. As before, we prepare a weak domain-wall in the spin polarization while keeping the other charge densities—including the hole density—constant.

For both the static and Floquet t-J models, we observe superdiffusive spin transport (with $z = 3/2$) via both the polarization transfer [Fig. 17.3(f)] and the collapse of the polarization profile. The numerical evidence that spin transport falls within the KPZ universality class is more subtle. In particular, the polarization gradient, $\partial_r q(r, t)$, exhibits a discrepancy with both the KPZ and Gaussian expectations [Fig. 17.3(d)]. However, the finite-time flow of $\partial_r q(r, t)$ approaches the KPZ scaling function in the same qualitative fashion as is observed in the $SU(3)$ case [insets, Fig. 17.3(a,d)]. Moreover, a careful comparison of the relative error to the Gaussian model suggests that rescaled diffusion cannot be the correct limiting behavior.

A few remarks are in order. First, we conjecture that finite-time effects are exacerbated in supersymmetric models owing to the presence of additional ballistic modes. To test this

conjecture, we decrease the hole density,[2] and indeed observe an improved convergence to KPZ universality [Fig. 17.3(e)]. Curiously, this suggests that KPZ dynamics might arise in supersymmetric systems for generic fermionic filling fractions. Second, our analysis for the EKS model arrives at identical conclusions [Fig. 17.3(f)].

17.4 Experimental proposal

Recent advances in the control and manipulation of alkaline-earth atoms in optical lattices have opened the door to studying $SU(N)$-symmetric spin models [570, 84, 415, 485, 605, 368, 585, 367, 513, 489]. In particular, at unit-filling in the Mott insulating phase, the lack of hyperfine coupling in the $ns^2\ {}^1S_0$ electronic ground state naturally leads to $SU(N)$-symmetric spin-exchange interactions [206, 240, 414, 513]:

$$H_{\text{SU}(N)} = J_{\text{SU}(N)} \sum_i \sum_{\alpha,\beta=1}^{N} s_i^{\alpha,\beta} s_{i+1}^{\beta,\alpha}, \tag{17.5}$$

where $s_i^{\alpha,\beta} = |\alpha\rangle \langle\beta|$ on site i; in one dimension, $H_{\text{SU}(N)}$ is integrable and precisely corresponds to the models considered above (e.g. Eq. 17.3).

The observation and characterization of KPZ transport requires the ability to address two main experimental challenges: (i) preparing near infinite-temperature states with a well-defined domain-wall polarization and (ii) measuring the tails of the scaling function with sub-percent accuracy. The former can be accomplished via a two step process: first, optical pumping via an intercombination transition (e.g. $ns^2\ {}^1S_0 \leftrightarrow nsnp\ {}^3P_1$) can be used to generate arbitrary magnetization distributions which are preserved upon cooling to the Mott insulator; second, with single-site addressing [32, 505, 95, 428, 410, 218, 567], a coherent optical drive can be applied to half the system in order to prepare the domain wall.

Achieving the latter is significantly more subtle. In order to distinguish between KPZ dynamics and rescaled diffusion, careful estimates suggest the need to experimentally resolve the scaling function with a relative error of $\sim 10^{-3}$. Achieving this error floor requires the ability to spatially resolve spin-transport dynamics over long time-scales and large distances. For concreteness, let us consider ^{87}Sr atoms loaded into a two-dimensional optical lattice [513, 424, 61]. Recent experiments have demonstrated the elegant use of cavity-enhancement to realize homogeneous lattices capable of supporting Mott insulators with a diameter of ~ 300 sites [424]. By implementing strong confinement in one direction, one can subsequently divide the system into ~ 250 independent chains, each with length ~ 150 sites. Assuming an on-site interaction energy, $U \sim 3$ kHz, and a tunneling rate, $t \sim 300$ Hz, yields a spin-exchange interaction, $J = 2t^2/U \approx 60$ Hz [424]. Optimizing for an evolution time of $\sim 50/J$ and assuming an experimental cycle time of ~ 10 s [513], we estimate that a relative error of $\sim 10^{-3}$, can be achieved within two days of measurement. Finally, the presence of a finite

---

[2]We note that when there are no holes, one recovers an SU(2)-symmetric model Heisenberg.

density ($\gtrsim 1\%$ [250]) of doublons and holes in the Mott insulator will perturb the polarization dynamics, but the exact nature of their effect remains an open question.

17.5 Outlook

The present chapter highlights how isolated quantum systems can exhibit myriad equilibrating dynamics. In this case, superdiffusion and the KPZ universality behavior arises from a delicate interplay between integrability and symmetry. This naturally begs the question: can other hydrodynamic phenomena emerge in isolated quantum systems [441]? If so, what are the requirements? If not, what are the limitations? At the same time, our understanding of the present KPZ behavior is still nascent. For example, although some arguments relate the magnetization dynamics to the noisy Burger's equation (known to induced KPZ dynamics) [73], the mapping between the microscopic motion of the quasi-particles of the system and the resulting KPZ dynamics remains elusive.

Chapter 18

Quantum gas microscopy of Kardar-Parisi-Zhang superdiffusion

In Chapter 17, we analyzed the emergence of the KPZ universal dynamics in the infinite temperature transport dynamics of a variety of integrable quantum systems (with non-Abelian symmetries and beyond). This very broad exploration was motivated by two recent discoveries. On the one hand, building on top of mounting evidence [252, 334, 151], it was found that non-Abelian symmetric integrable systems exhibit anomalous transport with $z = 3/2$ dynamical exponent [253]. This signals a stark departure from the expectation that transport should either be ballistic (with $z = 1$) or diffusive (with $z = 2$), depending on whether the system exhibits stable quasi-particles or not, respectively [241, 74]. On the other hand, it has been predicted that in the spin-1/2 quantum Heisenberg chain (the simplest non-Abelian symmetric integrable model), the transport is not only superdiffusive, but follows the KPZ universality class [612, 333, 334, 202, 127, 203, 73]. The appearance of KPZ scaling in such a quantum spin chain is particularly surprising because these quantum chains lack many of the properties shared by all canonical KPZ systems. In particular, while KPZ dynamics is generally robust in generic systems with noisy, non-linear dynamics, in quantum spin chains, the KPZ behavior occurs in under deterministic, linear evolution of very fine-tuned systems (i.e. integrable systems [85, 48, 251, 75]).

The combination of these two observations has fueled conjectures that the emergence of KPZ hydrodynamics in quantum many-body systems is significantly more general and applies to any integrable model exhibiting a non-Abelian symmetry [305, 253, 594]—we verified that this conjecture is indeed true in Chapter 17. Crucially, this suggests a fundamental difference from the mechanisms of canonical KPZ [452, 121, 305, 73, 304, 253].

Despite much interest, a full theory of KPZ hydrodynamics in the Heisenberg model remains elusive [47, 74]. As a result, experimentally characterizing the anomalous dynamical exponents of spin transport has been the subject of widespread effort [236, 262, 263, 487]. However, as a superdiffusive exponent can arise from a number of distinct microscopic origins [267], it is essential to characterize a system beyond the dynamical exponent to establish its hydrodynamical universality class.

In this chapter, we explore the superdiffusive dynamics of the ferromagnetic Heisenberg model using a quantum-gas microscope with single-site resolution and single-spin-sensitive detection in spin chains of up to 50 spins. Our main results are three fold. First, we observe superdiffusive spin transport with the dynamical exponent $z = 3/2$, consistent with KPZ hydrodynamics. Second, we demonstrate that both integrability and a non-Abelian symmetry are essential for observing superdiffusion: Breaking integrability by tuning dimensionality restores diffusion, and breaking the symmetry by preparing an initial state with net magnetization leads to ballistic transport [Fig. 18.1(A)]. Finally, leveraging the ability of our experimental setup to detect spin-resolved snapshots of the entire sample, we map the shot-to-shot dynamical fluctuations (i.e., the "full counting statistics") of the magnetization. These fluctuations carry clear signatures of the intrinsic non-linearity associated with KPZ hydrodynamics [226], and distinguish it from other potential mechanisms for superdiffusion such as Lévy flights [74].

18.1 Experimental system

In our experiment, we probed the transport dynamics of bosonic ^{87}Rb atoms trapped in an optical lattice; the atoms occupy the two hyperfine ground states $|\uparrow\rangle = |F = 1, m_F = -1\rangle$ and $|\downarrow\rangle = |F = 2, m_F = -2\rangle$ and their dynamics are captured by a two-species Bose-Hubbard model with on-site interaction U and tunnel coupling $\tilde{t}$. At unit filling and in the limit of strong interactions, the direct tunneling between lattice sites is suppressed and spin dynamics occur via second-order spin-exchange. The system can be mapped to the spin-1/2 XXZ model for $|\uparrow\rangle$ and $|\downarrow\rangle$ [149, 309], and, in one dimension (1D), is described by the Hamiltonian

$$\hat{H} = -J\sum_j \left(\hat{S}_j^x \hat{S}_{j+1}^x + \hat{S}_j^y \hat{S}_{j+1}^y + \Delta \hat{S}_j^z \hat{S}_{j+1}^z \right), \tag{18.1}$$

where Δ quantifies the interaction anisotropy and $J = 4\tilde{t}^2/U$ characterizes the spin-exchange coupling. In our system, the atomic scattering properties yield $\Delta \approx 1$ and the system maps to the isotropic ferromagnetic Heisenberg model.

We began our experiment by loading a spin-polarized 2D degenerate gas of approximately 2000 atoms into a square optical lattice with a spacing of $a = 532$ nm. We realized a homogeneous box potential over 50×22 sites by additionally projecting light at a wavelength of 670 nm with a digital micromirror device (DMD), preparing a Mott insulator with a filling of $n_0 = 0.93(1)$ in this box. Local spin control was realized using light at a wavelength of 787 nm on the DMD [186] to apply a site-resolved differential light shift between $|\uparrow\rangle$ and $|\downarrow\rangle$; subsequent microwave driving allowed for local flips of the spatially addressed spins.

Such quantum control enabled us to prepare spin domain walls [216, 333, 370, 334] by spatially addressing half the system. Subsequently, we prepared high-entropy states by globally rotating the spins away from the S^z-axis using a resonant microwave pulse and then locally dephasing them by projecting a site-to-site random spin-dependent potential, which we modified from shot to shot [Fig. 18.1(C)]. More precisely, our experiments focused
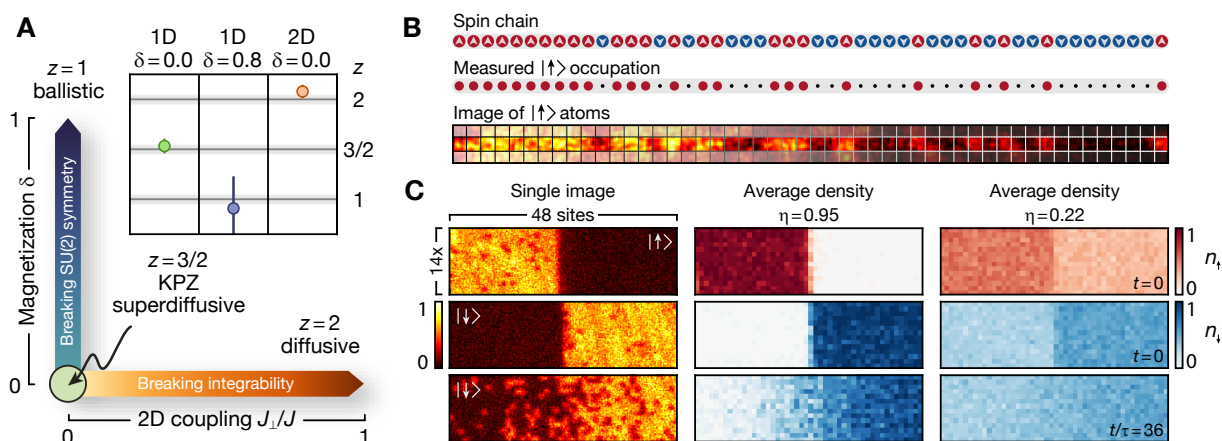
Figure 18.1: **Hydrodynamic transport in Heisenberg chains and schematic of the
experimental system. (A)** Dynamical exponents for finite-temperature Heisenberg chains.
Whereas integrable systems typically display ballistic transport (magnetized chains, $\delta >
0$), non-integrable systems are generically diffusive (2D Heisenberg model, $J_\perp > 0$). For
unmagnetized Heisenberg chains, transport is expected to fall into the KPZ universality
class with a superdiffusive exponent $z = 3/2$. Inset: By measuring polarization transfer
$P(t)$ across a domain wall, we directly observe these transport regimes: superdiffusion in
the unmagnetized case (green), ballistic transport at finite net magnetization (blue), and
diffusion in 2D (orange). Exponents are extracted by fitting $P(t) \propto t^{1/z}$; for the ballistic
case we additionally fit a vertical intercept to account for transient initial-time dynamics.
Error bars denote the standard deviation (s.d.) of the fit. **(B)** In each experimental run, we
measure the spin states of a Heisenberg chain (top) by removing one spin species (center)
and imaging the atomic site occupation (bottom). **(C)** The Heisenberg chains are realized in
a 2D atomic Mott insulator (analysis region depicted) with controllable inter-chain coupling.
Our setup allows us to prepare domain walls with high purity η (left, center column) and low
purity η (right). We measure the time evolution of both $|\uparrow\rangle$ (top) and $|\downarrow\rangle$ (center, bottom
row) atoms to extract the polarization transfer.

on tracking spin dynamics starting from a class of initial states comprising a spin domain wall with magnetization difference 2η in the middle of the spin chain: i.e., one half of the system has magnetization η and the other half of the system has magnetization $-\eta$. In the infinite-temperature limit, $\eta \to 0$, the relaxation of such states yields linear response transport coefficients, as the derivative of the spin profile is precisely the dynamical spin structure factor [333, 334].

In order to probe 1D spin dynamics in our system, we rapidly quenched the lattice depth along 1D tubes comprising 50 sites, which suddenly increased the spin-exchange coupling from zero to $J/\hbar = 64(1)\mathrm{s}^{-1}$. After tracking the spin dynamics for up to ~ 45 spin-exchange times $\tau = \hbar/J$, we removed one spin component and measured the remaining occupation via fluorescence imaging [Fig. 18.1(B)].

18.2 Superdiffusive spin transport

To explore the nature of anomalous spin transport in the 1D Heisenberg model, we initialize the spins in a high-entropy domain-wall state with $\eta = 0.22(2)$. We characterize the subsequent spin transport by measuring the polarization transfer, $P(t)$, defined as the average total number of spins that have crossed the domain wall by time t. The emergence of hydrodynamics is characterized by the power-law scaling of $P(t) \sim t^{1/z}$, and immediately enables us to extract the underlying dynamical exponent z. As depicted in Fig. 18.2(A), the data exhibit a superdiffusive exponent, $z = 1.54(7)$, consistent with KPZ scaling. By comparison, neither a diffusive ($z = 2$) nor ballistic ($z = 1$) exponent accurately capture the observed dynamics [Fig. 18.2(B)]. Somewhat surprisingly, we also observe a superdiffusive exponent of $z = 1.45(5)$ upon changing the initial state to a near-pure domain wall with $\eta = 0.95(2)$ [370, 191, 593, 74].

To further explore the superdiffusive dynamics, we investigate the spatially resolved spin profiles at $\eta = 0.22(2)$. Our experimental observations are in quantitative agreement with simulations based upon tensor-network numerical techniques [571, 593] and conform to KPZ dynamics [Fig. 18.2(A)]. Crucially, when appropriately rescaled by the dynamical exponent, all of the observed spatio-temporal profiles collapse onto a scaling form consistent with the KPZ scaling function [Fig. 18.2(C)].

18.3 Microscopic origins of superdiffusion

To understand why the combination of integrability and a non-Abelian symmetry leads to emergent superdiffusive transport, it is instructive to first consider the transport dynamics on top of a small net magnetization background [202, 203, 125, 129]. In our experiments, this corresponds to preparing domain walls with a finite overall magnetization δ, i.e. one half of the system has a magnetization $\eta + \delta$ and the other half $-\eta + \delta$. Stable quasiparticles then render spin transport ballistic [Fig. 18.1(A)], leading to a characteristic polarization-
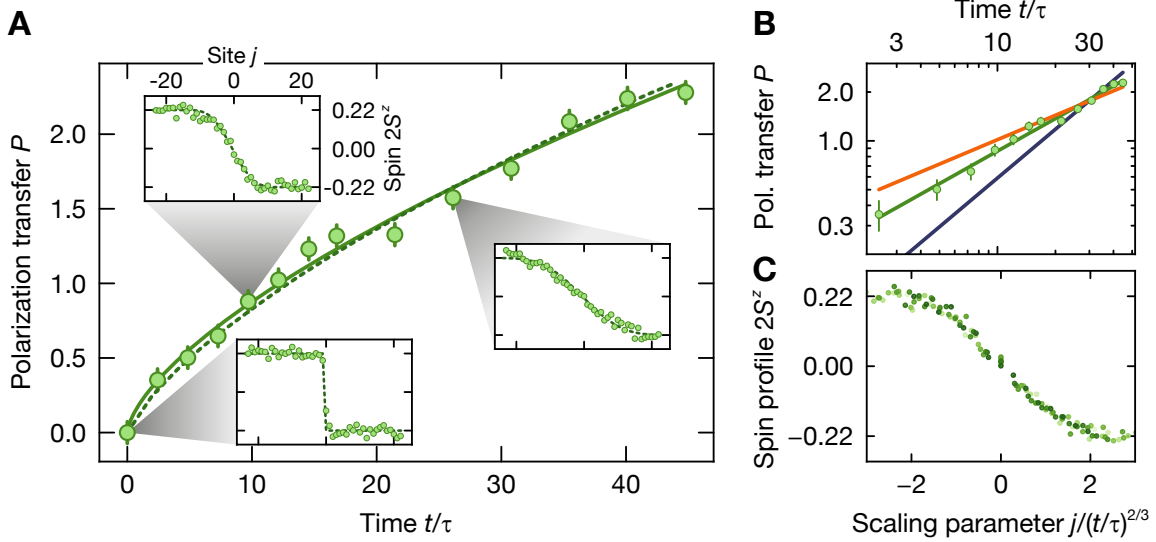
Figure 18.2: **Superdiffusive spin transport in a high-temperature Heisenberg chain.**
(A) The polarization transfer for a domain-wall initial state with a contrast of $\eta = 0.22(2)$
grows as a power law $[P(t) \propto t^{1/z}]$ with a fitted exponent $z = 1.54(7)$ (solid line), indicating
superdiffusive transport. The experimental data agrees well with numerical Heisenberg-
model simulations (dashed line). The insets show the averaged spin profiles $2S_j^z(t)$ at times
$t/\tau = 0, 10, 26$, which are compared to simulations (dashed lines). **(B)** Polarization transfer
in a double-logarithmic plot. The solid lines are power-law fits with fixed exponents, where
a distinction between $z = 3/2$ (green) and both $z = 2$ (brown) and $z = 1$ (blue) is visible.
(C) When rescaling time by the inverse dynamical exponent, the spatial spin profiles at
times $t/\tau = 5$ to 35 (light to dark green) collapse to a characteristic shape consistent with
the integrated KPZ function. Error bars denote the standard error of the mean (s.e.m).

transfer rate that scales linearly with net magnetization δ [203]. Even when $\delta = 0$ on average,
random local fluctuations of the magnetization will be present; thus, the net magnetization
in a typical region of size ℓ will scale as $1/\sqrt{\ell}$. Therefore, the average spin transport rate
across a region of size ℓ also scales as $1/\sqrt{\ell}$, implying that the transport time across the
region scales as $\ell/(1/\sqrt{\ell}) \sim \ell^{3/2}$, precisely yielding the KPZ exponent $z = 3/2$.

This intuitive analysis suggests two key requirements for superdiffusive transport: (i)
integrability ensures the presence of stable quasiparticles that move ballistically, and (ii) the
presence of a non-Abelian SU(2) symmetry makes the characteristic velocity of the ballistic
contribution to spin transport vanish. We can experimentally probe these requirements by
individually breaking either the integrability or the SU(2) symmetry of the system.

To break integrability, we turn on a finite inter-chain coupling $J_\perp$ by lowering the lat-
tice depth orthogonal to the 1D spin chains, which effectively causes the system to become
2D [528, 403]. We measure the dependence of the polarization transfer on the inter-chain
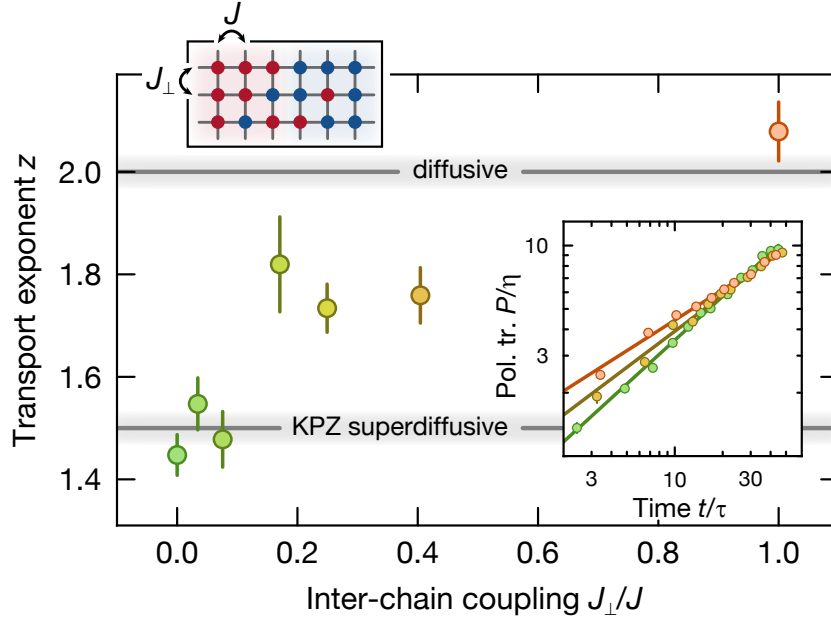
Figure 18.3: **Evolution towards diffusive transport under a breakdown of integrability.** Fitted power-law exponent z for the spin polarization transfer at different coupling strengths between individual 1D chains with initial domain walls with $\eta \approx 0.9$. Starting from superdiffusive transport in the purely 1D case, $z = 1.45(5)$, increased inter-chain coupling breaks the integrability of the system and leads to a crossover towards diffusive transport, reaching $z = 2.08(4)$ in the 2D case, as generically expected for non-integrable systems. The inset depicts the normalized polarization transfer $P(t)/\eta$ for $J_\perp/J = 0, 0.40(1)$ and $1.00(5)$ (green to orange). Error bars denote s.d. of the fit.

coupling, starting from an unmagnetized domain wall ($\eta \approx 0.9$, $\delta = 0$). As shown in Fig. 18.3, the extracted dynamical exponents exhibit a clear flow from superdiffusive transport when $J_\perp = 0$ to diffusive transport, $z = 2.08(4)$, when $J_\perp = J$. Interestingly, for $J_\perp/J \lesssim 0.1$ integrability is strictly broken but the transport dynamics remain consistent with superdiffusion within experimentally accessible timescales. This observation bolsters recent theoretical expectations, which suggest that superdiffusion can be particularly robust to perturbations that do not break the non-Abelian symmetry [128].

Next, let us explore the effect of breaking the underlying SU(2) symmetry using initial states with finite net magnetization δ. Working with an imbalanced domain-wall initial state [$\eta = 0.12(1)$, $\delta = 0.80(1)$], we observe two main differences compared to the unmagnetized ($\delta = 0$) case [Fig. 18.4(A)]. First, the polarization profile exhibits a fast ballistic component that follows the spin "light cone" of the dynamics [with a speed of $1/\tau$, dashed line in Fig. 18.4(A)]. This contribution arises from the fastest quasiparticles, which transport spin above the magnetized background [569]. Second, within this light cone, polarization spreads

substantially faster compared to the unmagnetized case; this comprises the bulk of the spin transport and is mediated by slower-moving, net-magnetization-carrying quasiparticles.

At early times, the polarization-transfer dynamics exhibit a superdiffusive power law, before crossing over to linear ballistic transport at later times. In particular, by fitting a power law to the late-time data, $t/\tau > 16$, we extract a dynamical exponent $z = 0.9(3)$, consistent with ballistic spin transport [Fig. 18.4(B)]. Although our results agree qualitatively with numerical simulations of the Heisenberg model, the magnitude of the measured polarization transfer is smaller; this can be understood as resulting from the presence of hole defects in the initial state [174]. In addition to verifying the ballistic nature of the spin dynamics, we can also directly extract the velocity of the underlying quasiparticles; by controlling the overall magnetization of the initial state, we observe the expected increase of the velocity with δ [Fig. 18.4(B)], an essential component for understanding the presence of KPZ superdiffusion in spin chains [203].

18.4 Observing KPZ hydrodynamics

Our previous observations have focused on characterizing superdiffusive spin transport; however, from the perspective of observing KPZ universality, this is insufficient, as multiple different classes of hydrodynamics can exhibit the same dynamical exponent of $z = 3/2$. To distinguish these classes, we go beyond measurements of the average polarization transfer and analyze the full distribution function of the polarization transfer $\mathrm{Pr}(P; t)$ across snapshots [226]. This distribution function can distinguish KPZ from potential alternatives such as Lévy flights: for all linear processes (such as Lévy flights or time-rescaled diffusion) the fluctuations of P at late times are necessarily symmetric about the mean; for KPZ, the limiting distribution $\mathrm{Pr}(P; t \to \infty)$ is the Tracy-Widom distribution, which is strongly asymmetric [448, 516].

Measuring the statistics of the polarization-transfer distribution therefore gives us a direct experimental observable to discern the underlying hydrodynamical transport equations; this analysis fundamentally relies on the single-shot nature and the single-spin sensitivity of our quantum-gas microscope. As we measure the occupation of a single spin species per snapshot, we approximate the polarization-transfer statistics by the statistics for the single-species atom-number transfer, $N_T^{\uparrow(\downarrow)} \approx P/2$, where $N_T^{\uparrow}$ is the number of $|\uparrow\rangle$ atoms on the side of the domain wall initialized with the opposite spin $|\downarrow\rangle$. We quantify the asymmetry of the distribution about its mean $\overline{P}$ by its skewness $(\mu_3(t) - \mu_3(0))/(\mu_2(t) - \mu_2(0))^{3/2}$, where $\mu_k(t) = \sum_P (P - \overline{P})^k \mathrm{Pr}(P; t)$ denotes the k-th central moment of the distribution.

To begin, we characterize the skewness of the polarization transfer starting from a high-purity domain wall $[\eta = 0.89(1),\ \delta = 0]$ for a 2D geometry with an inter-chain coupling strength $J_\perp/J = 0.25(1)$. The skewness of the polarization transfer distribution is overall small and is most consistent with a decay toward zero (Fig. 18.5) which corresponds to a fully symmetric distribution and which is expected for *linear* diffusive processes exhibited by the non-integrable 2D Heisenberg model.
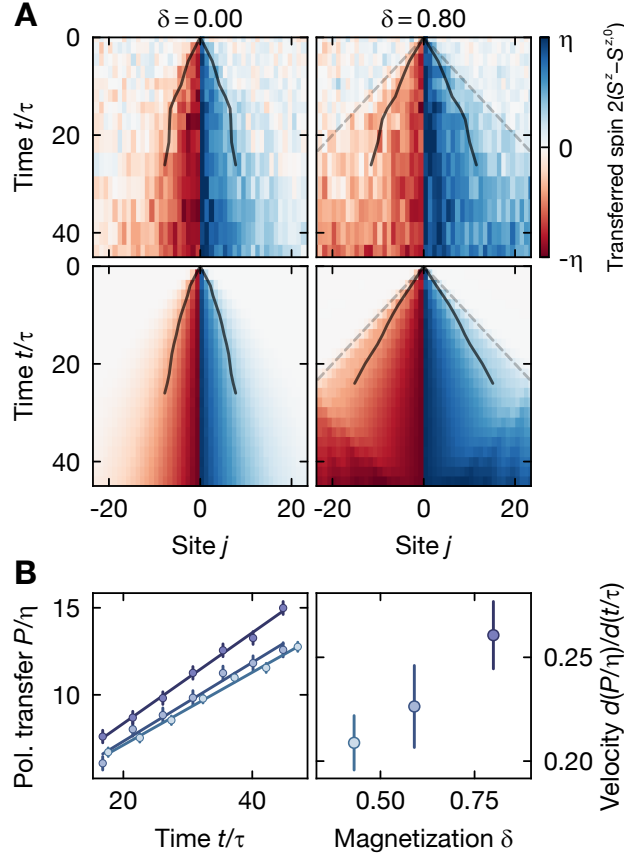
Figure 18.4: **Ballistic spin dynamics under broken SU(2) symmetry. (A)** Averaged
experimental (top) and numerical (bottom) spin profiles $S_j^z(t)$, from which the initial profile
$S_j^{z,0}$ is subtracted. (Left) Unmagnetized low-purity domain wall, $\delta = 0, \eta = 0.22(2)$ (from
Fig. 18.2). Spin transport results from the increase of the spin profile width, which scales with
the superdiffusive dynamical exponent. The black lines indicate the position j where the spin
profile crosses $|2S_j^z(t) - \delta|/\eta = 0.4$; because the profiles themselves are scale-invariant, the
position of any S^z value follows the $z = 3/2$ scaling. (Right) Magnetized domain wall, $\delta =
0.80(1), \eta = 0.12(1)$. At the outer edge the contribution of magnons is visible, transporting
spin with the speed of the spin "light cone" (dashed line), which was measured with a
quantum walk. The majority of the spin is carried by quasiparticles within the light cone,
leading to the width of the profile (solid line) growing faster than in the unmagnetized case.
The numerical simulation shows a qualitatively similar behavior. At $t/\tau \simeq 25$ the magnons
reach the system edge and are reflected. **(B)** To extract the ballistic polarization-transfer
velocity, we linearly fit the normalized polarization transfer after a crossover time, $t/\tau > 16$
(left). We observe a growth of the transfer velocity when increasing the initial domain-wall
magnetization δ (right, light to dark blue). Error bars denote s.d. of the fit.
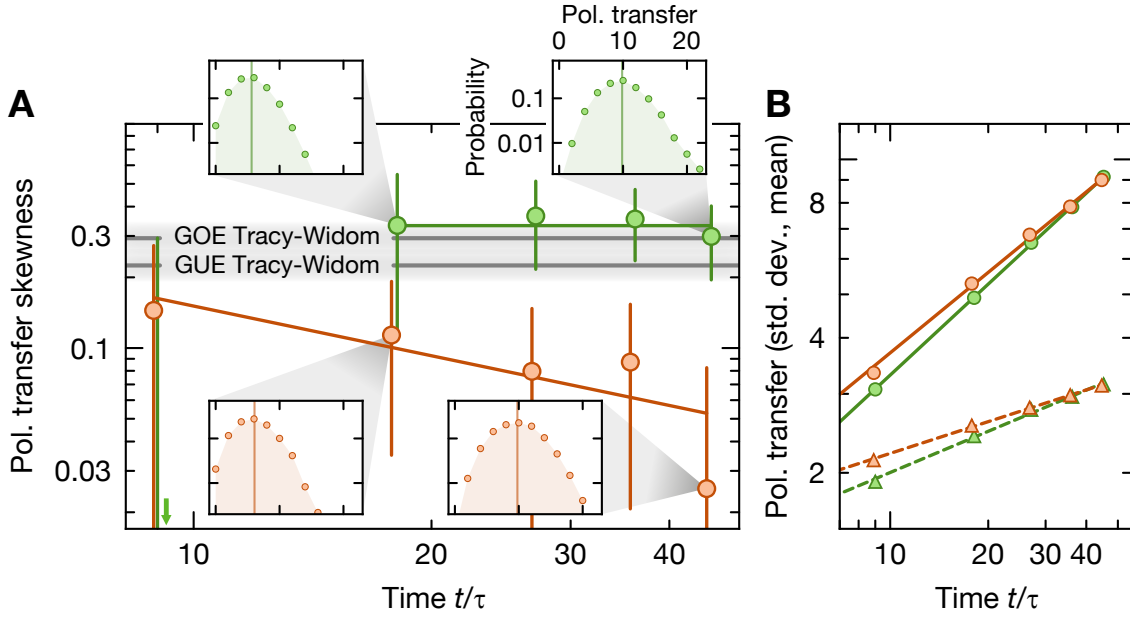
Figure 18.5: **Distribution function of polarization transfer.** **(A)** The probability
distribution asymmetry of the polarization transfer expected for KPZ transport is quantified
by the skewness. We compare the pure domain-wall dynamics in the 1D case (green) with the
non-integrable 2D case at $J_\perp/J = 0.25(1)$ (orange). Whereas the 2D case becomes symmetric
at late times, the 1D distribution remains asymmetric with a skewness of 0.33(8). Gray lines
indicate the skewness of the Gaussian-orthogonal-ensemble (GOE) and Gaussian-unitary-
ensemble (GUE) Tracy-Widom (TW) distributions [448]. Colored lines serve as guides to the
eye. (Insets) Probability distributions of the polarization transfer on a logarithmic scale. The
vertical line marks the mean of the distribution. **(B)** The mean (circles) of the polarization
transfer is consistent with the data shown in Fig. 18.3 and scales with the power-law (solid
lines) exponent $1/z = 0.67(1)$ in 1D; $1/z = 0.60(2)$ in 2D. The standard deviation (triangles)
features another characteristic transport exponent (the growth exponent [171]) which agrees
with the extracted power-law (dashed lines) exponent, $\beta = 0.31(1)$ in 1D; $\beta = 0.24(1)$ in
2D. Error bars denote the s.d. obtained from a bootstrap analysis.

If the 1D Heisenberg model is actually governed by non-linear KPZ hydrodynamics, one expects a markedly distinct behavior for the skewness as a function of time. In particular, the non-linearity of the KPZ equation would lead to a finite skewness, which is constant over time. We indeed observe that the skewness saturates to a finite value of 0.33(8) when starting from an initial state with $\eta = 0.91(2)$ and $\delta = 0$ (Fig. 18.5). In agreement with numerical simulations, this value is consistent with the skewness of the Gaussian-orthogonal-ensemble (GOE) Tracy-Widom (TW) distribution, 0.294 [448]. Directly ruling out linear transport processes, our experiment thus provides a strong indication that transport in the 1D quantum Heisenberg chain is indeed governed by KPZ hydrodynamics.

18.5 Discussion and conclusion

Our results support the theoretical conjecture that spin transport in the 1D Heisenberg model belongs to the KPZ universality class, with a superdiffusive transport exponent $z = 3/2$. We have experimentally demonstrated that both integrability and a non-Abelian symmetry are essential for stabilizing superdiffusive transport. Moreover, we exploit the single-spin sensitivity of our setup to extract the full distribution function of the polarization transfer. This distribution function exhibits a large skewness that does not decay in time, demonstrating that spin transport in this system belongs to a strongly coupled, non-linear dynamical universality class.

Our work builds and expands upon recent experimental explorations of Heisenberg-model spin dynamics. These experiments include neutron scattering studies of the quantum material KCuF$_3$ [487], as well as experiments probing the relaxation of spin-spiral initial states in ultracold gases [236, 262, 263]. In the 1D Heisenberg model, the relaxation of such spin-spiral states is non-generic because they are approximate eigenstates in the long-wavelength limit [74]. Empirically, spin spirals relax with a diffusive exponent $z = 2$. By considering a more generic family of domain-wall initial states, we are able to directly probe (and controllably move away from) the high-temperature linear-response limit where KPZ transport is conjectured to occur.

Our results open the door to a number of intriguing directions. First, the discrepancy between the relaxation of domain walls and spin spirals (away from linear response) indicates that relaxation in integrable systems is generally strongly state dependent; we lack a theory of this non-linear regime. Second, the robustness of our results along the crossover from the Heisenberg to the (non-integrable) Bose-Hubbard regime remains to be fully understood [128]. In this context, a comparison between the non-integrable Bose-Hubbard model and the integrable Fermi-Hubbard model [174] could be of particular interest. Finally, the observable we introduced to capture fluctuation effects—namely, the statistics of single shots of the polarization transfer—promises to be a powerful diagnostic tool for new phases of interacting quantum systems. This observable demonstrates the importance of experiments for the understanding more subtle transport dynamics. Although it is very difficult to compute analytically or numerically (except for specific models), the direct access to the full-counting

statistics in the quantum gas microscope makes the study a quantity natural to consider. This suggests that there exist other quantities that can provide new insights, and whose dynamics may be important to understand the hydrodynamics of the system.

More fundamentally, resolving and studying the properties of more complicated observables will be necessary steps in building an understanding of emergence of hydrodynamics; fortunately developments in quantum simulation platforms are helping in making this goal a reality by providing important clues for a future theoretical framework.

Chapter 19

Probing many-body noise in a strongly interacting two-dimensional dipolar spin system

Although one of the gold standards for atomic, molecular and optical experiments is the ability to prepare, isolate and control quantum degrees of freedom (or qubits) [454, 298, 554, 243, 133, 479, 79, 294, 544, 21, 234, 297, 307, 482, 96, 497, 371, 245], in most physical settings, the presence of a bath is not only a nuisance but also crucial to understand the system's dynamics. Whether the bath simply generates random, stochastic modifications to the qubit's Hamiltonian, or whether the qubit and bath can entangle with with another via coherent interactions, the end result is the same: even if the qubit starts in a pure, coherent quantum state, it inevitably approaches an incoherent mixed state—this process is known as decoherence. While a large effort goes into engineering quantum systems where the qubit is not affected by the presence of the outside world [298, 554, 243, 133, 479, 294, 544, 564], a complementary perspective embraces the presence of the bath and instead uses the qubit's *decoherence dynamics* to uncover properties of a strongly interacting bath [21, 234, 297, 307, 482, 96, 497, 17, 239, 79]. Under this perspective, the previously nefarious bath now becomes the strongly interacting system of interest. Discerning the extent to which the "many-body noise" can provide insights into transport dynamics, low-temperature order, and generic correlation functions of an interacting system remains an essential open question [90, 291].

In this chapter, we theoretically and experimentally tackle this question, studying how the decoherence dynamics of a probe qubit depends on the properties of its bath—in this case, a large ensemble of disordered and strongly-interacting spins.

Such an approach has immediate benefits: by mapping the dynamics of a system onto the decoherence of a probe, one avoids the exponential complexity typically associated with many-body tomography [16, 212]. Although this efficiency directly implies that one is able to gather less information, recent work has demonstrated that many-body noise spectroscopy can still provide important insight into a diverse array of physical phenomena, ranging from Cooper-paired superfluidity to quantum criticality and many-body localization [360, 17, 94,

239, 172, 68, 469, 235].

On the experimental front, probing the noise generated by a many-body system has a long tradition in the context of magnetic resonance spectroscopy [21, 234, 297, 307, 482, 96, 497]. Indeed, seminal work exploring the decoherence of paramagnetic defects in solids revealed the importance of many-body noise arising from strong dipolar interactions [21, 234, 297, 307, 482, 96, 497, 175]. Building upon this body of work, we start by presenting a theoretical framework which both unifies and generalizes existing results regarding the decoherence of a probe coupled to a strongly-interacting, many-body system. In addition to solid-state spin systems, our framework naturally applies to a broader class of quantum simulation platforms, including trapped ions [67, 268], Rydberg atoms [599, 598, 59], and ultracold polar molecules [402].

Our framework predicts a non-trivial temporal profile for the average coherence of probe spins, which exhibits a crossover between two distinct stretched exponential decays [Fig. 19.1] [21, 234, 297, 175, 307, 482, 96, 497]. Crucially, we demonstrate—both theoretically and experimentally—that the associated stretch powers contain a wealth of information about both the static and dynamical properties of the many-body spin system. We focus on three particular properties. First, the stretch power can distinguish between different forms of spectral diffusion, shedding light on the nature of local spin fluctuations. Second, the crossover in time between different stretch powers allows one to extract the many-body system's correlation time. Finally, the stretch power also contains direct signatures about the dimensionality and disorder intrinsic to the system.

This last point is particularly relevant given near-term prospects for engineering the dimensionality of spin systems embedded in solid-state platforms [407, 357, 155].

Indeed, while prior work in the solid-state has focused on dipolar spin ensembles in three dimensions [21, 234, 297, 175, 307, 482, 96, 497, 100], recent advances in material growth techniques have enabled the creation of two-dimensional *layers* of optically-active spin defects [407, 357, 155]. By combining nitrogen delta-doping during growth with local electron irradiation [407, 357, 155], we fabricate a diamond sample (S1) where paramagnetic defects are confined to a thin layer [Figs. 19.1(a,b)]. This layer contains a hybrid spin system consisting of two types of defects: spin-1 nitrogen-vacancy (NV) centers and spin-1/2 substitutional nitrogen (P1) centers. The dilute NV centers can be optically initialized and read out, making them a natural probe of the many-body noise generated by the strongly-interacting P1 centers.

Even once created, the non-destructive, *in situ* characterization of the effective "dimensionality" of our sample (i.e. whether the average spin-spin spacing is larger than the thickness of the layer) is challenging with conventional methods. To this end, we demonstrate how the decoherence dynamics of NV probes can be used to prove the two-dimensional nature of the P1 ensemble; we compare these results to measurements on a conventional three-dimensional ensemble.

Next, we show that the stretch power of the NV centers' coherence decay also reveals information about the nature of the many-body noise generated by the P1 system [234, 297, 482]. In particular, we demonstrate that the spin-flip dynamics are inconsistent with
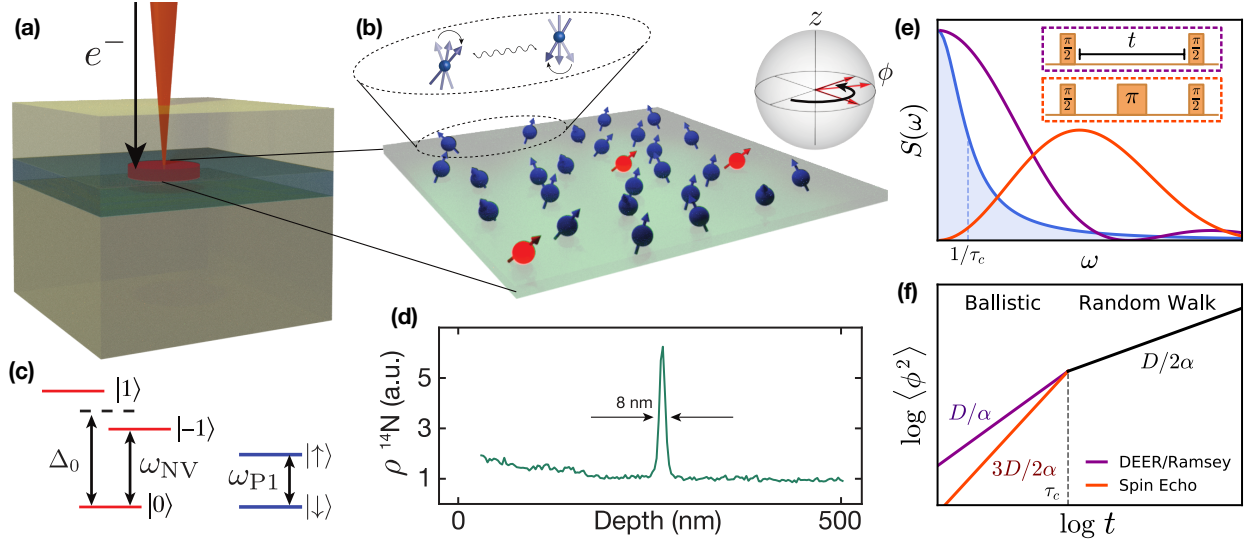
Figure 19.1: **Schematic of the different ingredients in our analysis of decoherence dynamics. (a)** A delta-doped layer of ^{14}N (green) is grown on a diamond substrate. NV centers are created via local electron irradiation (orange beam) and subsequent high-temperature annealing. **(b)** Schematic depiction of a two-dimensional layer of NV (red) and P1 (blue) centers. Dilute NV centers function as probe spins of the dense, disordered P1 system. The P1s exhibit spin-flip dynamics driven by magnetic dipole-dipole interactions (zoom). Ising interactions with the P1 system cause the NV to accumulate phase, ϕ, during noise spectroscopy (Bloch sphere). **(c)** NV and P1 level structure in the presence of a magnetic field, B, applied along the NV axis. We work within an effective spin-1/2 subspace of the NV center, $\{|0\rangle, |-1\rangle\}$, with level splitting, ω_{NV}. The corresponding P1 splitting, ω_{P1}, is strongly off-resonant from the NV transition. **(d)** Secondary ion mass spectrometry (SIMS) measurement of the density of ^{14}N as a function of depth for sample S1. The presence of a 2D layer is indicated by a sharp Nitrogen peak with a SIMS-resolution-limited 8 nm width. **(e)** The overlap between the many-body spectral function (blue) and the power spectrum of the filter function $|f(\omega; t)|^2$ determines the variance of the phase $\sim \chi$ [Eq. 19.2]. $|f(\omega; t)|^2$ for both a Ramsey/DEER pulse sequence (purple) and a spin echo pulse sequence (orange) are shown. **(f)** Schematic depiction of the variance of the phase, $\langle \phi^2 \rangle = -2\log C(t)$, as a function of the measurement duration t, for both Ramsey/DEER (purple) and spin echo (orange). The labeled slopes indicate the predicted stretch powers in both the early-time ballistic regime and the late-time random-walk regime [Table 19.1]; the crossover occurs at the correlation time, τ_c.

the conventional expectation of telegraph noise, but rather follow that of a Gauss-Markov
process [Table 19.1].

Finally, we actively control the noise spectral density of the many-body P1 system via
polychromatic driving [266]. In particular, we directly tune the correlation time of the P1
system and measure a corresponding change in the crossover timescale between coherent and
incoherent spin dynamics [196, 482].

19.1 Theoretical framework for decoherence dynamics induced by many-body noise

Let us begin by providing a framework for understanding the decoherence dynamics of probe
spins coupled to an interacting many-body system [21, 297, 246, 482, 175, 116, 136, 564,
307]—for additional details see Appendix E. The dynamics of a single probe spin gener-
ically depend on three properties: (i) the nature of the system-probe coupling,[1] (ii) the
system's many-body Hamiltonian H_{int}, and (iii) the measurement sequence itself. Crucially,
by averaging across the dynamics of many such probe spins, one can directly extract global
features of the many-body system [Fig. 19.1(b)]. We distinguish between two types of en-
semble averaging which give rise to distinct signatures in the decoherence: (i) an average
over *many-body trajectories* (i.e. both spin configurations and dynamics) yields informa-
tion about the microscopic spin fluctuations (for simplicity, we focus our discussion on the
infinite-temperature limit (i.e random locations of the system's spins) yields information
about both dimensionality and disorder.[2]), (ii) an average over *positional randomness*

To be specific, let us consider a single spin-1/2 probe coupled to a many-body ensemble
via long-range, $1/r^\alpha$ Ising interactions:

$$H_z = \sum_i \frac{J_z}{r_i^\alpha} \hat{s}_p^z \hat{s}_i^z, \tag{19.1}$$

where r_i is the distance between the probe spin $\hat{s}_p$ and the i-th system spin s_i.[3] Such
power-law interactions are ubiquitous in solid-state, atomic and molecular quantum plat-
forms (e.g. RKKY interactions, electric/magnetic dipolar interactions, van der Waals inter-
actions, etc.) [113, 479, 100, 67].

Physically, the system's spins generate an effective magnetic field at the location of the
probe (via their Ising interactions), which can be measured via Ramsey spectroscopy [inset,
Fig. 19.1(e)] [497]. In particular, we envision initially preparing the probe in an eigenstate
of $\hat{s}_p^z$ and subsequently rotating it with a $\pi/2$-pulse such that the normalized coherence,

---

[1]Although we have been explicitly distinguishing between the probe and the system, we note that our
framework also applies to the scenario where the probe itself is a part of the many-body system.

[2]The analysis is easily extended to finite temperature, but subtleties arise for low-temperature ordered
states.

[3]The Ising coupling J_z implicitly includes any angular dependence of e.g. dipolar interactions.

$C \equiv 2\langle \hat{s}_p^x \rangle = 1$. The magnetic field, which fluctuates due to many-body interactions, causes the probe to Larmor precess [inset, Fig. 19.1(b, e)]. The phase associated with this Larmor precession can be read out via a population imbalance, after a second $\pi/2$ pulse.

Average over many-body trajectories

For a many-body system at infinite temperature, $C(t) = 2\text{Tr}[\rho(t)s_p^x]$, where $\rho(t)$ is the full density matrix that includes both the system and the probe.[4] Let us treat $\hat{s}_i^z(t) \to s_i^z(t)$ as a classical, stochastic random variable, whose dynamics are determined by H_{int} (e.g. coherent flip-flop interactions $\hat{s}_i^+ \hat{s}_j^-$). In this case, the phase of the aforementioned Larmor precession is given by $\phi(t) = \int_0^t dt' \, J_z \sum_i s_i^z(t')/r_i^\alpha$. Assuming that $\phi(t)$ is Gaussian-distributed, one finds that the average probe coherence decays exponentially as $C(t) = \langle e^{-i\phi(t)} \rangle = e^{-\langle \phi^2 \rangle/2}$, where $\langle \phi^2 \rangle \sim \sum_i J_z^2 \chi(t)/r_i^{2\alpha}$ [234, 221, 133, 564]. Here, $\chi(t)$ encodes the response of the probe spins to the noise spectral density, $S(\omega)$, of the many-body system:

$$\chi(t) \equiv \int d\omega \, |f(\omega;t)|^2 S(\omega), \tag{19.2}$$

where $f(\omega;t)$ is the filter function associated with a particular pulse sequence (e.g. Ramsey spectroscopy or spin echo) of total duration t [Fig. 19.1(e)] [117, 563].

Intuitively, $S(\omega)$ quantifies the noise power density of spin flips in the many-body system; it is the Fourier transform of the autocorrelation function, $\xi(t) \equiv 4 \langle s_i^z(t)s_i^z(0) \rangle$, and captures the spin dynamics at the level of two-point correlations [299]. For Markovian dynamics, $\xi(t) = e^{-|t|/\tau_c}$, where τ_c defines the correlation time after which a spin, on average, retains no memory of its initial orientation.[5] In this case, $S(\omega)$ is Lorentzian and one can derive an analytic expression for χ [246, 196, 482, 175, 563].[6]

A few remarks are in order. The premise that many-body Hamiltonian dynamics produce Gaussian-distributed phases $\phi(t)$—while oft-assumed—is challenging to analytically justify [366, 297, 96, 482, 578]. Indeed, a well-known counterexample of non-Gaussian spectral diffusion occurs when the spin dynamics can be modeled as telegraph noise – i.e. stochastic jumps between discrete values $s_i^z = \pm s_i$ [96, 8]; the precise physical settings where such noise emerges remains the subject of active debate [366, 297, 96, 606, 196, 8, 607, 137, 577, 563, 38, 221, 133].

Average over positional randomness

The probe's decoherence depends crucially on the spatial distribution of the spins in the many-body system. For disordered spins, explicitly averaging over their random positions

---

[4]The full density matrix $\rho(t)$ includes both the system and the probe, and is time-evolved under the system interactions H_{int}, the probe-system coupling H_z, and the measurement pulse sequence.

[5]Note that the Markovian assumption is not necessarily valid for a many-body system at early times or for certain forms of interactions [136].

[6]In general, χ can be computed numerically for an arbitrary spectral function $S(\omega)$.

yields a decoherence profile:

$$C(t) = \int \prod_{i=1}^{N} \frac{d^D r_i}{V} \exp\left[\frac{-J_z^2 \chi(t)}{2r_i^{2\alpha}}\right] = e^{-an[J_z^2 \chi(t)]^{D/2\alpha}}, \qquad (19.3)$$

where a is a dimensionless constant, N is the number of system spins in a D-dimensional volume V at a density $n \equiv N/V$ [175]. By contrast, for spins on a lattice or for a single probe spin, the exponent of the coherence scales as $\sim J_z^2 \chi(t)$. A particularly elegant intuition, based upon resonance-counting, underlies the appearance of both the dimensionality and the interaction power-law in Eq. 19.3. Roughly, let us say that a probe spin is only coupled to system spins that induce a phase variance larger than some cutoff ϵ. This constraint on the minimum variance defines a volume of radius $r_{\max} \sim (J_z^2 \chi(t)/\epsilon)^{1/2\alpha}$ containing $N_s \sim n r_{\max}^D$ spins, implying that the total variance accrued at any given time is $\epsilon N_s \sim [J_z^2 \chi(t)]^{D/2\alpha}$. Thus, the positional average simply serves to count the number of spins to which the probe is coupled.

Decoherence profile

The functional form of the probe's decoherence, $C(t)$, encodes a number of features of the many-body system. We begin by elucidating them in the context of Ramsey spectroscopy. First, one expects a somewhat sharp cross-over in the behavior of $C(t)$ at the correlation time τ_c. For early times, $t \ll \tau_c$, the phase variance accumulates as in a ballistic trajectory with $\chi \sim t^2$, while for late times, $t \gg \tau_c$, the variance accumulates as in a random walk with $\chi \sim t$ [21, 246, 482]. This leads to a simple prediction: namely, that the stretch-power, β, of the probe's exponential decay (i.e. $-\log C(t) \sim t^\beta$) changes from D/α to $D/2\alpha$ at the correlation time [Fig. 19.1(f)].

Second, by considering other filter functions (i.e. moving away beyond Ramsey), one can probe even more subtle properties of the many-body noise. In particular, a spin-echo sequence filters out the leading order DC contribution from the many-body noise spectrum, allowing one to investigate higher-order correlation functions of the spin-flip dynamics. Different types of spin-flip dynamics naturally lead to different phase distributions. For the case of Gaussian noise, one finds that (at early times) $\chi \sim t^3$; however, in the case of telegraph noise the analysis is more subtle, since higher-order moments of $\phi(t)$ must be taken into account. This leads to markedly different early time predictions for β—dependent on both the measurement sequence as well as the many-body noise [Table 19.1].

At late times, however, one expects the probe's coherence to agree across different pulses sequences and spin-flip dynamics. For example, in the case of spin-echo, the decoupling π-pulse [inset, Fig. 19.1(e)] is ineffective on timescales larger than the correlation time, since the spin configurations during the two halves of the free evolution are completely uncorrelated. Moreover, this same loss of correlation implies that the phase accumulation is characterized by incoherent Gaussian diffusion regardless of the specific nature of the spin dynamics (e.g. Markovian versus non-Markovian, or continuous versus telegraph).
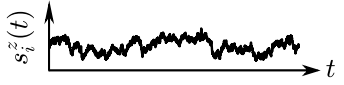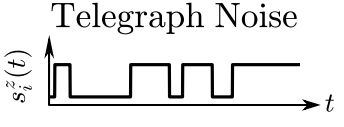
Many-Body Noise Properties	Measurement Sequence	Early-time (ballistic regime) stretch power	Late-time (random walk regime) stretch power
Gauss − Markov Noise	DEER/Ramsey	D/α	$D/2\alpha$
	Spin Echo	$3D/2\alpha$	$D/2\alpha$
Telegraph Noise	DEER/Ramsey	D/α	$D/2\alpha$
	Spin Echo	$1 + D/\alpha$	$D/2\alpha$

Table 19.1: **Stretch-power of decoherence dynamics for different measurement schemes and noise models.** Predicted early and late-time stretch powers of the probe spin decoherence profile when coupled to a $D-$dimensional system via power-law Ising interactions $\sim 1/r^\alpha$. We distinguish between Gaussian and telegraph spin-flip noise in the many-body system, which gives rise to different predictions for the early-time spin echo stretch power.

19.2 Experimentally probing many-body noise in strongly-interacting spin ensembles

Our experimental samples contain a high density of spin-1/2 P1 centers [blue spins, Fig. 19.1(b)], which form a strongly-interacting many-body system coupled via magnetic dipole-dipole interactions:

$$H_{\text{int}} = \sum_{i<j} \frac{J_0}{r_{ij}^3} \left[c_{ij}(\hat{s}_i^+ \hat{s}_j^- + \hat{s}_i^- \hat{s}_j^+) + \tilde{c}_{ij}\hat{s}_i^z \hat{s}_j^z \right], \tag{19.4}$$

where $J_0 = 2\pi \times 52$ MHz·nm^3, r_{ij} is the distance between P1 spins i and j, and $c_{ij}, \tilde{c}_{ij}$ capture the angular dependence of the dipolar interaction. We note that H_{int} contains only the energy-conserving terms of the dipolar interaction [616].

The probes in our system are spin-1 NV centers, which can be optically initialized to $|m_s = 0\rangle$ using 532 nm laser light. An applied magnetic field along the NV axis splits the $|m_s = \pm 1\rangle$ states, allowing us to work within the effective spin-1/2 manifold $\{|0\rangle, |-1\rangle\}$. Microwave pulses at frequency ω_{NV} are used to perform coherent spin rotations (i.e. for Ramsey spectroscopy or spin echo) within this manifold [Fig. 19.1(c)].

Physically, the NV and P1 centers are also coupled via dipolar interactions. However, for a generic magnetic field strength, they are highly detuned, i.e. $|\omega_{\text{NV}} - \omega_{\text{P1}}| \sim$ GHz, owing to the zero-field splitting of the NV center ($\Delta_0 = 2\pi \times 2.87$ GHz) [Fig. 19.1(c)]. Since typical interaction strengths in our system are on the order of $\sim$ MHz, the direct polarization
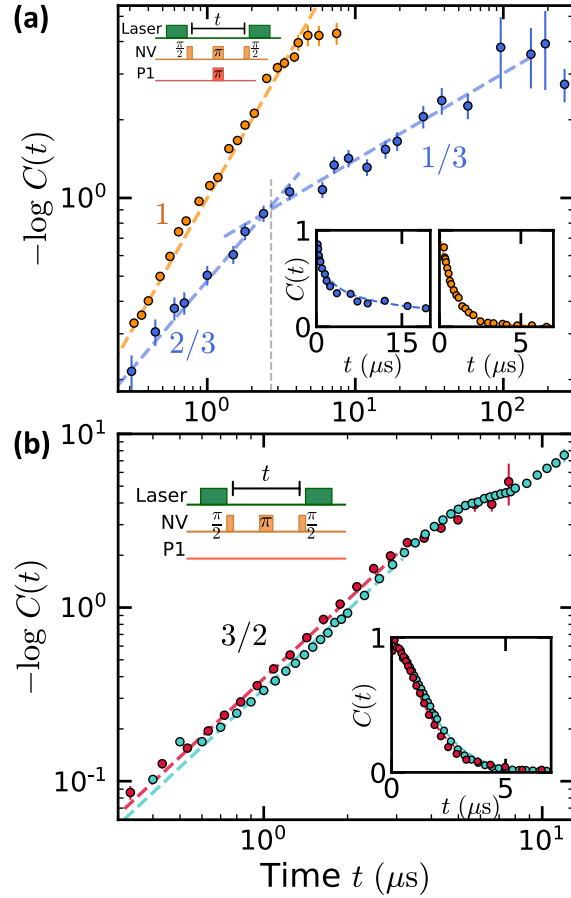
Figure 19.2: **Dimensionality dependence of decoherence dynamics. (a)** Depicts the normalized coherence for a DEER measurement on sample S1 (blue) and sample S2 (yellow) as a function of the free evolution time t. Dashed blue lines indicate the predicted early- and late-time stretch powers of 2/3 and 1/3, respectively, for a dipolar spin system in two dimensions. Dashed yellow line depicts the predicted early-time stretch power of 1 for a dipolar spin system in three dimensions [Table 19.1]. Together, these data demonstrate the two- and three-dimensional nature of samples S1 and S2, respectively. Lower right insets show the same data on a linear scale. Top left inset shows the DEER pulse sequence. **(b)** Spin echo measurements on three-dimensional dipolar spin ensembles in samples S3 (teal) and S4 (pink) clearly exhibit a stretch power of 3/2 (dotted lines) over nearly two decades in time. This is consistent with the presence of Gaussian noise and allows one to explicitly rule out telegraph noise. Lower right inset shows the same data on a linear scale. Top left inset shows the spin echo pulse sequence.

exchange between an NV and P1 is strongly off-resonant. This reduces the dipolar interaction between NV and P1 centers to a system-probe Ising coupling of precisely the form given by Eq. 19.1 with $\alpha = 3$.

19.3 Delta-doped sample fabrication

Sample S1 was grown via homoepitaxial plasma-enhanced chemical vapor deposition (PECVD) using isotopically purified methane (99.999% ^{12}C) [407]. The delta-doped layer was formed by introducing natural-abundance nitrogen gas during growth (5 sccm, 10 minutes) in between nitrogen-free buffer and capping layers. To create the vacancies necessary for generating NV centers, the sample was electron-irradiated with a transmission electron microscope set to 145 keV [357] and subsequently annealed at 850° C for 6 hours.

19.4 Two-dimensional spin dynamics

We begin by performing double electron-electron resonance (DEER) measurements on sample S1. While largely analogous to Ramsey spectroscopy [Table 19.1],[7] DEER has the technical advantage that it filters out undesired quasi-static fields (e.g. from hyperfine interactions between the NV and host nitrogen nucleus) [497, 134, 155]. As shown in Fig. 19.2(a) [blue data, inset], the NV's coherence decays on a time scale ~ 5 μs.

To explore the functional form of the probe NV's decoherence, we plot the negative logarithm of the coherence, $-\log C(t)$, on a log-log scale, such that the stretch power, β, is simply given by the slope of the data. At early times, the data exhibit $\beta = 2/3$ for over a decade in time [blue data, Fig. 19.2(a)]. At a timescale ~ 3 μs (vertical dashed line), the data crosses over to a stretch power of $\beta = 1/3$ for another decade in time. This behavior is in excellent agreement with that expected for two-dimensional spin dynamics driven by dipolar interactions [Fig. 19.1(f), Table 19.1].

Finally, for comparison, we perform DEER spectroscopy on a conventional three-dimensional NV-P1 system (sample S2). As shown in Fig. 19.2(a) (orange), the data exhibit $\beta = 1$ for a decade in time, consistent with the prediction for three-dimensional dipolar interactions [Table 19.1]. However, the crossover to the late-time "random walk" regime is difficult to experimentally access because the larger early-time stretch power causes a faster decay to the noise floor.

19.5 Characterizing microscopic spin-flip dynamics

To probe the nature of the microscopic spin-flip dynamics in our system, we perform spin-echo measurements on three dimensional samples [S3, S4 (Type IB)], which exhibit a significantly

---

[7]We note that this is the case for dense P1 ensembles where the NV's Ramsey signal is dominated by the P1 bath.

higher P1-to-NV density ratio. For lower relative densities (i.e. samples S1 and S2), the spin echo measurement contains a confounding signal from interactions between the NVs themselves (see Methods).

In both samples (S3, S4), we find that the coherence exhibits a stretched exponential decay with $\beta = 3/2$ for well over a decade in time [Fig. 19.2(b)]. Curiously, this is consistent with Gaussian spectral diffusion where $\beta = 3D/2\alpha = 3/2$ and patently inconsistent with the telegraph noise prediction of $\beta = 1 + D/\alpha = 2$. While in agreement with prior measurements on similar samples [38], this observation is actually rather puzzling and related to an enduring question in the context of dipolar spin noise [21, 234, 297, 175, 307, 482, 96, 497, 100].

In particular, one naively expects that spins in a strongly-interacting system should be treated as stochastic binary variables, thereby generating telegraph noise; for the specific case of dipolar spin ensembles, this expectation dates back to seminal work from Klauder and Anderson [297]. The intuition behind this is perhaps most easily seen in the language of the master equation—each individual spin sees the remaining system as a Markovian bath. The resulting local spin dynamics is then characterized by a series of stochastic quantum jumps, giving rise to telegraph noise. Alternatively, in the Heisenberg picture, the same intuition can be understood from the spreading of the operator $\hat{s}_i^z$; this spreading hides local coherences in many-body correlations, leading to an ensemble of telegraph-like, classical trajectories.

We conjecture that the origin of Gaussian spectral diffusion in our system is related to the presence of disorder, which strongly suppresses operator spreading [579]. To illustrate this point, consider the limiting case where the operator dynamics are constrained to a single spin. In this situation, the dynamics of $\hat{s}_i^z(t)$ follows a particular coherent trajectory around the Bloch sphere, and the rate at which the probe accumulates phase is continuous. Averaging over different trajectories of the coherent dynamics naturally leads to Gaussian noise.

19.6 Controlling the many-body spectral function

Finally, we demonstrate the ability to directly control the many-body noise spectrum for both two- and three-dimensional dipolar spin ensembles (i.e. samples S1, S2). In particular, we engineer the shape and linewidth of $S(\omega)$ by driving the P1 system with a polychromatic microwave tone [266]. This drive is generated by adding phase noise to the resonant microwave signal at ω_{P1} in order to produce a Lorentzian drive spectrum with linewidth $\delta\omega$ [Fig. 19.3(c)].

Microscopically, the polychromatic drive leads to a number of physical effects. First, tuning the Rabi frequency, Ω, of the drive provides a direct knob for controlling the correlation time, τ_c, of the P1 system. Second, since the many-body system inherits the noise spectrum of the drive, one has provably Gaussian statistics for the spin variables s_i^z. Third, our earlier Markovian assumption is explicitly enforced by the presence of a Lorentzian noise spectrum. Taking these last two points together allows one to analytically predict the precise form of
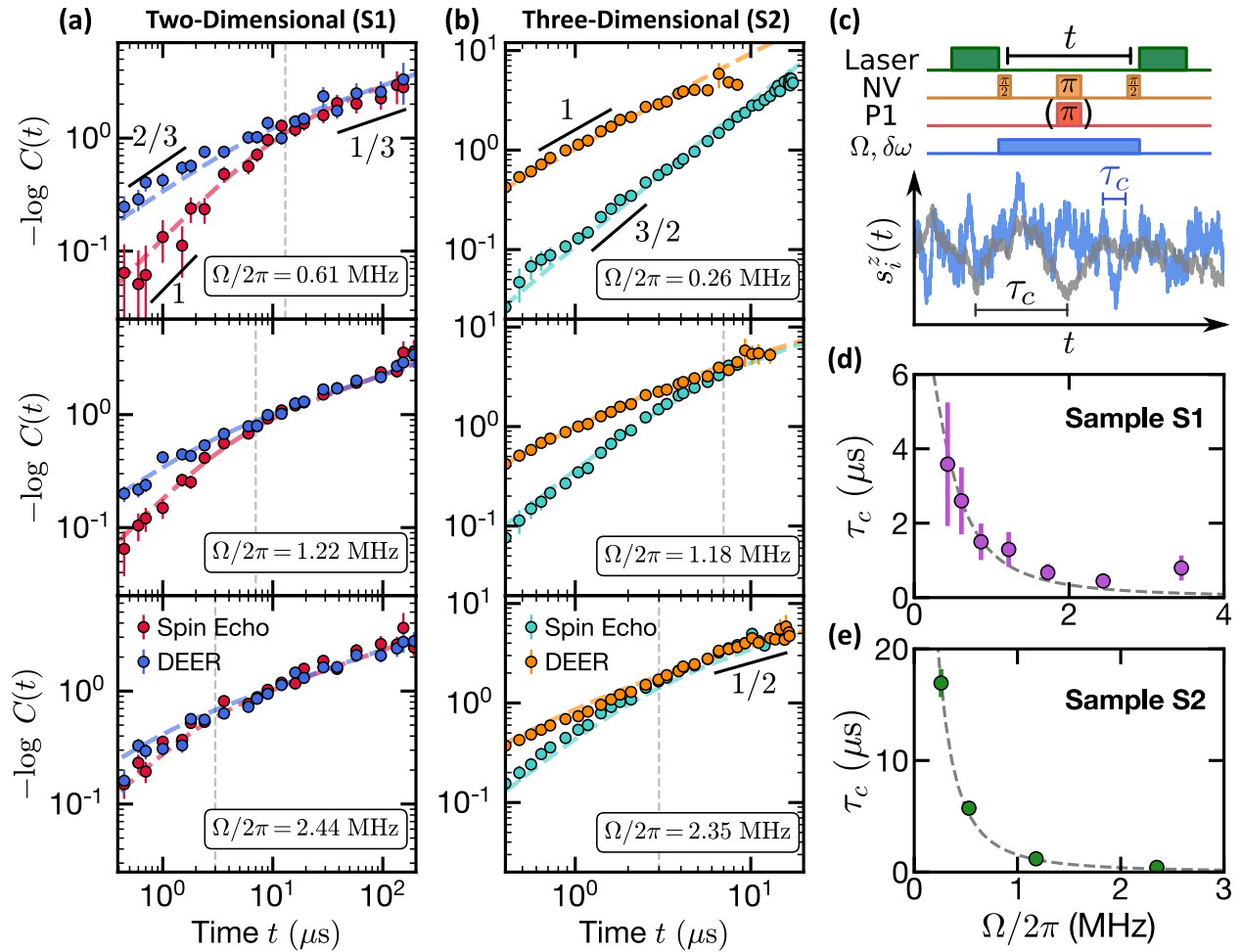
Figure 19.3: **Effect of an external drive on the noise of the spin ensemble.** **(a,b)** Measurements of DEER (blue, orange) and spin echo (red, teal) on two- and three-dimensional samples (S1, S2) for different powers of the polychromatic (i.e. incoherent) drive at fixed linewidth $\delta\omega = 2\pi \times (18, 20)$ MHz, respectively. The time at which the two signals overlap (vertical dashed lines) functions as a proxy for the correlation time and decreases as the power of the incoherent driving increases (top to bottom panels). The data is well-fit by analytic expressions for $\chi^{D/2\alpha}$ [Eq. 19.5] (dashed curves). **(c)** An incoherent drive field (light blue) with power $\sim \Omega^2$ and linewidth $\delta\omega$ is applied to the P1 spins during the free evolution time t of both DEER and spin echo sequences in order to tune the correlation time of the many-body system. In this case, $s_i^z(t)$ evolves as a Gaussian random process. **(d,e)** The correlation times, τ_c, extracted from fitting the data to Eq. 19.5 for samples S1 (purple) and S2 (green) are plotted as a function of Ω, and agree well with a simple theoretical model (dashed black curves).

the NV probe's decoherence profile, $-\log C(t) \sim \chi(t)^{D/2\alpha}$, for either DEER or spin-echo spectroscopy:

$$
\begin{aligned}
\chi^{\text{DEER}}(t) &= 2\tau_c t - 2\tau_c^2(1 - e^{-\frac{t}{\tau_c}}), \\
\chi^{\text{SE}}(t) &= 2\tau_c t - 2\tau_c^2(3 + e^{-\frac{t}{\tau_c}} - 4e^{-\frac{t}{2\tau_c}}).
\end{aligned}
\tag{19.5}
$$

We perform both DEER and spin-echo measurements as a function of the power ($\sim \Omega^2$) of the polychromatic drive for our two-dimensional sample (S1) [Fig. 19.3(a)]. As expected, for weak driving [top, Fig. 19.3(a)], the DEER signal (blue) is analogous to the undriven case, exhibiting a cross-over from a stretch power of $\beta = 2/3$ at early times to a stretch power of $\beta = 1/3$ at late times. For the same drive strength, the spin echo data (red) also exhibits a cross over between two distinct stretch powers, with the key difference being that $\beta = 3D/2\alpha = 1$ at early times. This represents an independent (spin-echo-based) confirmation of the two-dimensional nature of our delta-doped sample.

Recall that at late times (i.e. $t \gtrsim \tau_c$), one expects the NV's coherence $C(t)$ to agree across different pulses sequences [Fig. 19.1(f)]. This is indeed borne out by the data [Fig. 19.3]. In fact, the location of this late-time overlap provides a proxy for estimating the correlation time and is shown as the dashed grey lines in Fig. 19.3(a). As one increases the power of the drive [Fig. 19.3(a)], the noise spectrum, $S(\omega)$, naturally broadens. In the data, this manifests as a shortened correlation time, with the location of the DEER/echo overlap shifting to earlier time-scales [Fig. 19.3(a)].

Analogous measurements on a three dimensional spin ensemble (sample S2), reveal much the same physics [Fig. 19.3(b)], with stretch powers again consistent with a Gauss-Markov prediction [Table 19.1]. For weak driving, $C(t)$ is consistent with the early-time ballistic regime for over a decade in time [Fig. 19.3(b), top panel]; however, it is difficult to access late enough time-scales to observe an overlap between DEER and spin echo. Crucially, by using the drive to push to shorter correlation times, we can directly observe the late-time random-walk regime in three dimensions, where $\beta = 1/2$ [Fig. 19.3(b), bottom panel].

Remarkably, as evidenced by the dashed curves in Figs. 19.3(a,b), our data exhibits excellent agreement—across different dimensionalities, drive strengths, and pulse sequences—with the analytic predictions presented in Eq. 19.5. Moreover, by fitting $\chi^{D/2\alpha}$ simultaneously across spin echo and DEER datasets for each Ω, we quantitatively extract the correlation time, τ_c. Up to an $\mathcal{O}(1)$ scaling factor, we find that the extracted τ_c agrees well with the DEER/echo overlap time. In addition, the behavior of τ_c as a function of Ω, also exhibits quantitative agreement with an analytic model that predicts $\tau_c \sim \delta\omega/\Omega^2$ in the limit of strong driving [Fig. 19.3(d,e)].

Finally, we emphasize that although one observes $\beta = 3D/2\alpha$ in both the driven [Figs. 19.3(a,b)] and undriven [Fig. 19.2(b)] spin echo measurements, the underlying physics is extremely different. In the latter case, Gaussian spectral diffusion emerges from isolated, disordered, many-body dynamics, while in the former case, it is imposed by the external drive.

19.7 Conclusion and outlook

Our results demonstrate the diversity of information that can be accessed via the decoherence dynamics of a probe spin ensemble. For example, we shed light on a long-standing debate about the nature of spin-flip noise in a strongly-interacting dipolar system [366, 297, 96, 606, 196, 8, 607, 137, 577, 563, 38, 221, 133]. Moreover, we directly measure the correlation time of the many-body system and introduce a technique to probe its dimensionality. This technique is particularly useful for spin ensembles embedded in solids [83, 343, 194], where a direct, non-destructive measurement of nanoscale spatial properties is challenging with conventional toolsets.

One can imagine generalizing our work in a number of promising directions. First, the ability to fabricate and characterize strongly-interacting, two-dimensional dipolar spin ensembles opens the door to a number of intriguing questions within the landscape of quantum simulation. Indeed, dipolar interactions in 2D are quite special from the perspective of localization, allowing one to experimentally probe the role of many-body resonances [78, 591, 478]. In the context of ground state physics, the long-range, anisotropic nature of the dipolar interaction has also been predicted to stabilize a number of exotic phases, ranging from supersolids to spin liquids [587, 614, 101]. Connecting this latter point back to noise spectroscopy, one could imagine tailoring the probe's filter function to distinguish between different types of ground-state order [90, 291].

Second, dense ensembles of two dimensional spins also promise a number of unique advantages with respect to quantum sensing [407, 523, 100, 155]. For example, a 2D layer of NVs fabricated near the diamond surface would exhibit a significant enhancement in spatial resolution (set by the depth of the layer) compared to a three-dimensional ensemble at the same density, ρ [407, 466, 432]. In addition, for samples where the coherence time is limited by spin-spin interactions, a lower dimensionality reduces the coordination number and leads to an enhanced T_2 scaling as $\rho^{-\alpha/D}$.[8]

Third, our framework can also be applied to long-range-interacting systems of Rydberg atoms, trapped ions, and polar molecules [599, 598, 59, 67, 268, 402]. In such systems, the ability to perform imaging and quantum control at the single-particle level allows for greater freedom in designing methods to probe many-body noise. As a particularly intriguing example, one could imagine a non-destructive, time-resolved generalization of many-body noise spectroscopy, where one repeatedly interrogates the probe without projecting the many-body system.

Finally, although our work addresses head-on the distinction between the Gauss-Markov and telegraph noises, further investigation is necessary to understand under what conditions one description is better than the other. This is crucial in building a comprehensive framework that relates the microscopic quantum dynamics to the effective classical description. Fundamentally, this question mirrors our previous discussion of hydrodynamical phenom-

---

[8]While there exist surface spins on diamond which are also naturally confined to two dimensions, these spins exhibit significantly shorter coherence times compared to NV/P1 centers within the diamond lattice [523].

ena: although the system is invariably undergoes complex, quantum mechanical dynamics, we which to understand *if* there is a simpler classical description, and *how* that description depends on the microscopic details of the system. This suggests the intriguing possibility of there being different dynamical universality classes for quantum many-body noise.

Crucially, addressing this question will require a more in-depth analysis of the relationship between operator spreading and Gauss-Markov noise. On the one hand, new analytical and theoretical insights will be required. On the other hand, experiments can pave the way by allowing us to explore the importance of the relaxation rate, power-law of the interactions, strength of the disorder and the spin density [366, 196]. At the same time, different pulse sequences (e.g. stimulated echo), can provide a more fine-grained characterization of the many-body noise, and perhaps enable the extraction of the entire spectral diffusion kernel [21, 366, 547].

Part V

Appendices

Appendix A

Two-body resonance counting and avalanche instabilities at infinite-randomness

In Chapter 8, we discussed how, in the absence of interactions, the transitions we consider fall into an infinite-randomness universality class characterized by a divergent single-particle density of states and divergent mean and typical orbital localization lengths (diverging as $D(\varepsilon) \sim |\varepsilon \log^3 \varepsilon|^{-1}$, $\xi_{\mathrm{mean}} \sim |\log^2 \varepsilon|$, and $\xi_{\mathrm{typ}} \sim |\log \varepsilon|$ respectively in single particle energy ε). Here, we investigate how such divergences may potentially trigger delocalization via the accumulation of two-body resonances or via avalanche instabilities.

A.1 Two-body resonance counting

To begin, we expand on the resonance counting criterion for the stability of localization of a non-interacting chain at infinite randomness against perturbative interactions. We consider a non-interacting Anderson-localized chain characterized by its density of single-particle states (DOS) $D(\varepsilon)$ and the localization length $\xi(\varepsilon)$ of single-particle orbitals (with energy ε). At the infinite randomness fixed point, the localization length and DOS both diverge as $|\epsilon| \to 0$ and it is the interplay of such overlapping orbitals that could lead to two-body resonance proliferation. We assume each orbital has a "center" at position α and an exponentially scaling envelope $\psi_\alpha^* \sim \frac{1}{\sqrt{\xi(\varepsilon_\alpha)}} e^{-|x-\alpha|/\xi(\varepsilon_\alpha)}$ determined by its energy ε_α. The presence of multiple centers (e.g. two in a typical state produced by the strong disorder renormalization group treatment of the Ising model) does not parametrically modify the estimates below. Similarly, the presence of 'pairing' terms in the fermionization of the Ising model is not parameterically important.

We consider a generic local interaction, which we schematically model by a density-density operator $\sim V \int dx \, \hat{n}(x)\hat{n}(x)$. Writing it in terms of the non-interacting orbitals, we

have

$$V_{\alpha\beta\gamma\delta} = V \int dx \, \psi_\alpha(x)\psi_\beta(x)\psi_\gamma^*(x)\psi_\delta^*(x) \sim \frac{V}{\sqrt{\xi_\alpha\xi_\beta\xi_\gamma\xi_\delta}} \int dx \, e^{-(|x-\alpha|/\xi_\alpha+|x-\beta|/\xi_\beta+|x-\gamma|/\xi_\gamma+|x-\delta|/\xi_\delta)} .$$

(A.1)

Two-body resonances occur when $V_{\alpha\beta\gamma\delta} > |(\varepsilon_\alpha - \varepsilon_\delta) - (\varepsilon_\gamma - \varepsilon_\beta)|$. In general, any small finite strength of interactions produces some density of resonances, but this need not modify the ergodic properties of the system; instead it can "dress" the local conserved quantities to be many-particle operators—this is at the heart of MBL. However, if the number of resonances in a localization volume becomes sufficiently large, then the local character of the conserved quantity is lost and we expect delocalization. Counting the number of perturbative resonances, induced by interactions, can then identify instabilities to thermalization.

Owing to the localized nature of the single-particle orbitals, the matrix element will only be large whenever all four orbitals overlap. Without loss of generality, we can take α to be the orbital with *smallest* localization length $\xi_\alpha < \xi_\beta, \xi_\gamma, \xi_\delta$. For ease of notation let $\varepsilon = \varepsilon_\alpha$. This suggests the following organization of our counting: given such an orbital, first we compute how many other orbitals (labeled orbital δ) exist within a block of size $\ell = \xi_\alpha$ around α and with energy $\delta\varepsilon$ around ε; second, given the energy difference between orbital α and δ, what is the number of pairs of orbitals β and γ that have an energy difference within $V_{\alpha\beta\gamma\delta}$ of the initial pair. Under this organization, one must have that both estimates diverge: the first ensures that there is always an initial pair that can transition, while the second ensures that, given a particular pair of orbitals, additional pairs can resonantly transition. While the former can be simply estimated as $\delta\varepsilon D(\varepsilon)\ell$, the latter requires a more careful analysis. Fixing the pair of resonances α and δ, we must find the number of pairs of orbitals β and γ that satisfy three conditions: (1) the within ℓ distance from orbital α, (2) their localization length is larger than ℓ, and (3) their energy difference close to the energy difference between α and γ (where close is given by the strength of the matrix element). The number R of such pairs can be estimated as follows: given an orbital γ within the block ℓ, we need to find another orbital β whose energy is in a window of size $V_{\alpha\beta\gamma\delta}$ around $\varepsilon_\gamma - \delta\varepsilon$. At some energy $\varepsilon_\gamma < \varepsilon$, the number of such orbitals γ is $\sim \ell D(\varepsilon_\gamma)d\varepsilon_\gamma$ and the number of corresponding orbitals β is $\sim \ell D(\varepsilon_\beta)V_{\alpha\beta\gamma\delta}$, where $\varepsilon_\beta = \varepsilon_\gamma - (\delta\varepsilon)$. Integrating yields the total number of resonances:

$$R = \int_0^\varepsilon d\varepsilon_\gamma \ell D(\varepsilon_\gamma)\ell D(\varepsilon_\beta)V_{\alpha\beta\gamma\delta} \sim \int_0^\varepsilon d\varepsilon_\gamma \ell D(\varepsilon_\gamma)\ell D(\varepsilon_\beta)\frac{V\ell}{\sqrt{\xi_\alpha\xi_\beta\xi_\gamma\xi_\delta}} . \quad (A.2)$$

We make progress under the following approximation: take $\delta\varepsilon = C\varepsilon$ with a small C. Physically, this means that the initial orbitals have similar energies, and thus similar localization lengths, $\xi_\delta \approx \xi_\alpha = \ell$.

We can check that this counting argument reproduces previous work on interaction instabilities of localized systems in Ref. [396]. There, $D(\varepsilon)$ remains a constant, while the

localization length diverges as a power-law, $\xi(\varepsilon) \sim \varepsilon^{-\nu}$. The two conditions are then:

$$C\varepsilon D(\varepsilon)\xi(\varepsilon) \sim \varepsilon^{1-\nu} \tag{A.3}$$

$$R \sim V\ell^2 \int_0^\varepsilon d\varepsilon' \, |\varepsilon' + C\varepsilon|^{\nu/2}|\varepsilon'|^{\nu/2} \sim \ell^2|\varepsilon|^{\nu/2}|\varepsilon|^{1+\nu/2} \sim \varepsilon^{1-\nu} \tag{A.4}$$

Both quantities diverge when $1 - \nu < 0$, which agrees with previous estimates, $\nu > 1/d$ where $d = 1$, using a diagramatic approach.

We can turn to the infinite randomness fixed point, which is characterized by a Dyson singularity with $D(\varepsilon) \sim [\varepsilon \log^3 \varepsilon]^{-1}$ and $\xi(\varepsilon) \sim \log \varepsilon$. We note that the $\xi(\varepsilon)$ corresponds to the *typical* localization length. Owing to the bi-locality of the free fermion wave functions [179, 170], the average localization length captures the distance between the two localization centers while the typical localization length captures the spread around each center—the latter is responsible for the mixing between orbitals and thus controls the matrix element.

In such systems we have:

$$C\varepsilon \frac{1}{\varepsilon \log^3 \varepsilon} \log \varepsilon \sim \frac{1}{\log^2 \varepsilon} \to 0 \tag{A.5}$$

$$
\begin{aligned}
R &\sim V\ell^2 \int_0^\varepsilon d\varepsilon' \, \frac{|\log(\varepsilon' + C\varepsilon)|^{-3-1/2}|\log(\varepsilon')|^{-3-1/2}}{|\varepsilon' + C\varepsilon||\varepsilon'|} \\
&\gtrsim 2V\ell^2 \frac{|\log(\varepsilon)|^{-3-1/2}}{|\varepsilon|} \int_0^\varepsilon d\varepsilon' \, \frac{|\log(\varepsilon')|^{-3-1/2}}{|\varepsilon'|} \\
&\sim V\ell^2 \frac{|\log(\varepsilon)|^{-3-1/2}}{|\varepsilon|}|\log(\varepsilon)|^{-2-1/2} \sim \frac{1}{\varepsilon}|\log(\varepsilon)|^{-4} \tag{A.6}
\end{aligned}
$$

While the latter condition diverges as $\varepsilon \to 0$, the former does not. This means that, within a block of size ℓ we are not guaranteed to find an appropriate orbital to start the resonance process.

A.2   Avalanche instability

We now turn our attention to the susceptibility of infinite-randomness transitions to thermalization "avalanches" triggered by rare thermal bubbles induced by the presence of interactions. For a system with a distribution of localization lengths, it has shown that the *average* localization length $\bar{\xi}$ controls this instability: for $\bar{\xi} > 2/\log 2$, thermal bubbles lead to a global thermalization of the system [114]. When relating this prediction to the physics of the infinite-randomness fixed point, it is important to understand the different lengthscales. In particular, at the infinite-randomness fixed point, each orbital is located around two distinct positions whose separation is given by ξ_{mean}; around each position the orbital decays with a length scale given by ξ_{typ}. Crucially, it is the latter lengthscale that leads to the

avalanche instability as it control the number of ℓ-bits that can interact with a rare thermal region. Thus, while $\overline{\xi_{\text{mean}}} \sim \int_0^\varepsilon d\varepsilon \frac{1}{\varepsilon \log^3 \varepsilon} |\log^2(\varepsilon)|$ diverges logarithmically, the more appropriate $\overline{\xi_{\text{typ}}} \sim \int_0^\varepsilon d\varepsilon \frac{1}{\varepsilon \log^3 \varepsilon} |\log(\varepsilon)|$ remains finite and this criterion does not conclusively produce an ergodic instability. We highlight that the difference between a converging or divergent average localization length depends on a single logarithmic term; unaccounted channels or higher order terms might provide an additional corrections that lead to an absolute avalanche instability. We leave this analysis to future work.

Finally, let us note that the direct numerical observation of avalanche instabilities remains extremely challenging; the presence of a robust intervening ergodic region in our study suggests that an alternate mechanism might be at the heart of our observations.

Appendix B

Proofs for results in long-range prethermalization with an emergent symmetry

B.1 Short-ranged proof

In this appendix, we prove an improved version of the prethermalization theorem for *short-ranged* Hamiltonians. This improved version will eventually be the key to extending to the case of long-range power-law interactions.

Consider a finite set of sites Λ that characterize our system. Each site is assigned a finite Hilbert space, so the total Hilbert space becomes the tensor product of these local Hilbert spaces. One can then define any operator, as a sum of terms acting on different parts of the system:

$$Q = \sum_Z Q_Z \tag{B.1}$$

where Q_Z is an operator that acts on $Z \subseteq \Lambda$. The collection of Q_Z is often referred to as a potential [5]. Despite this decomposition not being unique, our result constructs new potentials from an initial input potential so this ambiguity does not affect our proof.

We begin by introducing a one-parameter norm [5]:

$$\|Q\|_\kappa = \sup_{x \in \Lambda} \sum_{Z \ni x} e^{\kappa |Z|} \|Q_Z\| \ . \tag{B.2}$$

The finiteness of this norm in the limit of infinite volume indicates that the interactions are decaying exponentially with the size of their support.

We can extend this definition to time-periodic potentials $Q(t)$ by considering the time-average of the instantaneous norms:

$$\|Q\|_\kappa = \frac{1}{T} \int_0^T dt \ \|Q(t)\|_\kappa. \tag{B.3}$$

The statement of our theorem is as follows

Theorem 5. *Suppose we have a time-periodic Hamiltonian $H(t) = H(t + T)$ which induces a Floquet evolution over a period T:*

$$U_f = \mathcal{T} \exp\left[-i \int_0^T dt\ H(t)\right] \tag{B.4}$$

$$= X\ \mathcal{T} \exp\left[-i \int_0^T dt\ D + E + V(t)\right] \tag{B.5}$$

such that D and E are time-independent and

$$X^N = \mathbb{1}\ , \tag{B.6}$$

$$[D, X] = 0\ . \tag{B.7}$$

Fix some $\kappa_0 > 0$, and define

$$\lambda = T \max\{\|D\|_{\kappa_0}, \|E\|_{\kappa_0}, \|V\|_{\kappa_0}\}, \tag{B.8}$$

Now fix any $0 < \mathfrak{C} < 1$. Then there exist constants $C_1, \ldots, C_5 > 0$, depending only on $\mathfrak{C}$ and κ_0, with the following properties.

If $\lambda \leq C_1$ (high-frequency regime), then there is a unitary transformation $\mathcal{U}$ which transforms the evolution to:

$$\mathcal{U}^\dagger U_f \mathcal{U} = X\ \mathcal{T} \exp\left[-i \int_0^T dt\ D^* + E^* + V^*(t)\right] \tag{B.9}$$

where:

$$\|D - D^*\|_{\kappa_*} T \leq C_3 \lambda^2, \tag{B.10}$$

$$\|V^*\|_{\kappa_*} T \leq C_2 \lambda^2 \left(\frac{1}{2}\right)^{n_*}, \tag{B.11}$$

$$\|E^*\|_{\kappa_*} T \leq C_2 \lambda^2 \left(\frac{1}{2}\right)^{n_*}. \tag{B.12}$$

and

$$\kappa_* = \mathfrak{C}\kappa_0, \quad n_* = \left\lfloor \frac{C_4}{\lambda} \right\rfloor. \tag{B.13}$$

Moreover, $\mathcal{U}$ is locality-preserving and close to the identity, in the following precise sense:

$$\|\mathcal{U}\Phi\mathcal{U}^\dagger - \Phi\|_{\kappa_*, \gamma_*} \leq C_5 \lambda \|\Phi\|_{\kappa_0, \gamma}, \tag{B.14}$$

for any potential Φ.

Note that this is very similar to Theorem 1 of Ref. [161]. It differs, however, in two important ways. First, scaling of n_* lacks the logarithm corrections with λ (which is proportional to the inverse frequency) found in Ref. [161]; as a result the bound on the size of the residual "error" terms (V^* and E^*) scales more stringently with frequency. Second, the norm $\|\cdot\|_{\kappa_*}$ with respect to which the final bounds are obtained has a parameter κ_* which *does not* depend on λ. Roughly, the κ_* for which a finite bound can be obtained can be thought of as setting upper an bound on the locality of the Hamiltonians; so the second condition means that D^*, V^*, and E^* do not become more non-local as the frequency increases (whereas the theorems of Refs. [5, 161] did not exclude this possibility).

The iteration

Following Ref. [161], the idea is to construct the necessary rotations iteratively. At step n of the iteration, there is a slightly rotated frame where the Floquet evolution operator U_f is in the form

$$\mathcal{U}_n^\dagger U_f \mathcal{U}_n = U_f^{(n)} = X \ \mathcal{T} \exp\left(-i \int_0^T dt \ \mathcal{H}_n(t)\right), \tag{B.15}$$

$$\text{with } X^N = \mathbb{1}. \tag{B.16}$$

We are interested in performing a unitary transformation, such that $\mathcal{H}_n$ becomes closer to a time independent term which commutes with the symmetry X. We begin by writing $\mathcal{H}_n(t)$ as the sum of two different contributions, D_n and $B_n(t)$. D_n corresponds to the time-independent part of $\mathcal{H}_n(t)$ which commutes with X—the "good" part—and it is given by

$$D_n = \langle\langle\mathcal{H}_n\rangle_T\rangle_X = \frac{1}{N}\sum_{k=0}^{N-1} X^{-k}\left[\frac{1}{T}\int_0^T dt \ \mathcal{H}_n(t)\right] X^k \tag{B.17}$$

where $\langle.\rangle_T$ corresponds to the time averaging across a period:

$$\langle O\rangle_T = \frac{1}{T}\int_0^T dt \ O(t) \ , \tag{B.18}$$

and $\langle.\rangle_X$ corresponds to the symmetrization with respect to X, defined as

$$\langle O\rangle_X = \frac{1}{N}\sum_{k=0}^{N-1} X^{-k}OX^k \ . \tag{B.19}$$

Together, time averaging and symmetrization guarantee that D_n is both time independent and commutes with X.

$B_n(t)$ is then the remaining "bad part" of $\mathcal{H}_n(t)$ and is composed of a time-independent term E_n which does not commute with X, and a time-dependent term $V_n(t)$:

$$B_n(t) = \mathcal{H}_n(t) - D_n = E_n + V_n(t) \tag{B.20}$$

where $V_n(t)$ is chosen such that

$$\langle V_n(t)\rangle_T = 0. \tag{B.21}$$

At each step of the iteration we reduce the norm of $B_n(t)$ by performing a transformation informed by $\mathcal{H}_n$. The construction for the iteration is exactly the one described in Ref. [161], and we do not repeat it here. We only differ from Ref. [161] in how we analyze the bounds satisfied by the iteration, as we describe in the next section.

Analysis of bounds

Now we prove bounds on the result of the iteration. Our first result is Lemma 2, a slightly modified form of Theorem 5 (Theorem 5 itself will eventually arise as a collorary), in which the constants more explicitly stated.

Lemma 2. *There are order 1 constants u and v (not depending on any other parameters) with the following properties.*

Suppose we have a time-periodic Hamiltonian $H(t) = H(t+T)$ which induces a Floquet evolution over a period T:

$$U_f = \mathcal{T}\exp\left[-i\int_0^T dt\ H(t)\right] \tag{B.22}$$

$$= X\ \mathcal{T}\exp\left[-i\int_0^T dt\ D + E + V(t)\right] \tag{B.23}$$

such that D and E are time-independent and

$$X^N = \mathbb{1}\ , \tag{B.24}$$

$$[D, X] = 0\ . \tag{B.25}$$

Fix some $\kappa_0 > 0$, and define

$$\lambda = T\|D\|_{\kappa_0}, \tag{B.26}$$

$$\mu = T\max\{\|V\|_{\kappa_0}, \|E\|_{\kappa_0}\}. \tag{B.27}$$

Now fix any $0 < \mathfrak{C} < 1$. Then suppose that

$$b \leq \mathfrak{C}^2 v, \tag{B.28}$$

where

$$b = \frac{1}{\kappa_0^2}6(N+3)\max\left\{\frac{12}{u}\left(\lambda + \frac{5}{2}\mu\right), \mu\kappa_0\right\}. \tag{B.29}$$

Then there is a unitary transformation $\mathcal{U}$ which transforms the evolution to:

$$\mathcal{U}^\dagger U_f \mathcal{U} = X \; \mathcal{T} \exp\left[-i \int_0^T dt \; D^* + E^* + V^*(t) \right] \tag{B.30}$$

where:

$$\|D - D^*\|_{\kappa_*} T \leq \frac{1}{2}\mu, \tag{B.31}$$

$$\|V^*\|_{\kappa_*} T \leq \mu \left(\frac{1}{2}\right)^{-n_*}, \tag{B.32}$$

$$\|E^*\|_{\kappa_*} T \leq \mu \left(\frac{1}{2}\right)^{-n_*}, \tag{B.33}$$

and

$$\kappa_* = \mathfrak{C}\kappa_0, \quad n_* = \left\lfloor \frac{(1 - \mathfrak{C}^2)}{b} \right\rfloor. \tag{B.34}$$

.

Moreover, $\mathcal{U}$ satisfies

$$\|\mathcal{U}\Phi\mathcal{U}^\dagger - \Phi\|_{\kappa_*} \leq e^{\mu/2\lambda}\frac{\mu}{2\lambda}\|\Phi\|_{\kappa_0} \tag{B.35}$$

for any potential Φ.

Proof. To prove Lemma 2, following Refs. [5, 161], we introduce a decreasing sequence of numbers $\kappa_n > 0$. The key difference between our analysis and that of Refs. [5, 161] is in how we choose this sequence κ_n. In particular, we choose this sequence in a way that is frequency-dependent, meaning that it depends on the parameters λ and μ that appeared in the statement of the lemma. The higher the frequency (i.e. the smaller λ and μ), the slower κ_n will decrease, which allows us to run the iteration to a larger order n_*.

First of all, let us define

$$d(n) = \|D_n\|_{\kappa_n}, \quad v(n) = \|V_n\|_{\kappa_n}, \quad e(n) = \|E_n\|_{\kappa_n}, \quad \delta d(n) = \|D_{n+1} - D_n\|_{\kappa_{n+1}}. \tag{B.36}$$

We recall the following bounds from Appendix A.4 of Ref. [161] (note that these bounds are independent of the choice of κ_n):

$$2\delta d(n), v(n+1), e(n+1) \leq \varepsilon_n, \tag{B.37}$$

where

$$\varepsilon_n = 2Tm(n)v'(n)[d(n) + 2v'(n)] , \tag{B.38}$$

$$m(n) = \frac{18}{(\kappa_n - \kappa_{n+1})\kappa_{n+1}} , \tag{B.39}$$

$$v'(n) = (N + 2)e(n) + v(n) . \tag{B.40}$$

Note that there is an extra factor of 2 in Eq. B.38, which corrects an error in Ref. [161].[1] These bounds hold provided that

$$3Tv'(n) \leq \kappa_n - \kappa_{n+1} \ . \tag{B.41}$$

These results can be recast in a more intuitive manner as follows. Our eventual goal is to argue by induction. Suppose our induction hypothesis is that, given some h that is independent of the iteration order:

$$d(n) + 2v'(n) \leq hT^{-1} \tag{B.42}$$

$$v(n), e(n) \leq \left(\frac{1}{2}\right)^n \mu T^{-1} \ . \tag{B.43}$$

Then we will make sure to *choose* κ_{n+1} in terms of κ_n such that the following conditions are satisfied:

$$\frac{1}{2} \geq 2(N+3)m(n)h, \tag{B.44}$$

$$\kappa_n - \kappa_{n+1} \geq 3(N+3)\mu. \tag{B.45}$$

The point is that Eq. B.45, combined with Eq. B.43, ensures that Eq. B.41 is satisfied, and then Eq. B.44 combined with the induction hypothesis ensures that

$$v(n+1), e(n+1), 2\delta d(n) \leq \left(\frac{1}{2}\right)^{n+1} \mu T^{-1}, \tag{B.46}$$

which, in turn, ensures that Eq. B.43, one of our induction hypothesis, is satisfied for $n \to n+1$ (we consider the other one later).

One way to ensure Eqs. (B.44) and (B.45) is to define

$$\kappa_{n+1} = \sqrt{\kappa_n^2 - \epsilon} \tag{B.47}$$

for some $\epsilon > 0$ that we will choose later. Then,

$$\frac{18}{m(n)} = \kappa_n \kappa_{n+1} - \kappa_{n+1}^2 \tag{B.48}$$

$$= \kappa_n^2 \left[\sqrt{1 - \frac{\epsilon}{\kappa_n^2}} - \left(1 - \frac{\epsilon}{\kappa_n^2}\right) \right] \tag{B.49}$$

$$\geq \kappa_n^2 \frac{u\epsilon}{\kappa_n^2} \tag{B.50}$$

---

[1]Specifically, [161] neglected to take into account that their modified definition of norm for time-dependent potentials – the time-average of the instantaneous norm rather than the supremum – necessitates an additional factor of 2 in the first equation of Section 4.2 in Ref. [5]

where $u < 1/2$ and v are new constants introduced such that

$$\sqrt{1-x} - (1-x) \geq ux \quad \text{for} \quad 0 \leq x \leq v \leq 1 \tag{B.51}$$

Computing explicitly for v, one obtains

$$v = \frac{1-2u}{(1-u)^2}. \tag{B.52}$$

Equation B.44 is then satisfied provided that

$$u\epsilon \geq 72(N+3)h, \tag{B.53}$$

$$\epsilon \leq v\kappa_n^2. \tag{B.54}$$

Meanwhile, for Eq. B.45 to be satisfied, we note that

$$\kappa_n - \kappa_{n+1} = \kappa_n \left(1 - \sqrt{1 - \frac{\epsilon}{\kappa_n^2}} \right) \tag{B.55}$$

$$\geq \frac{\epsilon}{2\kappa_n}. \tag{B.56}$$

Therefore, Eq. B.45 is satisfied provided that

$$\epsilon \geq 6(N+3)\mu\kappa_n . \tag{B.57}$$

In summary, the conditions on ϵ are that

$$6(N+3) \max \left\{ \frac{12}{u}h, \kappa_n\mu \right\} \leq \epsilon \leq v\kappa_n^2. \tag{B.58}$$

We choose to only continue the iteration while $\kappa_n \geq \mathfrak{C}\kappa_0$. Hence, Eq. B.58 is satisfied provided that

$$b \leq \epsilon/\kappa_0^2 \leq \mathfrak{C}^2 v, \tag{B.59}$$

where

$$b = \frac{6(N+3)}{\kappa_0^2} \max \left\{ \frac{12}{u}h, \kappa_0\mu \right\}. \tag{B.60}$$

Accordingly, we will set $\epsilon = b\kappa_0^2$; then Eq. B.59 requires only that

$$b \leq \mathfrak{C}^2 v. \tag{B.61}$$

With this choice, we see that $\kappa_n = \kappa_0\sqrt{1 - bn}$.

Finally, we can complete the argument. The main missing piece is to show that the induction hypothesis Eq. B.42 is satisfied. Indeed, from Eq. B.46 we have that

$$d(n) \le d(0) + \sum_{n=0}^{\infty} \left(\frac{1}{2}\right)^{n+2} \mu T^{-1} \tag{B.62}$$

$$\le \left[\lambda + \frac{\mu}{2}\right] T^{-1}, \tag{B.63}$$

and, thus,

$$d(n) + 2v'(n) \le d(n) + 2v'(0) \tag{B.64}$$

$$\le d(n) + 2(N+3)\mu T^{-1} \tag{B.65}$$

$$\le \left[\lambda + \frac{4(N+3)+1}{2}\mu\right] T^{-1} \tag{B.66}$$

Therefore, if we set $h = \lambda + \frac{4(N+3)+1}{2}\mu$, then given the assumptions of Lemma 2, we can continue the induction up to the maximum iteration order n_*.

Finally, we need to prove Eq. B.35. From the form of the iteration (see Ref. [161]), we have

$$\mathcal{U} = e^{iA_{n*}} \cdots e^{iA_0}, \tag{B.67}$$

where $\|A_n\|_{\kappa_n} \le Ne(n)T$. Let us define $\Phi_n = e^{iA_n}\Phi_{n-1}e^{-iA_n}$, $\Phi_0 = \Phi$. Then from Lemma 4.1 of Ref. [5] and Eqs. (B.43) and (B.44), and the fact that $h \ge \lambda$, we obtain

$$\|\Phi_{n+1}\|_{\kappa_{n+1}} \le \left[1 + m(n)N\left(\frac{1}{2}\right)^n \mu\right] \|\Phi_n\|_{\kappa_n} \tag{B.68}$$

$$\le \left[1 + \frac{\mu}{4\lambda}\left(\frac{1}{2}\right)^n\right] \|\Phi_n\|_{\kappa_n} \tag{B.69}$$

$$\le \exp\left[\frac{\mu}{4\lambda}\left(\frac{1}{2}\right)^n\right] \|\Phi_n\|_{\kappa_n}, \tag{B.70}$$

and, thus,

$$\|\Phi_n\|_{\kappa_n} \le \exp\left[\frac{\mu}{4\lambda}\sum_{n=0}^{\infty}\left(\frac{1}{2}\right)^n\right] \|\Phi\|_{\kappa_0} \tag{B.71}$$

$$= e^{\mu/2\lambda}\|\Phi\|_{\kappa_0} \tag{B.72}$$

Then, we also have

$$\|\Phi_{n+1} - \Phi_n\|_{\kappa_{n+1}} \le \frac{\mu}{4\lambda}\left(\frac{1}{2}\right)^n \|\Phi_n\|_{\kappa_n} \tag{B.73}$$

$$\le e^{\mu/2\lambda}\frac{\mu}{4\lambda}\left(\frac{1}{2}\right)^n \|\Phi\|_{\kappa_0}, \tag{B.74}$$

from which we conclude by summation and the triangle inequality that

$$\|\Phi_n - \Phi\|_{\kappa_n} \le e^{\mu/2\lambda} \frac{\mu}{2\lambda} \|\Phi_0\|_{\kappa_0}. \tag{B.75}$$

This completes the proof of Lemma 2. $\qquad\square$

Now let us state how to prove Theorem 5. Lemma 2 (with $\mu \sim \lambda$) already takes us most of the way there, but it does not give the $O(\lambda^2)$ scaling of $\|D - D^*\|_{\kappa_*}$ nor the $O(\lambda)$ scaling of $\|\mathcal{U}\Phi\mathcal{U}^\dagger - \Phi\|_{\kappa_*}$. The idea to fix this gap is that one should first do a single iteration of the procedure of Ref. [161], with $\kappa_0 - \kappa_1$ held fixed independently of λ (rather than the prescription above, for which $\kappa_1 - \kappa_0 \to 0$ as $\lambda \to 0$). In that case, we see from Eq. B.38 that $\epsilon_0 = O(\lambda^2)$. Now we apply Lemma 2 to the D_1, V_1, E_1 that result from the first iteration. We see that we can set the μ appearing in the statement of Lemma 2 to be $O(\lambda^2)$. Theorem 5 immediately follows.

B.2 Proof of Theorem 1

In this appendix, we prove our main theorem, Theorem 2 from Sec. 12.2. One of the principal ingredients is a new version of the prethermalization theorem for *short-range* interactions, which we describe in Appendix B.1. Here we extend this proof to range-indexed potentials, as introduced in Chapter 12; recall that these are formal sums,

$$\Phi = \sum_{l=0}^{\infty} \sum_{Z \in \mathcal{Z}_{R_l}} \Phi_{Z,l}, \tag{B.76}$$

where we have introduced a sequence $R_l = e^{\sigma l}$, and $\mathcal{Z}_{R_l}$ is the set of all R_l-ranged subsets of sites (recall the definition of R-ranged set from Sec. 12.2).

We define the formal commutator of two range-indexed potentials according to

$$(\mathrm{ad}_\Phi \Theta)_{Z,l} := [\Phi, \Theta]_{Z,l} = \sum_{\substack{l_1, l_2 \ge 0 \\ \max\{l_1, l_2\} = l}} \sum_{\substack{Z_1 \in \mathcal{Z}_{R_{l_1}}, Z_2 \in \mathcal{Z}_{R_{l_2}} \\ Z_1 \cap Z_2 \ne \emptyset, Z_1 \cup Z_2 = Z}} [\Phi_{Z_1,l_1}, \Theta_{Z_2,l_2}] \tag{B.77}$$

The idea is that we take the commutator of $[\Phi_{Z_1,l_1}, \Theta_{Z_2,l_2}]$ to be supported on $Z_1 \cup Z_2$, and then we observe that in fact, if Z_1 and Z_2 are non-disjoint R_{l_1}- and R_{l_2}-ranged sets respectively, then indeed $Z_1 \cup Z_2$ is a $\max\{R_{l_1}, R_{l_2}\} = R_{\max\{l_1, l_2\}}$-ranged set. This is true because an R'-ranged set is also an R-ranged set for $R > R'$, and the union of two non-disjoint R-ranged sets is also an R-ranged set.

Then, we define the exponential action of one potential on another according to

$$e^{\Phi} \Theta e^{-\Phi} = \sum_{n=0}^{\infty} \frac{1}{n!} \mathrm{ad}_\Phi^n \Theta, \tag{B.78}$$

Recall from Chapter 12 that we introduced a two-parameter norm for range-indexed potentials, according to

$$\|\Phi\|_{\kappa,\gamma} = \sum_{l=0}^{\infty} R_l^{\gamma} \sum_{Z \in \mathcal{Z}_{R_l}} e^{\kappa|Z|} \|\Phi_Z\|. \tag{B.79}$$

We will find it convenient to fix some κ_0, γ and define a one-parameter norm for range-indexed potentials:

$$\|\Phi\|_{\kappa} := \|\Phi\|_{\kappa,\gamma\kappa/\kappa_0} \tag{B.80}$$

$$= \sum_{l=0}^{\infty} \sum_{Z \in \mathcal{Z}_{R_l}} e^{\kappa(|Z|+\mu l)} \|\Phi_Z\|_{R_l}, \quad \mu = \sigma\gamma/\kappa_0 \ . \tag{B.81}$$

We emphasize that this is *not* the same norm as Eq. B.2 for a potential Φ which does not keep any information regarding the range.

Now we can prove the following key lemma:

Lemma 3. *Let Φ, Θ be range-indexed potentials, and let $0 < \kappa' < \kappa$. Then*

$$\|e^{\Phi}\Theta e^{-\Phi} - \Theta\|_{\kappa'} \leq \frac{18}{\kappa'(\kappa - \kappa')} \|\Phi\|_{\kappa} \|\Theta\|_{\kappa}. \tag{B.82}$$

Proof. This is analogous to Lemma 4.1 in Ref. [5]. Indeed, the proof carries through in exactly the same way, line by line, just replacing sums over Z with sums over (Z, l). The key fact for that proof was that for a collection of sets $S_0, \ldots, S_m$ which is connected (i.e. it cannot be separated into non-disjoint subcollections), the size of their union $P = \cup_{k=0}^{m} S_k$ can be bounded by the sum of the sizes of each S_i as:

$$|P| \leq -m + \sum_{j=0}^{m} |S_j| \ . \tag{B.83}$$

For us, the analogous fact is as follows. Let $S_0, \ldots, S_m$ be a connected collection of sets, and let $l_0, \ldots, l_m \geq 0$. Then we have that

$$|P| + \mu \max\{l_0, \ldots, l_m\} \leq -m + \sum_{j=0}^{m} (|S_j| + \mu l_j). \tag{B.84}$$

$\square$

In fact, Lemma 3 is already sufficient to allow us to extend Theorem 5 to range-indexed potentials! The reason is that the only two things we needed to prove Theorem 5 were the bounds Eq. B.36 and Lemma 4.1 of Ref. [5]. However, the *only* non-trivial property of potentials that was used in deriving Eq. B.36 in Refs. [5, 161] was Lemma 4.1 of Ref. [5] itself.

By generalizing Lemma 4.1 of Ref. [5] to Lemma 3 (which applied to range-indexed potentials) all of the argumentation in Theorem 2 from Sec. 12.2 immediately carries over.

B.3 Lieb-Robinson bounds for long-ranged interactions and the approximation of local observables

In this Appendix, we give the proof of Theorem 3 from Sec. 12.2.

We restrict our attention sets of sites Λ that can be embedded in a Cartesian space $\mathbb{R}^d$, such that for any $x \in \Lambda$ there exists $\boldsymbol{r}_x \in \mathbb{R}^d$ such that $\text{dist}(x, y) = |\boldsymbol{r}_x - \boldsymbol{r}_y|$. We also assume that there is a smallest distance $\min_{x,y} \text{dist}(x, y) = a$, which we normalize to be 1.

The important result that we will use is that there is a Lieb-Robinson bound for time-evolution by range-indexed potentials with bounded norm $\| \cdot \|_{\kappa,\gamma}$, so long as $\gamma > d$.

Lemma 4. *Lieb-Robinson bounds for generic graded potentials* *Let $\Phi(t)$ be a (time-dependent) graded potential with $\|\Phi\|_{\kappa,\gamma} < \infty$ for some $\kappa > 0$ and $\gamma > d$. Let A be an operator supported on the set $X \subseteq \Lambda$, and let B be an operator supported on $Y \subseteq \Lambda$. Define the time-evolution $\tau_t(A)$ as the time evolution of A according to $\frac{d}{dt}\tau_t(A) = i[\tau_t(A), \Phi(t)]$. Then for any η with $\frac{d+1}{\gamma+1} < \eta < 1$, there is a Lieb-Robinson bound:*

$$\frac{\|[\tau_t(A), B]\|}{\|A\|\|B\|} \leq 2|X|e^{vt - r^{1-\eta}} + K_1 \frac{\tau + \tau^\beta}{r^{\eta\gamma}}|X|^{n_*+2}, \tag{B.85}$$

where:

$$\beta = 1 + d/(1 - \eta), \tag{B.86}$$

$$n_* = \left\lceil \frac{\eta d}{\eta \alpha - d} \right\rceil, \tag{B.87}$$

$$\tau = vt, \tag{B.88}$$

$$v = K_2 \max\left\{ e^{-\gamma}\left(\frac{\gamma}{\kappa}\right)^\gamma, \kappa^{-1} \right\} \|\Phi\|_{\kappa,\gamma}, \tag{B.89}$$

and K_1 and K_2 are constants that depend only on the geometry of the system and on η, and we have defined

$$\|\Phi\|_{\kappa,\gamma} = \frac{1}{t}\int_0^t ds \|\Phi(s)\|_{\kappa,\gamma}. \tag{B.90}$$

Proof. This is a corollary of Theorem 1 in Ref. [163]. To show that the theorem applies, we need only ensure that the assumptions of Sec. I of Ref. [163] are satisfied. First observe that there is always a rescaling of time (which might be nonlinear) such that $\|\Phi(t)\|_{\kappa,\gamma}$ becomes independent of t and equal to $\|\Phi\|_{\kappa,\gamma}$.

Now define $\Phi_Z = \sum_{l=0}^{\infty} \Phi_{Z,l}$ (where we take $\Phi_{Z,l} = 0$ if Z is not an R_l-ranged set). Then we have, for any $x \in \Lambda$, $s \in [0, t]$:

$$\sum_{Z \ni x; \mathrm{diam}(Z) \geq r} \|\Phi_Z(s)\| \tag{B.91}$$

$$\leq \sum_{l=0}^{\infty} \sum_{x \in Z \in \mathcal{Z}_{R_l}; \mathrm{diam}(Z) \geq r} \|\Phi_{Z,l}(s)\| \tag{B.92}$$

$$\leq \sum_{l=0}^{\infty} \sum_{x \in Z \in \mathcal{Z}_{R_l}; \mathrm{diam}(Z) \geq r} e^{\kappa|Z|} e^{-\kappa r/R_l} \|\Phi_{Z,l}(s)\| \tag{B.93}$$

$$\leq \sum_{l=0}^{\infty} \sum_{Z \ni x} e^{\kappa|Z|} e^{-\kappa r/R_l} \|\Phi_{Z,l}(s)\| \tag{B.94}$$

$$= (\kappa r)^{-\gamma} \sum_{l=0}^{\infty} \sum_{Z \ni x} e^{\kappa|Z|} e^{-\kappa r/R_l} (\kappa r/R_l)^{\gamma} R_l^{\gamma} \|\Phi_{Z,l}(s)\| \tag{B.95}$$

$$\leq e^{-\gamma} \gamma^{\gamma} \|\Phi\|_{\kappa,\gamma} (\kappa r)^{-\gamma}, \tag{B.96}$$

where we used the fact that any R_l-ranged set $Z \in \mathcal{Z}_{R_l}$ satisfies $\mathrm{diam}(Z) \leq R_l|Z|$, and the fact that $\max_{x=[0,\infty)} e^{-\kappa x} (\kappa x)^{\gamma} = e^{-\gamma} \gamma^{\gamma}$.

Moreover, for any $x \in \Lambda$:

$$\sum_{y \in \Lambda} \sum_{Z \ni x, y} \|\Phi_Z(s)\| \tag{B.97}$$

$$\leq \sum_{Z \ni x} |Z| \|\Phi_Z(s)\| \tag{B.98}$$

$$\leq \sum_{Z \ni x} \frac{1}{\kappa} e^{\kappa|Z|} \|\Phi_Z(s)\| \tag{B.99}$$

$$\leq \frac{1}{\kappa} \|\Phi\|_{\kappa,0} \leq \frac{1}{\kappa} \|\Phi\|_{\kappa,\gamma} \tag{B.100}$$

Hence, we see that the assumptions of Theorem 1 of Ref. [163] are satisfied with

$$J = e^{-\gamma} (\gamma/\kappa)^{\gamma} \|\Phi\|_{\kappa,\gamma}, \tag{B.101}$$

$$\mathcal{C}_0 = \frac{1}{\kappa} \|\Phi\|_{\kappa,\gamma}. \tag{B.102}$$

Therefore, the Lieb-Robinson bound follows from Ref. [163]. □

Having proven that Lieb-Robinson bounds apply for range-indexed potentials with bounded norm provided that $\gamma > d$, we can now prove that small (in terms of the norm $\|.\|_{\kappa,\gamma}$) perturbations induce small changes in the dynamics of local observables. This will be encapsulated in Lemma 5. Combining Lemma 5 with Theorem 2 will then immediately imply Theorem 3.

Lemma 5. *Let $\Phi_1(t)$ and $\Phi_2(t)$ be two time-dependent range-indexed potentials, such that Φ_2 satisfies Lemma 4. Let $U_j(t) = \mathcal{T}\exp\left[-i\int_0^t \Phi_j(t)\right]$ be the corresponding time evolutions, and define $\Delta(t) = \Phi_1(t) - \Phi_2(t)$.*

Then, the difference in time evolved local operator O (initially support on the set $X \subseteq \Lambda$) under Φ_1 and Φ_2 is bounded by:

$$\left\| U_1^\dagger(t)OU_1(t) - U_2^\dagger(t)OU_2(t)] \right\| \leq$$
$$\leq |X| \|O\| \|\Delta\|_{0,0} t \times \left\{ K_3(1 + \tau^{d/(1-\eta)})|X| + K_4(\tau + \tau^\beta)|X|^{n_*+2} \right\}, \tag{B.103}$$

where we defined

$$\|\Delta\|_{0,0} = \frac{1}{t}\int_0^t ds \|\Delta(s)\|_{0,0}. \tag{B.104}$$

Here K_3 is another constant that depends only on the geometry of the lattice and on η (but not the system size), and K_4 depends on the geometry of the lattice, on η, and on γ, but not the system size. This result holds provided that η is as prescribed in Lemma 4 and also satisfies $\eta\gamma > d$.

Proof. We write the Lieb-Robinson bound from Lemma 4 as

$$\frac{\|[\tau_t(A), B]\|}{\|A\|\|B\|} \leq f(r), \tag{B.105}$$

where $f(r,t) = f_1(r,t) + f_2(r,t) + f_3(r,t)$, with

$$f_1(r,t) = 2\theta(\xi(t) - r), \tag{B.106}$$
$$f_2(r,t) = 2e^{vt-r^{1-\eta}}|X|\theta(r - \xi(t)), \tag{B.107}$$
$$f_3(r,t) = K_1\frac{\tau + \tau^\beta}{r^{\eta\gamma}}|X|^{n_*+2}, \tag{B.108}$$

Here θ is the Heaviside step function, $\tau = vt$, $\xi(t) = (vt)^{1/(1-\eta)}$, and we have also invoked the trivial commutator bound $\|[\tau_t(A), B]\| \leq 2\|A\|\|B\|$.

Now we use the fact that

$$\frac{d}{dt}(U_1 U_2^\dagger O U_2 U_1^\dagger) = -iU_1[\Delta, U_2^\dagger O U_2]U_1^\dagger. \tag{B.109}$$

Integrating this result, we obtain:

$$U_1(t)U_2^\dagger(t)OU_2(t)U_1^\dagger(t) - O = \tag{B.110}$$
$$- i\int_0^t ds\, U_1(s)[\Delta(s), U_2^\dagger(s)OU_2(s)]U_1^\dagger(s), \tag{B.111}$$

and, thus,

$$\|U_1^\dagger(t)OU_1(t) - U_2^\dagger(t)OU_2(t)\| \le \tag{B.112}$$

$$\le \int_0^t ds \|[\Delta(s), U_2^\dagger(s)OU_2(s)]\| \tag{B.113}$$

$$\le \int_0^t ds \sum_Z \|[\Delta_Z(s), U_2^\dagger(s)OU_2(s)]\|, \tag{B.114}$$

where we defined $\Delta_Z(s) = \sum_{l=0}^\infty \Delta_{Z,l}(s)$.

Now to bound the commutator we consider

$$\int_0^t \sum_Z \|[\Delta_Z(s), U_2^\dagger(s)OU_2(s)]\| \le \tag{B.115}$$

$$\le \int_0^t ds \sum_Z \|\Delta_Z(s)\| \|O\| f(\text{dist}(Z, X), s) \tag{B.116}$$

$$\le \int_0^t ds \sum_z \sum_{Z \ni z} \|\Delta_Z(s)\| \|O\| f(\text{dist}(z, X), s) \tag{B.117}$$

$$\le t\|\Delta\|_{0,0}\|O\| \sum_z f(\text{dist}(z, X), t) \tag{B.118}$$

$$\le t\|\Delta\|_{0,0}\|O\||X| \sup_x \sum_z f(\text{dist}(z, x), t), \tag{B.119}$$

and used the fact that $f(\cdot, t)$ is monotonic in t.

Then we observe that

$$\sum_z f_1(\text{dist}(z, x), t) \le V\{\xi(t)\}, \tag{B.120}$$

where $V\{\xi(t)\} \le K_3(1 + \xi(t)^d)$ is the number of points within distance $\xi(t)$ of a given point. Moreover, we also have

$$\sum_z f_2(\text{dist}(z, x), t) \tag{B.121}$$

$$= 2|X| \sum_{z, \text{dist}(x,z) \ge \xi(t)} e^{vt - \text{dist}(x,z)^{1-\eta}} \tag{B.122}$$

$$\le 2|X| \sum_{z, \text{dist}(x,z) \ge \xi(t)} e^{-[\text{dist}(x,z) - \xi(t)]^{1-\eta}} \tag{B.123}$$

$$\le 2|X| \sum_{y, \text{dist}(x,y) \le \xi(t)} \sum_z e^{-\text{dist}(y,z)^{1-\eta}} \tag{B.124}$$

$$\le V\{\xi(t)\} K_3 |X|, \tag{B.125}$$

where in Eq. B.123 we used Bernoulli's inequality. Finally, we have

$$\sum_z f_3(\text{dist}(z, x), t) \leq K_3(\tau + \tau^\beta)|X|^{n_*+2} \tag{B.126}$$

where

$$K_4 = K_1 \sup_y \sum_z \frac{1}{\text{dist}(z, y)^{\eta\gamma}}, \tag{B.127}$$

which is finite in the thermodynamic limit provided $\eta\gamma > d$. $\qquad\qquad\square$

B.4 Approximation of local observables for $\alpha > d$

In this appendix, we will deal only with potentials (not range-indexed potentials). Starting from a range-indexed potential we can construct a potential just by defining $\Phi_Z = \sum_{l=0}^\infty \Phi_{Z,l}$.

We define the Heisenberg evolution of a (time-independent) potential Θ by a (time-dependent) potential $\Phi(t)$ through the Dyson series for Heisenberg evolution, i.e.

$$\mathcal{E}_\Phi(t)\Theta := \sum_{n=0}^\infty i^n \int_0^t dt_1 \int_0^{t_1} dt_2 \cdots \int_0^{t_{n-1}} dt_n \times \text{ad}_{\Phi(t_1)} \cdots \text{ad}_{\Phi(t_n)}.\Theta, \tag{B.128}$$

where $\text{ad}_\Phi \Theta = [\Phi, \Theta]$. This satisfies

$$\frac{d}{dt}\mathcal{E}_\Phi(t) = i\text{ad}_{\Phi(t)}\mathcal{E}_\Phi(t) \tag{B.129}$$

Our key result is as follows.

Lemma 6. *Consider numbers $0 < \kappa' < \kappa$, and suppose that $3t\|\Phi\|_{\kappa'} \leq \kappa - \kappa'$. Then:*

$$\|\mathcal{E}_\Phi(t)\Theta - \Theta\|_{\kappa'} \leq \frac{18t}{\kappa'(\kappa - \kappa')}\|\Theta\|_\kappa\|\Phi\|_\kappa, \tag{B.130}$$

Here we defined

$$\|\Phi\|_\kappa = \frac{1}{T}\int_0^T dt \ \|\Phi(t)\|_\kappa. \tag{B.131}$$

Proof. This is basically a time-dependent version of Lemma 4.1 from Ref. [5]. The proof

proceeds in a nearly identical way. Indeed, we have

$$\|(\mathcal{E}_\Phi(t)\Theta)_P - \Theta_P\| \leq \sum_{n=1}^\infty \int_0^t dt_1 \int_0^{t_1} dt_2 \cdots \int_0^{t_{n-1}} dt_n \sum_{S_0,\cdots,S_m}^{c,P} \|\Theta_{S_0}\| \prod_{j=1}^n (2\|\Phi_{S_j}(t_j)\|) \quad (\text{B.132})$$

$$= \sum_{n=1}^\infty \frac{1}{n!} \int_0^t dt_1 \cdots \int_0^t dt_n \sum_{S_0,\cdots,S_m}^{c,P} \|\Theta_{S_0}\| \sum_{j=1}^n (2\|\Phi_{S_j}(t_j)\|) \quad (\text{B.133})$$

$$= \sum_{n=1}^\infty \frac{1}{n!} \sum_{S_0,\cdots,S_m}^{c,P} \|\Theta_{S_0}\| \sum_{j=1}^n (2t\|\overline{\Phi}_{S_j}\|) \quad (\text{B.134})$$

$$, \quad (\text{B.135})$$

where we defined $\|\overline{\Phi}_Z\| = \frac{1}{t} \int_0^t dt' \, \|\Phi_Z(t')\|$. The rest of the proof proceeds identically to Lemma 4.1 of Ref. [5]. $\qquad \square$

A corollary of this (or, in fact, of Lemma 4.1 of Ref. [5]) is as follows.

Lemma 7. *For any potential W, we have*

$$\|\mathrm{ad}_W \Theta\|_{\kappa'} \leq \frac{18}{\kappa'(\kappa - \kappa')} \|\Theta\|_\kappa \|W\|_\kappa. \quad (\text{B.136})$$

Proof. Just use the fact that

$$\mathrm{ad}_W = \lim_{t\to 0} \frac{\mathcal{E}_W(t) - \mathbb{1}}{t}. \quad (\text{B.137})$$

$\qquad \square$

Now we can prove a result about approximation of local observables.

Lemma 8. *Define $\lambda = \max\{\|\Phi\|_\kappa, \|\Phi'\|_\kappa\}$. Suppose that $12\lambda t \leq (\kappa - \kappa')$. Then*

$$\|\mathcal{E}_\Phi(t)\Theta - \mathcal{E}_{\Phi'}(t)\Theta\|_{\kappa'} \leq \mathcal{C}^3 \mathcal{M} t \|\overline{\Delta}\|_\kappa, \quad (\text{B.138})$$

where we defined $\Delta(t) = \Phi(t) - \Phi'(t)$, $\|\overline{\Phi}\|_\kappa = \frac{1}{t}\int_0^t \|\Phi(s)\|_\kappa ds$ (and similarly for Φ', Δ), and

$$\mathcal{M} = \frac{72}{\kappa'(\kappa - \kappa')}, \quad (\text{B.139})$$

$$\mathcal{C} = 1 + \mathcal{M}\lambda t \leq 1 + \frac{6}{\kappa'}. \quad (\text{B.140})$$

Proof. We introduce a sequence $\kappa = \kappa_0 > \kappa_1 > \kappa_2 > \kappa_3 > \kappa_4 = \kappa'$, such that $\kappa_j - \kappa_{j+1} = (\kappa - \kappa')/4$.

$$\frac{d}{ds}[\mathcal{E}_{\Phi'}^{-1}(s)\mathcal{E}_\Phi(s)] = -i\mathcal{E}_{\Phi'}^{-1}(s)\mathrm{ad}_{\Delta(s)}\mathcal{E}_\Phi(s) \quad (\text{B.141})$$

and therefore,

$$
\begin{aligned}
\left\| \frac{d}{ds} \mathcal{E}_{\Phi'}^{-1}(s) \mathcal{E}_{\Phi}(s) \Theta \right\|_{\kappa_3} &\leq \mathcal{C} \| \mathrm{ad}_{\Delta(s)} \mathcal{E}_{\Phi}(s) \Theta \|_{\kappa_2} \\
&\leq \mathcal{C} \mathcal{M} \| \Delta(s) \|_{\kappa_1} \| \mathcal{E}_{\Phi}(s) \Theta \|_{\kappa_1} \\
&\leq \mathcal{C}^2 \mathcal{M} \| \Delta(s) \|_\kappa \| \Theta \|_\kappa,
\end{aligned}
\tag{B.142}
$$

where we have invoked Lemmas 6 and 7. This then gives

$$
\begin{aligned}
\| \mathcal{E}_{\Phi'}^{-1}(t) \mathcal{E}_{\Phi}(t) \Theta - \Theta \|_{\kappa_3} &\leq \mathcal{C}^2 \mathcal{M} \| \Theta \|_\kappa \int_0^t ds \, \| \Delta(s) \|_\kappa \\
&= \mathcal{C}^2 \mathcal{M} \| \Theta \|_\kappa \| \Delta \|_\kappa t.
\end{aligned}
\tag{B.143}
$$

Finally, we obtain

$$
\begin{aligned}
\| \mathcal{E}_{\Phi}(t) \Theta - \mathcal{E}_{\Phi'}(t) \Theta \|_{\kappa'} &= \| \mathcal{E}_{\Phi'}(t) [\mathcal{E}_{\Phi'}^{-1}(t) \mathcal{E}_{\Phi}(t) \Theta - \Theta] \|_{\kappa'} \\
&\leq \mathcal{C}^3 \mathcal{M} \| \Theta \|_\kappa \| \Delta \|_\kappa t,
\end{aligned}
\tag{B.144}
$$

where we invoked Lemma 6 once more. $\qquad\square$

An immediate corollary is as follows.

Lemma 9. *Define $\lambda = \max\{ \| \Phi \|_\kappa, \| \Phi' \|_\kappa \}$. Suppose that $24\lambda t \leq \kappa$. Let O be an observable supported on a set S. Then*

$$
\| \mathcal{E}_{\Phi}(t) O - \mathcal{E}_{\Phi'}(t) O \| \leq \mathcal{C}^3 \mathcal{M} e^{\kappa |S|} t \| \Delta \|_\kappa,
\tag{B.145}
$$

where we defined $\Delta(t) = \Phi(t) - \Phi'(t)$, $\| \Phi \|_\kappa = \frac{1}{t} \int_0^t \| \Phi(s) \|_\kappa ds$ (and similarly for Φ', Δ), and

$$
\mathcal{M} = 288/\kappa^2,
\tag{B.146}
$$

$$
\mathcal{C} = 1 + \mathcal{M} \lambda t \leq 1 + \frac{12}{\kappa}.
\tag{B.147}
$$

Proof. We define $\kappa' = \kappa/2$ and treat O as a potential with a single term $O_S = O$. Then $\| O \|_\kappa = e^{\kappa |S|} \| O \|$. Moreover, we observe that $\delta := \mathcal{E}_{\Phi} O - \mathcal{E}_{\Phi'} O$, considered a potential, only takes nonzero values on sets Z that contain S. Therefore, given some $s \in S$, we have

$$
\| \delta \| \leq \sum_Z \| \delta_Z \| = \sum_{Z \ni s} \| \delta_Z \| \leq \| \delta \|_0 \leq \| \delta \|_{\kappa'},
\tag{B.148}
$$

and then the result follows from Lemma 8. $\qquad\square$

Lemma 9 then immediately implies Theorem 4 in Chapter 12.

Appendix C

Derivation of modifications to simple diffusion

C.1 Derivation of dynamical correction to diffusion

In this section, we show that a dynamical correction emerges due to the randomness of the local diffusion coefficient. Crucially, this effect can be seen from the disorder-averaged diffusion kernel, or Green's function:

$$G(\boldsymbol{k}, \omega) = \frac{1}{-i\omega + Dk^2 + \Sigma(\boldsymbol{k}, \omega)} \tag{C.1}$$

where $-i\omega + Dk^2$ describes the eventual diffusive dynamics at asymptotically late times and long wavelengths while the self-energy $\Sigma(\boldsymbol{k}, \omega)$ captures the corrections due to disorder averaging. Here in this section, we provide a derivation of such self-energy at the one-loop level, by considering a continuum model with a spatially random local diffusion coefficient. The actual coefficient ℓ^2 produced in this calculation depends on the UV-cutoff (as expected) and thus its detailed numerical form is of limited utility.

We assume that the diffusivity is $D(x) = D + \delta D(x)$ is Gaussian with

$$\overline{\delta D(x)\delta D(x')} = \Delta_D \delta(x - x') \tag{C.2}$$

The Martin-Siggia-Rose (MSR) [352] action generating the Green's function of the polarization $P(x, t)$ in a *fixed* diffusion environment $D(x)$ is given by

$$S_D = i \int dt d^dx \, \hat{P}(x,t)(\partial_t - D\vec{\nabla}^2)P(x,t) + i \int dt d^dx \, (\vec{\nabla}\hat{P}(x,t)) \cdot (\vec{\nabla}P(x,t))\delta D(x) \tag{C.3}$$

where $\hat{P}(x, t)$ is the MSR conjugate response field to $P(x, t)$. Here, $\langle \hat{P}(x,t)P(x',t')\rangle_D = -iG_D(x', t'; x, t)$ provides the fixed environment Green's function of the polarization. The action generating the disorder averaged Green's function can be obtained by integrating over

the fluctuations in $\delta D(x)$. Technically, this is straightforward because in the MSR approach, the normalization $Z_D = \int DPD\hat{P}e^{S_D} = 1$ is independent of the realization of $D(x)$; see Ref. [180] for more discussion. We obtain the effective action

$$S = S_0 + S_1 \tag{C.4}$$

$$S_0 = i \int dt d^d x\, \hat{P}(x,t)(\partial_t - D\vec{\nabla}^2)P(x,t) \tag{C.5}$$

$$S_1 = -\frac{\Delta_D}{2} \int dt dt' d^d x \left[(\vec{\nabla}\hat{P}(x,t)) \cdot (\vec{\nabla}P(x,t)) \right] \left[(\vec{\nabla}\hat{P}(x,t')) \cdot (\vec{\nabla}P(x,t')) \right] \tag{C.6}$$

We now compute $-iG(x,t) = \langle \hat{P}(0,0)P(x,t)\rangle$ using perturbation theory to leading loop order. The bare propagator, $-iG_0(\boldsymbol{k},\omega)$, can be taken as an arrow pointing from $\hat{P}$ to P:

$$\underset{\boldsymbol{k},\omega}{\longrightarrow} = \frac{-i}{-i\omega + Dk^2} \tag{C.7}$$

The interaction vertex (S_1) is

$$= -\frac{\Delta_D}{2}(\boldsymbol{q} \cdot (\boldsymbol{q}+\boldsymbol{k}))(\boldsymbol{q}' \cdot (\boldsymbol{q}' - \boldsymbol{k}))$$

We note that causality implies that any diagrams with closed P-loops are identically zero, since G_0 is retarded. As usual, we can organize the perturbative expansion for the full propagator $-iG$ in terms of a self-energy $G^{-1} = G_0^{-1} + \Sigma$,

$$\underset{\boldsymbol{k},\omega}{\Longrightarrow} = \underset{\boldsymbol{k},\omega}{\longrightarrow} + \underset{\boldsymbol{k},\omega}{\longrightarrow}\overbrace{\Sigma}\Longrightarrow \tag{C.8}$$

To one loop, the only diagram contributing to Σ is

$$\Sigma^{(1)}(\boldsymbol{k},\omega) = = -\frac{\Delta_D}{2} \int \frac{d^d q}{(2\pi)^d} \frac{(\vec{q}\cdot\vec{k})^2}{-i\omega + Dq^2}$$

This is clearly isotropic and quadratic in $\vec{k}$. It is straightforward to evaluate $\Sigma^{(1)}$ as an expansion in $-i\omega$ (in 3d):

$$\Sigma^{(1)} = -\frac{\Delta_D \Lambda^3}{36\pi^2 D}k^2 + \frac{\Delta_D \Lambda}{12\pi^2 D^2}(-i\omega)k^2 + \cdots \tag{C.9}$$

where Λ is a UV momentum cutoff. As expected we find a correction to the long-wavelength diffusion constant $D'k^2$ and a dynamical correction $\ell^2(-i\omega)k^2$.

C.2   Long-range modifications to diffusion

In building a description that goes beyond the leading order term, we first consider the problem in Fourier space, where it can be generically cast as:

$$\partial_t P_{\boldsymbol{k}}(t) = -f(\boldsymbol{k})P_{\boldsymbol{k}}(t), \tag{C.10}$$

where we have ignored the source and depolarization terms. Note that the diffusive nature of the dynamics arises as a leading order term Dk^2 in $f(\boldsymbol{k})$. In isotropic short-range interacting system, $f(\boldsymbol{k})$ can be expanded in a series of even powers in k:

$$f(\boldsymbol{k}) = Dk^2 + Ck^4 + \cdots . \tag{C.11}$$

When the polarization transfer rate is long-range (decays as $\sim 1/r^\alpha$ at large distances r) in a d-dimensional system, this simple expansion breaks down owing a divergent $(\alpha-d)$-order moment—this to a non-analyticity in $f(\boldsymbol{k})$. We now show how the long-range transfer $h(\boldsymbol{r})$ rate induces such terms in the decay rate of the Fourier modes

$$f(\boldsymbol{k}) = \int d^d\boldsymbol{r} \; [1 - \cos(\boldsymbol{k} \cdot \boldsymbol{r})]h(\boldsymbol{r}). \tag{C.12}$$

In particular, we consider a transfer rate where beyond some short-range cutoff r_0 the transfer decays simply decays as a power-law $\sim 1/r^\alpha$ for $\alpha > d$. Focusing on the long-range part (since any non-singular short-range contribution just leads to even terms) we have:

$$
\begin{aligned}
f_{\mathrm{lr}}(\boldsymbol{k}) &= \int \frac{1 - \cos(\boldsymbol{k} \cdot \boldsymbol{r})}{r^\alpha}d^d\boldsymbol{r} \\
&= \frac{\pi^{\frac{d}{2}}}{\Gamma(\frac{d}{2})} \int d\cos\theta \; dr \; \frac{1 - \cos(kr\cos\theta)}{r^\alpha}r^{d-1} = \frac{2\pi^{\frac{d}{2}}}{\Gamma(\frac{d}{2})} \int_{r_0}^\infty dr \left[1 - \frac{\sin(kr)}{kr}\right] r^{d-\alpha-1} \\
&= \frac{2\pi^{\frac{d}{2}}}{\Gamma(\frac{d}{2})} \left\{ \Gamma(d-\alpha-1)\sin\left(\frac{\alpha+1-d}{2}\pi\right)k^{\alpha-d} + \frac{r_0^{d-\alpha}}{d-\alpha}\left[-1 + {}_1F_2\left(\frac{d-\alpha}{2};\frac{3}{2},1+\frac{d-\alpha}{2};-\frac{k^2r_0^2}{4}\right)\right]\right\} \\
&= \frac{2\pi^{\frac{d}{2}}}{\Gamma(\frac{d}{2})} \left\{ \Gamma(d-\alpha-1)\sin\left(\frac{\alpha+1-d}{2}\pi\right)k^{\alpha-d} + \left[\frac{r_0^{d-\alpha+2}}{6(\alpha-d-2)}k^2 + \frac{r_0^{d-\alpha+4}}{120(d-\alpha+4)}k^4 + \mathcal{O}(k^6)\right]\right\},
\end{aligned}
\tag{C.13}
$$

where $\frac{2\pi^{\frac{d}{2}}}{\Gamma(\frac{d}{2})}$ is the surface area of a d-dimensional ball with unit radius, and ${}_1F_2(a_1; b_1, b_2; x)$ is the generalized hypergeometric function, which can be expanded as a power series of the variable x. The interpretation is simple: while the last term only contains terms with even power of k (similar to diffusion in short-range systems), the first term $(\sim k^{\alpha-d})$ captures the long-range nature, making the dynamics qualitatively different from short-range interacting systems. Therefore, with the presence of long-range interaction, $f(\boldsymbol{k})$ in general can be written as:

$$f(\boldsymbol{k}) = Dk^2 + C_{\mathrm{lr}}k^{\alpha-d} + Ck^4 + \cdots \tag{C.14}$$

where D, C_{lr} and C are model-dependent coefficients. This result immediately highlights three import regimes: When $d < \alpha < d + 2$, the leading power is no longer the k^2 term and instead a $k^{\alpha-d}$ term becomes the leading contribution—the system is no longer diffusive and enters the Lévy-flight regime [329, 506]. When $d + 2 < \alpha < d + 4$, the leading order term remains the diffusive term but the sub-leading correction that control the approach to diffusion is set by a $k^{\alpha-d}$ term [494]. When $d+4 < \alpha$, neither the leading nor the sub-leading term arises from the long-range transfer rate and the dynamics do not deviate significantly from the short-range case.

Appendix D

Rate equation for spin polarization dynamics

In this section we derive our semi-classical model using two different formalisms: the master equation and Fermi's golden rule [306, 328, 178, 177].

D.1 Master equation approach

In developing a master equation approach to the polarization transfer rate in our spin system, we begin by isolating a single pair of spins whose polarization dynamics we wish to study. Let us denote them by S and P (here we restrict our analysis of the NV center to the two lowest levels of interest in the polarization transfer dynamics dynamics) For each of the spins, let us associate Pauli operators $\sigma^z, \sigma^-, \sigma^+$. The two-spin Hamiltonian can be written as:

$$H = (\Delta + \delta_S)\frac{\sigma_S^z}{2} + (\Delta + \delta_P)\frac{\sigma_P^z}{2} + J_{zz}\sigma_S^z\sigma_P^z + J_\perp(\sigma_S^+\sigma_P^- + \sigma_S^-\sigma_P^+) \tag{D.1}$$

where we already focus on the approximate energy conserving terms $J_{zz}, J_\perp, \delta^S, \delta^P \ll \Delta$. The only two states that can exhibit dynamics due to the interactions live in the zero magnetization subspace $\{\lvert\uparrow_S\downarrow_P\rangle = \lvert A\rangle, \lvert\downarrow_S\uparrow_P\rangle = \lvert B\rangle\}$ with Hamiltonian:

$$H_{sub} = \delta\lvert A\rangle\langle A\rvert + J_\perp[\lvert A\rangle\langle B\rvert + \lvert B\rangle\langle A\rvert] \ , \tag{D.2}$$

where δ accounts for the energy mismatch between the two levels. In isolation, the population of the two states would coherently oscillate with a well-defined frequency; the presence of a bath of P1s and optical pumping leads to additional decoherence dynamics that modify the dynamics strikingly. These can be self-consistently included within the density matrix formalism, by adding a off-diagonal decoherence decay rate and optical pumping to an additional level.

	Rate $[\mu s^{-1}]$
$\Gamma_{\text{dec}} = k_{41} = k_{52} = k_{63}$	66 ± 5
k_{47}	7.9 ± 4.1
$k_{57} = k_{67}$	53 ± 7
k_{71}	1.0 ± 0.8
$k_{72} = k_{73}$	0.7 ± 0.5
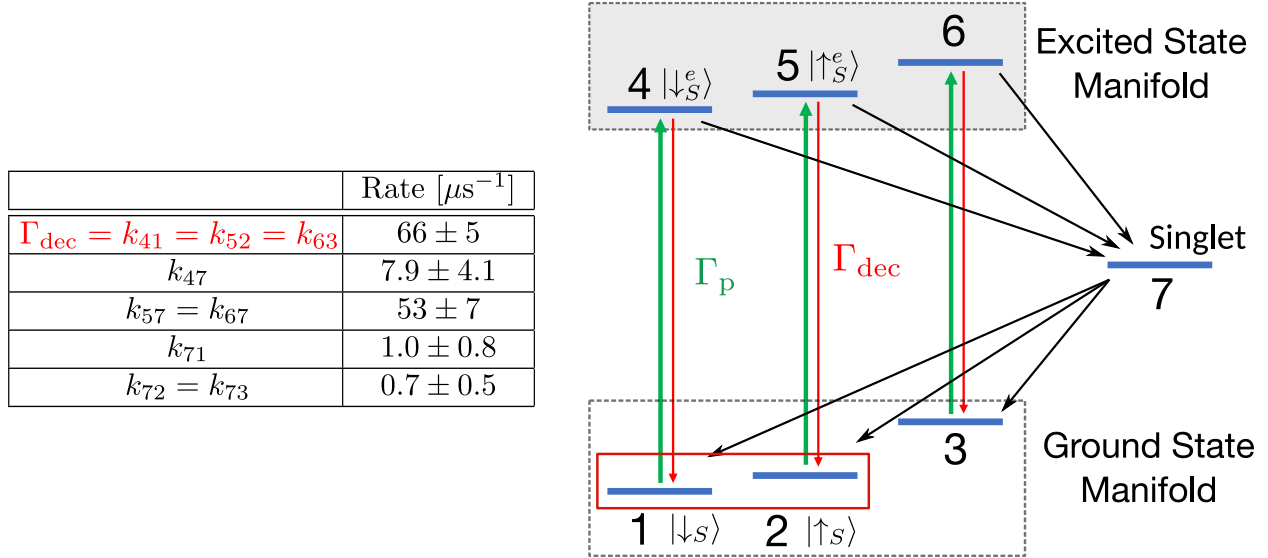
Figure D.1: **Transition rates between different nitrogen vacancy internal levels.** Diagram of the NV internal structure with $|m_s = 0\rangle = |\downarrow_S\rangle$ and $|m_s = -1\rangle = |\uparrow_S\rangle$ levels highlighted. The NV level structure is composed of a spin-1 ground state and excited manifold as well as a single level. Rates between the different NV levels (table) as measured in Refs. [465, 529].

Optical pumping to another state

In simulating the dynamics of the experiment, one important feature is the polarization of the NV via its internal structure. Briefly, the full structure of the NV includes two excited spin-1 manifolds, as well as a singlet level, Fig. D.1. The various decay rates between the different states (independently studied in Refs. [465, 529]) leads to a preferential polarization of the $|m_s = 0\rangle$ state in the ground state manifold, under spin-conserving optical polarization from the ground state to the excited states—let the rate of this process be Γ_{p} and the natural decay rate to be Γ_{dec}.

To study this effect, let us consider optical pumping of the ground state levels $|\uparrow_S\rangle$ and $|\downarrow_S\rangle$ to the corresponding excited states $|\uparrow_S^e\rangle$ and $|\downarrow_S^e\rangle$. In the full Hilbert space, these induce transition $|A\rangle = |\uparrow_S\downarrow_P\rangle \leftrightarrow |\uparrow_S^e\downarrow_P\rangle = |C\rangle$ and $|B\rangle = |\downarrow_S\uparrow_P\rangle \leftrightarrow |\downarrow_S^e\uparrow_P\rangle = |D\rangle$. The corresponding Linbladian quantum jump term for both pumping and decay are given by:

$$\dot{\rho}_{\text{opt+dec}} = -\frac{\Gamma_{\text{p}}}{2} \left[|A\rangle \langle A| \rho + \rho |A\rangle \langle A| - |C\rangle \langle C| \rho_{AA} + |B\rangle \langle B| \rho + \rho |B\rangle \langle B| - 2 |D\rangle \langle D| \rho_{BB} \right]$$
$$- \frac{\Gamma_{\text{dec}}}{2} \left[|C\rangle \langle C| \rho + \rho |C\rangle \langle C| - 2 |A\rangle \langle A| \rho_{CC} + |D\rangle \langle D| \rho + \rho \langle D|D\rangle - 2 |B\rangle \langle B| \rho_{DD} \right]$$
$$\tag{D.3}$$

which becomes a bit more insightful in matrix form:

$$
\dot{\rho}_{\text{opt+dec}} =
\left[
\begin{array}{cc|cc}
-\Gamma_{\text{p}}\rho_{AA} + \Gamma_{\text{dec}}\rho_{CC} & -\Gamma_{\text{p}}\rho_{AB} & -\bar{\gamma}\rho_{AC} & -\bar{\gamma}\rho_{AD} \\[2ex]
-\Gamma_{\text{p}}\rho_{BA} & -\Gamma_{\text{p}}\rho_{BB} + \Gamma_{\text{dec}}\rho_{DD} & -\bar{\gamma}\rho_{BC} & -\bar{\gamma}\rho_{BD} \\[2ex]
-\bar{\gamma}\rho_{CA} & -\bar{\gamma}\rho_{CB} & \Gamma_{\text{p}}\rho_{AA} - \Gamma_{\text{dec}}\rho_{CC} & -\Gamma_{\text{dec}}\rho_{CD} \\[2ex]
-\bar{\gamma}\rho_{DA} & -\bar{\gamma}\rho_{DB} & -\Gamma_{\text{dec}}\rho_{DC} & \Gamma_{\text{p}}\rho_{BB} - \Gamma_{\text{dec}}\rho_{DD}
\end{array}
\right]
$$

$$(D.4)$$

where $\bar{\gamma} = (\Gamma_{\text{p}} + \Gamma_{\text{dec}})/2$.

Immediately, we observe that the off-diagonal corrections with the $|C\rangle$ and $|D\rangle$ states are simply decaying. Since they start at zero, they remain zero and do not affect the dynamics of the system. The pumping only affects the dynamics between $|A\rangle$ and $|B\rangle$ by inducing an additional decoherence of off-diagonal ρ_{AB} term. The remaining dynamics affect only the diagonal component, which correspond to the populations in each of the levels.

This highlights that the presence of the complex structure of the NV center can be accounted by the diagonal components of the density matrix, up to an additional decoherence rate causes by the pumping to the excited manifold.

Extrinsic decoherence

By contrast, adding the extrinsic decoherence rate arising from other spins in the system is much simpler and corresponds to an additional decay of the off-diagonal terms with rate γ.

Putting everything together, the equations of motion are given by:

$$\dot{\rho}_{AA} = -iJ_{\perp}(\rho_{BA} - \rho_{AB}) - \Gamma_{\text{p}}\rho_{AA} + \Gamma_{\text{dec}}\rho_{CC} \tag{D.5}$$

$$\dot{\rho}_{BB} = -iJ_{\perp}(\rho_{AB} - \rho_{BA}) - \Gamma_{\text{p}}\rho_{BB} + \Gamma_{\text{dec}}\rho_{DD} \tag{D.6}$$

$$\dot{\rho}_{CC} = \Gamma_{\text{p}}\rho_{AA} - \Gamma_{\text{dec}}\rho_{CC} \tag{D.7}$$

$$\dot{\rho}_{DD} = \Gamma_{\text{p}}\rho_{BB} - \Gamma_{\text{dec}}\rho_{DD} \tag{D.8}$$

$$\dot{\rho}_{AB} = (i\delta - \gamma - \Gamma_{\text{exc}})\rho_{AB} - iJ_{\perp}(\rho_{BB} - \rho_{AA}) = [\dot{\rho}_{BA}]^{*} \tag{D.9}$$

while the remaining terms are zero. Adiabatically eliminating the coherence between $|A\rangle$ and $|B\rangle$, we get a modified set of equations for ρ_{AA} and ρ_{BB}:

$$\dot{\rho}_{AA} = -2|J_{\perp}|^{2}(\rho_{AA} - \rho_{BB})\frac{\gamma + \Gamma_{\text{p}}}{(\gamma + \Gamma_{\text{p}})^{2} + \delta^{2}} - \Gamma_{\text{p}}\rho_{AA} + \Gamma_{\text{dec}}\rho_{CC} \tag{D.10}$$

$$\dot{\rho}_{BB} = -2|J_{\perp}|^{2}(\rho_{BB} - \rho_{AA})\frac{\gamma + \Gamma_{\text{p}}}{(\gamma + \Gamma_{\text{p}})^{2} + \delta^{2}} - \Gamma_{\text{p}}\rho_{BB} + \Gamma_{\text{dec}}\rho_{DD} \tag{D.11}$$

Finally, we assume that the density matrix remains diagonal, $\rho_{AA} \approx \rho_{\uparrow\uparrow}^{S}\rho_{\downarrow\downarrow}^{P}$ and $\rho_{BB} \approx \rho_{\downarrow\downarrow}^{S}\rho_{\uparrow\uparrow}^{P}$. In a similar way we assume $\dot{\rho}_{AA}$ captures the polarization transfer rate so $\dot{\rho}_{AA} \approx \dot{\rho}_{\uparrow\uparrow}^{S} = -\dot{\rho}_{\downarrow\downarrow}^{P}$.

D.2   Fermi's golden rule

A different way to derive our semi-classical model is through Fermi's golden rule; polarization exchange corresponds to decay of a single spin to a bath composed of all other spin in the system. Owing to the presence of strong disorder (both on on-site fields and position), the spectrum of the bath modes should exbhibit important structure—peaked around the energy difference of each spin and with some broadening γ induced by interactions.

A more precise analysis of the decay closely follows the analysis of decay of an atom in electromagnetic field. Focusing on a two level spin $|s\rangle = \in \{|\uparrow\rangle, |\downarrow\rangle\}$ and a set of bath modes $|k\rangle$, the Hilbert space of the system undergoing decay can be written as $\{|\uparrow, 0\rangle = |e\rangle, |\downarrow, k\rangle = |g_k\rangle\}$, interacting via the Hamiltonian:

$$H = (\Delta + \delta)|e\rangle\langle e| + \sum_k \epsilon_k |g_k\rangle\langle g_k| + \sum_k J\big[|e\rangle\langle g_k| + |g_k\rangle\langle a|\big] \tag{D.12}$$

where $\Delta + \delta$ corresponds to the splitting of the spin of interest and ϵ_k the energy of the mode k of the bath. Moving into the the interaction picture of $|e\rangle$ and $|g_k\rangle$:

$$H_{int} = \sum_k J_k \left[e^{-i((\Delta+\delta)-\epsilon_k)t} |e\rangle\langle g_k| + e^{i((\Delta+\delta)-\epsilon_k)t} |g_k\rangle\langle e| \right] \ . \tag{D.13}$$

In the case when either of the spins is being pumped (like the NV must be during polarization), there will be an additional decoherence channel proportional to the strength of the pumping $\Gamma_{\rm p}$. Including this contribution is most straightforwardly done via the density matrix ρ, where it emerges as a decay of the off-diagonal component.

$$\dot\rho_{ee} = -i\sum_k J \left[e^{-i((\Delta+\delta)-\epsilon_k)t}\rho_{g_k e} - e^{i((\Delta+\delta)-\epsilon_k)t}\rho_{eg_k} \right] \tag{D.14}$$

$$\dot\rho_{eg_k} = -iJe^{-i((\Delta+\delta)-\epsilon_k)t}(\rho_{g_k g_k} - \rho_{ee}) - \Gamma_{\rm p}\rho_{eg_k} \tag{D.15}$$

Formally integrating the second equation assuming zero coherence at $t = 0$, $\rho_{eg_k}(t = 0) = 0$ yields:

$$\rho_{eg_k} = -iJ\int_0^t dt' \, (\rho_{g_k g_k}(t') - \rho_{ee}(t'))e^{-i((\Delta+\delta)-\epsilon_k)t'}e^{-\Gamma_{\rm p}(t-t')} \tag{D.16}$$

Inserting into the Eq. D.14 and focusing on the first term, we have:

$$e^{-i((\Delta+\delta)-\epsilon_k)t} \int_0^t dt' \, [\rho_{g_k g_k}(t') - \rho_{ee}(t')] e^{i((\Delta+\delta)-\epsilon_k)t'} e^{-\Gamma_{\mathrm{p}}(t-t')} \tag{D.17}$$

$$\approx \sum_k [\rho_{g_k g_k}(t) - \rho_{ee}(t)] \int_0^t dt' \, e^{[-i((\Delta+\delta)-\epsilon_k)-\Gamma_{\mathrm{p}}](t-t')} \tag{D.18}$$

$$\approx \lim_{t\to\infty} \sum_k (\rho_{g_k g_k}(t) - \rho_{ee}(t)) \frac{1 - e^{[-i((\Delta+\delta)-\epsilon_k)-\Gamma_{\mathrm{p}}]t}}{i((\Delta+\delta)-\epsilon_k)+\Gamma_{\mathrm{p}}} \tag{D.19}$$

$$\approx \sum_k (\rho_{g_k g_k}(t) - \rho_{ee}(t)) \frac{1}{i((\Delta+\delta)-\epsilon_k)+\Gamma_{\mathrm{p}}} \tag{D.20}$$

$$\approx (\rho_{BB} - \rho_{AA}) \int_{-\infty}^{\infty} d\epsilon \frac{\rho(\epsilon)}{i((\Delta+\delta)-\epsilon_k)+\Gamma_{\mathrm{p}}} \tag{D.21}$$

where, we have have taken $\rho_{g_k g_k}$ to be slowly varying across different modes g_k around the center frequency of the bath modes and thus the average $\overline{\rho_{g_k g_k}}$. Physically, this corresponds to coupling to a single other spin, where the bath modes correspond to a broadening of the spin energy levels and their occupation is determined by the state of the spin (either in $|\uparrow\rangle$ or $|\downarrow\rangle$). Considering the interaction of multiple such modes corresponds to summing over many independent channels as described above.

$\rho(\epsilon)$ is the density of states of the bath modes, allowing us to transform the sum into an integral, which is a necessary input in our theory. Motivated by the usual broadening in atomic physics, we take $\rho(\epsilon)$ to a Lorentzian, that in the rotating frame, is centered around Δ, with FWHM 2γ:

$$\rho(\epsilon) = \frac{1}{\pi} \frac{\gamma}{\gamma^2 + (\epsilon-\Delta)^2} \ . \tag{D.22}$$

As such δ alone captures the energy mismatch between the spin and the center of the bath. Solving for the integral in Eq. D.21 and including the second term (which is the complex conjugate of the first), we arrive at the formula for polarization transfer:

$$\dot{\rho}_{ee} = |J|^2 (\overline{\rho_{g_k g_k}} - \rho_{ee}) 2\,\mathrm{Re}\left[\frac{1}{(\gamma+\Gamma_{\mathrm{p}})+i\delta}\right] = -2|J|^2 \frac{\gamma+\Gamma_{\mathrm{p}}}{(\gamma+\Gamma_{\mathrm{p}})^2+\delta^2}(\rho_{ee} - \overline{\rho_{g_k g_k}}) \ . \tag{D.23}$$

Analogous to the master equation case, we assume that the density matrix is separable between the two spins involved analyzed and thus $\rho_{ee} = \rho_{\uparrow\uparrow}^{(1)}\rho_{\downarrow\downarrow}^{(2)}$ while $\overline{\rho_{g_k g_k}} = \rho_{\downarrow\downarrow}^{(1)}\rho_{\uparrow\uparrow}^{(2)}$ and $\dot{\rho}_{ee} \approx \dot{\rho}_{\uparrow\uparrow}^{(1)} = -\dot{\rho}_{\downarrow\downarrow}^{(2)}$.

Generalizing to many different spins corresponds to summing over the different bath spins that the first spin can decay to—each spin gives rise to a decay channel with slightly broadened levels and interacting with different couplings J. Labelling the bath spins with j, we arrive at the total depolarization of the initial spin as:

$$\dot{\rho}_{\uparrow\uparrow}^{(1)} = \sum_j -2|J_j|^2 \frac{\gamma+\Gamma_{\mathrm{p}}}{(\gamma+\Gamma_{\mathrm{p}})^2+\delta^2}(\rho_{\uparrow\uparrow}^{(1)}\rho_{\downarrow\downarrow}^{(j)} - \rho_{\downarrow\downarrow}^{(1)}\rho_{\uparrow\uparrow}^{(j)}) \tag{D.24}$$

under pumping of spin (1) of strength Γ_{p}.

Appendix E

Derivation of the decoherence profile in disordered spin systems

Here, we provide additional details for the derivation of the decoherence profile discussed in Chapter 19. Let us recall the setup. Our system consists of a probe spin $\hat{s}_p$ and a set of interacting system spins $\hat{s}_i$, coupled via long-range, Ising interactions:

$$H_z = \sum_i \frac{J_z g_i}{r_i^\alpha} \hat{s}_p^z \hat{s}_i^z. \tag{E.1}$$

Here, we explicitly separate J_z as an overall constant interaction strength from any possible angular dependence g_i. We note that decoherence of the probe spin is due to spectral diffusion (i.e. dephasing) rather than depolarization, because the probe-system coupling includes no spin-exchange terms. This situation is natural in the NV-P1 systems used in our experiments, since the NV and P1 centers are far detuned and spin-exchange interactions are strongly suppressed [616].

We now proceed to derive the decoherence decay profile of the probe spins, first by treating the quantum operator $\hat{s}_i^z$ as a classical variable s_i^z as in the main text. Later on, we will analyze the problem within a precise quantum description, and discuss the validity of different semi-classical approximations in different physical scenarios.

E.1 Average over trajectories

With a spin-1/2 probe initialized to point along the x-axis of the Bloch sphere, the coherence is simply defined as $C(t) = 2\langle s_p^x(t)\rangle$. We apply a pulse sequence, such as Ramsey or spin echo, in which π-pulses applied to the probe spin effectively flip the sign of the Ising interaction, H_z; let this sign be captured by the function $\eta(t';t)$. For a particular $\eta(t';t)$ applied on the probe spin up to the measurement duration t [Table E.1], we then have

$$s_p^x(t) = \frac{1}{2}\mathrm{Re}\left[e^{i\sum_i \frac{J_z g_i}{r_i^\alpha}\int_0^t \eta(t')s_i^z(t')dt'}\right]. \tag{E.2}$$

Explicitly, $\eta(t'; t)$ is the Fourier transform of the filter function $f(\omega; t)$ discussed in the main text. The phase

$$\phi(t) = \frac{J_z g_i}{r_i^\alpha} \int_0^t dt' \; \eta(t') s_i^z(t') \tag{E.3}$$

is a generalization of the phase $\phi(t)$ for a Ramsey sequence defined in the main text, which is obtained by setting $\eta(t') = 1$. The simplest case to treat analytically — although not necessarily the most physically relevant, as discussed in the main text — is that of Gaussian-distributed phases $\phi(t)$. Making this approximation for now, we obtain

$$\langle s_p^x(t) \rangle = \frac{1}{2} \exp \left\{ -\frac{1}{2} \left\langle \left| \sum_i \frac{J_z g_i \int_0^t dt' \; \eta(t') s_i^z(t')}{r_i^\alpha} \right|^2 \right\rangle \right\} = \frac{1}{2} \prod_i \exp \left\{ -\frac{1}{2} \left[\frac{J_z |g_i| \chi(t)^{\frac{1}{2}}}{2 r_i^\alpha} \right]^2 \right\}, \tag{E.4}$$

where

$$\chi(t) \equiv 4 \left\langle \left[\int_0^t dt' \; \eta(t') s_i^z(t') \right]^2 \right\rangle = \int_0^t dt' \int_0^t dt'' \; \eta(t') \eta(t'') \langle 4 s_i^z(t') s_i^z(t'') \rangle. \tag{E.5}$$

We assume the system spins are independent, and include a factor of 4 in the definition of $\chi(t)$ to normalize the correlation function of spin-1/2 particles. To evaluate $\chi(t)$ analytically, we assume a Markovian form for the correlation function

$$\xi(t') \equiv \langle 4 s_i^z(t_0) s_i^z(t_0 + t') \rangle = e^{-|t'|/\tau_c}, \tag{E.6}$$

where τ_c is the correlation time of the spins s_i, and we use the fact that $\langle 4 s_i^z(t_0) s_i^z(t_0) \rangle = 1$ at infinite temperature. Depending on the specific pulse sequence applied on the bath spins [as captured by $\eta(t')$], we can analytically obtain the expression for $\chi(t)$, as shown in Table E.1.

We note that Eq. E.5 can also be written in frequency space as:

$$\chi(t) = \int d\omega \; |f(\omega; t)|^2 S(\omega), \tag{E.7}$$

where $f(\omega; t)$ and $S(\omega)$ are the Fourier transforms of $\eta(t'; t)$ and $\xi(t')$, respectively. The preceding analysis thus constitutes a derivation of Eq. 19.2 in Chapter 19.

E.2 Average over positional randomness

Assuming the P1 spins s_i occupy a total volume V, the average signal over positional disorder can be evaluated as follows [175]:

$$
\begin{aligned}
\text{Signal} &= \frac{1}{2} \int \cdots \int \frac{d^D \vec{r}_1}{V} \frac{d^D \vec{r}_2}{V} \cdots \frac{d^D \vec{r}_N}{V} \prod_{i=1}^{N} \exp \left\{ -\frac{1}{2} \left[\frac{J_z |g_i| \chi(t)^{\frac{1}{2}}}{2 r_i^\alpha} \right]^2 \right\} \\
&= \frac{1}{2} \left[\int \frac{d^D \vec{r}}{V} \exp \left\{ -\frac{1}{2} \left[\frac{J_z |g_i| \chi(t)^{\frac{1}{2}}}{2 r^\alpha} \right]^2 \right\} \right]^N \\
&= \frac{1}{2} \left[1 - \frac{1}{V} \int \left(1 - \exp \left\{ -\frac{1}{2} \left[\frac{J_z |g| \chi(t)^{\frac{1}{2}}}{2 r^\alpha} \right]^2 \right\} \right) d^D \vec{r} \right]^N.
\end{aligned}
\tag{E.8}
$$

In the thermodynamic limit ($N, V \to \infty$ with fixed spin density $\frac{N}{V} = n$), we have

$$
\begin{aligned}
\text{Signal} &= \frac{1}{2} \exp \left\{ -n \int \left(1 - e^{-\frac{1}{2} \left[\frac{J_z |g| \chi(t)^{\frac{1}{2}}}{2 r^\alpha} \right]^2} \right) d^D \vec{r} \right\} \\
&= \frac{1}{2} \exp \left\{ -n \int \left(1 - e^{-\frac{1}{2} z^2} \right) r^{D-1} dr d\Omega \right\} \\
&= \frac{1}{2} \exp \left\{ -\frac{n}{\alpha} \left(\frac{J_z \chi^{\frac{1}{2}}}{2} \right)^{\frac{D}{\alpha}} \int \left(1 - e^{-\frac{1}{2} z^2} \right) z^{-\frac{D}{\alpha} - 1} dz \int |g|^{\frac{D}{\alpha}} d\Omega \right\} \\
&= \frac{1}{2} \exp \left\{ -\frac{n D A_D}{\alpha} \left[-\frac{\Gamma(-\frac{D}{2\alpha})}{2^{\frac{D}{2\alpha} + 1}} \right] \left[\frac{|\bar{g}| J_z \chi(t)^{\frac{1}{2}}}{2} \right]^{\frac{D}{\alpha}} \right\},
\end{aligned}
\tag{E.9}
$$

where we make the substitution $z = \frac{J_z |g_i| \chi(t)^{\frac{1}{2}}}{2 r_i^\alpha}$, $A_D = \frac{\pi^{\frac{D}{2}}}{\Gamma(\frac{D}{2} + 1)}$ is the volume of a D-dimensional unit ball, and $|\bar{g}| = \left(\frac{\int |g|^{\frac{D}{\alpha}} d\Omega}{\int d\Omega} \right)^{\frac{\alpha}{D}}$ is the averaged angular dependence over a D-dimensional solid angle. The integral converges when $D < 2\alpha$, which agrees with the intuition that when $D \geq 2\alpha$, the effective long-range coupling decays so slowly that any resonance counting blows up.

Combining the results in Table E.1 and Eq. E.9, we obtain the analytical form of the decoherence signal, averaged over the dynamical and positional randomness of the many-body system. In particular, for both the short-time and the long-time limits, the decay profiles are stretched exponentials, whose stretch powers and decay timescales are summarized in Table E.2.

We note that the positional disorder is crucial in determining the shape of the decoherence decay profile. As highlighted by the difference between Eq. E.4 (excluding positional averaging) and Eq. E.9 (including positional averaging), the decay associated with a single spatial configuration is qualitatively different from the decay after averaging over positional disorder. Intuitively, each positional configuration has its own decay profile, and the experimental signal is an average over these different decays. At different times, the main contribution to the averaged signal can come from different positional configurations. For example, if different positional configurations exhibit exponential decays with different decay rates, then at short times those with fast decay rates dominate the averaged signal, but at long times those with slow decay rates become dominant. With this in mind, the coherence is determined by many different positional realizations, rather than the decay of a specific spatial configuration. By contrast, we note that if the bath spins are on a regular lattice, the decay profile follows the shape of the single positional realization case (Eq. E.4). In particular, for a regular lattice, the spin echo always decays as a stretched exponential with a stretch exponent of 3, independent of D and α.

E.3 Quantum description

In the quantum description, the initial state of the full system (i.e. both the probe spin and the many-body system) is given by,

$$|\Psi_0\rangle = |\psi_0^s\rangle \otimes \left(\frac{|\uparrow\rangle + |\downarrow\rangle}{\sqrt{2}} \right), \tag{E.10}$$

where $|\psi_0^s\rangle$ is the initial state of the many-body system. The dynamics of the full system are governed by the time-dependent Hamiltonian, $H_{\text{tot}} = \eta(t')H_z + H_{\text{s}}$, where H_{s} is the Hamiltonian governing the intrinsic dynamics of the many-body system. After a measurement duration t, the initial state is transformed as

$$|\Psi(t)\rangle = \mathcal{T}e^{-i\int_0^t [\eta(t')H_z + H_{\text{s}}]dt'} |\Psi_0\rangle = \frac{(U_\uparrow |\psi_0^s\rangle) |\uparrow\rangle + (U_\downarrow |\psi_0^s\rangle) |\downarrow\rangle}{\sqrt{2}}, \tag{E.11}$$

where

$$U_\uparrow = \mathcal{T}e^{-i\int_0^t [\eta(t')\sum_i \frac{J_z g_i}{2r_i^\alpha} \hat{s}_i^z + H_{\text{s}}]dt'}, \qquad U_\downarrow = \mathcal{T}e^{i\int_0^t [\eta(t')\sum_i \frac{J_z g_i}{2r_i^\alpha} \hat{s}_i^z + H_{\text{s}}]dt'} \tag{E.12}$$

are the evolution operators acting only on the system spins $\hat{s}_i$ given the z-component of the probe spin. The coherence, $\langle \hat{s}_p^x \rangle$, corresponds to the overlap between the two evolution operators:

$$\langle \hat{s}_p^x \rangle = \text{Re}[\text{Tr}(U_\uparrow U_\downarrow^\dagger)]/\mathcal{N}, \tag{E.13}$$

where $\mathcal{N}$ is a normalization factor corresponding to the dimension of the system's Hilbert space.

Let us now move to the interaction picture by making the following substitution:

$$U_{\uparrow,\downarrow} = U_0 \tilde{U}_{\uparrow,\downarrow}$$
$$U_0 = \mathcal{T} \mathrm{e}^{-i \int_0^t H_\mathrm{s} dt'}. \tag{E.14}$$

Then the two evolution operators and the decoherence signal become

$$\tilde{U}_{\uparrow,\downarrow} = \mathcal{T} \mathrm{e}^{\mp i \int_0^t \eta(t') \sum_i \frac{J_z g_i}{2 r_i^\alpha} \hat{\tilde{s}}_i^z(t') dt'} \tag{E.15}$$

$$\langle \hat{s}_p^x \rangle = \mathrm{Re}[\mathrm{Tr}(\tilde{U}_\uparrow \tilde{U}_\downarrow^\dagger)]/\mathcal{N} = \mathrm{Re}[\mathrm{Tr}(\tilde{U}_\uparrow^2)]/\mathcal{N} \tag{E.16}$$

where

$$\hat{\tilde{s}}_i^z(t) = U_0^\dagger(t) \hat{s}_i^z(t) U_0(t). \tag{E.17}$$

The full quantum expression for the probe spin coherence $\langle \hat{s}_p^x \rangle$ obtained in Eq. E.16 provides several important insights into the semi-classical approach we used in the main text and in the previous sections. First, Eq. E.16 is formally the same as Eq. E.2, except that $\hat{\tilde{s}}_i^z(t)$ is now a quantum operator. Second, assuming that different spins $\hat{\tilde{s}}_i^z(t)$ are independent, the problem reduces to an evaluation of the eigenvalues of the single spin evolution operator $\tilde{U}_\uparrow$ for each spin i independently.

While Eq. E.16 already averages over all possible initial states of both $\hat{s}_i^z$ and its bath (i.e. other quantum degrees of freedom in H_s), one should also average the signal over the ensemble of the trajectories generated by the randomness of H_s (which arises, for example, from the polychromatic driving field, coupling to other classical degrees of freedom, positional and on-site disorder, etc.). This last point about two kinds of averages (one from different configurations of the many-body system and the other from the randomness of H_s) is essential for determining whether a telegraph or a continuous (Gaussian) random variable can better describe the many-body noise of $\hat{s}_i^z$. We note that, since the auto-correlator $\xi(t) \propto \langle \hat{\tilde{s}}_i^z(t) \hat{\tilde{s}}_i^z(0) \rangle$ always performs the two types of averages simultaneously, it does not contain the full information of the many-body noise.

E.4 Understanding decoherence dynamics in different physical scenarios

While Eq. E.15 provides the formula for the decoherence dynamics of a spin coupled to a dynamical bath, performing the necessary computation is intractable except in specific cases. In the following subsections, we describe two instructive examples where the explicit computation of Eq. E.15 can be performed and the relationship between the nature of the bath and the Gaussian or Telegraph noise is made clear.

Probe coupled to a single spin evolving under an external drive

First, we consider the case where the decoherence noise is generated by a single spin, whose dynamics are controlled by an external drive. In this case, the interaction Hamiltonian is

given by:

$$H_{\mathrm{s}} = \Omega[\hat{s}_i^x \cos\theta(t) + i\sin\hat{s}_i^y\theta(t)] \tag{E.18}$$

where Ω characterizes the strength of the drive and $\theta(t)$ is a time-dependent phase. The presence of such a time-dependent phase leads to the polychromatic drive described in the main text—$\theta(t)$ is chosen to follow a Gaussian stochastic process [266], and is randomized across different runs of the experiment. Crucially, for each run of the experiment, the dynamics induced by H_{s} generate a particular trajectory around the Bloch sphere without any loss of single-particle coherence. As a result, the continuous spin rotation leads to a continuous change in the strength of the noise generated—this leads to the natural description of $s_i^z(t)$ as a continuous classical variable.

We emphasize that within this framework, there is a single phase accumulated due to the noise for the particular driving $\theta(t)$. As a result, to obtain a Gaussian distributed noise, one must additionally average over different driving $\theta(t)$. In the experiment this corresponds exactly to the polychromatic drive, where the phase of each experimental run is sampled from a Gaussian-Markov process.

Probe coupled to a strongly interacting system

We now turn to the opposite limit, where the dynamics of the system are strongly interacting. In this case, the dynamics of $\hat{s}_i^z(t)$ mirror that of a spin interacting with a large bath and the dynamics can be captured via the formalism of quantum jumps and the master equation. In particular, the dynamics of $\hat{s}_i^z(t)$ is similar to that of a spin undergoing spontaneous emission and absorption with a photon/phonon bath—starting in either the state $|\uparrow\rangle$ or $|\downarrow\rangle$, the system undergoes quantum jumps into the opposite state at a rate given by $1/\tau_c$ [362]. Eq. E.15 can then be obtained by computing the decoherence decay averaged over all the possible quantum jump trajectories—this precisely corresponds to a telegraph-like classical noise.

A few remarks are in order. First, we note that unlike the single driven spin case, the different trajectories within a single realization ensure that the phase accumulated already corresponds to a distribution and no additional averaging is necessary. This contrasts with the single spin example, where an explicit averaging over the driving fields was necessary to obtain the distribution of accumulated phases.

Second, this behavior can also be understood in the picture of the operator evolution described in Eq. E.15. Due to its coupling with the Markovian bath, the operator $\hat{\tilde{s}}_i^z(t)$ quickly spreads across a large number of degrees of freedom. As a result, the operators at different times commute with each other, i.e. $[\hat{\tilde{s}}_z^i(t), \hat{\tilde{s}}_z^i(t')] = 0$. This immediately leads to two consequences: 1) the time-ordering in Eq. E.15 is trivial and the eigenvalues of the exponential are the exponential of the eigenvalues of $\int_0^t \eta(t')\hat{\tilde{s}}_i^z(t')dt'$; 2) $\hat{\tilde{s}}_i^z(t)$ can be diagonalized simultaneously for all times. In this common eigenbasis, each eigenvector (labelled by μ) has a time-dependent eigenvalue $\lambda_\mu(t)$ corresponding to the time-dependent operator $\hat{\tilde{s}}_i^z(t)$,

and eventually contributes an eigenvalue $\int_0^t \eta(t')\lambda_\mu(t')dt'$ to the spectrum of $\int_0^t \eta(t')\hat{\tilde{s}}_i^z(t')dt'$. Crucially, since $s_z^2(t) = 1/4$, $\lambda_\mu(t)$ can only be $\pm 1/2$.[1] In this language, the decay of spin correlations $\langle \hat{\tilde{s}}_i^z(t)\hat{\tilde{s}}_i^z(t')\rangle \propto \mathrm{e}^{-|t-t'|/\tau_c}$ is equivalent to the statement that the number of eigenvectors with $\lambda_\mu(t) = \lambda_\mu(t')$ decays exponentially in time with rate $1/\tau_c$. Assuming that each eigenvector is independent, the associated eigenvalue $\lambda_\mu(t)$ follows a Poisson process and jumps between $\pm 1/2$. The dynamics of each $\lambda_\mu(t)$ can then be understood as either a single quantum jump trajectory (in the quantum language), or a single classical telegraph noise realization (in the classical description).

Spin coupled to a generic many-body system

Taking the above two examples into consideration, whether a generic many-body system is described by the Gaussian or the telegraph random variable is determined by the speed of the operator spreading. If the spreading of the operator is slow, the dynamics of $\hat{\tilde{s}}_z^i(t)$ remain constrained to a few sites throughout the measurement duration and the system appears coherent-like (leading to continuous Gaussian noise). If the spreading of the operator is fast, $\hat{\tilde{s}}_z^i(t)$ quickly spreads across many spins and the rest of the system acts as an effective Markovian bath, leading to telegraph noise.

In our disordered, strongly-interacting system, we conjecture that disorder leads to the slow spread of $\hat{\tilde{s}}_i^z$, and the decay of the auto-correlator $\langle \hat{\tilde{s}}_i^z(0)\hat{\tilde{s}}_i^z(t)\rangle$ mostly results from the different trajectories of local dynamics (originating from different H_s owing to different initial configurations of the bath spins). This is consistent with our experimental observation of the spin-echo decay stretch power $\beta = 3D/2\alpha$ for a three-dimensional dipolar ensemble, and is characteristic of the Gaussian noise model.

---

[1]As long as the eigenspectrum of the original local operator is discrete, so will $\lambda_\mu(t)$; as a result, we expect the same telegraph noise description in the context of higher spin systems.

Sequence	$\eta(t';t)$	$\chi(t)$	Short-time $t \ll \tau_c$	Long-time $t \gg \tau_c$
Ramsey (DEER)	1	$2\tau_c t - 2\tau_c^2 \left(1 - e^{-\frac{t}{\tau_c}}\right)$	$t^2 - \frac{t^3}{3\tau_c}$	$2\tau_c t - 2\tau_c^2$
Spin Echo	$\begin{cases} 1 & 0 \le t' < t/2 \\ -1 & t/2 \le t' < t \end{cases}$	$2\tau_c t - 2\tau_c^2 \left(3 + e^{-\frac{t}{\tau_c}} - 4e^{-\frac{t}{2\tau_c}}\right)$	$\frac{t^3}{6\tau_c}$	$2\tau_c t - 6\tau_c^2$
XY-8	$\begin{cases} 1 & (m - \frac{1}{4})\tau_p \le t' < (m + \frac{1}{4})\tau_p \\ -1 & (m + \frac{1}{4})\tau_p \le t' < (m + \frac{3}{4})\tau_p \end{cases}$	$\frac{\tau_p^2}{12\tau_c} t$	$\frac{\tau_p^2}{12\tau_c} t$	$\frac{\tau_p^2}{12\tau_c} t$

Table E.1: **Phase accumulation for different pulse sequences.** Expressions of $\eta(t';t)$ and $\chi(t)$ for Ramsey/DEER, spin echo, and XY-8. In XY-8, we assume the inter-pulse spacing $\tau_p \ll \tau_c$.

	Profile	Stretch power	Decay timescale
Early-time Ramsey/DEER	$\exp\left[-n\left(C|\bar{g}|J_z t\right)^{\frac{D}{\alpha}}\right]$	$\frac{D}{\alpha}$	$\left(C|\bar{g}|n^{\frac{\alpha}{D}}J_z\right)^{-1}$
Early-time Echo	$\exp\left[-n\left(C|\bar{g}|J_z\sqrt{\frac{1}{6\tau_c}}t^{3/2}\right)^{\frac{D}{\alpha}}\right]$	$\frac{3D}{2\alpha}$	$(6\tau_c)^{\frac{1}{3}}\left(C|\bar{g}|n^{\frac{\alpha}{D}}J_z\right)^{-\frac{2}{3}}$
Late-time Ramsey/DEER and Echo	$\exp\left[-n\left(C|\bar{g}|J_z\sqrt{2\tau_c}t^{1/2}\right)^{\frac{D}{\alpha}}\right]$	$\frac{D}{2\alpha}$	$\left(\frac{1}{2\tau_c}\right)\left(C|\bar{g}|n^{\frac{\alpha}{D}}J_z\right)^{-2}$
XY8	$\exp\left[-n\left(C|\bar{g}|J_z\sqrt{\frac{\tau_p^2}{12\tau_c}}t^{1/2}\right)^{\frac{D}{\alpha}}\right]$	$\frac{D}{2\alpha}$	$\left(\frac{12\tau_c}{\tau_p^2}\right)\left(C|\bar{g}|n^{\frac{\alpha}{D}}J_z\right)^{-2}$

Table E.2: **Summary of early and late-time decoherence profile for different sequences.** Ensemble averaged decay profiles for Ramsey/DEER, spin echo, and XY-8 pulse sequences; $|\bar{g}|$ is the averaged angular dependence, and $C = \frac{1}{2}\left[-\frac{DA_D}{\alpha}\frac{\Gamma(-\frac{D}{2\alpha})}{2^{\frac{D}{2\alpha}+1}}\right]^{\frac{\alpha}{D}}$ is a dimensionless constant only depending on D and α.

Bibliography

[1] D. A. Abanin et al. "Distinguishing Localization from Chaos: Challenges in Finite-Size Systems". In: *Annals of Physics* 427 (2021), p. 168415. DOI: 10.1016/j.aop.2021.168415. arXiv: 1911.04501.

[2] D. A. Abanin et al. "Effective Hamiltonians, Prethermalization and Slow Energy Absorption in Periodically Driven Many-Body Systems". In: *Physical Review B* 95.1 (2017), p. 014112. DOI: 10.1103/PhysRevB.95.014112. arXiv: 1510.03405.

[3] Dmitry Abanin, Wojciech De Roeck, and François Huveneers. "A Theory of Many-Body Localization in Periodically Driven Systems". In: *Annals of Physics* 372 (2016), pp. 1–11. DOI: 10.1016/j.aop.2016.03.010. arXiv: 1412.4752.

[4] Dmitry Abanin, Wojciech De Roeck, and François Huveneers. "Exponentially Slow Heating in Periodically Driven Many-Body Systems". In: *Physical Review Letters* 115.25 (2015), p. 256803. DOI: 10.1103/PhysRevLett.115.256803. arXiv: 1507.01474.

[5] Dmitry Abanin et al. "A Rigorous Theory of Many-Body Prethermalization for Periodically Driven and Closed Quantum Systems". In: *Communications in Mathematical Physics* 354.3 (2017), pp. 809–827. DOI: 10.1007/s00220-017-2930-x. arXiv: 1509.05386.

[6] Dmitry A. Abanin et al. "Many-Body Localization, Thermalization, and Entanglement". In: *Reviews of Modern Physics* 91.2 (2019), p. 021001. DOI: 10.1103/RevModPhys.91.021001. arXiv: 1804.11065.

[7] Alexander G Abanov. "HYDRODYNAMICS OF CORRELATED SYSTEMS: Emptiness Formation Probability and Random Matrices". In: (2006).

[8] Eisuke Abe et al. "Electron Spin Phase Relaxation of Phosphorus Donors in Nuclear Spin Enriched Silicon". In: *Physical Review B* 70.3 (2004), p. 033204. DOI: 10.1103/PhysRevB.70.033204. arXiv: cond-mat/0402152.

[9] M. H. Abobeih et al. "Atomic-Scale Imaging of a 27-Nuclear-Spin Cluster Using a Single-Spin Quantum Sensor". In: *Nature* 576.7787 (2019), pp. 411–415. DOI: 10.1038/s41586-019-1834-7. arXiv: 1905.02095.

[10] E. Abrahams et al. "Scaling Theory of Localization: Absence of Quantum Diffusion in Two Dimensions". In: *Physical Review Letters* 42.10 (1979), pp. 673–676. DOI: `10.1103/PhysRevLett.42.673`.

[11] Kartiek Agarwal et al. "Anomalous Diffusion and Griffiths Effects near the Many-Body Localization Transition". In: *Physical Review Letters* 114.16 (2015), p. 160401. DOI: `10.1103/PhysRevLett.114.160401`. arXiv: `1408.3413`.

[12] AHusain314. *English: Shows Graphical Calculus of Yang Baxter Equation with 3 Strands Being Factorized into Permutations in Two Different Ways.* 2013.

[13] M. Aidelsburger et al. "Experimental Realization of Strong Effective Magnetic Fields in an Optical Lattice". In: *Physical Review Letters* 107.25 (2011), p. 255301. DOI: `10.1103/PhysRevLett.107.255301`.

[14] Anton Alekseev, Dai Jin, and Antti J. Niemi. "Provenance of Classical Hamiltonian Time Crystals". In: *Journal of High Energy Physics* 2020.8 (2020), p. 35. DOI: `10.1007/JHEP08(2020)035`. arXiv: `2002.07023`.

[15] Fabien Alet and Nicolas Laflorencie. "Many-Body Localization: An Introduction and Selected Topics". In: *Comptes Rendus Physique* 19.6 (2018), pp. 498–525. DOI: `10.1016/j.crhy.2018.03.003`. arXiv: `1711.03145`.

[16] Joseph B. Altepeter, Daniel F.V. James, and Paul G. Kwiat. "4 Qubit Quantum State Tomography". In: *Quantum State Estimation.* Ed. by Matteo Paris and Jaroslav Řeháček. Berlin, Heidelberg: Springer, 2004, pp. 113–145. DOI: `10.1007/978-3-540-44481-7_4`.

[17] Ehud Altman, Eugene Demler, and Mikhail D. Lukin. "Probing Many-Body States of Ultra-Cold Atoms via Noise Correlations". In: *Physical Review A* 70.1 (2004), p. 013603. DOI: `10.1103/PhysRevA.70.013603`. arXiv: `cond-mat/0306226`.

[18] B. L. Altshuler et al. "Quasiparticle Lifetime in a Finite System: A Non–Perturbative Approach". In: *Physical Review Letters* 78.14 (1997), pp. 2803–2806. DOI: `10.1103/PhysRevLett.78.2803`. arXiv: `cond-mat/9609132`.

[19] Gideon Amir, Ivan Corwin, and Jeremy Quastel. "Probability Distribution of the Free Energy of the Continuum Directed Random Polymer in 1+1 Dimensions". In: *Communications on Pure and Applied Mathematics* 64.4 (2011), pp. 466–537. DOI: `10.1002/cpa.20347`. arXiv: `1003.0443`.

[20] P. W. Anderson. "Absence of Diffusion in Certain Random Lattices". In: *Physical Review* 109.5 (1958), pp. 1492–1505. DOI: `10.1103/PhysRev.109.1492`.

[21] P. W. Anderson and P. R. Weiss. "Exchange Narrowing in Paramagnetic Resonance". In: *Reviews of Modern Physics* 25.1 (1953), pp. 269–276. DOI: `10.1103/RevModPhys.25.269`.

[22] A. V. Andreev, Steven A. Kivelson, and B. Spivak. "Hydrodynamic Description of Transport in Strongly Correlated Electron Systems". In: *Physical Review Letters* 106.25 (2011), p. 256804. DOI: `10.1103/PhysRevLett.106.256804`. arXiv: `1011.3068`.

[23] K. Arai et al. "Fourier Magnetic Imaging with Nanoscale Resolution and Compressed Sensing Speed-up Using Electronic Spins in Diamond". In: *Nature Nanotechnology* 10.10 (2015), pp. 859–864. DOI: `10.1038/nnano.2015.171`. arXiv: `1409.2749`.

[24] "Proof of a Theorem of A. N. Kolmogorov on the Invariance of Quasi-Periodic Motions under Small Perturbations of the Hamiltonian". In: *Collected Works: Representations of Functions, Celestial Mechanics and KAM Theory, 1957–1965*. Ed. by Vladimir I. Arnold et al. Berlin, Heidelberg: Springer, 2009, pp. 267–294. DOI: `10.1007/978-3-642-01742-1_21`.

[25] Y. Y. Atas et al. "The Distribution of the Ratio of Consecutive Level Spacings in Random Matrix Ensembles". In: *Physical Review Letters* 110.8 (2013), p. 084101. DOI: `10.1103/PhysRevLett.110.084101`. arXiv: `1212.5611`.

[26] Serge Aubry and Gilles André. "Analyticity Breaking and Anderson Localization in Incommensurate Lattices". In: *Ann. Israel Phys. Soc* 3.133 (1980), p. 18.

[27] S. Autti, V. B. Eltsov, and G. E. Volovik. "Observation of a Time Quasicrystal and Its Transition to a Superfluid Time Crystal". In: *Physical Review Letters* 120.21 (2018), p. 215301. DOI: `10.1103/PhysRevLett.120.215301`. arXiv: `1712.06877`.

[28] Sven Bachmann et al. "Automorphic Equivalence within Gapped Phases of Quantum Lattice Systems". In: *Communications in Mathematical Physics* 309.3 (2012), pp. 835–871. DOI: `10.1007/s00220-011-1380-0`.

[29] Yasaman Bahri and Ashvin Vishwanath. "Detecting Majorana Fermions in Quasi-One-Dimensional Topological Phases Using Nonlocal Order Parameters". In: *Physical Review B* 89.15 (2014), p. 155135. DOI: `10.1103/PhysRevB.89.155135`. arXiv: `1303.2600`.

[30] Yasaman Bahri et al. "Localization and Topology Protected Quantum Coherence at the Edge of Hot Matter". In: *Nature Communications* 6.1 (1 2015), p. 7341. DOI: `10.1038/ncomms8341`.

[31] Jinho Baik, Percy Deift, and Kurt Johansson. "On the Distribution of the Length of the Longest Increasing Subsequence of Random Permutations". In: *Journal of the American Mathematical Society* 12.4 (1999), pp. 1119–1178. DOI: `10.1090/S0894-0347-99-00307-0`.

[32] Waseem S. Bakr et al. "Probing the Superfluid to Mott Insulator Transition at the Single Atom Level". In: *Science* 329.5991 (2010), pp. 547–550. DOI: `10.1126/science.1192368`. arXiv: `1006.0754`.

[33] Satish Balay et al. "Efficient Management of Parallelism in Object-Oriented Numerical Software Libraries". In: *Modern Software Tools for Scientific Computing*. Ed. by Erlend Arge, Are Magnus Bruaset, and Hans Petter Langtangen. Boston, MA: Birkhäuser, 1997, pp. 163–202. DOI: `10.1007/978-1-4612-1986-6_8`.

[34] Leon Balents and Matthew P. A. Fisher. "Delocalization Transition via Supersymmetry in One Dimension". In: *Physical Review B* 56.20 (1997), pp. 12970–12991. DOI: `10.1103/PhysRevB.56.12970`. arXiv: `cond-mat/9706069`.

[35] Jonathan B. Balewski et al. "Rydberg Dressing: Understanding of Collective Many-Body Effects and Implications for Experiments". In: *New Journal of Physics* 16.6 (2014), p. 063012. DOI: `10.1088/1367-2630/16/6/063012`. arXiv: `1312.6346`.

[36] Eli Barkai and Stanislav Burov. "Packets of Diffusing Particles Exhibit Universal Exponential Tails". In: *Physical Review Letters* 124.6 (2020), p. 060603. DOI: `10.1103/PhysRevLett.124.060603`. arXiv: `1907.10002`.

[37] D. M. Basko, I. L. Aleiner, and B. L. Altshuler. "Metal-Insulator Transition in a Weakly Interacting Many-Electron System with Localized Single-Particle States". In: *Annals of Physics* 321.5 (2006), pp. 1126–1205. DOI: `10.1016/j.aop.2005.11.014`. arXiv: `cond-mat/0506617`.

[38] Erik Bauch et al. "Decoherence of Dipolar Spin Ensembles in Diamond". In: *Physical Review B* 102.13 (2020), p. 134210. DOI: `10.1103/PhysRevB.102.134210`. arXiv: `1904.08763`.

[39] Bela Bauer and Chetan Nayak. "Area Laws in a Many-Body Localized State and Its Implications for Topological Order". In: *Journal of Statistical Mechanics: Theory and Experiment* 2013.09 (2013), P09005. DOI: `10.1088/1742-5468/2013/09/P09005`. arXiv: `1306.5753`.

[40] Rodney J Baxter. *Exactly Solved Models in Statistical Mechanics*. 2016.

[41] Thomas Brooke Benjamin, Fritz Joseph Ursell, and Geoffrey Ingram Taylor. "The Stability of the Plane Free Surface of a Liquid in Vertical Periodic Motion". In: *Proceedings of the Royal Society of London. Series A. Mathematical and Physical Sciences* 225.1163 (1954), pp. 505–515. DOI: `10.1098/rspa.1954.0218`.

[42] Charles H. Bennett. "The Thermodynamics of Computation—a Review". In: *International Journal of Theoretical Physics* 21.12 (1982), pp. 905–940. DOI: `10.1007/BF02084158`.

[43] Charles H. Bennett and G. Grinstein. "Role of Irreversibility in Stabilizing Complex and Nonergodic Behavior in Locally Interacting Discrete Systems". In: *Physical Review Letters* 55.7 (1985), pp. 657–660. DOI: `10.1103/PhysRevLett.55.657`.

[44] Charles H. Bennett et al. "Stability of Temporally Periodic States of Classical Many-Body Systems". In: *Physical Review A* 41.4 (1990), pp. 1932–1935. DOI: `10.1103/PhysRevA.41.1932`.

[45] J. Berges, S. Borsanyi, and C. Wetterich. "Prethermalization". In: *Physical Review Letters* 93.14 (2004), p. 142002. DOI: 10.1103/PhysRevLett.93.142002. arXiv: hep-ph/0403234.

[46] Hannes Bernien et al. "Probing Many-Body Dynamics on a 51-Atom Quantum Simulator". In: *Nature* 551.7682 (2017), pp. 579–584. DOI: 10.1038/nature24622. arXiv: 1707.04344.

[47] B. Bertini et al. "Finite-Temperature Transport in One-Dimensional Quantum Lattice Models". In: *Reviews of Modern Physics* 93.2 (2021), p. 025003. DOI: 10.1103/RevModPhys.93.025003. arXiv: 2003.03334.

[48] Bruno Bertini et al. "Transport in Out-of-Equilibrium XXZ Chains: Exact Profiles of Charges and Currents". In: *Physical Review Letters* 117.20 (2016), p. 207201. DOI: 10.1103/PhysRevLett.117.207201. arXiv: 1605.09790.

[49] Lorenzo Bertini and Nicoletta Cancrini. "The Stochastic Heat Equation: Feynman-Kac Formula and Intermittence". In: *Journal of Statistical Physics* 78.5 (1995), pp. 1377–1401. DOI: 10.1007/BF02180136.

[50] E. Bettelheim, Alexander G. Abanov, and P. Wiegmann. "Nonlinear Quantum Shock Waves in Fractional Quantum Hall Edge States". In: *Physical Review Letters* 97.24 (2006), p. 246401. DOI: 10.1103/PhysRevLett.97.246401.

[51] Garrett Birkhoff. *Hydrodynamics*. 2015.

[52] George David Birkhoff. *Dynamical systems*. New York: American Mathematical Society., 1927.

[53] Mike Blake, Hyunseok Lee, and Hong Liu. "A Quantum Hydrodynamical Description for Scrambling and Many-Body Chaos". In: *Journal of High Energy Physics* 2018.10 (2018), p. 127. DOI: 10.1007/JHEP10(2018)127. arXiv: 1801.00010.

[54] S. Blanes et al. "The Magnus Expansion and Some of Its Applications". In: *Physics Reports* 470.5 (2009), pp. 151–238. DOI: 10.1016/j.physrep.2008.11.001.

[55] R. Blatt and C. F. Roos. "Quantum Simulations with Trapped Ions". In: *Nature Physics* 8.4 (4 2012), pp. 277–284. DOI: 10.1038/nphys2252.

[56] A. Bohrdt et al. "Scrambling and Thermalization in a Diffusive Quantum Many-Body System". In: *New Journal of Physics* 19.6 (2017), p. 063001. DOI: 10.1088/1367-2630/aa719b. arXiv: 1612.02434.

[57] Cameron Booker, Berislav Buča, and Dieter Jaksch. "Non-Stationarity and Dissipative Time Crystals: Spectral Properties and Finite-Size Effects". In: *New Journal of Physics* 22.8 (2020), p. 085007. DOI: 10.1088/1367-2630/ababc4.

[58] Pranjal Bordia et al. "Periodically Driving a Many-Body Localized Quantum System". In: *Nature Physics* 13.5 (2017), pp. 460–464. DOI: 10.1038/nphys4020. arXiv: 1607.07868.

[59] Victoria Borish et al. "Transverse-Field Ising Dynamics in a Rydberg-Dressed Atomic Gas". In: *Physical Review Letters* 124.6 (2020), p. 063601. DOI: 10.1103/PhysRevLett.124.063601. arXiv: 1910.13687.

[60] M. Born and R. Oppenheimer. "Zur Quantentheorie Der Molekeln". In: *Annalen der Physik* 389.20 (1927), pp. 457–484. DOI: 10.1002/andp.19273892002.

[61] Tobias Bothwell et al. "Resolving the Gravitational Redshift within a Millimeter Atomic Sample". In: *Nature* 602.7897 (2022), pp. 420–424. DOI: 10.1038/s41586-021-04349-7. arXiv: 2109.12238.

[62] G. S. Boutis et al. "Spin Diffusion of Correlated Two-Spin States in a Dielectric Crystal". In: *Physical Review Letters* 92.13 (2004), p. 137201. DOI: 10.1103/PhysRevLett.92.137201. arXiv: cond-mat/0308573.

[63] C. E. Bradley et al. "A 10-Qubit Solid-State Spin Register with Quantum Memory up to One Minute". In: *Physical Review X* 9.3 (2019), p. 031045. DOI: 10.1103/PhysRevX.9.031045. arXiv: 1905.02094.

[64] S. Bravyi and M. B. Hastings. "A Short Proof of Stability of Topological Order under Local Perturbations". In: *Communications in Mathematical Physics* 307.3 (2011), pp. 609–627. DOI: 10.1007/s00220-011-1346-2. arXiv: 1001.4363.

[65] S. Bravyi, M. B. Hastings, and F. Verstraete. "Lieb-Robinson Bounds and the Generation of Correlations and Topological Quantum Order". In: *Physical Review Letters* 97.5 (2006), p. 050401. DOI: 10.1103/PhysRevLett.97.050401. arXiv: quant-ph/0603121.

[66] Sergey Bravyi, Matthew Hastings, and Spyridon Michalakis. "Topological Quantum Order: Stability under Local Perturbations". In: *Journal of Mathematical Physics* 51.9 (2010), p. 093512. DOI: 10.1063/1.3490195. arXiv: 1001.0344.

[67] Joseph W. Britton et al. "Engineered Two-Dimensional Ising Interactions in a Trapped-Ion Quantum Simulator with Hundreds of Spins". In: *Nature* 484.7395 (7395 2012), pp. 489–492. DOI: 10.1038/nature10981.

[68] G. M. Bruun et al. "Probing Spatial Spin Correlations of Ultracold Gases by Quantum Noise Spectroscopy". In: *Physical Review Letters* 102.3 (2009), p. 030401. DOI: 10.1103/PhysRevLett.102.030401. arXiv: 0809.0312.

[69] Berislav Buca and Dieter Jaksch. "Dissipation Induced Nonstationarity in a Quantum Gas". In: *Physical Review Letters* 123.26 (2019), p. 260401. DOI: 10.1103/PhysRevLett.123.260401. arXiv: 1905.12880.

[70] Marin Bukov, Luca D'Alessio, and Anatoli Polkovnikov. "Universal High-Frequency Behavior of Periodically Driven Systems: From Dynamical Stabilization to Floquet Engineering". In: *Advances in Physics* 64.2 (2015), pp. 139–226. DOI: 10.1080/00018732.2015.1055918. arXiv: 1407.4803.

[71] Marin Bukov et al. "Heating and Many-Body Resonances in a Periodically Driven Two-Band System". In: *Physical Review B* 93.15 (2016), p. 155132. DOI: 10.1103/PhysRevB.93.155132. arXiv: 1512.02119.

[72] Marin Bukov et al. "Prethermal Floquet Steady States and Instabilities in the Periodically Driven, Weakly Interacting Bose-Hubbard Model". In: *Physical Review Letters* 115.20 (2015), p. 205301. DOI: 10.1103/PhysRevLett.115.205301. arXiv: 1507.01946.

[73] Vir B. Bulchandani. "Kardar-Parisi-Zhang Universality from Soft Gauge Modes". In: *Physical Review B* 101.4 (2020), p. 041411. DOI: 10.1103/PhysRevB.101.041411.

[74] Vir B. Bulchandani, Sarang Gopalakrishnan, and Enej Ilievski. "Superdiffusion in Spin Chains". In: *Journal of Statistical Mechanics: Theory and Experiment* 2021.8 (2021), p. 084001. DOI: 10.1088/1742-5468/ac12c7.

[75] Vir B. Bulchandani et al. "Bethe-Boltzmann Hydrodynamics and Spin Transport in the XXZ Chain". In: *Physical Review B* 97.4 (2018), p. 045407. DOI: 10.1103/PhysRevB.97.045407. arXiv: 1702.06146.

[76] Vir B. Bulchandani et al. "Solvable Hydrodynamics of Quantum Integrable Systems". In: *Physical Review Letters* 119.22 (2017), p. 220604. DOI: 10.1103/PhysRevLett.119.220604. arXiv: 1704.03466.

[77] L. A. Bunimovich and Ya G. Sinai. "Spacetime Chaos in Coupled Map Lattices". In: *Nonlinearity* 1.4 (1988), pp. 491–516. DOI: 10.1088/0951-7715/1/4/001.

[78] Alexander L. Burin. "Many-Body Delocalization in a Strongly Disordered System with Long-Range Interactions: Finite-size Scaling". In: *Physical Review B* 91.9 (2015), p. 094202. DOI: 10.1103/PhysRevB.91.094202.

[79] Jonas Bylander et al. "Dynamical Decoupling and Noise Spectroscopy with a Superconducting Flux Qubit". In: *Nature Physics* 7.7 (2011), pp. 565–570. DOI: 10.1038/nphys1994. arXiv: 1101.4707.

[80] Jianming Cai et al. "A Large-Scale Quantum Simulator on a Diamond Surface at Room Temperature". In: *Nature Physics* 9.3 (3 2013), pp. 168–173. DOI: 10.1038/nphys2519.

[81] Pasquale Calabrese, Pierre Le Doussal, and Alberto Rosso. "Free-Energy Distribution of the Directed Polymer at High Temperature". In: *EPL (Europhysics Letters)* 90.2 (2010), p. 20002. DOI: 10.1209/0295-5075/90/20002. arXiv: 1002.4560.

[82] Elena Canovi et al. "Quantum Quenches, Thermalization and Many-Body Localization". In: *Physical Review B* 83.9 (2011), p. 094431. DOI: 10.1103/PhysRevB.83.094431. arXiv: 1006.1634.

[83] Paola Cappellaro, Chandrasekhar Ramanathan, and David G. Cory. "Dynamics and Control of a Quasi-1D Spin System". In: *Physical Review A* 76.3 (2007), p. 032317. DOI: 10.1103/PhysRevA.76.032317. arXiv: 0706.0483.

[84] G. Cappellini et al. "Direct Observation of Coherent Interorbital Spin-Exchange Dynamics". In: *Physical Review Letters* 113.12 (2014), p. 120402. DOI: `10.1103/PhysRevLett.113.120402`.

[85] Olalla A. Castro-Alvaredo, Benjamin Doyon, and Takato Yoshimura. "Emergent Hydrodynamics in Integrable Quantum Systems out of Equilibrium". In: *Physical Review X* 6.4 (2016), p. 041065. DOI: `10.1103/PhysRevX.6.041065`. arXiv: `1605.07331`.

[86] Lorenzo Cevolani, Giuseppe Carleo, and Laurent Sanchez-Palencia. "Spreading of Correlations in Exactly-Solvable Quantum Models with Long-Range Interactions in Arbitrary Dimensions". In: *New Journal of Physics* 18.9 (2016), p. 093002. DOI: `10.1088/1367-2630/18/9/093002`. arXiv: `1604.05736`.

[87] Lorenzo Cevolani et al. "Universal Scaling Laws for Correlation Spreading in Quantum Systems with Short- and Long-Range Interactions". In: *Physical Review B* 98.2 (2018), p. 024302. DOI: `10.1103/PhysRevB.98.024302`. arXiv: `1706.00838`.

[88] Amos Chan and Thorsten B. Wahl. "Classification of Symmetry-Protected Topological Many-Body Localized Phases in One Dimension". In: *Journal of Physics: Condensed Matter* 32.30 (2020), p. 305601. DOI: `10.1088/1361-648X/ab7f01`. arXiv: `1808.05656`.

[89] Anushya Chandran et al. "Many-Body Localization and Symmetry Protected Topological Order". In: *Physical Review B* 89.14 (2014), p. 144201. DOI: `10.1103/PhysRevB.89.144201`. arXiv: `1310.1096`.

[90] Shubhayu Chatterjee, Joaquin F. Rodriguez-Nieva, and Eugene Demler. "Diagnosing Phases of Magnetic Insulators via Noise Magnetometry with Spin Qubits". In: *Physical Review B* 99.10 (2019), p. 104425. DOI: `10.1103/PhysRevB.99.104425`. arXiv: `1810.04183`.

[91] N. D. Chavda, H. N. Deota, and V. K. B. Kota. "Poisson to GOE Transition in the Distribution of the Ratio of Consecutive Level Spacings". In: *Physics Letters A* 378.41 (2014), pp. 3012–3017. DOI: `10.1016/j.physleta.2014.08.021`. arXiv: `1405.6321`.

[92] A. V. Chechkin et al. "Brownian yet Non-Gaussian Diffusion: From Superstatistics to Subordination of Diffusing Diffusivities". In: *Physical Review X* 7.2 (2017), p. 021002. DOI: `10.1103/PhysRevX.7.021002`. arXiv: `1611.06202`.

[93] Chi-Fang Chen and Andrew Lucas. "Finite Speed of Quantum Scrambling with Long Range Interactions". In: *Physical Review Letters* 123.25 (2019), p. 250605. DOI: `10.1103/PhysRevLett.123.250605`. arXiv: `1907.07637`.

[94] R. W. Cherng and Eugene Demler. "Quantum Noise Analysis of Spin Systems Realized with Cold Atoms". In: *New Journal of Physics* 9.1 (2007), pp. 7–7. DOI: `10.1088/1367-2630/9/1/007`. arXiv: `cond-mat/0609748`.

[95] Lawrence W. Cheuk et al. "Quantum-Gas Microscope for Fermionic Atoms". In: *Physical Review Letters* 114.19 (2015), p. 193001. DOI: `10.1103/PhysRevLett.114.193001`. arXiv: `1503.02648`.

[96] Meiro Chiba and Akira Hirai. "Electron Spin Echo Decay Behaviours of Phosphorus Doped Silicon". In: *Journal of the Physical Society of Japan* 33.3 (1972), pp. 730–738. DOI: 10.1143/JPSJ.33.730.

[97] Jae-yoon Choi et al. "Exploring the Many-Body Localization Transition in Two Dimensions". In: *Science* 352.6293 (2016), pp. 1547–1552. DOI: 10.1126/science.aaf8834. arXiv: 1604.04178.

[98] Joonhee Choi et al. "Robust Dynamic Hamiltonian Engineering of Many-Body Spin Systems". In: *Physical Review X* 10.3 (2020), p. 031002. DOI: 10.1103/PhysRevX.10.031002. arXiv: 1907.03771.

[99] Soonwon Choi, Norman Y. Yao, and Mikhail D. Lukin. "Quantum Metrology Based on Strongly Correlated Matter". In: *arXiv* (2017). arXiv: 1801.00042.

[100] Soonwon Choi et al. "Observation of Discrete Time-Crystalline Order in a Disordered Dipolar Many-Body System". In: *Nature* 543.7644 (2017), pp. 221–225. DOI: 10.1038/nature21426. arXiv: 1610.08057.

[101] L. Chomaz et al. "Long-Lived and Transient Supersolid Behaviors in Dipolar Quantum Gases". In: *Physical Review X* 9.2 (2019), p. 021012. DOI: 10.1103/PhysRevX.9.021012. arXiv: 1903.04375.

[102] Mykyta V. Chubynsky and Gary W. Slater. ""Diffusing Diffusivity": A Model for Anomalous and "Anomalous yet Brownian" Diffusion". In: *Physical Review Letters* 113.9 (2014), p. 098302. DOI: 10.1103/PhysRevLett.113.098302. arXiv: 1404.3573.

[103] Martin Claassen. "Flow Renormalization and Emergent Prethermal Regimes of Periodically-Driven Quantum Systems". In: *arXiv* (2021). arXiv: 2103.07485.

[104] E. F Codd. *Cellular Automata.* Elsevier Science, 2014.

[105] Alexandre Cooper et al. "Alkaline Earth Atoms in Optical Tweezers". In: *Physical Review X* 8.4 (2018), p. 041055. DOI: 10.1103/PhysRevX.8.041055. arXiv: 1810.06537.

[106] Ivan Corwin. "Kardar-Parisi-Zhang Universality". In: *Notices of the American Mathematical Society* 63.03 (2016), pp. 230–239. DOI: 10.1090/noti1334.

[107] Ivan Corwin. "Macdonald Processes, Quantum Integrable Systems and the Kardar-Parisi-Zhang Universality Class". In: *arXiv* (2014). arXiv: 1403.6877.

[108] Ivan Corwin. "The Kardar–Parisi–Zhang Equation and Universality Class". In: *Random Matrices: Theory and Applications* 01.01 (2012), p. 1130001. DOI: 10.1142/S2010326311300014. arXiv: 1106.1596.

[109] Ivan Corwin, Hao Shen, and Li-Cheng Tsai. "$\operatorname{ASEP}(q,j)$ Converges to the KPZ Equation". In: *Annales de l'Institut Henri Poincaré, Probabilités et Statistiques* 54.2 (2018), pp. 995–1012. DOI: 10.1214/17-AIHP829.

[110] Ivan Corwin et al. "Stochastic PDE Limit of the Six Vertex Model". In: *Communications in Mathematical Physics* 375.3 (2020), pp. 1945–2038. DOI: `10.1007/s00220-019-03678-z`.

[111] Ivan Corwin et al. "Tropical Combinatorics and Whittaker Functions". In: *Duke Mathematical Journal* 163.3 (2014). DOI: `10.1215/00127094-2410289`. arXiv: `1110.3489`.

[112] Jayson G. Cosme, Jim Skulte, and Ludwig Mathey. "Time Crystals in a Shaken Atom-Cavity System". In: *Physical Review A* 100.5 (2019), p. 053615. DOI: `10.1103/PhysRevA.100.053615`. arXiv: `1909.00266`.

[113] N. J. Craig et al. "Tunable Non-local Spin Control in a Coupled Quantum Dot System". In: *Science* 304.5670 (2004), pp. 565–567. DOI: `10.1126/science.1095452`. arXiv: `cond-mat/0404213`.

[114] Philip J. D. Crowley and Anushya Chandran. "Avalanche Induced Co-Existing Localised and Thermal Regions in Disordered Chains". In: *Physical Review Research* 2.3 (2020), p. 033262. DOI: `10.1103/PhysRevResearch.2.033262`. arXiv: `1910.10812`.

[115] Philip J. D. Crowley, Ivar Martin, and Anushya Chandran. "Topological Classification of Quasi-Periodically Driven Quantum Systems". In: *Physical Review B* 99.6 (2019), p. 064306. DOI: `10.1103/PhysRevB.99.064306`. arXiv: `1808.07884`.

[116] F. M. Cucchietti, J. P. Paz, and W. H. Zurek. "Decoherence from Spin Environments". In: *Physical Review A* 72.5 (2005), p. 052113. DOI: `10.1103/PhysRevA.72.052113`. arXiv: `quant-ph/0508184`.

[117] L. Cywinski et al. "How to Enhance Dephasing Time in Superconducting Qubits". In: *Physical Review B* 77.17 (2008), p. 174509. DOI: `10.1103/PhysRevB.77.174509`. arXiv: `0712.2225`.

[118] Luca D'Alessio and Anatoli Polkovnikov. "Many-Body Energy Localization Transition in Periodically Driven Systems". In: *Annals of Physics* 333 (2013), pp. 19–33. DOI: `10.1016/j.aop.2013.02.011`. arXiv: `1210.2791`.

[119] Luca D'Alessio and Marcos Rigol. "Long-Time Behavior of Periodically Driven Isolated Interacting Lattice Systems". In: *Physical Review X* 4.4 (2014), p. 041048. DOI: `10.1103/PhysRevX.4.041048`. arXiv: `1402.5141`.

[120] Han-Ning Dai et al. "Observation of Four-body Ring-exchange Interactions and Anyonic Fractional Statistics". In: *Nature Physics* 13.12 (2017), pp. 1195–1200. DOI: `10.1038/nphys4243`. arXiv: `1602.05709`.

[121] Avijit Das et al. "Kardar-Parisi-Zhang Scaling for an Integrable Lattice Landau-Lifshitz Spin Chain". In: *Physical Review E* 100.4 (2019), p. 042116. DOI: `10.1103/PhysRevE.100.042116`.

[122] Guillaume Dauphinais and David Poulin. "Fault-Tolerant Quantum Error Correction for Non-Abelian Anyons". In: *Communications in Mathematical Physics* 355.2 (2017), pp. 519–560. DOI: `10.1007/s00220-017-2923-9`. arXiv: `1607.02159`.

[123] Emily J. Davis et al. "Probing Many-Body Noise in a Strongly Interacting Two-Dimensional Dipolar Spin System". In: *arXiv* (2021). arXiv: `2103.12742`.

[124] Donald Andrew Dawson. "Stable States of Probabilistic Cellular Automata". In: *Information and Control* 34.93 (1977).

[125] Jacopo De Nardis, Denis Bernard, and Benjamin Doyon. "Diffusion in Generalized Hydrodynamics and Quasiparticle Scattering". In: *SciPost Physics* 6.4 (2019), p. 049. DOI: `10.21468/SciPostPhys.6.4.049`.

[126] Jacopo De Nardis, Denis Bernard, and Benjamin Doyon. "Hydrodynamic Diffusion in Integrable Systems". In: *Physical Review Letters* 121.16 (2018), p. 160603. DOI: `10.1103/PhysRevLett.121.160603`. arXiv: `1807.02414`.

[127] Jacopo De Nardis et al. "Anomalous Spin Diffusion in One-Dimensional Antiferromagnets". In: *Physical Review Letters* 123.18 (2019), p. 186601. DOI: `10.1103/PhysRevLett.123.186601`.

[128] Jacopo De Nardis et al. "Stability of Superdiffusion in Nearly Integrable Spin Chains". In: *Physical Review Letters* 127.5 (2021), p. 057201. DOI: `10.1103/PhysRevLett.127.057201`. arXiv: `2102.02219`.

[129] Jacopo De Nardis et al. "Universality Classes of Spin Transport in One-Dimensional Isotropic Magnets: The Onset of Logarithmic Anomalies". In: *Physical Review Letters* 124.21 (2020), p. 210605. DOI: `10.1103/PhysRevLett.124.210605`.

[130] Wojciech De Roeck and François Huveneers. "Stability and Instability towards Delocalization in MBL Systems". In: *Physical Review B* 95.15 (2017), p. 155129. DOI: `10.1103/PhysRevB.95.155129`. arXiv: `1608.01815`.

[131] Giuseppe De Tomasi, Frank Pollmann, and Markus Heyl. "Efficiently Solving the Dynamics of Many-Body Localized Systems at Strong Disorder". In: *Physical Review B* 99.24 (2019), p. 241114. DOI: `10.1103/PhysRevB.99.241114`.

[132] Jan de Gier et al. "Kardar-Parisi-Zhang Universality of the Nagel-Schreckenberg Model". In: *Physical Review E* 100.5 (2019), p. 052111. DOI: `10.1103/PhysRevE.100.052111`.

[133] G. de Lange et al. "Universal Dynamical Decoupling of a Single Solid-State Spin from a Spin Bath". In: *Science* 330.6000 (2010), pp. 60–63. DOI: `10.1126/science.1192739`. arXiv: `1008.2119`.

[134] Gijs de Lange et al. "Controlling the Quantum Dynamics of a Mesoscopic Spin Bath in Diamond". In: *Scientific Reports* 2.1 (1 2012), p. 382. DOI: `10.1038/srep00382`.

[135] Sylvain de Léséleuc et al. "Experimental Realization of a Symmetry Protected Topological Phase of Interacting Bosons with Rydberg Atoms". In: *Science* 365.6455 (2019), pp. 775–780. DOI: `10.1126/science.aav9105`. arXiv: `1810.13286`.

[136] Rogerio de Sousa. "Electron Spin as a Spectrometer of Nuclear-Spin Noise and Other Fluctuations". In: *Electron Spin Resonance and Related Phenomena in Low-Dimensional Structures*. Ed. by Marco Fanciulli. Berlin, Heidelberg: Springer, 2009, pp. 183–220. DOI: `10.1007/978-3-540-79365-6_10`. arXiv: `cond-mat/0610716`.

[137] Rogerio de Sousa and S. Das Sarma. "Theory of Nuclear-Induced Spectral Diffusion: Spin Decoherence of Phosphorus Donors in Si and GaAs Quantum Dots". In: *Physical Review B* 68.11 (2003), p. 115322. DOI: `10.1103/PhysRevB.68.115322`.

[138] Jean-Dominique Deuschel and Daniel W Stroock. *Large Deviations*. Boston u.a.: AMS Chelsea Publ., 2000.

[139] J. M. Deutsch. "Quantum Statistical Mechanics in a Closed System". In: *Physical Review A* 43.4 (1991), pp. 2046–2049. DOI: `10.1103/PhysRevA.43.2046`.

[140] Joshua M. Deutsch. "Eigenstate Thermalization Hypothesis". In: *Reports on Progress in Physics* 81.8 (2018), p. 082001. DOI: `10.1088/1361-6633/aac9f1`.

[141] Nishant Dogra et al. "Dissipation Induced Structural Instability and Chiral Dynamics in a Quantum Gas". In: *Science* 366.6472 (2019), pp. 1496–1499. DOI: `10.1126/science.aaw4465`. arXiv: `1901.05974`.

[142] Marcus W. Doherty et al. "The Nitrogen-Vacancy Colour Centre in Diamond". In: *Physics Reports* 528.1 (2013), pp. 1–45. DOI: `10.1016/j.physrep.2013.02.001`. arXiv: `1302.3288`.

[143] Anastasia Doikou et al. "Introduction to Quantum Integrability". In: *International Journal of Modern Physics A* 25.17 (2010), pp. 3307–3351. DOI: `10.1142/S0217751X10049803`. arXiv: `0912.3350`.

[144] Florian Dolde et al. "Room Temperature Entanglement between Distant Single Spins in Diamond". In: *Nature Physics* 9.3 (2013), pp. 139–143. DOI: `10.1038/nphys2545`. arXiv: `1212.2804`.

[145] Eytan Domany and Wolfgang Kinzel. "Equivalence of Cellular Automata to Ising Models and Directed Percolation". In: *Physical Review Letters* 53.4 (1984), pp. 311–314. DOI: `10.1103/PhysRevLett.53.311`.

[146] V. Dotsenko. "Bethe Ansatz Derivation of the Tracy-Widom Distribution for One-Dimensional Directed Polymers". In: *EPL (Europhysics Letters)* 90.2 (2010), p. 20003. DOI: `10.1209/0295-5075/90/20003`.

[147] Benjamin Doyon. "Diffusion and Superdiffusion from Hydrodynamic Projections". In: *Journal of Statistical Physics* 186.2 (2022), p. 25. DOI: `10.1007/s10955-021-02863-6`. arXiv: `1912.01551`.

[148] Benjamin Doyon. "Lecture Notes on Generalised Hydrodynamics". In: *SciPost Physics Lecture Notes* (2020), p. 18. DOI: `10.21468/SciPostPhysLectNotes.18`. arXiv: `1912.08496`.

[149] L.-M. Duan, E. Demler, and M. D. Lukin. "Controlling Spin Exchange Interactions of Ultracold Atoms in Optical Lattices". In: *Physical Review Letters* 91.9 (2003), p. 090402. DOI: `10.1103/PhysRevLett.91.090402`.

[150] Philipp T. Dumitrescu, Romain Vasseur, and Andrew C. Potter. "Scaling Theory of Entanglement at the Many-Body Localization Transition". In: *Physical Review Letters* 119.11 (2017), p. 110604. DOI: `10.1103/PhysRevLett.119.110604`. arXiv: `1701.04827`.

[151] Maxime Dupont and Joel E. Moore. "Universal Spin Dynamics in Infinite-Temperature One-Dimensional Quantum Magnets". In: *Physical Review B* 101.12 (2020), p. 121106. DOI: `10.1103/PhysRevB.101.121106`.

[152] M. V. Gurudev Dutt et al. "Quantum Register Based on Individual Electronic and Nuclear Spin Qubits in Diamond". In: *Science* 316.5829 (2007), pp. 1312–1316. DOI: `10.1126/science.1139831`.

[153] Freeman J. Dyson. "Existence of a Phase-Transition in a One-Dimensional Ising Ferromagnet". In: *Communications in Mathematical Physics* 12.2 (1969), pp. 91–107. DOI: `10.1007/BF01645907`.

[154] Kai W. Eberhardt et al. "Direct Observation of Nuclear Spin Diffusion in Real Space". In: *Physical Review Letters* 99.22 (2007), p. 227603. DOI: `10.1103/PhysRevLett.99.227603`.

[155] Tim R. Eichhorn, Claire A. McLellan, and Ania C. B. Jayich. "Optimizing the Formation of Depth-Confined Nitrogen Vacancy Center Spin Ensembles in Diamond for Quantum Sensing". In: *Physical Review Materials* 3.11 (2019), p. 113802. DOI: `10.1103/PhysRevMaterials.3.113802`. arXiv: `1901.11519`.

[156] Albert Einstein. *Investigations on the Theory of the Brownian Movement. Edited with Notes by R. Fürth. Translated by A. D. Cowper.* 1956.

[157] J. Eisert, M. Cramer, and M. B. Plenio. "Colloquium: Area Laws for the Entanglement Entropy". In: *Reviews of Modern Physics* 82.1 (2010), pp. 277–306. DOI: `10.1103/RevModPhys.82.277`.

[158] J. Eisert, M. Friesdorf, and C. Gogolin. "Quantum Many-Body Systems out of Equilibrium". In: *Nature Physics* 11.2 (2015), pp. 124–130. DOI: `10.1038/nphys3215`. arXiv: `1408.5148`.

[159] J. Eisert et al. "Breakdown of Quasilocality in Long-Range Quantum Lattice Models". In: *Physical Review Letters* 111.26 (2013), p. 260401. DOI: `10.1103/PhysRevLett.111.260401`. arXiv: `1309.2308`.

[160] Dominic V. Else, Bela Bauer, and Chetan Nayak. "Floquet Time Crystals". In: *Physical Review Letters* 117.9 (2016), p. 090402. DOI: 10.1103/PhysRevLett.117.090402. arXiv: 1603.08001.

[161] Dominic V. Else, Bela Bauer, and Chetan Nayak. "Pre-Thermal Phases of Matter Protected by Time-Translation Symmetry". In: *Physical Review X* 7.1 (2017), p. 011026. DOI: 10.1103/PhysRevX.7.011026. arXiv: 1607.05277.

[162] Dominic V. Else and Chetan Nayak. "Classification of Topological Phases in Periodically Driven Interacting Systems". In: *Physical Review B* 93.20 (2016), p. 201103. DOI: 10.1103/PhysRevB.93.201103. arXiv: 1602.04804.

[163] Dominic V. Else et al. "An Improved Lieb-Robinson Bound for Many-Body Hamiltonians with Power-Law Interactions". In: *Physical Review A* 101.2 (2020), p. 022333. DOI: 10.1103/PhysRevA.101.022333. arXiv: 1809.06369.

[164] Dominic V. Else et al. "Discrete Time Crystals". In: *Annual Review of Condensed Matter Physics* 11.1 (2020), pp. 467–499. DOI: 10.1146/annurev-conmatphys-031119-050658. arXiv: 1905.13232.

[165] Dominic V. Else et al. "Prethermal Strong Zero Modes and Topological Qubits". In: *Physical Review X* 7.4 (2017), p. 041062. DOI: 10.1103/PhysRevX.7.041062. arXiv: 1704.08703.

[166] I. G. Enting. "Crystal Growth Models and Ising Models: Disorder Points". In: *Journal of Physics C: Solid State Physics* 10.9 (1977), pp. 1379–1388. DOI: 10.1088/0022-3719/10/9/011.

[167] Laszlo Erdos, Benjamin Schlein, and Horng-Tzer Yau. "Rigorous Derivation of the Gross-Pitaevskii Equation". In: *Physical Review Letters* 98.4 (2007), p. 040404. DOI: 10.1103/PhysRevLett.98.040404. arXiv: math-ph/0612028.

[168] F. H. L. Essler et al. "Quench Dynamics in a Model with Tuneable Integrability Breaking". In: *Physical Review B* 89.16 (2014), p. 165104. DOI: 10.1103/PhysRevB.89.165104. arXiv: 1311.4557.

[169] Fabian H. L. Essler, Vladimir E. Korepin, and Kareljan Schoutens. "New Exactly Solvable Model of Strongly Correlated Electrons Motivated by High T_c Superconductivity". In: *Physical Review Letters* 68.19 (1992), pp. 2960–2963. DOI: 10.1103/PhysRevLett.68.2960. arXiv: cond-mat/9209002.

[170] F. Evers and A. D. Mirlin. "Anderson Transitions". In: *Reviews of Modern Physics* 80.4 (2008), pp. 1355–1417. DOI: 10.1103/RevModPhys.80.1355. arXiv: 0707.4378.

[171] F. Family and T. Vicsek. "Scaling of the Active Zone in the Eden Process on Percolation Networks and the Ballistic Deposition Model". In: *Journal of Physics A: Mathematical and General* 18.2 (1985), pp. L75–L81. DOI: 10.1088/0305-4470/18/2/005.

[172] Lara Faoro and Lev B. Ioffe. "Microscopic Origin of Low Frequency Flux Noise in Josephson Circuits". In: *Physical Review Letters* 100.22 (2008), p. 227005. DOI: 10.1103/PhysRevLett.100.227005. arXiv: 0712.2834.

[173] Michael Faraday. "On a Peculiar Class of Acoustical Figures; and on Certain Forms Assumed by Groups of Particles upon Vibrating Elastic Surfaces". In: *Abstracts of the Papers Printed in the Philosophical Transactions of the Royal Society of London* 3 (1837), pp. 49–51. DOI: 10.1098/rspl.1830.0024.

[174] Michele Fava et al. "Spin Crossovers and Superdiffusion in the One-Dimensional Hubbard Model". In: *Physical Review B* 102.11 (2020), p. 115121. DOI: 10.1103/PhysRevB.102.115121.

[175] Edward B. Fel'dman and Serge Lacelle. "Configurational Averaging of Dipolar Interactions in Magnetically Diluted Spin Networks". In: *The Journal of Chemical Physics* 104.5 (1996), pp. 2000–2009. DOI: 10.1063/1.470956.

[176] Johannes Feldmeier et al. "Anomalous Diffusion in Dipole- and Higher-Moment Conserving Systems". In: *Physical Review Letters* 125.24 (2020), p. 245303. DOI: 10.1103/PhysRevLett.125.245303. arXiv: 2004.00635.

[177] M. V. Fischetti. "Master-Equation Approach to the Study of Electronic Transport in Small Semiconductor Devices". In: *Physical Review B* 59.7 (1999), pp. 4901–4917. DOI: 10.1103/PhysRevB.59.4901.

[178] M. V. Fischetti. "Theory of Electron Transport in Small Semiconductor Devices Using the Pauli Master Equation". In: *Journal of Applied Physics* 83.1 (1998), pp. 270–291. DOI: 10.1063/1.367149.

[179] Daniel S. Fisher. "Critical Behavior of Random Transverse-Field Ising Spin Chains". In: *Physical Review B* 51.10 (1995), pp. 6411–6461. DOI: 10.1103/PhysRevB.51.6411.

[180] Daniel S. Fisher. "Random Walks in Random Environments". In: *Physical Review A* 30.2 (1984), pp. 960–964. DOI: 10.1103/PhysRevA.30.960.

[181] Michael Foss-Feig et al. "Nearly-Linear Light Cones in Long-Range Interacting Quantum Systems". In: *Physical Review Letters* 114.15 (2015), p. 157201. DOI: 10.1103/PhysRevLett.114.157201. arXiv: 1410.3466.

[182] Philipp Frey and Stephan Rachel. "Realization of a Discrete Time Crystal on 57 Qubits of a Quantum Computer". In: *Science Advances* 8.9 (2022), eabm7652. DOI: 10.1126/sciadv.abm7652.

[183] Aaron J. Friedman, Sarang Gopalakrishnan, and Romain Vasseur. "Diffusive Hydrodynamics from Integrability Breaking". In: *Physical Review B* 101.18 (2020), p. 180302. DOI: 10.1103/PhysRevB.101.180302. arXiv: 1912.08826.

[184] Aaron J. Friedman et al. "Localization-Protected Order in Spin Chains with Non-Abelian Discrete Symmetries". In: *Physical Review B* 98.6 (2018), p. 064203. DOI: 10.1103/PhysRevB.98.064203. arXiv: 1706.00022.

[185] Georg Frobenius. *Über Matrizen aus nicht negativen Elementen*. Reichsdr., 1912. 22 pp. Google Books: fuK3PgAACAAJ.

[186] Takeshi Fukuhara et al. "Quantum Dynamics of a Mobile Spin Impurity". In: *Nature Physics* 9.4 (2013), pp. 235–241. DOI: 10.1038/nphys2561.

[187] Peter Gacs. "A New Version of Toom's Proof". In: *arXiv* (2021). arXiv: 2105.05968.

[188] Peter Gacs. "Reliable Cellular Automata with Self-Organization". In: *Journal of Statistical Physics* 103.1/2 (2001), pp. 45–267. DOI: 10.1023/A:1004823720305. arXiv: math/0003117.

[189] Peter Gács. "Reliable Computation with Cellular Automata". In: *Journal of Computer and System Sciences* 32.1 (1986), pp. 15–78. DOI: 10.1016/0022-0000(86)90002-4.

[190] Victor Galitski and Ian B. Spielman. "Spin-Orbit Coupling in Quantum Gases". In: *Nature* 494.7435 (2013), pp. 49–54. DOI: 10.1038/nature11841. arXiv: 1312.3292.

[191] Oleksandr Gamayun, Yuan Miao, and Enej Ilievski. "Domain Wall Dynamics in the Landau–Lifshitz Magnet and the Classical-Quantum Correspondence for Spin Transport". In: *Physical Review B* 99.14 (2019), p. 140301. DOI: 10.1103/PhysRevB.99.140301. arXiv: 1901.08944.

[192] F. M. Gambetta et al. "Classical Stochastic Discrete Time Crystals". In: *Physical Review E* 100.6 (2019), p. 060105. DOI: 10.1103/PhysRevE.100.060105. arXiv: 1905.08826.

[193] F. M. Gambetta et al. "Discrete Time Crystals in the Absence of Manifest Symmetries or Disorder in Open Quantum Systems". In: *Physical Review Letters* 122.1 (2019), p. 015701. DOI: 10.1103/PhysRevLett.122.015701. arXiv: 1807.10161.

[194] Dorian A. Gangloff et al. "Witnessing Quantum Correlations in a Nuclear Ensemble via an Electron Spin Qubit". In: *Nature Physics* 17.11 (2021), pp. 1247–1253. DOI: 10.1038/s41567-021-01344-7. arXiv: 2012.11279.

[195] G. Gielis and R. S. MacKay. "Coupled Map Lattices with Phase Transition". In: *Nonlinearity* 13.3 (2000), pp. 867–888. DOI: 10.1088/0951-7715/13/3/320.

[196] M. Glasbeek and R. Hond. "Phase Relaxation of Photoexcited Triplet Spins in CaO". In: *Physical Review B* 23.8 (1981), pp. 4220–4235. DOI: 10.1103/PhysRevB.23.4220.

[197] Dominique Gobert et al. "Real-Time Dynamics in Spin-1/2 Chains with Adaptive Time-Dependent DMRG". In: *Physical Review E* 71.3 (2005), p. 036102. DOI: 10.1103/PhysRevE.71.036102. arXiv: cond-mat/0409692.

[198] N. Goldman et al. "Light-Induced Gauge Fields for Ultracold Atoms". In: *Reports on Progress in Physics* 77.12 (2014), p. 126401. DOI: 10.1088/0034-4885/77/12/126401. arXiv: 1308.6533.

[199] Herbert Goldstein, Charles Poole, and John Safko. *Classical mechanics*. San Francisco: Addison Wesley, 2002.

[200] Zhe-Xuan Gong et al. "Persistence of Locality in Systems with Power-Law Interactions". In: *Physical Review Letters* 113.3 (2014), p. 030602. DOI: 10.1103/PhysRevLett.113.030602. arXiv: 1401.6174.

[201] Zongping Gong, Ryusuke Hamazaki, and Masahito Ueda. "Discrete Time-Crystalline Order in Cavity and Circuit QED Systems". In: *Physical Review Letters* 120.4 (2018), p. 040404. DOI: 10.1103/PhysRevLett.120.040404. arXiv: 1708.01472.

[202] Sarang Gopalakrishnan and Romain Vasseur. "Kinetic Theory of Spin Diffusion and Superdiffusion in XXZ Spin Chains". In: *Physical Review Letters* 122.12 (2019), p. 127202. DOI: 10.1103/PhysRevLett.122.127202. arXiv: 1812.02701.

[203] Sarang Gopalakrishnan, Romain Vasseur, and Brayden Ware. "Anomalous Relaxation and the High-Temperature Structure Factor of XXZ Spin Chains". In: *Proceedings of the National Academy of Sciences* 116.33 (2019), pp. 16250–16255. DOI: 10.1073/pnas.1906914116. pmid: 31363047.

[204] Anna Goremykina, Romain Vasseur, and Maksym Serbyn. "Analytically Solvable Renormalization Group for the Many-Body Localization Transition". In: *Physical Review Letters* 122.4 (2019), p. 040601. DOI: 10.1103/PhysRevLett.122.040601. arXiv: 1807.04285.

[205] I. V. Gornyi, A. D. Mirlin, and D. G. Polyakov. "Interacting Electrons in Disordered Wires: Anderson Localization and Low-Temperature Transport". In: *Physical Review Letters* 95.20 (2005), p. 206603. DOI: 10.1103/PhysRevLett.95.206603. arXiv: cond-mat/0506411.

[206] A. V. Gorshkov et al. "Two-Orbital SU(N) Magnetism with Ultracold Alkaline-Earth Atoms". In: *Nature Physics* 6.4 (2010), pp. 289–295. DOI: 10.1038/NPHYS1535. arXiv: 0905.2610.

[207] Lawrence F. Gray. "A Reader's Guide to Gacs's "Positive Rates" Paper". In: *Journal of Statistical Physics* 103.1 (2001), pp. 1–44. DOI: 10.1023/A:1004824203467.

[208] M. Gring et al. "Relaxation and Prethermalization in an Isolated Quantum System". In: *Science* 337.6100 (2012), pp. 1318–1322. DOI: 10.1126/science.1224953.

[209] G. Grinstein. "Can Complex Structures Be Generically Stable in a Noisy World?" In: *IBM Journal of Research and Development* 48.1 (2004), pp. 5–12. DOI: 10.1147/rd.481.0005.

[210] Christian Gross and Immanuel Bloch. "Quantum Simulations with Ultracold Atoms in Optical Lattices". In: *Science* 357.6355 (2017), pp. 995–1001. DOI: `10.1126/science.aal3837`.

[211] Massimiliano Gubinelli and Nicolas Perkowski. "KPZ Reloaded". In: *Communications in Mathematical Physics* 349.1 (2017), pp. 165–269. DOI: `10.1007/s00220-016-2788-3`. arXiv: `1508.03877`.

[212] H. Haeffner et al. "Scalable Multi-Particle Entanglement of Trapped Ions". In: *Nature* 438.7068 (2005), pp. 643–646. DOI: `10.1038/nature04279`. arXiv: `quant-ph/0603217`.

[213] E. L. Hahn. "Spin Echoes". In: *Physical Review* 80.4 (1950), pp. 580–594. DOI: `10.1103/PhysRev.80.580`.

[214] Martin Hairer. "Solving the KPZ Equation". In: *Annals of Mathematics* 178.2 (2013), pp. 559–664. JSTOR: `23470800`.

[215] Asmi Haldar, Roderich Moessner, and Arnab Das. "Onset of Floquet Thermalisation". In: *Physical Review B* 97.24 (2018), p. 245122. DOI: `10.1103/PhysRevB.97.245122`. arXiv: `1803.10331`.

[216] Jad C. Halimeh et al. "Domain-Wall Melting in Ultracold-Boson Systems with Hole and Spin-Flip Defects". In: *Physical Review A* 89.6 (2014), p. 063603. DOI: `10.1103/PhysRevA.89.063603`.

[217] L. T. Hall et al. "Detection of Nanoscale Electron Spin Resonance Spectra Demonstrated Using Nitrogen-Vacancy Centre Probes in Diamond". In: *Nature Communications* 7.1 (1 2016), p. 10211. DOI: `10.1038/ncomms10211`.

[218] Elmar Haller et al. "Single-Atom Imaging of Fermions in a Quantum-Gas Microscope". In: *Nature Physics* 11.9 (2015), pp. 738–742. DOI: `10.1038/nphys3403`. arXiv: `1503.02005`.

[219] Timothy Halpin-Healy and Kazumasa A. Takeuchi. "A KPZ Cocktail-Shaken, Not Stirred...: Toasting 30 Years of Kinetically Roughened Surfaces". In: *Journal of Statistical Physics* 160.4 (2015), pp. 794–814. DOI: `10.1007/s10955-015-1282-1`.

[220] Timothy Halpin-Healy and Yi-Cheng Zhang. "Kinetic Roughening Phenomena, Stochastic Growth, Directed Polymers and All That. Aspects of Multidisciplinary Statistical Mechanics". In: *Physics Reports* 254.4 (1995), pp. 215–414. DOI: `10.1016/0370-1573(94)00087-J`.

[221] R. Hanson et al. "Coherent Dynamics of a Single Spin Interacting with an Adjustable Spin Bath". In: *Science* 320.5874 (2008), pp. 352–355. DOI: `10.1126/science.1155400`.

[222] Kun Hao et al. "Exact Solution of the Izergin-Korepin Model with General Non-Diagonal Boundary Terms". In: *Journal of High Energy Physics* 2014.6 (2014), p. 128. DOI: `10.1007/JHEP06(2014)128`. arXiv: `1403.7915`.

[223] Fenner Harper et al. "Topology and Broken Symmetry in Floquet Systems". In: *Annual Review of Condensed Matter Physics* 11.1 (2020), pp. 345–368. DOI: `10.1146/annurev-conmatphys-031218-013721`. arXiv: `1905.01317`.

[224] James William Harrington. "Analysis of Quantum Error-Correcting Codes: Symplectic Lattice Codes and Toric Codes". PhD thesis. California Institute of Technology, 2004. DOI: `10.7907/AHMQ-EG82`.

[225] A. B. Harris. "Effect of Random Defects on the Critical Behaviour of Ising Models". In: *Journal of Physics C: Solid State Physics* 7.9 (1974), pp. 1671–1692. DOI: `10.1088/0022-3719/7/9/009`.

[226] Alexander K. Hartmann et al. "High-Precision Simulation of the Height Distribution for the KPZ Equation". In: *EPL (Europhysics Letters)* 121.6 (2018), p. 67004. DOI: `10.1209/0295-5075/121/67004`.

[227] M. B. Hastings. "An Area Law for One Dimensional Quantum Systems". In: *Journal of Statistical Mechanics: Theory and Experiment* 2007.08 (2007), P08024–P08024. DOI: `10.1088/1742-5468/2007/08/P08024`. arXiv: `0705.2024`.

[228] M. B. Hastings. "Lieb-Schultz-Mattis in Higher Dimensions". In: *Physical Review B* 69.10 (2004), p. 104431. DOI: `10.1103/PhysRevB.69.104431`. arXiv: `cond-mat/0305505`.

[229] M. B. Hastings and Xiao-Gang Wen. "Quasi-Adiabatic Continuation of Quantum States: The Stability of Topological Ground State Degeneracy and Emergent Gauge Invariance". In: *Physical Review B* 72.4 (2005), p. 045141. DOI: `10.1103/PhysRevB.72.045141`. arXiv: `cond-mat/0503554`.

[230] Matthew B. Hastings and Tohru Koma. "Spectral Gap and Exponential Decay of Correlations". In: *Communications in Mathematical Physics* 265.3 (2006), pp. 781–804. DOI: `10.1007/s00220-006-0030-4`. arXiv: `math-ph/0507008`.

[231] Philipp Hauke and Luca Tagliacozzo. "Spread of Correlations in Long-Range Interacting Quantum Systems". In: *Physical Review Letters* 111.20 (2013), p. 207202. DOI: `10.1103/PhysRevLett.111.207202`. arXiv: `1304.7725`.

[232] Vicente Hernandez, Jose E. Roman, and Vicente Vidal. "SLEPc: A Scalable and Flexible Toolkit for the Solution of Eigenvalue Problems". In: *ACM Transactions on Mathematical Software* 31.3 (2005), pp. 351–362. DOI: `10.1145/1089014.1089019`.

[233] Vicente Hernández, Jose E. Román, and Vicente Vidal. "SLEPc: Scalable Library for Eigenvalue Problem Computations". In: *High Performance Computing for Computational Science — VECPAR 2002*. Ed. by José M. L. M. Palma et al. Berlin, Heidelberg: Springer, 2003, pp. 377–391. DOI: `10.1007/3-540-36569-9_25`.

[234] B. Herzog and E. L. Hahn. "Transient Nuclear Induction and Double Nuclear Resonance in Solids". In: *Physical Review* 103.1 (1956), pp. 148–166. DOI: `10.1103/PhysRev.103.148`.

[235] Daniel Hetterich et al. "Detection and Characterization of Many-Body Localization in Central Spin Models". In: *Physical Review B* 98.16 (2018), p. 161122. DOI: 10.1103/PhysRevB.98.161122. arXiv: 1806.08316.

[236] Sebastian Hild et al. "Far-from-Equilibrium Spin Transport in Heisenberg Quantum Magnets". In: *Physical Review Letters* 113.14 (2014), pp. 1–5. DOI: 10.1103/PhysRevLett.113.147205.

[237] Wen Wei Ho, Ivan Protopopov, and Dmitry A. Abanin. "Bounds on Energy Absorption and Prethermalization in Quantum Systems with Long-Range Interactions". In: *Physical Review Letters* 120.20 (2018), p. 200601. DOI: 10.1103/PhysRevLett.120.200601. arXiv: 1706.07207.

[238] Wade Hodson and Christopher Jarzynski. "Energy Diffusion and Absorption in Chaotic Systems with Rapid Periodic Driving". In: *Physical Review Research* 3.1 (2021), p. 013219. DOI: 10.1103/PhysRevResearch.3.013219. arXiv: 2102.13211.

[239] S. Hofferberth et al. "Probing Quantum and Thermal Noise in an Interacting Many-Body System". In: *Nature Physics* 4.6 (2008), pp. 489–495. DOI: 10.1038/nphys941. arXiv: 0710.1575.

[240] Christian Hofrichter et al. "Direct Probing of the Mott Crossover in the SU(N) Fermi-Hubbard Model". In: *Physical Review X* 6.2 (2016), p. 021030. DOI: 10.1103/PhysRevX.6.021030. arXiv: 1511.07287.

[241] P. C. Hohenberg and B. I. Halperin. "Theory of Dynamic Critical Phenomena". In: *Reviews of Modern Physics* 49.3 (1977), pp. 435–479. DOI: 10.1103/RevModPhys.49.435.

[242] F. den Hollander. *Large Deviations*. Providence, RI: American Mathematical Society, 2000.

[243] A. A. Houck et al. "Controlling the Spontaneous Emission of a Superconducting Transmon Qubit". In: *Physical Review Letters* 101.8 (2008), p. 080502. DOI: 10.1103/PhysRevLett.101.080502. arXiv: 0803.4490.

[244] Owen Howell et al. "Asymptotic Prethermalization in Periodically Driven Classical Spin Chains". In: *Physical Review Letters* 122.1 (2019), p. 010602. DOI: 10.1103/PhysRevLett.122.010602.

[245] S. Hsieh et al. "Imaging Stress and Magnetism at High Pressures Using a Nanoscale Quantum Sensor". In: *Science* 366.6471 (2019), pp. 1349–1354. DOI: 10.1126/science.aaw4352. arXiv: 1812.08796.

[246] P. Hu and S. R. Hartmann. "Theory of Spectral Diffusion Decay Using an Uncorrelated-Sudden-Jump Model". In: *Physical Review B* 9.1 (1974), pp. 1–13. DOI: 10.1103/PhysRevB.9.1.

[247] G. A. Hunt. "Some Theorems Concerning Brownian Motion". In: *Transactions of the American Mathematical Society* 81.2 (1956), pp. 294–319. DOI: 10.1090/S0002-9947-1956-0079377-3.

[248] David A. Huse, Rahul Nandkishore, and Vadim Oganesyan. "Phenomenology of Fully Many-Body-Localized Systems". In: *Physical Review B* 90.17 (2014), p. 174202. DOI: 10.1103/PhysRevB.90.174202. arXiv: 1408.4297.

[249] David A. Huse et al. "Localization Protected Quantum Order". In: *Physical Review B* 88.1 (2013), p. 014206. DOI: 10.1103/PhysRevB.88.014206. arXiv: 1304.1158.

[250] Eduardo Ibarra-García-Padilla et al. "Universal Thermodynamics of an SU(N) Fermi-Hubbard Model". In: *Physical Review A* 104.4 (2021), p. 043316. DOI: 10.1103/PhysRevA.104.043316. arXiv: 2108.04153.

[251] Enej Ilievski and Jacopo De Nardis. "Microscopic Origin of Ideal Conductivity in Integrable Quantum Models". In: *Physical Review Letters* 119.2 (2017), p. 020602. DOI: 10.1103/PhysRevLett.119.020602. arXiv: 1702.02930.

[252] Enej Ilievski et al. "Superdiffusion in One-Dimensional Quantum Lattice Models". In: *Physical Review Letters* 121.23 (2018), p. 230602. DOI: 10.1103/PhysRevLett.121.230602.

[253] Enej Ilievski et al. "Superuniversality of Superdiffusion". In: *Physical Review X* 11.3 (2021), p. 031023. DOI: 10.1103/PhysRevX.11.031023. arXiv: 2009.08425.

[254] John Z. Imbrie. "On Many-Body Localization for Quantum Spin Chains". In: *Journal of Statistical Physics* 163.5 (2016), pp. 998–1048. DOI: 10.1007/s10955-016-1508-x. arXiv: 1403.7837.

[255] Jun-ichi Inoue and Akihiro Tanaka. "Photoinduced Transition between Conventional and Topological Insulators in Two-Dimensional Electronic Systems". In: *Physical Review Letters* 105.1 (2010), p. 017401. DOI: 10.1103/PhysRevLett.105.017401. arXiv: 1006.5283.

[256] Matteo Ippoliti et al. "Many-Body Physics in the NISQ Era: Quantum Programming a Discrete Time Crystal". In: *PRX Quantum* 2.3 (2021), p. 030346. DOI: 10.1103/PRXQuantum.2.030346. arXiv: 2007.11602.

[257] A. G. Izergin and V. E. Korepin. "The Inverse Scattering Method Approach to the Quantum Shabat-Mikhaǐ Lov Model". In: *Communications in Mathematical Physics* 79.3 (1981), pp. 303–316.

[258] A. G. Izergin and V. E. Korepin. "The Quantum Inverse Scattering Method Approach to Correlation Functions". In: *Communications in Mathematical Physics* 94.1 (1984), pp. 67–92. DOI: 10.1007/BF01212350.

[259] D. Jaksch and P. Zoller. "Creation of Effective Magnetic Fields in Optical Lattices: The Hofstadter Butterfly for Cold Neutral Atoms". In: *New Journal of Physics* 5 (2003), pp. 56–56. DOI: 10.1088/1367-2630/5/1/356. arXiv: quant-ph/0304038.

[260] A. Jarmola et al. "Temperature and Magnetic Field Dependent Longitudinal Spin Relaxation in Nitrogen-Vacancy Ensembles in Diamond". In: *Physical Review Letters* 108.19 (2012), p. 197601. DOI: 10.1103/PhysRevLett.108.197601. arXiv: 1112.5936.

[261] Sangyong Jeon and Laurence G. Yaffe. "From Quantum Field Theory to Hydrodynamics: Transport Coefficients and Effective Kinetic Theory". In: *Physical Review D* 53.10 (1996), pp. 5799–5809. DOI: 10.1103/PhysRevD.53.5799. arXiv: hep-ph/9512263.

[262] Paul Niklas Jepsen et al. "Spin Transport in a Tunable Heisenberg Model Realized with Ultracold Atoms". In: *Nature* 588.7838 (7838 2020), pp. 403–407. DOI: 10.1038/s41586-020-3033-y.

[263] Paul Niklas Jepsen et al. "Transverse Spin Dynamics in the Anisotropic Heisenberg Model Realized with Ultracold Atoms". In: *Physical Review X* 11.4 (2021), p. 041054. DOI: 10.1103/PhysRevX.11.041054. arXiv: 2103.07866.

[264] Liang Jiang et al. "Majorana Fermions in Equilibrium and Driven Cold Atom Quantum Wires". In: *Physical Review Letters* 106.22 (2011), p. 220402. DOI: 10.1103/PhysRevLett.106.220402. arXiv: 1102.5367.

[265] Dai Jin et al. "Truncated Dynamics, Ring Molecules and Mechanical Time Crystals". In: *Physical Review A* 99.2 (2019), p. 023425. DOI: 10.1103/PhysRevA.99.023425. arXiv: 1810.00870.

[266] Maxime Joos et al. "Protecting Qubit Coherence by Spectrally Engineered Driving of the Spin Environment". In: *arXiv* (2021). arXiv: 2101.09654.

[267] M. K. Joshi et al. "Observing Emergent Hydrodynamics in a Long-Range Quantum Magnet". In: *arXiv* (2021). arXiv: 2107.00033.

[268] Manoj K. Joshi et al. "Quantum Information Scrambling in a Trapped-Ion Quantum Simulator with Tunable Range Interactions". In: *Physical Review Letters* 124.24 (2020), p. 240505. DOI: 10.1103/PhysRevLett.124.240505. arXiv: 2001.02176.

[269] Gregor Jotzu et al. "Experimental Realisation of the Topological Haldane Model". In: *Nature* 515.7526 (2014), pp. 237–240. DOI: 10.1038/nature13915. arXiv: 1406.7874.

[270] Leo P Kadanoff. "Scaling and Universality in Statistical Physics". In: *Physica A: Statistical Mechanics and its Applications* 163.1 (1990), pp. 1–14. DOI: 10.1016/0378-4371(90)90309-G.

[271] Leo P. Kadanoff. "Scaling Laws for Ising Models near ${T}_{c}$". In: *Physics Physique Fizika* 2.6 (1966), pp. 263–272. DOI: 10.1103/PhysicsPhysiqueFizika.2.263.

[272] Kunihiko Kaneko. "Overview of Coupled Map Lattices". In: *Chaos: An Interdisciplinary Journal of Nonlinear Science* 2.3 (1992), pp. 279–282. DOI: 10.1063/1.165869.

[273] Kunihiko Kaneko. "Period-Doubling of Kink-Antikink Patterns, Quasiperiodicity in Antiferro-Like Structures and Spatial Intermittency in Coupled Logistic Lattice*): Towards a Prelude of a "Field Theory of Chaos"". In: *Progress of Theoretical Physics* 72.3 (1984), pp. 480–486. DOI: `10.1143/PTP.72.480`.

[274] Kunihiko Kaneko and Tetsuro Konishi. "Transition, Ergodicity and Lyapunov Spectra of Hamiltonian Dynamical Systems". In: *Journal of the Physical Society of Japan* 56.9 (1987), pp. 2993–2996. DOI: `10.1143/JPSJ.56.2993`.

[275] PL Kapitza. "Dynamic Stability of a Pendulum with an Oscillating Point of Suspension". In: *Journal of experimental and theoretical physics* 21.5 (1951), pp. 588–597.

[276] Raymond Kapral. "Pattern Formation in Two-Dimensional Arrays of Coupled, Discrete-Time Oscillators". In: *Physical Review A* 31.6 (1985), pp. 3868–3879. DOI: `10.1103/PhysRevA.31.3868`.

[277] Mehran Kardar. *Statistical Physics of Particles*. Higher Education from Cambridge University Press. 2007. DOI: `10.1017/CBO9780511815898`. URL: `https://www.cambridge.org/highereducation/books/statistical-physics-of-particles/3CC2F33BD9F8DC56758DBDDB5B870558` (visited on 04/14/2022).

[278] Mehran Kardar, Giorgio Parisi, and Yi-Cheng Zhang. "Dynamic Scaling of Growing Interfaces". In: *Physical Review Letters* 56.9 (1986), pp. 889–892. DOI: `10.1103/PhysRevLett.56.889`.

[279] C. Karrasch, J. E. Moore, and F. Heidrich-Meisner. "Real-Time and Real-Space Spin- and Energy Dynamics in One-Dimensional Spin-1/2 Systems Induced by Local Quantum Quenches at Finite Temperatures". In: *Physical Review B* 89.7 (2014), p. 075139. DOI: `10.1103/PhysRevB.89.075139`. arXiv: `1312.2938`.

[280] Christian Kassel. *Quantum Groups*. New York: Springer-Verlag, 1995.

[281] Tadao Kasuya. "A Theory of Metallic Ferro- and Antiferromagnetism on Zener's Model". In: *Progress of Theoretical Physics* 16.1 (1956), pp. 45–57. DOI: `10.1143/PTP.16.45`.

[282] Jack Kemp, Norman Y. Yao, and Chris R. Laumann. "Symmetry Enhanced Boundary Qubits at Infinite Temperature". In: *Physical Review Letters* 125.20 (2020), p. 200506. DOI: `10.1103/PhysRevLett.125.200506`. arXiv: `1912.05546`.

[283] Jack Kemp et al. "Long Coherence Times for Edge Spins". In: *Journal of Statistical Mechanics: Theory and Experiment* 2017.6 (2017), p. 063105. DOI: `10.1088/1742-5468/aa73f0`. arXiv: `1701.00797`.

[284] Hans Keßler et al. "From a Continuous to a Discrete Time Crystal in a Dissipative Atom-Cavity System". In: *New Journal of Physics* 22.8 (2020), p. 085002. DOI: `10.1088/1367-2630/ab9fc0`. arXiv: `2004.14633`.

[285]   Hans Keßler et al. "Observation of a Dissipative Time Crystal". In: *Physical Review Letters* 127.4 (2021), p. 043602. DOI: `10.1103/PhysRevLett.127.043602`. arXiv: `2012.08885`.

[286]   Ilia Khait et al. "Spin Transport of Weakly Disordered Heisenberg Chain at Infinite Temperature". In: *Physical Review B* 93.22 (2016), p. 224205. DOI: `10.1103/PhysRevB.93.224205`. arXiv: `1603.06588`.

[287]   Vedika Khemani, Roderich Moessner, and S. L. Sondhi. "A Brief History of Time Crystals". In: *arXiv* (2019). arXiv: `1910.10745`.

[288]   Vedika Khemani, Ashvin Vishwanath, and D. A. Huse. "Operator Spreading and the Emergence of Dissipative Hydrodynamics under Unitary Evolution with Conservation Laws". In: *Physical Review X* 8.3 (2018), p. 031057. DOI: `10.1103/PhysRevX.8.031057`. arXiv: `1710.09835`.

[289]   Vedika Khemani et al. "Critical Properties of the Many-Body Localization Transition". In: *Physical Review X* 7.2 (2017), p. 021013. DOI: `10.1103/PhysRevX.7.021013`. arXiv: `1607.05756`.

[290]   Vedika Khemani et al. "Phase Structure of Driven Quantum Systems". In: *Physical Review Letters* 116.25 (2016), p. 250401. DOI: `10.1103/PhysRevLett.116.250401`. arXiv: `1508.03344`.

[291]   Jun Yong Khoo, Falko Pientka, and Inti Sodemann. "The Universal Shear Conductivity of Fermi Liquids and Spinon Fermi Surface States and Its Detection via Spin Qubit Noise Magnetometry". In: *New Journal of Physics* 23.11 (2021), p. 113009. DOI: `10.1088/1367-2630/ac2dab`. arXiv: `2103.05095`.

[292]   G. R. Khutsishvili. "Spin Diffusion and Magnetic Relaxation of Nuclei". In: *Zhur. Eksptl'. i Teoret. Fiz.* Vol: 42 (1962).

[293]   Jeongmin Kim, Chanjoong Kim, and Bong June Sung. "Simulation Study of Seemingly Fickian but Heterogeneous Dynamics of Two Dimensional Colloids". In: *Physical Review Letters* 110.4 (2013), p. 047801. DOI: `10.1103/PhysRevLett.110.047801`.

[294]   Z. Kim et al. "Decoupling a Cooper-pair Box to Enhance the Lifetime to 0.2 Ms". In: *Physical Review Letters* 106.12 (2011), p. 120501. DOI: `10.1103/PhysRevLett.106.120501`. arXiv: `1101.4692`.

[295]   Charles Kittel and Ching-Yao Fong. *Quantum Theory of Solids.* New York, N.Y.: Wiley, 2010.

[296]   Jonas A. Kjäll, Jens H. Bardarson, and Frank Pollmann. "Many-Body Localization in a Disordered Quantum Ising Chain". In: *Physical Review Letters* 113.10 (2014), p. 107204. DOI: `10.1103/PhysRevLett.113.107204`. arXiv: `1403.1568`.

[297]   J. R. Klauder and P. W. Anderson. "Spectral Diffusion Decay in Spin Resonance Experiments". In: *Physical Review* 125.3 (1962), pp. 912–932. DOI: `10.1103/PhysRev.125.912`.

[298] Daniel Kleppner. "Inhibited Spontaneous Emission". In: *Confined Electrons and Photons: New Physics and Applications*. Ed. by Elias Burstein and Claude Weisbuch. Boston, MA: Springer US, 1995, pp. 845–848. DOI: 10.1007/978-1-4615-1963-8_42.

[299] Sh. Kogan. *Electronic Noise and Fluctuations in Solids*. Cambridge: Cambridge University Press, 1996. DOI: 10.1017/CBO9780511551666.

[300] Marcus Kollar, F. Alexander Wolf, and Martin Eckstein. "Generalized Gibbs Ensemble Prediction of Prethermalization Plateaus and Their Relation to Nonthermal Steady States in Integrable Systems". In: *Physical Review B* 84.5 (2011), p. 054304. DOI: 10.1103/PhysRevB.84.054304.

[301] A. N. Kolmogorov. "On Conservation of Conditionally Periodic Motions for a Small Change in Hamilton's Function". In: *Dokl. Akad. Nauk SSSR* 98 (1954), p. 527.

[302] V. E. Korepin, N. M. Bogoliubov, and A. G. Izergin. *Quantum Inverse Scattering Method and Correlation Functions*. Cambridge Monographs on Mathematical Physics. Cambridge: Cambridge University Press, 1993. DOI: 10.1017/CBO9780511628832.

[303] Ivana Kovacic, Richard Rand, and Si Mohamed Sah. "Mathieu's Equation and Its Generalizations: Overview of Stability Charts and Their Features". In: *Applied Mechanics Reviews* 70.2 (2018). DOI: 10.1115/1.4039144.

[304] Žiga Krajnik, Enej Ilievski, and Tomaž Prosen. "Integrable Matrix Models in Discrete Space-Time". In: *SciPost Physics* 9.3 (2020), p. 038. DOI: 10.21468/SciPostPhys.9.3.038. arXiv: 2003.05957.

[305] Žiga Krajnik and Tomaž Prosen. "Kardar–Parisi–Zhang Physics in Integrable Rotationally Symmetric Dynamics on Discrete Space–Time Lattice". In: *Journal of Statistical Physics* 179.1 (2020), pp. 110–130. DOI: 10.1007/s10955-020-02523-1.

[306] H. J. Kreuzer. *Nonequilibrium Thermodynamics and Its Statistical Foundations*. 1981.

[307] Ryogo Kubo, N Hashitsume, and Morikazu Toda. *Statistical Physics. V. II V. II*. Berlin [etc.: Springer-Verlag, 1992.

[308] Georg Kucsko et al. "Critical Thermalization of a Disordered Dipolar Spin System in Diamond". In: *Physical Review Letters* 121.2 (2018), p. 023601. DOI: 10.1103/PhysRevLett.121.023601. arXiv: 1609.08216.

[309] A. B. Kuklov and B. V. Svistunov. "Counterflow Superfluidity of Two-Species Ultracold Atoms in a Commensurate Optical Lattice". In: *Physical Review Letters* 90.10 (2003), p. 100401. DOI: 10.1103/PhysRevLett.90.100401.

[310] P. P. Kulish and E. K. Sklyanin. "Solutions of the Yang-Baxter Equation". In: *Journal of Soviet Mathematics* 19.5 (1982), pp. 1596–1620. DOI: 10.1007/BF01091463.

[311] Yoshihito Kuno, Takahiro Orito, and Ikuo Ichinose. "Flat-Band Many-Body Localization and Ergodicity Breaking in the Creutz Ladder". In: *New Journal of Physics* 22.1 (2020), p. 013032. DOI: 10.1088/1367-2630/ab6352. arXiv: 1904.03463.

[312] Tomotaka Kuwahara, Takashi Mori, and Keiji Saito. "Floquet-Magnus Theory and Generic Transient Dynamics in Periodically Driven Many-Body Quantum Systems". In: *Annals of Physics* 367 (2016), pp. 96–124. DOI: 10.1016/j.aop.2016.01.012. arXiv: 1508.05797.

[313] Antonis Kyprianidis et al. "Observation of a Prethermal Discrete Time Crystal". In: *Science* 372.6547 (2021), pp. 1192–1196. DOI: 10.1126/science.abg8102. arXiv: 2102.01695.

[314] C. K. Lai. "Lattice Gas with Nearest-neighbor Interaction in One Dimension with Arbitrary Statistics". In: *Journal of Mathematical Physics* 15.10 (1974), pp. 1675–1676. DOI: 10.1063/1.1666522.

[315] L. D. Landau. "On the Theory of Phase Transitions". In: *Zh. Eksp. Teor. Fiz.* 7 (1937), pp. 19–32.

[316] R. Landauer. "Irreversibility and Heat Generation in the Computing Process". In: *IBM Journal of Research and Development* 5.3 (1961), pp. 183–191. DOI: 10.1147/rd.53.0183.

[317] A. Lasota, T.-Y. Li, and J. A. Yorke. "Asymptotic Periodicity of the Iterates of Markov Operators". In: *Transactions of the American Mathematical Society* 286.2 (1984), pp. 751–764. DOI: 10.1090/S0002-9947-1984-0760984-4.

[318] Chris R. Laumann and Norman Y. Yao. "Localization Goes Long". In: *Nature Physics* 12.10 (10 2016), pp. 894–895. DOI: 10.1038/nphys3854.

[319] Achilleas Lazarides, Arnab Das, and Roderich Moessner. "Equilibrium States of Generic Quantum Systems Subject to Periodic Driving". In: *Physical Review E* 90.1 (2014), p. 012110. DOI: 10.1103/PhysRevE.90.012110. arXiv: 1403.2946.

[320] Achilleas Lazarides and Roderich Moessner. "The Fate of a Discrete Time Crystal in an Open System". In: *Physical Review B* 95.19 (2017), p. 195135. DOI: 10.1103/PhysRevB.95.195135. arXiv: 1703.02547.

[321] Achilleas Lazarides et al. "Time Crystallinity in Dissipative Floquet Systems". In: *Physical Review Research* 2.2 (2020), p. 022002. DOI: 10.1103/PhysRevResearch.2.022002.

[322] Zala Lenarčič et al. "Critical Behavior near the Many-Body Localization Transition in Driven Open Systems". In: *Physical Review Letters* 125.11 (2020), p. 116601. DOI: 10.1103/PhysRevLett.125.116601. arXiv: 1910.01548.

[323] Pedro Lencastre et al. "From Empirical Data to Time-Inhomogeneous Continuous Markov Processes". In: *Physical Review E* 93.3 (2016), p. 032135. DOI: 10.1103/PhysRevE.93.032135.

[324] L. Lepori, A. Trombettoni, and D. Vodola. "Singular Dynamics and Emergence of Nonlocality in Long-Range Quantum Models". In: *Journal of Statistical Mechanics: Theory and Experiment* 2017.3 (2017), p. 033102. DOI: 10.1088/1742-5468/aa569d. arXiv: 1607.05358.

[325] Alessio Lerose et al. "Prethermal Quantum Many-Body Kapitza Phases of Periodically Driven Spin Systems". In: *Physical Review B* 100.10 (2019), p. 104306. DOI: 10.1103/PhysRevB.100.104306. arXiv: 1803.04490.

[326] Eyal Leviatan et al. "Quantum Thermalization Dynamics with Matrix-Product States". In: *arXiv* (2017). arXiv: 1702.08894.

[327] Fedor Levkovich-Maslyuk. "Lectures on the Bethe Ansatz". In: *Journal of Physics A: Mathematical and Theoretical* 49.32 (2016), p. 323004. DOI: 10.1088/1751-8113/49/32/323004. arXiv: 1606.02950.

[328] P. R. Levstein, H. M. Pastawski, and R. Calvo. "Spin Diffusion in Low-Dimensional Copper-Amino-Acid Complexes". In: *Journal of Physics: Condensed Matter* 3.12 (1991), pp. 1877–1888. DOI: 10.1088/0953-8984/3/12/018.

[329] P. Lévy. *Théorie de l'addition des variables aléatoires. 2. éd.* 1954.

[330] Elliott H. Lieb and Derek W. Robinson. "The Finite Group Velocity of Quantum Spin Systems". In: *Communications in Mathematical Physics* 28.3 (1972), pp. 251–257. DOI: 10.1007/BF01645779.

[331] Netanel H. Lindner, Gil Refael, and Victor Galitski. "Floquet Topological Insulator in Semiconductor Quantum Wells". In: *Nature Physics* 7.6 (2011), pp. 490–495. DOI: 10.1038/nphys1926. arXiv: 1008.1792.

[332] Marko Ljubotina, Lenart Zadnik, and Tomaž Prosen. "Ballistic Spin Transport in a Periodically Driven Integrable Quantum System". In: *Physical Review Letters* 122.15 (2019), p. 150605. DOI: 10.1103/PhysRevLett.122.150605. arXiv: 1901.05398.

[333] Marko Ljubotina, Marko Znidaric, and Tomaz Prosen. "Spin Diffusion from an Inhomogeneous Quench in an Integrable System". In: *Nature Communications* 8.1 (1 2017), p. 16117. DOI: 10.1038/ncomms16117. arXiv: 1702.04210.

[334] Marko Ljubotina, Marko Žnidarič, and Tomaž Prosen. "Kardar-Parisi-Zhang Physics in the Quantum Heisenberg Magnet". In: *Physical Review Letters* 122.21 (2019), p. 210602. DOI: 10.1103/PhysRevLett.122.210602.

[335] Cristóbal Lledó, Themistoklis Mavrogordatos, and Marzena Szymańska. "Driven Bose-Hubbard Dimer under Nonlocal Dissipation: A Bistable Time Crystal". In: *Physical Review B* 100.5 (2019), p. 054303. DOI: 10.1103/PhysRevB.100.054303. arXiv: 1901.04438.

[336] Jérôme Losson, John Milton, and Michael C. Mackey. "Phase Transitions in Networks of Chaotic Elements with Short and Long Range Interactions". In: *Physica D: Nonlinear Phenomena* 81.1 (1995), pp. 177–203. DOI: 10.1016/0167-2789(94)00203-3.

[337] I. Lovchinsky et al. "Magnetic Resonance Spectroscopy of an Atomically Thin Material Using a Single-Spin Qubit". In: *Science* 355.6324 (2017), pp. 503–507. DOI: `10.1126/science.aal2538`.

[338] David J. Luitz. "Long Tail Distributions near the Many Body Localization Transition". In: *Physical Review B* 93.13 (2016), p. 134201. DOI: `10.1103/PhysRevB.93.134201`. arXiv: `1601.04058`.

[339] David J. Luitz, François Huveneers, and Wojciech de Roeck. "How a Small Quantum Bath Can Thermalize Long Localized Chains". In: *Physical Review Letters* 119.15 (2017), p. 150602. DOI: `10.1103/PhysRevLett.119.150602`. arXiv: `1705.10807`.

[340] David J. Luitz, Nicolas Laflorencie, and Fabien Alet. "Many-Body Localization Edge in the Random-Field Heisenberg Chain". In: *Physical Review B* 91.8 (2015), p. 081103. DOI: `10.1103/PhysRevB.91.081103`. arXiv: `1411.0660`.

[341] David J. Luitz and Yevgeny Bar Lev. "Anomalous Thermalization in Ergodic Systems". In: *Physical Review Letters* 117.17 (2016), p. 170404. DOI: `10.1103/PhysRevLett.117.170404`. arXiv: `1607.01012`.

[342] David J. Luitz and Yevgeny Bar Lev. "Emergent Locality in Systems with Power-Law Interactions". In: *Physical Review A* 99.1 (2019), p. 010105. DOI: `10.1103/PhysRevA.99.010105`. arXiv: `1805.06895`.

[343] Daniil M. Lukin, Melissa A. Guidry, and Jelena Vučković. "Integrated Quantum Photonics with Silicon Carbide: Challenges and Prospects". In: *PRX Quantum* 1.2 (2020), p. 020102. DOI: `10.1103/PRXQuantum.1.020102`. arXiv: `2010.15700`.

[344] Francisco Machado et al. "Exponentially Slow Heating in Short and Long-range Interacting Floquet Systems". In: *Physical Review Research* 1.3 (2019), p. 033202. DOI: `10.1103/PhysRevResearch.1.033202`. arXiv: `1708.01620`.

[345] Francisco Machado et al. "Long-Range Prethermal Phases of Nonequilibrium Matter". In: *Physical Review X* 10.1 (2020), p. 011043. DOI: `10.1103/PhysRevX.10.011043`. arXiv: `1908.07530`.

[346] Ivaylo S. Madjarov et al. "High-Fidelity Entanglement and Detection of Alkaline-Earth Rydberg Atoms". In: *Nature Physics* 16.8 (2020), pp. 857–861. DOI: `10.1038/s41567-020-0903-z`. arXiv: `2001.04455`.

[347] Danuta Makowiec. "Stationary States of Toom Cellular Automata in Simulations". In: *Physical Review E* 60.4 (1999), pp. 3787–3796. DOI: `10.1103/PhysRevE.60.3787`.

[348] Krishnanand Mallayya, Marcos Rigol, and Wojciech De Roeck. "Prethermalization and Thermalization in Isolated Quantum Systems". In: *Physical Review X* 9.2 (2019), p. 021027. DOI: `10.1103/PhysRevX.9.021027`.

[349] Daniel Malz et al. "Seasonal Epidemic Spreading on Small-World Networks: Biennial Outbreaks and Classical Discrete Time Crystals". In: *Physical Review Research* 3.1 (2021), p. 013124. DOI: `10.1103/PhysRevResearch.3.013124`. arXiv: `2007.00979`.

[350] P. Mansfield. "Symmetrized Pulse Sequences in High Resolution NMR in Solids". In: *Journal of Physics C: Solid State Physics* 4.11 (1971), pp. 1444–1452. DOI: 10.1088/0022-3719/4/11/020.

[351] Matteo Marcuzzi et al. "Pre-Thermalization in a Non-Integrable Quantum Spin Chain after a Quench". In: *Physical Review Letters* 111.19 (2013), p. 197203. DOI: 10.1103/PhysRevLett.111.197203. arXiv: 1307.3738.

[352] P. C. Martin, E. D. Siggia, and H. A. Rose. "Statistical Dynamics of Classical Systems". In: *Physical Review A* 8.1 (1973), pp. 423–437. DOI: 10.1103/PhysRevA.8.423.

[353] Konstantin Matetski, Jeremy Quastel, and Daniel Remenik. "The KPZ Fixed Point". In: *Acta Mathematica* 227.1 (2021), pp. 115–203. DOI: 10.4310/ACTA.2021.v227.n1.a3. arXiv: 1701.00018.

[354] T. Matsuta, T. Koma, and S. Nakamura. "Improving the Lieb-Robinson Bound for Long-Range Interactions". In: *Annales Henri Poincaré* 18.2 (2017), pp. 519–528. DOI: 10.1007/s00023-016-0526-1. arXiv: 1604.05809.

[355] Barry M. McCoy and Tai Tsun Wu. "Theory of a Two-Dimensional Ising Model with Random Impurities. I. Thermodynamics". In: *Physical Review* 176.2 (1968), pp. 631–643. DOI: 10.1103/PhysRev.176.631.

[356] N. W. McLachlan. "Mathieu Functions of Fractional Order". In: *Journal of Mathematics and Physics* 26.1-4 (1947), pp. 29–41. DOI: 10.1002/sapm194726129.

[357] Claire A. McLellan et al. "Patterned Formation of Highly Coherent Nitrogen-Vacancy Centers Using a Focused Electron Irradiation Technique". In: *Nano Letters* 16.4 (2016), pp. 2450–2454. DOI: 10.1021/acs.nanolett.5b05304.

[358] Madan Lal Mehta. *Random Matrices*. Elsevier, 2004. 707 pp. Google Books: Kp3Nx03_gMwC.

[359] Florian Meinert et al. "Floquet Engineering of Correlated Tunneling in the Bose-Hubbard Model with Ultracold Atoms". In: *Physical Review Letters* 116.20 (2016), p. 205301. DOI: 10.1103/PhysRevLett.116.205301. arXiv: 1602.02657.

[360] C. J. Mertens, T. A. B. Kennedy, and S. Swain. "Many-Body Theory of Quantum Noise". In: *Physical Review Letters* 71.13 (1993), pp. 2014–2017. DOI: 10.1103/PhysRevLett.71.2014.

[361] Greg Meyer. *GregDMeyer/Dynamite v0.1.0*. Zenodo, 2020. DOI: 10.5281/zenodo.3606826.

[362] Pierre Meystre and Murray Sargent. *Elements of Quantum Optics*. Berlin: Springer, 2010.

[363] Xiao Mi et al. "Observation of Time-Crystalline Eigenstate Order on a Quantum Processor". In: *Nature* 601.7894 (2022), pp. 531–536. DOI: 10.1038/s41586-021-04257-w. arXiv: 2107.13571.

[364] A. A. Michailidis et al. "Slow Quantum Thermalization and Many-Body Revivals from Mixed Phase Space". In: *Physical Review X* 10.1 (2020), p. 011055. DOI: `10.1103/PhysRevX.10.011055`.

[365] Spyridon Michalakis and Justyna Pytel. "Stability of Frustration-Free Hamiltonians". In: *Communications in Mathematical Physics* 322.2 (2013), pp. 277–302. DOI: `10.1007/s00220-013-1762-6`. arXiv: `1109.1588`.

[366] W. B. Mims. "Phase Memory in Electron Spin Echoes, Lattice Relaxation Effects in CaW${\mathrm{O}}_{4}$: Er, Ce, Mn". In: *Physical Review* 168.2 (1968), pp. 370–389. DOI: `10.1103/PhysRev.168.370`.

[367] Martin Miranda et al. "Site-Resolved Imaging of a Bosonic Mott Insulator Using Ytterbium Atoms". In: *Physical Review A* 96.4 (2017), p. 043626. DOI: `10.1103/PhysRevA.96.043626`. arXiv: `1704.07060`.

[368] Martin Miranda et al. "Site-Resolved Imaging of Ytterbium Atoms in a Two-Dimensional Optical Lattice". In: *Physical Review A* 91.6 (2015), p. 063414. DOI: `10.1103/PhysRevA.91.063414`. arXiv: `1410.5189`.

[369] Gregoire Misguich et al. "Spin-Liquid Phase of the Multiple-Spin Exchange Hamiltonian on the Triangular Lattice". In: *Physical Review B* 60.2 (1999), pp. 1064–1074. DOI: `10.1103/PhysRevB.60.1064`. arXiv: `cond-mat/9812329`.

[370] Grégoire Misguich, Kirone Mallick, and P. L. Krapivsky. "Dynamics of the Spin-1/2 Heisenberg Chain Initialized in a Domain-Wall State". In: *Physical Review B* 96.19 (2017), p. 195151. DOI: `10.1103/PhysRevB.96.195151`. arXiv: `1708.01843`.

[371] Thomas Mittiga et al. "Imaging the Local Charge Environment of Nitrogen-Vacancy Centers in Diamond". In: *Physical Review Letters* 121.24 (2018), p. 246402. DOI: `10.1103/PhysRevLett.121.246402`. arXiv: `1809.01668`.

[372] Kaoru Mizuta, Kazuaki Takasan, and Norio Kawakami. "High-Frequency Expansion for Floquet Prethermal Phases with Emergent Symmetries: Application to Time Crystals and Floquet Engineering". In: *Physical Review B* 100.2 (2019), p. 020301. DOI: `10.1103/PhysRevB.100.020301`. arXiv: `1902.01126`.

[373] M. Moeckel and S. Kehrein. "Interaction Quench in the Hubbard Model". In: *Physical Review Letters* 100.17 (2008), p. 175702. DOI: `10.1103/PhysRevLett.100.175702`. arXiv: `0802.3202`.

[374] R. Moessner and S. L. Sondhi. "Equilibration and Order in Quantum Floquet Matter". In: *Nature Physics* 13.5 (2017), pp. 424–428. DOI: `10.1038/nphys4106`. arXiv: `1701.08056`.

[375] Philip J. W. Moll et al. "Evidence for Hydrodynamic Electron Flow in PdCoO$_2$". In: *Science* 351.6277 (2016), pp. 1061–1064. DOI: `10.1126/science.aac8385`. arXiv: `1509.05691`.

[376] Klaus Mølmer and Anders Sørensen. "Multiparticle Entanglement of Hot Trapped Ions". In: *Physical Review Letters* 82.9 (1999), pp. 1835–1838. DOI: `10.1103/PhysRevLett.82.1835`.

[377] C. Monroe et al. "Programmable Quantum Simulations of Spin Systems with Trapped Ions". In: *Reviews of Modern Physics* 93.2 (2021), p. 025001. DOI: `10.1103/RevModPhys.93.025001`. arXiv: `1912.07845`.

[378] Guy D. Moore and Kiyoumars A. Sohrabi. "Kubo Formulae for Second-Order Hydrodynamic Coefficients". In: *Physical Review Letters* 106.12 (2011), p. 122302. DOI: `10.1103/PhysRevLett.106.122302`. arXiv: `1007.5333`.

[379] Takashi Mori. "Floquet Prethermalization in Periodically Driven Classical Spin Systems". In: *Physical Review B* 98.10 (2018), p. 104303. DOI: `10.1103/PhysRevB.98.104303`. arXiv: `1804.02165`.

[380] Takashi Mori, Tomotaka Kuwahara, and Keiji Saito. "Rigorous Bound on Energy Absorption and Generic Relaxation in Periodically Driven Quantum Systems". In: *Physical Review Letters* 116.12 (2016), p. 120401. DOI: `10.1103/PhysRevLett.116.120401`. arXiv: `1509.03968`.

[381] Alan Morningstar, David A. Huse, and John Z. Imbrie. "Many-Body Localization near the Critical Point". In: *Physical Review B* 102.12 (2020), p. 125134. DOI: `10.1103/PhysRevB.102.125134`. arXiv: `2006.04825`.

[382] Alan Morningstar et al. "Avalanches and Many-Body Resonances in Many-Body Localized Systems". In: *arXiv* (2022). arXiv: `2107.05642`.

[383] J. Möser. "On Invariant Curves of Area-Preserving Mappings of an Annulus". In: *Nachr. Akad. Wiss. Göttingen, II* (1962), p. 1.

[384] Steven A. Moses et al. "New Frontiers with Quantum Gases of Polar Molecules". In: *Nature Physics* 13.1 (2017), pp. 13–20. DOI: `10.1038/nphys3985`. arXiv: `1610.07711`.

[385] Nevill Mott. *Metal-Insulator Transitions*. London: CRC Press, 1990. 296 pp. DOI: `10.1201/b12795`.

[386] Sanjay Moudgalya, David A. Huse, and Vedika Khemani. "Perturbative Instability towards Delocalization at Phase Transitions between MBL Phases". In: *arXiv* (2020). arXiv: `2008.09113`.

[387] Subroto Mukerjee, Vadim Oganesyan, and David Huse. "Statistical Theory of Transport by Strongly Interacting Lattice Fermions". In: *Physical Review B* 73.3 (2006), p. 035113. DOI: `10.1103/PhysRevB.73.035113`.

[388] Chaitanya Murthy and Mark Srednicki. "Bounds on Chaos from the Eigenstate Thermalization Hypothesis". In: *Physical Review Letters* 123.23 (2019), p. 230606. DOI: `10.1103/PhysRevLett.123.230606`. arXiv: `1906.10808`.

[389] Bruno Nachtergaele and Robert Sims. "A Multi-Dimensional Lieb-Schultz-Mattis Theorem". In: *Communications in Mathematical Physics* 276.2 (2007), pp. 437–472. DOI: 10.1007/s00220-007-0342-z. arXiv: math-ph/0608046.

[390] Bruno Nachtergaele and Robert Sims. "Lieb-Robinson Bounds and the Exponential Clustering Theorem". In: *Communications in Mathematical Physics* 265.1 (2006), pp. 119–130. DOI: 10.1007/s00220-006-1556-1. arXiv: math-ph/0506030.

[391] Bruno Nachtergaele and Robert Sims. "Lieb-Robinson Bounds in Quantum Many-Body Physics". In: *Entropy and the Quantum* 529 (2010), pp. 141–176. arXiv: 1004.2086.

[392] Bruno Nachtergaele and Robert Sims. "Locality Estimates for Quantum Spin Systems". In: *New Trends in Mathematical Physics*. Ed. by Vladas Sidoravičius. Dordrecht: Springer Netherlands, 2009, pp. 591–614. DOI: 10.1007/978-90-481-2810-5_39. arXiv: 0712.3318.

[393] Adam Nahum et al. "Quantum Entanglement Growth Under Random Unitary Dynamics". In: *Physical Review X* 7.3 (2017), p. 031016. DOI: 10.1103/PhysRevX.7.031016. arXiv: 1608.06950.

[394] Rahul Nandkishore, Sarang Gopalakrishnan, and David A. Huse. "Spectral Features of a Many-Body-Localized System Weakly Coupled to a Bath". In: *Physical Review B* 90.6 (2014), p. 064203. DOI: 10.1103/PhysRevB.90.064203.

[395] Rahul Nandkishore and David A. Huse. "Many Body Localization and Thermalization in Quantum Statistical Mechanics". In: *Annual Review of Condensed Matter Physics* 6.1 (2015), pp. 15–38. DOI: 10.1146/annurev-conmatphys-031214-014726. arXiv: 1404.0686.

[396] Rahul Nandkishore and Andrew C. Potter. "Marginal Anderson Localization and Many Body Delocalization". In: *Physical Review B* 90.19 (2014), p. 195115. DOI: 10.1103/PhysRevB.90.195115. arXiv: 1406.0847.

[397] Rahul M. Nandkishore and S. L. Sondhi. "Many Body Localization with Long Range Interactions". In: *Physical Review X* 7.4 (2017), p. 041021. DOI: 10.1103/PhysRevX.7.041021. arXiv: 1705.06290.

[398] B. N. Narozhny et al. "Hydrodynamics in Graphene: Linear-response Transport". In: *Physical Review B* 91.3 (2015), p. 035414. DOI: 10.1103/PhysRevB.91.035414. arXiv: 1411.0819.

[399] Frederik Nathan et al. "Anomalous Floquet Insulators". In: *Physical Review B* 99.19 (2019), p. 195133. DOI: 10.1103/PhysRevB.99.195133. arXiv: 1712.02789.

[400] N. Nessi, A. Iucci, and M. A. Cazalilla. "Quantum Quench and Prethermalization Dynamics in a Two-Dimensional Fermi Gas with Long-Range Interactions". In: *Physical Review Letters* 113.21 (2014), p. 210402. DOI: 10.1103/PhysRevLett.113.210402.

[401] Johann von NEUMANN and Arthur W Burks. *Theory of Self-Reproducing Automata. Edited and Completed by Arthur W. Burks.* Urbana; London: Illinois University Press, 1966.

[402] K.-K. Ni et al. "A High Phase-Space-Density Gas of Polar Molecules". In: *Science* 322.5899 (2008), pp. 231–235. DOI: `10.1126/science.1163861`.

[403] Matthew A. Nichols et al. "Spin Transport in a Mott Insulator of Ultracold Fermions". In: *Science* 363.6425 (2019), pp. 383–387. DOI: `10.1126/science.aat4387`. pmid: `30523079`.

[404] Nivedita, Henry Shackleton, and Subir Sachdev. "Spectral Form Factors of Clean and Random Quantum Ising Chains". In: *Physical Review E* 101.4 (2020), p. 042136. DOI: `10.1103/PhysRevE.101.042136`. arXiv: `2001.06732`.

[405] James O'Sullivan et al. "Signatures of Discrete Time Crystalline Order in Dissipative Spin Ensembles". In: *New Journal of Physics* 22.8 (2020), p. 085001. DOI: `10.1088/1367-2630/ab9fbe`.

[406] Vadim Oganesyan and David A. Huse. "Localization of Interacting Fermions at High Temperature". In: *Physical Review B* 75.15 (2007), p. 155111. DOI: `10.1103/PhysRevB.75.155111`. arXiv: `cond-mat/0610854`.

[407] Kenichi Ohno et al. "Engineering Shallow Spins in Diamond with Nitrogen Delta-Doping". In: *Applied Physics Letters* 101.8 (2012), p. 082413. DOI: `10.1063/1.4748280`. arXiv: `1207.2784`.

[408] Takashi Oka and Sota Kitamura. "Floquet Engineering of Quantum Materials". In: *Annual Review of Condensed Matter Physics* 10.1 (2019), pp. 387–408. DOI: `10.1146/annurev-conmatphys-031218-013423`. arXiv: `1804.03212`.

[409] Peter J Olver. "A Nonlinear Hamiltonian Structure for the Euler Equations". In: *Journal of Mathematical Analysis and Applications* 89.1 (1982), pp. 233–250. DOI: `10.1016/0022-247X(82)90100-7`.

[410] Ahmed Omran et al. "Microscopic Observation of Pauli Blocking in Degenerate Fermionic Lattice Gases". In: *Physical Review Letters* 115.26 (2015), p. 263001. DOI: `10.1103/PhysRevLett.115.263001`. arXiv: `1510.04599`.

[411] Roman Orus and Guifre Vidal. "The iTEBD Algorithm beyond Unitary Evolution". In: *Physical Review B* 78.15 (2008), p. 155117. DOI: `10.1103/PhysRevB.78.155117`. arXiv: `0711.3960`.

[412] Tobias J. Osborne. "Simulating Adiabatic Evolution of Gapped Spin Systems". In: *Physical Review A* 75.3 (2007), p. 032321. DOI: `10.1103/PhysRevA.75.032321`. arXiv: `quant-ph/0601019`.

[413] Edward Ott. "Strange Attractors and Chaotic Motions of Dynamical Systems". In: *Reviews of Modern Physics* 53.4 (1981), pp. 655–671. DOI: `10.1103/RevModPhys.53.655`.

[414] Hideki Ozawa et al. "Antiferromagnetic Spin Correlation of SU($\mathcal{N}$) Fermi Gas in an Optical Super-Lattice". In: *Physical Review Letters* 121.22 (2018), p. 225303. DOI: 10.1103/PhysRevLett.121.225303. arXiv: 1801.05962.

[415] Guido Pagano et al. "A One-Dimensional Liquid of Fermions with Tunable Spin". In: *Nature Physics* 10.3 (3 2014), pp. 198–201. DOI: 10.1038/nphys2878.

[416] Don N. Page. "Average Entropy of a Subsystem". In: *Physical Review Letters* 71.9 (1993), pp. 1291–1294. DOI: 10.1103/PhysRevLett.71.1291. arXiv: gr-qc/9305007.

[417] Daniela Pagliero et al. "Optically Pumped Spin Polarization as a Probe of Many-Body Thermalization". In: *Science Advances* 6.18 (2020), eaaz6986. DOI: 10.1126/sciadv.aaz6986. arXiv: 2005.00647.

[418] Arijeet Pal and David A. Huse. "Many-Body Localization Phase Transition". In: *Physical Review B* 82.17 (2010), p. 174411. DOI: 10.1103/PhysRevB.82.174411. arXiv: 1010.1992.

[419] Soham Pal et al. "Temporal Order in Periodically Driven Spins in Star-Shaped Clusters". In: *Physical Review Letters* 120.18 (2018), p. 180602. DOI: 10.1103/PhysRevLett.120.180602. arXiv: 1708.08443.

[420] Rajat K. Panda et al. "Can We Study the Many-Body Localisation Transition?" In: *EPL (Europhysics Letters)* 128.6 (2020), p. 67003. DOI: 10.1209/0295-5075/128/67003. arXiv: 1911.07882.

[421] Z. Papic, E. M. Stoudenmire, and Dmitry A. Abanin. "Many-Body Localization in Disorder-Free Systems: The Importance of Finite-Size Constraints". In: *Annals of Physics* 362 (2015), pp. 714–725. DOI: 10.1016/j.aop.2015.08.024. arXiv: 1501.00477.

[422] Arun Paramekanti, Leon Balents, and Matthew P. A. Fisher. "Ring Exchange, the Bose Metal, and Bosonization in Two Dimensions". In: *Physical Review B* 66.5 (2002), p. 054526. DOI: 10.1103/PhysRevB.66.054526. arXiv: cond-mat/0203171.

[423] S. A. Parameswaran and Romain Vasseur. "Many-Body Localization, Symmetry, and Topology". In: *Reports on Progress in Physics* 81.8 (2018), p. 082501. DOI: 10.1088/1361-6633/aac9ed. arXiv: 1801.07731.

[424] A. J. Park et al. "Cavity-Enhanced Optical Lattices for Scaling Neutral Atom Quantum Technologies". In: *arXiv* (2021). arXiv: 2110.08073.

[425] Daniel E. Parker, Romain Vasseur, and Thomas Scaffidi. "Topologically-Protected Long Edge Coherence Times in Symmetry-Broken Phases". In: *Physical Review Letters* 122.24 (2019), p. 240605. DOI: 10.1103/PhysRevLett.122.240605. arXiv: 1808.07485.

[426] Daniel E. Parker et al. "A Universal Operator Growth Hypothesis". In: *Physical Review X* 9.4 (2019), p. 041017. DOI: 10.1103/PhysRevX.9.041017. arXiv: 1812.08657.

[427] Ulrich Parlitz, Lutz Junge, and Ljupco Kocarev. "Subharmonic Entrainment of Unstable Period Orbits and Generalized Synchronization". In: *Physical Review Letters* 79.17 (1997), pp. 3158–3161. DOI: 10.1103/PhysRevLett.79.3158.

[428] Maxwell F. Parsons et al. "Site-Resolved Imaging of Fermionic Lithium-6 in an Optical Lattice". In: *Physical Review Letters* 114.21 (2015), p. 213002. DOI: 10.1103/PhysRevLett.114.213002. arXiv: 1504.04397.

[429] David Pekker et al. "The Hilbert-glass Transition: New Universality of Temperature-Tuned Many-Body Dynamical Quantum Criticality". In: *Physical Review X* 4.1 (2014), p. 011052. DOI: 10.1103/PhysRevX.4.011052. arXiv: 1307.3253.

[430] Pai Peng et al. "Floquet Prethermalization in Dipolar Spin Chains". In: *Nature Physics* 17.4 (4 2021), pp. 444–447. DOI: 10.1038/s41567-020-01120-z. arXiv: 1912.05799.

[431] Oskar Perron. "Zur Theorie der Matrices". In: *Mathematische Annalen* 64.2 (1907), pp. 248–263. DOI: 10.1007/BF01449896.

[432] Linh M. Pham et al. "NMR Technique for Determining the Depth of Shallow Nitrogen-Vacancy Centers in Diamond". In: *Physical Review B* 93.4 (2016), p. 045425. DOI: 10.1103/PhysRevB.93.045425. arXiv: 1508.04191.

[433] Andrea Pizzi, Johannes Knolle, and Andreas Nunnenkamp. "Higher-Order and Fractional Discrete Time Crystals in Clean Long-Range Interacting Systems". In: *Nature Communications* 12.1 (2021), p. 2341. DOI: 10.1038/s41467-021-22583-5. arXiv: 1910.07539.

[434] Andrea Pizzi, Andreas Nunnenkamp, and Johannes Knolle. "Bistability and Time Crystals in Long-Ranged Directed Percolation". In: *Nature Communications* 12.1 (2021), p. 1061. DOI: 10.1038/s41467-021-21259-4. arXiv: 2004.13034.

[435] Andrea Pizzi, Andreas Nunnenkamp, and Johannes Knolle. "Classical Prethermal Phases of Matter". In: *Physical Review Letters* 127.14 (2021), p. 140602. DOI: 10.1103/PhysRevLett.127.140602. arXiv: 2104.13928.

[436] Andrea Pizzi et al. "To Heat or Not to Heat: Time Crystallinity and Finite-Size Effects in Clean Floquet Systems". In: *Physical Review B* 102.21 (2020), p. 214207. DOI: 10.1103/PhysRevB.102.214207. arXiv: 2009.13527.

[437] Hoi Chun Po et al. "Radical Chiral Floquet Phases in a Periodically Driven Kitaev Model and Beyond". In: *Physical Review B* 96.24 (2017), p. 245116. DOI: 10.1103/PhysRevB.96.245116. arXiv: 1701.01440.

[438] Matteo Pompili et al. "Realization of a Multi-Node Quantum Network of Remote Solid-State Qubits". In: *Science* 372.6539 (2021), pp. 259–264. DOI: 10.1126/science.abg1919. arXiv: 2102.04471.

[439] Pedro Ponte et al. "Many-Body Localization in Periodically Driven Systems". In: *Physical Review Letters* 114.14 (2015), p. 140401. DOI: 10.1103/PhysRevLett.114.140401. arXiv: 1410.8518.

[440] Pedro Ponte et al. "Periodically Driven Ergodic and Many-Body Localized Quantum Systems". In: *Annals of Physics* 353 (2015), pp. 196–204. DOI: 10.1016/j.aop.2014.11.008.

[441] Vladislav Popkov et al. "Fibonacci Family of Dynamical Universality Classes". In: *Proceedings of the National Academy of Sciences* 112.41 (2015), pp. 12645–12650. DOI: 10.1073/pnas.1512261112. arXiv: 1505.04461.

[442] E. B. Postnikov, A. Chechkin, and I. M. Sokolov. "Brownian yet Non-Gaussian Diffusion in Heterogeneous Media: From Superstatistics to Homogenization". In: *New Journal of Physics* 22.6 (2020), p. 063046. DOI: 10.1088/1367-2630/ab90da.

[443] Ionut-Dragos Potirniche, Sumilan Banerjee, and Ehud Altman. "On the Stability of Many-Body Localization in $d>1$". In: *Physical Review B* 99.20 (2019), p. 205149. DOI: 10.1103/PhysRevB.99.205149. arXiv: 1805.01475.

[444] Ionut-Dragos Potirniche et al. "Floquet Symmetry-Protected Topological Phases in Cold Atomic Systems". In: *Physical Review Letters* 119.12 (2017), p. 123601. DOI: 10.1103/PhysRevLett.119.123601. arXiv: 1610.07611.

[445] Andrew C. Potter, Takahiro Morimoto, and Ashvin Vishwanath. "Classification of Interacting Topological Floquet Phases in One Dimension". In: *Physical Review X* 6.4 (2016), p. 041001. DOI: 10.1103/PhysRevX.6.041001. arXiv: 1602.05194.

[446] Andrew C. Potter, Romain Vasseur, and S. A. Parameswaran. "Universal Properties of Many-Body Delocalization Transitions". In: *Physical Review X* 5.3 (2015), p. 031033. DOI: 10.1103/PhysRevX.5.031033. arXiv: 1501.03501.

[447] Michael Prähofer and Herbert Spohn. "Exact Scaling Functions for One-Dimensional Stationary KPZ Growth". In: *Journal of Statistical Physics* 115.1 (2004), pp. 255–279. DOI: 10.1023/B:JOSS.0000019810.21828.fc.

[448] Michael Prähofer and Herbert Spohn. "Universal Distributions for Growth Processes in $1+1$ Dimensions and Random Matrices". In: *Physical Review Letters* 84.21 (2000), pp. 4882–4885. DOI: 10.1103/PhysRevLett.84.4882.

[449] Nicolas Privault. *Understanding Markov Chains: Examples and Applications*. 2018.

[450] Tomaz Prosen. "Ergodic Properties of a Generic Non-Integrable Quantum Many-Body System in Thermodynamic Limit". In: *Physical Review E* 60.4 (1999), pp. 3949–3968. DOI: 10.1103/PhysRevE.60.3949. arXiv: cond-mat/9808150.

[451] Tomaz Prosen. "Time Evolution of a Quantum Many-Body System: Transition from Integrability to Ergodicity in Thermodynamic Limit". In: *Physical Review Letters* 80.9 (1998), pp. 1808–1811. DOI: 10.1103/PhysRevLett.80.1808. arXiv: cond-mat/9707180.

[452] Tomaž Prosen and Bojan Žunkovič. "Macroscopic Diffusive Transport in a Microscopically Integrable Hamiltonian System". In: *Physical Review Letters* 111.4 (2013), p. 040602. DOI: 10.1103/PhysRevLett.111.040602.

[453] N. Provatas et al. "Flame Propagation in Random Media". In: *Physical Review E* 51.5 (1995), pp. 4232–4236. DOI: 10.1103/PhysRevE.51.4232.

[454] E. M. Purcell. "Spontaneous Emission Probabilities at Radio Frequencies". In: *Confined Electrons and Photons: New Physics and Applications*. Ed. by Elias Burstein and Claude Weisbuch. Boston, MA: Springer US, 1995, pp. 839–839. DOI: 10.1007/978-1-4615-1963-8_40.

[455] Atanu Rajak, Itzhack Dana, and Emanuele G. Dalla Torre. "Characterizations of Prethermal States in Periodically Driven Many-Body Systems with Unbounded Chaotic Diffusion". In: *Physical Review B* 100.10 (2019), p. 100302. DOI: 10.1103/PhysRevB.100.100302. arXiv: 1905.00031.

[456] Tibor Rakovszky, C. W. von Keyserlingk, and Frank Pollmann. "Dissipation-Assisted Operator Evolution Method for Capturing Hydrodynamic Transport". In: *arXiv* (2020). arXiv: 2004.05177.

[457] J. Randall et al. "Observation of a Many-Body-Localized Discrete Time Crystal with a Programmable Spin-Based Quantum Simulator". In: *Science* 374.6574 (2021), pp. 1474–1478. DOI: 10.1126/science.abk0603. arXiv: 2107.00736.

[458] Lord Rayleigh. "VII. On the Crispations of Fluid Resting upon a Vibrating Support". In: *The London, Edinburgh, and Dublin Philosophical Magazine and Journal of Science* 16.97 (1883), pp. 50–58. DOI: 10.1080/14786448308627392.

[459] Lord Rayleigh. "XXXIII. On Maintained Vibrations". In: *The London, Edinburgh, and Dublin Philosophical Magazine and Journal of Science* 15.94 (1883), pp. 229–235. DOI: 10.1080/14786448308627342.

[460] W-K. Rhim, A. Pines, and J. S. Waugh. "Time-Reversal Experiments in Dipolar-Coupled Spin Systems". In: *Physical Review B* 3.3 (1971), pp. 684–696. DOI: 10.1103/PhysRevB.3.684.

[461] W-K. Rhim, D. D. Elleman, and R. W. Vaughan. "Analysis of Multiple Pulse NMR in Solids". In: *The Journal of Chemical Physics* 59.7 (1973), pp. 3740–3749. DOI: 10.1063/1.1680545.

[462] Philip Richerme et al. "Non-Local Propagation of Correlations in Long-Range Interacting Quantum Systems". In: *Nature* 511.7508 (2014), pp. 198–201. DOI: 10.1038/nature13450. arXiv: 1401.5088.

[463] Marcos Rigol, Vanja Dunjko, and Maxim Olshanii. "Thermalization and Its Mechanism for Generic Isolated Quantum Systems". In: *Nature* 452.7189 (2008), pp. 854–858. DOI: 10.1038/nature06838. arXiv: 0708.1324.

[464] Eva Rittweger et al. "STED Microscopy Reveals Crystal Colour Centres with Nanometric Resolution". In: *Nature Photonics* 3.3 (3 2009), pp. 144–147. DOI: `10.1038/nphoton.2009.2`.

[465] Lucio Robledo et al. "Spin Dynamics in the Optical Cycle of Single Nitrogen-Vacancy Centres in Diamond". In: *New Journal of Physics* 13.2 (2011), p. 025013. DOI: `10.1088/1367-2630/13/2/025013`.

[466] T. Rosskopf et al. "Investigation of Surface Magnetic Noise by Shallow Spins in Diamond". In: *Physical Review Letters* 112.14 (2014), p. 147602. DOI: `10.1103/PhysRevLett.112.147602`.

[467] P. Roushan et al. "Spectroscopic Signatures of Localization with Interacting Photons in Superconducting Qubits". In: *Science* 358.6367 (2017), pp. 1175–1179. DOI: `10.1126/science.aao1401`.

[468] Jared Rovny, Robert L. Blum, and Sean E. Barrett. "Observation of Discrete-Time-Crystal Signatures in an Ordered Dipolar Many-Body System". In: *Physical Review Letters* 120.18 (2018), p. 180603. DOI: `10.1103/PhysRevLett.120.180603`. arXiv: `1802.00126`.

[469] Dibyendu Roy, Rajeev Singh, and Roderich Moessner. "Probing Many-Body Localization by Spin Noise Spectroscopy". In: *Physical Review B* 92.18 (2015), p. 180205. DOI: `10.1103/PhysRevB.92.180205`. arXiv: `1506.05116`.

[470] Rahul Roy and Fenner Harper. "Abelian Floquet Symmetry-Protected Topological Phases in One Dimension". In: *Physical Review B* 94.12 (2016), p. 125105. DOI: `10.1103/PhysRevB.94.125105`. arXiv: `1602.08089`.

[471] Rahul Roy and Fenner Harper. "Periodic Table for Floquet Topological Insulators". In: *Physical Review B* 96.15 (2017), p. 155118. DOI: `10.1103/PhysRevB.96.155118`. arXiv: `1603.06944`.

[472] Antonio Rubio-Abadal et al. "Floquet Prethermalization in a Bose-Hubbard System". In: *Physical Review X* 10.2 (2020), p. 021044. DOI: `10.1103/PhysRevX.10.021044`. arXiv: `2001.08226`.

[473] Antonio Rubio-Abadal et al. "Many-Body Delocalization in the Presence of a Quantum Bath". In: *Physical Review X* 9.4 (2019), p. 041014. DOI: `10.1103/PhysRevX.9.041014`.

[474] M. A. Ruderman and C. Kittel. "Indirect Exchange Coupling of Nuclear Magnetic Moments by Conduction Electrons". In: *Physical Review* 96.1 (1954), pp. 99–102. DOI: `10.1103/PhysRev.96.99`.

[475] Mark S. Rudner and Netanel H. Lindner. "Band Structure Engineering and Non-Equilibrium Dynamics in Floquet Topological Insulators". In: *Nature Reviews Physics* 2.5 (5 2020), pp. 229–244. DOI: `10.1038/s42254-020-0170-z`.

[476] D. Ruelle. "Statistical Mechanics of a One-Dimensional Lattice Gas". In: *Communications in Mathematical Physics* 9.4 (1968), pp. 267–278.

[477] Subir Sachdev. *Quantum Phase Transitions*. 2nd ed. Cambridge: Cambridge University Press, 2011. DOI: `10.1017/CBO9780511973765`.

[478] A. Safavi-Naini et al. "Quantum Dynamics of Disordered Spin Chains with Power-Law Interactions". In: *Physical Review A* 99.3 (2019), p. 033610. DOI: `10.1103/PhysRevA.99.033610`. arXiv: `1806.03339`.

[479] M. Saffman, T. G. Walker, and K. Molmer. "Quantum Information with Rydberg Atoms". In: *Reviews of Modern Physics* 82.3 (2010), pp. 2313–2363. DOI: `10.1103/RevModPhys.82.2313`. arXiv: `0909.4777`.

[480] Rahul Sahay et al. "Emergent Ergodicity at the Transition between Many-Body Localized Phases". In: *Physical Review Letters* 126.10 (2021), p. 100604. DOI: `10.1103/PhysRevLett.126.100604`. arXiv: `2008.08585`.

[481] Subhayan Sahu, Shenglong Xu, and Brian Swingle. "Scrambling Dynamics across a Thermalization-Localization Quantum Phase Transition". In: *Physical Review Letters* 123.16 (2019), p. 165902. DOI: `10.1103/PhysRevLett.123.165902`. arXiv: `1807.06086`.

[482] K. M Salikhov, S. A Dzuba, and A. M Raitsimring. "The Theory of Electron Spin-Echo Signal Decay Resulting from Dipole-Dipole Interactions between Paramagnetic Centers in Solids". In: *Journal of Magnetic Resonance (1969)* 42.2 (1981), pp. 255–276. DOI: `10.1016/0022-2364(81)90216-X`.

[483] Sarben Sarkar. "The Supersymmetric t ? J Model in One Dimension". In: *Exactly Solvable Models of Strongly Correlated Electrons*. Vol. Volume 18. Advanced Series in Mathematical Physics Volume 18. WORLD SCIENTIFIC, 1994, pp. 311–325. DOI: `10.1142/9789812798268_0029`.

[484] Tomohiro Sasamoto and Herbert Spohn. "Exact Height Distributions for the KPZ Equation with Narrow Wedge Initial Condition". In: *Nuclear Physics B* 834.3 (2010), pp. 523–542. DOI: `10.1016/j.nuclphysb.2010.03.026`. arXiv: `1002.1879`.

[485] F. Scazza et al. "Observation of Two-Orbital Spin-Exchange Interactions with Ultracold SU(N)-Symmetric Fermions". In: *Nature Physics* 10.10 (2014), pp. 779–784. DOI: `10.1038/nphys3061`. arXiv: `1403.4761`.

[486] Johannes Schachenmayer, Alexander Pikovski, and Ana Maria Rey. "Dynamics of Correlations in Two-Dimensional Quantum Spin Models with Long-Range Interactions: A Phase-Space Monte-Carlo Study". In: *New Journal of Physics* 17.6 (2015), p. 065009. DOI: `10.1088/1367-2630/17/6/065009`. arXiv: `1501.06593`.

[487] A. Scheie et al. "Detection of Kardar–Parisi–Zhang Hydrodynamics in a Quantum Heisenberg Spin-1/2 Chain". In: *Nature Physics* (2021), pp. 1–5. DOI: `10.1038/s41567-021-01191-6`.

[488] Max Schemmer et al. "Generalized HydroDynamics on an Atom Chip". In: *Physical Review Letters* 122.9 (2019), p. 090601. DOI: `10.1103/PhysRevLett.122.090601`. arXiv: `1810.07170`.

[489] Nathan Schine et al. "Long-Lived Bell States in an Array of Optical Clock Qubits". In: *arXiv* (2021). arXiv: `2111.14653`.

[490] Ch Schneider, Diego Porras, and Tobias Schaetz. "Experimental Quantum Simulations of Many-Body Physics with Trapped Ions". In: *Reports on Progress in Physics* 75.2 (2012), p. 024401. DOI: `10.1088/0034-4885/75/2/024401`.

[491] Ulrich Schollwoeck. "The Density-Matrix Renormalization Group". In: *Reviews of Modern Physics* 77.1 (2005), pp. 259–315. DOI: `10.1103/RevModPhys.77.259`. arXiv: `cond-mat/0409292`.

[492] Michael Schreiber et al. "Observation of Many-Body Localization of Interacting Fermions in a Quasi-Random Optical Lattice". In: *Science* 349.6250 (2015), pp. 842–845. DOI: `10.1126/science.aaa7432`. arXiv: `1501.05661`.

[493] E. Schrödinger. "Energieaustausch Nach Der Wellenmechanik". In: *Annalen der Physik* 388.15 (1927), pp. 956–968. DOI: `10.1002/andp.19273881504`.

[494] Alexander Schuckert, Izabella Lovas, and Michael Knap. "Non-Local Emergent Hydrodynamics in a Long-Range Quantum Spin System". In: *Physical Review B* 101.2 (2020), p. 020416. DOI: `10.1103/PhysRevB.101.020416`. arXiv: `1909.01351`.

[495] Thomas Schuster et al. "Floquet Hopf Insulators". In: *Physical Review Letters* 123.26 (2019), p. 266803. DOI: `10.1103/PhysRevLett.123.266803`. arXiv: `1903.02558`.

[496] Ilai Schwartz et al. "Robust Optical Polarization of Nuclear Spin Baths Using Hamiltonian Engineering of Nitrogen-Vacancy Center Quantum Dynamics". In: *Science Advances* 4.8 (2018), eaat8978. DOI: `10.1126/sciadv.aat8978`.

[497] A Schweiger and Gunnar Jeschke. *Principles of Pulse Electron Paramagnetic Resonance*. Oxford, UK; New York: Oxford University Press, 2001.

[498] Mordechai Segev, Yaron Silberberg, and Demetrios N. Christodoulides. "Anderson Localization of Light". In: *Nature Photonics* 7.3 (3 2013), pp. 197–204. DOI: `10.1038/nphoton.2013.30`.

[499] Kilian Seibold, Riccardo Rota, and Vincenzo Savona. "A Dissipative Time Crystal in an Asymmetric Non-Linear Photonic Dimer". In: *Physical Review A* 101.3 (2020), p. 033839. DOI: `10.1103/PhysRevA.101.033839`. arXiv: `1910.03499`.

[500] Dries Sels. "Markovian Baths and Quantum Avalanches". In: *arXiv* (2021). arXiv: `2108.10796`.

[501] Dries Sels and Anatoli Polkovnikov. "Thermalization of Dilute Impurities in One Dimensional Spin Chains". In: *arXiv* (2022). arXiv: `2105.09348`.

[502] Maksym Serbyn, Dmitry A. Abanin, and Zlatko Papić. "Quantum Many-Body Scars and Weak Breaking of Ergodicity". In: *Nature Physics* 17.6 (6 2021), pp. 675–685. DOI: 10.1038/s41567-021-01230-2.

[503] Maksym Serbyn, Z. Papić, and Dmitry A. Abanin. "Local Conservation Laws and the Structure of the Many-Body Localized States". In: *Physical Review Letters* 111.12 (2013), p. 127201. DOI: 10.1103/PhysRevLett.111.127201. arXiv: 1305.5554.

[504] Alfred Shapere and Frank Wilczek. "Classical Time Crystals". In: *Physical Review Letters* 109.16 (2012), p. 160402. DOI: 10.1103/PhysRevLett.109.160402. arXiv: 1202.2537.

[505] Jacob F. Sherson et al. "Single-Atom Resolved Fluorescence Imaging of an Atomic Mott Insulator". In: *Nature* 467.7311 (2010), pp. 68–72. DOI: 10.1038/nature09378. arXiv: 1006.3799.

[506] Michael F. Shlesinger, George M. Zaslavsky, and Uriel Frisch, eds. *Lévy Flights and Related Topics in Physics. Proceedings of the International Workshop, Held at Nice, France, 27-30 June, 1994*. Vol. 450. Lect. Notes Phys. Berlin: Springer-Verlag, 1995. DOI: 10.1007/3-540-59222-9.

[507] Ya. G. Sinai. "The Limiting Behavior of a One-Dimensional Random Walk in a Random Medium". In: *Theory of Probability & Its Applications* 27.2 (1983), pp. 256–268. DOI: 10.1137/1127028.

[508] Rajeev Singh, Jens H. Bardarson, and Frank Pollmann. "Signatures of the Many-Body Localization Transition in the Dynamics of Entanglement and Bipartite Fluctuations". In: *New Journal of Physics* 18.2 (2016), p. 023046. DOI: 10.1088/1367-2630/18/2/023046. arXiv: 1508.05045.

[509] Charles P. Slichter. *Principles of Magnetic Resonance*. Red. by Manuel Cardona et al. Vol. 1. Springer Series in Solid-State Sciences. Berlin, Heidelberg: Springer Berlin Heidelberg, 1990. DOI: 10.1007/978-3-662-09441-9.

[510] J. Smith et al. "Many-Body Localization in a Quantum Simulator with Programmable Random Disorder". In: *Nature Physics* 12.10 (10 2016), pp. 907–911. DOI: 10.1038/nphys3783.

[511] J. Smits et al. "Observation of a Space-Time Crystal in a Superfluid Quantum Gas". In: *Physical Review Letters* 121.18 (2018), p. 185301. DOI: 10.1103/PhysRevLett.121.185301. arXiv: 1807.05904.

[512] Ariel Sommer et al. "Universal Spin Transport in a Strongly Interacting Fermi Gas". In: *Nature* 472.7342 (2011), pp. 201–204. DOI: 10.1038/nature09989. arXiv: 1101.0780.

[513] Lindsay Sonderhouse et al. "Thermodynamics of a Deeply Degenerate SU(N)-Symmetric Fermi Gas". In: *Nature Physics* 16.12 (2020), pp. 1216–1221. DOI: 10.1038/s41567-020-0986-6. arXiv: 2003.02408.

[514] Frank Spitzer. *Principles of Random Walk.* Springer Science & Business Media, 2001. 438 pp. Google Books: `HI09jpb5o6cC`.

[515] Herbert Spohn. *Large Scale Dynamics of Interacting Particles.* Berlin: Springer, 1991.

[516] Herbert Spohn. "The $1 + 1$ Dimensional Kardar–Parisi–Zhang Equation: More Surprises". In: *Journal of Statistical Mechanics: Theory and Experiment* 2020.4 (2020), p. 044001. DOI: `10.1088/1742-5468/ab712a`.

[517] Mark Srednicki. "Chaos and Quantum Thermalization". In: *Physical Review E* 50.2 (1994), pp. 888–901. DOI: `10.1103/PhysRevE.50.888`. arXiv: `cond-mat/9403051`.

[518] Mark Srednicki. "The Approach to Thermal Equilibrium in Quantized Chaotic Systems". In: *Journal of Physics A: Mathematical and General* 32.7 (1999), pp. 1163–1175. DOI: `10.1088/0305-4470/32/7/007`. arXiv: `cond-mat/9809360`.

[519] David-Maximilian Storch, Mauritz van den Worm, and Michael Kastner. "Interplay of Soundcone and Supersonic Propagation in Lattice Models with Power Law Interactions". In: *New Journal of Physics* 17.6 (2015), p. 063021. DOI: `10.1088/1367-2630/17/6/063021`. arXiv: `1502.05891`.

[520] Steven H Strogatz and Mitchal Dichter. *Nonlinear Dynamics and Chaos with Student Solutions Manual: With Applications to Physics, Biology, Chemistry, and Engineering.* 2018.

[521] Stella Stylianidou, Nathan J. Kuwada, and Paul A. Wiggins. "Cytoplasmic Dynamics Reveals Two Modes of Nucleoid-Dependent Mobility". In: *Biophysical Journal* 107.11 (2014), pp. 2684–2692. DOI: `10.1016/j.bpj.2014.10.030`. pmid: `25468347`.

[522] J. Šuntajs et al. "Quantum Chaos Challenges Many-Body Localization". In: *Physical Review E* 102.6 (2020), p. 062144. DOI: `10.1103/PhysRevE.102.062144`. arXiv: `1905.06345`.

[523] A. O. Sushkov et al. "Magnetic Resonance Detection of Individual Proton Spins Using Quantum Reporters". In: *Physical Review Letters* 113.19 (2014), p. 197601. DOI: `10.1103/PhysRevLett.113.197601`. arXiv: `1410.3750`.

[524] Bill Sutherland. "Model for a Multicomponent Quantum System". In: *Physical Review B* 12.9 (1975), pp. 3795–3805. DOI: `10.1103/PhysRevB.12.3795`.

[525] Brian Swingle. "Unscrambling the Physics of Out-of-Time-Order Correlators". In: *Nature Physics* 14.10 (10 2018), pp. 988–990. DOI: `10.1038/s41567-018-0295-5`.

[526] Hossein Taheri et al. "All-Optical Dissipative Discrete Time Crystals". In: *Nature Communications* 13.1 (2022), p. 848. DOI: `10.1038/s41467-022-28462-x`. arXiv: `2012.07927`.

[527] Susumu Takahashi et al. "Quenching Spin Decoherence in Diamond through Spin Bath Polarization". In: *Physical Review Letters* 101.4 (2008), p. 047601. DOI: `10.1103/PhysRevLett.101.047601`. arXiv: `0804.1537`.

[528] Yijun Tang et al. "Thermalization near Integrability in a Dipolar Quantum Newton's Cradle". In: *Physical Review X* 8.2 (2018), p. 021030. DOI: 10.1103/PhysRevX.8.021030.

[529] J.-P. Tetienne et al. "Magnetic-Field-Dependent Photodynamics of Single NV Defects in Diamond: An Application to Qualitative All-Optical Magnetic Imaging". In: *New Journal of Physics* 14.10 (2012), p. 103033. DOI: 10.1088/1367-2630/14/10/103033.

[530] Manisha Thakurathi et al. "Floquet Generation of Majorana End Modes and Topological Invariants". In: *Physical Review B* 88.15 (2013), p. 155133. DOI: 10.1103/PhysRevB.88.155133. arXiv: 1303.2300.

[531] James Theiler. "Estimating Fractal Dimension". In: *JOSA A* 7.6 (1990), pp. 1055–1073. DOI: 10.1364/JOSAA.7.001055.

[532] Hugo Théveniaut et al. "Transition to a Many-Body Localized Regime in a Two-Dimensional Disordered Quantum Dimer Model". In: *Physical Review Research* 2.3 (2020), p. 033154. DOI: 10.1103/PhysRevResearch.2.033154. arXiv: 1902.04091.

[533] Thimothée Thiery et al. "Many-Body Delocalization as a Quantum Avalanche". In: *Physical Review Letters* 121.14 (2018), p. 140601. DOI: 10.1103/PhysRevLett.121.140601. arXiv: 1706.09338.

[534] D. J. Thouless. "Exchange in Solid 3He and the Heisenberg Hamiltonian". In: *Proceedings of the Physical Society* 86.5 (1965), pp. 893–904. DOI: 10.1088/0370-1328/86/5/301.

[535] Paraj Titum et al. "The Anomalous Floquet-Anderson Insulator as a Non-Adiabatic Quantized Charge Pump". In: *Physical Review X* 6.2 (2016), p. 021013. DOI: 10.1103/PhysRevX.6.021013. arXiv: 1506.00650.

[536] A. L. Toom. "Nonergodic multidimensional automata systems". In: *Problemy Peredachi Informatsii* 10.3 (1974), pp. 70–79.

[537] Andrei L Toom. "Stable and Attractive Trajectories in Multicomponent Systems". In: *Multicomponent random systems* 6 (1980), pp. 549–575.

[538] Hugo Touchette. "A Basic Introduction to Large Deviations: Theory, Applications, Simulations". In: *arXiv* (2012). arXiv: 1106.4146.

[539] Minh C. Tran et al. "Hierarchy of Linear Light Cones with Long-Range Interactions". In: *Physical Review X* 10.3 (2020), p. 031009. DOI: 10.1103/PhysRevX.10.031009. arXiv: 2001.11509.

[540] Minh C. Tran et al. "Locality and Digital Quantum Simulation of Power-Law Interactions". In: *Physical Review X* 9.3 (2019), p. 031006. DOI: 10.1103/PhysRevX.9.031006. arXiv: 1808.05225.

[541] Minh C. Tran et al. "Locality and Heating in Periodically Driven, Power-law Interacting Systems". In: *Physical Review A* 100.5 (2019), p. 052103. DOI: 10.1103/PhysRevA.100.052103. arXiv: 1908.02773.

[542] Minh C. Tran et al. "Optimal State Transfer and Entanglement Generation in Power-law Interacting Systems". In: *Physical Review X* 11.3 (2021), p. 031016. DOI: 10.1103/PhysRevX.11.031016. arXiv: 2010.02930.

[543] K. Tucker et al. "Shattered Time: Can a Dissipative Time Crystal Survive Many-Body Correlations?" In: *New Journal of Physics* 20.12 (2018), p. 123003. DOI: 10.1088/1367-2630/aaf18b.

[544] Alexei M. Tyryshkin et al. "Electron Spin Coherence Exceeding Seconds in High Purity Silicon". In: *Nature Materials* 11.2 (2012), pp. 143–147. DOI: 10.1038/nmat3182. arXiv: 1105.3772.

[545] G. V. Uimin. "One-Dimensional Problem for S = 1 with Modified Antiferromagnetic Hamiltonian". In: *Soviet Journal of Experimental and Theoretical Physics Letters* 12 (1970), p. 225.

[546] Stanislaw Ulam. *Proceedings of the International Congress on Mathematics*. Vol. 2. 1952.

[547] Eric Van Oort and Max Glasbeek. "Optically Detected Low Field Electron Spin Echo Envelope Modulations of Fluorescent N-V Centers in Diamond". In: *Chemical Physics* 143.1 (1990), pp. 131–140. DOI: 10.1016/0301-0104(90)85013-M.

[548] Lieven M. K. Vandersypen and Isaac L. Chuang. "NMR Techniques for Quantum Control and Computation". In: *Reviews of Modern Physics* 76.4 (2005), pp. 1037–1069. DOI: 10.1103/RevModPhys.76.1037. arXiv: quant-ph/0404064.

[549] Matthieu Vanicat, Lenart Zadnik, and Tomaž Prosen. "Integrable Trotterization: Local Conservation Laws and Boundary Driving". In: *Physical Review Letters* 121.3 (2018), p. 030606. DOI: 10.1103/PhysRevLett.121.030606. arXiv: 1712.00431.

[550] S. R. Srinivasa Varadhan, S. R. Srinivasa Varadhan, and S. R. Srinivasa Varadhan. *Large Deviations and Applications*. Philadelphia - Pa: Society for industrial and applied mathematics, 1984.

[551] Romain Vasseur et al. "Particle-Hole Symmetry, Many-Body Localization, and Topological Edge Modes". In: *Physical Review B* 93.13 (2016), p. 134207. DOI: 10.1103/PhysRevB.93.134207. arXiv: 1510.04282.

[552] Jordan Venderley, Vedika Khemani, and Eun-Ah Kim. "Machine Learning Out-of-Equilibrium Phases of Matter". In: *Physical Review Letters* 120.25 (2018), p. 257204. DOI: 10.1103/PhysRevLett.120.257204. arXiv: 1711.00020.

[553] V. I. Vichirko and N. Yu. Reshetikhin. "Excitation Spectrum of the Anisotropic Generalization of an SU3 Magnet". In: *Theoretical and Mathematical Physics* 56.2 (1983), pp. 805–812. DOI: 10.1007/BF01016823.

[554] Lorenza Viola, Emanuel Knill, and Seth Lloyd. "Dynamical Decoupling of Open Quantum Systems". In: *Physical Review Letters* 82.12 (1999), pp. 2417–2421. DOI: 10.1103/PhysRevLett.82.2417. arXiv: quant-ph/9809071.

[555] C. W. von Keyserlingk, Vedika Khemani, and S. L. Sondhi. "Absolute Stability and Spatiotemporal Long-Range Order in Floquet Systems". In: *Physical Review B* 94.8 (2016), p. 085112. DOI: 10.1103/PhysRevB.94.085112. arXiv: 1605.00639.

[556] C. W. von Keyserlingk, Frank Pollmann, and Tibor Rakovszky. "Operator Backflow and the Classical Simulation of Quantum Transport". In: *arXiv* (2021). arXiv: 2111.09904.

[557] C. W. von Keyserlingk and S. L. Sondhi. "1D Many-body Localized Floquet Systems II: Symmetry-Broken Phases". In: *Physical Review B* 93.24 (2016), p. 245146. DOI: 10.1103/PhysRevB.93.245146. arXiv: 1602.06949.

[558] C. W. von Keyserlingk and S. L. Sondhi. "Phase Structure of 1d Interacting Floquet Systems I: Abelian SPTs". In: *Physical Review B* 93.24 (2016), p. 245145. DOI: 10.1103/PhysRevB.93.245145. arXiv: 1602.02157.

[559] J. von Neumann. "Proof of the Ergodic Theorem and the H-theorem in Quantum Mechanics". In: *The European Physical Journal H* 35.2 (2010), pp. 201–237. DOI: 10.1140/epjh/e2010-00008-5.

[560] Ronen Vosk, David A. Huse, and Ehud Altman. "Theory of the Many-Body Localization Transition in One Dimensional Systems". In: *Physical Review X* 5.3 (2015), p. 031032. DOI: 10.1103/PhysRevX.5.031032. arXiv: 1412.3117.

[561] Thorsten B. Wahl and Benjamin Béri. "Local Integrals of Motion for Topologically Ordered Many-Body Localized Systems". In: *Physical Review Research* 2.3 (2020), p. 033099. DOI: 10.1103/PhysRevResearch.2.033099. arXiv: 2001.03167.

[562] Y. H. Wang et al. "Observation of Floquet-Bloch States on the Surface of a Topological Insulator". In: *Science* 342.6157 (2013), pp. 453–457. DOI: 10.1126/science.1239834. arXiv: 1310.7563.

[563] Zhi-Hui Wang and Susumu Takahashi. "Spin Decoherence and Electron Spin Bath Noise of a Nitrogen-Vacancy Center in Diamond". In: *Physical Review B* 87.11 (2013), p. 115122. DOI: 10.1103/PhysRevB.87.115122. arXiv: 1209.3365.

[564] Zhi-Hui Wang et al. "Comparison of Dynamical Decoupling Protocols for a Nitrogen-Vacancy Center in Diamond". In: *Physical Review B* 85.15 (2012), p. 155204. DOI: 10.1103/PhysRevB.85.155204.

[565] Haruki Watanabe and Masaki Oshikawa. "Absence of Quantum Time Crystals". In: *Physical Review Letters* 114.25 (2015), p. 251603. DOI: 10.1103/PhysRevLett.114.251603. arXiv: 1410.2143.

[566] J. S. Waugh, L. M. Huber, and U. Haeberlen. "Approach to High-Resolution Nmr in Solids". In: *Physical Review Letters* 20.5 (1968), pp. 180–182. DOI: 10.1103/PhysRevLett.20.180.

[567] David Wei et al. "Quantum Gas Microscopy of Kardar-Parisi-Zhang Superdiffusion". In: *arXiv* (2021). arXiv: 2107.00038.

[568] Simon A. Weidinger and Michael Knap. "Floquet Prethermalization and Regimes of Heating in a Periodically Driven, Interacting Quantum System". In: *Scientific Reports* 7.1 (2017), p. 45382. DOI: 10.1038/srep45382. arXiv: 1609.09089.

[569] Felix Weiner et al. "High-Temperature Spin Dynamics in the Heisenberg Chain: Magnon Propagation and Emerging Kardar-Parisi-Zhang Scaling in the Zero-Magnetization Limit". In: *Physical Review B* 101.4 (2020), p. 045115. DOI: 10.1103/PhysRevB.101.045115. arXiv: 1908.11432.

[570] Christof Weitenberg et al. "Single-Spin Addressing in an Atomic Mott Insulator". In: *Nature* 471.7338 (2011), pp. 319–324. DOI: 10.1038/nature09827. arXiv: 1101.2076.

[571] Christopher David White et al. "Quantum Dynamics of Thermalizing Systems". In: *Physical Review B* 97.3 (2018), p. 035127. DOI: 10.1103/PhysRevB.97.035127. arXiv: 1707.01506.

[572] Frank Wilczek. "Quantum Time Crystals". In: *Physical Review Letters* 109.16 (2012), p. 160401. DOI: 10.1103/PhysRevLett.109.160401. arXiv: 1202.2539.

[573] J. T. Wilson et al. "Trapping Alkaline Earth Rydberg Atoms Optical Tweezer Arrays". In: *Physical Review Letters* 128.3 (2022), p. 033201. DOI: 10.1103/PhysRevLett.128.033201. arXiv: 1912.08754.

[574] Kenneth G. Wilson. "Renormalization Group and Critical Phenomena. I. Renormalization Group and the Kadanoff Scaling Picture". In: *Physical Review B* 4.9 (1971), pp. 3174–3183. DOI: 10.1103/PhysRevB.4.3174.

[575] Kenneth G. Wilson. "Renormalization Group and Critical Phenomena. II. Phase-Space Cell Analysis of Critical Behavior". In: *Physical Review B* 4.9 (1971), pp. 3184–3205. DOI: 10.1103/PhysRevB.4.3184.

[576] Kenneth G. Wilson. "The Renormalization Group: Critical Phenomena and the Kondo Problem". In: *Reviews of Modern Physics* 47.4 (1975), pp. 773–840. DOI: 10.1103/RevModPhys.47.773.

[577] W. M. Witzel, Rogerio de Sousa, and S. Das Sarma. "Quantum Theory of Spectral Diffusion Induced Electron Spin Decoherence". In: *Physical Review B* 72.16 (2005), p. 161306. DOI: 10.1103/PhysRevB.72.161306. arXiv: cond-mat/0501503.

[578] W. M. Witzel and S. Das Sarma. "Quantum Theory for Electron Spin Decoherence Induced by Nuclear Spin Dynamics in Semiconductor Quantum Computer Architectures: Spectral Diffusion of Localized Electron Spins in the Nuclear Solid-State Environment". In: *Physical Review B* 74.3 (2006), p. 035322. DOI: 10.1103/PhysRevB.74.035322. arXiv: cond-mat/0512323.

[579] Wayne M. Witzel et al. "Quantum Decoherence of the Central Spin in a Sparse System of Dipolar Coupled Spins". In: *Physical Review B* 86.3 (2012), p. 035452. DOI: 10.1103/PhysRevB.86.035452.

[580] Stephen Wolfram. "Statistical Mechanics of Cellular Automata". In: *Reviews of Modern Physics* 55.3 (1983), pp. 601–644. DOI: `10.1103/RevModPhys.55.601`.

[581] David H. Wolpert. "Stochastic Thermodynamics of Computation". In: *Journal of Physics A: Mathematical and Theoretical* 52.19 (2019), p. 193001. DOI: `10.1088/1751-8121/ab0850`. arXiv: `1905.05669`.

[582] Jonathan Wurtz and Anatoli Polkovnikov. "Quantum Hydrodynamics in Spin Chains with Phase Space Methods". In: *Physical Review E* 101.5 (2020), p. 052120. DOI: `10.1103/PhysRevE.101.052120`. arXiv: `1808.08977`.

[583] Jonathan Wurtz, Anatoli Polkovnikov, and Dries Sels. "Cluster Truncated Wigner Approximation in Strongly Interacting Systems". In: *Annals of Physics* 395 (2018), pp. 341–365. DOI: `10.1016/j.aop.2018.06.001`. arXiv: `1804.10217`.

[584] Robert E Wyatt. *Quantum Dynamics with Trajectories Introduction to Quantum Hydrodynamics*. New York, NY: Springer New York, 2010.

[585] Ryuta Yamamoto et al. "An Ytterbium Quantum Gas Microscope with Narrow-Line Laser Cooling". In: *New Journal of Physics* 18.2 (2016), p. 023016. DOI: `10.1088/1367-2630/18/2/023016`.

[586] Bo Yan et al. "Realizing a Lattice Spin Model with Polar Molecules". In: *Nature* 501.7468 (7468 2013), pp. 521–525. DOI: `10.1038/nature12483`. arXiv: `1305.5598`.

[587] N. Y. Yao et al. "A Quantum Dipolar Spin Liquid". In: *Nature Physics* 14.4 (4 2018), pp. 405–410. DOI: `10.1038/s41567-017-0030-7`.

[588] Norman Y. Yao, Chris R. Laumann, and Ashvin Vishwanath. "Many-Body Localization Protected Quantum State Transfer". In: *arXiv* (2015). arXiv: `1508.06995`.

[589] Norman Y. Yao et al. "Classical Discrete Time Crystals". In: *Nature Physics* 16.4 (4 2020), pp. 438–447. DOI: `10.1038/s41567-019-0782-3`. arXiv: `1801.02628`.

[590] Norman Y. Yao et al. "Discrete Time Crystals: Rigidity, Criticality, and Realizations". In: *Physical Review Letters* 118.3 (2017), p. 030401. DOI: `10.1103/PhysRevLett.118.030401`. arXiv: `1608.02589`.

[591] Norman Y. Yao et al. "Many-Body Localization with Dipoles". In: *Physical Review Letters* 113.24 (2014), p. 243002. DOI: `10.1103/PhysRevLett.113.243002`. arXiv: `1311.7151`.

[592] Bingtian Ye, Francisco Machado, and Norman Y. Yao. "Floquet Phases of Matter via Classical Prethermalization". In: *Physical Review Letters* 127.14 (2021), p. 140603. DOI: `10.1103/PhysRevLett.127.140603`. arXiv: `2104.13927`.

[593] Bingtian Ye et al. "Emergent Hydrodynamics in Non-Equilibrium Quantum Systems". In: *Physical Review Letters* 125.3 (2020), p. 030601. DOI: `10.1103/PhysRevLett.125.030601`. arXiv: `1902.01859`.

[594] Bingtian Ye et al. "Universal Kardar-Parisi-Zhang Dynamics in Integrable Quantum Systems". In: *arXiv* (2022). arXiv: `2205.02853`.

[595] Kei Yosida. "Magnetic Properties of Cu-Mn Alloys". In: *Physical Review* 106.5 (1957), pp. 893–898. DOI: `10.1103/PhysRev.106.893`.

[596] Wing Chi Yu et al. "Discrete Time Crystal in Globally Driven Interacting Quantum Systems without Disorder". In: *Physical Review A* 99.3 (2019), p. 033618. DOI: `10.1103/PhysRevA.99.033618`. arXiv: `1807.07738`.

[597] Michael P. Zaletel and Frank Pollmann. "Isometric Tensor Network States in Two Dimensions". In: *Physical Review Letters* 124.3 (2020), p. 037201. DOI: `10.1103/PhysRevLett.124.037201`. arXiv: `1902.05100`.

[598] Johannes Zeiher et al. "Coherent Many-Body Spin Dynamics in a Long-Range Interacting Ising Chain". In: *Physical Review X* 7.4 (2017), p. 041063. DOI: `10.1103/PhysRevX.7.041063`. arXiv: `1705.08372`.

[599] Johannes Zeiher et al. "Many-Body Interferometry of a Rydberg-dressed Spin Lattice". In: *Nature Physics* 12.12 (12 2016), pp. 1095–1099. DOI: `10.1038/nphys3835`.

[600] Tian-Sheng Zeng and D. N. Sheng. "Prethermal Time Crystals in a One-Dimensional Periodically Driven Floquet System". In: *Physical Review B* 96.9 (2017), p. 094202. DOI: `10.1103/PhysRevB.96.094202`. arXiv: `1707.00404`.

[601] J. Zhang et al. "Observation of a Discrete Time Crystal". In: *Nature* 543.7644 (2017), pp. 217–220. DOI: `10.1038/nature21413`. arXiv: `1609.08684`.

[602] Liangsheng Zhang, Vedika Khemani, and David A. Huse. "A Floquet Model for the Many-Body Localization Transition". In: *Physical Review B* 94.22 (2016), p. 224202. DOI: `10.1103/PhysRevB.94.224202`. arXiv: `1609.00390`.

[603] Liangsheng Zhang et al. "Many-Body Localization Phase Transition: A Simplified Strong-Randomness Approximate Renormalization Group". In: *Physical Review B* 93.22 (2016), p. 224201. DOI: `10.1103/PhysRevB.93.224201`. arXiv: `1603.02296`.

[604] Wurong Zhang and D. G. Cory. "First Direct Measurement of the Spin Diffusion Rate in a Homogenous Solid". In: *Physical Review Letters* 80.6 (1998), pp. 1324–1327. DOI: `10.1103/PhysRevLett.80.1324`.

[605] X. Zhang et al. "Spectroscopic Observation of SU(N)-Symmetric Interactions in Sr Orbital Magnetism". In: *Science* 345.6203 (2014), pp. 1467–1473. DOI: `10.1126/science.1254978`. arXiv: `1403.2964`.

[606] G. M. Zhidomirov and K. M. Salikhov. "Contribution to the Theory of Spectral Diffusion in Magnetically Diluted Solids". In: *Soviet Journal of Experimental and Theoretical Physics* 29 (1969), p. 1037.

[607] Manjin Zhong et al. "Optically Addressable Nuclear Spins in a Solid with a Six-Hour Coherence Time". In: *Nature* 517.7533 (7533 2015), pp. 177–180. DOI: `10.1038/nature14025`.

[608] Hengyun Zhou et al. "Quantum Metrology with Strongly Interacting Spin Systems". In: *Physical Review X* 10.3 (2020), p. 031003. DOI: `10.1103/PhysRevX.10.031003`. arXiv: `1907.10066`.

[609] Bihui Zhu et al. "Dicke Time Crystals in Driven-Dissipative Quantum Many-Body Systems". In: *New Journal of Physics* 21.7 (2019), p. 073028. DOI: `10.1088/1367-2630/ab2afe`.

[610] Quntao Zhuang et al. "An Absolutely Stable Open Time Crystal". In: *arXiv* (2021). arXiv: `2110.00585`.

[611] Marko Znidaric, Antonello Scardicchio, and Vipin Kerala Varma. "Diffusive and Sub-diffusive Spin Transport in the Ergodic Phase of a Many-Body Localizable System". In: *Physical Review Letters* 117.4 (2016), p. 040601. DOI: `10.1103/PhysRevLett.117.040601`. arXiv: `1604.08567`.

[612] Marko Žnidarič. "Spin Transport in a One-Dimensional Anisotropic Heisenberg Model". In: *Physical Review Letters* 106.22 (2011), p. 220601. DOI: `10.1103/PhysRevLett.106.220601`.

[613] Marko Žnidarič. "Transport in a One-Dimensional Isotropic Heisenberg Model at High Temperature". In: *Journal of Statistical Mechanics: Theory and Experiment* 2011.12 (2011), P12008. DOI: `10.1088/1742-5468/2011/12/P12008`.

[614] Haiyuan Zou, Erhai Zhao, and W. Vincent Liu. "Frustrated Magnetism of Dipolar Molecules on a Square Optical Lattice: Prediction of a Quantum Paramagnetic Ground State". In: *Physical Review Letters* 119.5 (2017), p. 050401. DOI: `10.1103/PhysRevLett.119.050401`. arXiv: `1702.08517`.

[615] Randolph S. Zounes and Richard H. Rand. "Subharmonic Resonance in the Non-Linear Mathieu Equation". In: *International Journal of Non-Linear Mechanics* 37.1 (2002), pp. 43–73. DOI: `10.1016/S0020-7462(00)00095-0`.

[616] C. Zu et al. "Emergent Hydrodynamics in a Strongly Interacting Dipolar Spin Ensemble". In: *Nature* 597.7874 (7874 2021), pp. 45–50. DOI: `10.1038/s41586-021-03763-1`.